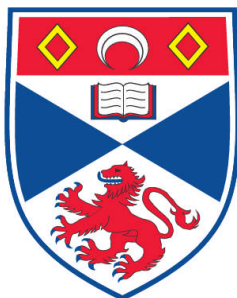


**THE IDENTIFICATION AND CHARACTERISATION OF THE
NORTH ATLANTIC HEINRICH EVENTS USING
ENVIRONMENTAL MAGNETIC TECHNIQUES**

Emilie R. Wadsworth

**A Thesis Submitted for the Degree of PhD
at the
University of St. Andrews**



2006

**Full metadata for this item is available in
Research@StAndrews:FullText
at:**

<http://research-repository.st-andrews.ac.uk/>

Please use this identifier to cite or link to this item:

<http://hdl.handle.net/10023/2782>

This item is protected by original copyright

**This item is licensed under a
Creative Commons License**

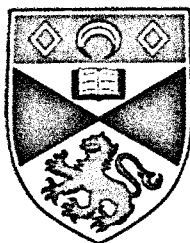
The Identification and Characterisation of the North Atlantic Heinrich Events using Environmental Magnetic Techniques

Emilie R Wadsworth

2005

A thesis submitted to the University of St Andrews for the
degree of Doctor of Philosophy

School of Geography & Geosciences,
University of St Andrews



Abstract

Heinrich Events (HEs) define intervals of major ice rafting from the Laurentide Ice Sheet (LIS) into the North Atlantic during that last glacial period. The discovery of potential European-sourced precursors to HEs suggests that the smaller, but climatically sensitive, European ice sheets (EIS) may have played a role in the triggering of HEs and their impact on global climates.

Environmental magnetism has proved itself to be a useful, rapid and non-destructive tool in the identification and quantification of provenance in sediments from numerous depositional environments. In this work, environmental magnetic analyses are applied to marine sediment records from the European margin of the NE Atlantic and known to contain ice-rafted debris (IRD) from both LIS and EIS sources. The primary aim of the work in this thesis is to evaluate the methodology as a means of distinguishing IRD provenance.

From the data obtained here it is possible to identify several magnetic events that correspond to the HEs and other layers of detrital material and which correlate well to previous standard petrological analyses performed on the same core materials. Magnetic signatures differ within the HEs, suggesting a changing balance of input from multiple sources as opposed to a single LIS source. The data suggest a phasing of these compositional differences through individual HEs. The potential of using environmental magnetic techniques in the identification of IRD provenance within marine sediments is discussed, as is the significance of the observed provenance variations within the cores studied.

Declarations

- i I, Emilie Rachel Wadsworth, hereby certify that this thesis, which is approximately 56000 words in length, has been written by me, that it is the record of work carried out by me and that it has not been submitted in any previous application for a higher degree.

Date 26/1/2006

Signature of Candidate



- ii I was admitted as a research student in September 2001 and as a candidate for the degree of PhD in September 2002; the higher study for which this is a record was carried out in the University St Andrews between 2001 and 2005.

Date 25/1/2006

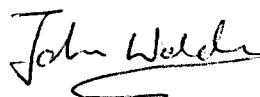
Signature of Candidate



- iii I hereby certify that the candidate has fulfilled the conditions of the Regulations and Resolutions appropriate for the degree of PhD in the University St Andrews and that the candidate is qualified to submit this thesis in application for that degree

Date 25-1-2006

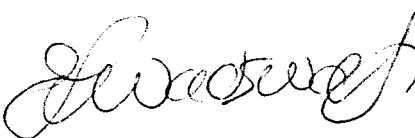
Signature of Supervisor



In submitting this thesis to the University of St Andrews, I understand that I am giving permission for it to be made available for use in accordance with the regulations of the University Library for the time being in force, subject to any copyright vested in the work not being affected thereby. I also understand that the title and abstract will be published, and that a copy of the work may be made and supplied to a *bona fide* library or research worker.

Date 26/1/2006

Signature of Candidate



Acknowledgements

Firstly, I would like to acknowledge the University of St Andrews, who part-funded the first year of this research project and have provided laboratory support throughout. I would also like to thank the Leverhulme Trust for funding the second two years of the research, enabling my progression onto a Ph.D program.

I would like to thank my supervisor, John Walden, for his hard work in conceiving, organising and implementing my project; for his efforts in procuring funding; for his constant faith in me; and for his encouragement, support and company throughout the last three years. I would also like to thank Dr Clare Peters for being an invaluable source of reference and knowledge of all things magnetic during the latter stages of my research. In addition, I would like to acknowledge Dr Bill Austin, Dr James Scourse and Dr Ian Hall for helping me with access to material and existing data, and for discussions on laboratory methods and data analysis; and Angus Calder for processing the XRD samples and help with interpretation. Vicky Peck and Sasha Leigh must also be acknowledged for their kind permission allowing me to include some of their data in the thesis. Many other people have contributed and helped me during my research, some of which are named in the relative sections of the thesis; the others, who know who they are, my thanks go to you all.

Finally, to Gavin, who has prevented this project from taking over my life; and Austin, who has provided a constant source of amusement – Cheers.

List of Contents

	Abstract	i
	Declarations	ii
	Acknowledgments	iii
	List of Contents	iv
	List of Figures	vii
	List of Tables	xv
1	Introduction	
	1.1 Project Rationale	1
	1.2 Environmental Magnetism	4
	1.3 Aims of the Project	7
	1.4 Structure of the Thesis	8
2	Literature Review	
	2.1 The Quaternary	10
	2.1.1 Evidence used for the Reconstruction of Past Climate Change	12
	2.1.2 Why is it so Important to Reconstruct Quaternary Environments	20
	2.2 Marine Sediments	21
	2.2.1 Methods of Analysis	22
	2.3 Heinrich Events	30
	2.3.1 Characteristics of Heinrich Events	31
	2.3.2 Potential Causes of Heinrich Events	35
	2.4 Current Issues Surrounding Heinrich Events	39
	2.4.1 External Forcing of Climate	40
	2.4.2 Internal Mechanisms for the Modification of Climate	41
	2.4.3 IRD Provenance	47
	2.4.4 Summary	56

2.5	Environmental Magnetism	58
2.5.1	Measurements used in Environmental Magnetism	59
2.5.2	Environmental Magnetism in Sediments	62
2.5.3	Mineral Identification	76
2.5.4	Provenance Studies with Environmental Magnetism	86
3	Site Context	91
3.1	The Ocean Margin EXchange Project	91
3.2	Core OMEX 2K	100
3.3	Core MD01-2461	107
4	Methods	114
4.1	Preliminary Analysis of OMEX 2K and MD01-2461	114
4.1.1	Core Physiology	114
4.1.2	Volume Susceptibility	115
4.2	Radiocarbon Dating and Chronology	121
4.2.1	Radiocarbon Dating	121
4.2.2	Chronology	124
4.2.3	Radiocarbon Dating and Chronology of OMEX 2K	131
4.3	Sample Preparation and Magnetic Analysis	135
4.3.1	Sample Preparation of OMEX 2K and MD01-2461	142
4.3.2	Magnetic Analysis of OMEX 2K and MD01-2461	144
4.4	Data Analysis	146
4.4.1	Correction for Carbonate	146
4.4.2	Magnetic Ratios	152
4.5	Statistics	152
4.5.1	Descriptive Statistics	152
4.5.2	Normality Tests	155
4.5.3	Tests of Variance	155

	4.5.4 Factor Analysis	156
5	Results and Discussion	158
	5.1 Chronology	158
	5.2 OMEX 2K: A Pilot Study	164
	5.2.1 Magnetic Analysis	166
	5.3 OMEX 2K: Environmental Interpretation	199
	5.3.1 The Heinrich Events	200
	5.3.2 Other aspects of OMEX 2K	207
	5.4 MD01-2461	210
	5.4.1 Chronology	210
	5.4.2 Magnetic Analysis	214
	5.4.3 Environmental Interpretation	232
	5.4.4 Comparison to OMEX 2K	240
	5.5 MD01-2461: H2 and H4	241
	5.5.1 H2 Magnetic Analysis	242
	5.5.2 Environmental Interpretation of H2	248
	5.5.3 Comparison to H2 in other cores	252
	5.5.4 H4 Magnetic Analysis	259
	5.5.5 Environmental Interpretation of H4	263
	5.5.6 Comparison to H4 in other cores	264
	5.6 Overview	272
6	Conclusions and Further Work	275
	References	277
	Appendices	325
	Appendix 1 – Biplots not referred to in the text	326
	Appendix 2 – Statistics	331

List of Figures

Figure No.	Title	Page No.
Fig. 1.1	The Characteristics of Heinrich Events	3
Fig. 1.2	The grouping of the Dansgaard-Oeschger cycles into Bond cycles, and the placing of the Heinrich Events	3
Fig. 1.3	The Thermohaline circulation and North Atlantic Deep Water circulation	6
Fig. 1.4	Location Map of the Celtic Margin and the cores OMEX 2K and MD01-2461	6
Fig. 2.1	The Oxygen Isotope record from the GRIP summit ice core	16
Fig. 2.2	Oxygen Isotope Ratios of surface water during times of glacial maxima and minima	16
Fig. 2.3	Photograph of Ice Rafted Debris from core OMEX 2K	28
Fig. 2.4	Examples of SEM images	28
Fig. 2.5	Map of the North Atlantic Ocean	32
Fig. 2.6	The Characteristics of Heinrich Events	33
Fig. 2.7	Magnetic Susceptibility records of four cores throughout the North Atlantic	33
Fig. 2.8	The grouping of the Dansgaard-Oeschger Cycles into Bond cycles, and the placing of the Heinrich Events	36
Fig. 2.9	Grey Level Reflectance of Heinrich Events compared to the GRIP ice core record	36
Fig. 2.10	The Astronomical Theory of Milankovitch	42
Fig. 2.11	The Internal mechanisms of climate control	42
Fig. 2.12	Map showing the global location of Heinrich-style events in the literature	45
Fig. 2.13	The Binge/Purge model proposed by Alley & MacAyeal (1994)	48

Fig. 2.14	Strontium-Neodymium analysis for Heinrich Event source areas	48
Fig. 2.15	SEM image of the nannoplankton <i>E. huxelyi</i> .	57
Fig. 2.16	Magnetic Susceptibility and pollen data for a core from the Lac du Bouchet, Central Massif, France	66
Fig. 2.17	Magnetic susceptibility record from two sites in the Chinese Loess Plateau showing the successive Loess-Palaeosol sequences	66
Fig. 2.18	The Natural Remanent Magnetisation of marine sediments compared to depositional and compositional factors	72
Fig. 2.19	Magnetic Analysis of marine sediments from the Equatorial Atlantic	72
Fig. 2.20	Magnetic Analysis of a marine core from the Portuguese Margin	74
Fig. 2.21	TEM images of the main Magnetotactic Bacterial Morphologies	79
Fig. 2.22	Lowrie-Fuller test results for magnetotactic bacteria	79
Fig. 2.23	Wohlforth-Cisowski test results for magnetotactic bacteria	79
	a) Normalised IRM acquisition and demagnetization	
	b) δ_{FC} versus δ_{ZFC}	
Fig. 2.24	Identification of magnetotactic bacteria using the graph of χ_{arm}/χ_{lf} versus χ_{arm}/χ_{fd}	80
Fig. 2.25	Acquisition curves and Saturation curves for Greigite	84
Fig. 2.26	The loss of magnetization on heating of Greigite	84
Fig. 2.27	Graph of χ versus SIRM for the identification of Greigite	85
Fig. 2.28	a) Graph of ARM ₄₀ /ARM versus SIRM/ χ	85
	b) Graph of ARM ₄₀ /ARM versus IRM ₁₀₀ /SIRM to determine the mineralogy of samples	

Fig. 2.29	SIRM/ARM versus χ_{fd} for various dust sets from Barbados, the North Atlantic and Japan	88
Fig. 3.1	Schematic of an ocean margin	93
Fig. 3.2	a) Map of the North Atlantic showing the location on the Celtic margin.	93
	b) Close-up of the Goban Spur and surrounding area	94
	c) Bathymetry of the Goban Spur	94
Fig. 3.3	Three-dimensional map of the Goban Spur bathymetry	96
Fig. 3.4	Location of the cores used in this study	97
Fig. 3.5	Diagram of the workings of a Kasten corer	99
Fig. 3.6	The mechanism of core shortening within gravity-dependent corers	99
Fig. 3.7	Sampling of a Kasten core	101
Fig. 3.8	X-radiographs of OMEX 2K	102
Fig. 3.9	Synthesis of existing data on OMEX 2K	103
Fig. 3.10	Mineralogical data on OMEX 2K	106
Fig. 3.11	The <i>Marion Dufresne</i> CALYPSO coring mechanism	108
Fig. 3.12	The workings of a piston corer	108
Fig. 3.13	Detailed schematic of a piston corer	109
Fig. 3.14	The process of sediment flow-in during the retrieval of a piston core	111
Fig. 3.15	Photographs showing bending of the laminae in a piston core due to friction, and the distortion of the laminae caused by, and evidence for, the process of sediment flow-in	111
Fig. 4.1	Descriptive core logs and photographs for OMEX 2K	116
Fig. 4.2	a) Photograph of the Philips PW1050/ Hiltonbrooks DG2	117

	XRD instrument	
	b) Photograph of the standard XRD sample holder	117
Fig. 4.3	Descriptive core logs and photographs for MD01-2461	119
Fig. 4.4	IRD record for MD01-2461 ($>150 \mu\text{m/g}$)	120
Fig. 4.5	Graph of the volume susceptibility for OMEX 2K measured in this study, and onboard ship during core retrieval.	120
Fig. 4.6	Correlation between the volume susceptibility measured in this study and that taken onboard ship during retrieval	123
Fig. 4.7	The Carbon Cycle	123
Fig. 4.8	a) Schematic of a Tandem Accelerator Mass Spectrometer b) Photograph of the ANTARES Tandem Accelerator Mass Spectrometer	126
Fig. 4.9	Graph showing the concentration of atmospheric ^{14}C since the thermonuclear weapons testing in the 1950s	126
Fig. 4.10	A Section of the INTCAL 98 calibration curve	128
Fig. 4.11	Example of a probability distribution for a radiocarbon date provided by the OxCal calibration program	128
Fig. 4.12	a) SEM images of the foraminifera <i>N. pachyderma</i> b) SEM images of the foraminifera <i>G. bulloides</i>	133
Fig. 4.13	OxCal probability distribution for the calibration of sample AA-53034 (60.5cm core depth)	134
Fig. 4.14	Photograph of the pots used for magnetic analysis	136
Fig. 4.15	Bartingtons Instruments Magnetic Susceptibility Meter (MS2) with the: a) MS2E volume susceptibility probe b) MS2B dual frequency sensor	136
Fig. 4.16	a) Screenshot from the Bartington Multisus Software v 2 showing the measurements of samples b) Screenshot from the Bartington Multisus Software v 2	137

	showing the drift test	
Fig. 4.17	Molspin a.f. demagnetiser with the: a) demagnetization attachment and b) steady biasing field generator used in imparting and ARM	140
Fig. 4.18	Molspin Pulse Magnetiser	140
Fig. 4.19	9 Tesla Pulse Magnetiser	140
Fig. 4.20	Molspin Minispin Magnetometer	140
Fig. 4.21	Graphs of percentage carbonate content and the parameters of magnetic susceptibility, χ_{arm} and SIRM before and after correction for carbonate content for OMEX 2K	148
Fig. 4.22	Correlation between the Carbonate content and Ca count data for MD01-2461	150
Fig. 4.23	Graphs of percentage carbonate content and the parameters of magnetic susceptibility, ARM and SIRM before and after correction for carbonate content for MD01-2461	151
Fig. 5.1	OxCal Multiplot for OMEX 2K Calibrated Ages	160
Fig. 5.2	a) Graph of Depth versus Age for OMEX 2K b) Graph of Age versus Depth for OMEX 2K	161
Fig. 5.3	a) Age Model for OMEX 2K b) Graph of the Sedimentation Rate along OMEX 2K	163
Fig. 5.4	Mineralogical Data for OMEX 2K taken from Scourse <i>et al.</i> , 2000.	167
Fig. 5.5	New Mineralogical Data for OMEX 2K	168
Fig. 5.6	Down-core magnetic properties of OMEX 2K	173
Fig. 5.7	Down-core magnetic properties of OMEX 2K by age	174

Fig. 5.8	Graph of Susceptibility, IRD and CaCO_3 for OMEX 2K	175
Fig. 5.9	Graph of magnetic properties that are common in the literature from the OMEX 2K data	176
Fig. 5.10	a) IRM acquisition ratios for OMEX 2K b) Demagnetisation ratios for OMEX 2K	182
Fig. 5.11	Graph of $\chi_{\text{arm}}/\chi_{\text{lf}}$ versus $\chi_{\text{arm}}/\chi_{\text{fd}}$ for the identification of magnetotactic bacteria in OMEX 2K	183
Fig. 5.12	Down-core record of ARM/SIRM for OMEX 2K	183
Fig. 5.13	Loss of magnetism over time for OMEX 2K	183
Fig. 5.14	Acquisition curves to 300 mT for OMEX 2K	186
Fig. 5.15	a) Down-core record of SIRM/ χ b) Down-core record of ARM ₋₄₀ /ARM	186
Fig. 5.16	a) Graph of ARM ₋₄₀ /ARM versus SIRM/ χ b) Graph of ARM ₋₄₀ /ARM versus IRM ₁₀₀ /SIRM for the identification of Greigite	187
Fig. 5.17	a) Biplot of χ_{lf} versus χ_{arm} b) Biplot of SIRM/ χ versus Soft IRM c) Biplot of χ_{lf} versus IRM ₋₁₀₀ /SIRM d) Biplot of χ_{arm}/χ versus Hard IRM	190 191
Fig. 5.18	Biplots from Bloemendal <i>et al.</i> , (1992): a) κ versus κ_{arm} , where $\kappa > 100$ and $\kappa_{\text{arm}} > 1000$ b) κ versus κ_{arm} , where $\kappa = 10-1000$ and $\kappa_{\text{arm}} = 100-10000$ c) κ versus κ_{arm} , where $\kappa < 200$ and $\kappa_{\text{arm}} < 1000$ d) $\kappa_{\text{arm}}/\kappa$ versus $S_{\text{(Bloemendal)}}$ – tightly grouped distribution e) $\kappa_{\text{arm}}/\kappa$ versus $S_{\text{(Bloemendal)}}$ – broadly spread distribution	194
Fig. 5.19	Biplots from Bloemendal <i>et al.</i> , (1992) for OMEX 2K a) κ versus κ_{arm} b) $\kappa_{\text{arm}}/\kappa$ versus $S_{\text{(Bloemendal)}}$	195
Fig. 5.20	a) κ versus κ_{arm} for the OMEX 2K temporal groups	195

	b) κ_{arm}/κ versus $S_{(Bloemendal)}$ for the OMEX 2K temporal groups	
Fig. 5.21	XRD trace for OMEX 2K	202
Fig. 5.22	Summary diagram for OMEX 2K data	206
Fig. 5.23	Factor Analysis for OMEX 2K	209
Fig. 5.24	Chronology for MD01-2461	211
Fig. 5.25	Age model for MD01-2461	213
Fig. 5.26	Graph of Susceptibility, IRD and $CaCO_3$ for MD01-2461	215
Fig. 5.27	Correlation between the susceptibility measured during this study and onboard ship for MD01-2461	216
Fig. 5.28	Down-core magnetic properties of MD01-2461	218
Fig. 5.29	Acquisition curves for MD01-2461	223
Fig. 5.30	a) Graph of χ_{arm}/χ_{lf} versus χ_{arm}/χ_{fd} for the identification of magnetotactic bacteria in MD01-2461 b) Down-core record of ARM/SIRM for MD01-2461	223
Fig. 5.31	a) Down-core record of SIRM/ χ b) Down-core record of ARM ₄₀ /ARM	224
Fig. 5.32	a) Graph of ARM ₄₀ /ARM versus SIRM/ χ b) Graph of ARM ₄₀ /ARM versus IRM ₁₀₀ /SIRM for the identification of greigite	224
Fig. 5.33	Biplots for MD01-2461	228-229
Fig. 5.34	Biplots from Bloemendal <i>et al.</i> , (1992) for MD01-2461 a) κ versus κ_{arm} b) κ_{arm}/κ versus $S_{(Bloemendal)}$	230
Fig. 5.35	a) κ versus κ_{arm} for the MD01-2461 temporal groups b) κ_{arm}/κ versus $S_{(Bloemendal)}$ for the MD01-2461 temporal groups	230
Fig. 5.36	Summary diagram for H2, H3, H4 and H5 from MD01-2461	237

Fig. 5.37	Factor Analysis for MD01-2461	238
Fig. 5.38	Down-core magnetic properties for the H2 section of MD01-2461	243
Fig. 5.39	Graph of χ_{arm}/χ versus $\chi_{\text{arm}}/\chi_{\text{fd}}$ for the identification of magnetotactic bacteria within the H2 section of MD01-2461	245
Fig. 5.40	a) Graph of ARM ₋₄₀ /ARM versus SIRM/ χ b) Graph of ARM ₋₄₀ /ARM versus IRM ₋₁₀₀ /SIRM for the identification of greigite	246
Fig. 5.41	Biplots for the H2 section of MD01-2461	249
Fig. 5.42	Down-core magnetic properties of the H2 section of MD95-2006	254
Fig. 5.43	a) Graph of $\chi_{\text{arm}}/\chi_{\text{lf}}$ versus $\chi_{\text{arm}}/\chi_{\text{fd}}$ for the identification of magnetotactic bacteria in MD95-2006 H2 b) Down-core record of ARM/SIRM for MD95-2006 H2	255
Fig. 5.44	a) Down-core record of SIRM/ χ b) Down-core record of ARM ₋₄₀ /ARM	255
Fig. 5.45	a) Graph of ARM ₋₄₀ /ARM versus SIRM/ χ b) Graph of ARM ₋₄₀ /ARM versus IRM ₋₁₀₀ /SIRM for the identification of greigite	256
Fig. 5.46	Biplots for the H2 section of MD95-2006	257
Fig. 5.47	Down-core magnetic properties of the H4 section of MD01-2461	260
Fig. 5.48	Biplots for the H4 section of MD01-2461	262
Fig. 5.49	Down-core magnetic properties of the H4 section of MD95-2006	265
Fig. 5.50	b) Graph of $\chi_{\text{arm}}/\chi_{\text{lf}}$ versus $\chi_{\text{arm}}/\chi_{\text{fd}}$ for the identification of magnetotactic bacteria in MD95-2006 H4 b) Down-core record of ARM/SIRM for MD95-2006 H4	267

Fig. 5.51	a) Down-core record of SIRM/ χ	267
	b) Down-core record of ARM ₋₄₀ /ARM	
Fig. 5.52	a) Graph of ARM ₋₄₀ /ARM versus SIRM/ χ	268
	b) Graph of ARM ₋₄₀ /ARM versus IRM ₋₁₀₀ /SIRM for the identification of greigite	
Fig. 5.53	Biplots for the H4 section of MD95-2006	269
Fig. 5.54	Factor Analysis for MD95-2006	271

List of Tables

Table No.	Title	Page No.
Table 2.1	The Quaternary Timescale	11
Table 2.2	Evidence for past climate change	14
Table 2.3	Dates of the six Heinrich Events	35
Table 2.4	Heinrich-style events identified across the globe	44
Table 2.5	Basic magnetic parameters	57
Table 3.1	The OMEX cores	97
Table 3.2	Sedimentation Rates for the OMEX cores	101
Table 4.1	The ^{14}C dates for OMEX 2K and their justifications	133
Table 4.2	Dates received from the NERC Radiocarbon Dating Facility in East Kilbride	134
Table 4.3	Procedure for imparting an ARM using the Molspin a.f. demagnetiser	139
Table 4.4	Procedure for demagnetising using the Molspin a.f. demagnetiser	139
Table 4.5	Procedure for imparting an IRM using the Molspin Pulse Magnetiser	143
Table 4.6	Procedure for imparting an IRM using the 9 Tesla Pulse Magnetiser	143
Table 4.7	Procedure for measuring magnetisations using the Molspin Minispin Magnetometer	143
Table 4.8	Samples from MD01-2461 selected for weight percentage carbonate analysis	150
Table 4.9	Table of Magnetic Ratios, including the ones used, and referred to in this study.	153

Table 5.1	Table of Calibrated Calendar Ages for OMEX 2K	160
Table 5.2	XRD samples chosen from OMEX 2K	169
Table 5.3	Magnetic Properties of some common minerals	170
Table 5.4	The Division of OMEX 2K into temporal groups	187
Table 5.5	Potential LIS and EIS samples from OMEX 2K and their magnetic/non-magnetic characteristics	202-203
Table 5.6	The Division of MD01-2461 into temporal groups	227
Table 5.7	Potential LIS and EIS samples from MD01-2461 and their magnetic characteristics	236
Table 5.8	Revised LIS and EIS samples from the H2 section of MD01-2461 and their magnetic characteristics	250
Table 5.9	Expanded list of LIS and EIS samples from the H4 section of MD01-2461 and their magnetic characteristics	251

1.0 Introduction

1.1 Project Rationale

The general concept of the ice rafting of sediment is now well established in the Quaternary/marine science research literature (e.g. Hemming 2004). Recently studies have shown that throughout the Pleistocene, great armadas of icebergs broke off from the pan-Atlantic ice sheets and drifted across the North Atlantic, slowly melting and releasing any sediments entrained within them (Heinrich, 1988; Bond *et al.*, 1992; Broecker *et al.*, 1993; Andrews *et al.*, 1993; van Kreveld *et al.*, 1996; Rasmussen *et al.*, 1997; Snoeckx *et al.*, 1999).

These “Heinrich Events” as they became known, are described as cold periods that exhibit significantly enhanced ice-rafting, occurring roughly every 7-10 thousand years (kyr) for a duration of approximately 1000 years (Heinrich, 1988; Bond *et al.*, 1993; Andrews, 2000). Heinrich Events (HEs) left a lasting impression in the sediments of the North Atlantic, in the form of Heinrich Layers (HLs)(Heinrich, 1988). These horizons are characterised by a high concentration of coarse lithic grains (Ice Rafted Debris - IRD); a decrease in foraminiferal abundance, with those foraminifera present being dominated by the species *N. pachyderma (sinistral.)*; light planktonic $\delta^{18}\text{O}$ values and an increased magnetic susceptibility (Fig. 1.1)(Bond *et al.*, 1992; Broecker *et al.*, 1992; Andrews *et al.*, 1993; van Kreveld *et al.*, 1996; Rasmussen *et al.*, 1997). Six distinct layers have been found throughout the Pleistocene so far (labelled H1-H6), plus the Younger Dryas IRD event, which some authors have called H0 (Andrews *et al.*, 1995).

The HEs form part of climatic cycles called Bond Cycles (Bond *et al.*, 1993, Broecker, 1994), which span on average 10 kyr. The climate gets progressively colder, until an abrupt warming returns the climate to its original state and ends a cycle. The HEs occur just prior to this warming (Fig. 1.2)(Bond *et al.*, 1993; Williams *et al.*, 1998). Further analysis has also associated HEs with low sea surface temperatures (SSTs) and sea surface salinities (SSSs), and a reduction

(and possible collapse) of oceanic circulation, notably reduced North Atlantic Deep Water (NADW) formation and the reduction of the global Thermohaline Circulation (THC)(Fig. 1.3)(Maslin *et al.*, 1995; Oppo & Lehman, 1995; Seidov & Maslin, 1999). Heinrich Events are suggestive of major, and possibly abrupt, climate changes on relatively short time-scales throughout the Pleistocene (Bond *et al.*, 1993; Bond & Lotti, 1995; Stoker, 1998). This has made the determination of their causes and mechanisms a significant component in understanding Quaternary climate change. Current competing hypotheses include external forcing, such as climate fluctuations or THC perturbations (Scourse *et al.*, 2000), and internal instability of the Laurentide Ice Sheet (LIS)(MacAyeal, 1993).

The association of Dansgaard-Oeschger cycles (D-O cycles; short 500-2000 year climate cycles found in the Greenland Ice Cores, GRIP and GISP2 (Dansgaard & Oeschger, 1989)) and Bond cycles with HEs (Fig. 1.2), implies a climatic connection, but whether HEs are the cause or effect of these climate variations has yet to be established (Stoker, 1998). Climate cooling would increase the growth of ice sheets, and therefore increase iceberg calving. In turn, this would inject fresh, polar water into the ocean, altering temperature and salinity and inducing a weakening of oceanic circulation (Manabe & Stouffer, 1995). Alternatively, THC perturbations will affect the transport of water temperatures and salinity around the oceans, which could induce the melting of icebergs, affecting albedo, evaporation rates and, therefore, climate (Briggs *et al.*, 1997).

The theory of internal ice sheet instability was proposed by MacAyeal (1993) and Alley & MacAyeal (1994), in the form of a binge/purge mechanism. They suggested that the basal sediments of the Hudson Bay and Strait periodically froze and thawed, creating a slipway for the ice, thereby enhancing ice rafting. The cause of this freezing and thawing was suggested as either geothermal heat, or a response to the pressure of the ice reacting to a critical mass reached every 7-10 kyr. Climate oscillations could also be caused by the accumulation and ablation of the LIS, as the strength and position of the northerly winds would be affected by the height of the ice sheet (Clark, 1994)(See Section 2.4).

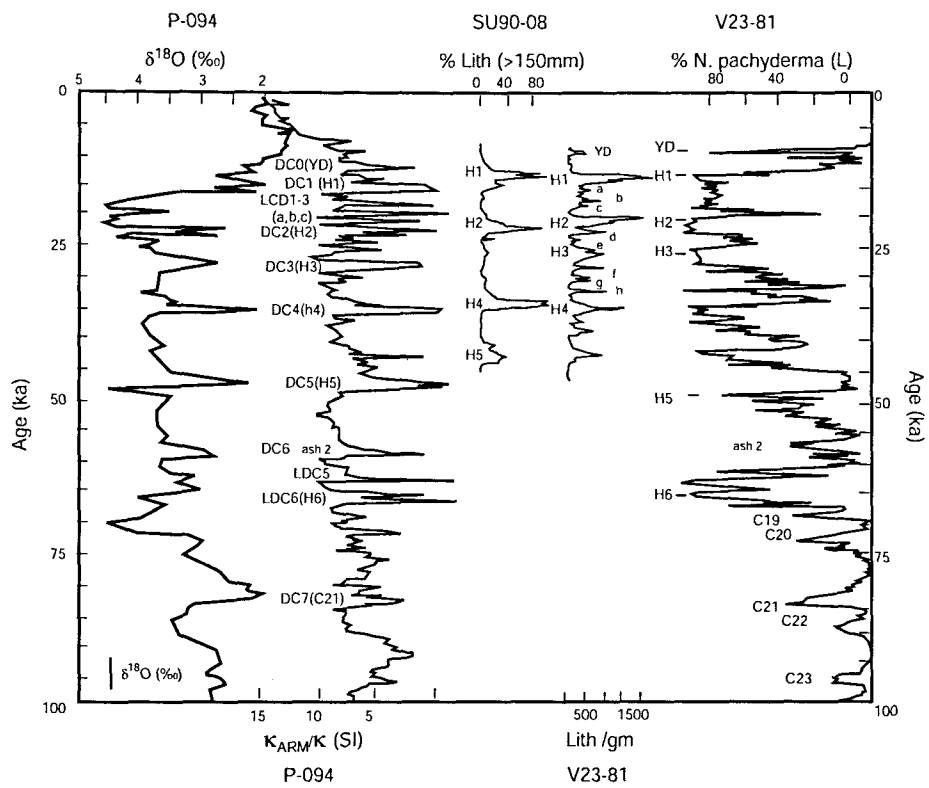


Fig. 1.1: The Characteristics of the North Atlantic Heinrich Events, including low oxygen isotope ($\delta^{18}\text{O}$) values, low $\kappa_{\text{ARM}}/\kappa$ values, high lithic grains counts and abundances, and high percentage of *N. pachyderma* (s)(Maher *et al.*, 1999).

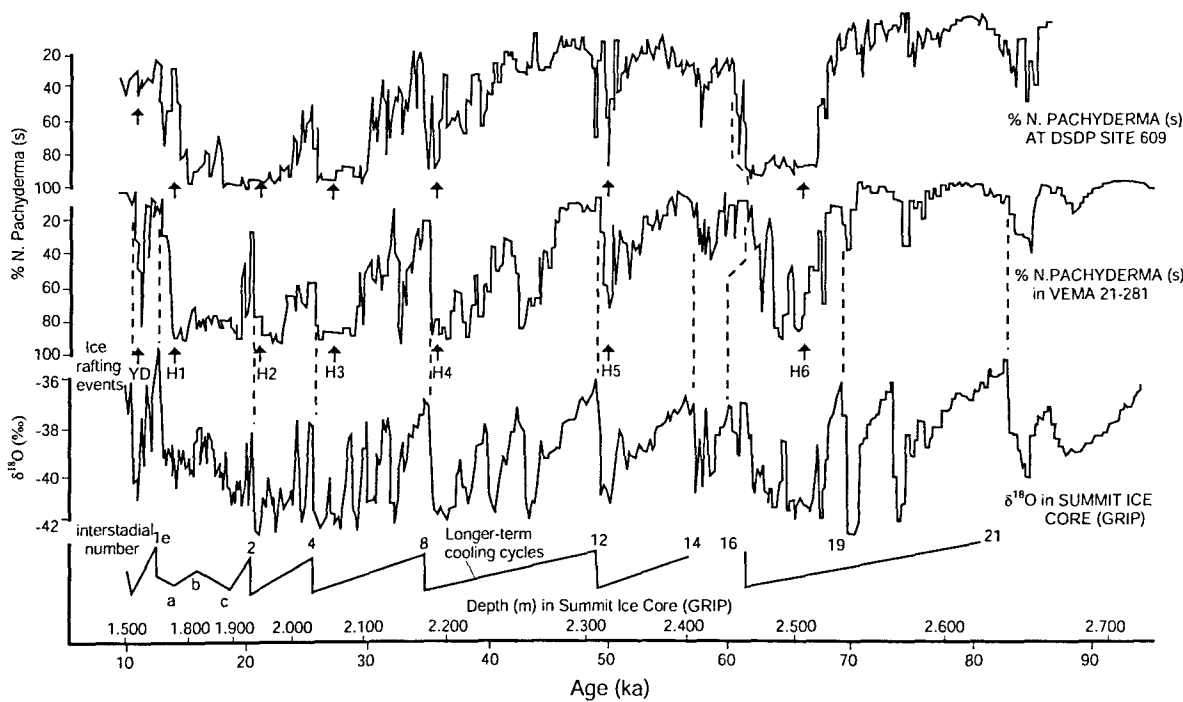


Fig. 1.2: Correlation between Foraminifera analysis of two marine cores and the GRIP ice core showing the D-O cycles, Heinrich Events and Bond cycles (the longer cooling cycles)(re-drawn from Bond *et al.*, 1993).

It has long been established that the LIS was the major contributor to the HEs, and much work has been done on cores from that side of the Atlantic (Broecker *et al.*, 1993; Andrews *et al.*, 1993; MacAyeal, 1993; Alley & MacAyeal, 1994). However, recent isotopic and mineralogical work on the sediment fine fraction has indicated a European/Nordic contribution (Hemming *et al.*, 1998; Snoeckx *et al.*, 1999). In 2000, whilst studying cores from the Celtic Margin, Scourse *et al.*, found what appeared to be a small IRD event approximately 1000 years prior to H2. It was comprised of chalk and therefore said to be of British origin. Scourse *et al.*, suggested that this may be a “precursor event” and attributed it to the response of the British Ice Sheet (BIS) to some hemispheric external force. As the BIS was a smaller ice sheet than the LIS, it would have responded to that force quicker. Also, being nearer to the Celtic Margin, BIS icebergs would have reached this area first. The temporal relationship between different inputs of material is, therefore, an important element in determining the ultimate cause of HEs.

Provenance is also a key issue in solving the mystery surrounding the cause of HEs. The identification of which ice sheets were involved, coupled with a reliable age-depth model could provide detailed information on the mechanisms at work before, after and during a HE. Current methods of research are often time consuming and must work in tandem with other data to provide the necessary information mentioned above. Therefore, a single technique with the ability to differentiate between source areas, and thereby look in detail at the phasing throughout a HE is greatly needed.

1.2 Environmental Magnetism

Environmental magnetic techniques provide a means of characterising the iron mineral types, concentrations and grain sizes within a rock, sediment or soil (Verosub & Roberts, 1995). As such, they can be used to provide a compositional signal (or ‘fingerprint’) that can be used in the same fashion as other compositional analyses such as X-ray Diffraction (XRD), heavy mineral counts or isotope analysis. However, in contrast to some other compositional

methods, environmental magnetic analyses are relatively quick and simple to use (Walden *et al.*, 1987; Oldfield, 1991). They are also inexpensive, very sensitive and non-destructive to the sample, so the material can subsequently be used for other analysis (Oldfield, 1991; Dekkers, 1997). To date, environmental magnetic methods have been used, with varying degrees of success, in several provenance studies (e.g. Begét & Hawkins, 1989; Yu & Oldfield, 1989; 1993). Provenance studies include identifying a material in terms of its lithological character, its formation processes, as well as determining the geographical source of the material and differentiating between transport mechanisms and pathways (Bloemendal *et al.*, 1992; Verosub & Roberts, 1995). Magnetic methods have been used to analyse the materials in a variety of sedimentary environments, such as lakes (Dearing & Flower, 1982), loess (Begét & Hawkins, 1989), and oceans (Bloemendal & de Menocal, 1989).

The main magnetic parameters: Susceptibility (χ), Anhysteretic Remanent Magnetism (ARM), Isothermal Remanent Magnetism (IRM) and Saturation Isothermal Remanent Magnetism (SIRM), along with various associated ratios (see Section 4.4 and Table 4.9) give detailed information on the mineral magnetic concentration, magnetic grain size and mineral type within a material. A mixture of these parameters can lead to a comprehensive characterisation of the material being analysed. Comparing these characters to other samples from different areas can help with the identification of provenance. Within a marine core spanning a relatively large timescale, it can be assumed that several different sources will provide material through a variety of transport mechanisms (Seibold & Berger, 1982; Briggs *et al.*, 1997). This can be postulated because of the known changes in climate, ocean circulation and ice sheet limits that took place during the Pleistocene (e.g. Dansgaard & Oeschger, 1989; Bond *et al.*, 1993; Alley & MacAyeal, 1994; Lambeck, 1995; Oppo & Lehman, 1995; Elliot *et al.*, 2002). Changes in magnetic properties down-core should reflect these changes in provenance, transport methods, and pathways (e.g. Bloemendal *et al.*, 1992; 1993), and therefore, the propensity exists to characterise each source or mechanism magnetically.

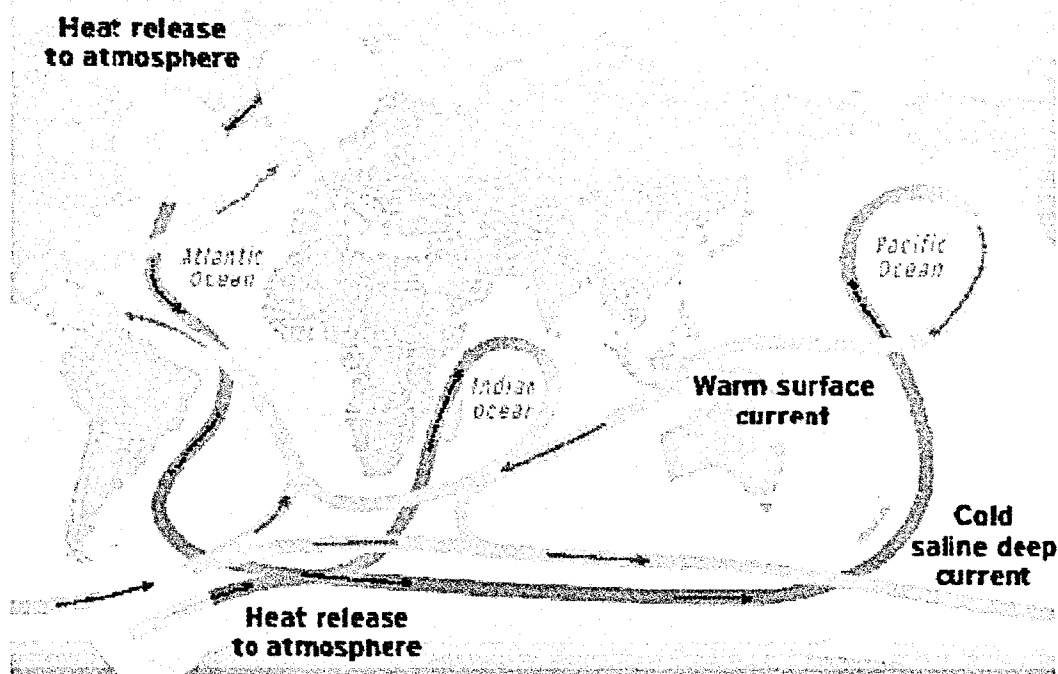


Fig. 1.3: The Thermohaline Circulation (THC), the main mechanism for moving heat and salinity around the global ocean. The North Atlantic Deep Water (NADW) is the blue section within the North Atlantic. It is formed by the sinking of water in the Nordic Sea as it releases its heat and travels southward to the Southern Ocean (<http://www.ucsusa.org>, 2004)

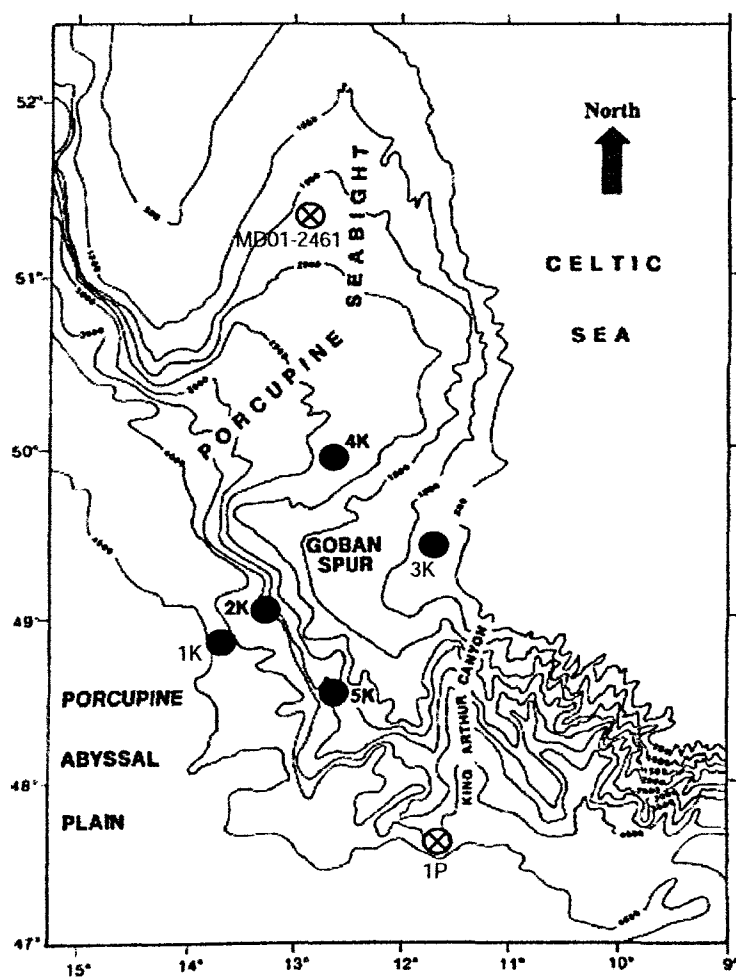


Fig. 1.4: Location of the OMEX cores and MD01-2461 (Hall & McCave, 1998a & b). Solid circles are kasten cores, crossed circles are piston cores.

1.3 Aims of the study.

Using sediments from a number of selected marine sediment cores, the aims of this study are primarily to:

- Evaluate the potential of using environmental magnetic techniques as a provenance tool in marine sediments;
- Characterise the HLs and inter-HL sediments in terms of magnetic grain type, size and concentration;
- Identify and explain the down-core variations in magnetic parameters;
- If possible, determine the provenance of the sediments, particularly those associated with the HLs.

Additionally, if the magnetic signature for each of the source areas identified above can be determined, it may be possible at some stage to attempt un-mixing of the HE signal into quantifiable concentrations from each source. Such information could make a useful contribution to the establishment of a causal mechanism for Heinrich Events that satisfies all the current criteria in terms of source areas, phasing and climatic and oceanographic effects, however, this is unlikely to be achieved during the timescale of this study.

These aims are going to be addressed by using high resolution, basic magnetic measurements of susceptibility (χ), Isothermal Remanent Magnetism (IRM), Saturation Isothermal Remanent Magnetism (SIRM), and Anhysteretic Remanent Magnetism (ARM) and associated ratios (Table 4.9) on two marine cores taken from the Celtic Margin (Fig. 1.4). The first one is a 245 cm Kasten core (OMEX 2K, 40°5.29N, 13°25.9W, Fig. 1.4), which contains a record of the last 30 kyr, including H1 and H2. OMEX 2K is used as a pilot study for the methods, to assess their potential for addressing the aims laid out above, before the acquisition of a longer core. This second core, MD01-2461 (51°45'N, 12°55'W, Fig. 1.4) is a 2226 cm Piston core, which reaches back into the last interglacial period (>125 kyr BP). An improved age model for OMEX 2K will be developed through the

addition of 7 new ^{14}C dates to the ones previously obtained by Scourse *et al.*, (2000). Extensive petrological data is also available for OMEX 2K, with simple IRD counts in place for MD01-2461. Certain samples may also be subjected to more advanced magnetic analysis using a Vibrating Sample Magnetometer (VSM), and a Superconducting Quantum Interference Device (SQUID). These instruments enable more detailed information about the magnetic minerals present in a material to be extracted by performing full hysteresis loops, low, and high temperature measurements. For further information on these, see Lees & Dearing, 1999 and Evans & Heller, 2003.

1.4 Structure of the Thesis

Chapter 2 provides a basic background to climate change research, and the rationale of using marine sediments. Two sections will explore the phenomenon of Heinrich Events and detail the current issues surrounding them, as well as some of the other ongoing research attempting to answer the questions posed by HEs. The final section introduces the subject of Environmental Magnetism, how it came about as a technique, the methods involved and what it has the potential to achieve. It also looks at some of the many studies from all aspects of environmental science to have used these methods.

Chapter 3 is a short introduction to the site context. It details the purpose of the Ocean Margin EXchange (OMEX) project, which retrieved one of the cores used in this study; the methods of obtaining deep-sea cores; and discusses the previous analysis performed on the OMEX 2K core. MD01-2461 is also described, and the previous analysis discussed, however, as this is a recent core, much of the non-magnetic analysis is still ongoing.

Chapter 4 is concerned with the methods used in this study. It outlines the processes used for core logging, IRD counting and XRD, along with two detailed sections on Radiocarbon dating and its application to this work. The next two sections explain the environmental magnetic measurements used, the

instrumentation involved, and the subsequent data analysis. Finally, a brief introduction to some of the basic statistical methods used is included.

The results and discussion are provided in Chapter 5. Here, the age-depth model for OMEX 2K is discussed, as is the basis for a chronology for MD01-2461. A comprehensive study of the magnetic characters of the sediments is explained here, and they are interpreted in terms of their provenance and transport mechanisms. A comparison of the two cores, and other North Atlantic material are provided, followed by an overview of all the findings discussed above.

The sixth, and final chapter contains the principle findings of this study, and outlines further work identified during the project. Appendices on page 325 contain additional biplots drawn for both the cores, to show the interactions of various parameters (Appendix 1) and the raw statistics performed on all cores and subsections (Appendix 2).

2.0 Literature Review

2.1 The Quaternary

The Quaternary is in the latest period of the Earth's history (the Cainozoic era) and it spans approximately the last 2 million years (ma)(Williams *et al.*, 1998; Maher *et al.*, 1999). It comprises of the Holocene (10 kyr BP – present) and the Pleistocene (~ 2 ma BP – 10 kyr BP). Some 2.4 ma BP, major ice sheets began to form over most of North America and Europe. By the onset of the Pleistocene, much of the Northern Hemisphere was experiencing glacial conditions (Table 2.1)(Ahnert, 1996; Briggs *et al.*, 1997). Within the Pleistocene, as many as 50 glacial – interglacial cycles are thought to have taken place, with some authors record the Holocene as an interglacial itself; and therefore an extension of the Pleistocene (Lowe & Walker, 1997; Maher *et al.*, 1999).

The climate changes of the Quaternary have left their imprint on terrestrial landforms, sediment sequences and floral and faunal remains, for example in tree rings, peat bogs, foraminifera shells and corals etc. The analysis of these can give valuable insights into the extent of Quaternary environment instability (Lowe & Walker, 1997; Stauffer, 1999). The use of proxy records contained in stable isotopes and nuclides, such as ^{18}O , ^{14}C , ^{10}Be , and ^{26}Al etc are also helpful in assessing past climates, as once incorporated into the climate system, their behaviour is very predictable (Lal, 2004). For example, oxygen isotope ratios from marine sediment records are good indicators of sea surface temperature and salinity (Wefer *et al.*, 1999).

The study of Quaternary environments is necessary because it can help in our understanding of climate and improves our ability to make predictions of future climate change (Maher *et al.*, 1999). Given the major implications that climatic conditions, and changes to those conditions, have on both natural and human systems, this predictive ability is seen as of increasing importance at both national and international levels of government.

Table 2.1: The Quaternary Timescale (Ahnert, 1996)

Years Before Present	North Germany	Alps	United Kingdom	North America
-10 000		Beginning of the Holocene		
	Weichsel	Wurm	Devensian	Wisconsin
-70 000		(Glacial)		
	Eem-	Riss/Wurm	Ipswichian	Sangamon
-120 000		(Interglacial)		
	Saale	Riss	Wolstonian	Illinoian
-180 000		(Glacial)		
	Holstein	Mindel/Riss	Hoxnian	Yarmouth
-260 000		(Interglacial)		
	Elster	Mindel	Anglian	Kansan
-420 000		(Glacial)		
	Cromer	Gunz/Mindel	Cromerian	Aftonian
-820 000		(Interglacial)		
		(Glacial)	Beestonian	
		(Interglacial)	Pastonian	
	Menap	Gunz	Baventian	Nebraskan
-1.2 million		(Glacial)		
	Waal	Donau/Gunz	Antian	Unknown
-1.4 million		(Warm period)		
	Eburon	Donau	Waltonian	Unknown
-1.7 million		(Cold period)		
	Tegelen	Biber/Donau		Unknown
-2.2 million		(Warm period)		
	Bruggen	Biber		Unknown
-2.4 million		(Cold period)		

2.1.1 Evidence used for the reconstruction of past climatic change

Lowe and Walker (1997) classify the evidence used to evaluate past climatic changes into broadly geomorphological, lithological and biological types (although overlap does exist between each type) and a brief introduction to the nature of these evidence types will now be presented. Table 2.2 provides an extensive list of the types of evidence for climate changes, some of which will be discussed below.

One of the major influences on the geomorphology of a landscape, particularly a non- or post-volcanic one, is the movement of ice. The growth and retreat of continental ice sheets is a major response to climate change and may also influence climate in a complex fashion. Therefore the presence of typical glacial landform features, such as corries, U-shaped valleys and moraines are indicative of the extent of ice coverage (Broecker, 1995; Lowe & Walker, 1997).

The ice coverage throughout the Quaternary glaciations has been mapped principally by identifying the positions of terminal moraines, outwash deltas and meltwater channels using remote sensing, aerial photography and satellite imagery. Advances in dating techniques, particularly that of thermoluminescence dating, has helped identify the chronology of these glacial – interglacial cycles (Lowe & Walker, 1997). The systematic mapping of glacial extent in North America began c.1860 and was mainly based on the recognition of terminal moraines. It soon spread to Europe and Asia, and by 1894, maps had been compiled showing the worldwide distribution of ice during the most recent glacial stage (Table 2.2) (Lowe & Walker, 1997). Terminal moraines, outwash deltas, and meltwater channels mark the maximum position of ice, recessional moraines indicate periods of stability in advances and retreats, and frost shattering can show the upper altitude limit of ice sheets and/or glaciers (Briggs *et al.*, 1997; Lowe & Walker, 1997).

Certain periglacial landforms, such as rock glaciers (active, lobate accumulations of rock debris); pingos (dome-shaped hills created by uplift from an ice body below the ground); and protalus ramparts (a ridge of debris that has been expelled from a snow-filled niche) have evolved in present-day arctic/alpine regions. The identification of comparable relic features means that the climatic conditions of that time can be approximated (Lowe & Walker, 1997).

Sea-level changes can also be suggestive of past climates (Broecker, 1995), and are identifiable by features such as raised beaches and former coastal features standing above present sea-level, as well as off shore submerged landforms, e.g. caves, coral reefs and river valleys. Data from marine sediments, both lithological and biological (e.g. microfossil abundance, type of sediment, grain size), can provide a more detailed picture of sea-level by inferring the oceanic conditions at various times (Lowe & Walker, 1997; Williams *et al.*, 1998).

Low-latitude features also provide evidence of changing climates away from the dramatic influence of glaciation. Features such as pluvial lakes, fluvial landforms (e.g. relic drainage channels and alluvial channels) and dunefields reflect changes in prevailing climatic conditions. Expanded pluvial lakes and dry river channels suggest that there were once wetter conditions than today (e.g. Ancient Lake Bonneville, Utah; the Sahel, West Africa), whereas sand dunes standing where they couldn't form in today's climate suggests former periods of aridity (e.g. the Southern fringe of the Sahara Desert; the Northern fringe of the Kalahari Desert)(Lowe & Walker, 1997).

Geomorphology can give an indication of large-scale environmental conditions associated with glaciation, but the examination of sediment sequences can give particulars about small-scale climate changes and, importantly, the chronological order in which they occurred. This can be helpful in identifying what processes were at work and how they affected the environment (Lowe & Walker, 1997).

Table 2.2: Evidence for, and methods used to assess past climate change (compiled from Broecker, 1995; Briggs *et al.*, 1997; Lowe & Walker, 1997; Williams *et al.*, 1998; Benn & Evans, 1998).

Type of Evidence	Specific tools/methods	Examples
Geomorphological	Glacial Landforms	Extent of ice cover and ice sheets. Direction of ice movement. Palaeotemperature estimates using comparisons to present-day features and climates
	Periglacial Landforms	Palaeoclimatic inferences using comparisons to present-day features. e.g. Rock glaciers, protalus ramparts, pingos
	Sea Level	Relative and absolute sea level changes Eustatic changes
	River Terraces	Relic terraces show periods of wetter and probably warmer climates
	Low Latitude Landforms	Pluvial lakes and Fluvial landforms show wetter periods. Dunefields show drier periods
Lithological	Glacial Sediments	Rate of melting, ice thickness, glacier topography and ice extent inferred from particle size and shape, type of deposit, level of stratification, erratics etc.
	Periglacial Sediments	Mean annual air temperatures are specific for some structures e.g. Ice wedges
	Palaeosols	Relic soils that have formed under different conditions to those present today. Comparisons to present-day soils with similar characteristics
	Loess/Windblown Deposits	Loess deposits occur during cold, dry phases, with warmer periods encouraging soil formation Wind direction reconstructed from grain size and mineral composition of loess
	Deep-Sea/Lacustrine Sediments	Types of deposits represent types of sediment transport. e.g. IRD = ice rafting, which can only occur during cold periods. Foraminiferal oozes suggest warmer, higher productivity times. The fossils themselves have information on the prevailing conditions (see below & Section 2.2.1)
	Cave Sediments/Speleothems	Mineral deposits of CaCO_3 , deposition rates slow during cold stages and increase during warm
	Ice Cores	Annual layering of ice, contains information on atmospheric dust content, chemical composition and stable isotopes e.g. $\delta^{18}\text{O}$ = temperature, salinity, ice volume and therefore sea level
Biological	Pollen Analysis	Reconstruction of vegetation history and land use
	Diatoms	Hold information on the pH, oxygen content, mineral concentration, temperature and salinity of water
	Fossils	Palaeoclimatic inferences using comparisons to present-day species e.g. Chronimids, ostracods, bivalves, plants, and also large animal remains
	Foraminifera	Species abundance suggests general water conditions. Isotopes (e.g. $\delta^{18}\text{O}$, ^{13}C etc.) give more information on temperature, salinity, productivity and oceanic circulation patterns

Lacustrine and marine sediments are especially useful, as they are relatively undisturbed. The evidence held within them can give details about water temperatures and salinity which are associated with ice cover, atmospheric conditions and ocean circulation patterns (De Dekker, 1997). Loess records provide a means to test the reconstruction of palaeo-winds, as well as general glacial - interglacial changes (Muhs *et al.*, 2003).

Ice cores provide the most detailed records of atmospheric parameters at high resolution during the Quaternary (Augustin *et al.*, 2004). They store information which includes local temperatures and precipitation, moisture conditions and wind strength, as well as aerosol fluxes of marine, volcanic and terrestrial origin, solar activity levels and changes in atmospheric gas compositions (Petit *et al.*, 1999; Stauffer, 1999; Augustin *et al.*, 2004). For example, the GRIP and GISP2 cores have given valuable insight to the climatic conditions over Greenland by the analysis of gases trapped within the ice layers (GRIP members, 1993). Shackleton (1963) developed the $^{18}\text{O}/^{16}\text{O}$ ratio ($\delta^{18}\text{O}$) as a proxy for continental ice volume, which was subsequently used to identify glacial-interglacial cycles within the ice cores, and marine carbonate records (Fig. 2.1). When used by Dansgaard & Oeschger (1989) on the two Greenland Ice Cores, warm-cold cycles of 500 – 2000 years (subsequently named Dansgaard-Oeschger, or D-O cycles) were noticed throughout the last glacial stage. These were also recognised by Johnsen *et al.*, (1992) in the GRIP core, and by the GRIP members (1993) in the GISP2 core. Dansgaard *et al.*, (1993) picked up the same signal spanning into the last interglacial (~250 kyr BP) in the GRIP core and a core from Vostok, East Antarctica.

A second core was taken at Vostok in 1998, and was subsequently used to identify and analyse the past four glacial cycles in terms of temperature, dust content, marine input (sodium concentrations), ice volume ($\delta^{18}\text{O}$) and the concentration of the atmospheric gases CO_2 and CH_4 (Stauffer, 1999; Petit *et al.*, 1999). The results are still being interpreted.

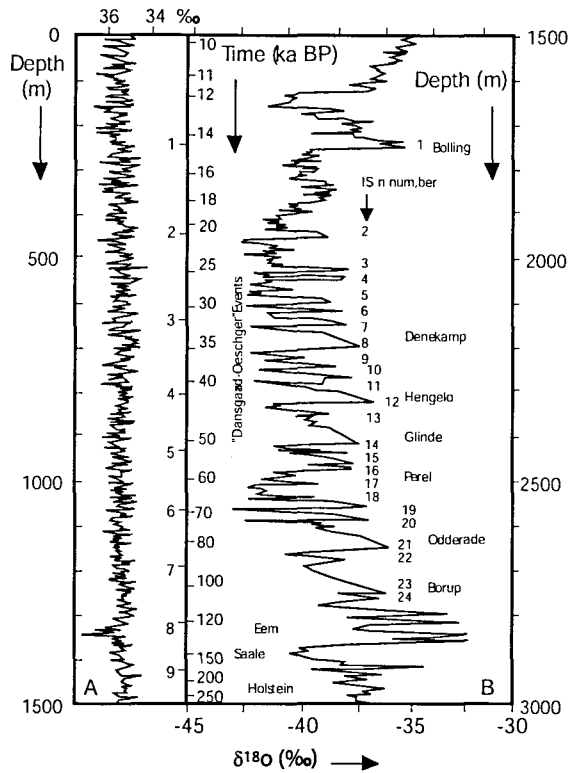


Fig. 2.1: The GRIP ice core Oxygen Isotope record. On the left is the Holocene and the right, the Pleistocene. The numbers are the glacial interstadials with the peaks representing the Dansgaard-Oeschger cycles (re-drawn from Williams *et al.*, 1998).

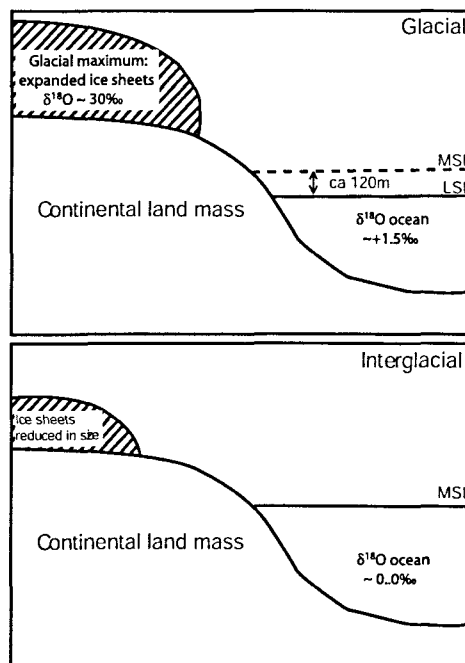


Fig. 2.2: The impact of glacial and interglacial stages on the oxygen isotope composition of sea water (Lowe & Walker, 1997).

The D-O cycles mentioned above were also noted within the four major cycles at Vostok (Petit *et al.*, 1999), suggesting that these variations occurred on a global scale. This record is currently being extended back to approximately 820 kyr BP by the analysis of a new Antarctic core, EDC2 (Augustin *et al.*, 2004).

A wide range of proxies have been used to extract environmental information from ice cores and marine/lacustrine sediments. These methods include:

- Particle size and shape analysis, which helps determine transport and deposition mechanisms (King & Buckley, 1968).
- Organic content is particularly useful in lacustrine sediment analysis where it can indicate past productivity (Lowe & Walker, 1997)
- Metallic element measurements and sediment properties are also useful in the study of lakes and oceans. The concentration of ions such as Calcium, Potassium, Sodium and Magnesium can be indicators of the erosional history of a catchment area (Mackereth, 1965; 1966). Ratios of elements such as Mg/Ca and Ca/Fe are good estimates of sea surface temperatures and climatic variations (Wefer *et al.*, 1999).
- Clay mineralogy can provide information on the origins and chemical changes such as erosion that have taken place. It is particularly useful in the analysis of glacial diamicts (Willman *et al.*, 1963; 1966).
- Stable isotope measurements are usually used as a proxy for temperature (Williams *et al.*, 1998; Lal, 2004) and have been used to great effect on the Greenland ice cores as mentioned above (Dansgaard & Oeschger, 1989; Johnsen *et al.*, 1992; GRIP members, 1993).
- Magnetic analysis identifies changes in the composition, concentration and grain size of the magnetic minerals present in sediments. These changes reflect lithological variations and can be interpreted as changes in the origin, transport mechanism and pathway of the sediments, as well as post-depositional processes which affect them. They are usually climatically influenced (Stoner *et al.*, 1996; Maher *et al.*, 1999).
- Microfossil assemblages are suggestive of climatic state, as many species are temperature and salinity specific and are unable to tolerate changes

(Williams *et al.*, 1998; Wefer *et al.*, 1999), therefore the quantitative assessment of assemblages can give general temperature estimates (Wefer *et al.*, 1999).

Both in a terrestrial and lacustrine/marine context, fossils and other flora and faunal remains can suggest environmental conditions such as temperatures and rainfall through time. In using such evidence for climatic and environmental reconstruction, the Principle of Uniformitarianism has to be applied – that is, it has to be assumed that, if they still exist, the species of plants and animals lived in similar conditions in the past as those in which they are found today (Lowe & Walker, 1997).

Pollen analysis is one of the most successful and widely used biological techniques. Individual pollen grains are selected and identified from within a sediment sequence, and a profile of the vegetation can be built up (Williams *et al.*, 1998). Direct temperature estimates can also be made (mean January and July temperatures) as well as quantitative climate estimates (Walker, 2001). Pollen dispersal is a problem that must be taken into consideration however, as pollen grains can travel by wind, water or animals and birds (Williams *et al.*, 1998), which can make it difficult to evaluate whether the pollen assemblage represents either a local or regional pollen source. However, recent studies of current pollen transport have helped to lessen the problem by identifying factors that are involved in pollen transport, deposition and subsequent incarceration, and analysing the influences on the pollen grains. It is suggested that, in general, wind blown pollen does not travel very far in comparison to other redistribution methods (Lowe & Walker, 1997), and pollination by animals is considered much more efficient (Williams *et al.*, 1998), therefore, the majority of pollen reaching a site should be local and be dispersed by water and wind (Lowe & Walker, 1997). Further difficulties are created by differential pollen production between plant species (that is, proportions of pollen may not equate to proportions of plant coverage) and this also needs to be accounted for when using pollen data to reconstruct past vegetation communities (Lowe & Walker, 1997).

A wide range of other biological methods are used as indicators of climatic and environmental change. The key ones include:

- The study of diatoms. Different species of diatoms are very sensitive to different levels of pH, oxygen content, mineral concentration, temperature and salinity (Williams *et al.*, 1998). Changes in any of these will have a major effect on the composition and structure of the diatom community, therefore environmental changes will be recorded in diatom fossils
- Fossil remains can include a variety of biological materials (e.g. plants, insects or molluscs). Coleopteran beetle fossils are the most widely used, due to their abundance and robustness, ensuring that their remains are easily identifiable (Lowe & Walker, 1997). An important factor governing Coleopteran distribution is climate, particularly temperature, and they respond quickly to climatic changes making them excellent proxies (Broecker, 1995; Walker, 2001). Due to relative evolutionary stability they are also likely to have lived in similar conditions to today (Coope, 1997).
- Chironomids (midges) are also strongly influenced by summer lake surface temperatures in arctic and alpine environments, and they react rapidly to changes in these environments. Studies of modern - day assemblages and their July temperature tolerance has helped to create a “data-base” of summer temperature estimates during the late glacial (Walker, 2001).
- Foraminiferal analysis is restricted to marine environments, but in a similar way to diatoms, they are extremely sensitive to temperature and salinity. They also record ^{18}O and ^{16}O compositions within their skeletons (Lowe & Walker, 1997; Williams *et al.*, 1998).
- Large animal remains are generally the least used, due to the infrequency of finds. Simple identification can lead to inferences regarding climate (Lowe & Walker, 1997).

2.1.2 Why is it so important to reconstruct Quaternary environments?

The theory that the present is the key to the past (the Principle of Uniformitarianism) is now generally accepted (Lowe & Walker, 1997), and it has also been argued that the past is also the key to the future (Briggs *et al.*, 1997; Maher *et al.*, 1999). By developing our understanding of the processes and causes of past climatic and environmental change, models of future changes can be developed (both conceptual and mathematical). In turn, modelling various responses of the biosphere, hydrosphere and cryosphere to climatic changes, can not only provide information about former environments, but also help predict what may happen if a similar climate change were to take place again. The modelling process can also take into account the additional effect of human activity, if such a climate flux should take place, or our probability of inducing it (Williams *et al.*, 1998).

Reconstructing specific Quaternary environments could provide information on human evolution, and our effect on the success or demise of other plant and animal species. It could also help in the structure of management strategies for soil erosion, floods, droughts, coastal erosion and conservation etc. (Williams *et al.*, 1998).

Before c.1988, Milankovitch's Astronomical Theory was thought of as the dominant mechanism for climate change, until evidence of shorter, less constant changes were found (e.g. Fillon & Duplessy, 1980; Heinrich, 1988; Bond *et al.*, 1993; GRIP members, 1993). The evidence for rapid climate change has grown significantly during recent years, and there has been a subsequent change of focus from orbital frequency fluctuations (20, 40 and 100 ka), to "abrupt" frequencies i.e. <10 ka. Causal mechanisms for these abrupt changes and the influence of the atmosphere, ice sheets, and the oceans are the subjects of most current interest in the literature. These abrupt changes will be discussed in further detail in Sections 2.3 and 2.4.

2.2 Marine Sediments

Marine sediments have two main constituents; terrigenous detritus (derived from land by erosion) and biogenic detritus (mainly skeletal remains of microfossils) (Seibold & Berger, 1982; Dawson, 1992; Cortijo *et al.*, 1995). The biogenic material can be sub-divided into a series of oozes (King, 1974), and the terrigenous section into grain sizes (Seibold & Berger, 1982). For example, Atlantic sediments are mainly made up from *Globigerina* ooze (a predominately planktonic foraminifera based material) and terrigenous material deposited by turbidity currents and ice rafting (King, 1974).

The terrigenous component of marine sediments can be deposited on the ocean floor by a number of methods; river input redistributed by turbidity currents and bottom currents (Seibold & Berger, 1982); wind, particularly that associated with monsoons; and melt-out from icebergs or sea ice (Lowe & Walker, 1997). During glacial periods, ice would have been the principal agent transporting sediment into the main ocean basins, though the lowering of sea levels would have caused rivers and outwash streams to run down continental shelves taking large quantities of unconsolidated sediment with them, this would have been limited to continental margins and not affect deep sea environments (Lowe & Walker, 1997). In water-transported materials, assuming similar particle densities, larger grained particles fall out of suspension first, and so tend to accumulate nearer the coast. In ice-rafted debris (IRD), this principle does not apply and, as a consequence, IRD is often identified within deep-sea sediment cores because of the presence of larger particle sizes, typically coarser than the silt and/or clay dominated non-IRD sediment found in an off-shore marine setting (Ruddiman, 1977; Seibold & Berger, 1982).

Many deep-sea cores provide long, continuous records that span much of the Cainozoic era, and they have good global coverage (Williams *et al.*, 1998). They are also a relatively undisturbed sequence as the ocean is primarily a depositional environment with little erosion or redistribution of sediment taking place (Dawson,

1992; Lowe & Walker, 1997). Marine sediments are, therefore, excellent uninterrupted records of oceanic conditions during the Quaternary (Seibold & Berger, 1982).

2.2.1 Methods of Analysis

Some of the most detailed evidence of environmental change in the oceans is found in the chemical and isotope content of the marine organisms within the sediments, particularly useful are the ratios of oxygen isotopes (^{16}O and ^{18}O)(Lowe & Walker, 1997). The presence of various species of foraminifera can indicate general temperature variations (Section 2.1.1), but isotopic analyses from their shells, particularly the $\text{O}^{16}:\text{O}^{18}$ ratio, can be used to determine temperature estimates (King, 1974; Wefer *et al.*, 1999). A brief introduction to the most significant forms of analysis is provided below as this provides an essential context for the work presented in this thesis.

Oxygen isotopes

Oxygen exists naturally in three forms: ^{18}O , ^{17}O , and ^{16}O . The ratio of $^{18}\text{O}:\text{}^{16}\text{O}$ ($\delta^{18}\text{O}$) is used in oxygen isotope analysis because of the way the isotopes behave within the climate system (Lowe & Walker, 1997). Water (H_2^{16}O) molecules in surface waters will evaporate more readily than the heavier H_2^{18}O molecules, resulting in the ocean surface becoming relatively enriched in H_2^{18}O i.e. it is isotopically heavier and will yield more positive $\delta^{18}\text{O}$ values (Lowe & Walker, 1997; Williams *et al.*, 1998). As evaporation is temperature dependent and warmer atmospheric temperatures are able to absorb heavier molecules, the relative enrichment of H_2^{18}O can be used as a climatic indicator; the more enriched the water, the cooler the climate (Lowe & Walker, 1997). During glacial times, large quantities of the evaporated H_2^{16}O is trapped in glaciers and ice sheets, leaving the ice relatively depleted in, and the oceans enriched in, H_2^{18}O (~1.5‰ is an accepted value for glacial marine sediments)(Fig. 2.2). This is reversed during interglacials, when glaciers and ice sheets undergo melting. Values of 0‰ are found during times of minimum global ice cover (Lowe & Walker, 1997).

Inferences of past sea-level can also be drawn from oceanic $\delta^{18}\text{O}$ records; more ice (higher $\delta^{18}\text{O}$) means a lower global sea-level (Shackleton, 1987).

The $\delta^{18}\text{O}$ composition of sea water over time can be reconstructed using the shells of marine foraminifera from sediment cores (Williams *et al.*, 1998). Foraminifera are typically small, unicellular organisms that build a carbonate shell around themselves; these shells therefore record the $\delta^{18}\text{O}$ value of the sea water at that time. The $\delta^{18}\text{O}$ record of fossilised organisms found in sediment cores can reveal detailed information on the temperature, salinity and sea-level of the ocean at that particular time (see above)(Dawson, 1992; Williams *et al.*, 1998; Wefer *et al.*, 1999). As described above, isotopically heavier (more positive $\delta^{18}\text{O}$ values) suggest colder phases and lowered sea-level, whilst isotopically lighter (less positive, or more negative $\delta^{18}\text{O}$ values) suggest warmer periods with higher sea-levels. This applies to both planktonic (surface dwelling), and benthic (bottom dwelling) organisms (Lowe & Walker, 1997; Williams *et al.*, 1998).

In recent years, several authors have looked closer at the oxygen isotope technique and used it, sometimes in conjunction with other methods, to recreate climatic and ocean conditions at various points throughout the Quaternary. Oppo *et al.*, (1998) used the technique to identify ocean cooling cycles of approximately 6 kyr duration throughout Marine Isotope Stages 10-13 (500 kyr – 340 kyr BP). McManus *et al.*, (1999) used benthic oxygen isotope values from sub-polar marine sediments to trace climate changes over a 500 kyr period. They determined that temperatures fluctuated both within glacials as well as between glacials and interglacials, and that ice sheets reached a critical size and collapsed when the benthic $\delta^{18}\text{O}$ value reached 3.5‰. Benthic $\delta^{18}\text{O}$ values are seen as representative of global ice cover, as well as deep ocean temperature (Shackleton, 1987), so it is therefore possible that the 3.5‰ threshold indicates a certain level of ice cover in a certain location; the advection of sea ice; or the growth of an ice sheet to a specific height or shape. McManus *et al.*, (1999) state emphatically that whatever the extent of glaciation at this value, it constitutes a major, and persistent, threshold. van Kreveld *et al.*, (2000) used oxygen isotopes

to calculate sea temperatures in the Irminger Basin (S. Iceland) between 60 kyr – 18 kyr BP, and then combined them with estimates of global ice volume to determine approximate ocean salinity values. They found that salinity records varied with temperature records, indicating that an influx of cold, fresh water was the cause of the variations. Shackleton *et al.*, (2000) correlated the benthic oxygen isotope record from an Iberian (South of Portugal) core to the Greenland ice cores, and suggested that fluctuations in ice volume indicated by the marine core were also the cause of the atmospheric temperature shifts in Greenland. Oxygen isotope records of the GRIP and GISP2 ice cores from Greenland are so detailed that they have also been used as a chronostratigraphical tool (Fig. 2.1)(Lal, 2004).

Carbon Isotopes

Carbon isotopes are also taken up by foraminifera, with shell $^{13}\text{C}:^{12}\text{C}$ ratios reflecting biological and environmental controls on isotopic fractionation (Mulitza *et al.*, 1999; Wefer *et al.*, 1999). Stable carbon isotopes ratios are a good estimate of sea surface fertility and nutrient availability, as well as temperature indicators (Lowe & Walker, 1997; Mulitza *et al.*, 1999). The fractionation of carbon isotopes between the ocean and atmosphere is temperature dependent as it is controlled by CO_2 exchange; the utilisation and removal of carbon in solids; and the re-supply of dissolved carbon from subsurface water, all of which in turn are controlled by temperature. Lower temperatures mean greater fractionation, and therefore higher $\delta^{13}\text{C}$ ratios (Mulitza *et al.*, 1999; Wefer *et al.*, 1999). Stable carbon isotope data from planktonic species can provide information on the productivity of an area, as it is influenced by carbon utilisation (more productivity, increased utilisation); benthic species records also show ventilation changes (i.e. vertical ocean circulation)(Lowe & Walker, 1997; Williams *et al.*, 1998). Ventilation is the process that takes oxygenated water to the deep ocean, therefore during times of reduced circulation, $\delta^{13}\text{C}$ will also decrease (Raymo *et al.*, 1990; Wefer *et al.*, 1999).

Microfossil Assemblages

Species of marine benthic and planktonic foraminifera have proved to be invaluable in climate reconstruction and global correlations (Lowe & Walker, 1997) because relatively few species of foraminifera exist, and it has been possible to define their respective biogeographical boundaries (Williams *et al.*, 1998) with quantitative counting of species leading to temperature and salinity estimates (Wefer *et al.*, 1999). Reference sets have also been created to provide a tool for comparisons to known climatic conditions (Wefer *et al.*, 1999). Many types of planktonic foraminifera grow their shell chambers in different directions (called coiling), depending on the surrounding temperature. For example, *Neoglobobulimina pachyderma* coils to the left (sinistral) in temperatures below 9°C and to the right (dextral) in temperatures above 9°C (Williams *et al.*, 1998; Bauch *et al.*, 2003). The coiling behaviour of foraminifera was utilised by Ruddiman & McIntyre (1976) and Kellogg (1976) to reconstruct the migration of the Polar Front for the last 150 kyr. Temperature data from cores around the Nordic Seas and the current position of the Polar Front were analysed. Four climatic regimes with varying polar front positions were recorded, mapping its evolution over the last glacial-interglacial cycle.

Sediment Analysis

Particle size analysis is routinely performed on marine sediments. Grain size data is generally used for reconstructing the velocity of oceanic currents, particularly in the 10-63 µm size range, which is also termed the sortable silt fraction (Hall & McCave, 1998a; Hall *et al.*, 1998). The mean particle size in this range reflects the prevailing current regime, as size will increase with increased current strength (Hall & McCave, 1998a; Gröger *et al.*, 2003). Cold periods in the North Atlantic are characterised by slower currents and an increase in clay percentage (particle size <2 µm), as well as overall accumulation. Warm periods consist of faster currents, lower deposition and silt domination (Hall & McCave, 2000; Gröger *et al.*, 2003). Grain alignment and the trajectory of the deposits can also be used to reconstruct the direction of the currents (Williams *et al.*, 1998; Hall & McCave, 1998a; Hall *et al.*, 1998).

Lithological and petrological analysis can help to identify the types and provenance of material, and thereby give inferences into the transport mechanisms and origin of the sediment (e.g. Scourse *et al.*, 2000). See Section 2.4.3 for further discussion.

In the context of the research contained in the thesis, the presence of ice rafted debris (IRD), which often introduces a distinct particle size assemblage to the 'normal', water transported sediment, is of particular interest. IRD is defined as particles or clasts of terrigenous origin deposited in a lacustrine or glacial marine environment by either icebergs, sea ice or lake ice (Fig. 2.3)(Section 2.3)(Wilson & Austin, 2001; Hemming *et al.*, 2002). While IRD can be found in low concentrations throughout many marine sediment cores, within the North Atlantic marine sediments, IRD is often concentrated into distinct layers, termed Heinrich Layers (Section 2.3). The presence of IRD was first noted by Bramlette & Bradley (1941), but there was not a full and comprehensive examination until Conolly & Ewing (1965), who observed a distinct change in sediment composition and concentration with geographical distribution. Unlike most marine and fluvial environments, there is no relationship between the grain size of the IRD and transport velocity (Lowe & Walker, 1997). Usually, the larger the grain size, the stronger and quicker the transport mechanism, as these particles will fall out of suspension first. IRD, however, is entrained within an iceberg, and therefore the melting of the ice will release particles of all sizes represented within the icebergs sediment load. Given the manner in which sediments are entrained within a glacier (from both sub-glacial and supra-glacial sources), this may include a wide range of particle sizes

Compositional Analysis.

A variety of techniques are now routinely available that can achieve a detailed analysis of the mineralogical and elemental composition of marine sediments. Optical mineralogy is the most basic of these, and involves the identification by eye (usually via a standard petrological microscope) of the different lithologies within a particular grain size range. This can reveal information on the types of

minerals present (and hence their potential provenance) and their relative abundance (e.g. Scourse *et al.*, 2000). The percentage of certain types of lithic grains can be used as very specific petrologic tracers, e.g. volcanic grains from Iceland (Bond *et al.*, 1997).

Electron Microscopy was developed in the 1930s (Goodhew, 1975) and provides higher magnification than a standard light microscope. Instead of shining a light onto the object to enhance the image, directed rays of electrons are rastered over the object. The interaction between the electrons in the beam and the specimen (the scattering) yields information which is used to build a monograph (or photograph) of the specimen (e.g. Fig 2.4)(Goodhew, 1975; van der Biest & Thomas, 1976). Transmission Electron Microscopy (TEM) improved the resolution of the image from c.300 nm in optical microscopes, to 15 nm (Heywood, 1971), enabling quick and easy identification of minerals. Scanning Electron Microscopy (SEM) has more recently bridged the gap between optical and TEM with an average resolution of 50 nm. SEM uses a scanning beam of electrons to give a life-like three-dimensional image of the specimen (Heywood, 1971; Hearle, 1972), so despite its lower resolution it is often preferred to TEM. Due to the high resolution nature of TEM and SEM, they are also able to provide information on particle chemistry and fabric structures, making these methods excellent compositional tools (e.g. Bell & Walker, 2000; Vaniman *et al.*, 2002). TEM and SEM have been used in a variety of studies, including the identification of minerals (Channell & Hawthorne, 1990; Thouveny *et al.*, 1994), grain sizes, shapes and surface morphologies (Kirschvink & Chang, 1984; Stockhausen & Zolitschka, 1999; Snowball & Torii, 1999), the characterisation of bacterial magnetite (Vali *et al.*, 1987; Towe & Moench, 1981), lithogenic and petrologic identification (Calanchi *et al.*, 1998) and micropaleontology (Karega, 1995; Findlay & Giraudeau, 2000).

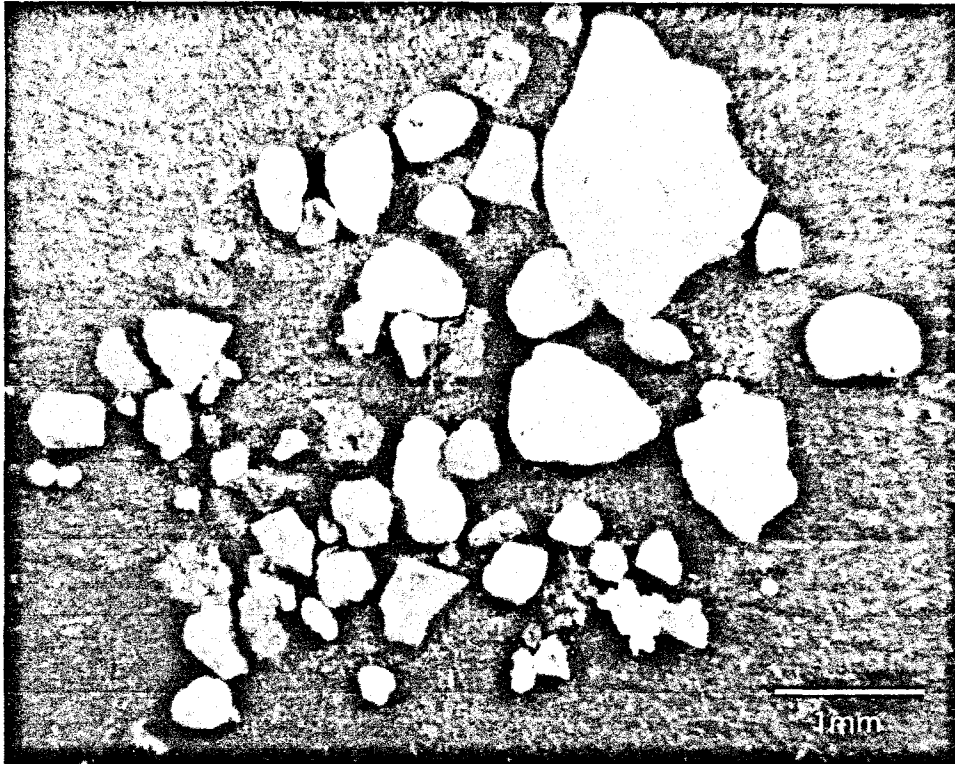


Fig. 2.3: Photograph of Ice-Rafted Debris from core OMEX 2K.

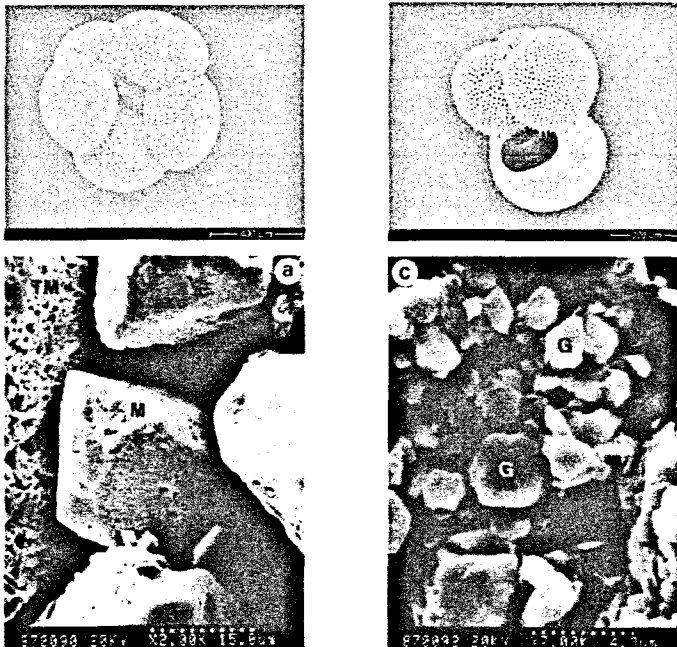


Fig 2.4: Examples of SEM images; a) a variety of the foraminifera *N. pachyderma* (image courtesy of Dr. A. Cage); b) *G. bulloides* (image courtesy of Dr. A. Cage); c) an octahedral magnetite (M) grain with a large etched titanomagnetite (TM) grain to it's left (taken from Horng *et al.*, 1998); d) fine-grained greigite (G) particles (taken from Horng *et al.*, 1998).

X-ray techniques, such as fluorescence (XRF) and diffraction (XRD), can identify and quantify the minerals present in a bulk sample (XRD)(Hardy & Tucker, 1988), and the elemental structure of that sample (XRF)(Fairchild *et al.*, 1988), whilst still being relatively non-destructive (some sample preparation may be required, depending on the environment)(Stallard *et al.*, 1995). XRF utilises the characteristic X-rays that are emitted by atoms when hit with an external radiation source, such as an x-ray beam (Williams, 1987; Stallard *et al.*, 1995; Jansen *et al.*, 1998). X-ray diffraction monitors the scattering of electrons that are hit with the beam whilst the sample is rotating at a regular speed (Hardy & Tucker, 1988), as this is dependent on mineralogy (Norrish & Chappell, 1967; Lowe & Walker, 1997). Many studies have taken advantage of the relatively easy to use methods of XRD and XRF (e.g. Cranfield & Berner, 1987; Hilton, 1990; Kris *et al.*, 1990; Stallard *et al.*, 1995; Roberts, 1995; Valkovic & Bogdanoic, 1996; Kirtay *et al.*, 1998; Jansen *et al.*, 1998; Rendle *et al.*, 2002; Moros *et al.*, 2004).

Mineral magnetic analysis provides another compositional tool and, in appropriate circumstances, can be used as an alternative to the methods described above. The method has received some attention from marine sedimentologists and magnetic susceptibility is now routinely performed on marine sediment cores with whole core traces being taken on board ship soon after recovery. The identification of magnetic minerals, their grain size and concentration can be used to infer terrigenous particle flux, bioproductivity, past oceanic and atmospheric circulation patterns and climates as these processes can all be reflected in the provenance and transport mechanisms of the sediment (Kissel *et al.*, 1999; Frederichs *et al.*, 1999). The use of magnetic analysis within the marine environment will be further discussed in Section 2.5.2.

2.3 Heinrich Layers

In 1988, in what is now regarded as something of a milestone paper in Quaternary Science, Heinrich reported analyses from 13 piston cores from the North Atlantic. Within each of these cores, he observed six distinct peaks of coarse lithic grains within the top few meters (Marine Isotope Stage 5 and upward). Planktonic foraminifera samples from 3 representative cores (Me69-17, Me69-19 and M01-32, see Fig 2.5) demonstrated a match between the lithic grain and the polar foraminifera records, and an inverse relationship between the temperate foraminifera and lithic grain record. Heinrich interpreted these layers as evidence of enhanced ice rafting controlled by cyclic changes in the Earth's axis occurring every 11000 ± 1000 years, regardless of glacial state. He went on to suggest that the Little Ice Age (c. 1500 – 1900 AD) was also a result of ice-rafting, but as it occurred during an interglacial period there were insufficient icebergs to leave a signal in the marine environment.

Bond *et al.*, (1997) added to the above argument by identifying periods of ice rafting on a 1470 year cycle throughout the Holocene, using the concentration of lithic grains within sediment cores. They were supported by Bianchi & McCave (1999) who, also using grain-size analysis, were able to determine fluctuations in Iceland-Scotland Overflow Water (ISOW) with a periodicity of 1500 years during the Holocene. Some of these were correlated to known climatic events, such as the Little Ice Age.

Heinrich Events have subsequently become the focus of many researchers' attention, and are the subject of a considerable body of literature. Some aspects of Heinrich Events are discussed in the following sections, however recent reviews by Andrews (1998; 2000); and an extensive publication by Hemming (2004), are cited for more detailed information.

2.3.1 Characteristics of Heinrich Events

The layers containing higher concentrations of coarse lithic grains have subsequently become known as “Heinrich Layers” (Bond *et al.*, 1992, Broecker *et al.*, 1992). Continued research by various workers (Bond *et al.*, 1992; Broecker *et al.*, 1992; Broecker *et al.*, 1993; Andrews *et al.*, 1993; van Kreveld, *et al.*, 1996; Rasmussen *et al.*, 1997; Hemming *et al.*, 2002; Fig. 2.5), have demonstrated that these Heinrich Layers have very distinct characteristics (Fig. 2.6). First, they have a high lithic grain concentration, assumed to be the result of increased ice-rafting. Second, they record a decrease in foraminiferal abundance, indicating a drop in marine productivity, or dilution due to increased sedimentation. Third, the foraminifera that are in evidence are dominated by *N. pachyderma*, suggesting a polar environment. Fourth, they show an increase in detrital carbonate deposits which, based upon detailed provenance work by Broecker *et al.*, (1992) and Bond *et al.*, (1993), have been used to indicate that the Laurentide Ice Sheet (LIS) was the major supplier of IRD. Finally, Heinrich Layers display light $\delta^{18}\text{O}$ values from planktonic foraminifera, which are interpreted as a lowering of SSTs and SSSs due to the melting of icebergs.

The six most obvious layers first identified by Heinrich (1988) have subsequently been observed within a large number of North Atlantic marine sediment cores (e.g. Bond *et al.*, 1992; Broecker *et al.*, 1992; Broecker *et al.*, 1993; Andrews *et al.*, 1993; van Kreveld *et al.*, 1996; Rasmussen *et al.*, 1997; Hemming *et al.*, 2002)(Fig. 2.5), and were dated using AMS ^{14}C dating by Bond *et al.*, (1993)(Table 2.3). They have an approximate duration of 1000 years, occur every 7 – 10 kyrs (Andrews, 2000); and have an average thickness of 10-15 cm (Dowdeswell *et al.*, 1995). Heinrich Layers within the Hudson Strait region appear to consist of three distinct sedimentary units, suggesting a three-step process to their formation involving the growth of the LIS followed by massive ice rafting and then the waning of the LIS (Rashid *et al.*, 2003).

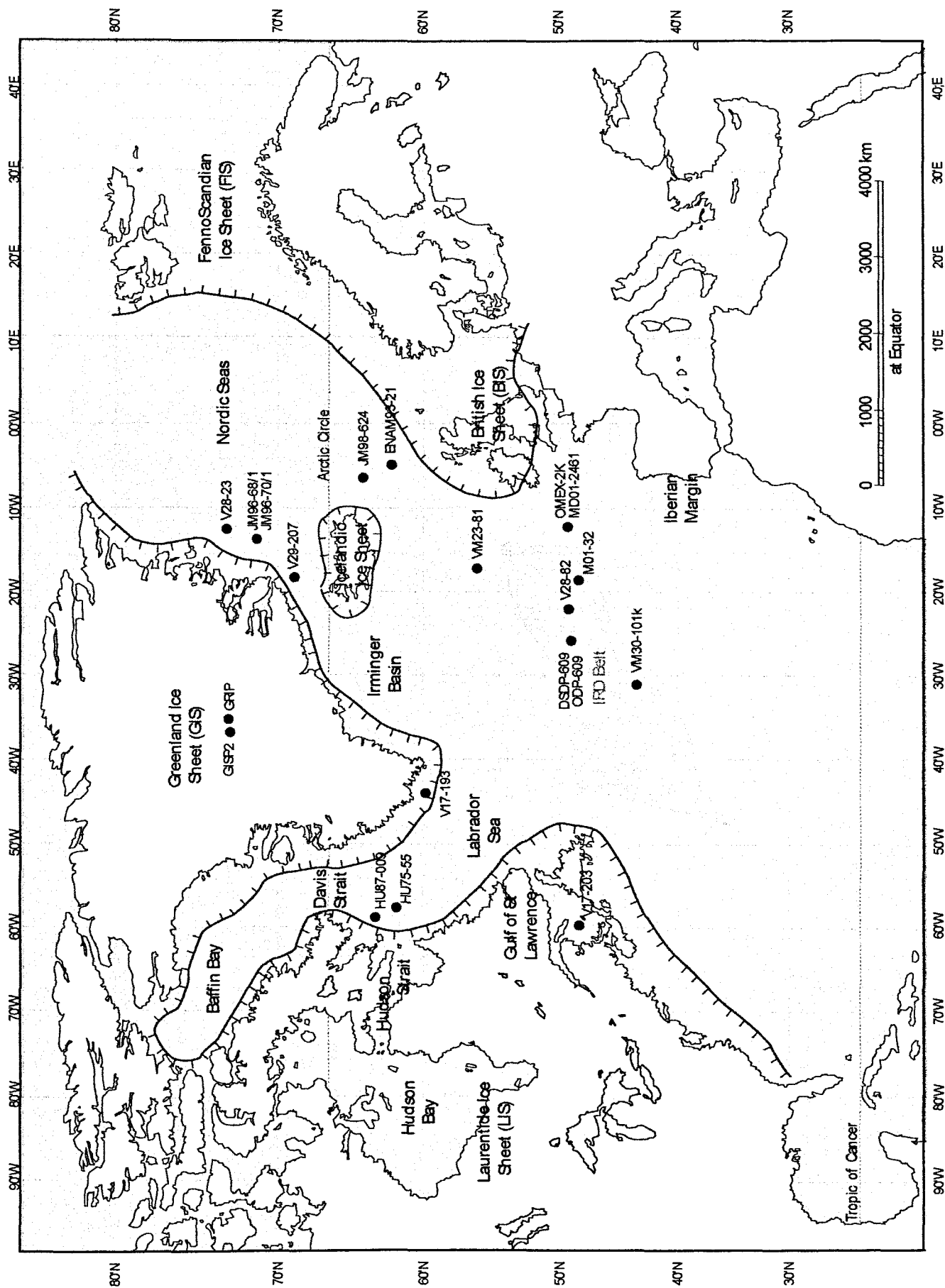


Fig. 2.5: Map of the North Atlantic Ocean, showing the major ice sheets during the last glacial cycle, and some of the areas and cores mentioned within this study (Outline map courtesy of Graeme Sandeman, University St Andrews).

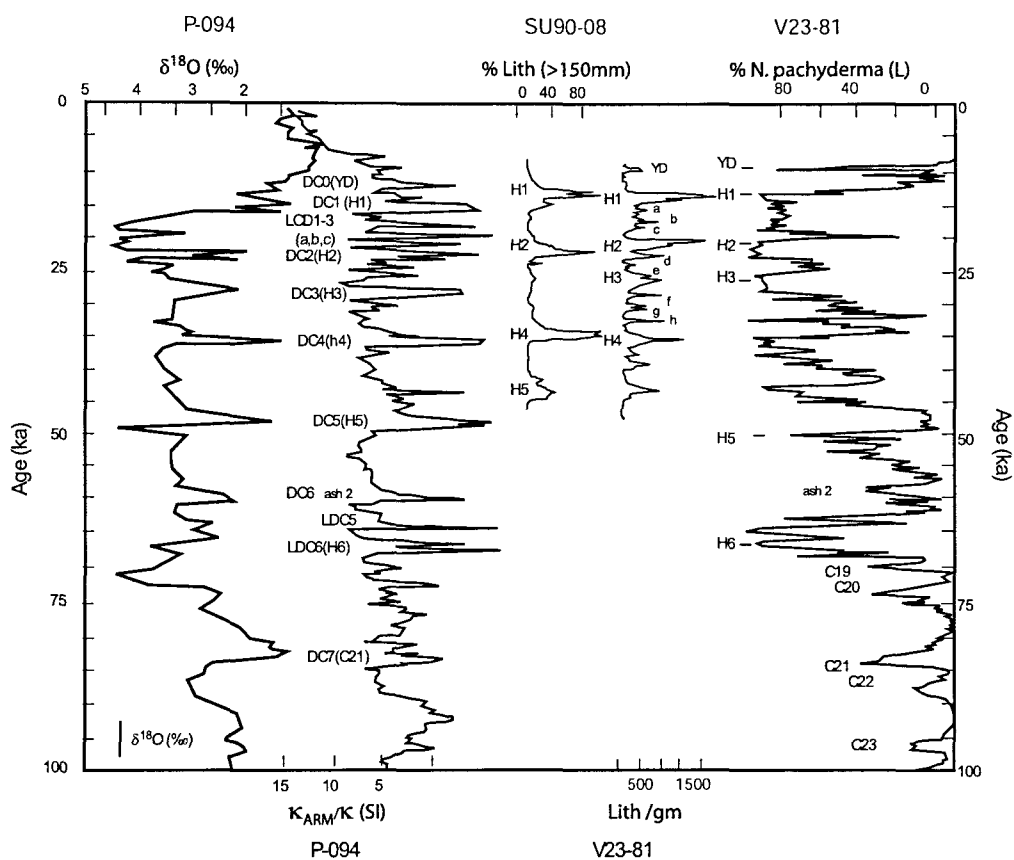


Fig. 2.6: The Characteristics of Heinrich Events, including oxygen isotope data, magnetic susceptibility, lithic grain counts and concentrations, and Foraminifer counts (Maher *et al.*, 1999).

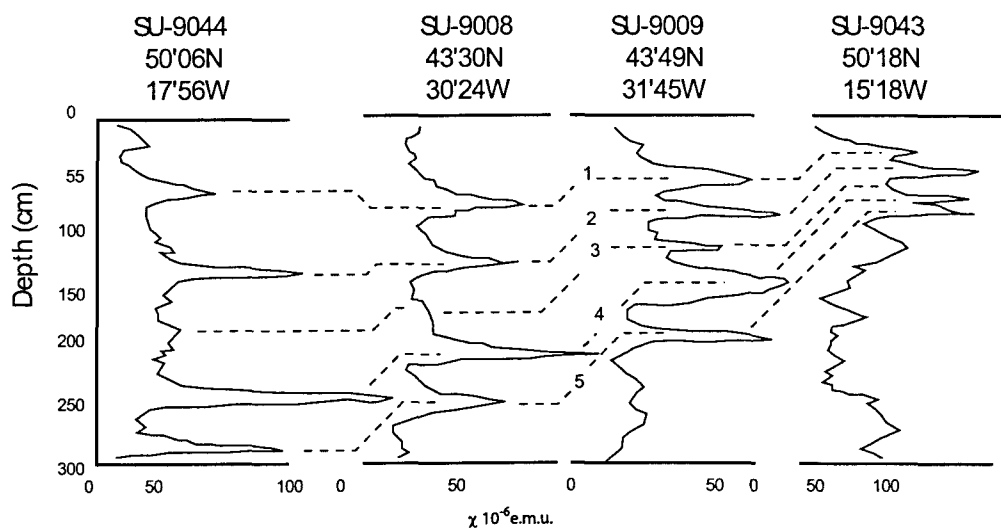


Fig. 2.7: Magnetic susceptibility of 4 cores from the North Atlantic performed during a study by Grousset *et al.*, 1993.

Heinrich Layers (HL) became the subject of immense interest within a few years with Bond *et al.*, (1992; 1993) interpreting the increased IRD, low $\delta^{18}\text{O}$ values and increased *N. pachyderma* abundance as evidence of lowered SSTs and SSSs caused by melting ice. In turn, lowered SSTs slowed melting, ensuring that icebergs could travel further with a possible effect on the Thermohaline Circulation (THC)(Palliard & Labeyrie, 1994). Broecker *et al.*, (1993) suggested that the abundant limestone fragments and the high ^{40}K - ^{40}Ar ages of the clay particles pointed towards the LIS as the major source.

The above was supported by Andrews *et al.*, (1993) who examined two cores from the Labrador Sea (HU75-55 and HU87-099; Fig. 2.5) and identified two ice streams full of detrital carbonate which extended out from the Hudson Strait dated at ~15 kyr and 20 kyr BP (coincident with H1 and H2). Andrews *et al.*, (1993) also used magnetic susceptibility as a possible indicator of HL provenance, suggesting that another characteristic of HLs is a high bulk magnetic susceptibility. Grousset *et al.*, (1993) demonstrated a similar effect after performing magnetic susceptibility measurements on approximately 20 cores from all over the North Atlantic (Fig. 2.7). They also noticed variations in the distribution of the HLs. H1, 2, 4 & 5 were generally found in all cores, but H3 & 6 were confined to cores from central and eastern locations. In a recent study by Rashid *et al.*, (2003), 24 cores from the Labrador Sea did pick up an H3 signal, identified by a slight increase in carbonate content, coarser grains and lighter $\delta^{18}\text{O}$ values. Rashid *et al.*, (2003) suggested a Hudson Strait origin for H3 layers in the Labrador Sea, as the layers thinned further out to sea. However, they still agreed with a Greenland and European Ice Sheet (GIS, EIS; Fig. 2.5) source for H3 in the Northeast Atlantic.

Table 2.3: AMS ¹⁴C dates for Heinrich Events. Taken from Bond *et al.*, (1993). All dates are uncalibrated radiocarbon dates.

HE	Radiocarbon Date (kyr BP)
H1	14.5-13.5
H2	22-19
H3	27
H4	35.5
H5	52
H6	69

2.3.2 Potential Causes of Heinrich Events

Heinrich Events are a widely accepted phenomenon with authors now debating their cause rather than their existence. In 1993, Bond *et al.*, correlated the climate cycles found in the Greenland ice cores (see Section 2.1.1; Fig. 2.1) with evidence of ice-rafting from the North Atlantic sediments (Fig. 2.8). They noticed, after further examination of the GRIP core, that the Dansgaard-Oeschger cycles (D-O cycles) lasting 500 – 2000 years were in fact bundled into larger climate cycles themselves. These Bond cycles (Broecker, 1994) collected the D-O cycles into a series of progressively cooler events, which abruptly terminated with a dramatic shift to warmer temperatures (Alley, 1998). They span on average 10 – 15 kyrs and $\delta^{18}\text{O}$ stratigraphy puts Heinrich Events as occurring immediately prior to the rapid warming (Alley, 1998; Williams *et al.*, 1998). This was also observed by Maslin *et al.*, (1995) who, using SSS and SST data, calculated the climatic rebound as lasting for approximately 2000 years before returning to average glacial conditions. A direct link between air temperatures above Greenland and the Atlantic Ocean is thus indicated, though the causes of either, or indeed both, remains a mystery (Broecker, 1994).

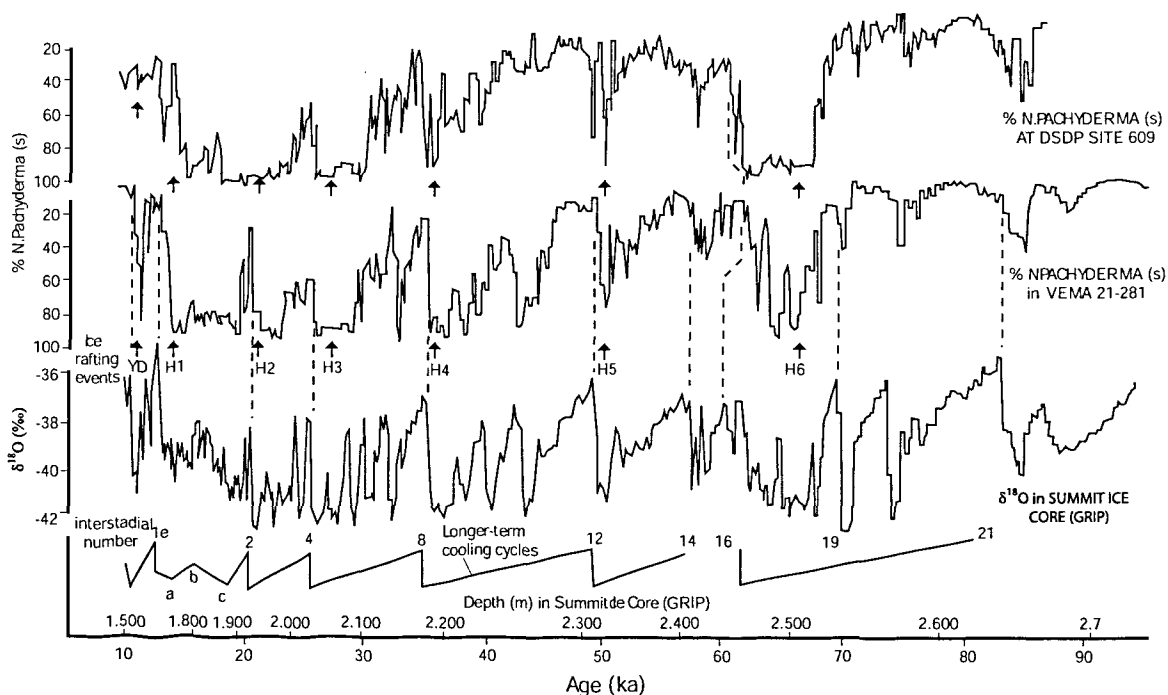


Fig. 2.8: Correlation between Foraminifera analysis of two marine cores and the GRIP ice core showing the D-O cycles, Heinrich Events and Bond cycles (the longer cooling cycles)(re-drawn from Bond *et al.*, 1993).

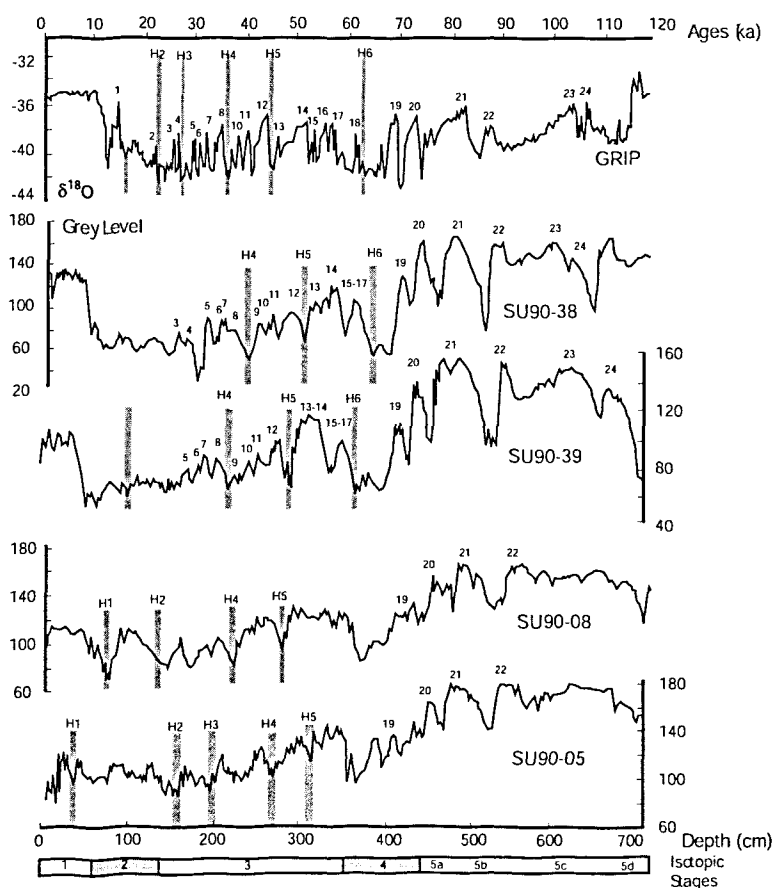


Fig. 2.9: The correlation of grey level reflectance of cores SU90-38, SU90-39, SU90-08 and SU90-05 with the GRIP ice core, Heinrich Events and D-O cycles (re-drawn from Cortijo *et al.*, 1995).

As a consequence of high-resolution foraminiferal and lithic analysis of three marine cores, Bond & Lotti (1995) and van Kreveld *et al.*, (1996) noted the presence of what have now become called “IRD events”. These are small layers of slightly increased IRD with intervals of 2 – 3 kyrs, comparable to the D-O cycles. They suggested that these climate oscillations caused the injection of icebergs into the Atlantic, but on a much smaller scale than the HEs. The build up of slightly cooler D-O cycles reached a critical temperature causing the massive collapse of ice sheet margins, resulting with a HE, and the end of a Bond cycle (Fig. 2.8).

The D-O signals were also picked up by Cortijo *et al.*, (1995) with grey reflectance analysis; by Helmke *et al.*, (2002) in colour intensity records; and in sedimentological, isotopic and foraminiferal variations by Rasmussen *et al.*, (1997). Grey reflectance obtains a colour level value for the intensity of reflected light from a sediment. The sediment is digitised by a Tri-Charged-Coupled-Device (TCCD) Colour camera, which consists of two neon glow lights. The intensity of the reflection is expressed as a numerical value somewhere between 0 (black) and 255 (red, blue or green level). The green level was selected by Cortijo *et al.*, (1995) because it is the most responsive to the presence of CaCO_3 , which is thought to reflect climatic variations. They were able to correlate the marine grey level signature to the $\delta^{18}\text{O}$ record from planktonic foraminifera from the same core, and the GRIP ice core record. The lowest grey level values correspond to HE's with a cyclic pattern in between (Fig. 2.9).

Variations in red-green intensity were found to be connected to the input of IRD on millennial time-scales by changes in the concentration of iron-bearing terrigenous material, red indicating more iron (Helmke *et al.*, 2002). Colour is ultimately linked to ice volume, as this controls the flux of sediment to the oceans, therefore, as HE's involve a rapid change in ice volume, they will also result in rapid colour changes (Helmke *et al.*, 2002).

Oceanic Circulation

After Palliard & Labeyrie (1994) noted that North Atlantic Deep Water (NADW) formation during the glacial stadials occurred in and around the IRD belt (Fig. 2.5), the effects of the input of fresh polar water to the ocean system also became of interest. Therefore, the impact this fresh, polar water would have on the NADW, the THC, and associated currents was studied. Palliard & Labeyrie (1994) were testing a theory put forward by Bond *et al.*, (1993) that stated the decrease in meltwater following a HE caused the THC to strengthen, giving rise to abrupt climate warming. Using a simple climate model, it was found that the massive ice discharges during a HE initially stopped the THC and caused North Atlantic cooling. The circulation was restarted shortly after, causing the abrupt warming suggested by Bond *et al.*, (1993)(Fig. 2.8).

Oppo & Lehman (1995) generated a record of surface and deepwater variability using benthic and planktonic foraminifera and found that NADW production was reduced during times of cold or dropping temperatures and *vice versa*, on a time-scale comparable to the D-O cycles. The suggestion of reduced NADW production was supported by Vidal *et al.*, (1997) during a study of benthic $\delta^{18}\text{O}$ and $\delta^{13}\text{C}$ data. The time period surrounding H4 (37 kyr BP – 33 kyr BP) was analysed specifically and it was found that NADW production was reduced at 35 kyr BP (H4 main event) though it could have continued to operate in areas less affected by the salinity changes. Soon after H4, NADW production returned to a similar distribution as before. Elliot *et al.*, (2002), too, found reductions in NADW production on millennial time-scales, with the HE's bringing the largest reduction, substantiating the previous work by both Oppo & Lehman (1995), and Vidal *et al.*, (1997). Additionally, sea ice break up has been noted in the polar North Atlantic during Heinrich Events (Dokken & Hald, 1996), which has been interpreted as the emergence of a vigorous surface circulation pattern caused by meltwater influx in lower latitudes, resulting in the advection of warmer water into the polar regions.

Sea surface temperature and salinity oscillations on D-O timescales during the last deglaciation was also noted by Kroon *et al.*, (1997) in a study of a core from the Barra Fan (N-W Scottish margin). The authors argued that such variations were probably a result of British Ice Sheet (BIS) fluctuations, representing a connection between BIS instability, N-W European climates (indicated by *Coleopteran* assemblages) and Atlantic circulation patterns. This was expanded by Gröger *et al.*, (2003) who using sortable silt analysis, have established three modes of NADW circulation that have prevailed over the last 800 kyr. Firstly, a strong circulation, with a coarse sortable silt fraction, and strong bottom current is found during interglacials. Secondly, a slower NADW circulation with finer sortable silts is prominent throughout glacial periods. Finally, a third state involving the episodic shutdown of circulation, with an extremely fine sortable silt fraction is found during glacial to interglacial transitions.

In terms of Heinrich Events in general, Seidov & Maslin (1999) modelled the response of the NADW to meltwater episodes caused by a variety of scenarios, including different iceberg origins. It was found that regardless of the provenance of the ice, there would be a complete shut down of the THC if there was enough ice reaching pivotal areas (i.e. deep overturn regions). However, if the event was confined to the Nordic Seas, THC production would only be weakened. This was in support of the theory of Jansen & Veum (1990) who argued that lowered salinity is dependent on the rate of deglaciation, not meltwater pathways.

2.4 Current Issues Surrounding Heinrich Events

As indicated above, the existence of Heinrich Events is now well-established based upon IRD evidence within the marine sedimentary record. Within the North Atlantic region, the spatial distribution of IRD has also been mapped in some detail (Fig. 2.5). Perhaps the most significant ongoing debate surrounds the causes of Heinrich Events and, in particular, the role of major iceberg discharge into the North Atlantic within the global climate system.

Furthering our understanding of the causes of Heinrich Events is of considerable interest given the two, major theories currently being debated within the research literature, namely external forcing (such as climate; Seidov & Maslin, 1999) and internal ice sheet instability (Oerlemans, 1993; Alley, 1998). Clearly, if external forcing is the driving force behind the occurrence of Heinrich Events, then the Events themselves are a response to climate change. In contrast, if Heinrich Events are triggered by the internal dynamics of major ice sheets, their occurrence may be less intimately linked to external climatic forcing, though they can represent the cause of the rapid climatic changes. In both cases, the fresh water discharge into the ocean system generated during Heinrich Events may have a major influence upon internal components of the climatic system.

2.4.1 External forcing of climate

Originally, HEs were attributed to Milankovitch style orbitally forced climate changes (Heinrich, 1988), with the well documented changes in the Earth's orbital parameters altering the amount of energy reaching the surface, affecting surface temperatures (Dawson, 1992; Lowe & Walker, 1997; Williams *et al.*, 1998). The Milankovitch cycles have periodicities of approximately 413 kyr, 123 kyr, 95 kyr, 54 kyr, 42 kyr, 21 kyr and 19 kyr (Berger *et al.*, 1989; Dawson, 1992; Briggs *et al.*, 1997)(Fig. 2.10). The D-O cycles, Bond cycles and Heinrich Events, however, all have much shorter periodicities, making it difficult to link Heinrich Events with orbital changes, and suggesting that an alternative forcing mechanism is required (Pallard & Labeyrie, 1994; Williams *et al.*, 1998). Bond *et al.*, (1993) and Bond & Lotti, (1995) have demonstrated the link between the atmospheric oscillations above Greenland and IRD events indicating a common cause or trigger in the climate system (Stoker, 1998).

During the analysis of the Bond cycles (Bond *et al.*, 1992), it was noted that each HE appeared to have been preceded by a cooling of the ocean surface, implying that the HEs were a response to, not a cause of, climate change. Bond *et al.*, (1999) also noted two petrological tracers of different origin (Icelandic glass, and

haematite-stained grains from red-bed sedimentary rocks) throughout an entire sediment core. As the icebergs carrying these tracers came from different sources, the fact that there is continued mixing of the tracers throughout the entire core suggests that icebergs from both source areas were arriving at the site simultaneously. This was interpreted by Bond *et al.*, (1999) as the influence of climate on unstable ice, rather than internal ice sheet instability, because internal ice sheet variability would not cause independent ice sheets to surge simultaneously. After further analysis, Bond *et al.*, (1999) suggested that HEs 1, 2, 4 and 5, were caused by glaciological mechanisms triggered by the cooling D-O cycles. H3 and H6 were also glaciogenic, but simply due to falling temperatures. During the several thousands of years immediately after an HE, the slowly re-growing ice in the Hudson Strait would be insensitive to the 1-2kyr cycles, explaining the lack of a D-O cycle signal between the HEs.

2.4.2 Internal mechanisms for modification of climate

Climate can be influenced internally by a number of factors such as atmospheric composition, changes in albedo due to ice cover, ocean temperatures and salinity (Fig. 2.11)(Briggs *et al.*, 1997). The oceans are a major part of the global climate cycle, therefore any changes in conditions will be reflected in the climate and *vice versa* (Ruddiman, 2003). The climate system has made vast and often abrupt changes during the Quaternary, involving all of the components (Broecker, 2000). The two mechanisms that have been suggested and are still under debate are atmospheric changes and reorganisations in the oceanic THC (Broecker, 2003).

The THC is the mechanism by which temperature and salinity are distributed throughout the oceans, and is one of the chief forces behind the oceanic circulation (Whittow, 1984; Lowe & Walker, 1997). The colder, denser waters in the high latitudes sink, causing warmer, less dense water from the tropics to be drawn up to replace it. In turn, the colder water is fed down to the tropics to compensate for the removal of the warmer water. The warmer water then cools

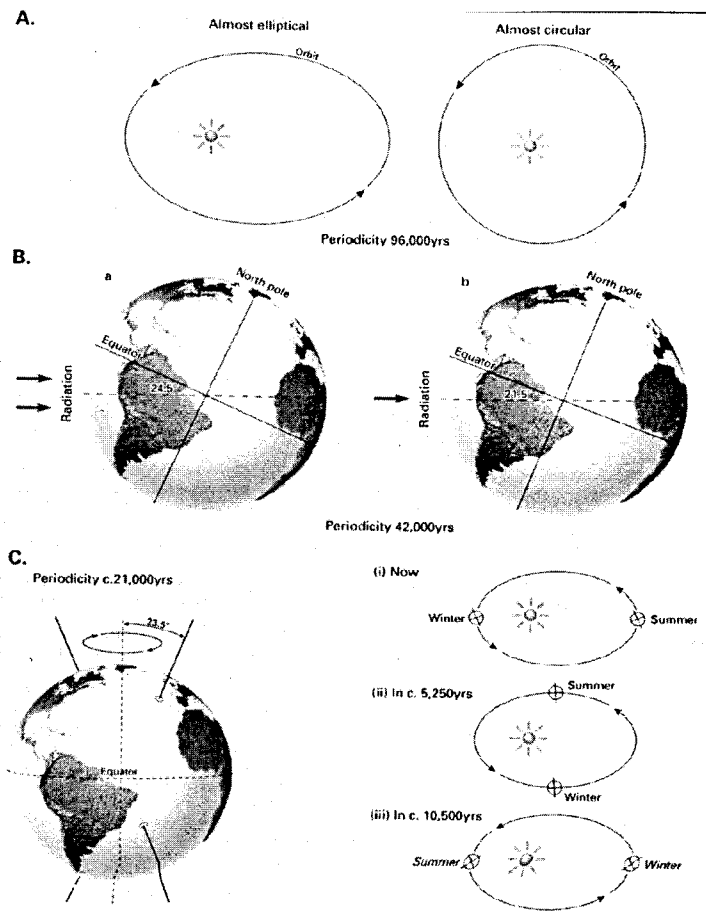


Fig. 2.10: Milankovitch's Astronomical Theory of climate change. A) Eccentricity of the orbit; B) Obliquity of the ecliptic; C) Precession of the equinoxes. (Lowe & Walker, 1997).

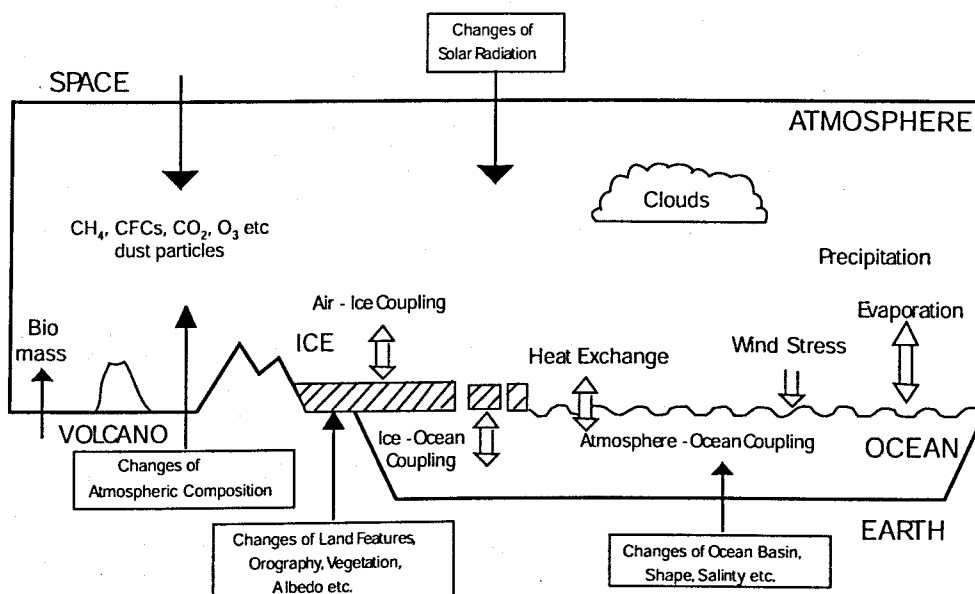


Fig. 2.11: The internal mechanisms of climate control. Re-drawn from Briggs *et al.*, 1997).

as it loses heat to the atmosphere and begins to sink, creating a continuous cycle (Fig. 1.3)(Williams *et al.*, 1998). Oceanic circulation throughout the HEs has been discussed in an earlier section (2.3.2). Reduction in THC production will slow down the transfer of heat northward, resulting in a cooling of SSTs, the expansion of sea ice, and therefore a lowering of atmospheric temperatures. A major problem with the above scenario is the initial cause of the THC shutdown. Prior to the Younger Dryas (YD), the collapse of the proglacial Lake Agassiz through deglaciation forced a massive input of freshwater into the North Atlantic, weakening the THC (Broecker, 2003). Melting of the HE icebergs has been modelled as being enough to slow down circulation, but no accurate chronology has yet been created to determine when the climate change began in relation to the THC reduction.

Although the exact sequence of events is still not fully understood, the concepts discussed above have caused changes in the THC to be accepted as the main mechanism that amplifies some initial pulse or distortion of sea surface properties that leads to abrupt climate change (Kandiano *et al.*, 2004; Ewen *et al.*, 2004). The intensity of the climate change during, and after each HE, and the length of time the THC takes to recover are all strongly dependent on the background climate state (Prange *et al.*, 2004), potentially explaining the differences between the HEs.

Several studies have revealed events throughout the globe, and throughout the climate system, with apparent temporal correlation to the HEs and D-O cycles, suggesting a climatic link, rather than ice sheet instability (see below and Broecker, 1994). Table 2.4 gives a brief synopsis of some of the studies. A fuller compilation of studies undertaken and underway can be found in Voelker (2002). Fig. 2.12 maps a selection of the studies listed both here and in Voelker (2002), to give an idea of the locations affected by “Heinrich-like” signals.

Table 2.4: Some studies showing apparent correlation with the North Atlantic Heinrich Events throughout the globe. More studies can be found in Voelker (2002).

Reference	Location of Study	Description of Findings
Grimm <i>et al.</i> , 1993	Lake Tulane, Florida	Vegetation cycles alternating between pine and oak, indicating changes in temperature and atmospheric moisture. ^{14}C dates put the pine episodes with the HEs.
Lowell <i>et al.</i> , 1994	New Zealand Southern Alps and Chilean Andes	Glacial advances identified by moraines have ^{14}C dates corresponding to the HEs.
Thouveny <i>et al.</i> , 1994	Lac du Bouchet, France	Magnetic susceptibility records and pollen traces vary on times scales comparable to the D-O cycles.
Porter & An, 1995	Chinese Loess Plateau	Layers of grain size maxima caused by variations in the strength of the Asian monsoon coincide with the HEs.
Behl & Kennett, 1996	Santa Barbara Basin	Layers of laminated clays indicating periods of oxygenation on D-O time scales.
Whitlock & Bartlein, 1997	Cascade Range, NW America	Alternations between steppe and forest vegetation match the marine $\delta^{18}\text{O}$ stratigraphy.
Benson <i>et al.</i> , 1998	Mono Lake, California	Low lake levels are coincident with the HEs, indicating enhanced dryness of America during the HEs. Suggested as the result of the southward displacement of the polar jet stream by the growth of the LIS.
Schulz <i>et al.</i> , 1998	Arabian Sea	Biological productivity oscillations caused by fluctuations in the strength of the Asian Monsoon correlate to the D-O cycles and HEs.
Allen <i>et al.</i> , 1999	Lago Grande di Monticchio, Italy	Pollen analysis, magnetic susceptibility and biogenic silica data have revealed temperature and atmospheric moisture cycles comparable to the D-O cycles.
Dreger, 1999	Norwegian Sea	IRD layers with HE dates, also planktonic foraminifera and isotopes show sea surface temperature and salinity variations.
Schmelzer, 1999	Southern Red Sea	Upwelling events shown by benthic foraminifera occurred during the HEs.
Wang <i>et al.</i> , 1999	South China Sea	Climate fluctuations on millennial time scales. Monsoonal flooding occurred during colder periods in time with the HEs.
Behling <i>et al.</i> , 2000	NE Brazilian Margin	Planktonic isotopes, XRF and CaCO_3 content reveal increases in sedimentation during HEs and temperature cycles similar to the D-O cycles.
Colmenero <i>et al.</i> , 2000	Gulf of Cadiz	Cold sea surface temperatures, input of IRD and a stable thermohaline circulation were all coincident with the HEs.
Kanfousch <i>et al.</i> , 2000	SE Atlantic	IRD layers occur on millennial time scales, correlating to increases in NADW production and HEs.
Leuschner <i>et al.</i> , 2000	Arabian Sea	Aeolian dust fluxes are compatible with D-O cycles and the laminated clay beds in the Santa Barbara basin (Behl & Kennett, 1996).
Sagnotti <i>et al.</i> , 2001	Western Antarctic	Finely laminated beds with ^{14}C dates concurrent with the HEs. They are deficient in organic matter suggesting times of extended sea ice.
Chappell, 2002	Huon Peninsula, Papua New Guinea	Cycles of sea level shown by coral terraces last approximately 6-7 kyr. The cycles end with a rise of 10-15m lasting 1-2kyr, and correspond to the HEs.

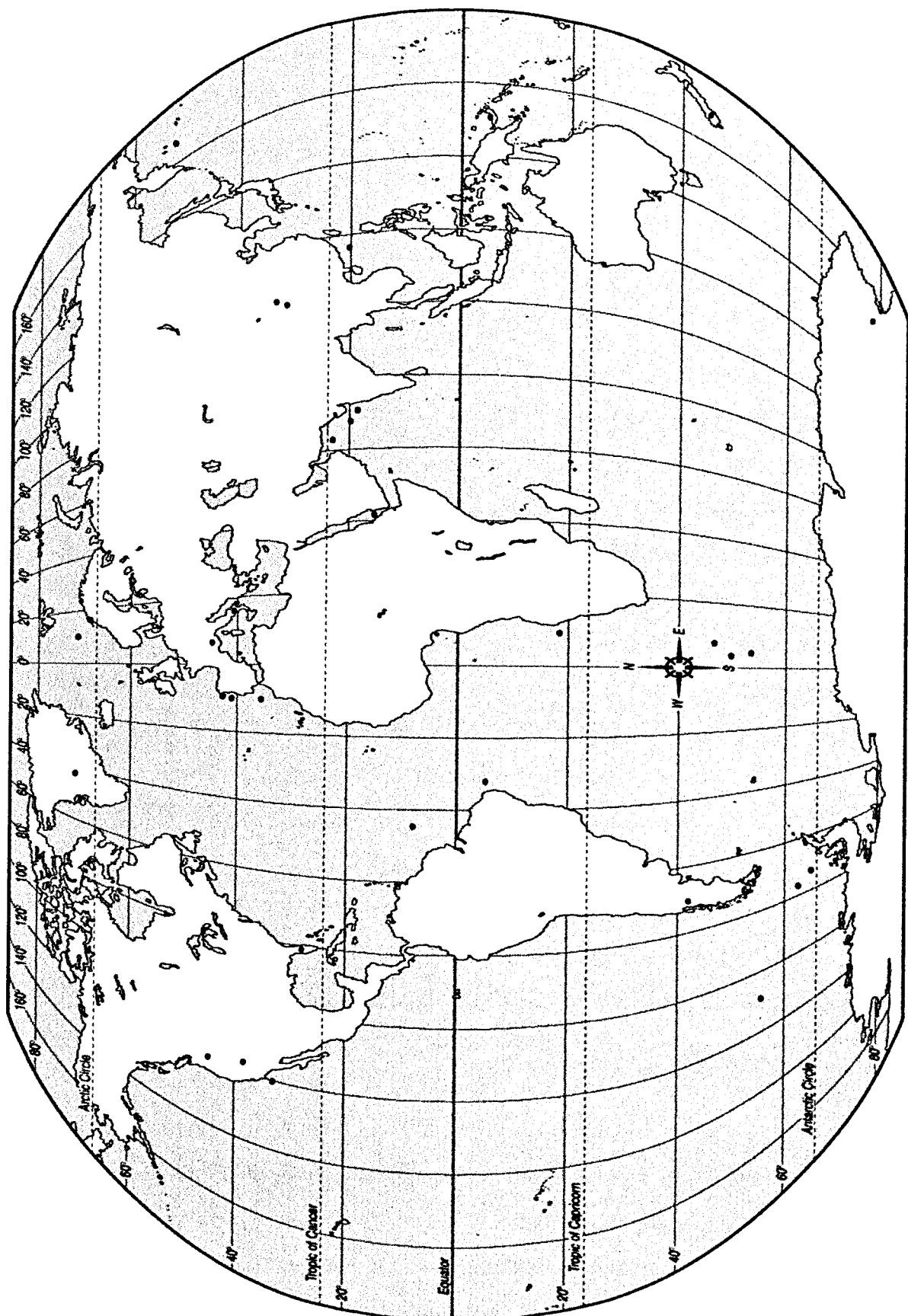


Fig. 2.12: Map showing the location of "Heinrich-like" events noted around the globe, from Table 2.4

Internal Ice Sheet Instability

Oelermans (1993) examined the possibility of HEs being caused by the response of the Laurentide Ice Sheet (LIS) to climate cooling using an orbitally forced model of the LIS. His results showed that H1 occurred during a relatively warm period, before deglaciation of the LIS had started, whereas H2 and H3 occurred during the very cold last glacial cycle when the LIS would be growing and from which, Oelermans (1993) inferred that HEs were the result of internal LIS variability and not climate.

The idea was developed by MacAyeal (1993) and Alley & MacAyeal (1994), who proposed a binge/purge mechanism to the LIS as a cause of the HEs (Fig. 2.13). This was based on the idea of the freezing and thawing of the Hudson Bay and Hudson Strait basal sediments to provide a periodic slipway for ice. The first stage was the binge phase, where the sediment is frozen allowing the LIS to grow unhindered. The second stage is the purge phase, where the basal sediments thaw, creating a lubricated pathway for the ice. The suggested cause of the freezing and thawing could be geothermal heat or a response to pressure from the thickness of the ice. The latter could explain the 7kyr periodicity as, with a relatively constant accumulation rate, a critical mass-related pressure point would be reached in a relatively constant time-scale.

Manabe & Stouffer (1995) used a coupled ocean-atmosphere model to simulate the response of climate to freshwater inputs to the North Atlantic. They noticed a stepped weakening and strengthening structure to the THC evolution, which was reflected in the atmosphere by cooling-warming cycles and lends strength to the idea that HEs caused the climate oscillations and were not a response to them.

McCabe & Clark (1998) established the involvement of the BIS in H1 however, they also noted a “dynamic collapse” of the LIS approximately 800 years prior to the BIS surge and attributed the BIS surge to a response to the subsequent THC disruption.

Hunt & Malin (1998) suggested the possibility of earthquakes at the sea-ice margin resulting from crustal failures due to ice pressure during the binge phase of the Alley & MacAyeal model. The 7kyr periodicity could again, be explained by a critical pressure point for crustal failure. Evidence was taken from the NE Canadian coast, which showed that seismic activity had taken place due to post-glacial rebound.

Abundant, and apparently convincing evidence has been presented for both arguments, however, the actual causal mechanism for HEs is still under immense debate. It is imperative that the causal mechanism is established, as it holds vital clues to the way the climate system works and changes independently of anthropological influence.

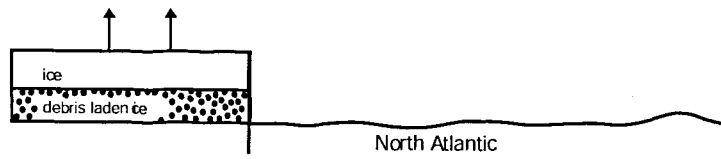
2.4.3 IRD Provenance

A key issue in solving the internal-external debate is provenance of the IRD. If the ice sheets involved can be identified, and the order in which they released their icebergs determined, it may be possible to form a sequence of events leading up to and during a HE that might, ultimately, determine the cause (Hemming *et al.*, 2002). Several IRD provenance studies have taken place in recent years, which have used a variety of techniques (e.g. Revel *et al.*, 1996; Gwiazda *et al.*, 1996 a & b; Snoeckx *et al.*, 1999; Grousset *et al.*, 2000).

Optical Mineralogy and Electron Microscopy

Compositional analysis involving the physical identification and counting of the lithic grains present in a core has been extensively used in the study of IRD provenance (e.g. Heinrich, 1988; Broecker, 1993; Andrews *et al.*, 1993; Bond & Lotti, 1995; Cortijo *et al.*, 1997; Bond *et al.*, 1997; Scourse *et al.*, 2000; Knutz *et al.*, 2001). The identification of petrologic tracers, such as Iceland volcanic ash, and haematite stained grains from North America, have helped with this (see Section 2.4.1).

BingePhase:



Purge Phase:

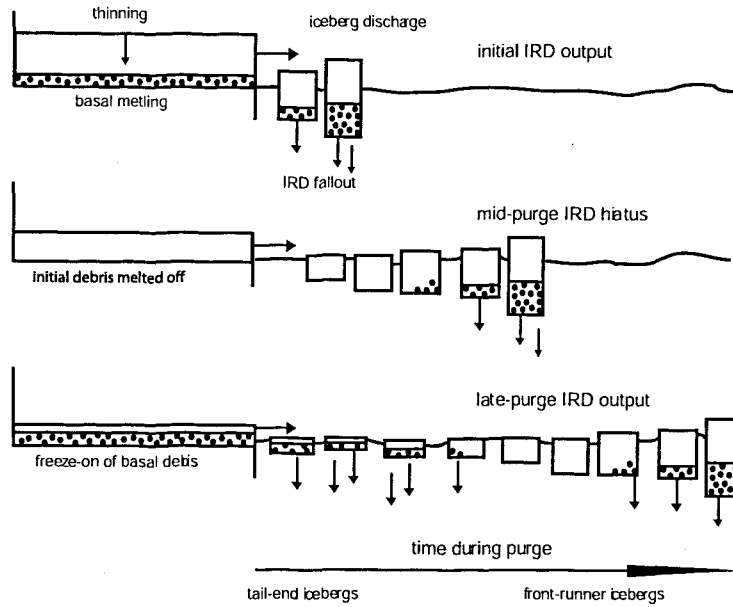


Fig. 2.13: The Binge/Purge model put forward by Alley & MacAyeal (1994)(re-drawn).

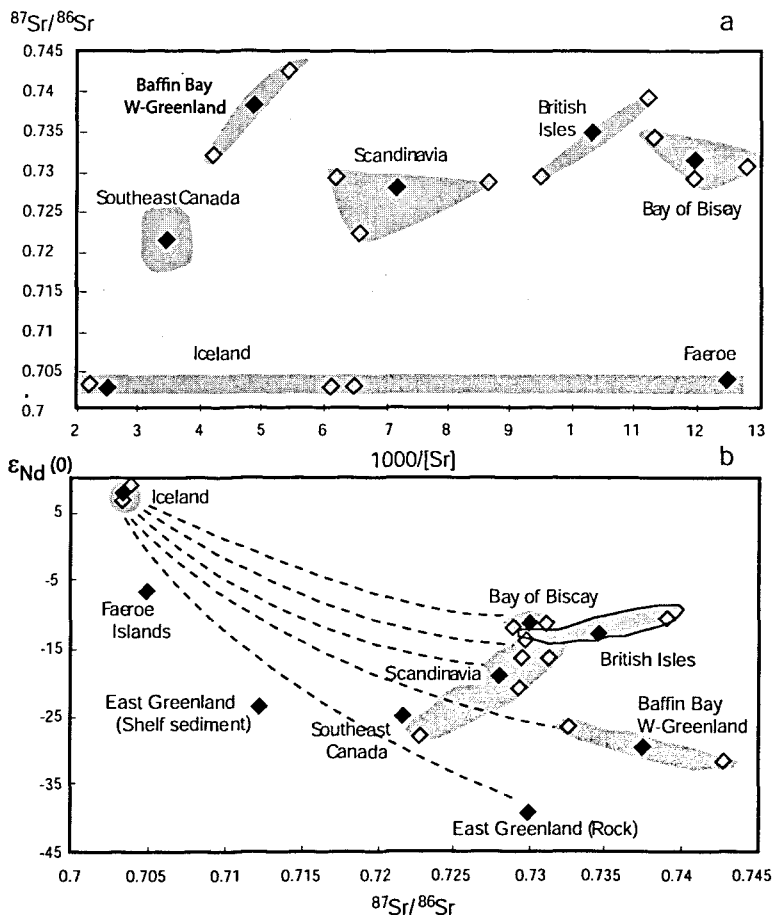


Fig 2.1 4: Sr-Nd analysis by Revel et al., 1996 (re-drawn). a) $^{87}\text{Sr}/^{86}\text{Sr}$ ratios plotted against $1000/[\text{Sr}]$ for each source region. b) $^{87}\text{Sr}/^{86}\text{Sr}$ ratios plotted against $^{143}\text{Nd}/^{144}\text{Nd}$ ratios (expressed here as $\epsilon_{\text{Nd}}(0)$) also for source areas. Open diamonds are specific samples from each of the source areas. Solid diamonds represent the mean value for all the samples from each source area.

XRD and XRF

X-ray techniques have been used to some extent in studies of IRD provenance, although these methods have not been as widely performed as the more traditional methods of optical identification. Again, the identification of elemental composition or mineral types has helped to gain information on mineral provenance, authigenic or diagenetic alterations, and transport mechanisms (e.g. Kirschvink & Chang, 1984; Snowball & Thompson, 1988; Roberts, 1995; Walden *et al.*, 1996; Zahn *et al.*, 1997; Moros *et al.*, 2004).

Strontium (Sr) and Neodymium (Nd)

The Sr composition of seawater at any given time is determined by the isotopic ratios of the various source materials (Faure, 1986; Capo *et al.*, 1998). This can depend on their age and their origin (Elderfield, 1986), and therefore help with sediment provenance identification. Each of the inputs into the oceans has an isotopically distinct Sr signal that can be separated and identified. Changes in the Sr composition over long periods of time are associated with tectonic uplift, whereas shorter timescales reflect climate change. Climate change can strongly affect the amount, and the isotopic composition of Sr entering the worlds' oceans through rivers by changing the intensity of weathering processes as well as the types of rocks subject to weathering (Capo *et al.*, 1998).

The Nd composition reflects the age of the rocks that it originates from, as it is derived from the weathering of rocks which were created by magmas from the mantle (Peipgras & Wasserburg, 1980), and any mixing or transportation that has subsequently taken place (Faure, 1986; Stordal & Wasserburg, 1986). Therefore, it is very geographically distinct (Piotrowski *et al.*, 2004), and can again assist in the determination of provenance. The high atomic masses of Nd isotopes, coupled with only a single oxidation state (Nd^{3+}), means that little fractionation occurs to Nd over time, and hence, these isotopes are free from some of the uncertainties that other isotopes in sea-water experience (Piotrowski *et al.*, 2004). Peipgras & Wasserburg (1980) found significant differences in Nd concentration with water depth, which can indicate water mixing. Nd in NADW is also isotopically distinctive

and can therefore help identify sources of NADW, and possible circulation pathways (Vance & Burton, 1999).

Both Strontium and Neodymium are recorded in the shells of foraminifera, and can be separated from sediment samples by chemical procedures. Strontium is separated by leaching the sample in 1 N HCl, and dissolving in HF and HNO₃ at 220°C for 36 hours. The sample is then dried and soaked in 12 N HCl at 200°C for 12 hours before being passed through a Sr-spec resin in 3 N HNO₃ (Hemming *et al.*, 1998). The Sr composition is measured by Inductively Coupled Plasma-Mass Spectrometry (ICP-MS)(Snoeckx *et al.*, 1999).

Neodymium is separated from Samarium (Sm) by being dissolved in 1 N HCl and spiked with a Rare Earth Element (REE) spike containing ¹⁴⁵Nd and ¹⁴⁹Sm. The Nd is separated using methyliatic acid on cation resin (Hemming *et al.*, 1998), and measured by a TIMS multi-collector mass spectrometer (Snoeckx *et al.*, 1999).

In 1996, Revel *et al.*, used combined Sr-Nd analysis on the lithic fraction of sediments from six North Atlantic piston cores to deduce their origin and transport pathways. Comparisons with the Sr-Nd compositions of potential source areas revealed that the main source regions of the IRD were the Canadian Shield (particularly the Baffin Bay area and Western Greenland), Iceland, and Europe (Britain and Scandinavia). They therefore concluded that the Heinrich layers originated from all the circum-Atlantic ice sheets (Fig. 2.14).

Snoeckx *et al.*, (1999) used the same methods on H3 and H4 from 17 cores from around the North Atlantic. Their results agreed with Revel *et al.*, (1996) confirming a Scandinavian and European input as well as a Laurentide one for both HEs. However, during H3, they found a dominant European signal, whereas in H4 it was dominantly Laurentide. They also noticed a European signal early in H4, prior to the main Laurentide H4 event in the same core SU92-28 (Fig. 2.5), which was interpreted as the European Ice Sheets (EIS) releasing their icebergs first,

indicating a hemispheric involvement in HEs. They stated that if it can be shown that the European Ice Sheets surged first, then the behaviour of the LIS might not be the sole influence behind HEs as is currently commonly thought. Several possible mechanisms for this were discussed, including the release of EIS icebergs prior to the LIS in response to some global forcing such as North Atlantic drift or climate, and the simultaneous release by both the LIS and EIS. The location of SU92-28 (the Portuguese coast) would simply mean that the EIS icebergs arrived there first. Either way, an internal LIS instability cause could not explain the findings.

A similar pattern to Snoeckx *et al.*, (1999) findings was noted by Auffret *et al.*, (2002), who also used Sr-Nd analysis. It was found that for both H1 and H2, the LIS icebergs were preceded by the European icebergs by 1-1.5 kyr. These findings were also supported by Knutz *et al.*, (2002) for H1; using multiproxy analysis, the “precursor” as it became known, to H1 was found to be meltwater discharge from European Ice Sheets, though whether it was a trigger for H1 or a quicker response to common climate forcing was left undecided with possible evidence for both.

In 2000, Grousset *et al.*, presented Sr-Nd isotope analysis of 7 cores. They also recognised a European precursor event in H1, H2, H4 and H5. Using ^{14}C AMS dating on H2, they were able to establish that the EIS iceberg discharge did predate the LIS one. They did accept that it could be due to the fact that the core they dated was from the European margin and therefore a travel time for the LIS icebergs would have to be included. Other suggested causes were the EIS responding to a global trigger first as it was smaller; or even triggering the LIS response itself. They also discussed the possibility of the LIS surging due to internal dynamics every 7 – 10 kyrs and the EIS surging as a result of the D-O cycles every 1.5 kyrs. The shorter cyclicity of the EIS was supported by Knutz *et al.*, (2001), in a study of a core from the Rockall Trough (NW Scotland). Sixteen glaciomarine events were identified by IRD abundance, with lithic petrology attributing the material to the British Tertiary Province on the Hebridian Shelf. Tuning the data (using IRD and planktonic foraminifera abundance) to another

North Atlantic core, and then to the GISP2 $\delta^{18}\text{O}$ record, gave the glaciomarine events a periodicity of 2-3 kyr.

In 2001, Grousset *et al.*, used lithological analysis as well as Sr-Nd to establish circum-Atlantic ice sheet involvement in the Heinrich Events, and that the IRD was deposited in a particular order. This was determined as a European/Icelandic precursor followed by the LIS main event and finally Baffin Bay material. They suggested that, as they found the 3-step structure in a core from the centre of the Ruddiman IRD belt, it would record the order in which the ice sheets discharged their icebergs.

Farmer *et al.*, (2003), however, whilst recognising a three-step structure using Sr-Nd compositions, with a low ϵ_{Nd} ($^{143}\text{Nd}/^{144}\text{Nd}$ ratio) input from the Hudson Strait flanked above and below by higher ϵ_{Nd} values, suggested that the final input could either be from the EIS, like the precursor, or a different LIS ice stream

The authors above have firmly established the involvement of all circum-Atlantic ice sheets in the Heinrich Event discharges, despite the ambiguity surrounding the actual contributions from each ice sheet, and the sequence of their discharges.

Lead

Lead analysis of single feldspar grains can be used to identify specific continental sources whilst multigrain composites can show the relative contributions of each source (Vitrac *et al.*, 1981; Gwiazda *et al.*, 1996a). Lead exists in 4 forms: ^{204}Pb , ^{206}Pb , ^{207}Pb and ^{208}Pb . The isotopic composition of lead ores varies in rocks and sediments in different regions due to geological controls (Bjorlykke *et al.*, 1993; Renberg *et al.*, 2002). Lead isotope ratios reflect the Uranium-Lead and Thorium-Lead ratios of the sources (Chillrud *et al.*, 2003). As the Uranium and Thorium decay, Lead isotopes are created and a ratio is left which is specific to the source rocks. This is because the isotopic composition of Lead is dependent on the quantity of Uranium or Thorium present at the beginning of the decay, which is

controlled by metamorphism during the formation of the rocks (Gwiazda *et al.*, 1996a). As with Sr and Nd, Pb is separated by chemical procedures (leaching in HCl, dissolution in HF:HClO₄:HNO₃, and separation by anion exchanges, Dixon *et al.*, 1990; Birkeland *et al.*, 1993a & b; Bjorlykke *et al.*, 1993) and is analysed for provenance using a silica gel-phosphoric technique (Hemming *et al.*, 1998).

The ratio of ²⁰⁶Pb/²⁰⁷Pb isotopes has become popular over recent years as a tool able to trace the provenance of lead ores in a variety of environments, including snow and ice (e.g. Rosman *et al.*, 1997; Simonetti *et al.*, 2000), peat bogs (Mackenzie *et al.*, 1998; Weiss *et al.*, 1999), soils (Bindler *et al.*, 1999; Prohaska *et al.*, 2000) and sediments (Brannvall *et al.*, 1999; 2001; Monna *et al.*, 1999).

Specific to the marine environment, studies by Gwiazda *et al.*, (1996a; 1996b) used Pb isotope analysis on H2 and H3 from cores throughout the North Atlantic. Their results showed that for H2, all the single grains came from the Canadian Shield, with which the multigrains were in agreement. Gwiazda *et al.*, (1996a) interpreted this as evidence supporting the ping-pong model of MacAyeal (1993). For H3, however, they found a definite multi source signal, which was attributed to foraminiferal dissolution, or low productivity (Gwiazda *et al.*, 1996b). Hemming *et al.*, (1998) also carried out Pb analysis on all the HEs in core V28-82 (Fig. 2.5). It was found that the IRD in H1, H2, H4 and H5 was dominantly LIS in origin, but with some additional material from the Gulf of St Lawrence, Europe and Iceland. They suggested glacial mechanisms as the cause. Benson *et al.*, (2003) also identified a Hudson Strait source using Pb, Nd and Rare Earth Element (REE) analysis for samples from the Northwest Labrador Sea.

Nannofossils

Nannofossils are the remains of calcareous nanoplankton, such as coccoliths (Fig. 5.15)(Lowe & Walker, 1997). They live in the top 200m of the water column and thrive in areas of upwelling or pronounced mixing (Brasier, 1980). The age and geographic distribution of reworked nannofossils can determine their origin (Rahman, 1995). Nanoplankton live in specific geographical zones, due to their

sensitivity to climate regimes, as well as specific stratigraphical ranges (Donally, 1989). These “zonations” have been mapped by workers such as Thierstein (1976) and Backman (1984), thus reworked nannofossils have become a useful tool in sourcing the surrounding sediment. Rahman (1995) conducted a study of reworked nannofossils in the North Atlantic and found that the nannofossils with ages synchronous with H1 and H2 originated in NW Europe, even in the core from the Labrador Sea. The results were used as evidence that both the LIS and EIS were involved in H1 and H2, and that a near-synchronous response to some common mechanism was seen by the circum-Atlantic ice sheets. Climatic and eustatic sea level changes were suggested.

Provenance sequencing

As discussed above, where IRD contributions from different sources can be shown to be sequenced, such evidence may assist in determining the causal mechanism/processes driving a HE. Several workers have used the various IRD provenance methods outlined above to investigate variations in IRD provenance, both within a single HE and between HEs.

Auffret *et al.*, (1996) studied the bulk physical properties of H1-5 and found a two-stage pattern to the events. The first phase is characterised by glacial conditions and high productivity, the second by increased carbonate deposition and reduced productivity. The second phase is also associated with a decrease in ocean salinity caused by the sudden influx of fresh water.

In 1998, Elliot *et al.*, proposed 2 systems oscillating at different rates as a cause for the HEs and D-O cycles. After sediment and $\delta^{18}\text{O}$ analysis, they suggested that every 5-10 kyr, there would be massive discharges from the continental ice sheets in response to the Bond cycles, and every 1.2-3.8 kyrs, the high latitude coastal ice sheets would release smaller quantities of icebergs in timings associated with the D-O cycles. This was supported by Knutz *et al.*, (2001), who used lithic analysis on a European margin core. They found evidence of 16 glaciomarine events, including equivalents to H1-4. They were dated as having a

periodicity of 2-3 kyr, suggesting that the BIS fluctuated in time with the D-O cycles.

Scourse *et al.*, (2000) studied the lithological characteristics of H1 and H2, on a core from the European margin (OMEX 2K; Fig 2.5). They found a chalk fingerprint with a BIS signal predating the H2 Laurentide Ice Sheet (LIS) signal (a carbonate peak) by only 700 – 1000 yrs, suggesting that the European Ice Sheets (EIS) could have played a bigger role in HEs than previously thought. The idea of the EIS causing the LIS discharge was dismissed, as a larger lag time would be needed between the two signals. It was therefore suggested that all the ice sheets responded to the same external stimuli, but the proximity of the core to the BIS ensured that the European icebergs got there prior to the LIS icebergs.

Richter *et al.*, (2001) also found glaciomarine deposits in a core from the western Irish margin. They noticed a series of IRD events rich in detrital carbonate and (meta) sediment rock fragments, indicative of Irish ice and ice streams which can be correlated to Irish terrestrial evidence of ice sheet retreats and advances.

Kirby & Andrews (1999) analysed the characteristics of H3 and H4 and their surrounding sediments from a Labrador Sea core. They found that the ice margin prior to H4 extended further than before either H1 or H2, and, that the collapse associated with H4 was so massive that the Hudson Strait was completely gutted of ice. The ice did not have time to advance to its original position before H3, explaining the more European-like signal to H3.

2.4.3 Summary

In summary, all Heinrich Layers appear to show some degree of a multi-source provenance signal, but in varying quantities (Rahman, 1995; Revel *et al.*, 1996; Gwiazda *et al.*, 1996a & b; Snoeckx *et al.*, 1999; Grousset *et al.*, 2001) H1, H2, H4 & H5 appear to be predominantly LIS in origin (Hemming *et al.*, 1998), whereas H3 is dominantly European in origin (Snoeckx *et al.*, 1999). A three-step

structure to the HEs has also been proposed by some workers where, firstly a European/Icelandic precursor (Snoeckx *et al.*, 1999; Grousset *et al.*, 2000; Grousset *et al.*, 2001) is followed by a LIS main event (Snoeckx *et al.*, 1999; Scourse *et al.*, 2000; Grousset *et al.*, 2001), and finally an input of Baffin Bay material (Revel *et al.*, 1996; Grousset *et al.*, 2001).

The reason for the more European signal in H3 has been suggested as a complete gutting of the Hudson Strait during H4. The ice did not have sufficient time to advance that far again and the LIS iceberg supplies were therefore depleted during H3 (Kirby & Andrews, 1999). It has also been suggested that the HEs are a response, primarily of the LIS to the Bond cycles, and that the smaller IRD events identified by Bond & Lotti (1995), are the result of smaller, coastal ice sheets (the BIS, Iceland Ice Sheet etc) responding to the D-O cycles (Elliot *et al.*, 1998; Grousset *et al.*, 2001; Knutz *et al.*, 2001; Richter *et al.*, 2001).

The consensus as to the sequence of events during a HE is yet to be determined, but current evidence does tend to suggest a structure individual to each HE (Auffret *et al.*, 1996; Cortijo *et al.*, 1997; Lagerklint & Wright, 1999).

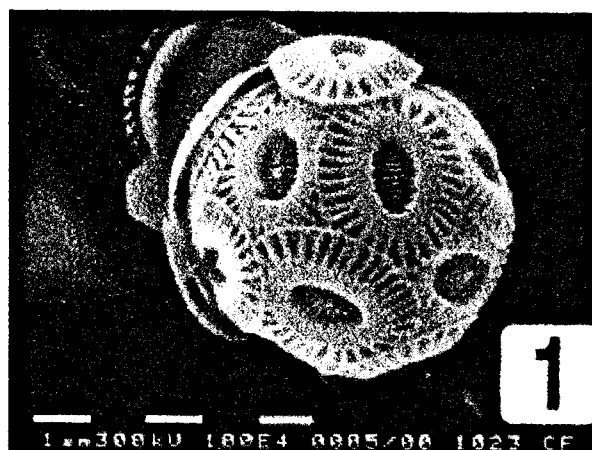


Fig. 2.15: SEM image of a nannofossil (*Emiliana huxleyi*)(Findlay & Giraudeau, 2000)

Table 2.5: Common mineral magnetic parameters, and their interpretation (Thompson & Oldfield, 1986; Maher, 1988; Oldfield, 1991; King & Channell, 1991; Verosub & Roberts, 1995; Stoner et al., 1996; Dekkers, 1997; Dunlop & Ozdemir, 1997; Lowe & Walker, 1997; Dearing, 1999; Smith, 1999; Tarling & Turner, 1999; Shu et al., 2001; Evans & Heller, 2003).

Parameter	Interpretation
Magnetic Susceptibility (χ)	A measure of how easily a material can be magnetised. This is directly proportional to the concentration and grain size of ferro- and ferrimagnetic minerals present. It can therefore be used to identify the types of minerals present as well as their concentrations. χ increases with increasing grain size. Units = $10^{-8} \text{m}^3 \text{kg}^{-1}$
Frequency Dependence Susceptibility (χ_{fd})	The difference between mass specific magnetic susceptibilities measured at different frequencies. An indication of the presence of superparamagnetic grains (SP) is given if values rise above ~6%. Units = %
Anhyseretic Remanent Magnetism (ARM)	This is the magnetisation of a sample acquired in a biasing DC field within a decreasing field. It is very sensitive to variations in grain size, particularly in the single domain size. It is usually expressed as χ_{arm} (i.e. normalised for the size of the biasing field) for comparative reasons. Units = $10^{-5} \text{m}^3 \text{kg}^{-1}$.
Isothermal Remanent Magnetism (IRM)	A measure of the intensity of the magnetisation remaining in a sample after removal from a magnetic field. Can be expressed as low field (e.g. 40mT field), or high field ($\geq 300 \text{ mT}$). Can be indicative of mineral type as different types respond to different field sizes. Units = $10^{-5} \text{Am}^2 \text{kg}^{-1}$.
Saturated Isothermal Remanent Magnetisation (SIRM)	The magnetisation at which the sample becomes saturated after exposure to varying IRMs i.e. it will magnetise no further. It is primarily dependent on mineral concentration and grain size (value increases with decreasing grain size), and is often the name given to the highest field exposed to the sample. Units = $10^{-5} \text{Am}^2 \text{kg}^{-1}$.
Saturation Magnetisation (M_s) or Sample Remanence (M_r)	The saturation magnetisation of a sample is a measure of its magnetisation when it is still in the presence of the inducing field (as opposed to its remanence, once it's been removed from the field = SIRM). The sample remanence is the measurement of a sample's magnetization at lower than saturation fields (IRM equivalent). Units for both = $\text{Am}^2 \text{kg}^{-1}$ (mass normalised).
Coercive Force ($(B_0)_c$) and Remanent Coercivity ($(B_0)_{cr}$).	The coercive force is the size of the field required to reverse the saturation magnetisation to zero. It is not an actual "force". The remanent coercivity is the field needed to obtain a remanence of zero after the removal of the field. This requires a large negative field. Units for both = Am^{-1} .
Viscous Remanent Magnetisation (VRM)	A VRM is the resulting magnetisation within a sample during exposure to a new magnetic field, or the gradual change of the initial magnetisation over time. It can often occur as magnetic particles realign themselves a new field direction during storage, or due to superparamagnetic grain relaxation (see Dunlop & Ozdemir, 1997 for further details).
Thermoremanent Magnetisation (TRM)	A magnetization acquired by cooling from a high temperature. This can occur naturally during the material formation, or through laboratory inducement. Indications of the mineralogy of a sample can be gained through its high or low temperature behaviour. A TRM is also very stable, and so will record the lineation of the field in which it was acquired, and be proportional to its size.

2.5 Environmental Magnetic Analysis

Introduction

Environmental magnetism involves the application of rock and mineral magnetic techniques to situations in which the transport, deposition, or transformation of magnetic grains is influenced by environmental processes in the atmosphere, hydrosphere and lithosphere (Verosub and Roberts, 1995). In a pioneering early paper, Thompson *et al.*, (1980) introduced the idea of applying extensive magnetic measurements to environmental studies, when they illustrated the use of the basic parameters of magnetic susceptibility (χ), saturation isothermal remanence magnetisation (SIRM) and remanent coercivity ($(B_o)_{CR}$) on sediment samples from a range of environments such as the atmosphere, lithosphere and lacustrine settings. While Mackareth (1971) had documented the variation in Natural Remanent Magnetisation (NRM; see Section 2.5.1 below) recorded in lacustrine sediments on a 2700 year frequency and suggested that lake sediments can record directional changes in the horizontal component of the Earth's magnetic field, it was the Thompson *et al.*, (1980) paper that led the way for further research and shortly after, Thompson and Oldfield (1986) published a major review of the techniques and the potential applications.

Environmental magnetic techniques have a great many uses. The methods are now routinely applied in a variety of research contexts, including palaeoclimate studies (e.g. Chinese Loess Plateau analysis, Heller and Liu, 1984; Maher and Thompson, 1992; Forster and Heller, 1997), palaeoceanographic studies (e.g. magnetic analysis of marine sediments, Karlin *et al.*, 1990a, 1990b; Bloemendal *et al.*, 1992; Stoner *et al.*, 1996), provenance analysis of sediments (e.g. Yu & Oldfield, 1989), studies of anthropologically-induced pollution (e.g. Hunt, 1986) and archaeological investigations (e.g. Sternberg, 1987; McClean and Kean, 1993; Batt, 1999).

The speed of the techniques and the simplicity with which they can be applied are just two of the reasons why environmental magnetism has such appeal to the

environmental scientist (Oldfield, 1991; Dekkers 1997). Other advantages are that the methods are inexpensive, non-destructive to the sediment or sample, and they can be used in a range of environments, for a range of needs. Additionally, in many circumstances, the sample preparation is simple, and the measurements extremely sensitive, so even ultra-fine minerals with compositions in the order of 0.5% iron can be detected (Dekkers, 1997). This makes magnetic analysis two or three times more sensitive than routine XRD analysis. The techniques also have the propensity to address problems currently inaccessible to other scientific methods (e.g. chemical analysis, XRD and spectroscopy (Oldfield, 1991; Verosub and Roberts, 1995)). Magnetic measurements have also been successful in characterising sediments for lithological correlation and provenance indication to a comparable level as more traditional forms of analysis e.g. XRD, XRF and heavy mineral analysis (Walden *et al.*, 1996).

2.5.1 Measurements used in Environmental Magnetism

Below, and in Table 2.5 is a discussion on the major parameters measured during routine environmental magnetic analysis.

Rocks, sediments and soils often acquire a magnetic remanence through natural processes, generally during their formation. This is known as a Natural Remanent Magnetisation (NRM), and often reflects the Earth's Geomagnetic Field at the time of formation (Dekkers, 1997; Thompson & Oldfield, 1986). The NRM was the initial focus of attention during early studies of magnetoclimatology, however it wasn't long before other magnetic properties began to be investigated and found to be more useful (Thompson *et al.*, 1980; Evans & Heller, 2003).

One of the most widely and routinely used magnetic measurements is that of magnetic susceptibility (κ or χ). Susceptibility is a measure of how easily magnetised a material is, and is primarily dependent on magnetic concentration (ferrimagnetic content)(Table 2.5)(Lindsley *et al.*, 1966; Thompson & Oldfield, 1986; Verosub & Roberts, 1995). It is also influenced by both the magnetic

assemblages present, and their grain sizes (Lindsley *et al.*, 1966; Walden, 1999a). Ferrimagnetic minerals (such as magnetite and maghaemite) have higher susceptibilities than antiferromagnetic minerals (e.g. haematite). However, when ferrimagnetic minerals are scarce, other minerals (even only slightly magnetic ones) can contribute significantly to χ , though the actual value will still be relatively low (Thompson & Oldfield, 1986).

By measuring susceptibility at different frequencies (0.46kHz and 4.6kHz - low frequency and high frequency respectively - are used by the Bartington equipment used in this study), it is possible to identify the presence of fine-grained magnetic particles within a sample. High frequency susceptibility (χ_{hf}) will have a slightly lower value than the low frequency susceptibility (χ_{lf}) when fine-grained super-paramagnetic (SP) particles are present (Dearing, 1999) Super-paramagnetic grains (0.001-0.03 μm) are ferrimagnetic or anti-ferromagnetic grains that, due to their size, do not hold a magnetic remanence (Thompson & Oldfield, 1986; Tarling & Turner, 1999). The difference between the two susceptibility frequencies is called the frequency dependence of susceptibility (χ_{fd})(Table 2.5). Materials dominated by coarse-grained minerals should display χ_{fd} values of zero, whilst samples with a significant presence of ultra-fine SP grains will show values of >6% (Dearing, 1999).

Anhyseretic Remanent Magnetisation (ARM)(Table 2.5) is another grain size parameter, but is most useful when used in combination with other parameters, such as χ and Saturation Isothermal Remanent Magnetisation (see below). ARM is responsive to the concentration of single domain ferrimagnetic grains (SD < 0.01 μm), when corrected for the influence of the field the magnetisation was grown in (expressed as χ_{arm})(Dunlop & Özdemir, 1997; Verosub & Roberts, 1995; Evans & Heller, 2003). When normalised for concentration (χ_{arm}/χ), it becomes a grain size indicator for ferrimagnetic minerals, which if used with care, is especially useful if SP grains are present (Verosub & Roberts, 1995; Evans & Heller, 2003). The ratio of ARM/SIRM is also influenced by the grain size of magnetite; samples with a large SD fraction present will yield higher ratios (Evans & Heller, 2003).

Isothermal Remanent Magnetisation (IRM)(Table 2.5) is the level of magnetisation acquired by a specimen after it has been exposed to a given magnetic field (Thompson & Oldfield, 1986; Dunlop & Özdemir, 1997; Tarling & Turner, 1999). The magnitude of the remanence is dependent on the strength of the magnetic field applied, as well as the mineral types within the sample (Thompson & Oldfield, 1986). A sample will become “saturated” when the material has become as magnetised as its mineralogy will allow, meaning that the IRM will no longer increase even if stronger fields are used (Verosub & Roberts, 1995). The highest IRM value is termed the Saturation Isothermal Remanent Magnetisation (SIRM)(Table 2.5), and is a measurement of the magnetisation left in a sample once it has been removed from the maximum inducing field (Thompson & Oldfield, 1986). It must be remembered, however, that while SIRM is the name given to the magnetisation corresponding to the highest field used in a given study, in some laboratories, this field may only be 1 Tesla (T). Many magnetic minerals may not be ‘saturated’ as a result of this field strength.

Used in isolation, SIRM is mainly a measure of ferrimagnetic content, though it can be influenced by other minerals, (a high concentration of the other grains will lower the SIRM), and grain size (e.g. SIRM is higher for SD grains than multidomain grains (MD = $>10\ \mu\text{m}$) for magnetite). When combined with χ , it is normalised for (ferrimagnetic) concentration and can be a good grain size indicator, varying indirectly with size (King & Channell, 1991). An increase in SIRM/χ suggests a decrease in grain size, however, workers must be aware that as SP grains have high χ values but low SIRM/χ values ($<0.01\ \text{kAm}^{-1}$), they can become confused with MD grains if this parameter is used alone (Thompson *et al.*, 1980; Thompson & Oldfield, 1986). Additionally, the ratio SIRM/ARM varies directly with grain size (King & Channell, 1991).

Once a sample has been saturated, it can be exposed to more IRM fields in the opposite direction to the previous fields. These are termed backfields and can be used as a mineralogical tool (Thompson & Oldfield, 1986; Evans & Heller, 2003). A ratio known as the 100 backfield ratio (also known in some cases as the S-

ratio), is IRM at 100mT backfield normalised by SIRM ($IRM_{100}/SIRM$). It is used to identify the relative importance of hard (antiferromagnetic) to soft (ferrimagnetic) minerals, the idea being that the ferrimagnetic minerals should be saturated by 100 mT, therefore any remanence left will be due to antiferromagnetic grains (Thompson & Oldfield, 1986).

It must be made clear that SIRM is different to another parameter often used, called the Saturation Magnetisation (M_s)(Table 2.5). This is a measurement of the magnetisation of a sample whilst it is still in the presence of the saturation magnetic field, M_s is a size independent parameter, particularly useful when combined with SIRM or χ . Values of M_s for pure magnetite are around the 480 kAm⁻¹ area, whilst values of haematite are c.2.5 kAm⁻¹ (Thompson & Oldfield, 1986), and pyrrhotite are c.15 kAm⁻¹ (Rochette *et al.*, 1990).

There are two other parameters often used in magnetic analysis, especially in conjunction with saturation magnetisation; the coercive force ($(B_o)_c$) and remanent coercivity ($(B_o)_{cr}$)(Table 2.5). $(B_o)_c$ is the size of the field required to reduce a magnetisation to zero (similar to an IRM backfield, except the magnetisation is measured while the field is still present)(Smith, 1999), whereas $(B_o)_{cr}$ is the size of the field required to reduce the remanent magnetisation to zero (i.e. once the field has been removed)(Thompson & Oldfield, 1986; Evans & Heller, 2003). $(B_o)_{cr}$ usually requires a larger negative field than $(B_o)_c$ (Evans & Heller, 2003). These two parameters are mainly influenced by ferrimagnetic grain size (Thompson & Oldfield, 1986; Smith, 1999)

More details on these various measurements and their associated ratio can be found in Section 4.4 and Table 4.9.

2.5.2 Environmental Magnetism in Sediments

Variations in the magnetic properties of sediments reflect changes in the composition, concentration and grain size of magnetic minerals present in the

material (Thompson & Oldfield, 1986; Stoner *et al.*, 1996; Dearing, 1999). For example, in a lake sediment sequence, down-core variations in the parameters arise from changes in detrital input (e.g. aeolian, ice rafting etc.), provenance, land use and erosion, biogenic dilution and post-depositional changes such as authigenesis (the *in-situ* formation of sedimentary materials) and diagenesis (the compaction and cementation of sedimentary materials)(Karlin, 1990b; Lean & McCave, 1998; Stockhausen & Zolitschka, 1999; Watkins & Maher, 2003).

Given its wide applicability within a variety of environmental contexts, the rapid and inexpensive nature of the analysis, and the ubiquitous nature of iron oxides within many environmental systems, magnetic analysis is slowly becoming a popular tool with which to study sediments.

Lake Sediments

Lake sediments are composed of material from different origins that have arrived by a variety of transport pathways (e.g. bedrock weathering, soil erosion, fluvial transport, volcanic activity and wind transport), which has resulted in a range of magnetic signatures for the lake sediments themselves (Mackereth, 1971; Thompson & Oldfield, 1986). Magnetic measurement have, both despite and because of this, helped to reconstruct the erosional history of catchment areas and from that, their vegetational, land use and climatic evolution (Thompson & Oldfield, 1986).

The most basic mineral magnetic measurement is magnetic susceptibility (Table 2.5). Measured on either a volume or mass-specific basis (Section 2.5.1), it can provide a quick and simple way to identify down core mineral variations. These, in turn, can be attributed to changes in sediment source, climate variations or the result of a change in land use (Thompson & Oldfield, 1986; Eriksson & Sandgren, 1999). It is also a useful tool for cross core correlation (Thompson *et al.*, 1980). It has been possible to correlate susceptibility traces with changes in pollen records, particularly grass pollen, indicating that there is a link between magnetic mineral concentration and vegetation (Pennington *et al.*, 1972).

A number of examples can be given that demonstrate the usefulness of magnetic measurements within a lake sediment context. For instance, several studies of Lough Neagh, Northern Ireland have taken place, (e.g. Thompson, 1973; Thompson *et al.*, 1975; Dearing & Flower, 1982). Thompson *et al.*, (1975) noted that IRM could identify the magnetic minerals present in the lake and that susceptibility could not only correlate between cores, but is also directly related to the rate of erosion in the basin, and therefore, the pattern of erosion could be deduced. After comparing magnetic susceptibility to the chemical and pollen changes within the sediments, they were able to suggest that χ is directly and positively linked to the amount of inorganic material being washed into the lake from the surrounding catchment area, which, in turn, is an indication of changing land use. The authors also stressed that this is only a record for Lough Neagh and that the link may not work in all cases. Susceptibility peaks were found to correspond to rainfall maximums and are assumed to represent hydrological and erosional controls such as deforestation and cultivation (Dearing & Flower, 1982).

The link between erosion and χ had previously been found in a study of Loch Lomond by Thompson & Morton (1979). They noticed that down-core susceptibility variations were related to grain size i.e. peak susceptibilities were recorded by fine particles (see Section 2.5.1), indicating increased erosion of fine surface particles due to deforestation, and was validated with pollen analysis (Thompson & Morton, 1979).

A study of Lough Fea, also in Northern Ireland (Thompson & Oldfield, 1986) showed that SIRM measurements correlated with chemical indicators of erosion, e.g. Potassium, Sodium and Magnesium (Mackereth, 1966), suggesting again that magnetic minerals are linked to erosion, and therefore vegetation and land use. The study also showed that magnetic minerals within lacustrine environments are sensitive to climate, particularly at the Pleistocene-Holocene boundary, and human activity.

Several authors (Peck *et al.*, 1994; Thouveny *et al.*, 1994; Rosenbaum, 1996; Vlag *et al.*, 1996) used magnetic methods on lake sediments to try to identify the glacial-interglacial cycles within the Pleistocene. For example, Thouveny *et al.*, (1994) analysed the magnetic properties of lacustrine cores from the Massif Central, France, and compared the results with the ice core records from the GRIP project (Fig. 2.16). The susceptibility results were plotted against the $\delta^{18}\text{O}$ measurements for the GRIP ice core. The correlation was very good, with climate oscillations present that have similar wave-lengths and time-scales with the marine isotope stages, reinforcing the idea that lake sediments can record climatic behaviour.

Glacial Sediments

A number of workers have attempted to use magnetic measurements, especially magnetic susceptibility, as a provenance tool in studies of glacial sediments (e.g. Vonder Haar & Johnson, 1973; Gravenor & Stupavsky, 1974; Chernicoff, 1983; Walden *et al.*, 1987; 1992; 1996). As in other sedimentary environments, the success, or otherwise, of the method, is dependent on measurable and distinctive lithological differences within the range of possible source areas (Oldfield, 1999). In a series of papers, Walden *et al.*, (1987; 1992; 1996) undertook a study of the glacial diamicts on the Isle of Mann using the magnetic parameters of susceptibility, SIRM and coercivity. It was found that the characteristics of both the clasts and matrix components within the diamict assemblage studied could be used for both site correlation and, at a broad level, provenance indication. The data obtained suggested sediment sources that were consistent with more traditional field data (e.g. till fabrics) for the same sediments. The compositional relationships between the various diamict samples suggested by their environmental magnetic properties were also consistent with those based upon more traditional compositional methods such as clast lithological analysis, heavy mineral analysis, XRF and clay XRD (Walden *et al.*, 1996). Walden & Addison, (1995) have also used magnetics to evaluate the weathering history of glacial sediments in North Wales successfully.

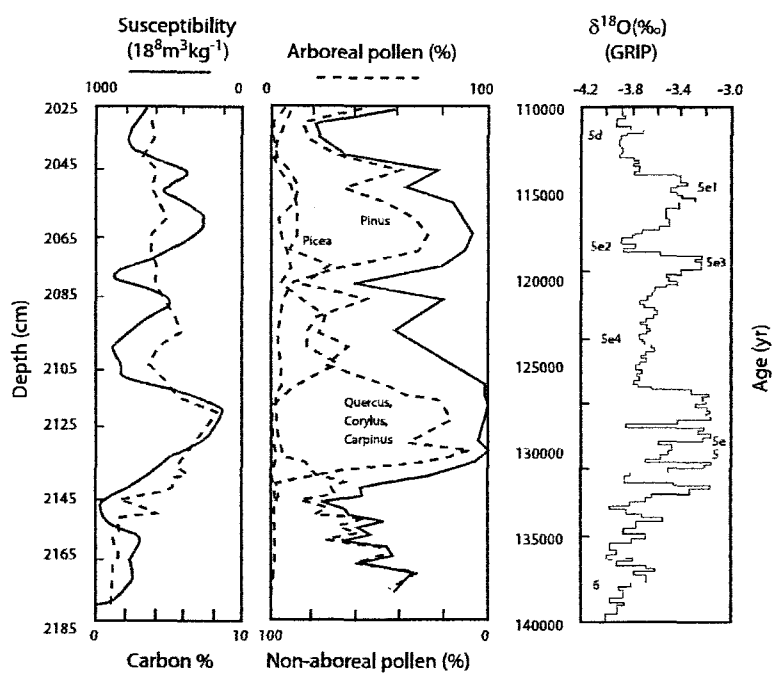


Fig. 2.16: Susceptibility, organic carbon and pollen data for Lac du Bouchet (Central Massif, France) against the GRIP $\delta^{18}\text{O}$ data (re-drawn from Thouveny *et al.*, 1994).

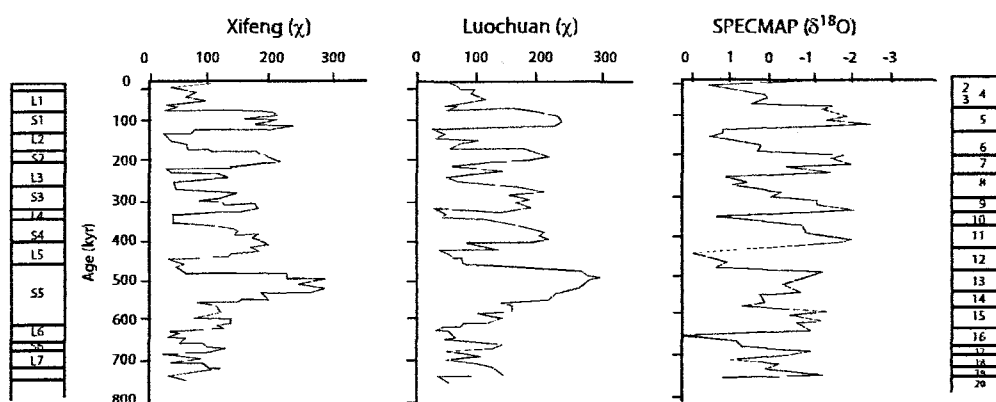


Fig. 2.17: The susceptibility record of two sites in the Chinese Loess Plateau and the SPECMAP Oxygen Isotope curve. On the right are the successive loess (L) and palaeosol (S) sequences, on the left are the marine isotope stages (re-drawn from Verosub & Roberts, 1995).

Walden & Ballantyne (2002) assessed the possibility of using magnetic techniques to identify glacial trim-lines (former maximum ice-surface altitudes) and found that the magnetic parameters show distinctive signatures between samples above and below the trim-lines, though the difference is ultimately dependent on lithology. For example, Walden & Ballantyne (2002) found that concentration-dependent parameters were higher above the trim-line than below for basalt, but lower above than below for sandstone. It was thought that the different responses of the two lithologies to periods of long-term sub-aereal weathering/pedogenesis was the cause.

Soils and Loess

Magnetic measurements in soils are very responsive to both the particle size of the magnetic components (the magnetic grain size) and the overall particle size distribution of the soil (Mullins, 1997). As described above (Section 2.5.1) a number of magnetic parameters are sensitive to the magnetic grain size and can be used to draw inferences as to the presence of ultra-fine magnetic particles. However, this sensitivity also makes bulk soil measurements more difficult to interpret than measurements made on single grain size fractions (Thompson & Oldfield, 1986). Walden and Slattery (1993) demonstrated how variations in particle size properties may influence bulk magnetic properties of a sample. This issue is complicated, however, by the fact that some magnetic grains (themselves fine grained) may be present as an inclusion within larger host grains and will not be easily segregated by standard laboratory procedures used to achieve separation of discrete size fractions for magnetic analysis (Walden & Slattery, 1993).

Perhaps the most significant application of magnetic measurements within the context of soils is in analyses of loess sediment sequences. Loess is a climatically sensitive wind blown deposit and, as with marine sediments, can form a major archive of evidence for palaeoclimatic variation through the Quaternary (Zhu *et al.*, 2004). The actual character of a loess or palaeosol sequence is a direct result of the climatic action on the dust arriving at the area. An immense amount of

research has taken place on loess deposits during the last 20 years or so (Balsam *et al.*, 2004).

The identification of pedogenically produced ultra-fine grained magnetite has proved central to the interpretation of many loess sediment sequences, particularly the extensive loess-palaeosol sediments within China which are thought to provide a continuous sedimentary record spanning the whole of the Quaternary (Maher *et al.*, 1999). Magnetic susceptibility variations in loess sequences can be correlated to the oscillations within the deep-sea oxygen isotope stages of the Pleistocene (Liu *et al.*, 1995; Dunlop & Özdemir, 1997; Tang *et al.*, 2003). Loess sequences in the Chinese Loess Plateau, Tajikstan and the Czech Republic consist of alternating layers of loess, indicating cold, dry glacials or stadials, and palaeosols, indicating warm and humid interglacials or interstadials (Evans & Heller, 1994; Maher, 1998; Heslop *et al.*, 2002). The palaeosols are more magnetic than the loess, with higher susceptibilities, a higher NRM, and a higher Viscous Remanent Magnetisation (VRM)(Table 2.5, Fig. 2.17, Verosub & Roberts, 1995). While several explanations for these variations have been proposed, Maher & Thompson (1992) identified the presence of ultra-fine grained magnetite similar in form to that formed by pedogenesis in other soil environments.

Examination of the magnetic properties of loess has made it possible to reconstruct past climate records from the complete sediment sequence, including rainfall records (Banerjee *et al.*, 1993). Maher & Thompson (1992; 1999) have studied the Chinese Loess Plateau in great detail. They were able to create an accurate chronology to the sequence using the strong correlation between the magnetic susceptibility of the loess and the $\delta^{18}\text{O}$ record from a Pacific Ocean core. This correlation suggested that both were linked to the same climatic signal. Maher & Thompson (1992, 1999) used the magnetic parameters of susceptibility, SIRM, IRM and ARM to calculate palaeo-rainfall and reconstruct the climate evolution over the Quaternary. Maher *et al.*, (1994) noticed that the rainfall today matches the current ferrimagnetic iron-oxide content in the soil of the Chinese

Loess Plateau. Therefore, using susceptibility to calculate the concentration of ferrimagnetic minerals present over time, it was possible to make assumptions about the rainfall (Dekkers, 1997). Low temperature measurements of susceptibility and Thermoremanent Magnetisation (TRM)(Table 2.5) can differentiate between magnetic grain sizes of magnetite and haematite. Such measurements have helped in the determination of weathering processes at work in Asian Loess-Palaeosol sequences, due to the strong relationship between the destruction of the paramagnetic signal, the enhancement of the ferrimagnetic signal, and weathering processes such as the diagenetic formation of iron oxides (Sartori *et al.*, 1999).

The Alaskan Loess record is the reverse of the Chinese record, with the less magnetic palaeosols forming during wet and humid interglacials/interstadials, whilst the highly magnetic loess formed in colder, drier glacials/stadials (Begét *et al.*, 1990; King & Channell, 1991; Maher, 1998; Muhs *et al.*, 2003). One of the explanations for this is the “wind vigour” model (Evans & Heller, 2001; Liu *et al.*, 2003a). At higher latitudes (e.g. Alaska, Siberia, and Southern Argentina), glacial winds were stronger due to a higher temperature gradient between the poles and the tropics (Parkin, 1974). The stronger winds are assumed to be more effective at transporting dense iron-oxide grains, and therefore result in a higher concentration of magnetic minerals and a higher susceptibility at the poles (Begét & Hawkins, 1989; Begét *et al.*, 1990; Evans & Heller, 2001). Other reasons suggested were the gleying of the palaeosols preventing the formation of (or leading to the destruction of) magnetic minerals (Evans & Heller, 2001); or weathering during pedogenesis (Begét *et al.*, 1990).

Marine Sediments.

Due to the undisturbed nature of marine sediments (Lowe & Walker, 1997), they have the potential to provide excellent records of past environments (Seibold & Berger, 1982). Combined with the sensitive nature of magnetic techniques, a very accurate chronological sequence of oceanic and climatic conditions can be formed

(Verosub & Roberts, 1995). The magnetic properties of marine sediments are controlled by biogenic dilution, sediment source and sediment transport mechanisms, along with possible diagenetic and authigenic alteration (Lean & McCave, 1998; Stoner & Andrews, 1999; Frederichs *et al.*, 1999). As these factors are ultimately controlled by climate, magnetic properties can be indicators of palaeoceanographic conditions (Bloemendal *et al.*, 1993).

Some workers have found that the authigenic growth and diagenetic alteration of magnetic minerals in sediments can significantly contribute to the magnetic signal (Hilton & Lishman, 1985; Hilton, 1986). Methods have been developed for the identification and quantification of these minerals and will be discussed later.

As with lake sediments, susceptibility is a useful tool for cross core correlation, particularly with the North Atlantic Heinrich Layers (Stoner & Andrews, 1999). Stoner & Andrews (1999) also showed that Heinrich Layers can be characterised using other magnetic parameters such as ARM, IRM and SIRM ratios, and thus the magnetic properties of marine sediments are dependent on sediment source and transport mechanism. This will be explored further later in the chapter.

Wollin *et al.*, (1978) found a link between climate and the intensity of the Earth's geomagnetic field, which they suggested was the result of the Earth's orbit eccentricity causing a weakened dipole changing the Earth's geomagnetic field and somehow effecting climate. This was disproved by Kent (1982) and Bloemendal (1983), who showed that NRM is dependent on the magnetic concentration and composition of the sediments, and not on geomagnetic field intensity (Fig. 2.18). Kent (1982) also proposed that the variations in composition reflect changes in depositional conditions and therefore possibly as a result of climate changes (Fig. 2.18)(Frederichs *et al.*, 1999).

Robinson (1986) reinforced this idea when he compared magnetic parameters (NRM, χ , ARM and IRM, and associated ratios) with climate indicators (CaCO₃ content and $\delta^{18}\text{O}$). He demonstrated that as χ , ARM and IRM are a function of

carbonate content they would ultimately record climate variations. The magnetic variations themselves were an outcome of changing sediment source and fluxes, which are controlled by climate, though it has been established that bacterially precipitated magnetite can dominate the material in calcareous deep-sea sediments, and be a significant source of NRM (Kirschvink & Chang, 1984).

In 1988, Bloemendal *et al.*, made one of the first comprehensive examinations of marine sediments when they analysed 11 cores from the Equatorial Atlantic using χ , IRM and SIRM, NRM, and M_s (see Section 2.5.1 and Table 2.5)(Fig. 2.19). The magnetic measurements seemed well correlated and showed an inverse relationship to the oxygen isotope record. Robinson (1990) showed whole core magnetic susceptibility records for several cores from Leg 115 of the Ocean Drilling Program. It was found that χ is not only a good indicator of palaeoclimate, but can also detect areas in deep-sea cores affected by drilling disturbances, pipe-rust and loss of material between successive core sections.

In 1992, Bloemendal *et al.*, proposed that variations in selected magnetic parameters within marine sediments were due to a) the sediment lithology, b) sediment provenance and c) diagenetic, authigenic and/or biogenic alterations. This was further substantiated by Bloemendal *et al.*, (1993) who suggested that variations in the magnetic properties on sub-Milankovitch timescales were a result of fluctuations in carbonate productivity, transport pathways and mechanisms, and cycles associated with continental aridity/humidity.

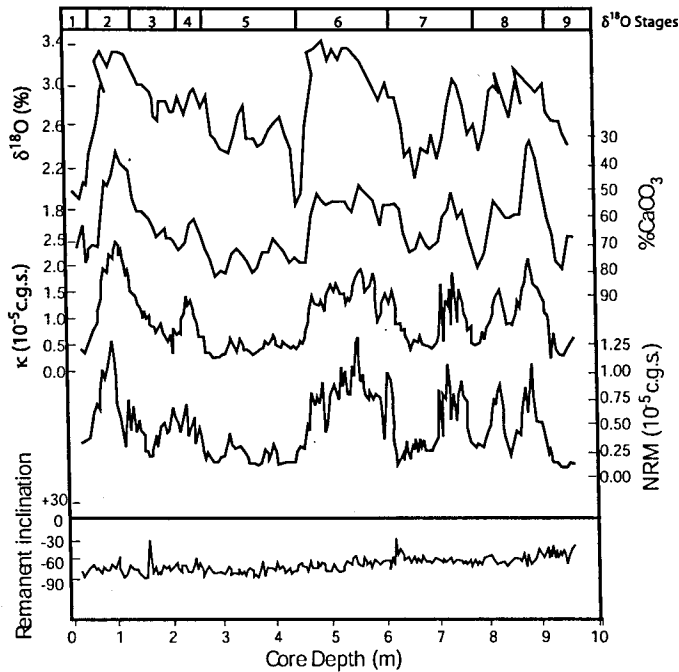


Fig.2.18: Results from Kent (1982 (re-drawn)) showing the NRM of marine sediments compared to depositional and compositional factors.

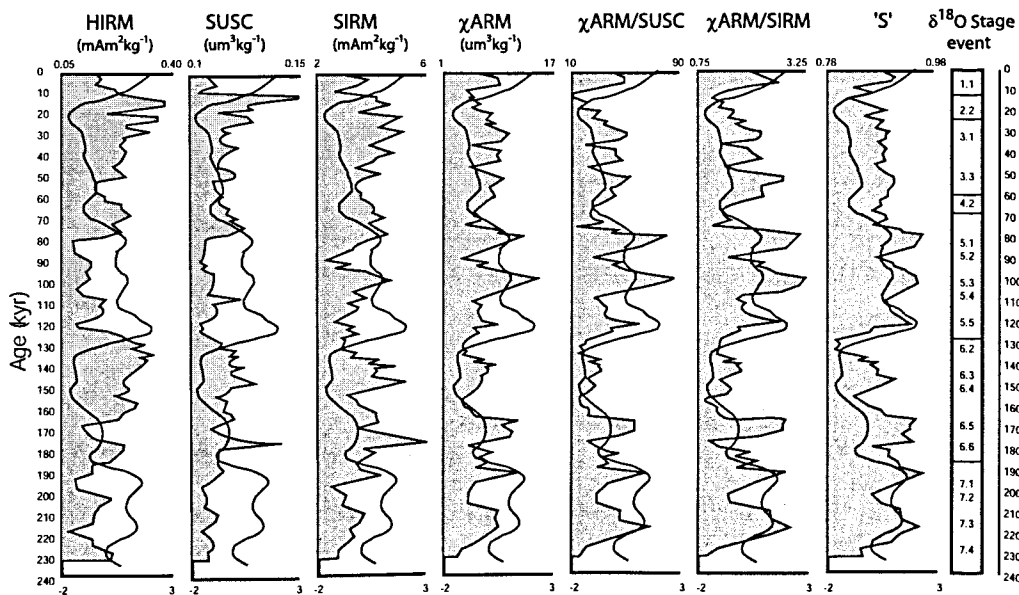


Fig. 2.19: Magnetic characteristics of a sediment core from the Equatorial Atlantic (Re-drawn from Bloemendal *et al.*, 1988). The solid black line on each plot is the relevant part of the SPECMAP Oxygen Isotope curve.

Heinrich Events

Some previous research work has focussed on the mineral magnetic characterisations of Heinrich Events, particularly that of high magnetic susceptibility (Andrews *et al.*, 1993).

Robinson *et al.*, (1995) focussed on magnetic susceptibility variations in a North East Atlantic core and its ability to pick up the Heinrich Layer signal. After comparing the χ to the IRD content, with and without correction for CaCO_3 content, they decided that χ was actually only slightly dependent on CaCO_3 (that is, dilution of the magnetic signal by organic carbonate was not a major concern in the interpretation of the results). They suggested that susceptibility depended much more on the concentration and grain size of the magnetic minerals present as a result of icebergs being able to carry larger quantities of coarser grained material to deep-sea environments, resulting in higher susceptibilities within Heinrich Layers. The χ -IRD link was used on over 80 cores throughout the Atlantic to reconstruct patterns of iceberg flow, and therefore, possible palaeo-surface currents. Robinson *et al.*, (1995) proposed that at the last glacial maximum (LGM) there was a slow, warm current flowing northward between 47° and 62°N which carried the icebergs during H2 to the central IRD belt (45° -52° N, Ruddiman, 1977, Fig 2.5) where they melted.

Thouveny *et al.*, (2000) continued the magnetic examination of Heinrich layers by studying 2 cores (MD95-2039 and MD95-2042) from the Portuguese margin using χ , ARM, IRM, related ratios and HIRM (Fig. 5.20). Using these measurements, they were able to detect a series of lesser IRD layers, which indicated that though ice rafting was a frequent process in this area, it was not always to the extent which produced a full Heinrich Layer (Fig. 5.20). It was concluded that though the parameters showed distinct characteristics at the HLs (Higher χ , higher IRM_{3000} and low $\text{ARM}_{30}/\text{ARM}$), provenance could not be distinguished for the IRD using magnetic measurements alone. The first three HLs in core MD95-2042 show χ signatures of a similar order ($\sim 300 \times 10^{-9} \text{m}^3 \text{kg}^{-1}$, Fig. 2.20), Thouveny *et al.*, (2000) therefore, discount the ability of χ to differentiate origin, based on the

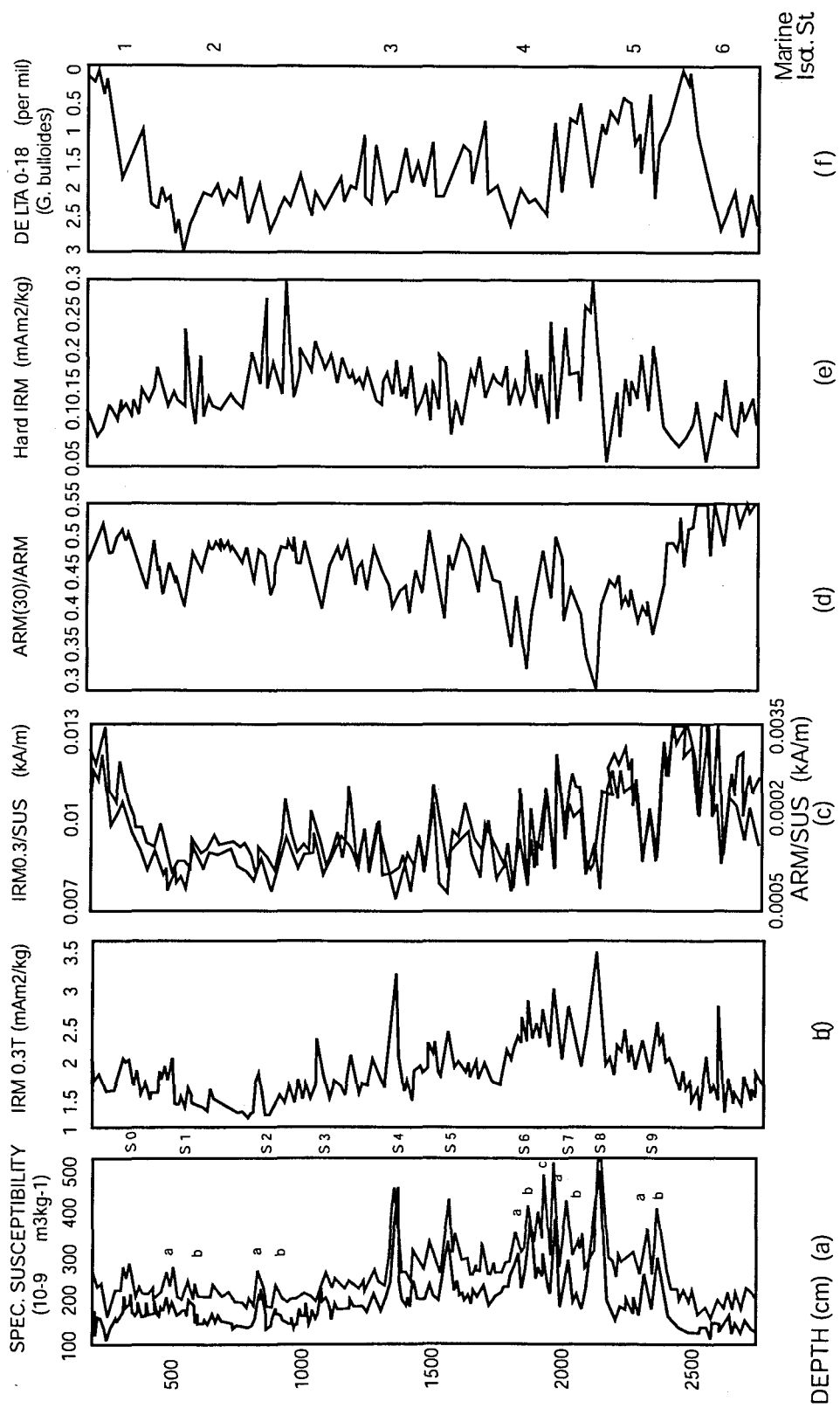


Fig. 2.20: Magnetic measurements made on a core from the Portuguese margin by Thouveny *et al.*, (2000)(re-drawn).

assumption that the LIS is responsible for the high χ in HLs, thus H1 and H2 should have higher χ values than H3 - a pattern that does not actually emerge.

In 1999, Kissel *et al.*, used the magnetic measurements of χ , NRM, IRM and ARM on seven marine cores distributed across the North Atlantic and Nordic Seas. All the cores showed short-term variations on similar levels to each other, and with the Greenland oxygen isotope record. It was suggested that the concentration of magnetic minerals is dependent on the existing climate, due to its interaction with oceanic circulation. From the uniform mineralogy found, they determined that there was only one source for the magnetic minerals within all the cores and therefore suggested that variations in the magnetic parameters had to be due to the efficiency, or mode of transport, namely the deep ocean currents. Low concentrations of IRD were found in the sediments, suggesting limited ice rafting. Wind deposition was also discounted due to the large geographical area covering the cores, leaving oceanic currents as the only acceptable mechanism (Kissel *et al.*, 1999). The HEs in all seven of these cores displayed, in contrary to all other studies, low susceptibility values. Kissel *et al.*, (1999) attributed this to the reduction in oceanic circulation found during stadial intervals, which would reduce the efficiency of the transport method. Six of these cores were from the Nordic Seas, with the seventh from the Bermuda Rise, therefore, they were not in the direct iceberg trajectories from the LIS during the HEs (as shown by the lack of IRD) and the magnetic material must have been transported to the sites by other methods (i.e. oceanic currents, as discussed above). As the high magnetic susceptibility found at the HEs has been attributed to the LIS (Andrews *et al.*, 1993), the lack of LIS material at these locations, combined with the assumption that oceanic currents must have been the dominant transport mechanism to these points, could explain the drop in magnetic susceptibility.

In material from the Portuguese Margin, Moreno *et al.*, (2002) identified discrete layers of very fine titanomagnetite associated with Heinrich Layers, in contrast to sediments containing higher concentrations of haematite/goethite outside the HLs. The variations in titanomagnetite and haematite were found to be directly

linked to cold and warm sections of climate cycles, leading to the suggestion that the titanomagnetite was transported by winnowing bottom currents from a remote source during cold periods, whilst haematite/goethite arrived by river and aeolian transport from the neighbouring continents in warmer times. The specific magnetic characteristics of HEs are similar to those expressed by Thouveny *et al.*, (2000), with high χ and SIRM values and low ARM values.

With the exception of the Kissel *et al.*, (1999) paper, all studies of HEs using magnetic measurements have come up with the same characteristics; a high concentration of coarse-grained ferrimagnetic minerals (high χ and SIRM, and low ARM ratios).

2.5.3 Mineral Identification

The sections above discuss detrital and lithogenic magnetic minerals and their analysis in terms of climatically induced changes to the system they are in. This is an intrinsic part of the study contained in this thesis, and therefore any magnetic minerals in the sediment that are not deposited through this manner, must be accounted for. Two main magnetic minerals are discussed extensively within the literature as forming within marine sediments after their deposition; biogenic magnetite and diagenetic greigite. The next two sections will detail the characteristics of biogenic magnetite and greigite, their importance to the interpretation of magnetic data, and methods for their identification. All other minerals in the marine sediments within this research are thought to be inorganic and detrital in origin, and therefore will not be described here.

Magnetotactic Bacteria

Iron cultivating bacteria in freshwater and marine sediments have been found to orient themselves with, and navigate along the Earth's, or a local, geomagnetic field (Blakemore, 1975; 1982; Frankel *et al.*, 1979; Moskowitz *et al.*, 1988). These magnetotactic bacteria (MTB) have flagella (a long, whip-like appendage used for locomotion; Sinclair, 2001) to aid movement; are aquatic (found in fresh,

brackish and marine waters; Vali *et al.*, 1987); are typically microaerophilic; inhabit the microaerobic sediment layer; and have the ability to synthesise intracellular iron grains known as magnetosomes (Blakemore, 1982; Moskowitz *et al.*, 1988; Zablotskii *et al.*, 2001).

Analysis has shown these magnetosomes to be magnetite in mineralogy (Towe & Moench, 1981; Kirschvink & Lowenstam, 1979; Moskowitz *et al.*, 1988) and of single domain grain size (average width-length ratio of 0.63 (Towe & Moench, 1981; Frankel *et al.*, 1979; 1981; Vali *et al.*, 1987; Moskowitz *et al.*, 1988)). They are usually found in chains with the individual magnetic moments aligned to produce a larger net magnetic moment (Chang & Kirschvink, 1989), and have one of three distinct particle morphologies: sub-rounded cubes and rectangles; elongated hexagonal prisms; and teardrop or irregular shapes, such as bullets and arrowheads (Chang & Kirschvink, 1989; Evans & Heller, 2003)(Fig. 2.21). Thus, they can be distinguished from their inorganic counterparts, which have very different morphologies (Towe & Moench, 1981; Chang & Kirschvink, 1989).

Magnetite, especially in the SD size range, is an important mineral in the world of palaeo- and environmental magnetism, as it is one of the main minerals that hold a stable remanent magnetisation in sediments (Kirschvink & Lowenstam, 1979; Paasche *et al.*, 2004). The potentially different sources of magnetic minerals in sediments have an impact on reconstructing geomagnetic palaeointensities, the appropriateness of empirically derived mixing models for sediment provenance identification, and on the interpretation of climatically modulated magnetic properties (Oldfield, 1992). Therefore, as a study attempting to use environmental magnetic analysis as a means of provenance indication, it is important to identify and, hopefully, quantify the contribution of biogenic magnetite to the magnetic record within the sediments under examination (Kirschvink & Lowenstam, 1979; Blakemore, 1982; Oldfield, 1992). The contribution of MTB to the overall magnetic signal, in lake and marine environments particularly, varies between sites and between cores (Oldfield, 1999; Evans & Heller, 2003). In some cases it might be minor, whilst in others it

could contribute significantly (e.g. Maher & Taylor, 1988; Dunlop & Özdemir, 1997).

For studies only involving pure cultures of MTB, or only looking at the MTB themselves, methods relatively destructive to the sediment can be used. Electron-optical methods, such as transmission and scanning electron microscopy, electron diffraction and electron microprobe analysis have been used (Towe & Moench, 1981; Kirschvink & Chang, 1984; Chang & Kirschvink, 1989; Snowball, 1994) to identify and characterise MTB and their magnetosomes, particularly in deep-sea sediments (Petersen *et al.*, 1986; Stolz *et al.*, 1986). These kind of studies have revealed the characteristics discussed previously and are used, along with sedimentation rates to calculate bacterial abundance.

Rock magnetic analysis on bulk sediments has also been used to try to ascertain the presence of MTB, though most of this has been done using the characterisation of MTB cultures themselves (Petersen *et al.*, 1986; Moskowitz *et al.*, 1993). Petersen *et al.*, (1986) used the functional dependence of the Lowrie Fuller test (see Lowrie & Fuller 1971; Dunlop & Özdemir 1997) on IRM and ARM/IRM to distinguish SD biogenic material from lithogenic material. Bacterial magnetite has Lowrie-Fuller test statistic (ΔLF) values of 4-8 mT (40-80 Oe)(Fig. 2.22). Moskowitz *et al.*, (1993) identified magnetic parameters diagnostic of MTB, consisting of ARM/SIRM with values of 0.15-0.25; δ_{FC}/δ_{ZFC} (the loss of remanence by a sample when cooled through the Verwey transition in the presence of a 2500 mT field (δ_{FC}), divided by the remanence lost when cooled in a zero field (δ_{ZFC})) values of greater than 2; and Wohlfarth-Cisowski test (a test of the relationship between IRM acquisition and af demagnetisation curves for a sample; Dunlop & Özdemir, 1997) statistic (R_{af}) values of >0.5 (Fig. 2.23). Oldfield (1994) added to this the magnetic ratios of χ_{arm}/χ_{lf} and χ_{arm}/χ_{fd} with high values for both indicative of magnetic bacteria ($\chi_{arm}/\chi_{lf} > 40$ and $\chi_{arm}/\chi_{fd} > 1$)(Fig. 2.24). Watkins & Maher (2003) agreed with Oldfield (1994) following extensive analysis of North Atlantic surface sediments.

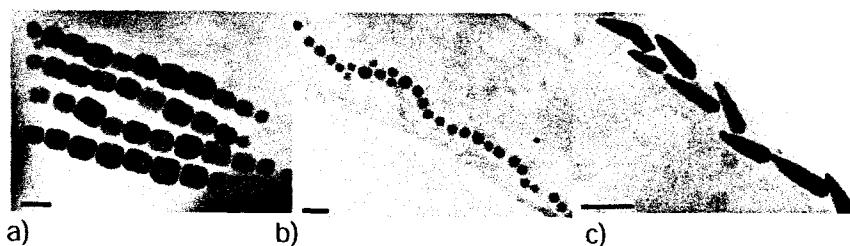


Fig. 2.21: Examples of magnetosome morphology; a) sub-rounded cubes and rectangles, b) hexagonal prisms and c) teardrop shapes (Schuler, 1999; Anon, 2004 - www.mpi-bremen.de).

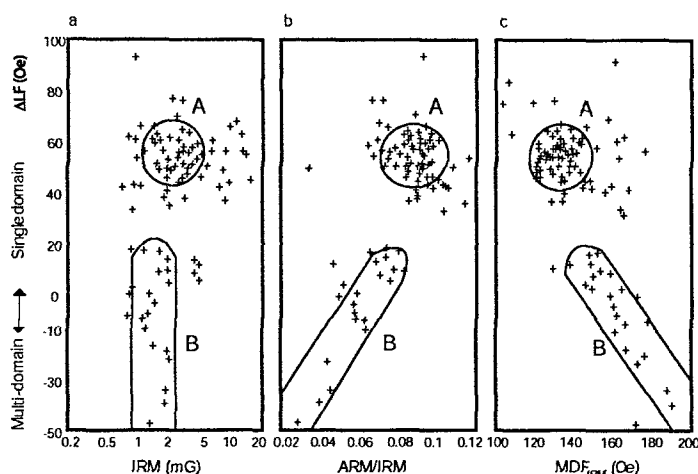


Fig. 2.22: Functional dependence of the Lowrie Fuller test parameter ΔLF against a) IRM; b) ARM/IRM; and c) MDF_{IRM} . Data set A represents single domain particles of biogenic origin, set B contains coarser material and is presumably of lithogenic origin (re-drawn from Petersen *et al.*, 1986).

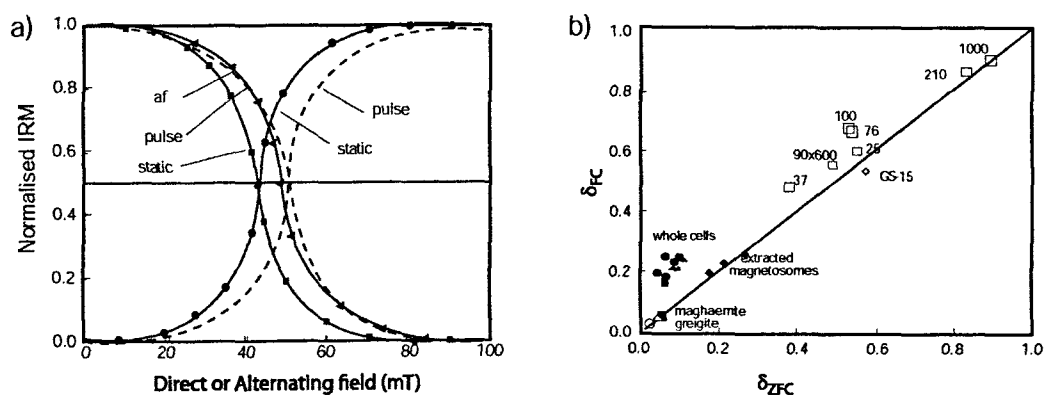


Fig. 2.23: a) Normalised IRM acquisition and demagnetisation. Dot = static acquisition; Solid square = static DF demagnetisation; Circle = pulse acquisition; Square = pulse DF demagnetisation; Triangle = AF demagnetisation; (Wohlforth Cisowski test) (re-drawn from Moskowitz *et al.*, 1993). b) δ_{fc} versus δ_{zfc} for biogenic and inorganic samples. Numbered samples are lithogenic in origin (re-drawn from Moskowitz *et al.*, 1993).

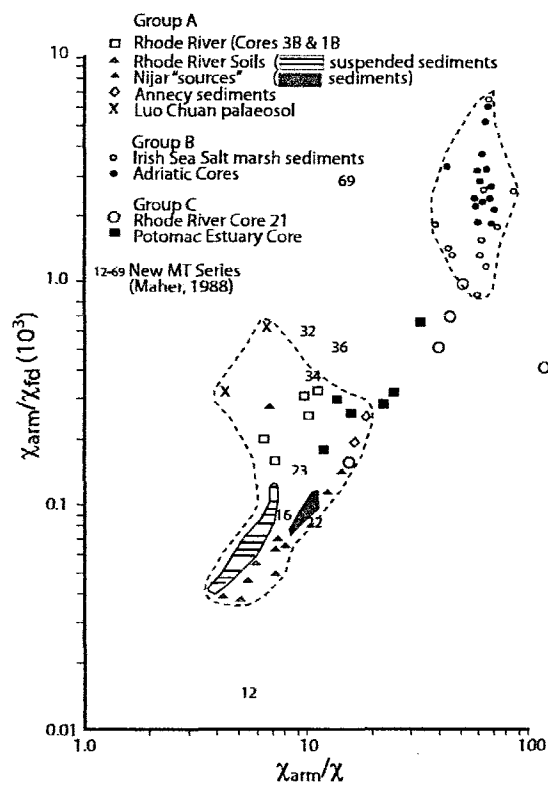


Fig. 2.24: Plot of χ_{arm}/χ versus χ_{arm}/χ_{fd} . Two groups are apparent: A (see legend) are detrital in origin, whilst B are bacterial (Oldfield, 1992).

The above are recent advances, and have had little testing. They therefore must be treated with caution. Further explanation of the methods employed in this study can be found in Section 4.4 and Table 4.9.

Greigite

Greigite (Fe_3S_4) is a ferrimagnetic iron sulphide mineral that forms in sulphate reducing sedimentary environments (Roberts, 1995; Sagnotti & Winkler, 1999). It was first identified as a new mineral in 1964 by Skinner *et al.*, until then being known as melnikovite, a form of pyrite (FeS_2) and not a mineral in its own right (Lee & Jin, 1995; Roberts, 1995). Greigite forms by the process of diagenesis (post depositional changes to sediments; Whittow, 1984) at the expense of detrital iron-bearing minerals, especially magnetite in shallow burial (Roberts & Turner, 1993; Hallam & Maher, 1994; Roberts, 1995).

Several factors are thought to control the production of greigite. Sulphate reducing conditions are essential, and are themselves dependent on the availability of organic matter or bacteria to produce hydrogen sulphide (H_2S), and an oxygen deficiency (Karlin *et al.*, 1987; Kris *et al.*, 1990; Roberts & Turner, 1993; Horng *et al.*, 1998). Sedimentation rate also affects greigite formation: higher sedimentation rates generally reduce the potential for greigite production as the amount of time magnetic minerals are in contact with sulphate reducing bacteria is reduced and sediments are buried more quickly (Cranfield & Berner, 1986).

Greigite is a chemically stable, remanence-bearing ferrimagnetic mineral (Dunlop & Özdemir, 1997). A magnetic remanence due to the presence of diagenetic greigite will compete with, and possibly obscure the original detrital signal (Karlin *et al.*, 1987; Roberts, 1995). The production of greigite therefore has major implications for palaeomagnetic and palaeoclimatic studies, as they are dependent on the detrital signal. Any alteration of the mineral magnetic composition of sediments can affect the accuracy and interpretation of palaeomagnetic records and disrupt any mineral magnetic based provenance studies (Karlin *et al.*, 1987;

Snowball, 1991; Roberts, 1995). Hilton and Lishman (1985) and Hilton (1986) have also found that magnetic minerals formed in reducing conditions and can account for up to 70% of the magnetic signal in a sediment.

Greigite is a very distinct mineral and can be identified in a variety of ways. Firstly it oxidises rapidly when exposed to air (Snowball & Thompson, 1988; Hilton, 1990; Snowball, 1991). This can result in a dramatic reduction in magnetic intensity during normal sample storage, shown by losses in χ and SIRM. Snowball & Thompson (1988) measured the susceptibility of a core taken from Llyn Geirionydd, North Wales in 1978, and then again in 1986. There had been a 90% reduction of susceptibility over the 8 years, due to greigite oxidation. Snowball (1991) suggested that the loss in magnetisation could be used as a diagnostic tool for the presence of greigite.

Greigite also has very distinct IRM properties (Peters & Thompson, 1998). Between fields of 40-200 mT, normalized IRM data rises from ≤ 0.02 to ≥ 0.9 (Fig. 2.25a)(Peters & Thompson, 1998), and reaches saturation by 300 mT (Fig. 2.25b)(Kris *et al.*, 1990; Hallam & Maher, 1994). Greigite also shows a loss of magnetisation on heating to around 200°C, which can be used as an identifying property (Fig. 2.26)(Snowball & Thompson, 1988; Sagnotti & Winkler, 1999).

Snowball (1991) noted that values of $\text{SIRM}/\chi \geq 70 \text{ kAm}^{-1}$ were characteristic of greigite, especially when coupled with low 100 backfield ratios ($\text{IRM}_{100}/\text{SIRM} = \sim 0.8$). SIRM/χ values of haematite and goethite have are similar to those for greigite ($\sim 260 \text{ kAm}^{-1}$ and 57 kAm^{-1} respectively, Peters & Dekkers, 2003), hence the necessity to combine the ratio with other diagnostic parameters. Hallam & Maher (1994) however, suggested greigite displayed SIRM/χ values of 20-50 kAm^{-1} , though SIRM for their study was IRM_{300} , as greigite should reach saturation by then. It has been generally accepted that values around 70 kAm^{-1} are diagnostic of greigite (Oldfield, 1999; Sagnotti & Winkler, 1999). $\text{ARM}_{40}/\text{ARM}$ values of between 0.45-0.85 are also indicative of greigite when used in conjunction with $\text{IRM}_{100}/\text{SIRM}$ ratios of < 0.6 (Peters & Thompson, 1998). Maher *et al.*, (1999)

have suggested that ARM₄₀/ARM values of 0.3 are indicative of greigite, but only when combined with SIRM/ χ values of $>70 \text{ kAm}^{-1}$.

Roberts & Turner (1993) also used a combination of SIRM (IRM₈₀₀ mT) and χ ; values of $11\text{-}12 \cdot 10^{-4} \text{ Am}^2 \text{ kg}^{-1}$ for SIRM and $11\text{-}12 \cdot 10^{-8} \text{ m}^3 \text{ kg}^{-1}$ for χ , are indicative of greigite (Fig. 2.27). Peters & Thompson (1998) presented a comprehensive study of the magnetic minerals magnetite, titanomagnetite, haematite, pyrrhotite and greigite, in order to find magnetic parameters to distinguish them. Both greigite and pyrrhotite were found to have high SIRM/ χ values (pyrrhotite the higher), but as greigite has a higher ARM stability, it is possible to distinguish between the two using ARM₄₀/ARM. Peters & Thompson (1998) used the above ratios and properties of magnetic minerals to draw biplots for the identification of several common minerals, including greigite. Fig.2.28a & b shows these biplots and demonstrated their usefulness in assessing the presence of the various magnetic minerals.

As with the analysis into magnetotactic bacteria, the characteristics mentioned here are merely a synopsis of the data collected from a number of studies, and are not necessarily conclusive. Further analysis and testing is needed but, in the context of the current study, it is possible to use these characteristics to assess whether the presence of greigite may have any impact upon the detrital magnetic signal contained within the core sediments.

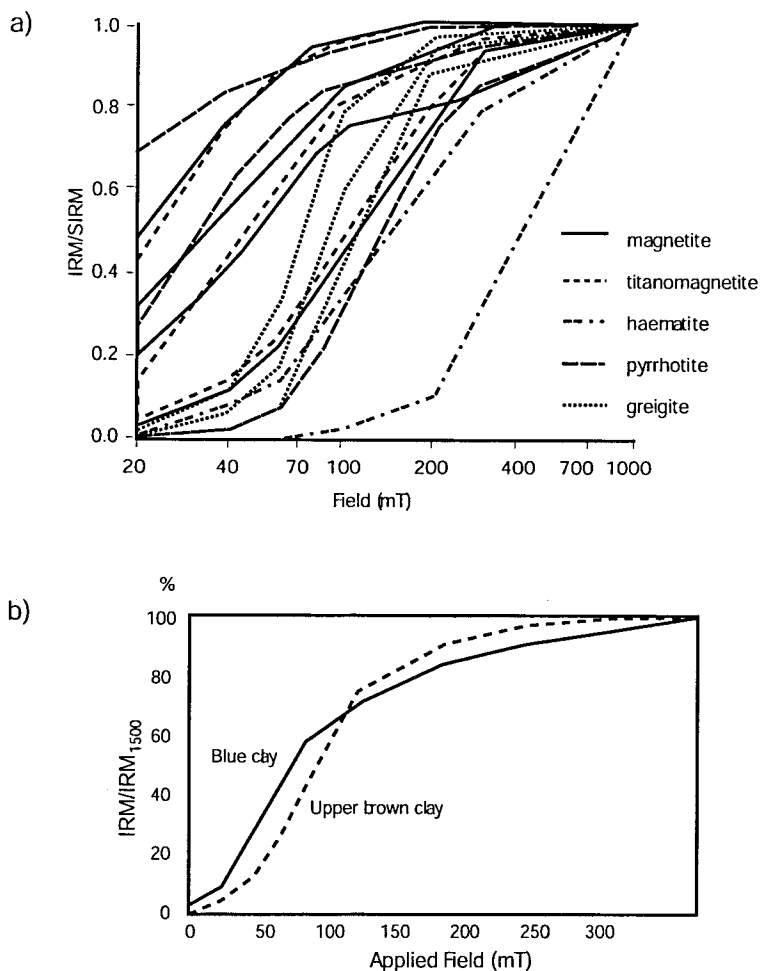


Fig. 2.25: a) IRM acquisition curves of a variety of magnetic minerals from, re-drawn from Peters & Thompson, 1998) b) IRM acquisition for greigite samples. Saturation is reached by 300mT (re-drawn from Kris *et al.*, 1990)

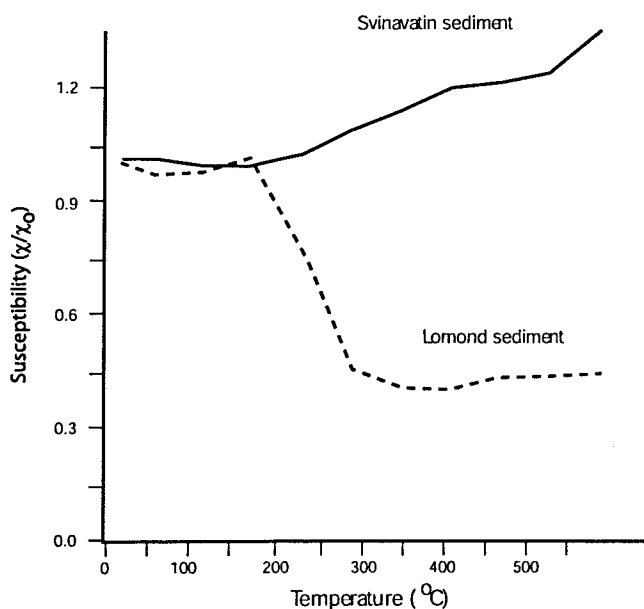


Fig. 2.26: Magnetic susceptibility changes following the stepwise heating of sediments. The Svinavatin sediments show changes usually associated with magnetite; the Loch Lomond sediments show those associated with greigite (re-drawn from Snowball & Thompson, 1988).

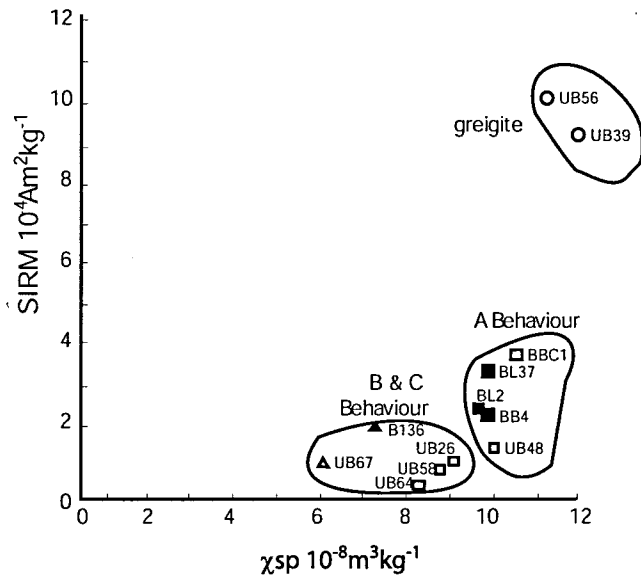


Fig. 2.27: Greigite identifying parameters of c versus SIRM (re-drawn from Roberts & Turner, 1993). The A, B, and C behaviour refers to the palaeomagnetic behaviour of the samples.

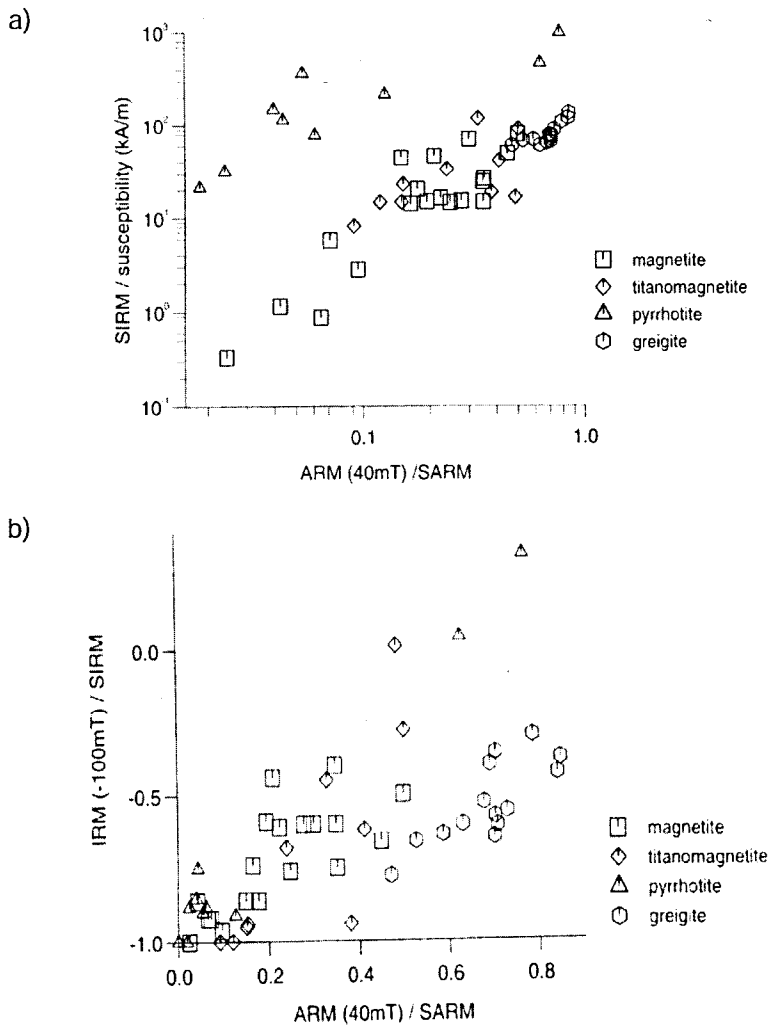


Fig. 2.28: The distinction of greigite from other magnetic minerals using plots of a) $ARM_{40}/ARM \text{ v } SIRM/\chi$ and b) $IRM_{100}/SIRM \text{ v } ARM_{40}/ARM$ (Peters & Thompson, 1998).

2.5.4 Provenance Studies with Environmental Magnetism

Provenance studies can take many forms. They can help identify the origin of a material in terms of its lithological structure, as well as how it was formed. In sedimentary environments, they can determine the geographical source of the material, and they can differentiate between transport mechanisms and pathways (Verosub & Roberts, 1995).

In lake studies, concentration dependent magnetic parameters have been shown to vary with changes of soil type, soil processes and land use (e.g. Pennington *et al.*, 1972; Thompson *et al.*, 1975; Thompson & Oldfield, 1986; Eriksson & Sandgren, 1999) and, therefore a link between certain magnetic signatures contained within a lake sediment sequence and specific vegetation and soil types within the lake catchment has been established (Verosub & Roberts, 1995). For example, Dearing & Flower (1982) found susceptibility peaks corresponding to rainfall maxima and after a study of the surrounding vegetation and soil, concluded that magnetic susceptibility recorded periods of erosion due to deforestation and/or cultivation (see Section 2.5.2). They argued that increased run-off and stream discharge resulted in the deposition of coarser and more magnetic sediments in the lake through channel erosion, and not the top soil erosion that is usually cited for increased lake sediment susceptibility.

Yu & Oldfield (1989) developed a multivariate mixing model for differentiating sediment sources in lacustrine environments, using the Rhode River as a case study. Source areas were identified and samples collected. The sediments were mixed in known concentrations and their magnetic properties measured. From the results, a regression model was created using linear functions, which could help to identify and quantify the proportion of material from each source area within a sediment sample. This method was developed further by the same authors in 1993, using only susceptibility, ARM and IRM to model sediment sources for a reservoir catchment in Nijar, Spain. The reservoir filled in during the 19th Century, and whilst the model was successful in identifying all the contemporary sediment

sources, the cause of this infill was not established. A similar study was reported by Peters & Turner (1999), on sediments from Lake Paringa, South Island, New Zealand. A suite of magnetic measurements were made to characterise the magnetic minerals present within the lake sediments, and attribute them to a source, or origin.

Magnetic measurements are particularly useful in analysing contemporary pollution (Thompson & Oldfield, 1986) as well as in studies of palaeoclimate, especially palaeowind intensity (Maher *et al.*, 1999). It has been found that SIRM, ARM, χ and χ_{fd} can distinguish between the ferrimagnetic component of atmospheric dust, soil particles of various regions and ash from industrial sources (Verosub & Roberts, 1995), as well as between weathering regimes for the soil contingent (Oldfield *et al.*, 1985). Harder IRM/SIRM values and higher SIRM/ χ values are indicative of typical haematite material from arid and semi-arid regions. Dusts from Barbados have been found to show seasonal variations, while Atlantic sediments can be split into groups according to their SIRM values. The most polluted materials have maximum SIRM values, the highest SIRM/ARM ratios and the lowest χ_{fd} values, which are all comparable to fossil fuel power station fly-ash and originate from the Northwest Atlantic. The least polluted have minimum SIRM, the lowest SIRM/ARM and highest χ_{fd} values, are comparable to the Barbados summer dusts and are North African in origin (Fig. 2.29)(Oldfield *et al.*, 1985). Shu *et al.*, (2001) collected samples of atmospheric particles from 11 sites across Shanghai, China. Sources of the particles were inferred using magnetic analysis and a chemical mass balance model (CMB). It was ultimately concluded that χ , SIRM, Hard IRM, Soft IRM and χ_{arm} are all able to successfully estimate the concentration of the main metal elements in atmospheric dust.

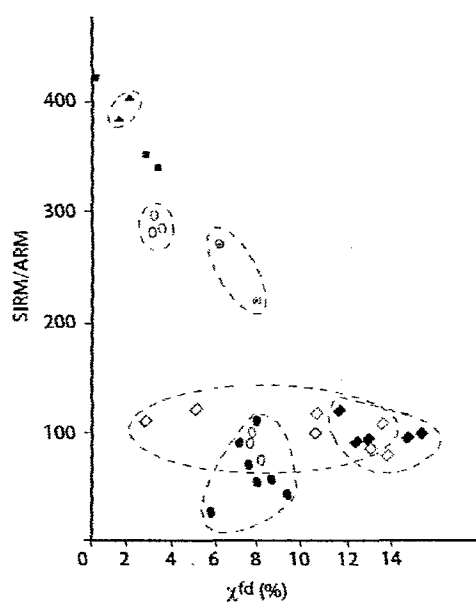


Fig. 2.29: SIRM/ARM versus χ_{fd} % for various dusts sets from Barbados, the North Atlantic and the Sea of Japan (Re-drawn from Oldfield *et al.*, 1985).

■ represents re-suspended particle sizes fly-ash used for comparison; ▲ = inland Sea of Japan dusts; ○ = North Sea and North Atlantic dusts (most polluted); ⊙ = North Atlantic dusts; ● = North Atlantic dusts (least polluted); ◇ = Barbados summer dusts; ◆ = Barbados winter dusts.

Begét & Hawkins (1989) studied the Alaskan Loess deposits, finding that χ recorded wind intensities, and therefore provenance. They suggested that high χ was characteristic of proximal deposits, because far travelled loess would be depleted in magnetic minerals, possibly because larger particles are not carried as far, or due to magnetite fractionation during aeolian transport (Begét *et al.*, 1990). Despite this, consideration must be given to the fact that during glacials, winds were stronger (Parkin, 1974) and therefore, larger particles could be transported further. Aeolian dust in deep-sea sediments have been characterised by high quartz/illite ratios, high kaolinite/illite/chlorite ratios and high antiferromagnetic content (i.e. high HIRM values)(Maher *et al.*, 1999).

In marine studies, it has been shown that high susceptibility denotes the interglacial periods in the North Atlantic and Indian Ocean (Bloemendal & de Menocal, 1989) and *vice versa* in the Somali Basin (Verosub & Roberts, 1995). Susceptibility is representative of terrigenous input, and changes are therefore the result of the Asian monsoon on ice rafting in this area. Following the onset of the Quaternary, changes in cyclicity in the Indian Ocean reflect the response of the Asian Summer Monsoon to the increase of global ice cover (Bloemendal & de Menocal, 1989). The parameters SIRM/ARM and S-ratio (the 100 backfield ratio in this instance) reflect changes in the input of dust to the Arabian Sea, which is also controlled by the Asian Summer Monsoon (Maher *et al.*, 1999). Bloemendal *et al.*, (1992) have also shown that specific magnetic ratios can give insights into sediment type and number of transport pathways or source regions delivering sediment to an area. Watkins & Maher (2003) have characterised present-day sediments in the North Atlantic, and identified the climatic and oceanographic controls on their magnetic signatures.

As demonstrated by the examples cited above, environmental magnetic analysis of sediments has helped to identify provenance and transport pathways within a variety of sedimentary environments and on a range of spatial scales, from local to global (Liu *et al.*, 2003b; Watkins & Maher, 2003). This thesis is going to concentrate on the magnetic characteristics of Heinrich Layer sediments from the

European margin, the main aim being to identify provenance for the various sedimentary components and to determine a magnetic signature for each source area. It may then be possible to separate the different signatures, quantify their relative contributions and any changes in those contributions with time.

3.0 Site Context

The work contained in this thesis is based on the analysis of two marine cores: OMEX 2K, a 2.5 m Kasten core; and MD01-2461, a 22 m giant piston core. Both of the cores were retrieved from the Celtic Margin as part of wider research projects. OMEX 2K was retrieved in 1995 during a EU sponsored project set up to study exchange at ocean margins (Hall & McCave, 1998a). In 2001, MD01-2461 was collected for a NERC funded project looking at ice-ocean-climate interaction in the North East Atlantic, as this area is considered an optimal sentinel to record signs of THC and ice sheet variability (NERC Research Grant Proposal, Scourse *et al.*, 2001).

In terms of the aims of this thesis, OMEX 2K and MD01-2461 are ideally located. It has previously been established that the Celtic Margin was reached by Heinrich Event icebergs of both Laurentide and European origin (e.g. Hall & McCave, 1998a & b; Scourse *et al.*, 2000). Therefore, these sediments not only have the ability to characterise HEs, but also have the potential to differentiate between provenances as different sources are already established. In addition to this, an extensive collection of data is already available on OMEX 2K.

3.1 The Ocean Margin EXchange (OMEX) project.

The Ocean Margin EXchange project (OMEX) was set up and run by the European Union in 1994 to measure and model exchange processes at passive ocean margins. Its main objective was to gain a better understanding of processes at ocean margins and how they affect, and are influenced by, the environment (Hall & McCave, 1998a; van Weering *et al.*, 1998a; 2001).

Ocean Margins are the regions of transition between the thick continental crust and the thin oceanic crust (Roberts & Montadert, 1979; Seibold & Berger, 1982). They have varying characteristics depending on their location within a tectonic plate, but are generally made up of a coastal zone, continental shelf, continental

slope, continental rise and abyssal plain (Fig. 3.1)(King, 1974). There are two main types: Atlantic (or passive) and Pacific (or active). Passive margins occur when the plate margin is in the middle of the ocean and are characterised by rifting. They are made up of layers of increasingly younger sediment and are slowly sinking (Seibold & Berger, 1982). Unless they are very young, they are free from earthquakes and volcanism (Roberts & Montadert, 1979). Active margins are associated with collision margins, folding, faulting and volcanism. They are caused by the sinking of the oceanic crust below the continents, causing the continental crust to fracture and uplift and are therefore classed as rising (Roberts & Montadert, 1979; Seibold & Berger, 1982). Ocean margins contain ~ 60% of the total oceanic sediments (Roberts & Montadert, 1979).

The main site chosen for study within OMEX was the Goban Spur, on the Western edge of the Celtic Shelf (Figs. 3.2a, b, & c and 3.3)(Hall & McCave, 1998a). This area is affected by three main water masses; North Atlantic Central Water (NACW), Mediterranean Outflow Water (MAO), and North Atlantic Deep Water (NADW); which impose a significant influence on sediment transport (van Weering *et al.*, 2001; McCave *et al.*, 2001). The Goban Spur is a gently sloping shelf to a depth of 1400m, with a slightly steeper slope leading to the top of the Pendragon Escarpment, which itself drops to a depth of 4500m (de Graciansky *et al.*, 1981; van Weering *et al.*, 1998b; 2001). This then levels off to the Porcupine Abyssal Plain which covers an area of 10 000 km² to the base of the Mid-Atlantic Ridge (49°N, 12°W and northwards, Figs. 3.2 & 3.3)(Heezen & Laughton, 1960). To the Southeast of the Spur, a series of gullies run down the slopes, creating the Celtic Fan while to the North is the Porcupine Seabight, a semi-enclosed depression that corresponds to an Early Cenozoic sediment basin (Fig. 3.2b & c)(de Graciansky *et al.*, 1981; van Weering *et al.*, 1998b; 2001).

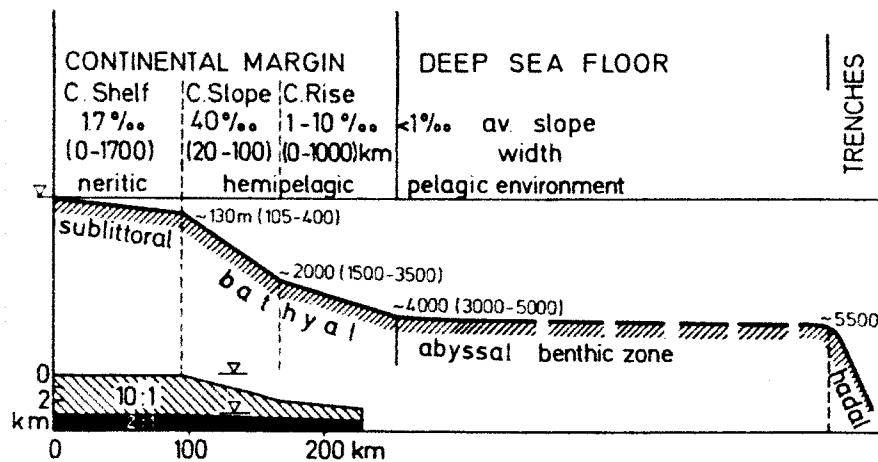


Fig. 3.1: A typical ocean margin profile (Seibold & Berger, 1981).

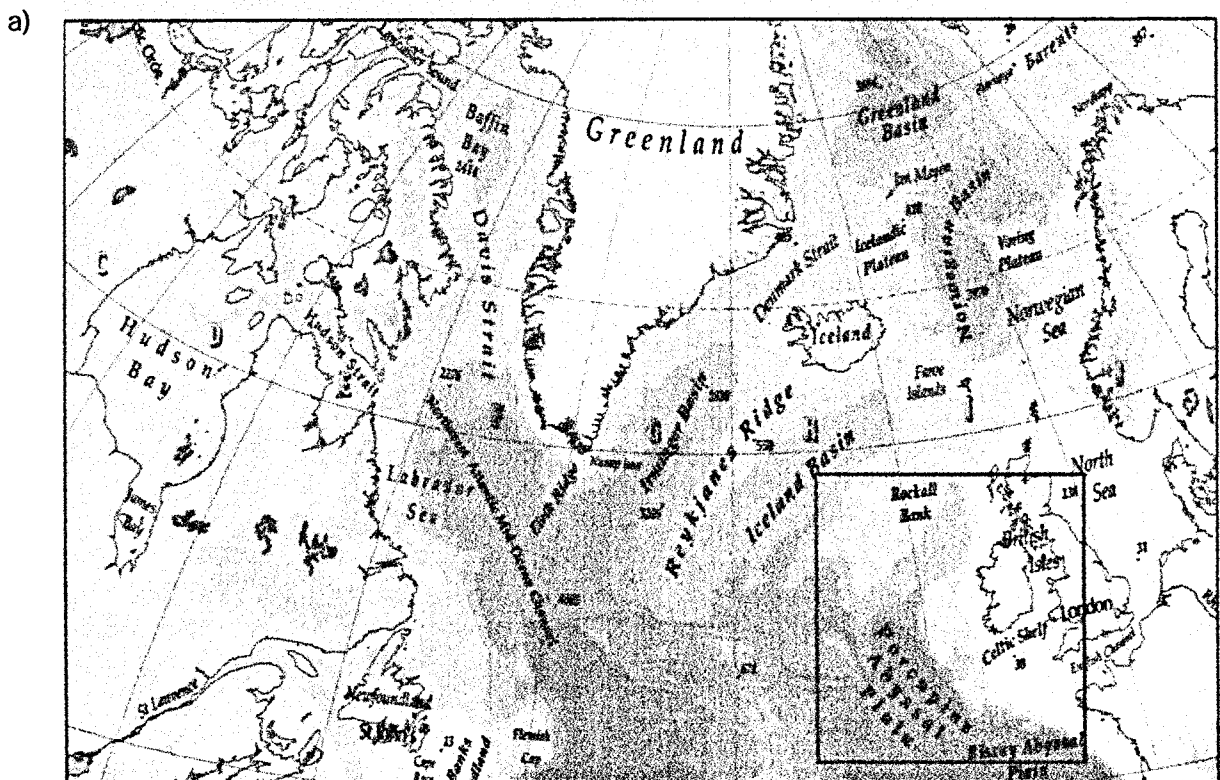


Fig. 3.2a: The North Atlantic Ocean (Times Concise Atlas of the World, 1999). The Goban Spur and the Celtic Margin is highlighted, further detailed maps are found in Figs 3.2b and c (over page).

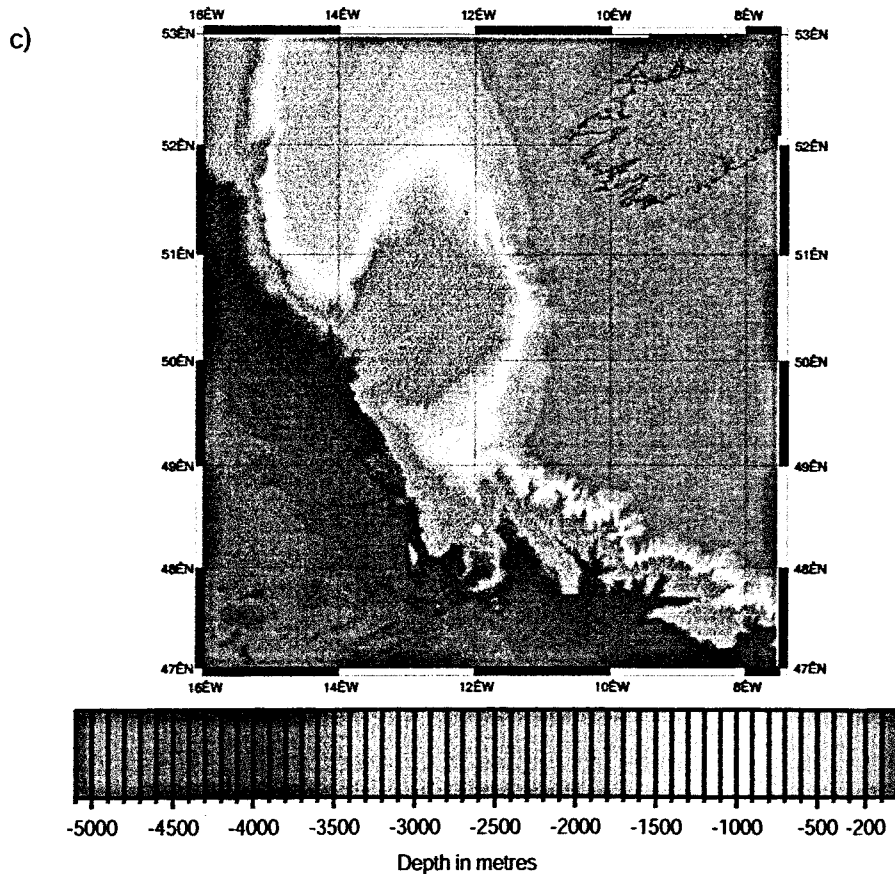
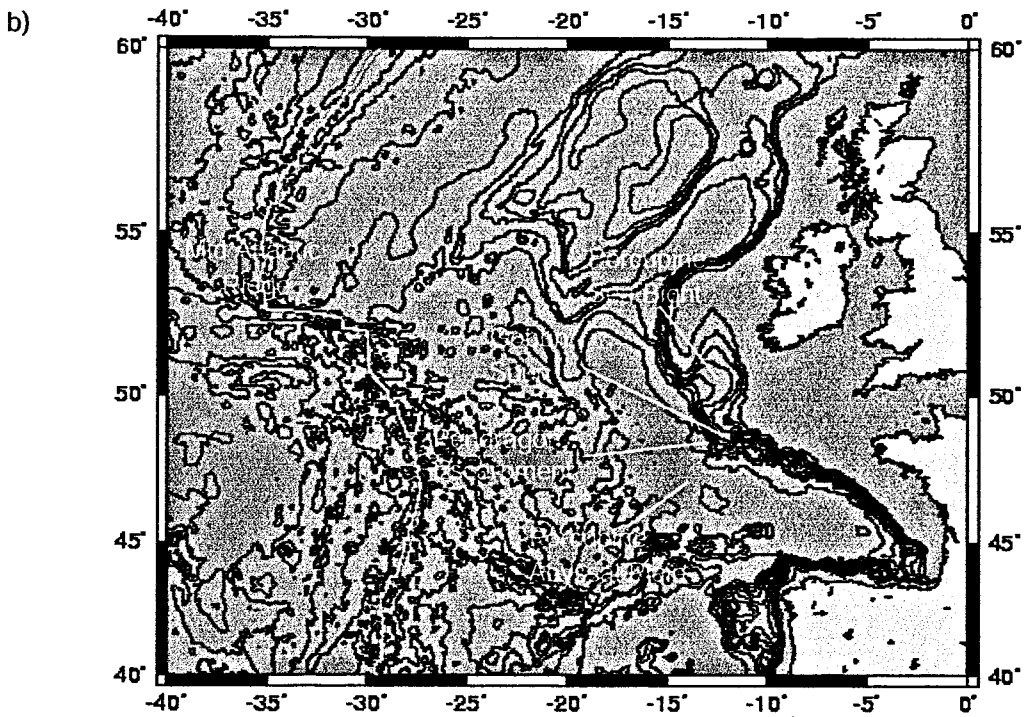


Fig. 3.2: b) A close-up of the Goban Spur and surrounding area (www.aquarius.geomar.de/cgi-bin.pl, 2002). b) Bathymetric map of the Goban Spur (Lowry *et al.*, 1997 - OMEX dataset CD-ROM).

The sediments on the Goban Spur are relatively thin compared to other ocean margins. The basement rocks are cut by Hercynian faults formed during major earth movement in the Devonian and Carboniferous periods (408.5 - 290 ma). They are covered with layers of sediment, the bottom most of which are syn-rift deposits - thick layers of sediment that accumulated in the “troughs” of the faults as they formed. They are the reason that the Goban Spur has a level topography despite the disturbed basement blocks (de Graciansky *et al.*, 1981).

During the RRS *Charles Darwin* cruises 84 and 94 in 1994 and 1995, five Kasten cores were taken from the Goban Spur along a rough transect running from approximately 11°-14°W, with the fifth from within the Porcupine Sea-Bight (50°N)(Table 3.1, Figs. 3.2b & c and 3.4)(Hall & McCave, 1998b).

A 4m long, 0.15m square corer barrel was used (Hall & McCave, 1998a & b). This corer is a stainless steel barrel with cross section dimensions of 15 x 15 cm with a core catcher of standard dimensions (from the Institute of Oceanographic Sciences, IOS) and a core head (Fig. 3.5). A circular hole in the core head allows water to escape during descent and can be closed to prevent the sediment being washed out, and slumping once the core is on board ship and stored horizontally. The core catcher is placed on the bottom of the core barrel. It has a shutter like system composed of two doors held to the inside wall of the barrel by tension. When the corer is lifted, two levers on the outside of the barrel are forced down by the surrounding sediment, releasing the tension and shutting the doors (Zangger & McCave, 1990).

The Kasten corer was designed by Kuehl *et al.*, (1985) and improved by Zangger & McCave (1990) with a view to lessening the problems of core shortening and re-penetration which is common in open barrel gravity cores (Zangger & McCave, 1990). Core shortening is thought to arise from friction between the wall of the corer and the adjacent sediment (Fig. 3.6)(Emery & Hulsemann, 1964; Weaver & Schulthesis, 1983). Shortening in gravity cores was found to be dependent on the type of sediment and water content, but is estimated at 50% of the penetration,

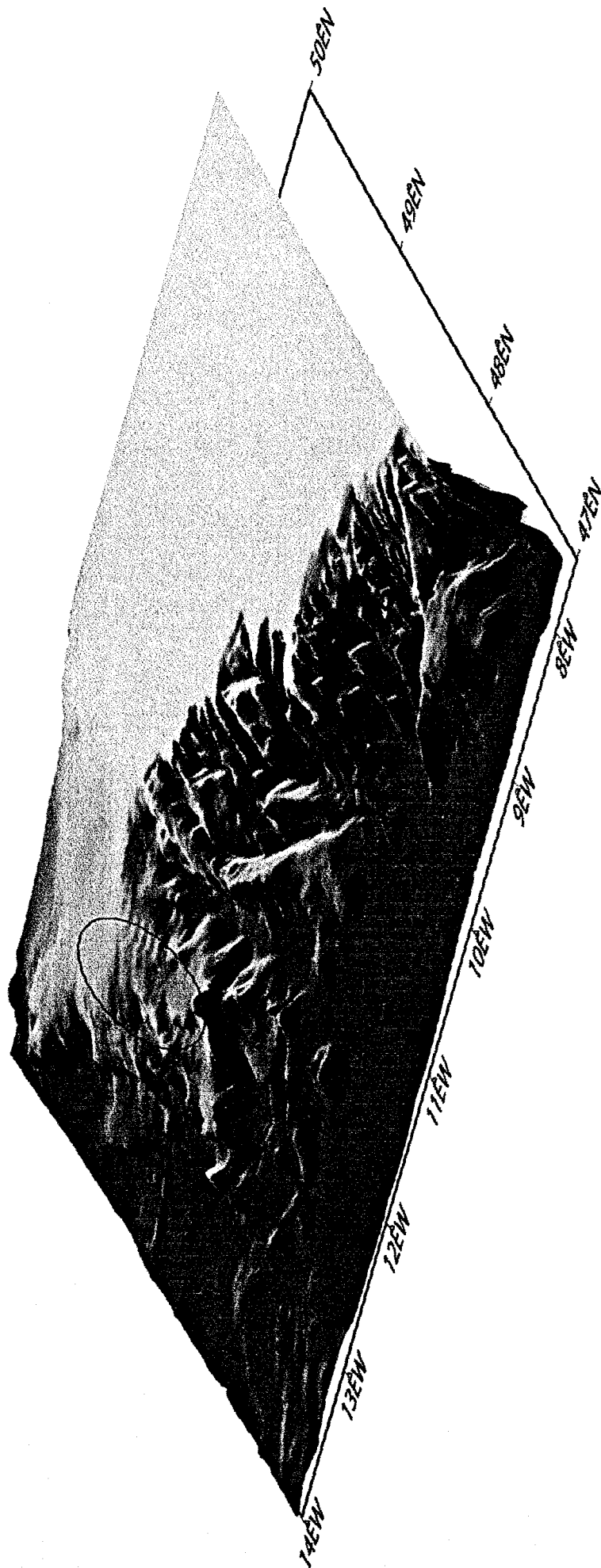


Fig. 3.3: 3-D Bathymetric profile of the Goban Spur. The OMEX cores and MD01-2461 are around 49°N, 12°W as highlighted (Lowry *et al.*, 1997 - OMEX dataset CD-ROM).

Table 3.1: The OMEX cores taken onboard the *RV Charles Darwin* in 1995 (Hall & McCave1998a).

Cruise	Core (OM)	Date	Type	Length (cm)	Latitude (N)	Longitude (W)	Water depth (m)
CD 84	1K	23.1.94	4m Kasten	337	48°58.60'	13°39.83'	4494
CD 84	2K	24.1.94	4m Kasten	254	49°5.29'	13°25.90'	3658
CD 84	3K	31.1.94	3m Kasten	265	49°22.70'	11°11.62'	806
CD 94	4K	7.6.95	4m Kasten	371	49°59.25'	12°31.06'	2280
CD 94	5K	12.6.95	4m Kasten	391	48°50.07'	12°39.95'	2333
BAS	1P	9.93	15m Piston	1532	47°58.80'	11°48.50'	3652

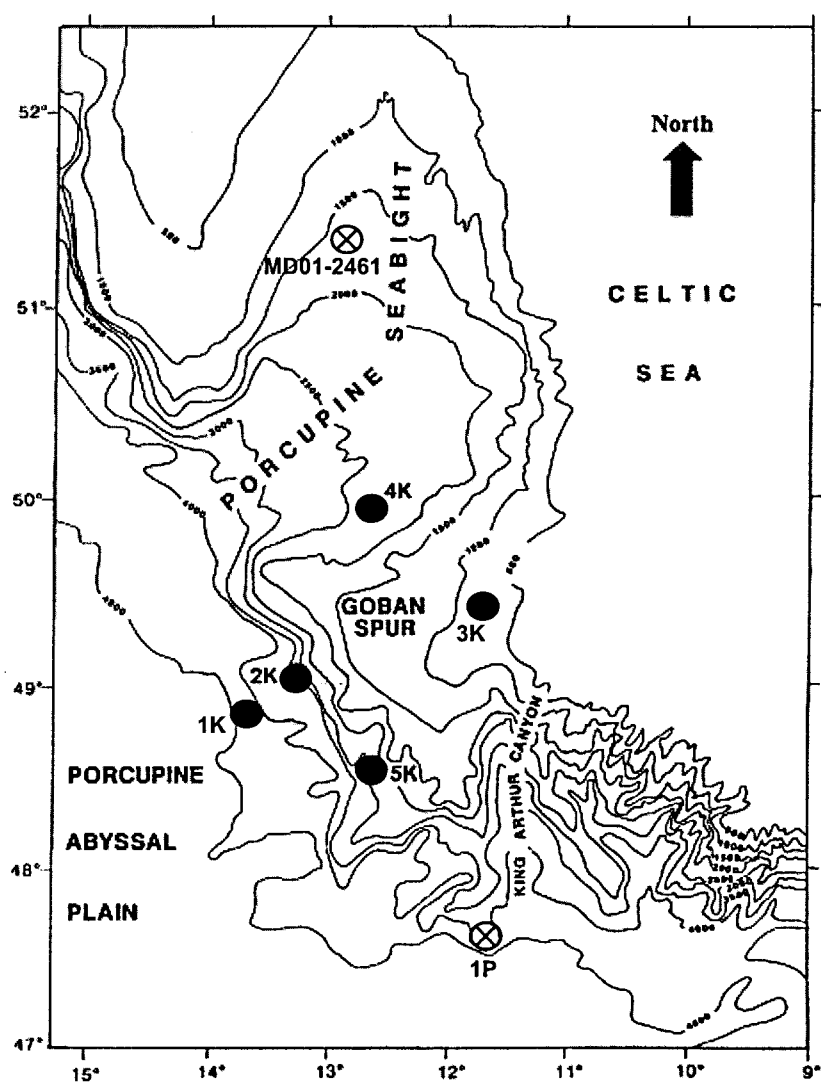


Fig. 3.4: Location of the OMEX cores and MD01-2461 (Hall & McCave, 1998a & b) Solid circles are kasten cores, crossed circles are piston cores.

with little shortening taking place above 50 cm depth, and below 50 cm, shortening increases with depth (Emery & Hulsemann, 1964). The large cross-sectional area of the new Kasten corer means that less shortening takes place, however it is still susceptible to re-penetration (Weaver & Schulthesis, 1990).

Re-penetration is caused by cable recoil or slackening, often due to the corer pulling free of the sediment when the ship is at the high point in the swell (Weaver & Schulthesis, 1983; Zangger & McCave, 1990). The new Kasten corer limits this re-penetration by the addition of shutter-like doors that close when levers are pushed downwards by sediment external to the corer (Zangger & McCave, 1990), and the addition of a sliding, 30kg weight that stabilises the core barrel (Kuehl *et al.*, 1985). Kasten cores, on average, can now return intact, undisturbed sediments down to ~3m penetration, below which shortening of a maximum of only 20% can occur (Skinner & McCave, 2003).

Once in the lab, the core can be secured in two carpenters' vices and the lid removed. U-channel samples can then be taken by inserting two 6 x 6 cm pieces of drainpipe into the sediment. An 8 cm threaded T-bar is then attached to a thin sheet of steel on the inside of the barrel on the opposite side to the lid and wound in, forcing the sheet up and the sediment out. The drainpipes can then be removed using cheese-wire. Photos and X-rays can then be taken and further sub-samples, if necessary (Fig. 3.7)(Zangger & McCave, 1990).

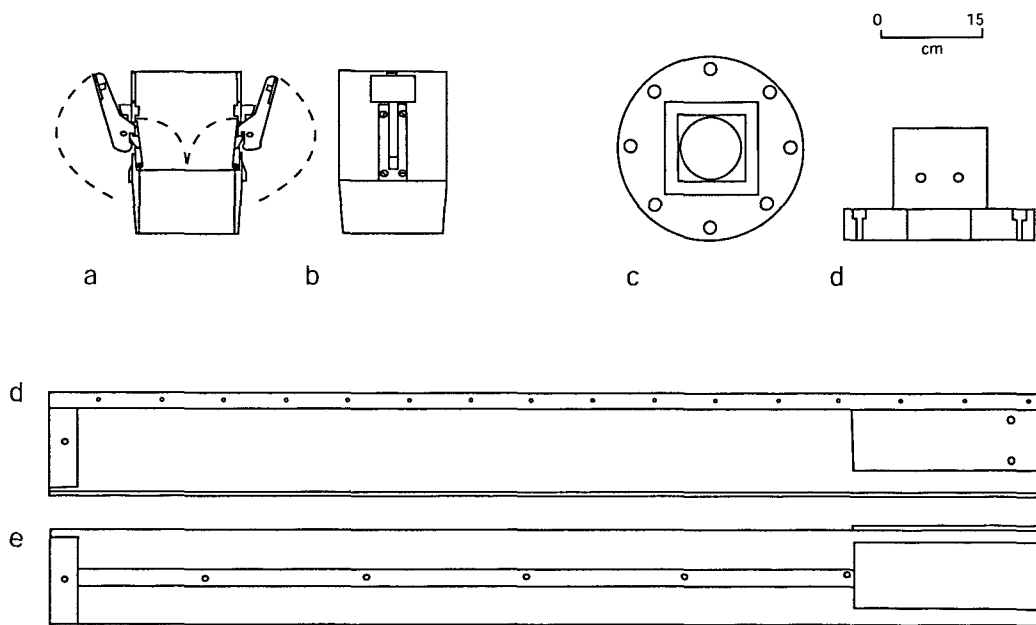


Fig. 3.5: The corer designed by Zangger & McCave. a) and b) constitute the core catcher; c) and d) the core head; e) and f), the core barrel (re-drawn from Zangger & McCave, 1990).

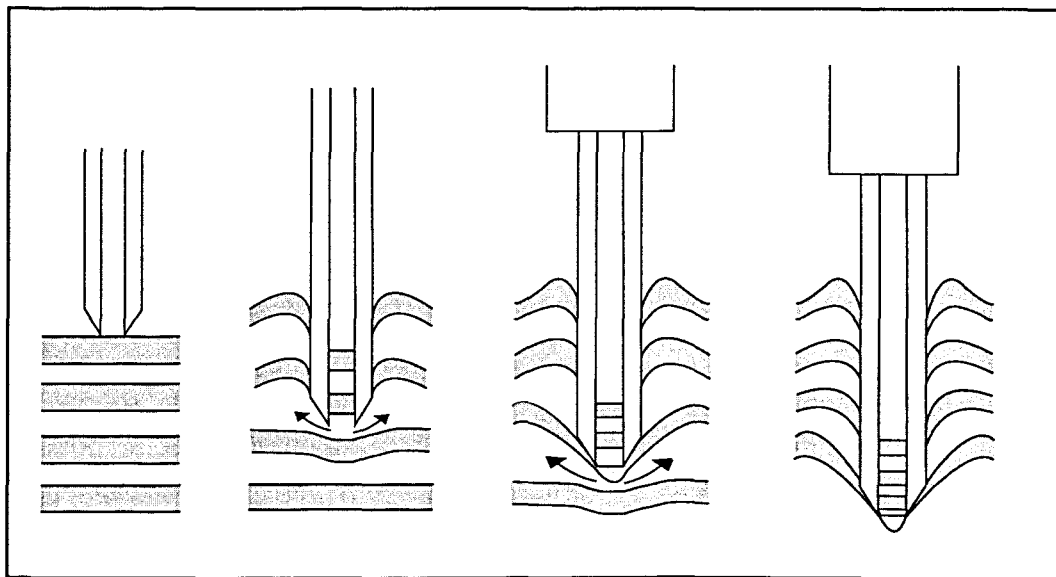


Fig. 3.6: The shortening of sediment cores during open barrel gravity coring. (re-drawn from Weaver & Schulthesis, 1983)

3.2 Core OMEX-2K

OMEX 2K was one of the cores extracted in the above fashion (Fig. 3.4) and was recovered from 49°5.29'N, 13°25.90'W, 3658 m water depth on 24.1.1994 (Hall & McCave, 1998a & b). The core was logged descriptively and X-radiographs taken to help determine the sediment structure (Fig. 3.8). Water content was determined on samples taken every 4cm. These samples were then sieved using a 63µm sieve, dried and weighed to determine the coarse grain percentage. Magnetic susceptibility measurements were made along the whole core whilst still onboard ship, and later, on a mass specific basis with the sub samples. Subsequently, AMS ¹⁴C dating was carried out, as was CHN analysis for organic and inorganic carbon, and grain size distribution for both the terrigenous and carbonate fractions (Fig. 3.9)(Hall & McCave, 1998a & b).

The magnetic susceptibility and water content profiles of the OMEX cores detected turbidities and pulses of meltwater, both of which deliver a large quantity of lithic particles to the sediment. Due to the presence of these higher concentrations of lithic particles, the X-rays contain dark, opaque bands, with the meltwater pulses containing abundant dropstones.

The AMS ¹⁴C dating provided a basis for estimating sedimentation rates within the OMEX cores, combined with the identification of chronological markers, such as the vedde ash layer and the ice-rafting pulses of Heinrich Events 1 and 2, and the correlation with features in oxygen isotope profiles (Hall & McCave, 1998a). Sedimentation rates decrease with depth along the Goban Spur, but also show a distinct glacial-interglacial pattern with glacial rates being higher (Table 3.2)(Hall & McCave, 1998a). The flux of non-carbonate sand (grains > 63 µm; Hall & McCave, 1998a) is used as a proxy for ice rafting (e.g. Manighetti & McCave, 1995). *High fluxes record an increase in ice rafting and can therefore identify Heinrich Layers.* Variations in grain size distribution can reflect prevailing current direction and speed, as well as pick out the HLs. Average particle size will increase with stronger currents, as finer silts and clays are carried away (Hall & McCave,

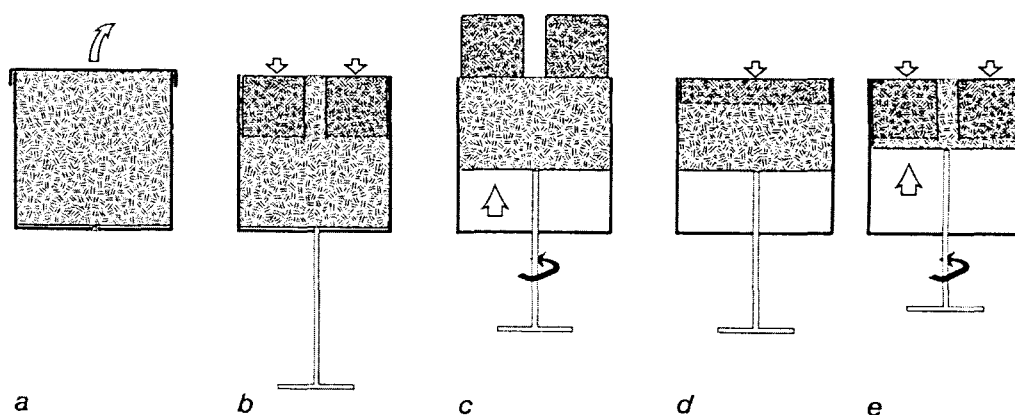


Fig. 3.7: The sampling techniques for the Zangger & McCave corer; a) lift the lid; b) push in two u-channels; c) screw out the sediment; d) cut off the u-channels; e) repeat the process (Zangger & McCave, 1990).

Table 3.2: The OMEX cores and their sediment accumulation rates (Hall & McCave, 1998a).

Interval	Horizon	Age (cal. yr BP)	Sediment accumulation rate (cm ka-1)
OM-3K (806m water depth)			
Present – Vedde Ash	Top – 76	0 – 11.980	6.6
OM-5K (2333m water depth)			
Present – Vedde Ash	Top – 64	0 – 11.980	5.6
Vedde Ash – H1	65 – 152	11.980 – 18.500	15.9
H1 – H2	152 – 332	17.500 – 25.150	23.5
OM-2K (3658m water depth)			
Present – 7584	Top – 36.5	0 – 7584	5.1
7584 – Vedde Ash	36.5 – 48	7584 – 11.980	2.6
Vedde Ash – 14846	48 – 73	11.980 – 14.84	8.7
14846 – H1	73 – 82	14.846 – 17.500	3.4
H1 – LGM	82-112	17.500 – 21.000	8.6
LGM – H2	112 – 178	21.000 – 25.150	15.9
OM-1K (4494m water depth)			
Present – Vedde Ash	Top – 42	0 – 11.980	3.7
Vedde Ash – H1	42 – 98	11.980 – 17.500	10.1
H1 – LGM	98 – 132	17.500 – 21.000	9.7
LGM – H2	132 – 194	21.000 – 25.15	14.9
OM-4K Porcupine Seabight (2280m water depth)			
Present – 5123	Top – 36.5	0 – 5123	7.6
5123 – Vedde Ash	36.5 – 76	5123 – 11.980	5.8
Vedde Ash – 14462	76 – 115.5	11.980 – 14.462	15.9
14462 – H1	115.5 – 136	14.462 – 17.500	6.8
H1 – H2	136 – 308	17.500 – 25.150	22.5
OM-1P King Arthur Canyon (3652m water depth)			
Present – Vedde Ash	Top – 70	0 – 11.980	6.1
Vedde Ash – H1	70 – 159	11.980 – 17.500	16.1
H1 – H2	159 – 339	17.500 – 25.150	23.5

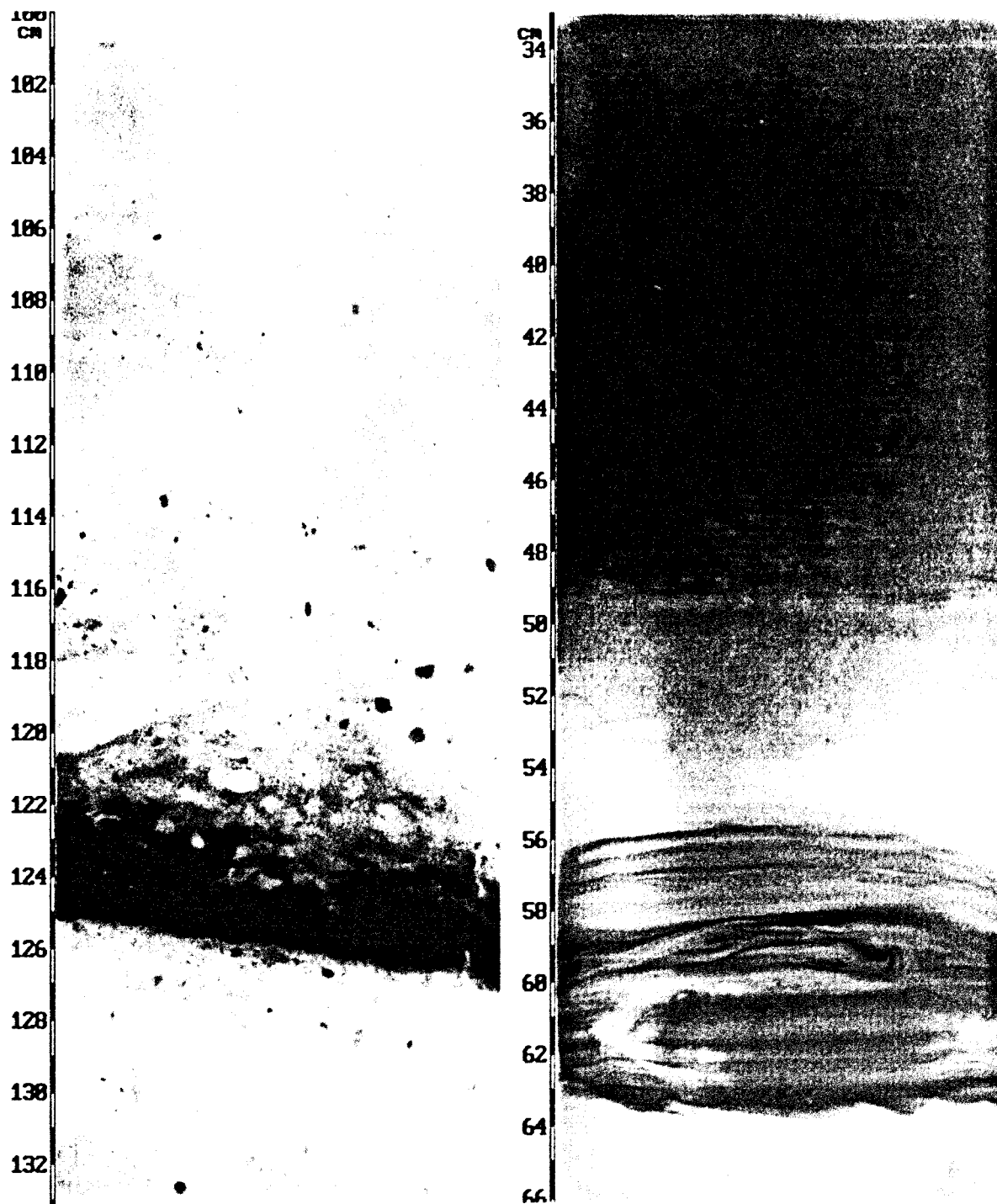


Fig. 3.8: X-radiographs taken of OMEX 2K. The dark bands are possibly due to distortion of the sediments during the coring process. Lithic particles are clearly visible, especially around 114-132 cm (X-rays courtesy of Dr. I. Hall, University of Cardiff and Lowry *et al.*, 1997 - OMEX dataset CD-ROM).

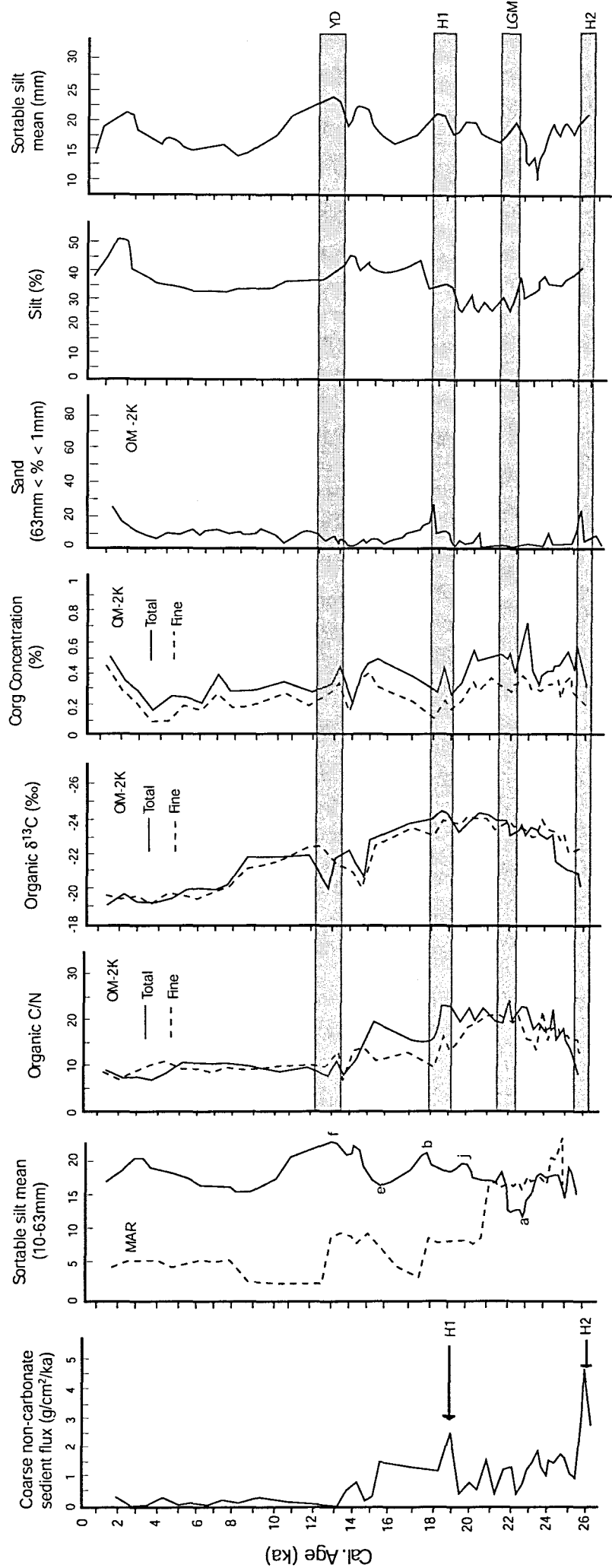


Fig. 3.9: Synthesis of data for OMEX 2K from onboard analysis and initial analysis by Hall & MacCave, 1998a & b (re-drawn).

1998a). Silt is generally accepted as an indicator for current strength, which is often influenced by topography and slope gradient. The particle size analysis on the OMEX cores indicates that velocity increases with slope steepness. (Fig. 3.9)(Hall & McCave, 1998a). Shifts in the $\delta^{13}\text{C}$ of organic carbon (Fig. 3.9) from low values at the glacial maximum, and increasing throughout the Holocene reflects the change in transport mechanism due to coastline retreat. As the sea-level rose, less wind transport would take place, being replaced by current redistribution (Hall & McCave, 1998b).

During a study by Scourse *et al.*, (2000) the dominant lithological groupings of OMEX 2K were determined using visual differences and X-ray analysis of elemental content. These were quartz, volcanic glass (rhyolitic and basaltic), porphyry, dolomite, mica and chalk (Fig. 3.10)(Scourse *et al.*, 2000). The rhyolitic glass peak (depth 54 cm depth) is the result of Vedde Ash being transported by ice during the late LGM (Last Glacial Maximum) and mixed with the uppermost sediments. As noted earlier, dolomite is thought to be typical of LIS-scoured IRD material. Dolomite is found to be prominent during both H1 and H2 (at depths 82 cm and 180 cm respectively), and is co-incident with peaks in the whole-core magnetic susceptibility data. In contrast, chalk peaks are found both during and just prior to the H2 main event. Scourse *et al.*, (2000) suggest this chalk is characteristic of LGM sediments from the Celtic shelf (SEM observations revealed that the chalk contained well-preserved late Cretaceous coccoliths, pithonellid calcispheres – calcareous fossil species - and planktonic foraminifera). Detailed analysis of individual chalk grains by light microscopy shows the presence of diverse well-preserved nannofossil assemblages including marker species indicative of the mid-late Campanian (in the late Cretaceous, approx 130 – 65 ma; Lowe & Walker, 1997). The chalk peak prior to H2 may indicate the possibility of a British precursor event to H2. Similar chalk peaks were absent from H1 and Scourse *et al.*, (2000) argued that this was because the BIS had retreated some 400 km north by this time (Bowen *et al.*, 1986).

Scourse *et al.*, (2000) also suggested that the mica within OMEX 2K was characteristic of Celtic shelf material. Bowen *et al.*, (1986) have reported that the main drainage of the Irish ice was through a lobe of ice projecting out onto the shelf just south of the Goban Spur, and this would explain the presence of BIS material. The lithological studies provide direct evidence that the BIS was involved in the Heinrich Events, though the LIS input was greater than the BIS (Scourse *et al.*, 2000).

The two chalk peaks in and around H2 suggest two pulses of BIS activity: one precursor and one during the main event but slightly later than the LIS dolomite peak. ^{14}C dates indicate a lag time of 740-1360 years between the precursor and main event, which agrees with estimates from other Northeast Atlantic cores (e.g. Snoeckx *et al.*, 1999). The precursor contains only non-LIS material suggesting that the BIS responded rapidly to some external forcing which resulted in the destabilisation of the LIS a few hundred years later. During the H2 main event, it is thought that the lobe projecting from the Irish margin responded to the sea level rise caused by the LIS discharge, explaining the BIS input to the main H2 event (Scourse *et al.*, 2000).

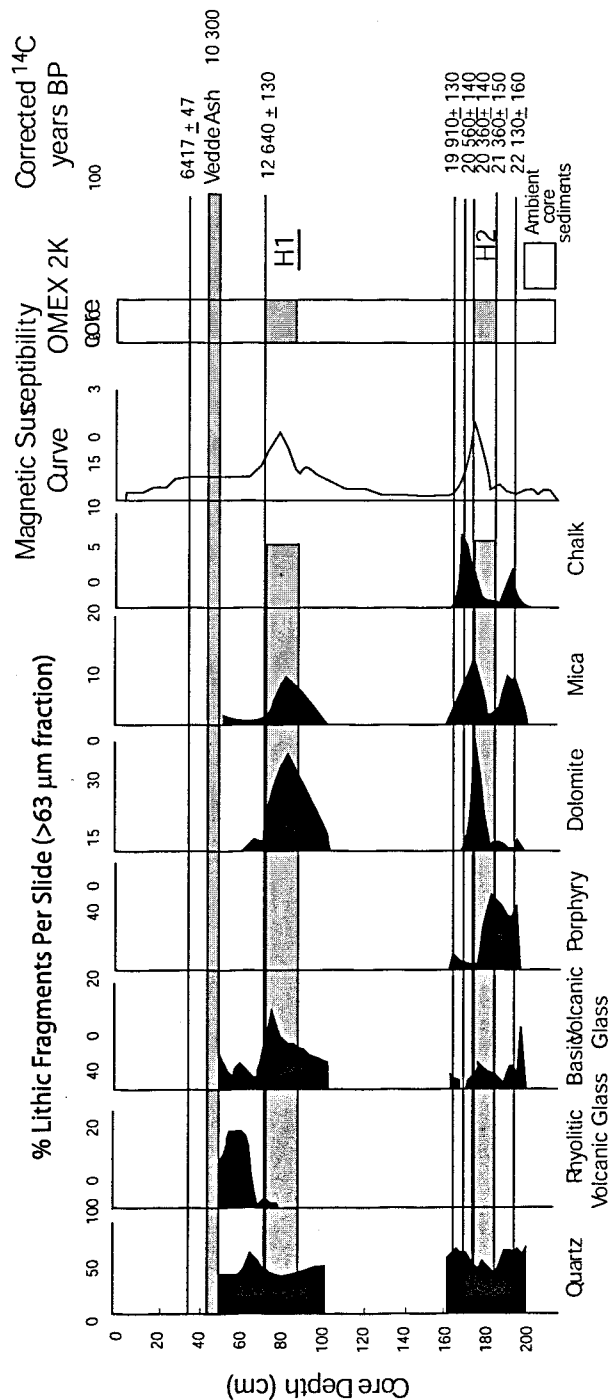


Fig. 3.10: Lithological data for OMEX 2K (re-drawn from Scourse et al., 2000). The lithic particles are expressed as a percentage per slide, therefore are only representative of relative abundance, not absolute values. Analysis was only performed on material surrounding the Heinrich Layers explaining the absence of data between 100cm and 160cm, and 45cm upwards. The Dolomite is characteristic of LIS-sourced material (Andrews et al., 1993), suggesting that icebergs from the LIS were able to travel as far as the Celtic margin. The Chalk and Mica is typical of glacial sediments from the BIS, via the Irish Sea ice stream (Scourse et al., 2000), particularly at the LGM (21–18 kya, Lowe & Walker, 1997). From this information, Scourse et al., (2000) derived a two-phase structure to H2, with a pulse of BIS material pre-dating the main HE (which itself consists of BIS and LIS sediments), by 740–1360 years. Several suggestions were made to explain this, the most likely being the existence of lag times. Both ice sheets could have been responding to the same external stimuli (climate, oceanic circulation and the THC, sea level etc), but BIS material reached the Celtic margin first. Either the BIS could have responded quicker, as it was smaller, or the proximity of the BIS to the Celtic margin meant that icebergs surging simultaneously with the LIS would reach the area first. Another explanation was that European instability caused the collapse of the LIS by altering oceanic circulation and raising sea level. The time lag for this method, however, might have to have been longer than the 740–1360 years suggested here by radiocarbon dating.

3.3 Core MD01-2461

During an IMAGES cruise aboard the *RV Marion Dufresne* in 2001, the Goban Spur site was revisited and a giant piston core (MD01-2461) was taken slightly further north from the OMEX cores in the Porcupine Seabight at 51°45'N, 12°55'W, 1153 m water depth (Figs. 3.2 & 3.7).

The *Marion Dufresne* hosts a giant piston core handling system known as CALYPSO which can retrieve cores of up to 65 m (Fig. 3.11)(Anon, 2004), the longest having been recorded at 64.40 m in the Gulf of California in 2002 (Beaufort *et al.*, 2002). The system consists of a 70 m steel tube, with an 8-10 ton weight, a mechanical trigger and piston, and an aramide hoisting cable (Calais *et al.*, 2003; Anon, 2004). The core is slowly lowered to the sea floor, with a preliminary weight attached. The weight hits the sea floor some metres before the core, releasing the tube from the main cable and allowing it to fall to the seabed. Once the tube has penetrated the sediment, the piston takes over, holding up sediment as the core is retrieved. A core-catcher ensures that no material escapes as the core is being brought back to the surface (Fig. 3.12).

Piston coring itself developed through the need to increase penetration and retrieve longer cores (Weaver & Schulthesis, 1990). The corers are hollow steel tubes with an internal sliding steel, that produces a weak vacuum, causing the sediment to move up the tube, without disturbing the layers (Fig. 3.13). As surface sediment is often lost during piston coring, a small gravity or box core is often attached to the trigger weight to recover the top 1-1.5 m of sediment (Weaver & Schulthesis, 1990; Buckley *et al.*, 1994). Piston coring was so successful, that the idea of giant piston coring was suggested by Wood's Hole Oceanographic Institution in 1967, in an attempt to retrieve up to 50m of sediment (Weaver & Schulthesis, 1990). As this involved larger and heavier coring equipment, stronger wires and more powerful winches were required, which meant that few ships were capable of such operations (Hollister *et al.*, 1973).

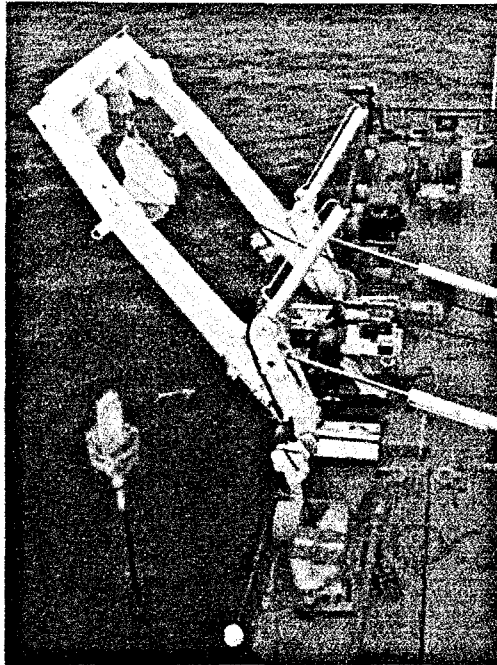


Fig. 3.11: The CALYPSO giant piston coring mechanism aboard the *RV Marion Dufresne* (Calais *et al.*, 2003 0 www.univ-brest.fr/IUEM/Universite_flottante/md).

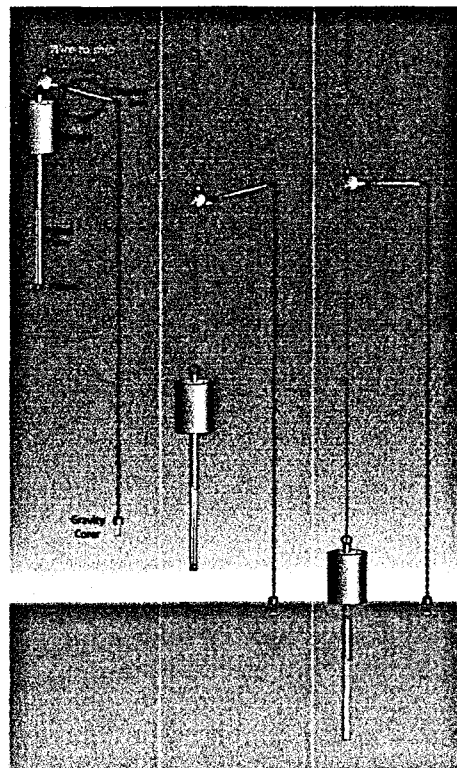


Fig. 3.12: A schematic of a giant piston coring mechanism (www.usgs.mil/pacarea/iceops/cpmanual, 2004)

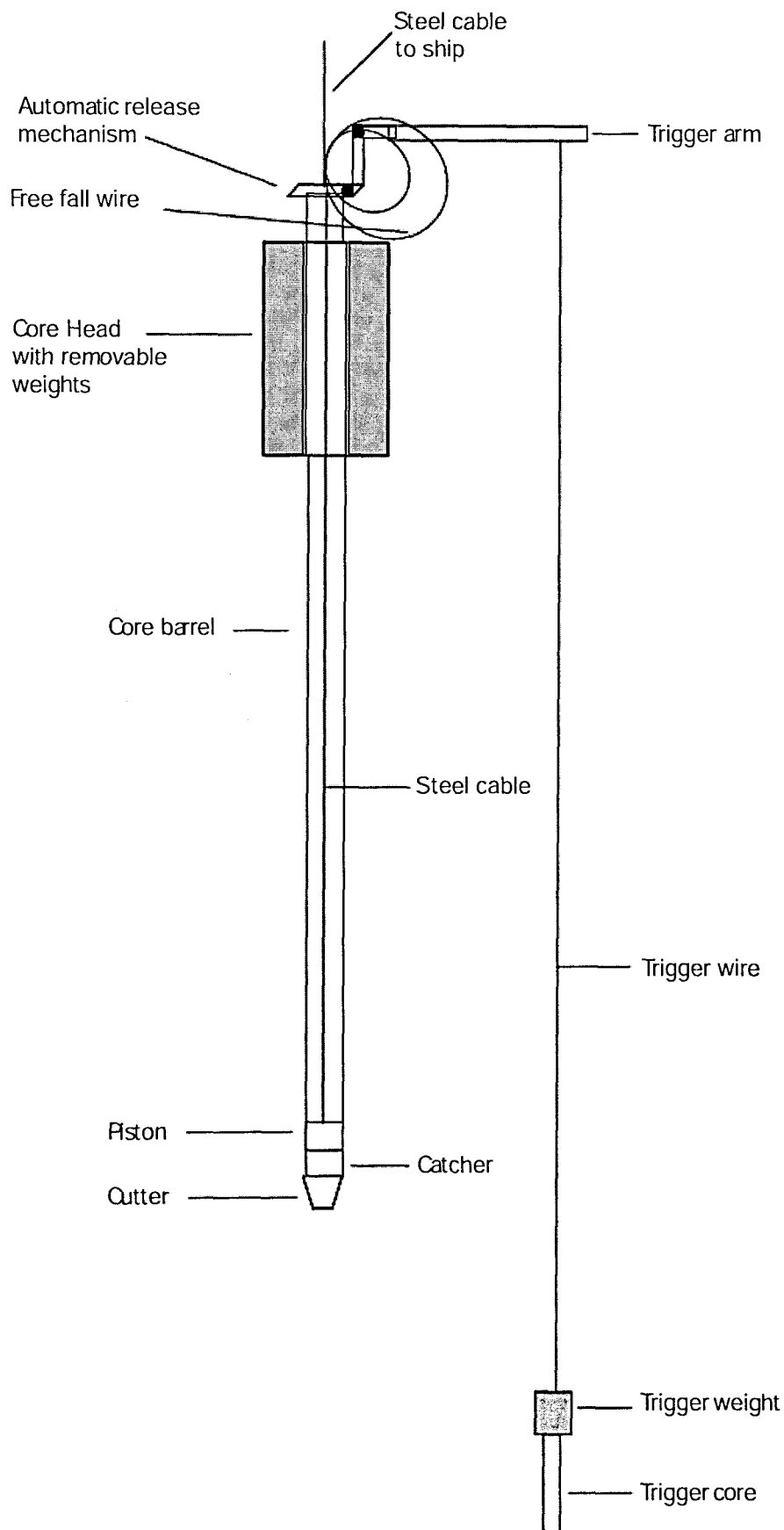


Fig. 3.13: A giant piston corer, similar to that used on the *RV Marion Dufresne*. (re-drawn from Hollister *et al.*, 1973 and Weaver & Schulthesis, 1990).

Problems with the piston coring method became apparent shortly after they became widely used, in the form of vertical disturbances (Bouma & Boerma, 1968; McCoy, 1985). These disturbances were described as “vertical line patterns” or a “rounding of the laminae” (Fig. 3.14)(Bouma & Boerma, 1968) and were identified as both the shrinking and stretching of the core due to missing sediments, or sediment flow-in (McCoy, 1985; Buckley *et al.*, 1994). Suggestions for the cause of these disruptions are in the coring processes themselves; the core barrel may not penetrate vertically or may fall over on impact which will distort the laminations in any sediment collected; friction between the sediment and the core liner can cause bending of the laminae and in very severe cases, shrinking of the core (Blomquist, 1985); if the core barrel does not penetrate to its full extent, then a sucking-up of additional material may occur when the piston begins to lift, as it is not in contact with the sediment (Fig. 3.15) - this can also occur mid-core if the upward movement of the piston exceeds the downward movement of the corer (McCoy, 1985); and the delayed stopping of the piston at the sediment surface may cause the loss of the top layers (Bouma & Boerma, 1968; Winterhalter, 1970; Stow & Asku, 1978; Buckley *et al.*, 1994).

Several improvements have been made to the system over the last 30 years, including the changing of the “rope” used to hoist the corer (Schilling *et al.*, 1988), the addition of an automatic release system, as seen on the *Marion Dufresne*, which induces free fall to maximise the force of the impact (Winterhalter, 1970) and the addition of a piston immobiliser to prevent the upward movement of the piston after penetration has ceased (Bader & Paquette, 1956). Even a few millimetres of motion during sampling can cause distortion (Richards, 1966). A second core (usually a Gravity or Kasten core) is taken at each site to ensure retrieval of the surface sediments, and to compare with the Piston core for core stretching. The development of a Stationary Piston Core (STACOR) involving a system which holds the piston in the same place (and, therefore, the sediment surface), while the corer slides past has also helped with the collection of long (over 25m) undisturbed cores (Weaver & Schulthesis, 1990; Buckley *et al.*, 1994).

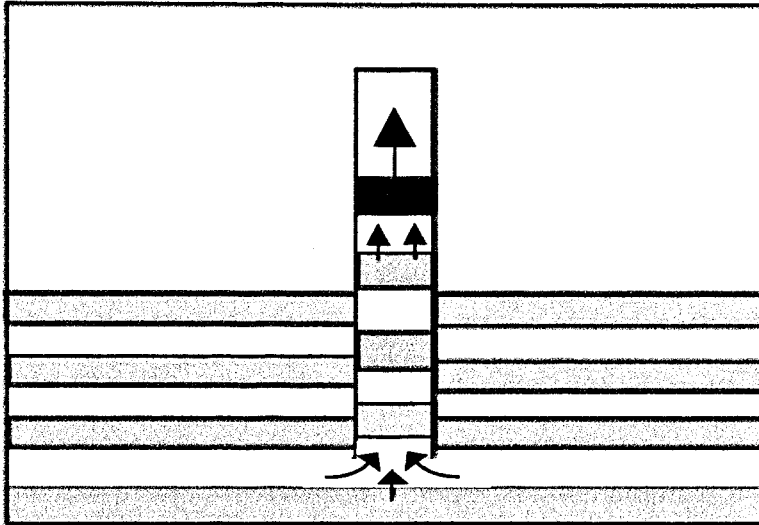


Fig. 3.14: The sucking-up of sediment from outside the core barrel by suction due to the piston not being in contact with the sediment when it begins to lift (re-drawn from Skinner & McCave, 2003).

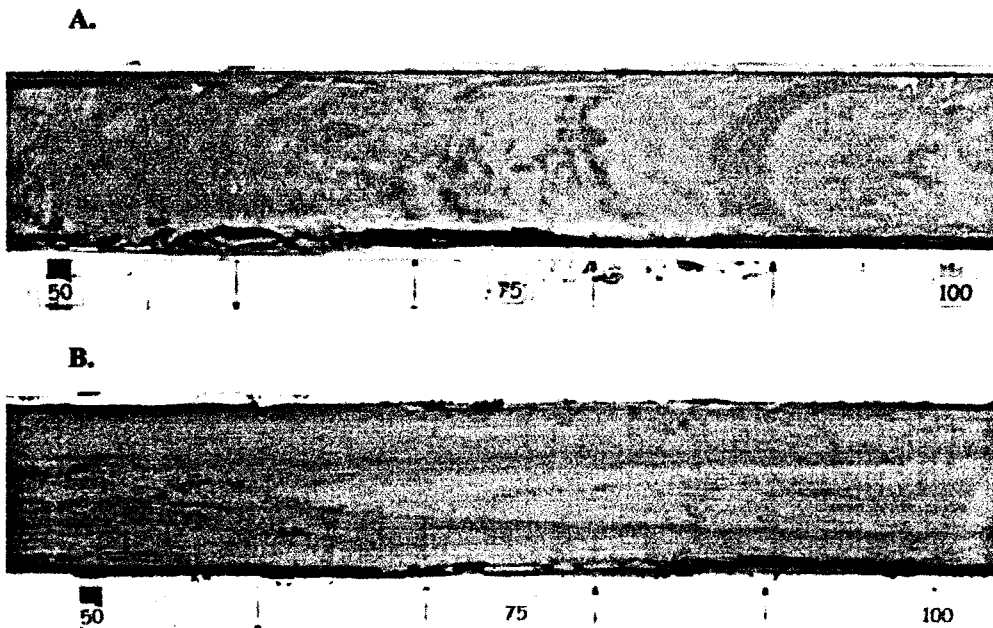


Fig. 3.15: A) Bending of the laminae in piston core MD01-2446, section IIb. B) Extreme suction of excess material due to "flow-in" in piston core MD01-2443, section XIXb (Taken from Skinner & McCave, 2003)

The main problem caused by distortion to a sediment core is the disruption to the stratigraphic continuity by either extending or shortening the core (McCoy, 1985; Blomquist, 1985). The alteration of the original laminae affects the ability of the core to produce accurate sedimentation rates or determine chronostratigraphical sequences (McCoy, 1985; Buckley *et al.*, 1994).

After extensive modelling of coring techniques based on soil mechanics and testing on marine cores, Skinner & McCave (2003) determined that stretching was likely to take place between ~5 and 15m depth in a piston core, depending on cable length (therefore, water depth). In MD01-2461, it is expected that stretching took place between 5-15m depth extending the sediment by 1.5-2.5 times (I.N. McCave, Pers Comm, 2004).

Once onboard the ship, the core is cut into manageable 1.5m sections, labelled, sawn in half lengthways and then opened using the cheese-wire technique mentioned in Section 3.1 (Fig. 3.16). One half is archived whilst the other is used for preliminary analysis, including sediment logging, spectrophotometric measurements, photographs along with porosity, density, P-wave velocity and amplitude and magnetic susceptibility made using a multi-sensor logging tool (MST). The working half of the core is then packed and cold stored.

MD01-2461 was retrieved and used as part of a NERC funded project entitled “Sequencing Ocean-Ice-Climate Interactions in the North East Atlantic.” The project involves collaboration between the University of Wales, Bangor, the University of Cardiff, the University of St Andrews, University of Cambridge, University of Bordeaux, and the Natural History Museum (NHM), with much of the work contributing to PhD theses. Work to date includes palaeoclimate analysis using IRD, some mineralogical work and foraminifera work by Vicky Peck in Cardiff, and examination of coccoliths by Craig Koch in the NHM.

The work in this thesis will concentrate on the environmental magnetic analysis of both cores: OMEX 2K and MD01-2461. Access to material from both the cores

was granted by Dr James Scourse (University of Wales, Bangor), and Dr Ian Hall (University of Cardiff). OMEX 2K was selected for a pilot study of the techniques because of its extensive previous analysis and, following its success, the Principal Investigators of the above NERC research project (Sequencing Ice-Ocean-Climate Interaction in the North East Atlantic) granted access to MD01-2461. This second core provided the opportunity to develop the pilot study and look at the same events in different cores, as well as to extend the record back in time to study all the HEs at a single location.

4.0 Methodology

4.1 Preliminary Analysis of OMEX 2K and MD01-2461

4.1.1 Core Physiology

Two U-channels from the core OMEX 2K were made available for analysis (by Dr Ian Hall, Cardiff University and Dr James Scourse, University of Wales, Bangor), along with the X-radiographs taken of the original Kasten core (Fig. 3.8). The X-rays were examined and the number of visible lithic grains counted at a resolution of 2 cm, as described in Austin & Kroon (2001) and Andrews & Barber (2002). While a somewhat crude form of analysis, these data provide a first order, non-destructive approximation of the variations in IRD concentrations with depth. The U-channels were then visually described in terms of the texture, colour (using the Munsell Soil Colour Chart, 1973) and the presence of coarse grains, visible foraminifera and anything else of interest. Photographs were also taken for a visual record of the core surface (Fig. 4.1). X-ray Diffraction (XRD) analysis was provided by Angus Calder (University St Andrews), on a small number of samples from OMEX 2K. 18 samples were selected at various depths with differing mineralogical signatures (identified from the mineralogical data provided by Dr. M Fruze; see below), the samples were crushed to $<10\text{ }\mu\text{m}$ with an agate ball mill and dried in a drying oven at 80°C . Approximately 1 g of sediment was used for the XRD analysis and packed into standard Philips sample holders (Fig. 4.2b) in order to produce a random orientation. The samples were then run in a Philips PW1050/ Hiltonbrooks DG2 instrument (Fig. 4.2a) using a Colbalt anode tube. The data was analysed with WinXRD version 2 software using the ICDD powder diffraction file by Angus Calder, and the percentage abundance of each mineral present was calculated using Rietveld refinement methods.

The original plaquettes from MD01-2461 used for taking X-rays were made available by Dr Ian Hall, Cardiff University. Photographs and core logs were taken onboard ship and were also provided by Dr James Scourse, University of Bangor

(Fig. 4.3). Lithic grain counts were made by Vicky Peck, Cardiff University, as part of her PhD analysis (Peck, unpublished data). Samples were dried in a drying oven at c. 30°C, following which the residues were weighed and then dry sieved at 150 μm . The number of lithic grains greater than 150 μm in size were counted under a microscope at each depth (every 4 cm) and expressed as the number of grains per gram of sediment (Fig. 4.4).

4.1.2 Volume Susceptibility

Using a MS2E1 High Resolution Susceptibility Sensor attached to a Bartington Instruments Susceptibility Meter (Fig. 4.15a), the whole-core volume magnetic susceptibility (κ) was measured along OMEX 2K. The meter was set to SI units with a range of 0.1 and linked to a computer running Bartington Instruments computer software; Multisus v.2. Susceptibility measurements were then taken at 1 cm intervals. A background reading was taken between each measurement, to correct the results for background “noise”. Once the entire core had been measured, the process was repeated, and an average taken for each of the U-channels. In a number of small sections of the core measurements were not possible as the sediment was damaged or missing, mainly because of shrinking and drying out during storage. There were a total of 10 cm worth of sediment missing from the core (the gaps packed with tissue), with a further 30 cm worth of sediment fractured and disturbed, equating to 16.6% of the recovered core material. Most of the damaged material was still able to produce a reading, though the effect of the uneven surfaces is unknown. These sections are noted on Fig. 4.5, along with the volume susceptibility. Fortunately, the damage only transpired into two completely missing samples when the core was sub-sampled (100 cm depth and 235 cm depth). The damaged sections appear to have had little impact on the resultant magnetic susceptibility when compared to the subsequent mass specific measurements. The missing sections have registered a low measurement, with the exception of the gaps below 225 cm, which appear to have a volume susceptibility record similar to the mass specific susceptibility measured later, probably due to the influence of surrounding material.

OMEX 2K Goban Spur (2333 m)

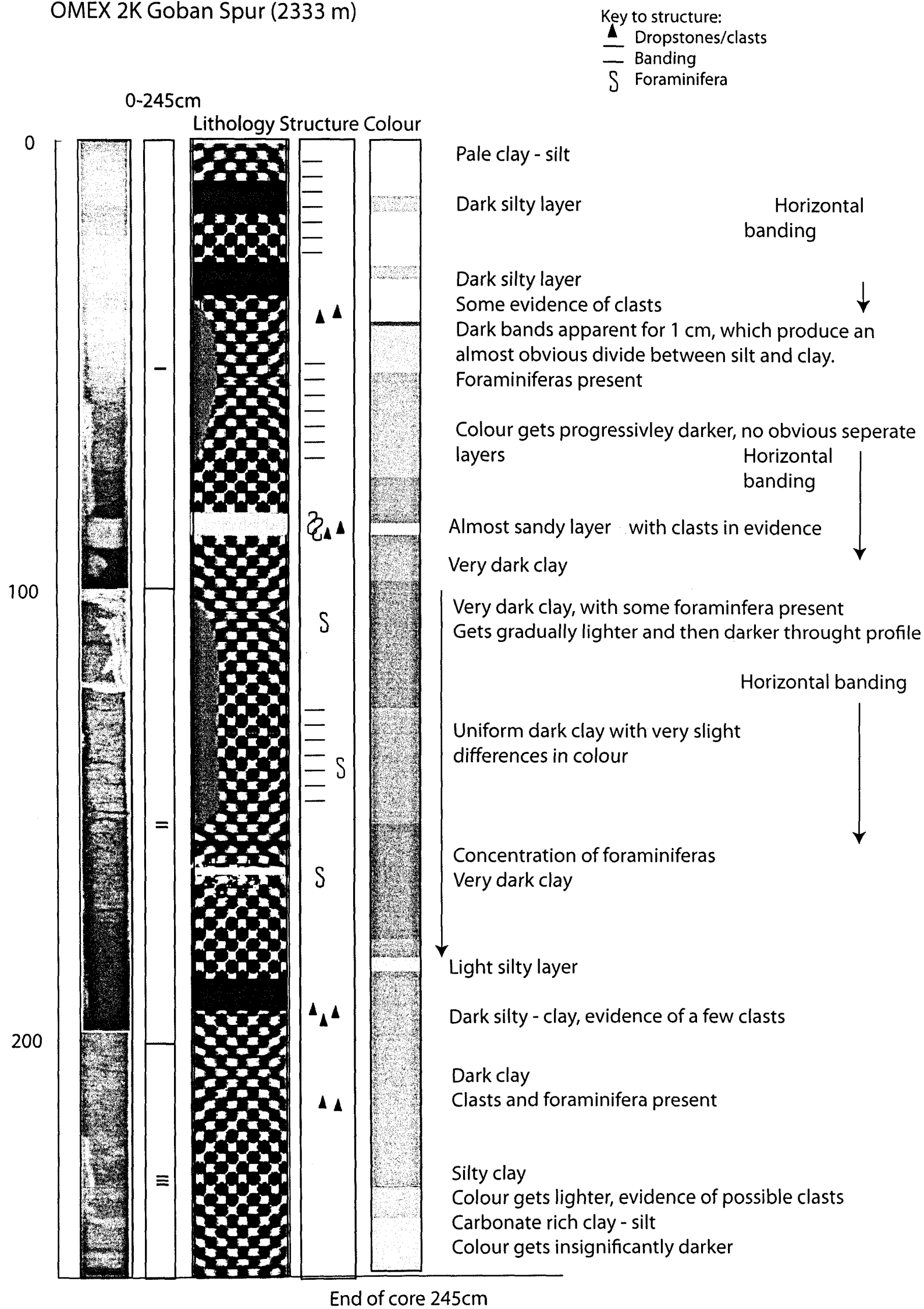
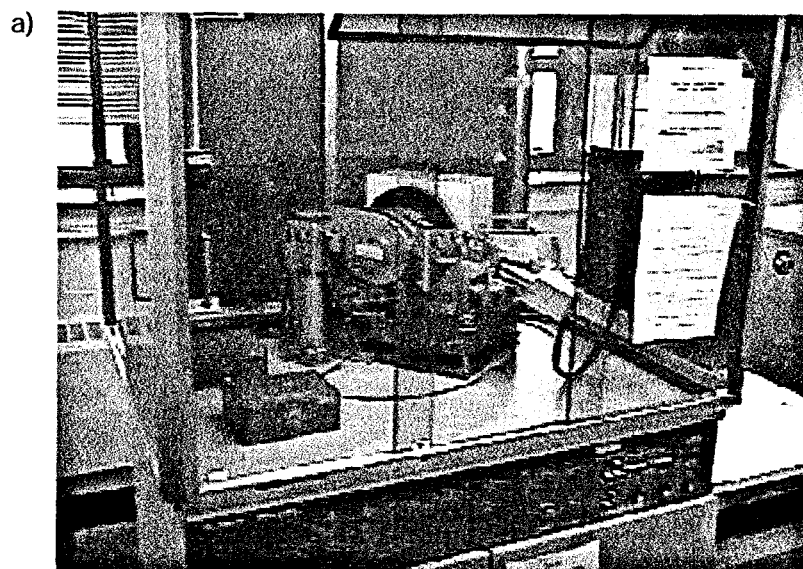


Fig. 4.1: Core logs, photographs and descriptions from OMEX 2K



b)

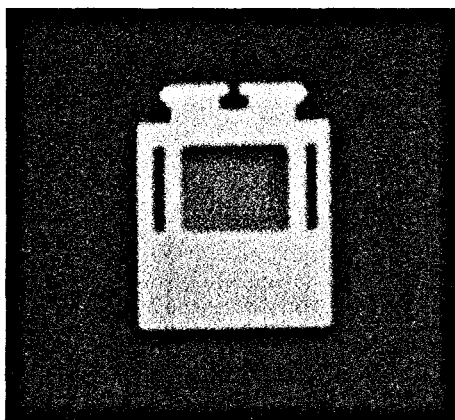


Fig. 4.2: Philips PW1050/Hiltonbrooks DG2 X-ray Diffractometer (a), with a close up of a standard sample pot (b).

In contrast, the damaged sediment below 225 cm shows a lower volume susceptibility than the dual frequency susceptibility (Section 4.3).

To establish whether there had been any alteration in magnetic susceptibility of OMEX 2K during the storage of the core, the volume susceptibility curve produced above was compared to that in Scourse *et al.*, (2000), which was recorded on board ship after the core had been taken (Fig. 4.5). A correlation was performed on the two datasets, which returned a relatively strong positive correlation (0.667) (Fig. 4.6). While some variation would be expected between the two data sets due to the different instrumentation used and the higher resolution of the data from this thesis, this statistically significant correlation suggests that the long-term storage of OMEX 2K has not had a major effect on its magnetic properties, and we can be confident about the reliability of future data obtained from this core.

Volume susceptibility was measured on the MD01-2461 plaquettes, again using the MS2E1 High Resolution Susceptibility sensor attached to a Bartington Instruments Susceptibility Meter (Fig. 4.15b) for comparison to the ship data. Unfortunately, it was found that the plaquettes containing the sediment were metallic, and therefore unsuitable for *in situ* or palaeomagnetic analysis, including volume susceptibility measurements made in this way, although sediment sub-samples taken from the plaquettes would still be suitable for mass-specific environmental magnetic methods. Alternative pre-sampled sub-samples were provided by Dr James Scourse (originally taken for Dinoflagellate work, but not intended to be processed for several more months), so it was decided to keep the plaquettes intact and retain them for future use. As environmental magnetic techniques are non-destructive, the samples used could be returned for Dinoflagellate analysis at a later date. Samples had been taken at 2cm resolution between depths of 120 –1499 cm, yielding a total of 690 samples.

MD01-2461 Porcupine West (1135 m).

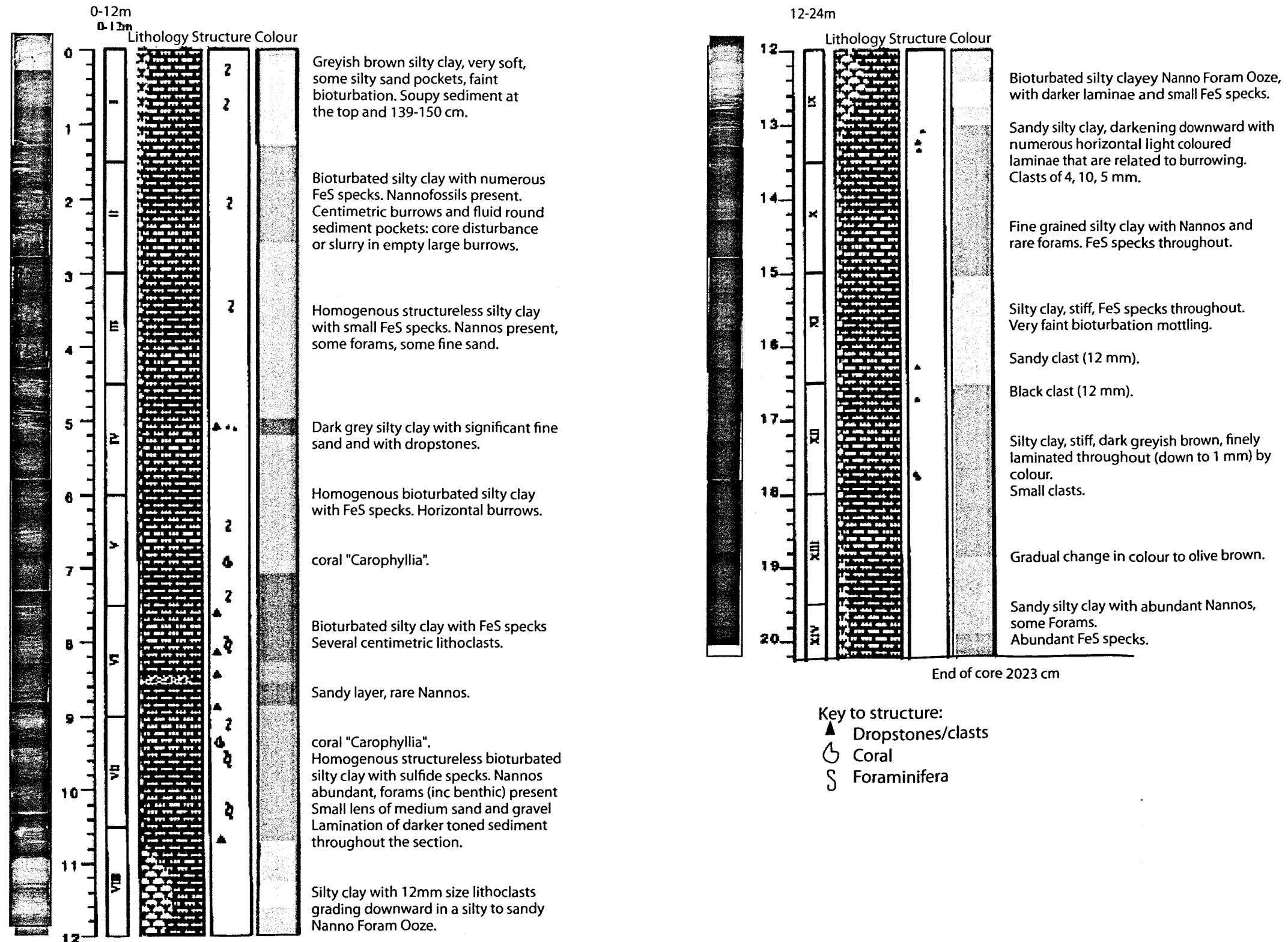


Fig. 4.2: Core logs, photographs and description for MD01-2461. All taken onboard the RV Marion Dufresne (Courtesy of Dr. J Scourse, 2003).

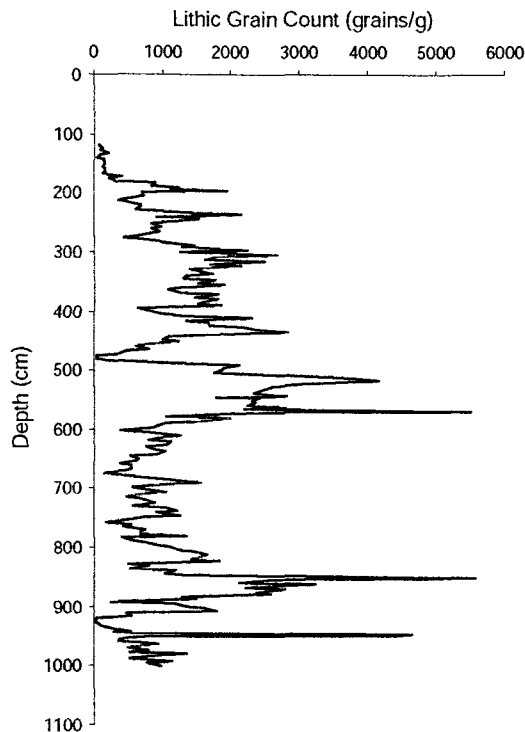


Fig. 4.4: Lithic grain count for MD01-2461. Grain >150 μ m per gram of sediment (Peck, unpublished data).

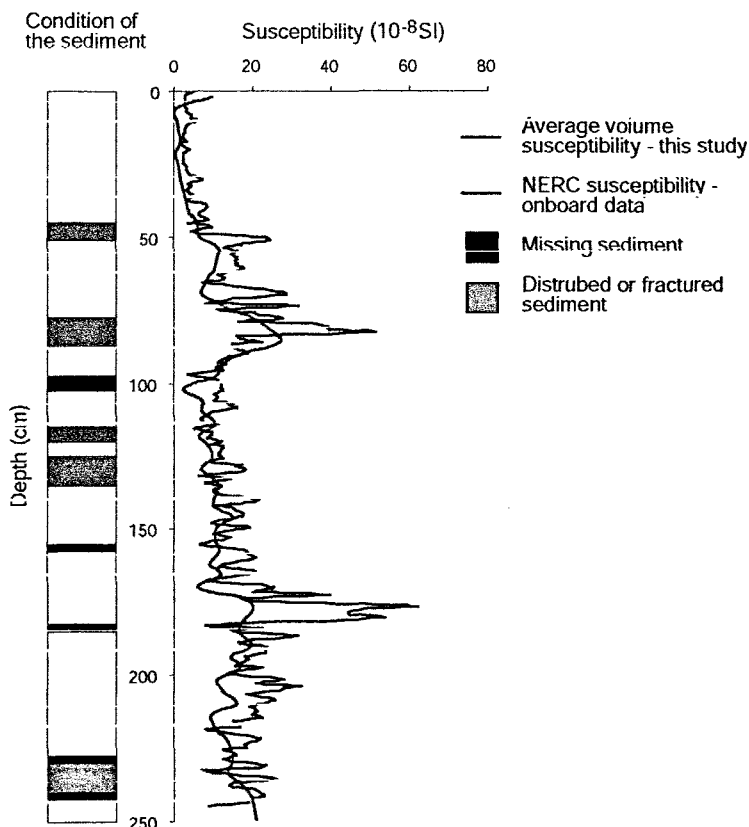


Fig. 4.5: Volume susceptibility from this study (2001) compared with that measured onboard ship immediately after the core was retrieved (1995). Data taken from the OMEX 2K CD ROM dataset (Lowry *et al.*, 1997). On the left is the record of the condition of the sediment during the susceptibility measurements made in 2001. Black squares record areas of missing sediment, grey show areas of disturbed sediment. The damaged sediment appears to have little influence on the susceptibility, with the exception of the two sections below 225cm depth. The missing sediment records low, or no, susceptibility, also with the exception of the section below 225cm.

4.2 Radiocarbon Dating and Chronology

Chronostratigraphy is the classification of a stratigraphical record in terms of time (Whittow, 1984; Lowe & Walker, 1997). It determines the correct sequence of events in a rock or sedimentary record and relates it to time (Lowe & Walker, 1997; Sinclair, 2001). Chronostratigraphy is necessary to improve the resolution of stratigraphic sequences, in order to examine the temporal relationships between various lines of proxy evidence used as indicators of events such as sea level and climate change (Kidd & Hailwood, 1993). A variety of techniques are available to develop a chronology, including radiocarbon dating, uranium/thorium dating, oxygen isotope stratigraphy, lead dating, and dendrochronology. Different techniques provide different levels of precision, and are capable of providing age control over different timescales. Therefore, the requirements of the project must be determined before a method is selected. A crude stratigraphy will suffice for the analysis of long-term changes, however, a study of shorter variations, such as the Dansgaard-Oeschger cycles, require a much higher resolution chronology.

4.2.1 Radiocarbon Dating

Radiocarbon dating is one method utilised within chronostratigraphy and works using the principle that the decay of ^{14}C is at a constant rate (Bowman, 1990). It is the primary dating technique within the context of this work, due to the abundance of foraminifera shells available, and has been used on OMEX 2K (see below). First developed by Willard Libby in the late 1940s, radiocarbon dating has become a successful technique taking advantage of the unstable and weakly radioactive properties of the ^{14}C isotope. ^{14}C is constantly formed in the atmosphere and readily combines with oxygen to form carbon dioxide (Bowman, 1990; Doyle *et al.*, 1994; ANSTO, 2003). It then rapidly cycles through the atmosphere, hydrosphere (dissolving in the oceans) and the biosphere (photosynthesis and incorporation into the food chain)(Fig. 4.7)(Bowman, 1990; Doyle *et al.*, 1994; ANSTO, 2003). When the organisms that take up the ^{14}C die, the interaction with new atmospheric ^{14}C ceases and the unstable ^{14}C begins to

decay at a constant rate (Bowman, 1990; Lowe & Walker, 1997). Therefore, the number of ^{14}C atoms in an organism at its death (which is assumed to be the same number of ^{14}C atoms in a modern specimen of the same material), minus the number of ^{14}C remaining in the organism at the time of measurement, can be used to calculate the time elapsed since death (Bowman, 1990; Williams *et al.*, 1998). This technique however makes 5 major assumptions (Bowman, 1990; Broecker, 1995; Lowe & Walker, 1997):

- There is a constant concentration of ^{14}C in the atmosphere, both spatially and temporally;
- The biosphere has the same concentration of ^{14}C as the atmosphere;
- The concentration of ^{14}C is constant throughout the whole of the biosphere;
- Exchange of ^{14}C ceases immediately and only at death;
- The concentration of ^{14}C only decays after death.

Radiocarbon dating takes two forms: Radiometric (often called conventional radiocarbon dating) and Accelerator Mass Spectrometric (AMS). Radiometric dating detects the activity of the sample; that is, the number of electrons emitted per unit time and weight of sample by the decay of ^{14}C (Wand *et al.*, 1884; Bowman, 1990; ANSTO, 2003). It involves one of two methods: gas proportional counting or liquid scintillation counting, both of which need large samples and often take several days to perform (Lowe & Walker, 1997). AMS is a more recent technique, which is more efficient than radiometric techniques, as it is quicker and uses much smaller sample sizes (1-5 mg as opposed to 1-5 g). The AMS method directly detects the number, or a proportion of the number of ^{14}C atoms in a sample, relative to ^{13}C or ^{12}C atoms (Wand *et al.*, 1984; Bowman, 1990; ANSTO, 2003). It works in the same way as normal mass spectrometers (applying a magnetic field to a moving charged particle in order to deflect it), however, normal mass spectrometers are not sensitive enough to detect ^{14}C as it is often masked by other elements. AMS uses large voltage differences to speed up the particles, enabling the differentiation between elements of similar weights (e.g. ^{14}C and ^{14}N)(Lowe & Walker, 1997).

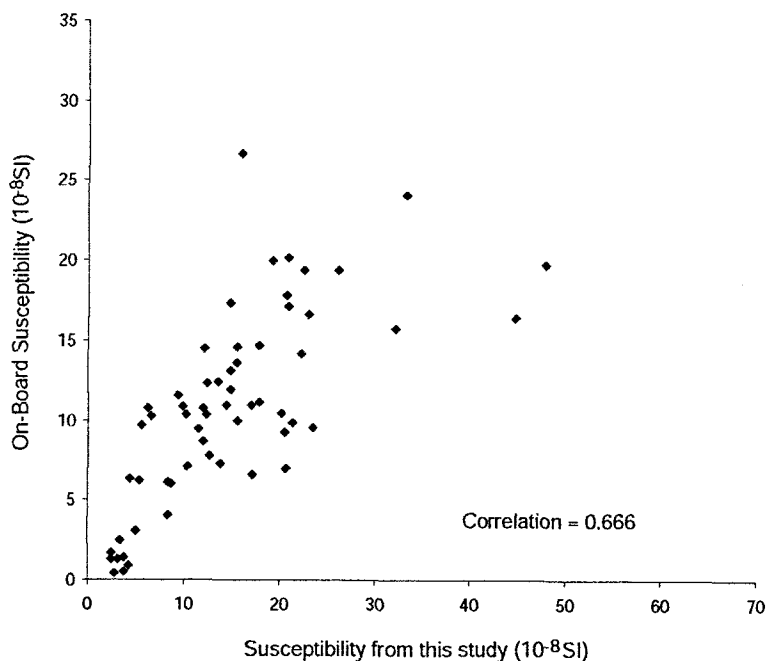


Fig. 4.6: Correlation between the susceptibility of OMEX 2K taken on board ship in 1995 and during this study in 2001.

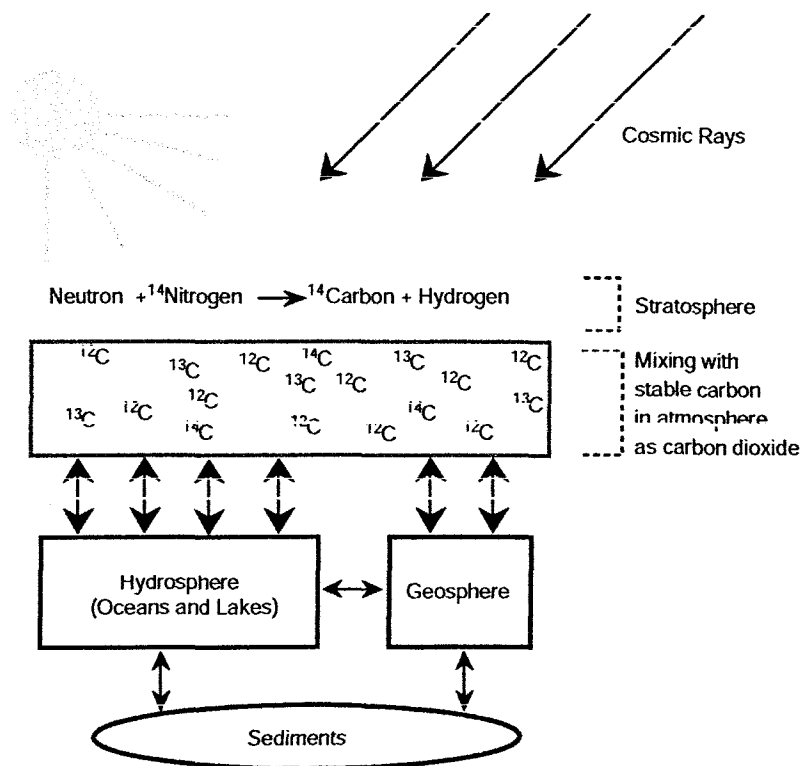


Fig. 4.7: The production and cycle of carbon through the atmosphere, hydrosphere, geosphere and biosphere. (re-drawn from Anon, date unknown - www.qub.ac.uk, 2004).

The most common detection system used is a tandem accelerator (Fig. 4.8a & b) (Bowman, 1990; Lowe & Walker, 1997). Samples are firstly converted to graphite and mounted on a metal disc to create a target for the accelerator (ANSTO, 2002). The original sample (foraminifera, shell, bone, wood etc.) is sandblasted with 30 μ alumina and etched in dilute HCl to remove 10-20% of the surface carbonate. They are then treated with 50% phosphoric acid under vacuum, the CO₂ recovered is dried and reacted with molten lithium metal and water to form acetylene (Wand *et al.*, 1984; Gillespie *et al.*, 1986). The acetylene is then pyrolyzed by a hot tantalum wire, on which graphite is deposited (Wand *et al.*, 1984; Gillespie *et al.*, 1986). Within the tandem accelerator, Cesium ions are fired at the graphite sample, producing negatively ionised C atoms, which are accelerated towards a positive terminal. ¹⁴N atoms are eliminated before they reach the detector, as they don't form negative ions. The ions are then sent through a "stripper" which removes four electrons, creating C³⁺. The C³⁺ ions are now repulsed from the positive terminal and are accelerated again through focusing magnets where deflection occurs. The concentration of ¹⁴C, ¹³C and ¹²C can be measured due to their different weights, and hence, different deflections. Once the ¹⁴C:¹²C ratio is measured, it is compared to standards which are made up from a material of known ¹⁴C activity, giving a sample/modern ratio from which a radiocarbon age can be calculated in years Before Present (BP) (Lowe & Walker, 1997).

4.2.2 Chronology

The radiocarbon ages produced by ¹⁴C dating are not calendar ages and must be calibrated in order to convert them to the calendar timescale (Pilcher, 1991). Variations in the production of ¹⁴C through time have resulted in a discrepancy between calendar years and radiocarbon years (Williams *et al.*, 1998). Radiocarbon ages are quoted in years BP (before present), with present defined at AD 1950 (Bowman, 1990; Lowe & Walker, 1997; ANSTO, 2003). AD 1950 is used because of the industrial effect, and more importantly, the impact of thermonuclear weapons testing on modern day atmospheric ¹⁴C levels (Williams *et*

al., 1998). Nuclear bombs release ^{14}C into the atmosphere, and testing has almost doubled the ^{14}C present in today's atmosphere (Fig. 4.9) (Higham, 2003; Anon, 2003). This has rendered organisms from the past 45-50 years unnaturally high in ^{14}C , and hence, AD 1950 (or pre-bomb, as it is known), has become accepted as "present" (Lowe & Walker, 1997; Higham, 2003). There is an upside to the nuclear bomb testing, however, as the large quantities of carbon released has been traced through the carbon cycle, improving our understanding of carbon mixing and exchange (Higham, 2003).

Calibration curves have been created by comparing ^{14}C dates to independently derived dates for the same stratigraphical event, using techniques such as dendrochronology (tree-ring sequences), varve chronologies and Th/U dating of corals (Stuiver & Reimer, 1993; Goslar *et al.*, 1995; Bard *et al.*, 1998; ANSTO, 2003). Dendrochronology has produced accurate calibration curves back to 11.9 kyr BP (Bard *et al.*, 1998; Hughen *et al.*, 1998; Geyh & Schluchter, 1998; Stuiver *et al.*, 1998) with corals and laminated marine sediments extending the curve to approximately 24 kyr BP (Stuiver *et al.*, 1998; Geyh & Schluchter, 1998) and more recently, work on the varved sediments of Lake Suigetsu, Japan (Kitagawa & van der Plincht 1998; 2000) and Caricao Basin (Hughen *et al.*, 2004) has produced a high resolution curve back to over 45 kyr BP. An internationally agreed calibration curve (INTCAL98, Stuiver *et al.*, 1998) for both the atmosphere and the marine environment provides the most reliable calibration procedure at present. A section of this curve can be seen in Fig. 4.10. Marine samples are subject to a marine reservoir effect, which must be taken into account before calibration (Bowman, 1990), hence a separate calibration curve for the marine environment is required. Unfortunately, because the mixing rates in the ocean are significantly slower than the atmosphere, marine reservoir ages exhibit significant geographical variations (Heier-Nielsen *et al.*, 1995; Stuiver *et al.*, 1998).

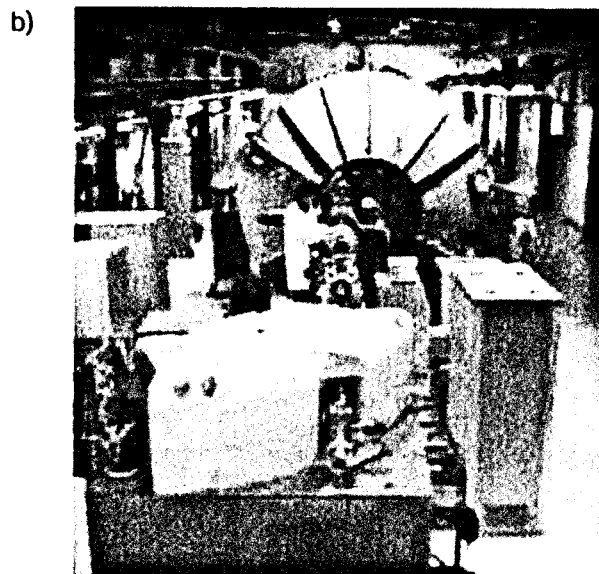
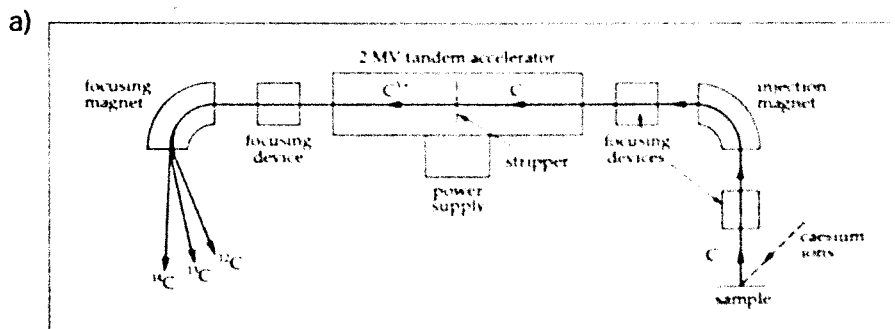
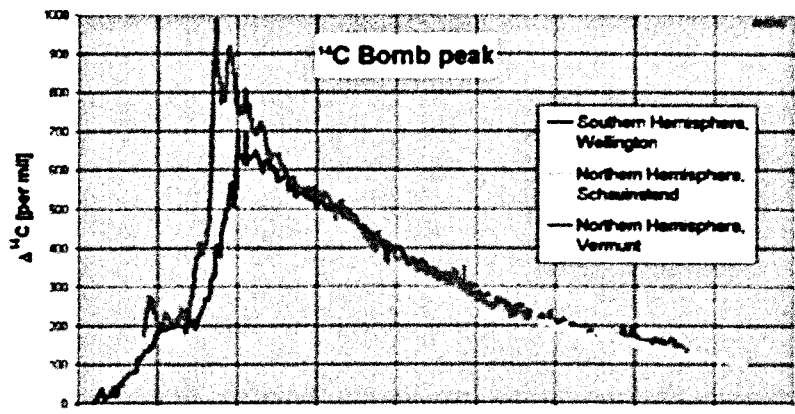


Fig. 4.8: a) Schematic of a Tandem Accelerator Mass Spectrometer (Bowman, 1990). b) Photograph of the ANTARES (Australian National Tandem for Applied Research) Tandem Accelerator in Australia (ANSTO, 2003 -www.ansto.gov.au)



Radiocarbon in atmospheric CO₂ dissolves into the oceans at the sea-air interface and can subsequently be taken up by the marine organisms present (such as plankton, algae, molluscs, foraminifera and fish). The organism will normally retain the ¹⁴C:¹²C ratio of the water. This ratio is, however, different to that of the contemporaneous atmosphere due to inequalities between the input of atmospheric ¹⁴C and its removal by transport or radio-decay. This gives marine organisms an apparent age, significantly older than their actual age, because the ¹⁴C:¹²C ratio of sea water is distorted by the large “reservoir” of older water (Bard *et al.*, 1994; Austin *et al.*, 1995; Waelbroeck *et al.*, 2001). This apparent age is called the marine reservoir age (Bowman, 1990; Heier-Nielsen *et al.*, 1995; Lowe & Walker, 1997). The marine reservoir age is dependent on oceanic and climatic variables such as upwelling, mixing rate, wind speed, deep water formation and ice cover which means it varies between oceans and regions, and has also varied over time (Heier-Nielsen *et al.*, 1995; Austin *et al.*, 1995; Stuiver *et al.*, 1998; Bard *et al.*, 1998). The modern standard reservoir age for the surface waters of the North Atlantic region is close to 400 years (Heier-Nielsen *et al.*, 1995; Stuiver *et al.*, 1998; Geyh & Schluchter, 1998). Pacific Ocean reservoir ages have been estimated between 580-788 years (Lowe & Walker, 1997; Waelbroeck *et al.*, 2001), with Southern Ocean and other high latitude ages as large as 1200 years (Bard *et al.*, 1994; Austin *et al.*, 1995; Waelbroeck *et al.*, 2001). Reservoir ages for the North Atlantic during the Younger Dryas have also been estimated at 700 years (Bard *et al.*, 1994; Austin *et al.*, 1995) with larger ages for the end of H1 (1230 ± 600 to 1940 ± 750 years)(Waelbroeck *et al.*, 2001).

Radiocarbon ages determined from surface dwelling marine organisms must be corrected for the reservoir age prior to calibration, which for North Atlantic cores involves the subtraction of 400 years from the ¹⁴C date (Heier-Nielsen *et al.*, 1995).

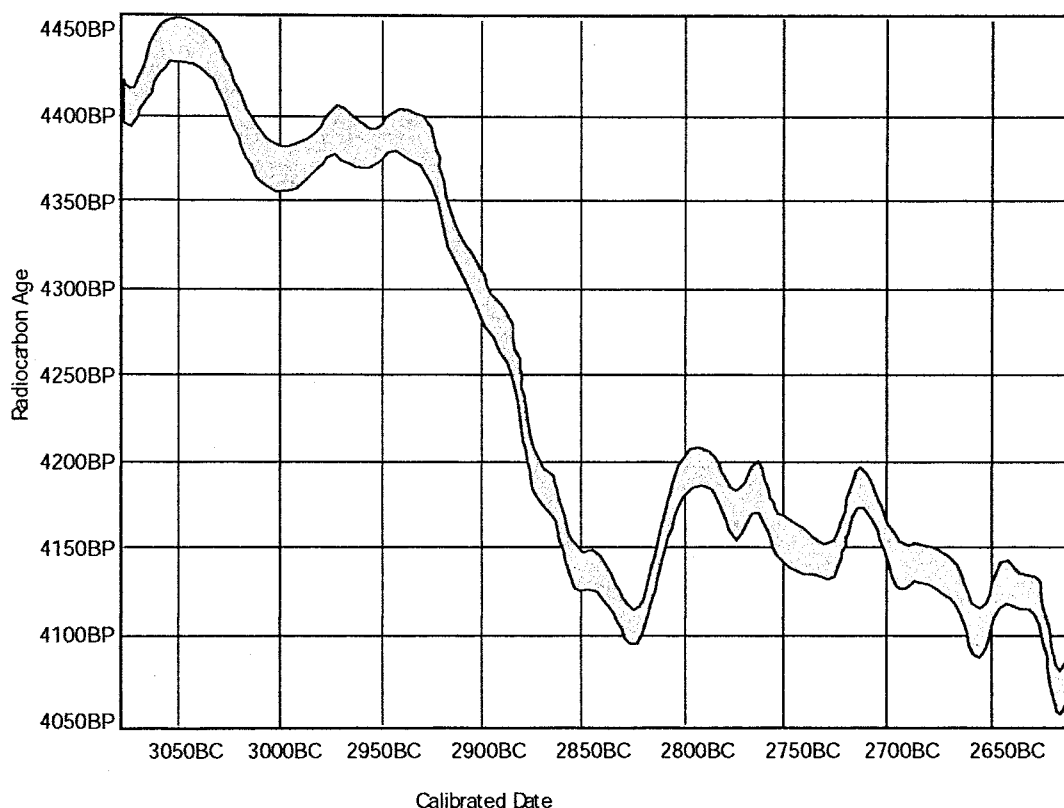


Fig. 4.10: A section of the INTCAL98 calibration curve. (Re-drawn from Stuiver *et al.*, 1998; Higham, 2003).

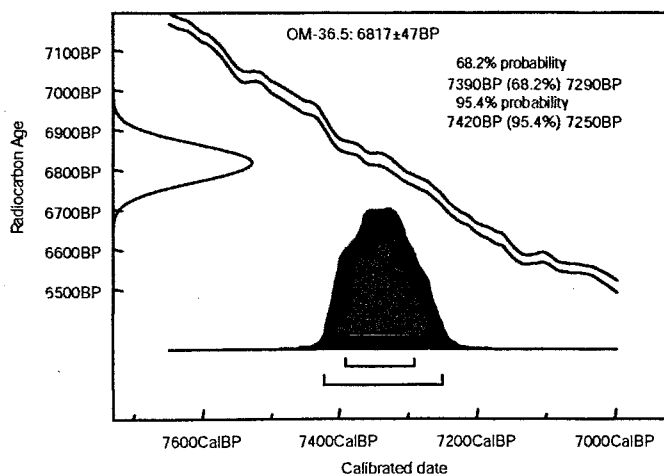


Fig. 4.11: An example of a probability distribution created by the OxCal 3.8 computer calibration software. The blue lines are the 14C calibration curves; the upper line is the atmospheric curve, the lower line, the marine curve. The red line on the right is the distribution given by the original 14C date provided by the radiocarbon lab. The solid black distribution on the x-axis is the intercept of the conventional 14C date with the calibration curve (i.e. the red and the blue lines). An age from within that distribution is selected as the calibrated 14C age, the methods for which is explained in the main text.

In order to create a stratigraphic sequence for a marine core, samples of a species of foraminifera must be picked from the sediment and sent to a radiocarbon dating centre (further details on this procedure can be found below in Section 4.2.3, and below in Section 4.2.1). Once the ^{14}C dates have been received, the first step is to correct for the relevant reservoir age. In this work, the 400 year North Atlantic standard was used.

Once this is done, the computer programme OxCal 3.8 (Bronk Ramsey, 1995) can then be used to calibrate the ages. It utilises the 310 year moving average INTCAL98 marine calibration curve from Stuiver *et al.*, 1998. The OxCal 3.8 software generates a probability distribution for each ^{14}C age (e.g. Fig. 4.11). A series of possible ages are calculated from intercepts between the ^{14}C age and the calibration curve at both the 68.2% probability and 95.4% probability ranges. One of these ages must be selected by either calculating the mean age from the 95.4% probability range, as suggested by Pilcher (1991), or by calculating a weighted-mean from the probability distribution (Telford *et al.*, 2004a). Beyond approximately 20 kyr BP, the marine calibration curve is poorly constrained, which means samples older than this cannot be calibrated using OxCal 3.8 (OxCal, 1995). In these cases, the Bard Age Equation (Eqn. 4.1, Bard *et al.*, 1998) can be used to determine the calibrated age. This has the apparent advantage of giving a single date, rather than a range of possible dates from which one must be selected. However, this has the limitation that the age uncertainty is unknown and possibly large. The equation was also developed using only a few samples from corals (approx 50), the majority of which were younger than 25 kyr BP; with Uranium-Thorium dates and radiocarbon dates measured in tandem (Bard *et al.*, 1998).

The Bard Equation is one of relatively few methods available for calibration beyond 20 kyr BP. Alternatives include tuning proxy records to one of the Greenland Ice Cores (e.g. Bond *et al.*, 1993; Bond & Lotti, 1995;), or extrapolating back using average sedimentation rates from dates younger than 20 kyr (e.g. Broecker *et al.*, 1992; Bond *et al.*, 1992). A recent paper by Hughen

et al., (2004) provides high resolution calibration data back to 50 kyr based on the correlation of ^{14}C dates on the varved sediments of the Cariaco Basin to the annual layers in the GISP2 record. These two proxy records have previously been noted to be near-synchronous (Huguen *et al.*, 1998; 2000), and the method appears to be a more precise one than the Bard Equation, but it has yet to be validated and accepted by the calibration world. Therefore, in the present study, ^{14}C ages older than 20 kyr have been corrected (see above) and calibrated using Equation 4.1.

Bard Age Equation:

$$\text{Calibrated Age (years BP)} = -3.0126 \times 10^{-6} \times (^{14}\text{C age BP})^2 + 1.2896 \times (^{14}\text{C age BP}) - 1005$$

$$\text{Where } ^{14}\text{C age BP} = \text{conventional radiocarbon age} - \text{the marine reservoir correction} \quad (\text{Eqn 4.1})$$

Once the dates have been selected, the development of an age-depth model is essential to be able to determine an age for any given depth along the core. The usual procedure involves plotting the calendar ages against depth and fitting a polynomial trendline (Telford *et al.*, 2004a). The equation of this trendline will attribute an age to any depth along the core.

There are several issues that must be borne in mind when dealing with radiocarbon dates. A calibrated radiocarbon date is not an “absolute” date in that there are many sources of error that must be taken into account. Not only do calibration issues, such as the selection of the age from the range provided by the raw radiocarbon date, and the application of a correct reservoir age limit the precision of the age (e.g. Heier-Nielsen *et al.*, 1995; Austin *et al.*, 1995; Stuiver *et al.*, 1998), but the documented variation in ^{14}C production both spatially and temporally (e.g. Williams *et al.*, 1998), means that there have been different ratios of isotopes available to organisms, and that the number of ^{14}C atoms in an organism at its death may be significantly different to today’s specimens (Bartlein *et al.*, 1995). ^{14}C production is influenced by the Earth’s geomagnetic field

intensity, as this controls the quantity of cosmic rays that reach our atmosphere, creating radiogenic nuclides like ^{14}C . Fluctuations in the Earth's geomagnetic field intensities over the last 45 kyr have resulted in at least 80% of the ^{14}C production variation (Laj *et al.*, 1996). All these factors mean that care must be taken when developing a chronology for any stratigraphical sequence.

4.2.3 ^{14}C Dating and Chronology of OMEX 2K

Previous ^{14}C dates have been obtained and reported from the OMEX 2K core by Hall & McCave, (1998a) and Scourse *et al.*, (2000), mainly concentrating on the area surrounding H2. During the course of this study, a successful application was made to NERC for the ^{14}C dating of 7 additional points along the core within this project, in order to help constrain the area around H1 and the Younger Dryas. Table 4.1 details these points and the reasons they were chosen for dating. Sample residues (i.e. the material of various size fractions left after sieving and drying), were provided by Dr James Scourse, who had carried out the preliminary lithological analysis. For the cold water samples (i.e. in and around the HEs), the polar planktonic foraminifera *Neogloboquadrina pachyderma* (s) (Fig. 4.12a) was selected for picking, because of its overwhelming abundance (Table 4.1). For samples representing warmer waters (between HEs), benthic *Globigerina bulloides* (Fig. 4.12b) was selected again because of abundance (Table 4.1). It must be acknowledged that the species of foraminifera picked for dating may have a slight impact on the resulting dates (Broecker *et al.*, 1984; 1988). Different species may inhabit different levels in the ocean thermocline, thereby taking up carbon of differing ages (due to the reservoir effect discussed above) (Bard *et al.*, 1987). The lower in the water column they live, the older the ^{14}C they will be likely to incorporate into their shells. These differences, however, are also important as they help identify palaeocirculation patterns (Broecker *et al.*, 1984; 1988).

The species used in this study have been recorded (see Tables 4.1 and 5.1), however, it is not known which species of foraminifera were used by Hall & McCave, (1998a), or Scourse *et al.*, (2000). Each sample was dry sieved using a

mesh size of $>150\ \mu\text{m}$ and at least 1000 individual foraminifera were picked for the dating process, typically yielding 12 mg of sample. Once the foraminifera had been picked, they were sent to the NERC Radiocarbon Dating Laboratory at East Kilbride for ^{14}C AMS dating.

The dates received from East Kilbride (Table 4.2) were calibrated using OxCal 3.8 as described above. The mean date from the 95.4% probability range was selected, as suggested by Pilcher, (1991) because the data required to calculate the weighted-means of the distributions were not readily available. If there were several possible solutions within the 95.4% probability range, the one with the highest probability within the range was selected. For example, the probability distribution from OxCal 3.8 for sample AA-53034, age 11926 ± 67 years BP is shown in Fig. 4.13, and includes a table explaining which calibrated age was selected and how.

The marine calibration curve at this time (11926 ± 67 years BP) is highly variable, creating a complex probability distribution. OxCal 3.8 has generated 4 possible intervals for this age; one at 68.2% probability and three at 95.4% probability (12.7%, 80.3% and 2.4%) The mean for these three intervals were calculated, and the age with the highest probability (80.3%) was selected (Fig. 4.13). The age selected for sample AA53034 therefore was 13350 ± 200 years BP.

Samples KIA8068-KIA8072 (Table 4.2) are older than the limits of the marine calibration curve in OxCal 3.8, therefore the Bard age equation (Eqn. 4.1) was used to calibrate those ^{14}C ages. Table 5.1 shows all the ages for OMEX 2K. Once all the radiocarbon ages were calibrated, they were plotted against depth in order to develop an age model for OMEX 2K. The age model will be further discussed in Section 5.1.

Table 4.1: ¹⁴C dates and their justifications. Taken from the NERC ¹⁴C Dating application.

Depth (cm)	Justification
41.5	Immediately above the Vedde Ash layer and coincident with a marked transition in magnetic variables. Possible Younger Dryas/Holocene Boundary. Species: <i>G. bulloides</i>
60.5	Possibly the onset of the Younger Dryas event. Marked with minima in χ and Soft IRM prior to both showing increases. Species: <i>G. bulloides</i> .
68.5	Constraint of timing marked shifts in magnetic properties. Also confirmation of existing dates and constraint of age-depth model. Species: <i>G. bulloides</i> .
88.5	Possible onset of the main H1 event. A transition in χ and soft IRM from low to high values. Species: <i>N. pachyderma</i> .
92.5	Zone of any H1 precursor events. Minima in -100 backfield ratios. Species: <i>N. pachyderma</i> .
108.5	As above.
138.5	Peak in soft IRM and χ_{arm} . Improvement of age-depth relations between H1 and H2. Species: <i>N. pachyderma</i> .

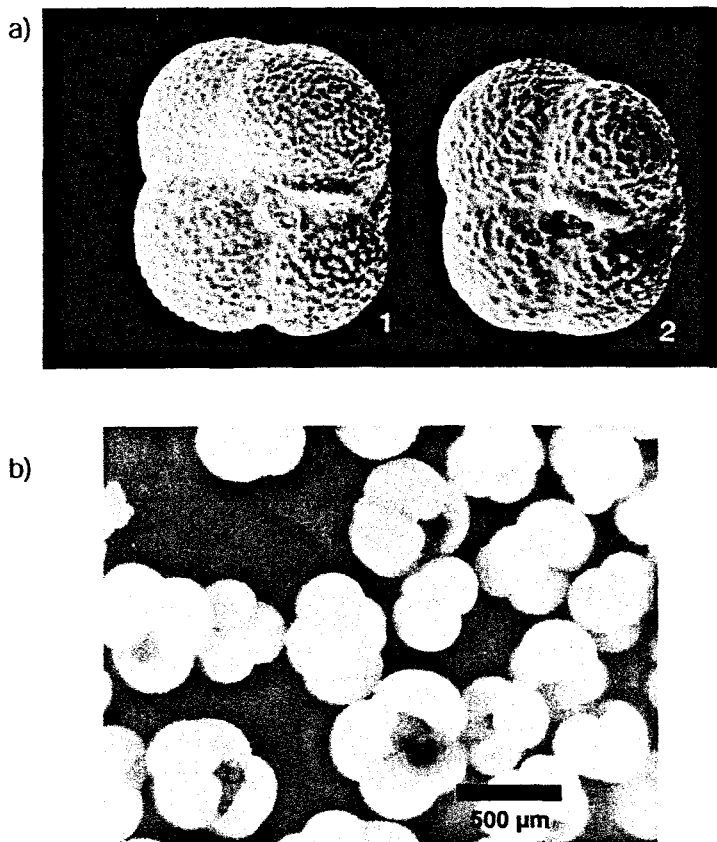
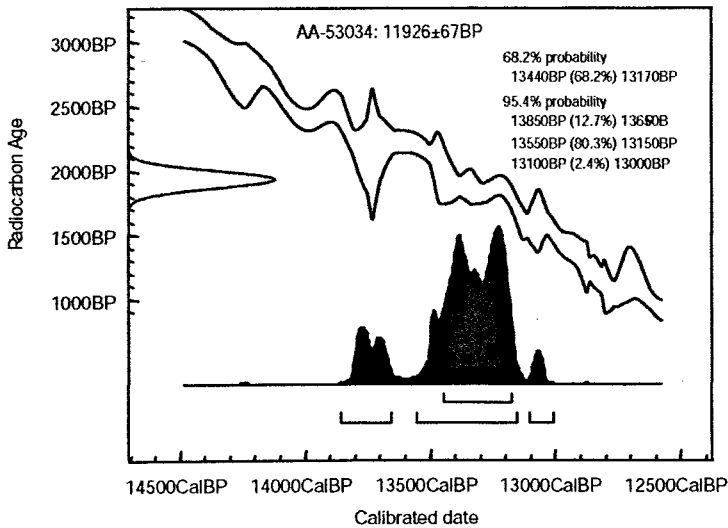


Fig. 4.12: a) SEM images of *N. pachyderma*, apertural view; b) Photograph of a *G. bulloides* radiocarbon dating sample. All images courtesy of Dr. B. Austin.

Table 4.2: ^{14}C dates obtained for OMEX 2K.

Code	Depth (cm)	Conventional Radiocarbon Age (BP $\pm 1\sigma$)	Species of Foraminifera
CM-36.5	36.5	6817 \pm 47	
AA-53034	60.5	11926 \pm 67	<i>G. bulloides</i>
AA-53035	68.5	12514 \pm 61	<i>G. bulloides</i>
CM-73	73	13040 \pm 70	
AA-53036	88.5	14324 \pm 76	<i>N. pachyderma</i>
AA-53057	92.5	14721 \pm 76	<i>N. pachyderma</i>
AA-53058	108.5	15950 \pm 99	<i>N. pachyderma</i>
AA-53039	138.5	18010 \pm 200	<i>N. pachyderma</i>
KA-8068	166.5	20310 \pm 130	
KA-8069	170.5	20960 \pm 140	
KA-8070	174.5	20760 \pm 140	
KA-8071	186.5	21790 \pm 150	
KA-8072	198.5	22530 \pm 160	



Code	Depth	68.2% Max	68.2% Min	68.2% Mean	95.4% Max	95.4% Min	95.4% Mean
AA-53034	60.5	13400	13170	13305	13850 (12.7%) 13550 (80.3%) 13100 (20.4%)	3650 (12.7%) 13150 (80.3%) 13000 (2.4%)	13750 13350 13050

Fig. 4.13: The probability distribution of the calibrated age BP of sample AA-53034, radiocarbon age 11926 \pm 67. Produced by OxCal 3.8. The table below is the determination of the calibrated age for this sample. The age picked was 13350 years BP (i.e. that with the highest percentage).

4.3 Sample Preparation and Magnetic Analysis

The processes described in the next few sections are performed using machines that hold 10 ml plastic pots into which the material under analysis must be immobilised. Samples are weighed, wrapped in “cling-film” and packed into the pots. The “cling-film” is used as it has no magnetic signature and helps to immobilise the sediment within the pots. The pots are clearly labelled, with an arrow drawn on the bottom, to ensure constant orientation of the sample during the measurements (Fig. 4.14). Dearing (1999) states that 5g of sediment should be sufficient for routine magnetic analysis.

Low frequency mass specific susceptibility (χ) is a measure of how magnetic a material is (see Section 2.5.1). This was measured using a Bartington MS2 Susceptibility Meter with a Dual Frequency MS2B sensor (Fig. 4.15b) set to the low frequency setting (Dearing, 1999). The meter was connected to a PC running the Multisus v.2 software (Fig. 4.16). This software controls the operation of the meter and automates elements of the measurement process. Low frequency, mass-specific magnetic susceptibility data for each sample is stored within a data file for later transfer to Microsoft Excel.

This procedure is then repeated for each sample with the MS2B on the high frequency setting. The two frequencies give two susceptibility readings for the same sample (χ_{lf} and χ_{hf}), which are used to calculate the frequency dependence of susceptibility ($\chi_{fd\%}$) using the equation:

$$\chi_{fd\%} = \frac{(\chi_{lf} - \chi_{hf}) / \text{mass}}{10} \quad (\text{Eqn. 4.2})$$



Fig 4.14: Photo of sample pots used for magnetic analysis, containing samples from MD01-2461. The pots are labeled with the name of the core (2461), the depth (in this case, 580 cm depth) and an arrow along the bottom to ensure constant orientation throughout the measurements.

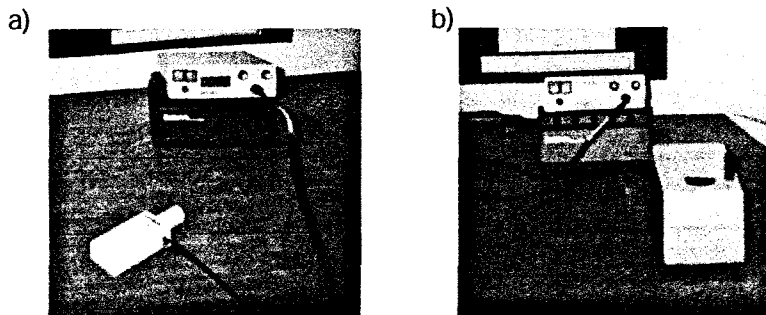


Fig. 4.15: Bartington Instruments MS2 Susceptibility Meters with the a) MS2E Volume Susceptibility probe and; b) MS2B Dual Frequency sensor.

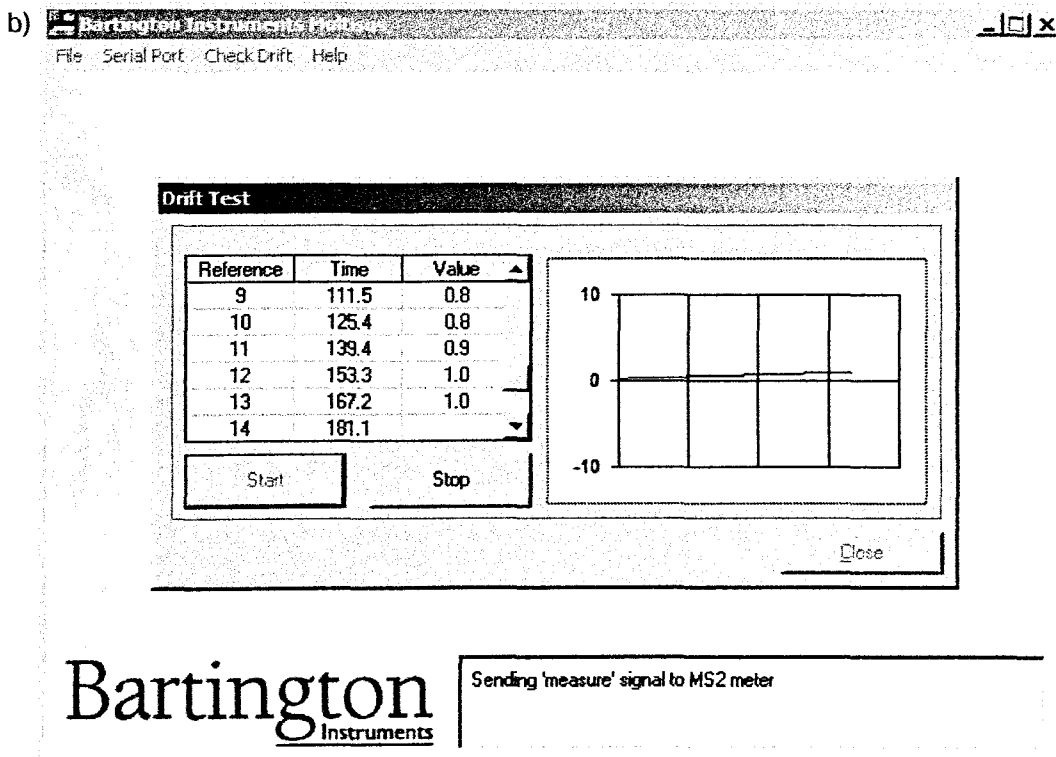
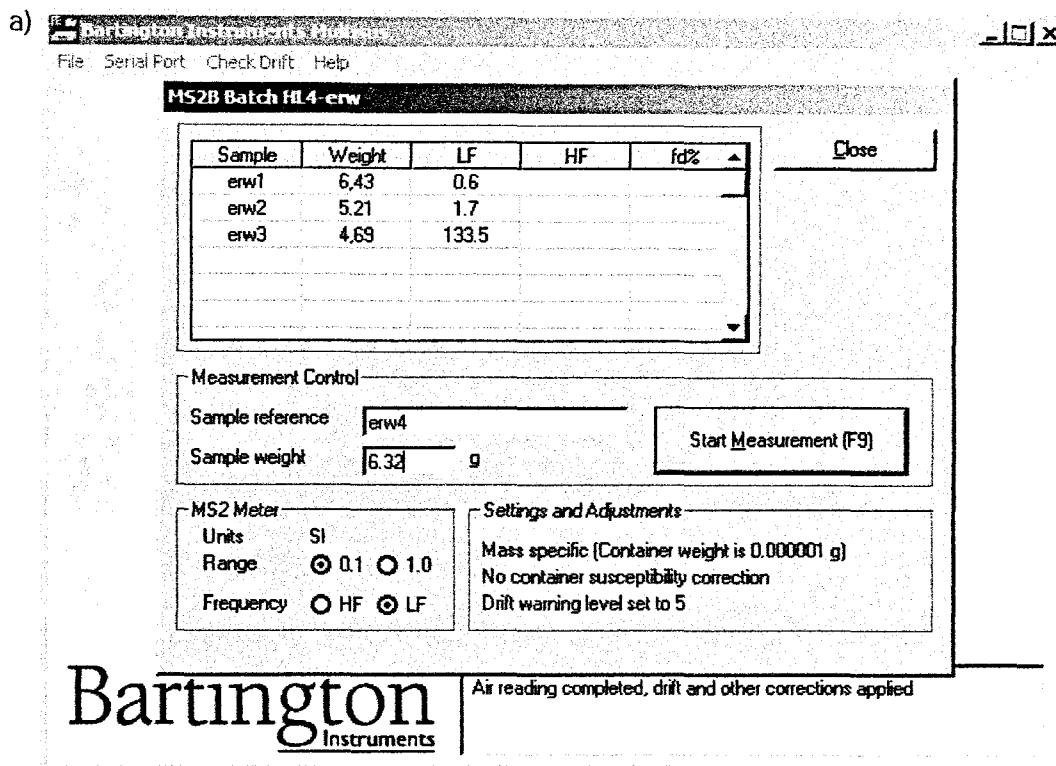


Fig. 4.16: Bartington Multisus Software v. 2 for the electronic measurement of magnetic susceptibility. The software automatically gives mass specific values, if requested, and calculates the frequency dependence of susceptibility. a) measurement of susceptibility, input a reference number, the sample weight and measure. The software prompts a "first air" reading before the sample measurement and a "second air" measurement after to correct for any background interference. The value on the screen is mass specific; b) The drift test screen, used to test for any ambient, background noise prior to any sample measurements.

$\chi_{fd\%}$ detects the presence of ultra-fine superparamagnetic (SP) materials (<0.03 μm) as the response of SP grains is dependent on the frequency of the applied field (Maher, 1988; Bloemendal *et al.*, 1992, Verosub & Roberts, 1995), it is a proxy for magnetic grain size. Samples with ultra-fine superparamagnetic minerals present will record a slightly lower value when measured at the high frequency level, while samples without fine-grained magnetic minerals should show identical χ_{lf} and χ_{hf} values and an $\chi_{fd\%}$ of 0% (Dearing, 1999).

After the susceptibility measurements were completed, Anhysteretic Remanent Magnetism (ARM) was measured on each sample. This has been shown to have a distinct relationship to magnetic grain, or domain, size (Smith, 1999), and is measured using an a.f. demagnetiser with an ARM attachment (Fig 4.17a & b). The sample is placed in the ARM attachment, within which a steady biasing field of 0.04 mT (31.84 Am^{-1}) is generated. The attachment is slid into the a.f. demagnetiser which generates an alternating field of 100 mT. For full details of the procedure, see Table 4.3.

Generally, ARM is converted into susceptibility of ARM (χ_{arm}) to allow for the size of the biasing field. This is because the size of the ARM induced is proportional to the size of the biasing field (Walden, 1999b). This conversion is done using the following equation:

$$\chi_{arm} (10^{-5}\text{m}^3\text{kg}^{-1}) = \frac{\text{ARM} (10^{-5}\text{Am}^2\text{kg}^{-1})}{\text{Steady Biasing Field} (\text{Am}^{-1})} \quad (\text{Eqn. 4.3})$$

Where the:

$$\text{Steady Biasing Field} (\text{Am}^{-1}) = \frac{\text{Steady Biasing Field (mT)}}{4\pi \times 10^{-7}} \quad (\text{Eqn. 4.4})$$

χ_{arm} has been shown to be highly characteristic of stable, single domain ferrimagnetic grains, such as magnetite, in the size range 0.02 – 0.4 μm . Ferrimagnetic grains above or below this range will have significantly lower values of χ_{arm} (Maher, 1988; Walden, 1999b).

Table 4.3: Procedure for using the Molespin a.f. demagnetiser to impart an ARM (based on Walden, 1999b).

Step	Procedure
1	Install the ARM sample holder arm.
2	Connect the power supply which generates the steady biasing field, and set the size of the field to 0.04mT (31.84 Am^{-1}).
3	Turn on the power supply to the main demagnetiser, the power indicator light should come on.
4	Turn the variac control dial clockwise to a reading of 9.5 (almost full deflection) on the VU meter. If the value is set to high an automatic cut out may be tripped and the needle will slowly decrease to zero. If this happens, turn the dial anticlockwise to zero and start again.
5	Set the size of the alternating field to its maximum 100mT (though some machines may read zero).
6	Set the rate at which the alternating field is reduced to zero. Setting C generally gives a suitable decay rate (0.016mT per cycle).
7	Insert the sample into the sample holder, making sure it is aligned correctly. Generally the sample should be inserted upright into the holder with the arrow on the pot facing into the arm. Some experimentation may be required for a new instrument to ensure the correct orientation for both the demagnetiser and the magnetometer. Insert the arm into the main body of the demagnetiser.
8	Press the start button. The biasing field and a.f. field will be generated whilst the set of lights (Up, Down and Pause) go through their sequence. When the Ready light comes on, the sample can be removed.
9	The induced ARM can then be measured on the magnetometer, as described in table 4.6. Any lengthy delay between ARM inducement and measurement should be avoided.
10	Repeat steps 7-9 until all samples have been processed. The machine will heat up during the procedure and must be turned off regularly to cool. Consult the manufacturers handbook for advice on how often this should occur.
11	When the sample set is completed, turn the variac control anticlockwise to zero and press start. Let the machine go through a full cycle like this and then switch off both the power to the demagnetiser and the biasing field generator.

Table 4.4: Procedure for demagnetising, both fully and partially, using the Molespin a.f. demagnetiser (based on Walden, 1999b).

Step	Procedure
1	Install the demagnetiser arm, ensuring the motor which drives the rotation of the sample is connected to the main body of the demagnetiser.
2	Turn on the power, the power indicator light should come on.
3	As for the ARM inducement, set the VU meter to 9.5 using the variac control, the rate of decay to C, and the field size to 100mT (40mT for a partial demagnetisation).
4	Place the sample in the holder and switch the "Rotation" dial to "on". Slide to sample holder in to the main body of the machine with the sample rotating.
5	Press the start button. Again the set of lights will go through their sequence and the sample can be removed when the Ready light comes on. This process takes about 30 seconds (15 for a partial demagnetisation) and all (or part) of the remanence will have been destroyed.
6	Repeat steps 4-5 until all sample have been demagnetised. The machine will heat up during the procedure and must be allowed to cool at regular intervals.
7	When all samples are demagnetised, turn the variac control anticlockwise to zero and press start. Allow the machine to run a full cycle and switch off the power to the main body of the demagnetiser.

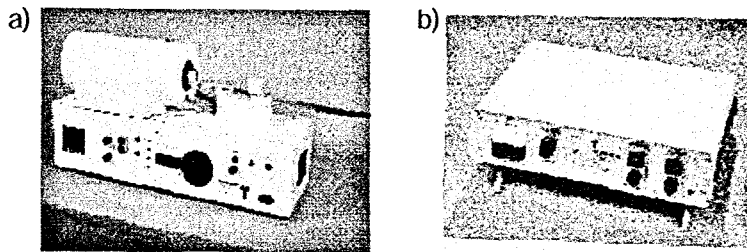


Fig. 4.17: a) Molspin a.f. demagnetiser with demagnetisation attachments; b) steady biasing field generator. This has a separate attachment not shown in picture (Molspin, date unknown - www.molspin.com/demagx).

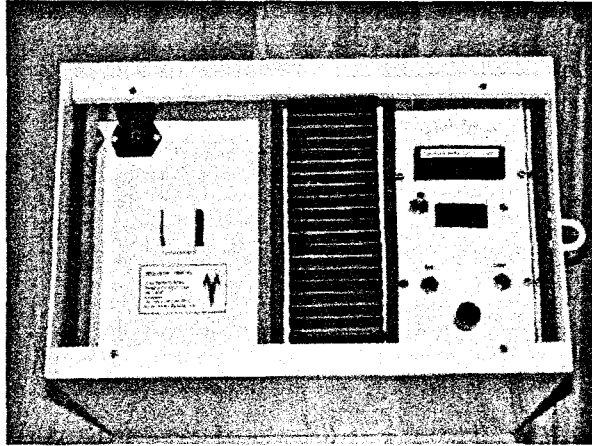


Fig. 4.18: Molspin Pulse Magnetiser (Molspin, date unknown - www.molspin.com/pulsemag).

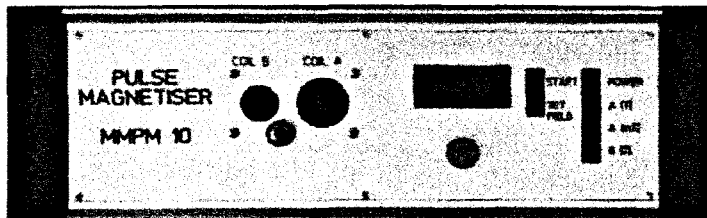


Fig. 4.19: 9 Tesla Pulse Magnetiser (Shaw, date unknown - www.magnetic-measurements.com/mmtpm).

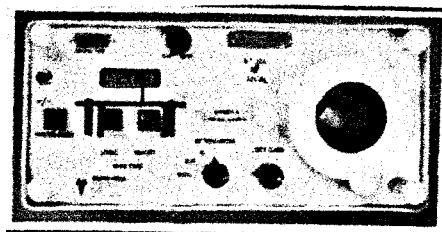


Fig. 4.20: Molspin Minispin Magnetometer (Molspin, date unknown - www.molspin.com/mspintxt).

Once the ARM measurements are complete, the ARM attachment is removed, and the sample can be demagnetised, either fully or partially. A partial demagnetisation of 40 mT can help to reveal information about the mineral composition of a material (Peters & Thompson, 1998; Maher *et al.*, 1999). To do this, the sample is rotated within an alternating field of 40 mT for a partial demagnetisation and 100 mT for a full demagnetisation. Demagnetisation must take place before the inducement of any IRMs in a field smaller than that used in the a.f. demagnetiser to induce the ARM (generally 100mT)(Walden, 1999b). For a full methodology see Table 4.4.

Isothermal Remanence Magnetisations (IRM) are measurements of how responsive a sample is to different magnetic fields. They can give information on both the concentration of magnetic minerals, but also the mineral types present in a material. A series of IRMs may be induced into a sample, providing the fields get progressively larger. A sample will eventually become saturated (known as the SIRM) which means that it will no longer respond to higher magnetic fields. This is very suggestive of mineral composition (Verosub & Roberts, 1995). Once the SIRM has been reached, or the sample has been subjected to the highest IRM possible, “backfields” may then be induced. These are exactly the same as IRMs described above, however the sample is turned around in the sample holder and the field is induced “backwards”. Negative values are generally given by backfields, and are used in similar ways to their forward field counterparts in assessing mineralogy.

IRMs can be induced with fields up to 9000 mT (9T) using a Molspin Pulse Magnetiser and a PM9 (9T) Magnetiser (Figs. 4.18 and 4.19), although in this study the maximum field used for routine measurements was 3T as this is the largest field that can be imparted on samples in the standard 10 ml plastic pots. Samples are placed into the magnetisers with their orientation one way for a forward field and the opposite for a backfield. After each field (ARM or IRM) is induced, the response is measured using the Molspin Magnetometer (Fig. 4.20).

The detailed methods for these various steps are described in Tables 4.5, 4.6 and 4.7.

4.3.1 Sample Preparation for OMEX 2K and MD01-2461

As only a limited amount of material was available for sub-sampling for mass specific magnetic measurements for OMEX 2K, it was decided (based on Dearing, 1999) that approximately 5g of material would be sufficient for each sample to provide an accurate reading. Samples were taken every 1 cm. As the U-channels were approximately 4 cm wide, a 2 cm wide trench was needed to provide adequate material. A line was scoured down the middle, and across at 1 cm intervals using a scalpel and ruler. The trench was cut using the scalpel and a scoop to collect the material, which was placed in “cling” film, weighed to 2 decimal places and packed into a 10 ml plastic container, immobilising the sediment. The pots were clearly labelled with a number (corresponding to its depth) and an arrow along the base to ensure consistent orientation of the sample during subsequent measurements.

For the MD01-2461 core, samples were sent from Dr James Scourse in sample bags of average size 13.5 cm by 9 cm. It was decided that the bags could be pushed into the standard plastic containers and held in place with sellotape, thus ensuring no loss of sediment. Twenty empty bags of the same size were weighed and measured for susceptibility. The average weight of the bags was then subtracted from the weight of each sample. The susceptibility measurements were to ensure that there would be no effect on the measurements from the bags themselves, and as these produced zero susceptibility, no adjustment of the data obtained from the samples measured in this format was thought necessary. The samples were then weighed and packed into the 10 ml plastic pots, making sure that the sediment was immobilised and securing in place with sellotape. The containers were labelled according to depth, with an arrow along the bottom to ensure constant orientation.

Table 4. 5: Procedure for using the Molspin pulse magnetiser to induce forward and backward magnetic fields (based on Walden, 1999b).

Step	Procedure
1	Switch on the pulse magnetiser by plugging it in and switching it on at the mains.
2	Hold down the "Set" button whilst rotating the black control dial. The needle on the larger VU display will indicate the field set. Once the required field is reached, release the Set button.
3	Press the "Start" button once. The field will be generated. For small field this will be almost instantaneous, but for larger fields it could take up to 30 seconds. The needle on the larger VU display will swing into place as the field is generated.
4	Where the needle of the larger VU display settles is the actual field generated. Check it is correct, if not repeat step two until it is. This field will be generated every time the Start button is pressed until it is changed.
5	Place the sample in the holder with the correct orientation. For a forward field the arrow should be pointing vertically downwards, for a backfield, vertically upwards. Lower the sample into the chamber.
6	Press the Start button. Once the larger VU needle has swung into place, the field has been generated and the sample can be removed.
7	Repeat steps 5 - 6 until all samples have experienced the chosen field. Avoid lengthy delays between field inducement and measurement.
8	Once all samples have been processes, switch off the pulse magnetiser to allow cooling before another field is chosen.

Table 4. 6: Procedure for using the 9 tesla pulse magnetiser to induce IRM field of 1000mT (1T) and above.

Step	Procedure
1	Switch on the magnetiser using the power button on the front panel.
2	Press the "Set Field" button and use the black control dial to select the field.
3	Press the "Start" button. The field will be induced. Check that the field shown on the LDC screen is correct, if not repeat step two until it is.
4	Once the chosen field is correct, place the sample into the wooden sample holder, ensuring correct orientation (the arrow pointing outward of the machine for a forward field and inward for a backfield) and press start.
5	Once the field size appears on the LDC, the field has been induced and the sample may be removed. The field may need re-adjusting after a few samples. Avoid lengthy delay between inducement and measurement.
6	Switch off the magnetiser at the power button on the front panel.

Table 4. 7: Procedure for measuring the magnetisation of samples on the MolspinMinispin Magnetometer with computer control (based on Walden, 1999b).

Step	Procedure
1	Switch on the magnetometer, ensuring that the separate power supply is also on, and connected. Allow 10 mins to warm up. Switch on the computer attached to the magnetometer.
2	Select an Attenuator setting of 10, unless it is known that the samples are only weakly magnetic, in which case use a setting of 1.
3	Calibrate the magnetometer by placing the calibration sample into the sample holder, ensuring that it is orientated correctly. Use the controls on the computer to run the sample.
4	Once a sample is induced with a magnetisation (IRM or ARM), place it into the sample holder, ensuring that the arrow is orientated correctly. Lower into the sample chamber, avoiding any disturbance that may realign the sample within the holder.
5	Follow the instructions on the computer to measure the sample. The sample should spin for approximately 6 seconds.
6	Repeat steps 4 and 5, re-calibrating regularly until all the sample are measured. Save the data on the computer regularly.
7	When all analysis is complete, switch off the battery and mains power supply.

It was decided to sub-sample across H2 and H4 of MD01-2461 for higher resolution analysis. Using the whole core magnetic data, and IRD data supplied by Vicky Peck at Cardiff University (Peck, unpublished), depths of 490-590 cm for H2 and 790-920 cm for H4 were selected. H4 is estimated to cover 840-890 cm depth, with a possible precursor event around 890-910 (Vicky Peck, Pers Comm, 2003 and magnetic data). Ash Zone II is centered around 950 cm, so H5 is placed between 915-930 cm. The whole core χ_{lf} data has the peak of H4 slowly declining to c. 810 cm, so it was decided to sample 20cm prior to this, to ensure all of H4 was taken. This selection of samples may also have incorporated H5, as the possible H4 precursor and H5 are very close to each other. There were no such problems surrounding H2.

The original plaquettes were sub-sampled at 1 cm resolution across the potential HLs. Taking the average density of the sediment to be 1.6 gcm^{-3} , it was calculated that a trench 3 cm wide was needed to provide enough sediment for the magnetic analysis. A line was scoured 3 cm wide, and at 1 cm intervals sediment was collected using a scalpel and scoop. The sediment was weighed, wrapped in “cling film” and packed into 10 ml plastic containers in much the same way as the OMEX 2K samples. The pots were clearly labelled and the sediment securely immobilised (Fig. 4.14).

4.3.2 Magnetic Analysis of OMEX 2K and MD01-2461

The mass specific magnetic susceptibility (χ) was measured for each sample using a Bartington Instruments MS2B Dual Frequency Sensor (Fig. 4.15b), which was linked to the Bartington Multisus software (Fig. 4.16). The meter was set to SI units ($10^{-8} \text{ m}^3 \text{ kg}^{-1}$) and the 0.1 sensitivity range. Two readings were taken at both high (χ_{hf}) and low (χ_{lf}) frequency settings and the average taken. These average values of χ_{hf} and χ_{lf} were then used to calculate the frequency dependent susceptibility ($\chi_{fd\%}$). This was done for all OMEX 2K and MD01-2461 samples, including the H2 and H4 sub-sections.

Once the susceptibility measurements were completed, the Anhysteretic Remanence Magnetisation (ARM) and the Isothermal Remanence Magnetisation (IRM) measurements were started, using the methods discussed above (Section 4.3), and in Walden (1999b). A Molspin a.f. demagnetiser with an ARM attachment (Fig. 4.17) was used to induce the ARM into the sample. The alternating field was set to the maximum, 100mT, and the VU meter to the maximum deflection of 9.7. Each sample had an ARM induced, which was then measured on a calibrated Magnetometer with the attenuator set to 1 (Fig. 4.20). The magnetometer was connected to a computer with suitable software to calibrate, measure the appropriate values, and record the results in a database compatible with Microsoft Excel.

The ARM attachment was then removed from the demagnetiser, which was reset to an alternating field of 40 mT, to create a partial demagnetisation (ARM₄₀). Each sample was partially demagnetised, and the remaining remanence was again measured by the magnetometer. The demagnetisation field was put back to 100 mT, and the samples completely demagnetised. The ARM results were converted to χ_{arm} (susceptibility of ARM) as discussed above (Section 4.3 and Equations 4.3 & 4.4). In this case, the steady biasing field used was 0.04 mT, which converts to 31.84 Am⁻¹, therefore:

$$\chi_{arm} (10^{-5} \text{m}^3 \text{kg}^{-1}) = \frac{\text{ARM}}{31.84} \quad (\text{Eqn 4.5})$$

The IRM measurements were taken using a Molspin Pulse Magnetiser, which can induce fields of up to 1000 mT (1T)(Fig. 4.18), and a Magnetic Measurement Ltd Pulse Magnetiser 9 (PM9), which induces fields up to 9000 mT (9T)(Fig. 4.19). Eleven fields were initially chosen for the OMEX 2K IRMs, as suggested by Walden (1999b). They were: 20f (forward field), 40f, 100f, 300f, 500F, 1000f, 40b (backfield), 100b, 300b, 2000f and 3000f. Each field was induced and the resulting magnetisation measured by the magnetometer. Once the OMEX 2K data analysis was completed, it was noted that the backfield data provided as much information as the forward field data. Therefore, considering the large number of samples for MD01-2461, it was decided to omit the time-consuming

demagnetisation process and forward field measurements, by saturating the MD01-2461 samples in a forward field of 3000mT straight after the ARM-40 measurements, and inducing backfields at 40b, 100b, 300b and 1000b.

The IRM values were normalised for weight (IRM/mass) to calculate mass specific ratios, and for concentration (IRM/SIRM) to give acquisition ratios for each field. These were used to draw acquisition plots for each sample, which can show the dominant magnetic behaviour present in the sample, e.g. ferrimagnetic or canted antiferromagnetic (see Section 5.2).

4.4 Data Analysis

4.4.1 Correction for Carbonate Content

Environmental magnetic analysis measures the magnetic signal within a sediment, which in the case of deep sea sediments is held within the inorganic fraction (with the exception of any magnetotactic bacteria, discussed in Section 2.5.2). As the productivity and biological activity of a body of water varies, so does the content of carbonate, and therefore the amount of dilution of the inorganic fraction by the organic fraction (Stoner & Andrews, 1999; Evans & Heller, 2003). This may cause alteration in, or masking of, the magnetic signal (principally due to dilution) that is a response to changing biological activity, not IRD deposition (Robinson *et al.*, 1995). Therefore, it is important to effectively normalise the magnetic data for carbonate content, removing the influence of any organic fraction (e.g. Lean & McCave, 1998). In this study, it is acknowledged that there is inorganic carbonate present as IRD, but it is considered a priority to remove any biological impact.

Carbonate content data for the OMEX 2K core was retrieved from the NERC OMEX Project Data Set CD ROM (Lowry *et al.*, 1997). The data was based on measurements of total inorganic carbon using CHN after thermal combustion of the organic fraction (Ian Hall, *Pers Comm* 2002), and is expressed as a percentage of the total sample material. The CaCO₃ measurements were taken on

samples spaced every 4cm, therefore, to match the high resolution 1 cm analysis performed here, estimates were made using consecutive CaCO_3 measurements. This was done by taking an average of two consecutive values, (average 1), as the centre value, and then filling in the gaps, with the mean of average 1 and the adjacent CaCO_3 value (average 2; see below).

e.g.

64	
Average 2	—
Average 1	—
Average 2	—
67	

When all the samples had CaCO_3 values, the magnetic data were “corrected”, i.e. the proportion of carbonate was subtracted from the sample mass, leaving the mass of only the inorganic material. The NERC data expressed CaCO_3 as a percentage of the material in the sample, therefore the weights of the samples used for the mass specific magnetic analysis were divided into percentage CaCO_3 and percentage inorganic material and the percentage CaCO_3 then subtracted.

e.g.

Weight = 6.65 g

% Carbonate = 64%

$$\rightarrow \left[\frac{6.65}{100} \times 64 \right] = 4.265$$

$$\rightarrow 6.65 - 4.265 = 2.185$$

Corrected weight = 2.185 g

CaCO_3 corrected (i.e. CaCO_3 free) values of each of the mass specific parameters were calculated for each sample. Fig. 4.21 shows the percentage carbonate curve and the parameters of susceptibility, ARM and SIRM for OMEX 2K before and after correction for carbonate.

The most common detection system used is a tandem accelerator (Fig. 4.8a & b) (Bowman, 1990; Lowe & Walker, 1997). Samples are firstly converted to graphite and mounted on a metal disc to create a target for the accelerator (ANSTO, 2002). The original sample (foraminifera, shell, bone, wood etc.) is sandblasted with 30 μ alumina and etched in dilute HCl to remove 10-20% of the surface carbonate. They are then treated with 50% phosphoric acid under vacuum, the CO₂ recovered is dried and reacted with molten lithium metal and water to form acetylene (Wand *et al.*, 1984; Gillespie *et al.*, 1986). The acetylene is then pyrolyzed by a hot tantalum wire, on which graphite is deposited (Wand *et al.*, 1984; Gillespie *et al.*, 1986). Within the tandem accelerator, Cesium ions are fired at the graphite sample, producing negatively ionised C atoms, which are accelerated towards a positive terminal. ¹⁴N atoms are eliminated before they reach the detector, as they don't form negative ions. The ions are then sent through a "stripper" which removes four electrons, creating C³⁺. The C³⁺ ions are now repulsed from the positive terminal and are accelerated again through focusing magnets where deflection occurs. The concentration of ¹⁴C, ¹³C and ¹²C can be measured due to their different weights, and hence, different deflections. Once the ¹⁴C:¹²C ratio is measured, it is compared to standards which are made up from a material of known ¹⁴C activity, giving a sample/modern ratio from which a radiocarbon age can be calculated in years Before Present (BP)(Lowe & Walker, 1997).

4.2.2 Chronology

The radiocarbon ages produced by ¹⁴C dating are not calendar ages and must be calibrated in order to convert them to the calendar timescale (Pilcher, 1991). Variations in the production of ¹⁴C through time have resulted in a discrepancy between calendar years and radiocarbon years (Williams *et al.*, 1998). Radiocarbon ages are quoted in years BP (before present), with present defined at AD 1950 (Bowman, 1990; Lowe & Walker, 1997; ANSTO, 2003). AD 1950 is used because of the industrial effect, and more importantly, the impact of thermonuclear weapons testing on modern day atmospheric ¹⁴C levels (Williams *et*

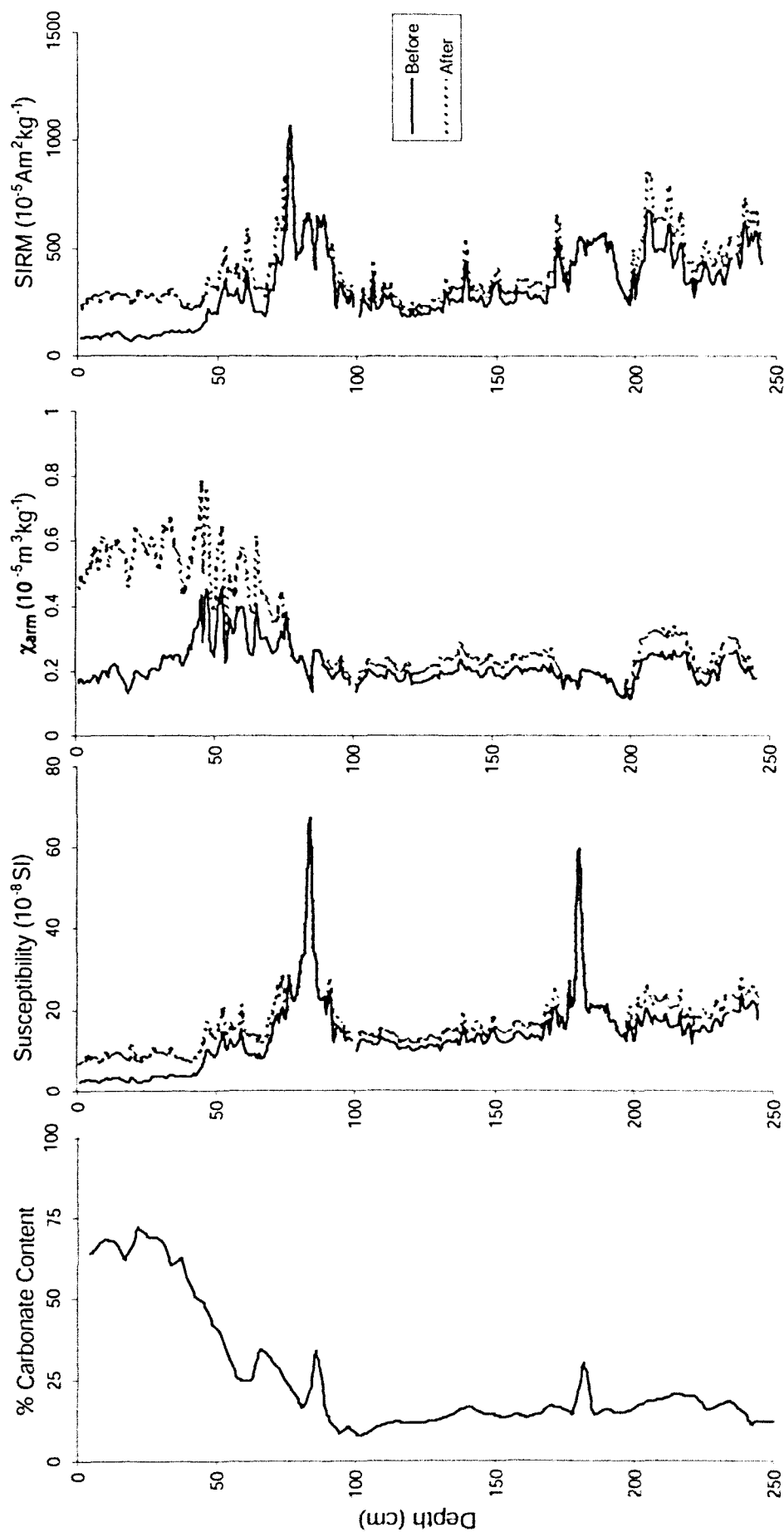


Fig 4.21: The parameters of susceptibility, χ_{arm} and SIRM for OMEX 2K, before correction for carbonate content (solid black line) and after correction (dashed red line). It is apparent that carbonate content appears to have little effect on the magnetic properties of OMEX 2K prior to the Holocene, during which biological activity has increased dramatically with warmer ocean temperatures. The peaks seen in the Carbonate Content record at the HEs is due to the high input of inorganic carbonate at these times.

Extensive carbonate content data is not, as yet, available for the MD01-2461 core, however, 19 samples from various points along the core were measured for CaCO₃ content by Dr Ian Hall, Cardiff University for the purpose of subtracting inorganic carbonate influence from the magnetic results. The 19 samples were selected from the Calcium XRF trace for the core, and represented a range of Ca count values (Table 4.8).

Once the percentage weight of CaCO₃ was measured for the samples, the values were compared to their original Ca values and a regression performed (Fig. 4.22). A line of best fit, in this case a fourth order polynomial curve, was placed on the graph, to give an equation that would provide a CaCO₃ content value for any Ca value along the core (Eqn. 4.6, Table 4.8). Other studies have suggested that this is a reasonably robust prediction of weight percentage CaCO₃ (e.g. Röhl *et al.*, 2000). Using this equation, a percentage weight of carbonate content was calculated for every sample along the length of the core (Fig. 4.23). The magnetic data was then corrected for carbonate content using the methods described above for OMEX 2K, and carbonate free mass specific parameters were calculated (Fig. 4.23).

$$\text{Carbonate Content (\%)} = \frac{(1.311 \times 10^{-13} \times \text{Ca}^4) - (2.369 \times 10^{-9} \times \text{Ca}^3) + (1.400 \times 10^{-5} \times \text{Ca}^2) - (0.023 \times \text{Ca}) + 26.893}{1} \quad (\text{Eqn 4.6})$$

Table 4.8: Samples from core MD01-2461 measured for weight percentage carbonate content by Dr. I. Hall (Cardiff University), their corresponding Ca counts from the XRF scan, and the predicted carbonate content calculated from equation 4.6.

Sample Depth (cm)	Weight percentage CaCO ₃	Ca XRF counts	CaCO ₃ content prediction
19	47.7	5423.8	48.61679
41	50.9	4908.5	46.89652
47	50.8	4170.8	42.76329
82	42.8	3780.4	40.02308
103	43.4	4529.3	43.66054
109	41.1	2790.4	29.8356
130	36.0	3483.1	33.6376
192	23.2	2208.7	23.62145
258	14.5	1440.7	18.42964
260	17.9	2788.8	25.81662
313	15.6	1609.5	16.97676
464	20.9	2146.6	21.36259
480	17.2	1450.9	16.43821
513	19.5	1120.1	16.40699
630	20.5	1949.8	22.22493
696	16.8	1494.9	17.33382
749	25.2	4055.9	34.50374
774	23.9	2428	24.72938
846	21.5	2074.6	21.13183
851	37.8	3562.8	31.49228
923	34.8	4295.3	41.20632
949	19.9	1566.2	19.25601
1032	16.9	1095.9	15.61
1094	41.9	5287.2	48.04506
1117	58.7	8079.9	62.50472
1123	50.3	6185.9	53.23343
1153	60.5	68794	57.04582
1165	61.1	7102.3	55.28818
1197	47.9	6157.5	50.83132

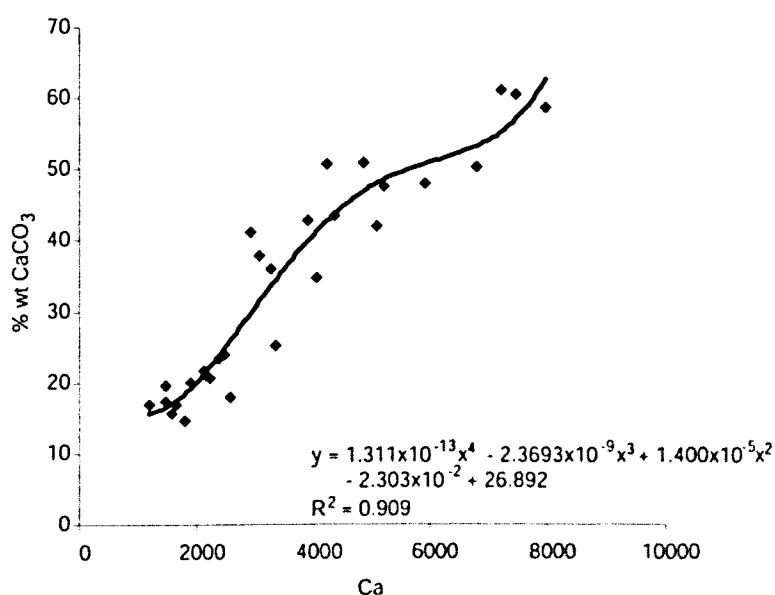


Fig. 4.22: Correlation between the Ca XRF data and Carbonate content data for 19 samples along the MD01-2461 core. The equation of the fourth order polynomial trendline will give a carbonate content value for any Ca value from the core enabling the magnetic data to be corrected for any organic carbonate present.

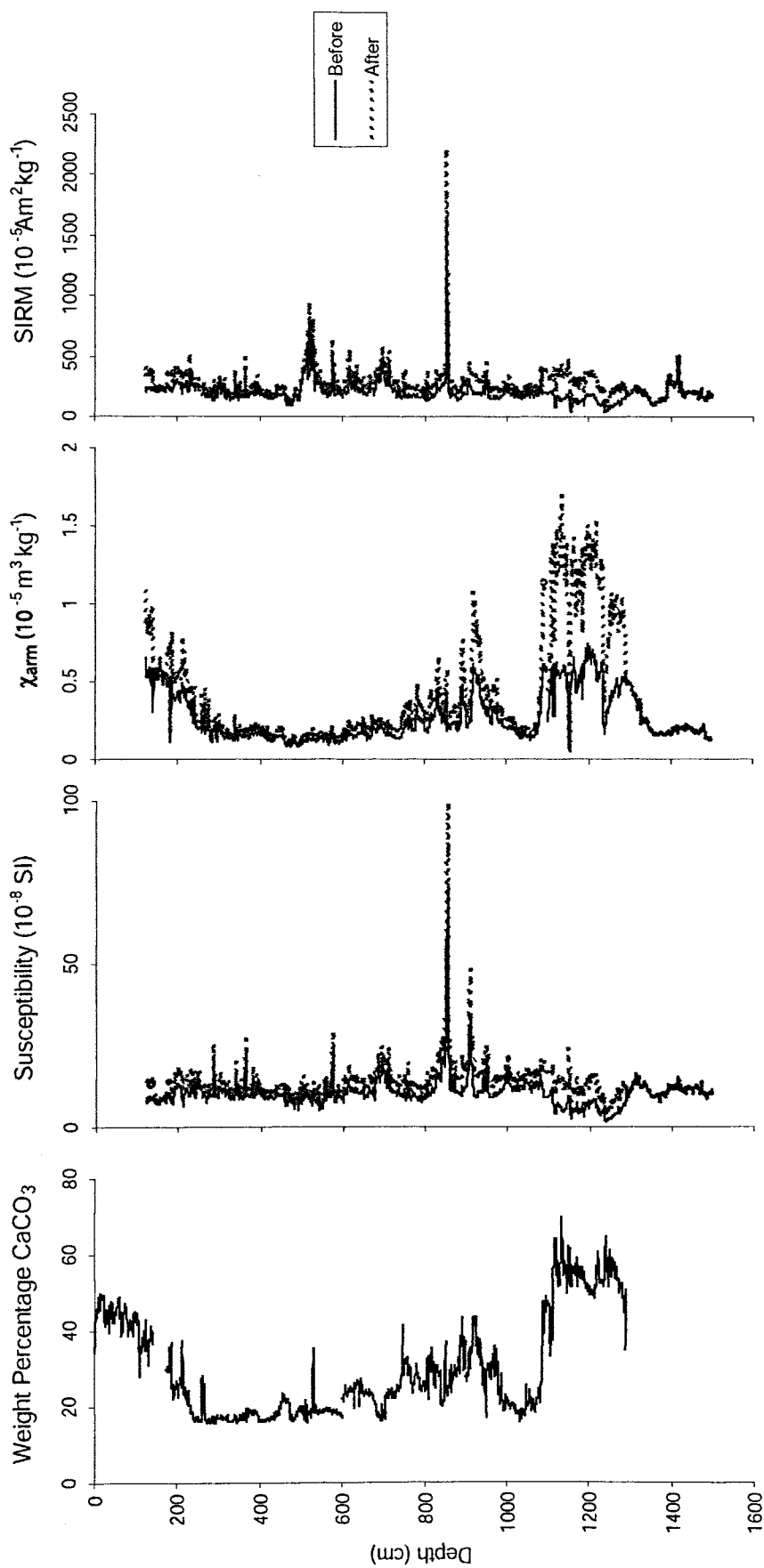


Fig 4.23: The parameters of susceptibility, χ_{arm} and SIRM for MD01-2461, before correction for carbonate content (solid black line) and after correction (dashed red line). It is apparent that carbonate content appears to have little effect on the magnetic properties of MD01-2461 with the exception of the interglacial events (the Holocene and MIS 5e).

4.4.2 Magnetic Ratios

Magnetic ratios can reveal additional information about the magnetic characteristics of a material when used to complement the individual measured parameters. For example, the ratio of ARM with other parameters such as χ_{ir} or SIRM can be diagnostic of grain size (King & Channell, 1991), and when used with ARM₄₀ it is indicative of the presence of greigite (Peters & Thompson, 1998; Maher *et al.*, 1999). Table 4.9 details some magnetic ratios, including the ones used in this study (highlighted in Table 4.9 in red). The ratios will also be discussed fully in Chapter 5.

The importance of identifying the presence of magnetotactic bacteria and the mineral greigite is discussed within Section 2.5.2. Table 4.9 includes some of the parameters and ratios used to analyse sediments for bacterial magnetite and greigite (e.g. Moskowitz *et al.*, 1988; Kris *et al.*, 1990; Snowball, 1991; Oldfield, 1992; Peters & Thompson, 1998). A number of these parameters are based upon measurements that have routinely been performed in this study and are therefore used here to gain a first-order insight into the likely presence of either magnetotactic bacteria or greigite. The parameters most useful to this study are χ_{arm}/χ and χ_{arm}/χ_{fd} for magnetotactic bacteria, and SIRM/ χ , ARM₄₀/ARM and IRM₁₀₀/SIRM, the saturation properties and loss of magnetisation for greigite.

4.5 Statistical Analysis

4.5.1 Descriptive Statistics

Descriptive statistics were calculated, using Minitab (version 14) on the carbonate free data of both the OMEX 2K core and the MD01-2461 core (Appendices 2bi, 2ci, 2di and 2ei). Statistics such as mean, median, standard deviation, upper and lower quartiles and standard error of the mean were calculated both for the whole core data and individual sections of both cores.

Table 4.9: A series of magnetic ratios, including the ones used in this study. Taken from Bloemendal *et al.*, (1988); Bloemendal *et al.*, (1992); Bloemendal *et al.*, (1993); Hallam & Maher, (1994); Hilton, (1990); King & Channell, (1991); Kris *et al.*, (1990); Moskowitz *et al.*, (1988); Oldfield, (1992); Peters & Thompson (1998); Petersen *et al.*, (1986); Roberts & Turner, (1993); Snowball, (1991); Snowball & Thompson, (1988); Thompson & Oldfield, (1986); Verosub & Roberts, (1995); Walden *et al.*, (1987); Walden (1999b), Walden & Ballentyne, (2002); Watkins & Maher, (2003); Yu & Oldfield (1989).

Ratio or Parameter	Calculation and Interpretation
ARM and χ_{arm}	ARM is the magnetisation of a material acquired in a biased, decreasing DC field. It is sensitive to changes in grain size and usually normalised for the size of the biasing field and expressed as χ_{arm} . χ_{arm} is proportional to the concentration of ferromagnetic minerals in the 0.02–0.4 μm size range, values will drop significantly for minerals either above or below this range. Units = $10^{-5}\text{m}^3\text{kg}^{-1}$
ARM_{40} ARM	This is mainly a mineralogical parameter, which is used to help identify greigite (values of 0.45–0.85) and pyrrhotite (when plotted against SIRM/ χ , pyrrhotite is situated at the top left). When plotted against $\text{IRM}_{100}/\text{SIRM}$, greigite is positioned at the bottom right and influenced by size. Pseudo-single domain (PSD) grains have the lowest ratios, and single domain (SD) grains have the highest ratios.
ARM/SIRM	Ratios of ARM/SIRM for MTB are between 0.15 – 0.25 at an applied field of 0.1 mT. When plotted against the cross over point for R_{df} (from the demagnetisation curves, see below) they produce a distinct group with cross over points >0.5.
ARM/ χ and χ_{arm}/χ	These parameters are used for the identification of grain sizes of ferrimagnetic minerals, as it is inversely proportional to magnetite grain size in the 0.1–10 μm range. They are essentially the same variable, but are both used in this study for ease of comparison to data in the literature. High values of both indicate fine-grained particles and low values indicate the presence of coarse grains. Units = kAm^{-1}
Hard IRM	$\text{HIRM} = \frac{(\text{SIRM} - \text{IRM}_{300})}{\text{Weight}}$ for forward fields, $= \frac{\text{SIRM}((\text{IRM}_{300}/\text{SIRM}) + 1)}{2}$ for backfields It measures the concentration of high coercivity minerals like haematite and goetite. Higher values indicate hard mineral presence. Units = $10^{-5}\text{Am}^2\text{kg}^{-1}$
IRM_{100} SIRM	This is also a mineralogical parameter, also known as the 100 backfield ratio. Displays the proportion of higher coercivity minerals to lower coercivity minerals, has values of between +1 and –1, with higher values representing ferrimagnetic behaviour and lower values, canted antiferromagnetic behaviour. No units.
$\text{IRM}_{100}/\text{SIRM}$ v $\text{ARM}_{40}/\text{ARM}$ (graph)?	Greigite plots on the far right, with $\text{ARM}_{40}/\text{ARM}$ values of 0.5–0.8 and $\text{IRM}_{100}/\text{SIRM}$ values of –0.25–0.7.
IRM acquisition properties	Rapid increase in normalised IRM from ≤ 0.02 – ≥ 0.9 between the fields of 40 – 200 mT, with complete saturation reached by 300 mT. Used for the identification of diagenetic greigite.
Lowrie-Fuller test	Functional dependence of the Lowrie-Fuller test (ΔF) plotted against IRM, ARM/IRM and MDF_{IRM} . Two data sets were clearly distinguishable, one of single domain (SD) particles of biogenic origin, and the other test of lithogenic origin, containing coarser particles. Higher values of ΔF represent organic particles. Further information and methods for this test can be found in Lowrie & Fuller (1972) and Dunlop & Ozdemir (1997).
Loss of magnetisation	Loss of magnetisation during storage, due to the oxidation of greigite. Shown by a dramatic loss in χ over a few years.
R_{df} and R_{af}	The Wohlfarth-Cisowski test provides an R-value, in this case using DF magnetisation and AF demagnetisation curves. Bacterial magnetite is shown by R_{df} values of ≈ 0.5 and R_{af} values >0.5. Further information on this test can be found in Dunlop & Ozdemir (1997).
S-parameter	The S-parameter is a ratio that has become confused over the years, with different authors adapting it to their needs, which are dependent on the measurements they are able to make. It is essentially accepted as similar to the 100 backfield ratio (see above) though sometimes utilising 300 backfield measurements, and details the same information. However, in this study, for comparison to previous work, the S-parameter takes on two different forms, one is 100 backfield ratio, the other very different. $S_{(\text{snowball})}$ is used in Snowball (1991) for the identification of greigite, and takes the same form of the 100 backfield ratio ($\text{IRM}_{100}/\text{SIRM}$). $S_{(\text{Bloemenda})}$ however is calculated by the equation: $\frac{(-\text{IRM}_{300}/\text{SIRM}) + 1}{2}$ and is used as a provenance indicator in terms of sediment source and transport pathways. Both ratios are dimensionless.

Ratio or Parameter	Calculation and Interpretation
SIRM/ χ	Another grain size indicator, which also displays mineralogical type. Haematite displays values of above 200kAm ⁻¹ , with pyrrhotite even higher (~1000kAm ⁻¹). Magnetite is shown by values of 1.5-50 kAm ⁻¹ , increasing as grain size decreases. Greigite displays values of >30kAm ⁻¹ . High superparamagnetic (SP) material has values of <0.01 kAm ⁻¹ as the ultra-fine material only contributes to χ and not SIRM and therefore can be confused with very coarse grained magnetite. Units = kAm ⁻¹
SIRM/ARM and SIRM/ χ_{arm}	These vary directly with grain size in the 0.1-100 μ m (SD) range. Higher values show a lower concentration of fine-grained ferrimagnetic minerals, and therefore and increased average size, whilst low values indicate a higher concentration of SD ferrimagnetic minerals. Again, both are used in this study for ease of comparison to the literature. Units = kAm ⁻¹
SIRM/ χ_v ARM ₄₀ /ARM (graph)	Greigite plots on the right hand side, towards the top, with ARM ₄₀ /ARM values of between 0.5-1.0 and SIRM/ χ values of 40-100.
Soft IRM	Soft IRM = $\frac{IRM_{40}}{\text{mass}}$ Also a mineralogical indicator, and is proportional to the concentration of low coercivity, ferrimagnetic minerals such as magnetite and maghaematite. Units = 10 ⁻⁵ Am ² kg ⁻¹
χ_{arm}/χ_{fd}	$\chi_{arm}/\chi_{fd} > 1$ is diagnostic of bacterial magnetite. When plotted against χ_{arm}/c it shows distinct patterns – bacterial magnetite plots in the top right hand corner, whilst inorganic material falls into the bottom left corner.
δ_{FC}/δ_{ZFC}	δ is representative of the amount of remanence lost on warming through the Verway transition in either zero field (ZFC) or a strong field (FC). $\delta_{FC}/\delta_{ZFC} > 2$ signifies MTB.

4.5.2 Normality Tests

In order to decide what types of inferential statistical analysis might be used with the magnetic data, Normality tests were performed on each of the parameters using Minitab. This test produces a P-value that shows if the distribution is normal or not. Where $P > 0.05$ the data set is normal (Hull, 1998). These were performed on both cores, and the individual H2 and H4 sections of MD01-2461, and can be found in Appendix 2bii, Appendix 2cii and Appendices 2dii and eii respectively.

4.5.3 Tests of Variance

The *Kruskal-Wallis* test was selected as a non-parametric test (i.e. it can be used on either normally distributed or non-normally distributed data sets) to detect any significant differences between the medians of the sample groups (Gibbons, 1993). There must be at least 3 groups, and if only 3, there must be at least 5 samples in each group (Fowler *et al.*, 1998). Minitab version 14 gives a P value and an H value during the test. H is the test statistic, P is the significance level and shows whether the null hypothesis (H_0) is accepted or rejected. In the Kruskal-Wallis test, H_0 states that the samples come from identical populations with identical medians, whereas H_1 states that at least one group must be significantly different from the rest of the groups (Davis, 2002; Texassoft, 2004).

In this study, the Kruskal Wallis test was used on the whole core data from both OMEX 2K and MD01-2461, to test for any significant difference between the medians of the various time segments within the core (Holocene, H1, etc.). In this case H_0 is the hypothesis that there is no significant difference between the core groups, and H_1 says that there is a difference between the groups. See Appendix 2a (Pg 332) for the full procedure and P-value tables.

The *Mann Whitney U* test is also a non-parametric test and is used in the same way as the Kruskal-Wallis test, but is designed for only 2 populations with as few as 4 observations in each sample (Fowler *et al.*, 1998; Davis, 2002). The Mann

Whitney U test was used to test for any significant difference between the potential LIS and European fractions within the H1 and H2 sections of OMEX 2K, and the H2 and H4 sections of MD01-2461. As with the Kruskal-Wallis test, the Null hypothesis (H_0) states that there is no significant difference between the populations, whereas H_1 states that there is. Minitab version 14 again produces a P value and if $P \leq 0.05$, H_0 is rejected and there is a significant difference between the populations. See Appendix 2a (Pg 333) for a full procedure.

4.5.4 Factor Analysis

Factor analysis is a multivariate statistical technique with the primary purpose of determining the number and nature of any underlying common factors which affect the measurable surface attributes of a population, and if there is any pattern to their influences (Tucker & MacCallum; 1997, Davis, 2002).

Surface attributes are the directly measurable variables used on a population, in this case, χ , ARM, IRM, and their associated ratios. The theory surrounding factor analysis is that there exists internal attributes, i.e. unobservable characteristics, which cannot be directly measured, but do exert some kind of influence on the surface attributes. Internal attributes can also be called factors, and consist of common factors, which affect more than one surface attribute; and unique factors, which effect only one. Factor analysis attempts to quantify these common factors and to assess the patterns of their influence on the population (Tucker and MacCallum, 1997).

Two types of factor analysis can be used: R-mode and Q-mode. R-mode techniques attempt to uncover the interrelations between the variables; whilst Q-mode techniques try to find patterns or groupings of the samples within their arrangement in “multivariate space” The two techniques can be used simultaneously (Walden *et al.*, 1991; Davis, 2002). The full methods for factor analysis can be found in Appendix 2a (Pg 333), however the best way to illustrate the uses of factor analysis is by a worked example. This can also be found in Appendix 2a (Pg 334-337 and is based on Walden & Smith (1995). Many of the

steps described are now automated by Minitab version 14, simply by selecting the Factor Analysis options from the Stats menu, however a knowledge of the processes are useful for the interpretation of the resulting data.

5.0 Results and Discussion

This chapter will deal with the data analysis and environmental interpretation of OMEX 2K and MD01-2461. The age model for OMEX 2K will be discussed first, and the results in later sections will all be provided in terms of both age and depth. The environmental magnetic analysis will then be addressed, along with descriptions and discussions of the variety of analytical methods used. All the data (magnetic and non-magnetic) will be discussed and interpreted in the context of the aims set out in Section 1.3. This format will be applied to the data for MD01-2461, followed by comparisons to OMEX 2K and another core (MD95-2006) with available magnetic data.

Ultimately, a chronology for MD01-2461 using the same methods as OMEX 2K will be developed, and whilst a radiocarbon dating application for MD01-2461 has been granted, the samples will not be processed during the time-scale of this study. An approximate time-scale for MD01-2461 has been created for the purpose of some general data analysis, and this will be discussed in Section 5.4.1. This section, therefore, deals solely with the age-depth model for OMEX 2K.

5.1 Chronology for OMEX 2K

Using the methods described in Section 4.2.3, a calendar age was assigned to each radiocarbon date for OMEX 2K (Table 5.1). A multiplot showing these ages is created by OxCal, plotting the probability distribution of the dates against calendar age (years BP)(Fig. 5.1). This is a good way to see potential calibration problems, such as the KIA- samples here, which are just too old to be calibrated by the marine calibration curve in OxCal; and the uncertainty surrounding the samples in the Younger Dryas and Holocene, which have the potential to yield multiple calibration solutions. An OxCal multiplot also provides a good visualisation of the probability plots in comparison to each other: Fig 5.1 for example, shows the broad probability distributions given by older samples compared to younger ones and this is due to the limited resolution of the calibration curve for ages

older than c. 11 kyr BP.

Once all the radiocarbon ages were calibrated, they were plotted against depth in order to develop an age model for the core (Fig. 5.2a & b). A trendline was fitted to the data, which gives an equation for the model. A third order polynomial trendline and a sixth order polynomial trendline were both fitted to the data for OMEX 2K. The third order polynomial was selected for its simplicity. The sixth order curve intercepts the mean ages with greater precision, but it was decided that for this study, simplicity throughout MIS 2 & 3 (Marine Isotope Stages 2 and 3, which span 12 –59 thousand radiocarbon years BP; Lowe & Walker, 1997) was more important than precision in the Holocene. In addition, given the uncertainty in age at any one dated point, there is a danger in over or under estimating sedimentation rate changes with higher order curves. There was also found to be remarkable similarity between the two models below c. 60 cm depth, which is the area of primary concern here. It is acknowledged that the model must be treated with caution above 60 cm depth, due to the disparity between the fitted trendlines, and the date at 36.5 cm depth.

Using the equation for the third order polynomial curve (Fig. 5.2), any age (calendar years BP) can be attributed to any depth (cm) along the core. The equation is:

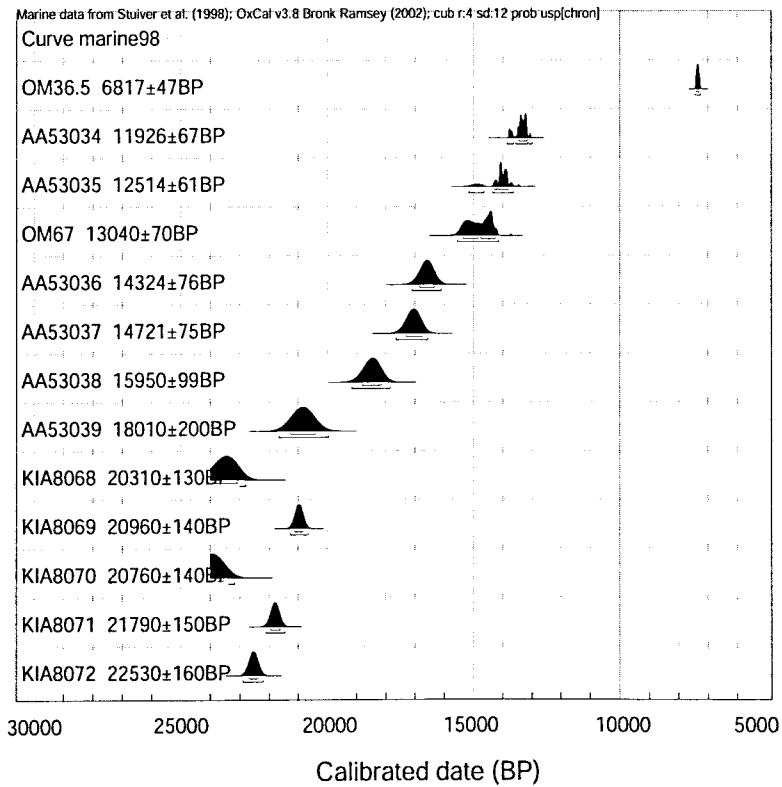
$$\text{Age (yr BP)} = (2.3969 \times 10^{-3} \times \text{depth}^3) - (1.184 \times \text{depth}^2) + (273.033 \times \text{depth})$$

(Eqn 5.1)

Age models are also useful in assessing sedimentation rate changes over time (i.e. the amount of material deposited in a certain timescale, usually centimeters per thousand years). Sedimentation rates display the variations in sediment delivery to a core site, which is ultimately dependent upon the transport mechanisms at work and therefore, climate (Wilson & Austin, 2002). The sedimentation rates within OMEX 2K will be discussed in Section 5.3.1.

Table 5.1: Calibrated Calendar Ages for OMEX 2K

Code	Depth (cm)	Conventional Radiocarbon Age (BP $\pm 1\sigma$)	Calibrated Age (BP)
OM-36.5	36.5	6817 ± 47	7335
AA -53034	60.5	11926 ± 67	13450
AA -53035	68.5	12514 ± 61	14000
OM-73	73	13040 ± 70	14850
AA -53036	88.5	14324 ± 76	16600
AA -53037	92.5	14721 ± 75	17100
AA -53038	108.5	15950 ± 99	28500
AA -53039	138.5	18010 ± 200	21400
KIA -8068	166.5	20310 ± 130	23476
KIA -8069	170.5	20960 ± 140	24235
KIA -8070	174.5	20760 ± 140	24002
KIA -8071	186.5	21790 ± 150	25664
KIA -8072	198.5	22530 ± 160	26058

**Fig. 5.1:** Multiplot showing the age distributions of all the dates for OMEX 2K taken from OxCal.

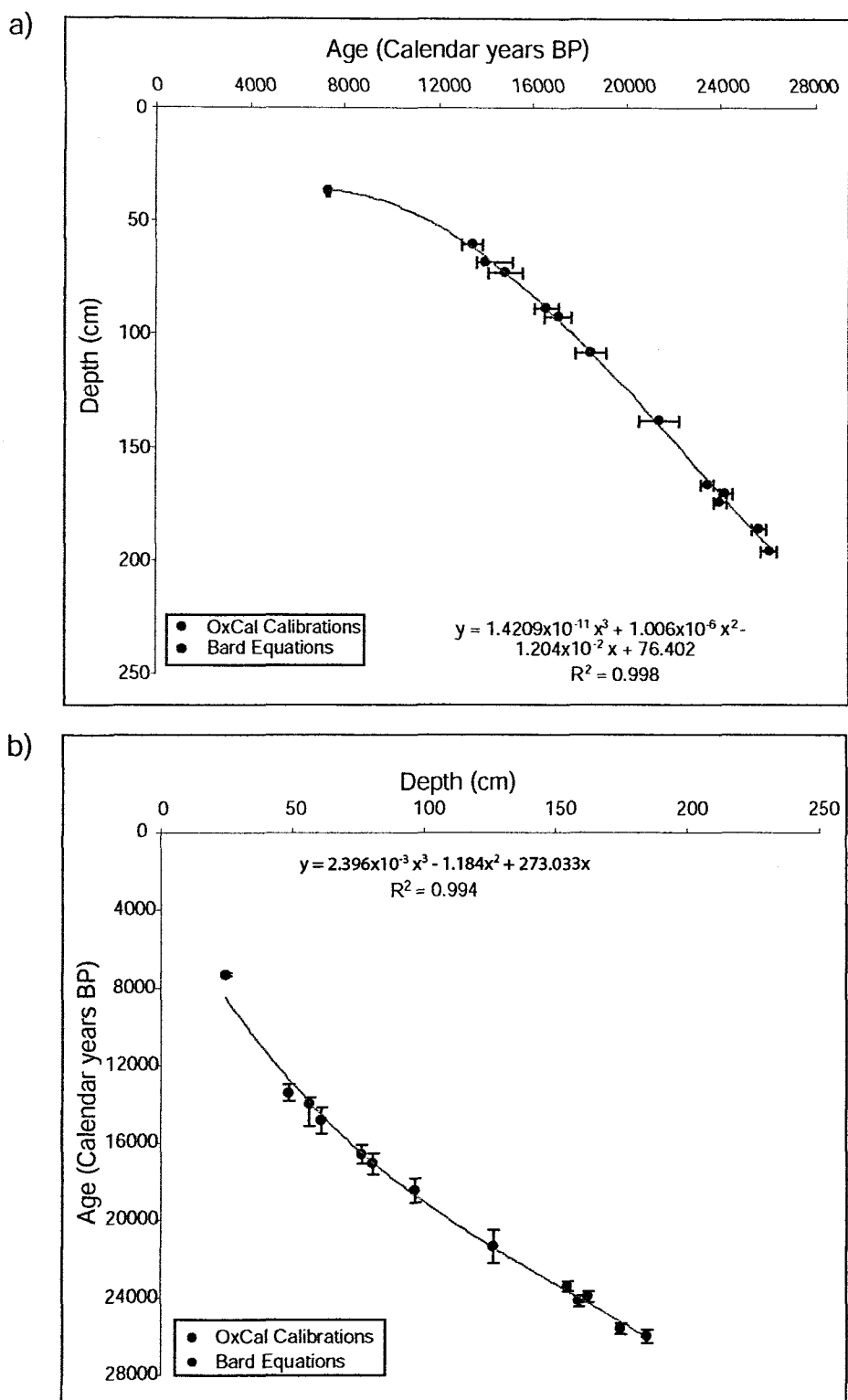


Fig. 5.2: a) Graph of age versus depth for OMEX 2K. The equation of the third order polynomial curve, seen on the graph will provide a depth (cm) for any age (years BP) along the core. b) Graph of depth versus age for OMEX 2K. The equation of the third order polynomial curve, seen on the graph will provide an age (years BP) for any depth (cm) along the core.

Calibration Issues for OMEX 2K

There are various issues surrounding the calibration of radiocarbon ages, especially in the marine environment. These have been discussed in some detail in Section 4.2. The factors affecting the calibration of OMEX 2K will now be addressed.

The first issue raised in the calibration of OMEX 2K is that of a marine reservoir correction. There is extensive discussion in the literature on the spatial and temporal variations in marine reservoir age, and many suggestions are made as to which should be used (see Section 4.2.2). Spatially, reservoir ages change both between and within oceans. This creates problems for selecting a correction relevant to a specific area. Temporally, each date potentially has its own correction age, as they are influenced by oceanic and climatic variables, such as mixing rate, wind speed, ice cover and up welling (Heier-Nielsen *et al.*, 1995; Stuiver *et al.*, 1998). The Younger Dryas in the North East Atlantic has been estimated as having a reservoir age of 700 years while at the end of Heinrich Event 1, this age is suggested at 1230-1940 years (Austin *et al.*, 1995; Waelbroeck *et al.*, 2001)(see Section 4.2). This makes the selection of a reservoir age difficult, as it is impossible to apply a separate, and accurate, correction to each date, especially to those below H1 for which no estimates have been made as yet. As a result, and in the absence of any great confidence in an alternative approach, the standard modern-day reservoir correction for the North Atlantic (400 years) was applied in the construction of the OMEX-2K age model.

Once the reservoir correction had been applied (OxCal 3.8 does this automatically during the calibration process), the next issue to be resolved was the selection of a single age from within the intervals provided by OxCal 3.8 for each ^{14}C sample. Ideally, a weighted average process would have been used, which enables the height of the probability distribution to be taken into consideration rather than just the time span. Unfortunately, the relevant data to use this method was not available for OMEX 2K. The next best method was used, which was to calculate the mean age from the range with the highest probability (Pilcher, 1991).

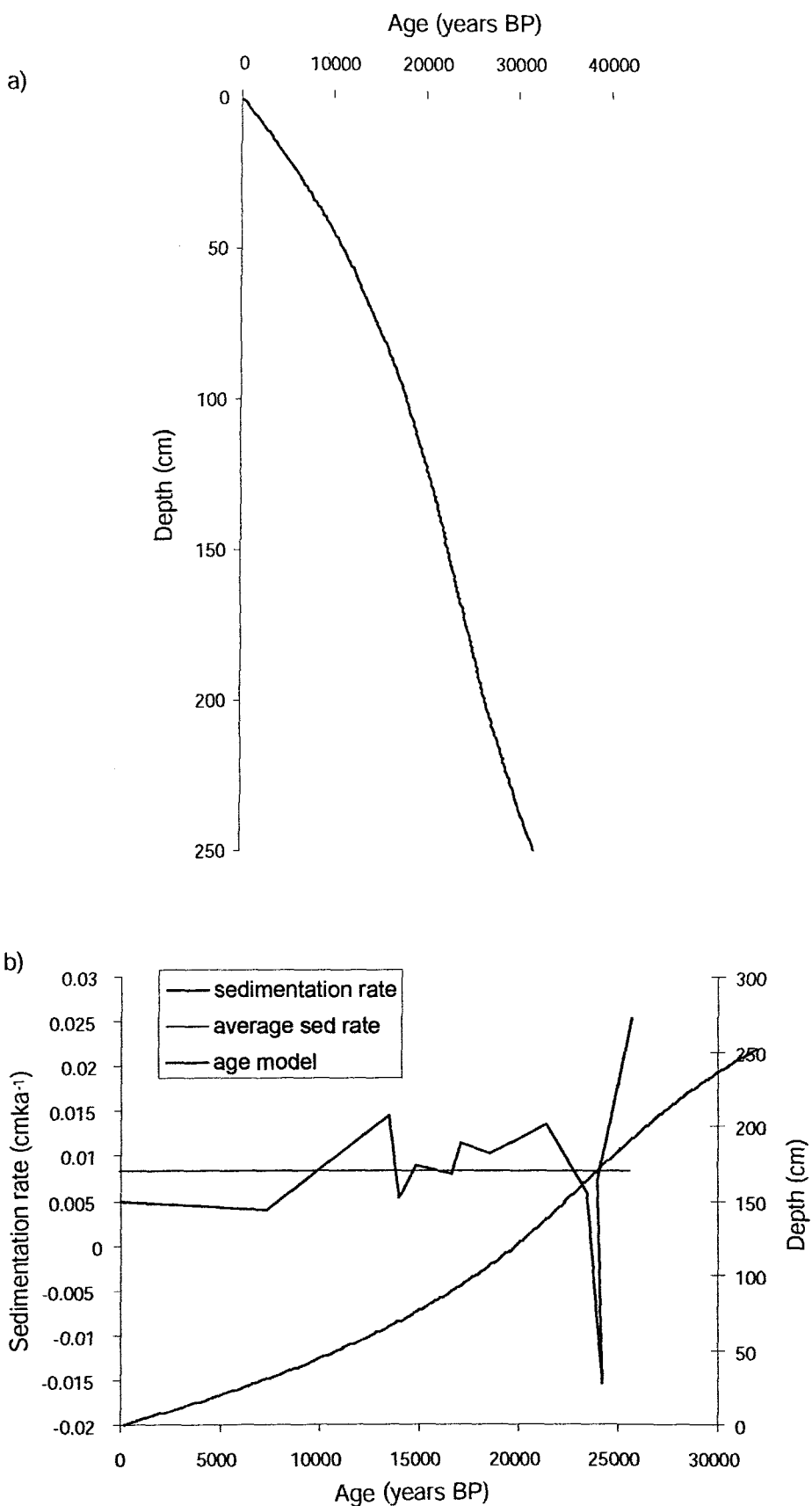


Fig. 5.3: a) Age model for OMEX 2K, created using Equation 5.1; b) Sedimentation rates for OMEX 2K created using the age model. The black line is the sedimentation rate against time; the red line is the age model taken from 5.3a); the blue line is the average sedimentation rate for the whole of the core.

Five of the radiocarbon dates were obtained from Scourse *et al.*, (2000) with permission, but were too old for OxCal 3.8 to calibrate accurately, given the limits of the INTCAL98 calibration curve (Stuiver *et al.*, 1998). This meant that the Bard Age Equation was used (Eqn 4.1; Bard *et al.*, 1998 - see Section 4.2.2 for a further discussion). Despite its limitations, the Bard Equation was employed in this study because it provides the simplest approach to radiocarbon calibration beyond the limits of INTCAL98 (Bard *et al.*, 1990).

Finally, the application of the polynomial trendline has problems associated with it. The precision of the trendline through the dates can affect the outcome, as can the degree of the polynomial used. A higher order will intercept the mean ages with greater precision, but will create a more complex equation, and can over or under estimate the age model at these points (Telford *et al.*, 2004b). This was demonstrated in Section 4.2.2, where the sixth order polynomial used gave a higher level of precision, but a significantly more complex equation. It also didn't vary significantly from the third order polynomial curve below 60 cm depth – probably due to the number of dates below this depth. As this study is focused on the Pleistocene, it was decided that a simpler model would be more beneficial to a precise one in the Holocene.

With these limitations acknowledged, an age-depth model for OMEX 2K is shown in Fig. 5.3. Having established this model for OMEX 2K, all subsequent results will be presented on both a depth and age basis.

5.2 OMEX 2K: A pilot study

As described earlier (Section 1.3), the OMEX 2K core was chosen as the basis for a pilot study with the main aim of evaluating the potential of high resolution environmental magnetic methods to differentiate between and identify IRD provenance. Mineralogical analysis performed by Scourse *et al.*, (2000) has demonstrated that OMEX 2K contains not only the first two Heinrich Layers, but

also both European and Laurentide IRD (Fig. 5.4).

Seven dominant mineral types were originally counted and converted into relative abundance by Scourse *et al.*, (2000). Major dolomite peaks were found to correspond with the magnetic susceptibility highs at the Heinrich Layers (constrained by AMS ^{14}C dating), with chalk and mica peaks just prior to the H2 dolomite maximum. Dolomite is characteristic of LIS-sourced material (Andrews *et al.*, 1993), suggesting that icebergs from the LIS were able to travel as far as the Celtic margin. The chalk and mica is typical of glacial sediments from the BIS via the Irish Sea ice stream, particularly at the LGM (21-18 kya, Lowe & Walker, 1997). Volcanic glass from Iceland is also found both after and preceding the HLs. Given this mineralogical and chronological control, and the availability of suitable archive core sample material, OMEX 2K was thought an ideal core to use in evaluating environmental magnetic techniques as a provenance discriminator.

Subsequent to the start of the pilot study, a more detailed mineralogical and lithological analysis of OMEX 2K was undertaken by Dr M. Fruze and Dr J. Scourse (University of Wales, Bangor). These data are reproduced here (with permission; Fig. 5.5). They confirm the general findings reported in Scourse *et al.*, (2000) but also reveal some interesting further features. Large quantities of rhyolitic tephra is found at the Younger Dryas, accompanied by a peak in quartz with biotite. Below H1 (c. 90cm) there is a steady increase in all types of quartz down to 100 cm, where it peaks, along with basaltic tephra. The quartz and tephra remain abundant through to a depth of 114 cm, where they are joined by peaks in both mica (muscovite) and chalk. The ambient sediments between the Heinrich Events appear to be characterised by various types of quartz (including clear, rounded quartz and biotite) and mica (biotite). A chalk peak is found at c. 168 cm, just after the main H2 dolomite peak, as well as the “precursor event” originally identified by Scourse *et al.*, (2000). Peaks in both mica (biotite) and quartz (with biotite) are found between the main H2 event and “precursor event”, with a further maximum in mica at 202 cm depth. Below this, the dominant lithologies are basaltic tephra and mica (muscovite).

XRD analysis was performed on 18 samples from OMEX 2K (see Section 4.1.1). These points were selected due to their interesting magnetic or IRD properties, as shown by the preliminary magnetic data, and the data discussed above. Table 5.2 shows the depths picked for XRD analysis and gives the reason for the selection of each sample. The results will be discussed later in the chapter (Section 5.3.1).

The environmental magnetic analysis of OMEX 2K was performed as described in Section 4.3. From these analyses, a range of magnetic parameters and inter-parametric ratios were calculated (Table 4.9). These data are presented as both depth and age plots in Figs. 5.6 & 5.7.

5.2.1 Magnetic Analysis

This section will discuss the magnetic results for OMEX 2K, starting with the initial results, down-core plots and acquisition data, and their basic interpretation. The quantification of magnetotactic bacteria and greigite will follow (see Section 2.5.2), and then some more detailed analysis of the magnetic data. Section 5.3 contains the environmental interpretation of the data.

The first magnetic analysis to be performed in this study was volume magnetic susceptibility (κ). As mentioned previously (Section 2.5.1), susceptibility is a measure of the concentration of magnetic minerals and, in particular, is sensitive to the concentration of ferrimagnetic minerals (e.g. magnetite)(Thompson & Oldfield, 1986; Verosub & Roberts, 1995). Fig. 5.8a shows the down-core record of volume magnetic susceptibility for OMEX 2K taken during this analysis, alongside the NERC susceptibility record taken on board ship (from the OMEX project CD ROM; Lowry *et al.*, 1997)(Fig. 5.8b).

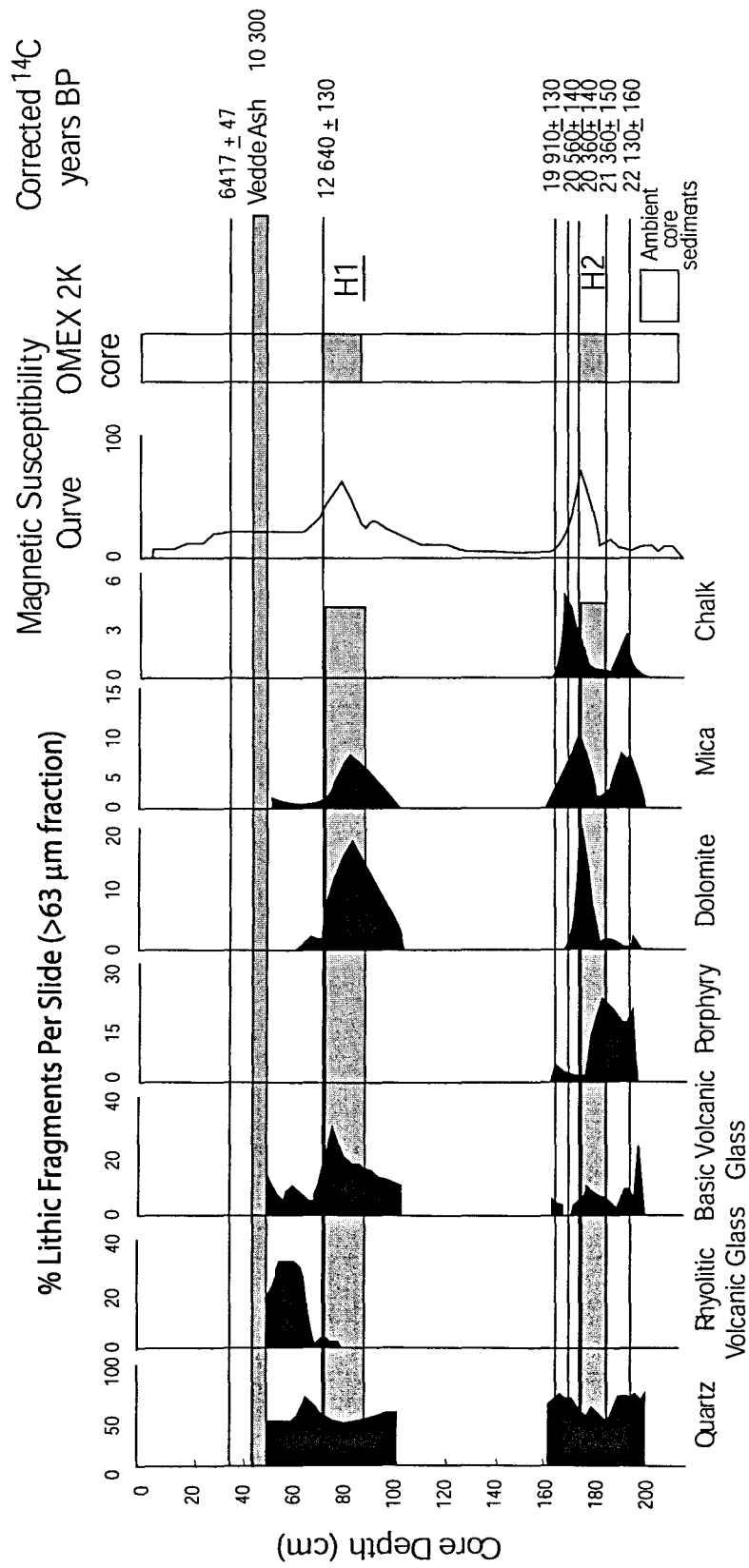


Fig. 5.4: Lithological data for OMEX 2K (re-drawn from Scourse *et al.*, 2000). See Fig 3.10 legend for further discussion.

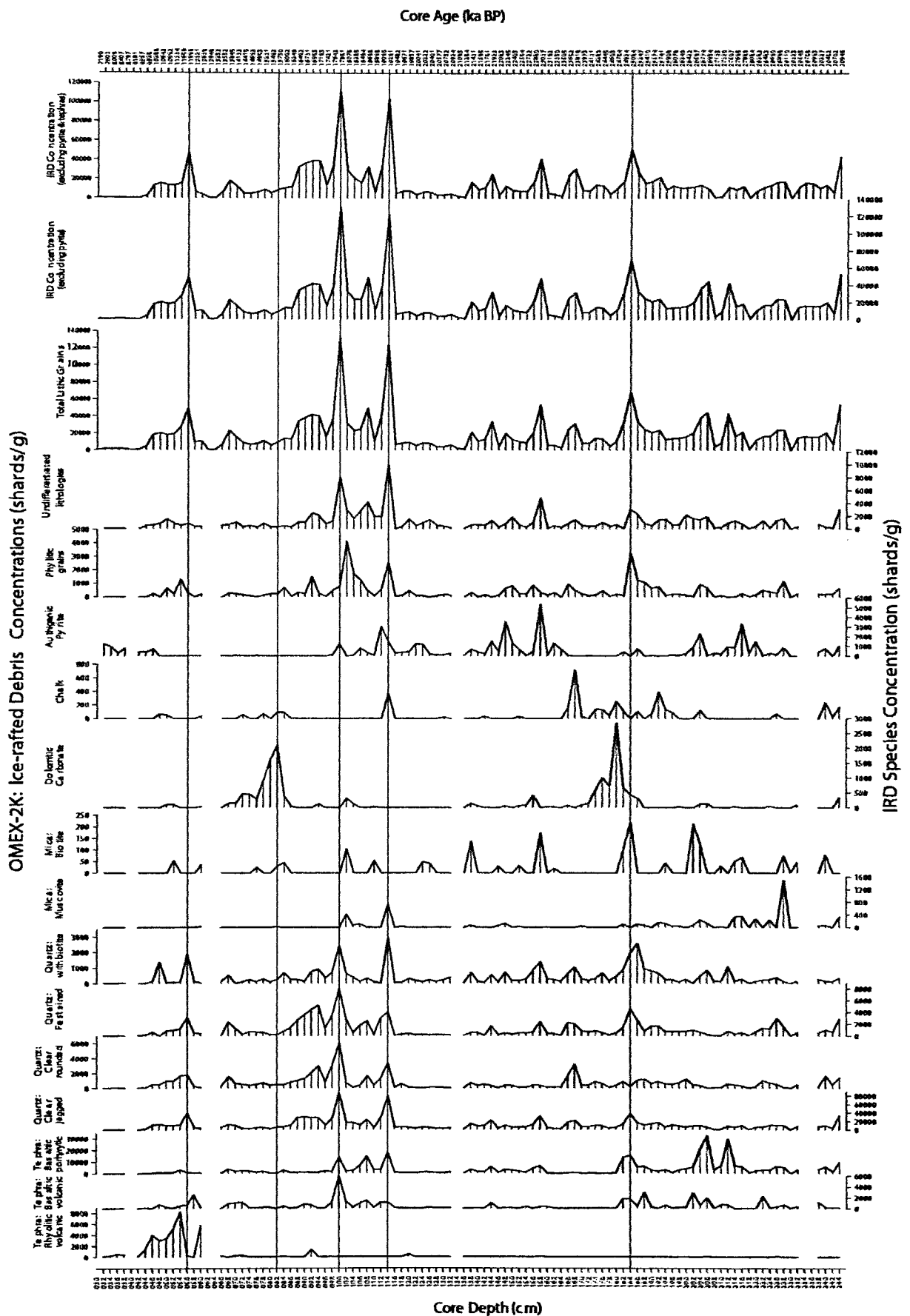


Fig. 5.5: Mineralogical data from OMEX 2K carried out by Dr. M. Furze (University of Wales, Bangor) in 2003. Many of the patterns seen in the Scourse *et al.*, (2000) paper are identifiable here, but the more detailed analysis also reveals some further information surrounding the Younger Dryas, before H1, and before H2.

Table 5.2 : Samples from OMEX 2K selected for XRD analysis and the reasons why.

Sample	Reason for Selection
13	Modern day sediments (c. 3000 years BP)
25	Modern day sediments (c. 6000 years BP)
54	Sample from the Vedde Ash layer picked out by Scourse et al., (2000)
83	Peak of H1
84	Peak of H1
92	IRD peak in the lithic grain count, identified as quartz by Furze (unpublished)
108	Quartz and tephra peaks
130	Ambient glacial sediments
131	Ambient glacial sediments
167	Chalk peak identified by Furze (unpublished) above H2
168	Chalk peak identified by Furze (unpublished) above H2
180	Peak of H2
181	Peak of H2
190	Chalk peak below H2, named as a European precursor by Scourse et al., (2000)
191	Chalk peak below H2, named as a European precursor by Scourse et al., (2000)
202	Tephra and mica peaks
205	Tephra and quartz peaks
212	Tephra, quartz and mica peaks

Parameter	Mineral Magnetite	Haematite	Maghaemite	Greigite	Pyrrhotite	Goetite	Titano magnetite	Illmeno haematite
χ ($10^{-6}\text{m}^3\text{kg}^{-1}$)	250-1200	0.3-4	250-850	120	50	0.3-1.3	170-200	25
κ	2.4-2.8		$125 \cdot 10^{-6}$					
χ_{arm} ($10^{-6}\text{m}^3\text{kg}^{-1}$)	70-10510	10	300-400	250-900			150-600	
χ_{fd} (%)	0.4-11							
ARM ($\text{mAm}^2\text{kg}^{-1}$)	18-110	0.002		110	80	0.005	80-480	480
SIRM ($\text{Am}^2\text{kg}^{-1}$)	10-40	0.2-0.3	5-35	11	4.5	0.01-1	7-12	8
χ_{arm}/χ or ARM/ χ	0.1-13 0.03-0.3	0.01	1-1.5	1.8-9.8 0.9	1.6	1.0	0.3-4 0.5-2.4	19
SIRM/ χ (kAm^{-1})	4-50	500		100	500	70	10-60	320
IRM ₁₀₀ /SIRM	-0.87	+0.5		-0.8				
Hard IRM ($10^{-5}\text{Am}^2\text{kg}^{-1}$)	4.042 (60% haematite) 0.462 (20% haematite)							
M_i (kAm^2) ($\text{Am}^2\text{kg}^{-1}$)	480 92	2.5 0.5	380	~125 20	~80 20	~0 0.5	24	30
Curie Temp ($^{\circ}\text{C}$)	580	675	590-675	330	320	120	200	100

Table 5.3: Table of common magnetic minerals and some of thier typical magnetic characteristics (Taken from Thompson & Oldfield, 1986; Peters & Thompson, 1998; Maher et al., 1999; Smith, 1999; Evan & Heller, 2003; Peters & Dekkers, 2003)

The original, on board trace is at 4 cm resolution, and therefore shows less detail than the record measured here, but the general trends are still fairly obvious. The gaps at 100 cm and 235 cm (due to lack of sample material at those depths) can also be inferred from the original data. The two Heinrich Layers are clearly visible on both profiles, with peaks at 84 cm (16.06 kyr BP) and 181 cm (24.88 kyr BP), showing a dramatic increase in the concentration of magnetic minerals. When compared with the lithic grain count data (Fig 5.8c), it is evident that peaks of large grains (around 1 mm in size) correspond to the peaks in susceptibility (see Fig. 5.8 legend). These results suggest that the increases in magnetic concentration are due to large terrigenous particles (IRD). The average κ value is 15.078×10^{-5} SI, with a range of $1.7\text{--}61.9 \times 10^{-5}$ SI. As mentioned above, the highest values are found in the HEs, the lowest values, however are found in the Holocene (above 50cm depth)(Descriptive statistics can be found in Appendix 2bi, Pg 338)

Also noted in the susceptibility record are slight increases at 47-62 cm (10.55-13.02 kyr BP), c.190 cm (25.62 kyr BP) and 200-221cm (26.47 – 28.43 kyr BP). The first two potentially correlate with the Younger Dryas (YD) and H2 Precursor event (suggested by Scourse *et al.*, 2000) respectively, and are also visible in the IRD grain count data. There were no corresponding mineralogical data beneath 200 cm from the Scourse *et al.*, (2000) paper, however, the newer lithological analysis by Dr. M Fruze described previously details a large input of mica (biotite) at 202 cm and basaltic tephra at both 205 cm and 212 cm (Fig. 5.5).

The various mass-specific magnetic parameters and ratios described in Section 4.4 give a more detailed account of the variations in magnetic concentrations, mineralogy and grain size along the whole length of the core. Figs. 5.6 & 5.7 show the down-core profiles for each of the parameters. Fig. 5.9 contains the ratios that are commonly reported within the environmental magnetic literature. To aid comparison, Table 5.3 contains average values of the various parameters for the more common magnetic minerals taken from the literature (Thompson & Oldfield, 1986; Peters & Thompson, 1998; Maher *et al.*, 1999; Smith, 1999;

Evans & Heller, 2003; Peters & Dekkers, 2003).

Mass specific magnetic susceptibility (χ) was the first measurement made on the sub-samples of OMEX 2K, at both low (χ_{lf}) and high (χ_{hf}) frequencies. Frequency dependence of susceptibility was calculated as in Section 4.3. Convention dictates that low frequency susceptibility is used over the high frequency susceptibility, therefore, χ will now refer to χ_{lf} . The χ record (Fig 5.9) replicates that of the volume susceptibility, with average values of 16.98×10^{-8} SI, and a range of $6.41 - 67.20 \times 10^{-8}$ SI. The highest points again occur at the HLs and the lowest in the Holocene.

χ_{arm} is indicative of the concentration of single domain (SD) grains within the core (Table 4.9) From the plot in Fig. 5.9, it is possible to say that there is an increase in SD grains between 225-200 cm (28.84-26.47 kyr BP), decreases at the HLs (perhaps due to an increase in MD grains), with a slight peak at 139 cm (21.56 kyr BP). After H1, there is an abrupt and rapid rise until ~50 cm (~11.07 kyr BP)(possibly the termination of the YD) and the signal becomes very erratic for the rest of the Holocene. Maximum and minimum values are 0.78 and $0.118 \times 10^{-5} \text{m}^3 \text{kg}^{-1}$ and occur at a depth of 45cm and H2 (182 cm) respectively. The average value is $0.322 \times 10^{-5} \text{m}^3 \text{kg}^{-1}$. Pure magnetite powders have yielded χ_{arm} results of $800 \times 10^{-5} \text{m}^3 \text{kg}^{-1}$ for average grain sizes of $0.05 \mu\text{m}$; and $80 \times 10^{-5} \text{m}^3 \text{kg}^{-1}$ for average grain sizes of $1 \mu\text{m}$ (Evans & Heller, 2003). Using these data for pure magnetite, it would suggest that concentrations of sub-micron sized magnetite within the OMEX 2K sediments might vary between 0.00000944% and 0.0000624%. Within other marine sediments, values of χ_{arm} during glacial conditions have been suggested to be below $0.00001 \times 10^{-5} \text{m}^3 \text{kg}^{-1}$ with interglacial values increasing by an order of magnitude to $0.0001 - 0.0003 \times 10^{-5} \text{m}^3 \text{kg}^{-1}$ (Lean & McCave, 1998). All the OMEX 2K data fall well above the glacial estimate of χ_{arm} .

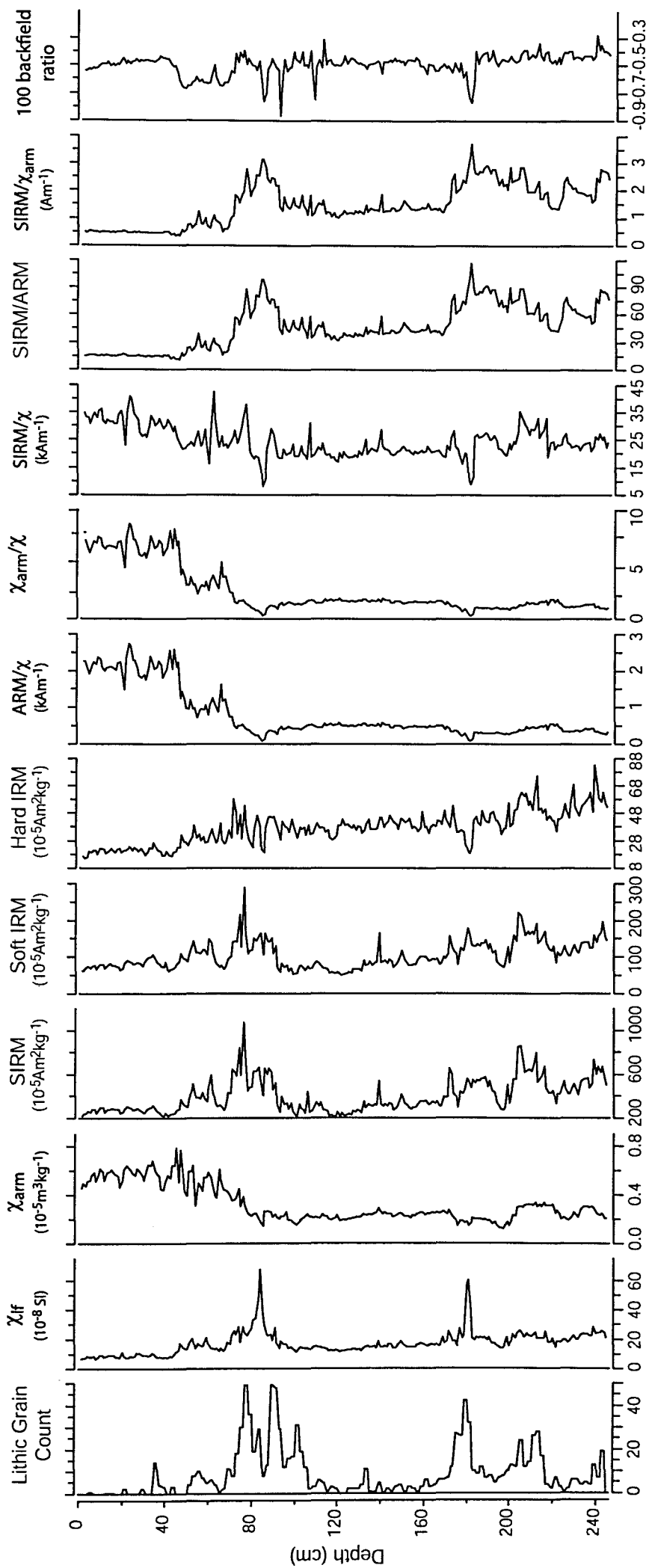


Fig. 5.6: Down-core properties of OMEX 2K against depth. See text for a full discussion.

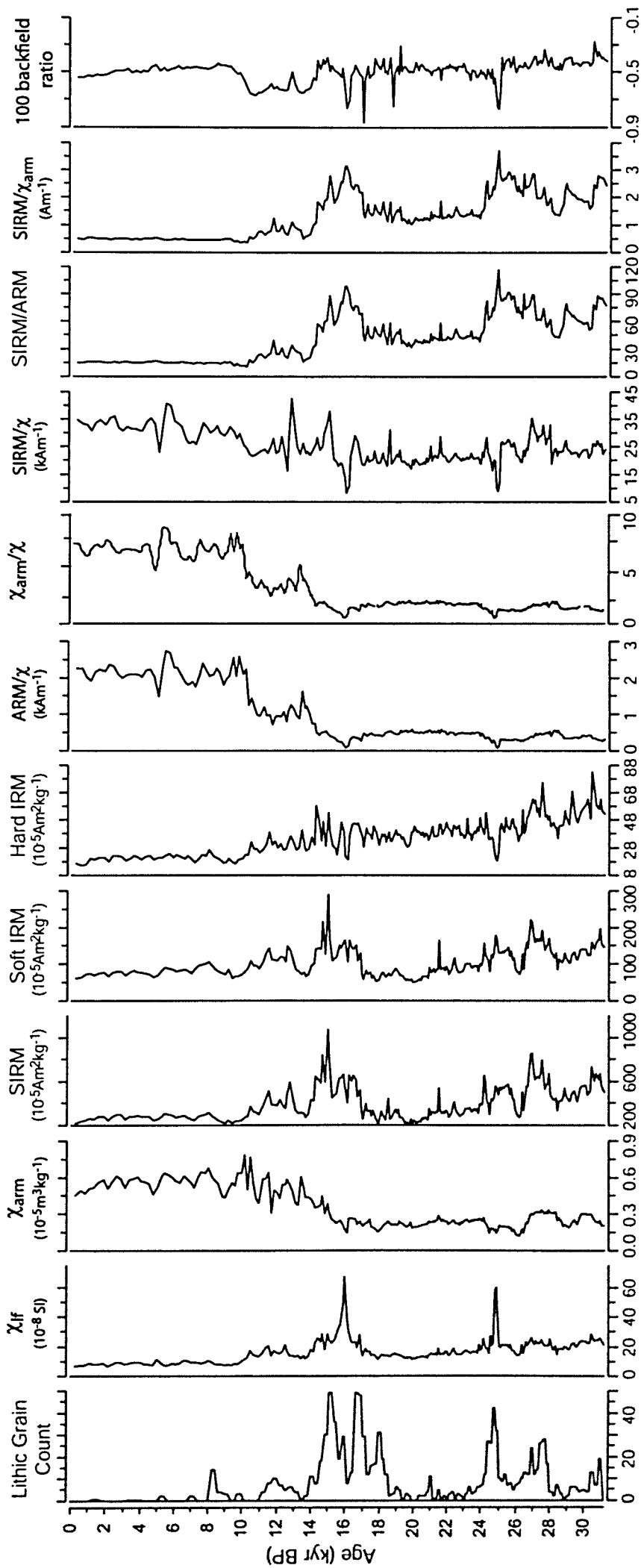


Fig. 5.7: Down-core magnetic properties of OMEX 2K against age. See text for further discussion.

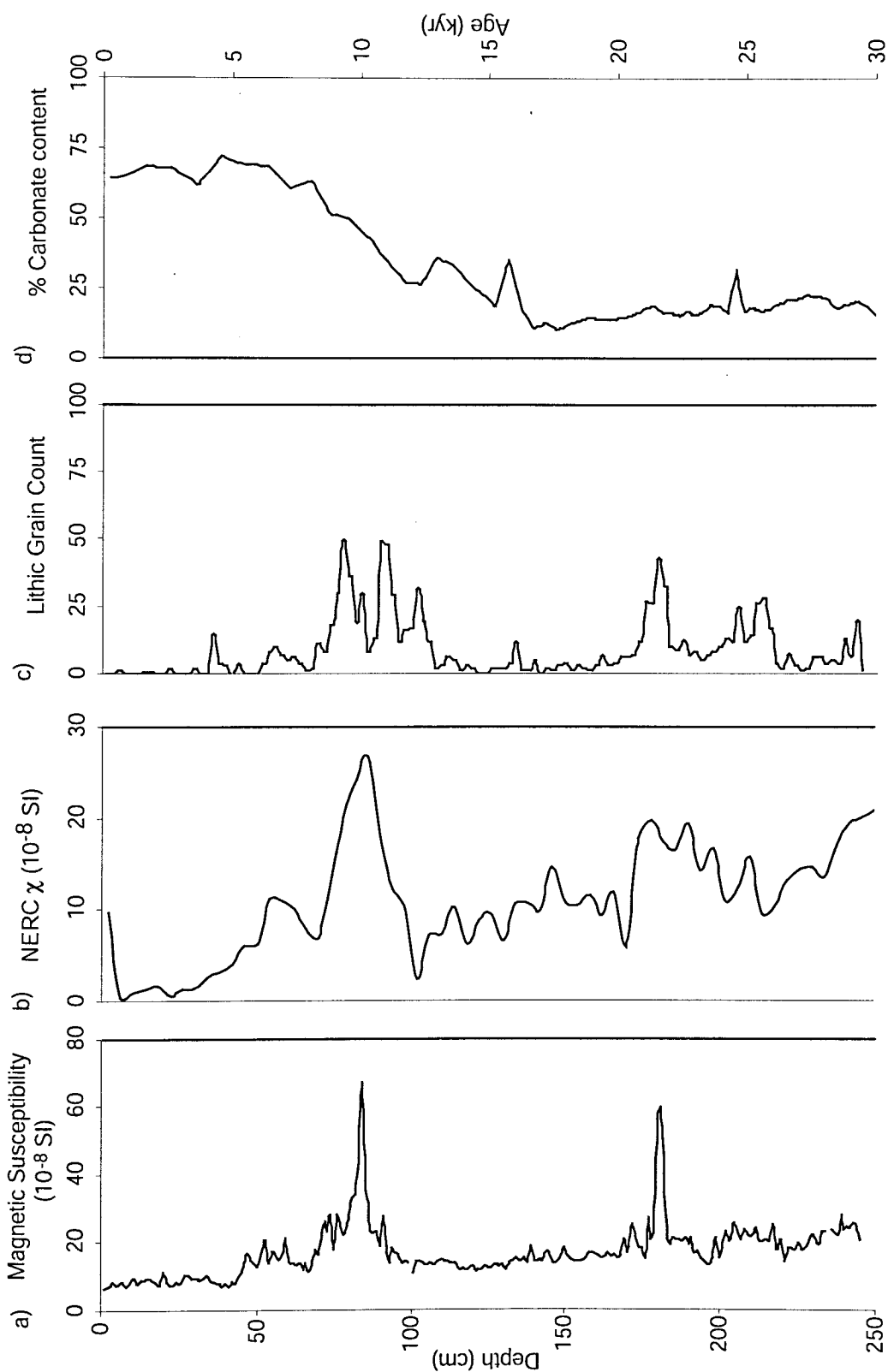


Fig. 5.8: a) Magnetic susceptibility measured during this study, and b) onboard ship in 1995 (taken from the NERC CD-ROM dataset; Lowry *et al.*, 1997). c) Lithic grain count from X-rays of OMEX 2K and d) the percentage carbonate content (taken from the NERC CD-ROM dataset; Lowry *et al.*, 1997).

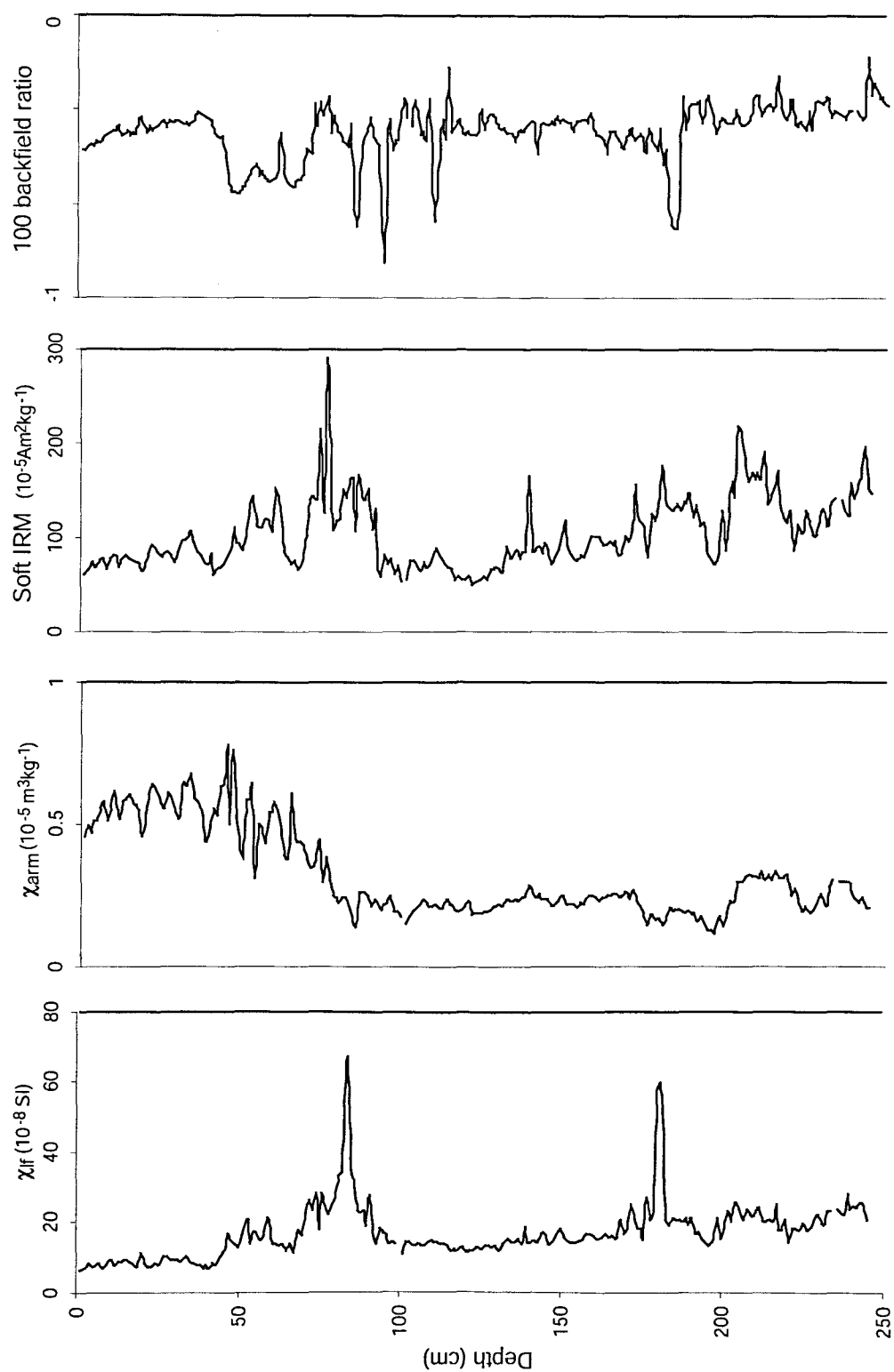


Fig. 2.9: Some magnetic properties of OMEX 2K; a) Magnetic susceptibility; b) Susceptibility of ARM; c) Soft IRM and; d) 100 backfield ratio.

The Soft IRM record shows variations in the concentration of low coercivity ferrimagnetic minerals, such as magnetite. A prolonged increase in low coercivity minerals can be seen between 225-200 cm (28.84-26.47 kyr BP), with smaller peaks at 189 cm (25.49 kyr BP), H2 and 139 cm (21.56 kyr BP). There is a rise at H1, but only because of the short-lived dip seen just prior to it (this could be the interval between a H1 precursor event and H1). A large rise in the concentration of ferrimagnetic minerals also occurs at ~75 cm (14.89 kyr BP), followed by a smaller two-peaked increase at the YD. The Holocene becomes more stable, and demonstrates a decrease in soft magnetic mineral concentration. Hard IRM, by definition, is the opposite of Soft IRM and represents the concentration of harder (high coercivity) magnetic minerals, such as haematite, however, they do not necessarily work in direct opposition with each other as additional factors play a part. This is demonstrated by the rise in Hard IRM that matches the rise in Soft IRM at 225-200 cm (28.84-26.47 kyr BP)(Figs. 5.6 & 5.7). A possible cause could be that the general increase in magnetic mineral concentration seen in the χ_{if} curve is due to a rise in both low and high coercivity minerals, and not just an input of one. Both of the HLs are dominated by lower coercivity minerals (a drop in Hard IRM), suggesting an increased input of only low coercivity minerals. Between the HLs, the signal takes on a seemingly cyclic pattern, which continues after H1 with larger, generally decreasing cycles, followed by lowering values over the YD. The Holocene is characterised by a consistently low hard mineral content. The average value of Soft IRM is $103.89 \times 10^{-5} \text{Am}^2 \text{kg}^{-1}$, the range is 49.44 (at 121 cm) to $290.47 \times 10^{-5} \text{Am}^3 \text{kg}^{-1}$ (at 76 cm). Hard IRM has an average of $37 \times 10^{-5} \text{Am}^2 \text{kg}^{-1}$ and a range of 14.96 (2 cm depth) to $82.78 \times 10^{-5} \text{Am}^3 \text{kg}^{-1}$ (239 cm depth).

IRM₁₀₀/SIRM (the 100 backfield ratio) is a slightly more specific mineralogical parameter, differentiating between magnetite (lower values; nearer to -1, reflecting its low coercivity behaviour) and haematite (higher values; nearer to 1, reflecting its high coercivity behaviour)(Table 5.3). Note that in these data, SIRM = IRM_{3000 mT}, although this ratio is often referenced to an SIRM measured at 1000 mT in the literature. The response of this ratio is consistent with both the

concentration dependent Soft and Hard IRM records in that it suggests a decrease in haematite concentration during the HLs, and at 139 cm (21.56 kyr BP), and an apparently constant mineralogy throughout the YD and Holocene. IRM₋₁₀₀/SIRM varies between -0.27 and -0.86, with an average of -0.49. The lowest point is at 92 cm depth, though the two next are the peak HE samples (-0.761 and -0.764). The highest point is at 239 cm. Peters & Thompson, (1998) estimated that IRM₋₁₀₀/SIRM values of -0.8 corresponded to magnetite whilst values of 0.5 corresponded to haematite (Table 5.3). From this, it is possible to infer that the sediments in OMEX 2K have a signal that is influenced more by magnetite than haematite.

ARM/ χ and χ_{arm}/χ are essentially the same variable (as described in Table 4.9), so will be discussed here solely as χ_{arm}/χ . They are both included in the plots to aid comparison between published results. χ_{arm}/χ is associated with the size of ferrimagnetic minerals (e.g. magnetite), with higher values indicating finer grains (Table 4.9). A slight rise in χ_{arm}/χ is seen at 225 cm (28.84 kyr BP), gradually declining to 200 cm (26.47 kyr BP). The record is then relatively stable, with the exception of the two dips at the HLs (down to values of 0.263 and 0.242), and a very small drop at 89 cm (16.67 kyr BP)(a possible H1 precursor?). After H1, there is a large, abrupt leap to approximately 75 cm (24.41 kyr BP), followed by high variability with an overall decline throughout the YD. At 50 cm (11.07 kyr BP), there is another large rise, followed by a series of cycles during the rest of the Holocene. This can be interpreted as being due to a predominance of coarse grains throughout the Pleistocene, especially at the HLs, with a rapid change to finer grains after H1. Within the finer-grained Holocene however, there is a great deal of variability. The average value for χ_{arm}/χ is 2.506, with a range of 0.242 - 8.619. Lowest values occur at the HEs, with the highest points in the Holocene. Table 5.3 records the average values of χ_{arm}/χ for Magnetite, Titanomagnetite, Maghematite and Greigite. On comparison to Table 5.3, the OMEX 2K samples all fall within the range of magnetite, agreeing with the 100 backfield ratio above.

SIRM/ χ can also be a magnetic grain size indicator, though it is also suggestive of

mineralogy. Lower values ($1.5\text{--}50\text{ kAm}^{-1}$) represent magnetite and vary indirectly with size, while higher values ($>50\text{ kAm}^{-1}$) characterise haematite. Very high results ($>70\text{ kAm}^{-1}$), on the other hand, are indicative of pyrrhotite (Peters & Thompson, 1998). The results here show that the dominant mineral is magnetite, with increasing grain size at the HLs. Noticable decreases in size occur at 225–200 cm (28.84–26.47 kyr BP), 139 cm (21.56 kyr BP), 115 cm (19.43 kyr BP), and the YD. The Holocene has a very variable signature, although grain size generally becomes finer overall. Minima in SIRM/χ are at the HEs (8.25 and 8.97 kAm^{-1}), maxima during the YD and Holocene (highest point = 42.42 kAm^{-1}). The average value is 24.42 kAm^{-1} . These all clearly fall within the magnetite range of $1.5\text{--}50\text{ kAm}^{-1}$ (Table 5.3).

$\text{SIRM}/\chi_{\text{arm}}$ (or SIRM/ARM , again both plotted in order to compare with published data) is a measure of SD ($<0.1\text{ }\mu\text{m}$) grains, with lower values indicating more SD grains. Higher values indicate a low concentration of grains in this range, and therefore, a higher overall magnetic grain size. It has been suggested that values falling around 1 kAm^{-1} are consistent with single domain magnetite, while values of $\sim 10\text{ kAm}^{-1}$ are representative of multidomain magnetite (Bloemendal *et al.*, 1993). Peaks in the OMEX 2K data occur at 189 cm (25.49 kyr BP), H2, 139 cm (21.56 kyr BP), 89 cm (16.67 kyr BP) (a possible H1 precursor?), H1 and the YD. All these record times of decreased SD grain presence, possibly due to increasing presence of MD grains. The rest of the record remains consistently low, suggesting that grain size remained relatively constant, with the occasional increase occurring at the HLs, 200 cm (26.47 kyr BP), 139 cm (21.56 kyr BP) and the YD. The average $\text{SIRM}/\chi_{\text{arm}}$ value is 1.494 kAm^{-1} , and the range is $0.348\text{--}3.705\text{ kAm}^{-1}$. The highest values are again found at the HEs, with the lowest occurring during the Holocene.

Summary

At 225–200 cm (28.84–26.47 kyr BP) there is an overall increase in magnetic concentration, with the extra input consisting of both high and low coercivity minerals. Magnetic grain size, particularly of low coercivity minerals, also

increases. The concentration of SD grains increases at 200 cm (26.47 kyr BP), indicating a decrease in overall grain size. The “precursor” (as defined by Scourse *et al.*, 2000 at ~191 cm, 25.66 kyr BP) is characterised by a relatively low overall magnetic concentration, with a drop in the concentration of fine grained magnetite. The decline in fine grains is probably due to the increase in MD grains. There is an increased concentration at H2, which seems to be caused by an input of low coercivity minerals (e.g. magnetite) and grain size increased to the MD range. At 139 cm (21.56 kyr BP), there is an increase in coarse-grained magnetically soft minerals, with a significant decline in haematite. In the zone of any H1 precursor event, there seems to be an overall increase in magnetic grain size. H1 itself has a drop in magnetically hard minerals but also a rise in magnetic grain size and overall concentration. The YD and Holocene signals display a significant deviation from previous signatures, with a rapid, overall decline in magnetic minerals, though a much finer grain size to anything seen before is found in the minerals that are present. This grain size record is highly variable, however, it never reaches pre YD levels.

IRM Acquisition Curves

The raw IRM data was used to draw acquisition curves that show the “rate” at which a material becomes magnetically saturated (Walden, 1999). This can be indicative of mineralogy. Magnetically soft minerals acquire their IRM remanence easily and therefore become saturated at lower field strengths, whereas magnetically hard minerals saturate at higher field strengths (Walden, 1999). For example, magnetite, a ferrimagnetic mineral (i.e. a low coercivity mineral) will have all but reached saturation by 200mT, but haematite, a canted anti-ferromagnetic mineral (i.e. a higher coercivity mineral), will only reach saturation in fields of 1000mT or more. This is ultimately due to the crystal lattice structure of the mineral, and dependent on the number of paired electrons and their lineation (Smith, 1999).

The raw IRM data are converted into acquisition ratios by normalising for concentration (IRM/SIRM - in this case SIRM = IRM₃₀₀₀ mT). It is then plotted

against field strength, which is expressed as a logarithmic scale for forward fields and a linear scale for backfields. Fig. 5.10 shows the acquisition plots for all of the OMEX 2K samples, with standard acquisition curves from Peters and Thompson, (1998) and Walden, (1999) super-imposed. The standards were created by measuring natural samples of single mineralogy, normalising for concentration and plotting as above. Although the interpretation of these plots is relatively simple, caution must be practiced, as natural samples are very rarely made up from one type of mineral, and curves may be composites based upon the mixture of minerals present, and their relative proportions (Walden, 1999).

The plots for OMEX 2K (Fig. 5.10) show an abundance of softer magnetic minerals, as the majority of samples reach saturation by c. 800 mT. There is clearly a mixture of minerals involved however, which is evident from comparison with the standard ratios, and also from the samples that reach saturation at higher fields. There are two samples that clearly reach saturation before any of the others, particularly in the forward fields. These samples are the “peak” Heinrich Event samples at 84 cm depth and 181 cm depth. The three other samples seen in the backfield plot are also Heinrich Event samples. These distinctive samples appear to consist of a markedly different mixture of minerals to the ambient glacial sediments, dominated by a ferrimagnetic composition. The short-lived nature of the Laurentide input to the Heinrich Layers is supported by this data.

Magnetotactic Bacteria

As discussed in Sections 2.5.3 and 4.4.3, various magnetic parameters can be used to potentially quantify the concentration of magnetotactic bacteria (MTB) in deep-sea sediments. If the magnetic data are to offer insights into the provenance of the inorganic IRD sediment fraction of marine cores such as OMEX 2K, it is important that the influence of non-detrital (post depositional) magnetic components can be shown to be absent or of minimal importance to the overall magnetic composition.

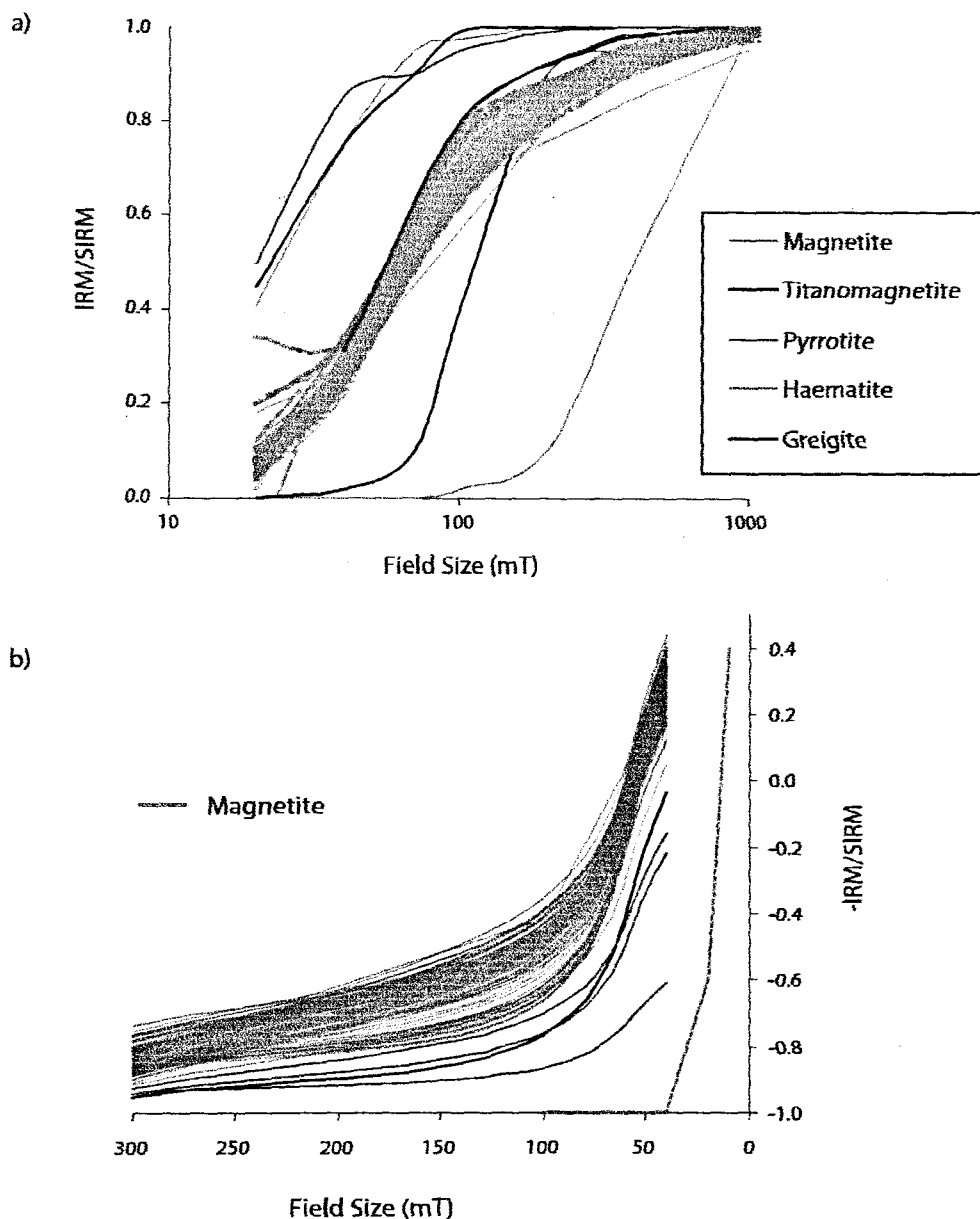


Fig. 5.10: IRM Acquisition curve for both (a) forward and (b) backfield IRM acquisitions for the whole of OMEX 2K. Superimposed are standard curves for magnetite from Walden, 1999 (backfields) and Peters & Thompson, 1998 (forward fields). The peak Heinrich Event samples are relatively easily distinguished from the rest of the core; they are the two that saturate first in (a) and are among the samples seen at the base of the backfield acquisition curve (red lines correspond to H1 samples; blue to H2). The five samples that are separate from the main group in (b) are all from either the H1 or the H2 sections of OMEX 2K, as identified by the down-core magnetic susceptibility. This lends evidence to the suggestion that the mineral characteristics associated with the HEs are short-lived. These curves show that the OMEX 2K sediments have a low coercivity minerals abundance, particularly that of magnetite (evident from the backfield acquisition plot).

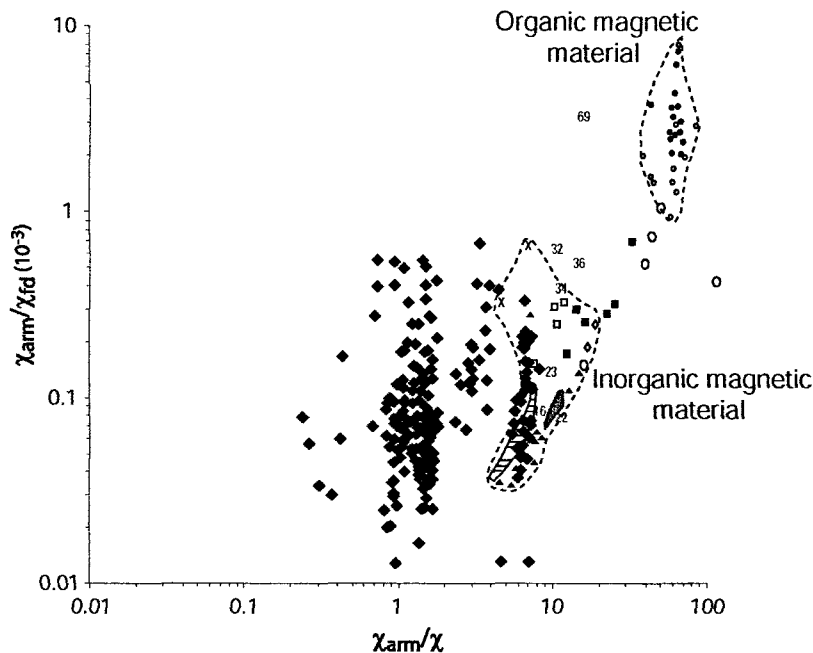


Fig. 5.11: Graph of χ_{arm}/χ versus χ_{arm}/χ_{fd} used for the identification of magnetotactic bacteria. The original plot from Oldfield (1991) is superimposed on the figure to aid comparison. Bacterial magnetic material should plot with χ_{arm}/χ values of >40 and χ_{arm}/χ_{fd} values of >1 . This is not the case for the OMEX 2K sediments, suggesting minimal influence of organic magnetite

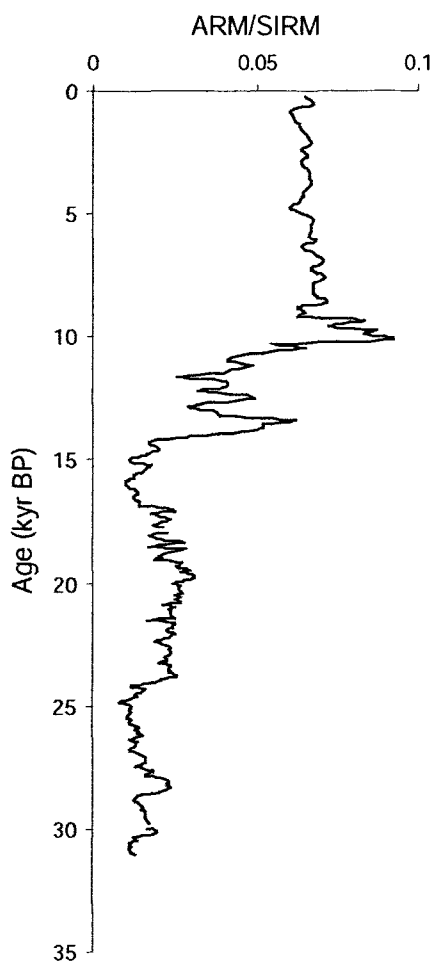


Fig. 5.12: ARM/SIRM for OMEX 2K used as an indication for the presence of magnetotactic bacteria (values of 0.15-0.25).

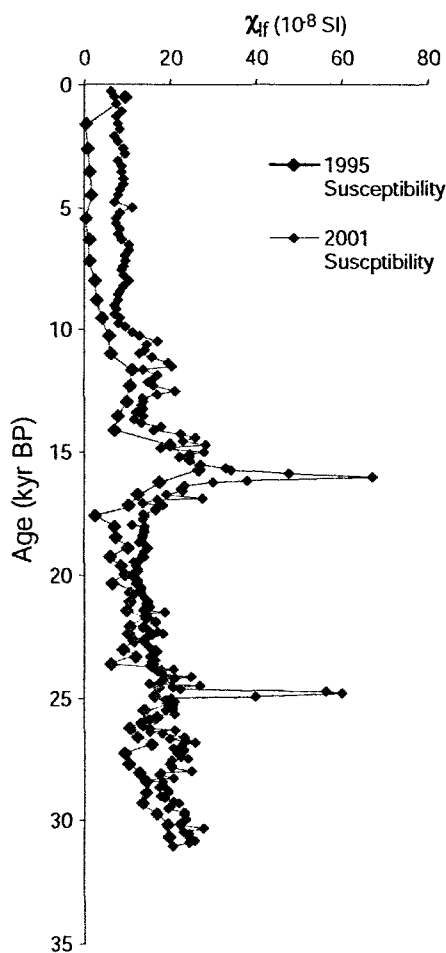


Fig. 5.13: Loss of susceptibility over time for OMEX 2K, used as an indicator for the presence of the mineral greigite.

In this study, the most appropriate parameters to assess the contribution of magnetotactic bacteria are χ_{arm}/χ , $\chi_{\text{arm}}/\chi_{\text{fd}}$ and ARM/SIRM, as they are measured in the routine magnetic analysis performed. Oldfield, (1992) suggests that values of $\chi_{\text{arm}}/\chi > 40$ and $\chi_{\text{arm}}/\chi_{\text{fd}} > 1$ are representative of bacterial magnetite. ARM/SIRM ratios between 0.15-0.25 are also suggestive of MTB (Moskowitz *et al.*, 1986).

Figs. 5.11 & 5.12 show the graphs of χ_{arm}/χ v. $\chi_{\text{arm}}/\chi_{\text{fd}}$ and ARM/SIRM v. depth for OMEX 2K. Fig 5.11 clearly shows the OMEX 2K samples falling well below the range of $\chi_{\text{arm}}/\chi_{\text{fd}}$ that Oldfield, (1992) suggested for magnetotactic bacteria. Fig. 5.12 agrees with this, showing ARM/SIRM ratios that never reach above 0.1 kAm⁻¹. Given this spatial distribution, it can be inferred that organic magnetic minerals contribute minimally to the sediments in OMEX 2K.

Greigite

For similar reasons as above, it is important to assess the contribution of greigite to the magnetic signature of the sediments in OMEX 2K. As discussed in Section 4.4, the magnetic ratios of SIRM/ χ , ARM₄₀/ARM and S (S=IRM₁₀₀/SIRM); the saturation properties; and any loss of magnetisation during storage can be used to indicate the influence of greigite on the magnetic signature of the sediments. In all cases, SIRM = IRM₁₀₀₀. The S-ratio here (S=IRM₁₀₀/SIRM) is taken from Snowball (1991) and is different to a ratio used by Bloemendal *et al.*, (1992)(S=[(-IRM₃₀₀/SIRM)+1]/2) which is also called S and will be discussed later in the chapter. Hence, the denotations S_(Bloemendal) and S_(Snowball) will be used to differentiate between the two.

Any loss of magnetisation can be identified by comparing the volume magnetic susceptibility of the core taken onboard ship in 1995, with the volume susceptibility measured during this study in 2001 (Fig. 5.13). Fig. 5.13 shows that there has been no reduction in susceptibility, rather that there appears to have been an increase (approx 3% increase on average). This is suggested to be due to increased sensitivity of the measurements taken in 2001, and a more stable environment, or simply a difference in equipment.

During the routine magnetic analysis of the OMEX 2K core, IRM acquisition was measured to a maximum field of 3000 mT. Acquisition curves of up to 300 mT are shown in Fig. 5.14. If greigite has a significant influence upon these materials, it would be expected that they would reach saturation prior to 300mT (Kris *et al.*, 1990; Hallam & Maher, 1994). This is clearly not the case, suggesting minimal presence of greigite.

The ratios of SIRM/χ , $\text{ARM}_{-40}/\text{ARM}$ and $S_{(\text{Snowball})}$ are indicative of greigite. SIRM/χ ratios of 70 kAm^{-1} and above, combined with $S_{(\text{Snowball})}$ values of -0.8 ; or $\text{ARM}_{-40}/\text{ARM}$ values between 0.45 - 0.85 , for example. However, $\text{ARM}_{-40}/\text{ARM}$ values of 0.3 are also suggestive of greigite when coupled with SIRM/χ values of $>70 \text{ kAm}^{-1}$. The results of these ratios must be looked at in tandem, as singly they can be confused with other minerals. For example, magnetite has $S_{(\text{Snowball})}$ values of between -0.9 to -0.4 , however it has much lower $\text{ARM}_{-40}/\text{ARM}$ values than greigite (Snowball, 1991). Fig. 5.15 shows downcore plots of these ratios. The SIRM/χ record for OMEX 2K appears to vary around approximately 35 kAm^{-1} , with this decreasing to c. 20 kAm^{-1} between the two Heinrich Events and then increasing back to 35 kAm^{-1} . The highest value is 42.42 kAm^{-1} . For the majority of the $\text{ARM}_{-40}/\text{ARM}$ record, values fall around the lower limit of greigite (0.45), with slight increases at the Heinrich Events (0.67 and 0.64) and 121 cm (0.99). These plots also suggest a limited influence of greigite, with few samples falling within the necessary ranges. This can be analysed further using the biplots discussed below.

Previous workers (particularly Peters & Thompson, 1998) have used biplots to identify greigite, specifically those of $\text{ARM}_{-40}/\text{ARM}$ versus SIRM/χ and $\text{ARM}_{-40}/\text{ARM}$ versus $S_{(\text{Snowball})}$. Again, in these studies, $\text{SIRM} = \text{IRM}_{1000}$. Peters & Thompson, (1998) collated their mineralogical data onto biplots, in order to provide a single method with which to distinguish between various magnetic minerals. These biplots have been reproduced for this study, with the original ones from Peters & Thompson, (1998) overlain for comparison (Figs. 5.16a & b). Fig. 5.16a shows the graph of $\text{ARM}_{-40}/\text{ARM}$ v. SIRM/χ , the results for OMEX 2K plot within the

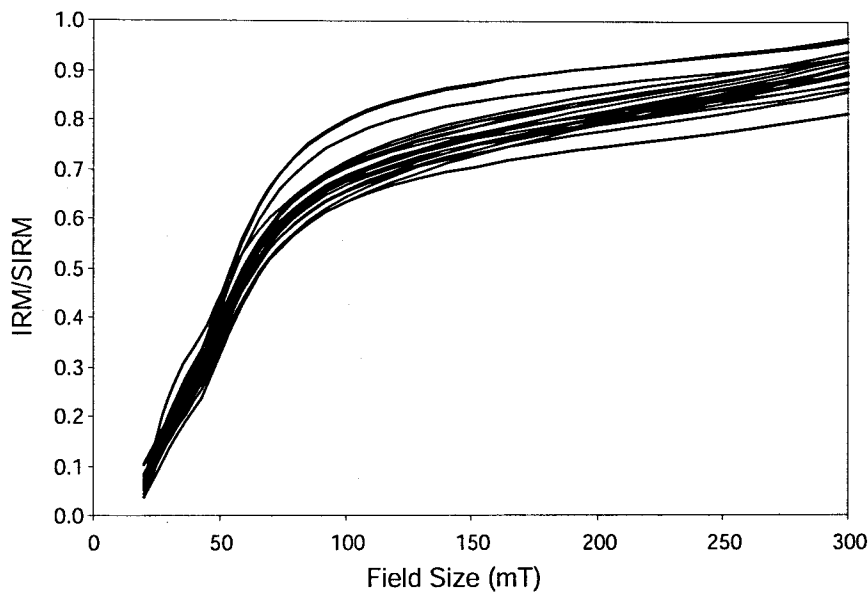


Fig. 5.14: IRM acquisition for OMEX 2K, to a maximum of 300 mT. Saturation is not quite reached by 300 mT, suggesting limited influence of greigite on the sediments.

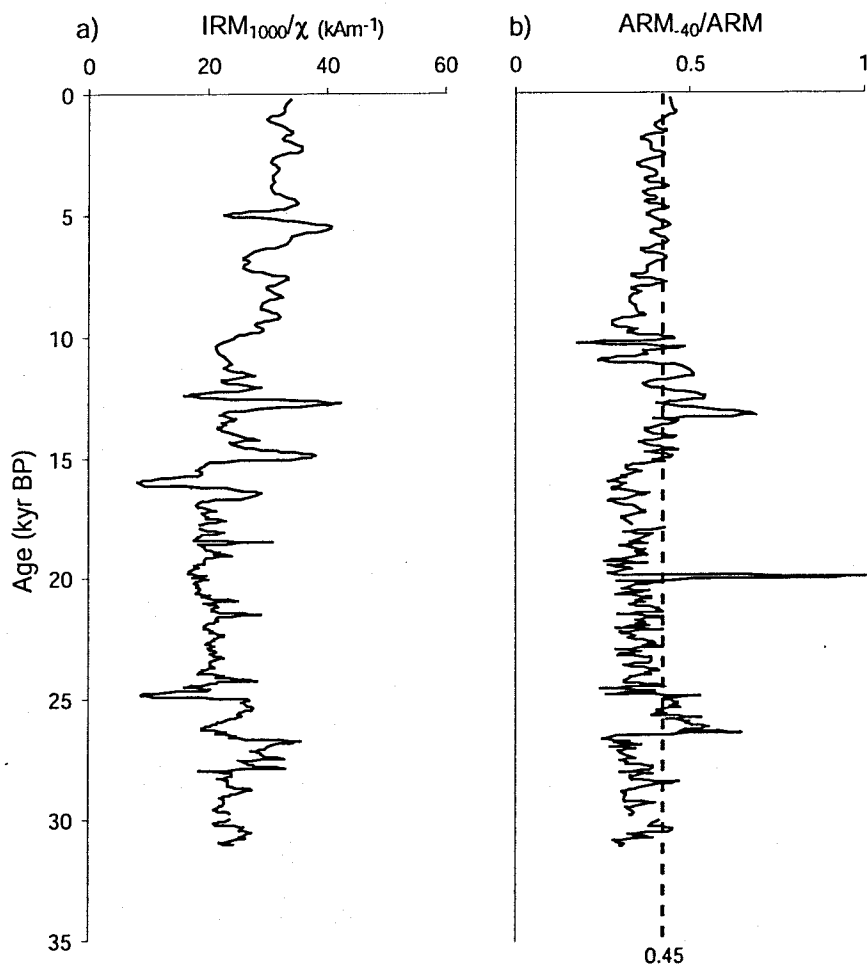


Fig. 5.15: a) Down-core plot of SIRM/χ . Values above 70 kAm^{-1} are indicative of greigite; b) Down-core plot of $\text{ARM}_{40}/\text{ARM}$. Values between 0.45-0.85 are suggestive of greigite.

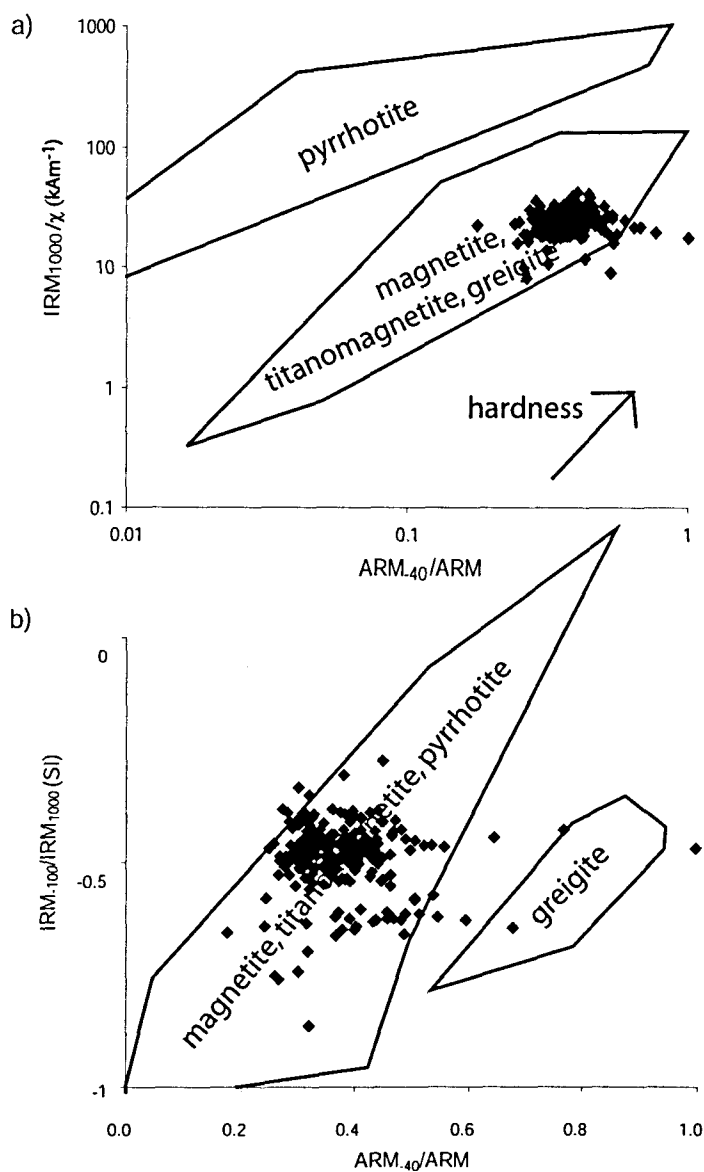


Fig. 5.16: a) Plot of ARM_{40}/ARM versus IRM_{100}/χ , used by Peters & Thompson (1998) for the differentiation of magnetic minerals; b) Plot of ARM_{40}/ARM versus IRM_{100}/IRM_{1000} also used by Peters & Thompson (1998) for the identification of greigite.

Table 5.4: Group sections for biplots.

Group name	Depth	Age (years BP)
Holocene	0-50 cm	271-1099
Younger Dryas	54-63 cm	1167-1310
H1	73-91 cm	1483-1685
Pre H1	95-140 cm	1731-2160
Post H2	143-170 cm	2184-2397
H2	175-184 cm	2437-2508
Precursor	188-197 cm	2541-2616
Pre H2	200-245 cm	2642-3107

ranges for magnetite, titanomagnetite and greigite, as interpreted by Peters and Thompson, (1998). Fig. 5.16b, however, shows ARM-40/ARM v. $S_{(Snowball)}$, which is a useful plot that can distinguish greigite from the other main magnetic minerals in a sediment, unlike Fig. 5.16a. Here, it places three samples within the greigite range. As these are individual samples (from 64cm depth, 121cm depth and 122cm depth), and because the majority of OMEX 2K values fall clumped within the magnetite range, it can be said that greigite does not significantly influence the magnetic characteristics of the sediments in OMEX 2K and will not obscure the climatic signal (C. Peters, Pers. Comm. 2004).

Using the analysis shown here, it is possible to suggest that there is little greigite in the OMEX samples, and certainly not enough to influence the environmental interpretation of the magnetic data.

Biplots

In order to examine the temporal changes in sediment properties in greater detail, the data was split into sections, according to age. Table 5.4 details these groups, and their corresponding depths and ages. These groups were used to draw biplots for the magnetic data showing the different characteristics within the sections. The biplots (Fig. 5.17 and Appendix 1a) quite clearly demonstrate the differences of the magnetic characteristics between, and within the sections (for example, H2), that cannot be seen as clearly in the down-core records. Kruskal-Wallis tests (Section 4.5) were also performed on each of the temporal groups in Table 5.4 for each of the magnetic parameters to test if there is any statistically significant difference between the magnetic characteristics of the separate groups. For each of the parameters discussed in Section 5.2.1, the Kruskal-Wallis tests returned a P-value of 0.000, which means that the null hypothesis of no significant difference must be rejected. Therefore, statistically speaking, there are differences in the magnetic characteristics between the temporal groups shown in Table 5.4. The Kruskal-Wallis tests can be found in Appendix 2biii (Pg 342-343).

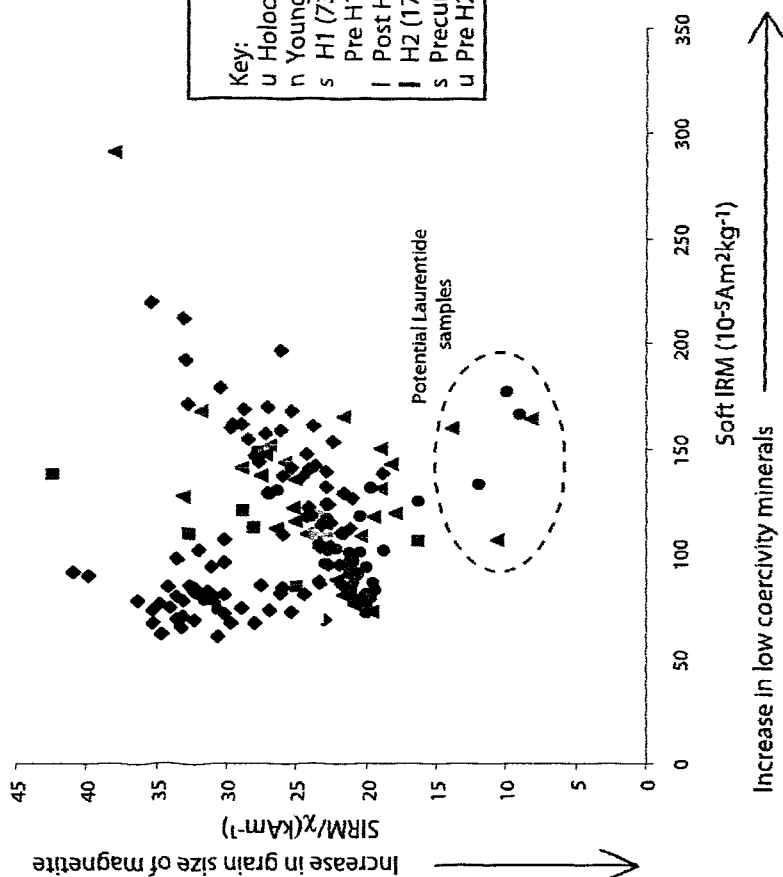
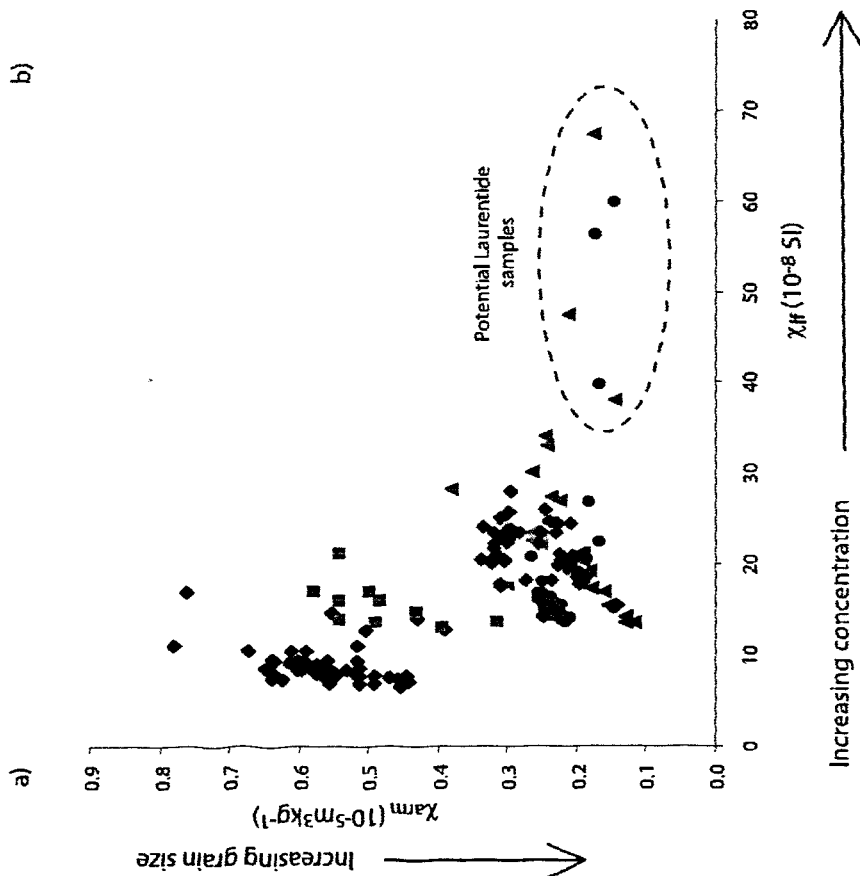
Fig. 5.17a shows the biplot of χ_{lf} v. χ_{arm} . It is evident that the HLs have low χ_{arm}

and high χ_{if} , suggesting a larger magnetic grain size and concentration than the ambient glacial sediments and *vice-versa*. Six HL samples have a very high concentration of magnetic minerals compared to the other HL samples, three come from H1 and the other three from H2, indicating a variation in magnetic signature within the HLs, possibly suggesting provenance variations. “Precursor” samples have signatures which vary between the Pre H2 and HE sample groups, suggesting a provenance similar to the ambient sediments and part of the HLs. In the case of OMEX 2K, the ambient sediments will be dominated with European material, hinting that this may also be the case for the precursor event, and hence, the samples from within the HLs that display magnetic signatures similar to the precursor may also be European in origin. The Holocene displays the lowest χ_{if} and the highest χ_{arm} values, with the ambient glacial sediment showing low values of both parameters.

Soft IRM v. SIRM/ χ (Fig. 5.17b) also reveals a set of HL samples with different characteristics to both the ambient glacial sediments, and the other samples within the HLs. These six samples have much lower SIRM/ χ values (larger grains of magnetite) and are the same six samples as identified in Fig. 5.17a. Precursor samples are characteristically similar to the remainder of the HL samples, and the Pre H2 samples as before. The rest of the samples have similar SIRM/ χ ratios, with the exception of the Holocene, and are only really distinguishable by their Soft IRM ratios. A single sample from H1 (from the end of H1 at a depth of 76 cm) has a very distinct signature on this plot, with an exceptionally high Soft IRM value and a relatively high SIRM/ χ ratio. This corresponds to the secondary dolomite peak found in Fig. 5.5 just above the main H1 peak.

Fig. 5.17c shows the graph of χ_{if} v. IRM₁₀₀/SIRM (100 backfield ratio), six HL samples are again obviously different, with significantly lower IRM₁₀₀/SIRM values (low coercivity behaviour) and higher χ_{if} (higher concentration) than the rest of the HLs. They are the same six samples as mentioned above. An additional sample is also identifiable by this plot with its very low IRM₁₀₀/SIRM ratio from within the Pre H1 samples (108cm depth). When compared with the IRD data discussed at

b)



Key:

- u Holocene (0-50cm)
- n Younger Dryas (54-63cm)
- s H1 (73-91cm)
- l Pre H1 (95-140cm)
- l Post H2 (143-170cm)
- l H2 (175-184cm)
- s Precursor (188-197cm)
- u Pre H2 (200-245cm)

Fig. 5.17: Biplots for some of the magnetic parameters measured on OMEX 2K. a) χ_{H} versus χ_{am} , b) Soft IRM versus SIRM/χ , c) χ_{H} versus $\text{IRM}_{-100}/\text{SIRM}$, d) χ_{am}/χ versus Hard IRM.

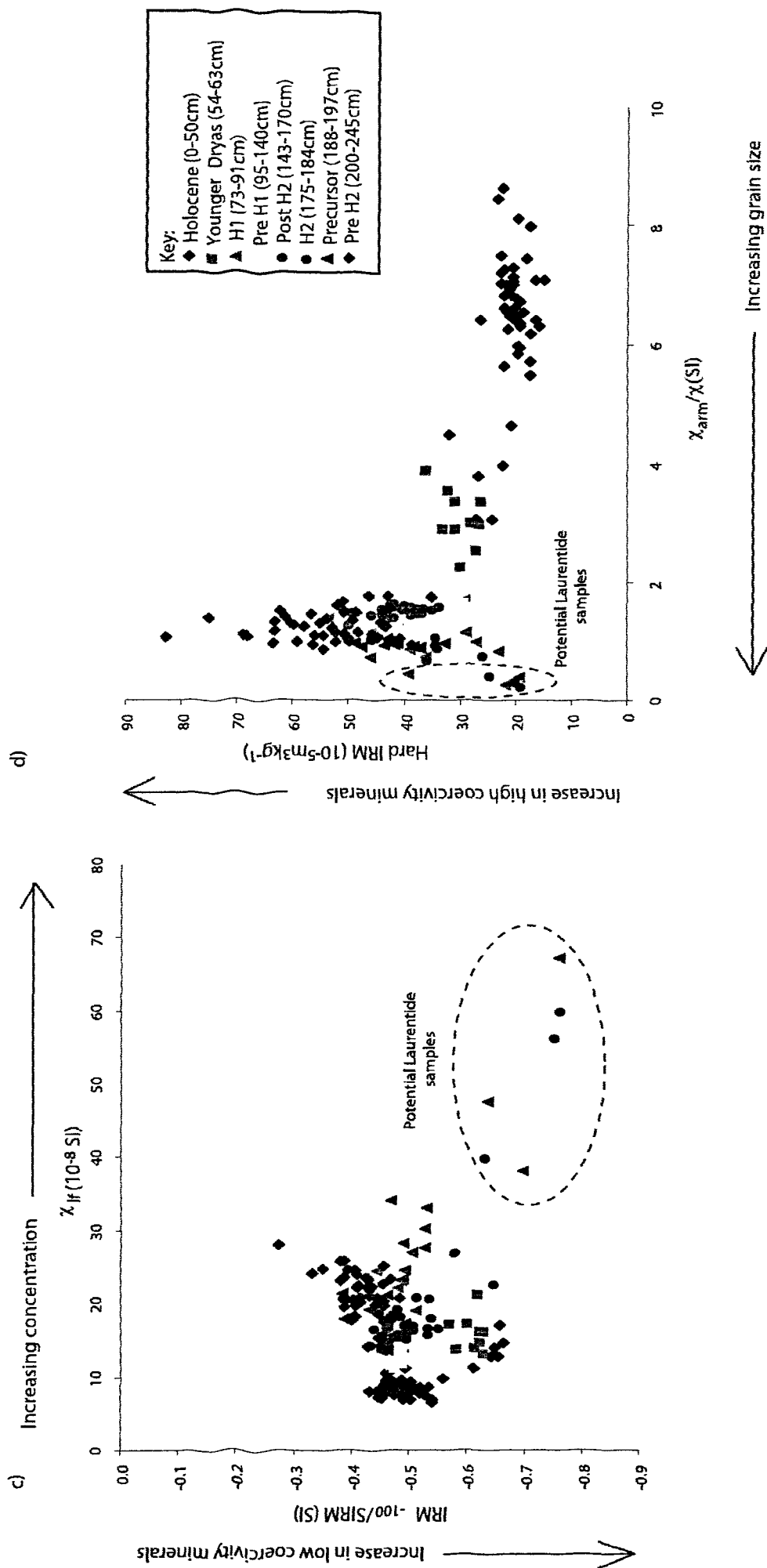


Fig. 5.17: Biplots for some of the magnetic parameters measured on OMEX 2K. c) χ_{lf} versus IRM₋₁₀₀/SIRM, d) χ_{arm}/χ versus Hard IRM.

the beginning of this section, this samples appears to contain large quantities of quartz, basaltic tephra and mica (muscovite). The rest of the groups are bunched together relative to the HL samples, however, there is still distinct clustering apparent.

The plot of χ_{arm}/χ v. Hard IRM (Fig. 5.17d) reveals a group of nine samples which have very low χ_{arm}/χ values (larger grain size) and low Hard IRM values (lower coercivity behaviour) which are comparable to the Holocene values. Five of these nine samples have been previously identified, whilst the others are one additional H2 sample and three H1 samples. The sixth sample noted in the previous plots is identifiable by it's low χ_{arm}/χ value, but has a significantly higher Hard IRM value than the other nine; similar to the other HL samples. The Holocene and YD also have low Hard IRM, though have progressively higher χ_{arm}/χ ratios, suggesting increasing grain size. The other ambient sediments, plus the precursor and Pre H2 samples have higher Hard IRM and relatively low χ_{arm}/χ values, i.e. a higher coercivity mineralogy and larger magnetic grain size.

Summary

The biplots display some of the very obvious differences between the magnetic characteristics of the groups, which were hinted at in the depth profiles, such as the HLs having a higher magnetic concentration and grain size, and being magnetically softer. They also show differences in characteristics within the groups as well. Six samples from H1 and H2 have particularly high concentrations and larger magnetic grain sizes; they also appear to have a lower coercivity signature and higher magnetite content. All this suggests that there is variation in magnetic signature within the HLs themselves, as well as between the temporal sections of the core. It is possible that these variations are associated with provenance. The precursor samples have a similar signature to the remaining HL samples and the Pre H2 samples, indicating a provenance similar to these. In the case of the OMEX 2K core, its location dictates that the ambient sediments (Pre H2, Post H2 and Pre H1) will be dominated by European material. This suggests that Europe is also the source for the precursor samples. The samples from the

HLs with similar characteristics to the precursor material may also, therefore, be European in origin.

From this reasoning, it is possible to suggest that the HL samples with signatures differing from the precursor material are Laurentide in origin.

Comparison to published data

In 1992, Bloemendal *et al.*, published results from a study of the magnetic characteristics of various marine sediments. They included material from the North Atlantic, Labrador Sea and Arctic Ocean, as well as the W North Pacific, Central Pacific and the Sierra Leone Rise. These existing data for marine sediments are being used here as a comparison for OMEX 2K to aid the interpretation in terms of more specific sediment type and provenance.

Bloemendal *et al.*, (1992) suggested that plots of κ versus κ_{arm} and κ_{arm}/κ versus S_{-300} were diagnostic of sediment types and provenance/transport pathways (S_{-300} is different to the S-ratio used earlier in the identification of greigite, and is referred to in this thesis as $S_{(Bloemendal)}$). Sediments that plotted in the top right corner of κ v. κ_{arm} (e.g. Fig. 5.18a; $\kappa > 100$, $\kappa_{arm} > 1000$; κ and κ_{arm} = SI units) are characteristic of glacio-marine sediments and material transported by bottom currents and wind. Sediments that plot in the mid ranges (e.g. Fig. 5.18b; $\kappa = 10$ -1000, $\kappa_{arm} = 100$ -10000 SI units) are generally foraminiferal oozes with wind-blown silts and clays occurring during glacials. Finally sediments that sit in the bottom left section (e.g. Fig. 5.18c; $\kappa < 200$, $\kappa_{arm} < 1000$ SI units) are characteristic of carbonate rich sediments. A wide distribution of samples in this area is suggestive of an intermittent flux (or transport) of terrigenous magnetic material, with lowest values occurring when the flux is weak. A narrow cluster of samples indicates a continuous deposition of carbonates, or the effect of reduction diagenesis on magnetic minerals.

The graph of κ_{arm}/κ v. $S_{(Bloemendal)}$, where $S = [(-IRM_{-300}/SIRM)+1]/2$ is indicative of provenance in terms of the number of sources/transport pathways (Bloemendal

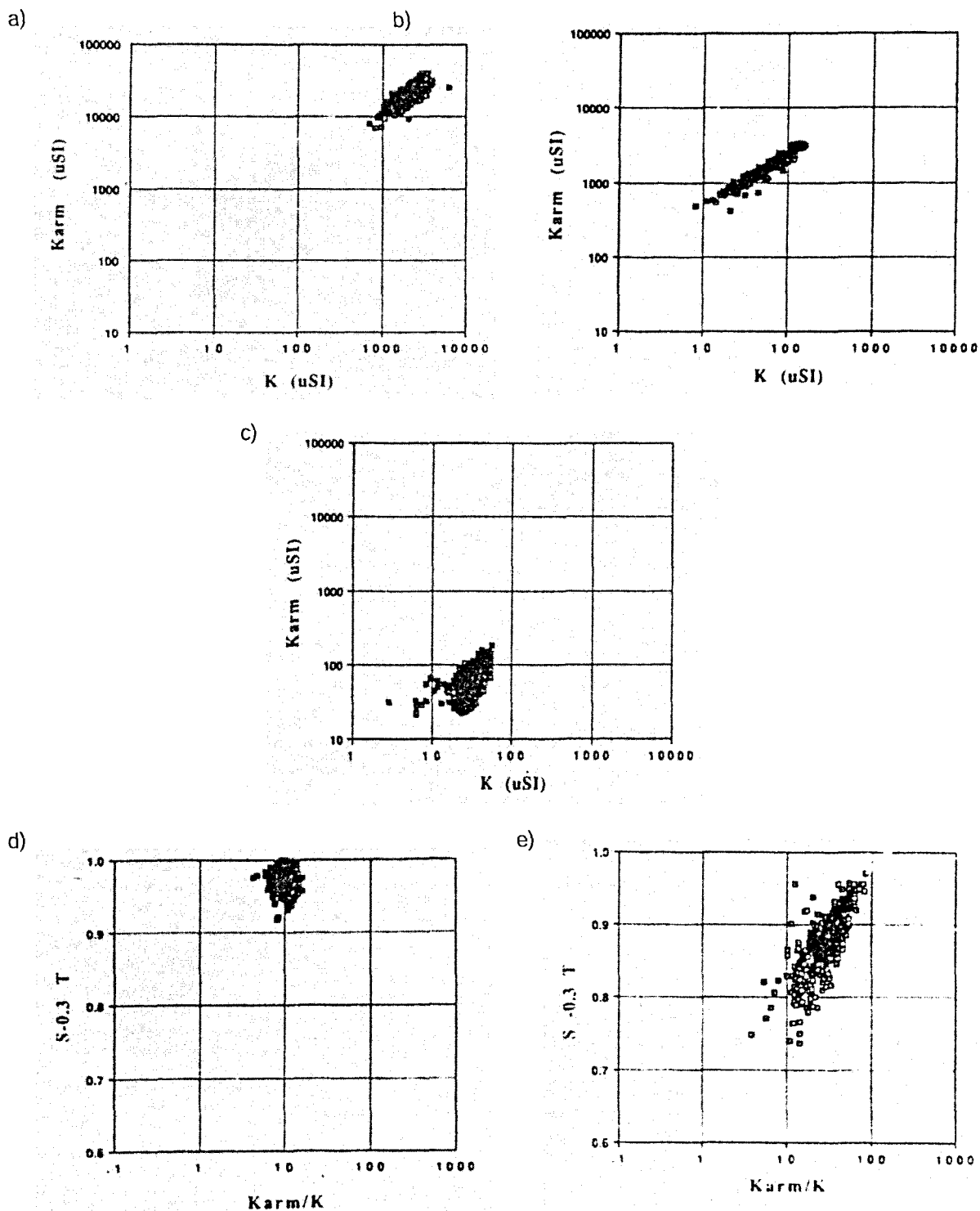


Fig. 5.18: a)-c) Plots taken from Bloemendal et al., (1992) showing the κ versus κ_{arm} values for a range of marine sediments. a) shows sediments falling in the top right corners, and are examples of glacio-marine sediments and material blown by wind or transported by bottom currents ($\kappa > 100$; $\kappa_{arm} > 1000$). b) shows samples falling in the mid-ranges, which are representative of foraminiferal oozes with wind blown silts and clays occurring during glacial periods ($\kappa = 10$ -1000; $\kappa_{arm} = 100$ -10000). c) shows sediments in the bottom left corner, and is characteristic of carbonate rich sediments ($\kappa < 200$; $\kappa_{arm} < 1000$). d) & e) κ_{arm}/κ versus S values for a range of marine sediments. d) shows a tightly grouped distribution which is linked to only one source or transport pathway. e) shows a broadly spread distribution, which is interpreted as several sources or transport pathways.

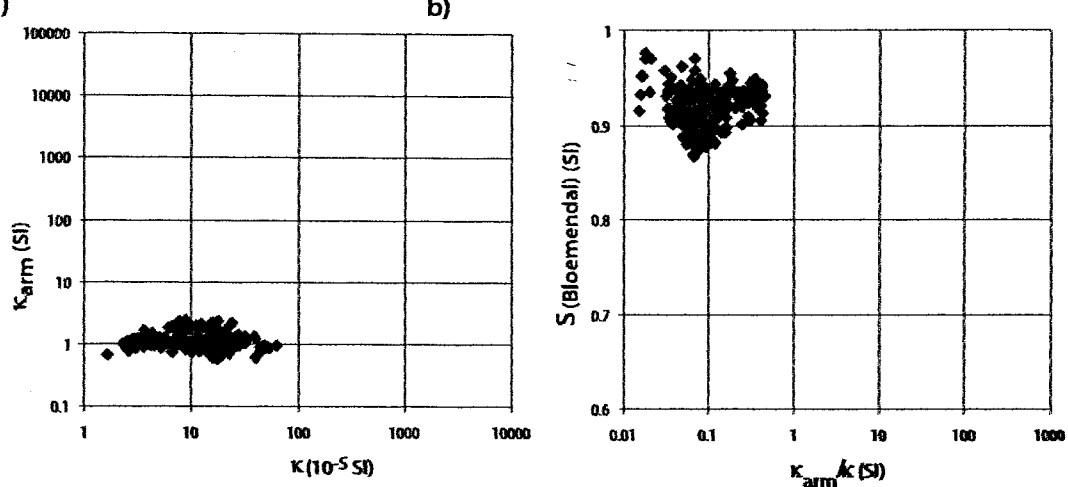


Fig. 5.19: Whole-core plots of: a) κ versus κ_{arm} and b) κ_{arm}/κ versus $S_{(Bloemendal)}$ for OMEX 2K. In comparison to the discussion in Bloemendal *et al.*, 1992 and the diagrams taken from that paper (Fig. 5.18), these data are suggestive of a relatively intermittent flux of carbonate-rich sediments from more than one source, or by more than one transport mechanism.

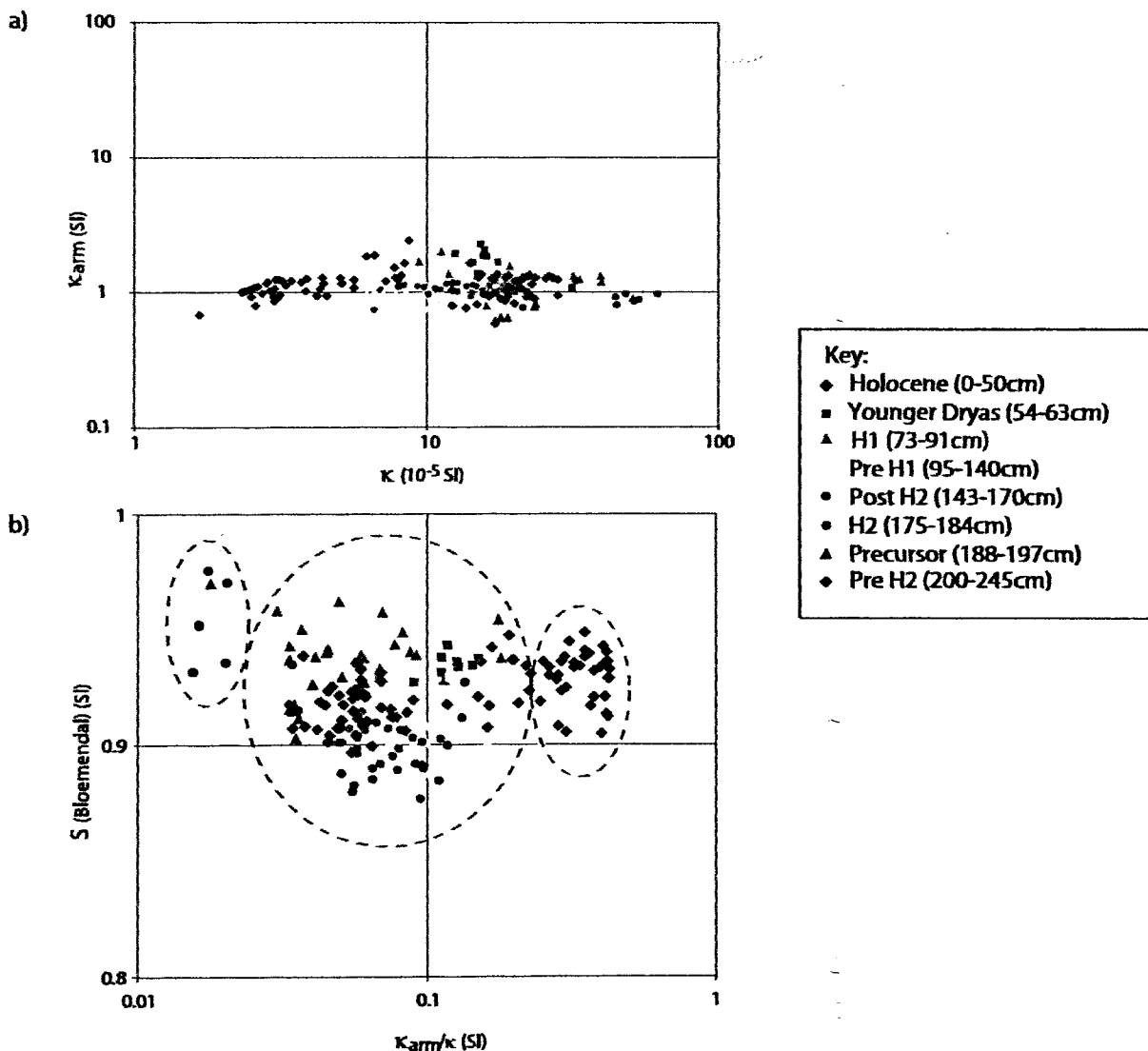


Fig. 5.20: Enlargements of the plots in Fig. 5.19: a) κ versus κ_{arm} and b) κ_{arm}/κ versus $S_{(Bloemendal)}$ for the temporal groups within OMEX 2K. These plots show that there is variation in the sources and transport pathways both between and within the different groups. The dashed lines show the clustering discussed in the text.

et al., 1992). A tightly grouped distribution (e.g. Fig. 5.18d) is suggestive of one source/pathway, whereas a broadly spread group (e.g. Fig. 5.18e) is representative of two or more sources/pathways. The placing of the values along the κ_{arm}/κ axis can also be diagnostic of origin: $\kappa_{arm}/\kappa > 10$ is detritus or aeolian material, $\kappa_{arm}/\kappa < 10$ is glacio-marine material.

Fig. 5.19a shows the biplot of κ v. κ_{arm} for OMEX 2K. The data is grouped along the $\kappa_{arm} = 1$ gridline, with κ values of between 1-100. Using the interpretation of Bloemendal *et al.*, (1992), it can be inferred that the material within OMEX 2K is dominated by carbonate rich sediments. While the data fall into one group, they are widely distributed and does show clustering of the various core sections. After comparison with Fig. 5.18, taken from the Bloemendal *et al.*, (1992) paper, which shows the distributions of two sites constituting carbonate rich sediments, it can be suggested that there appears to be intermittent transportation of carbonate rich sediments to the site of OMEX 2K. It may be possible to ascertain the times that the transport of sediments broke down by looking at graphs of κ_{arm} v κ for the separate temporal groups. While not directly related to provenance or transport, the fact that there is known to be different climatic states, effecting ice cover, oceanic circulation and transport mechanisms between the Holocene and pre YD times could be reflected in these graphs. Volume susceptibility measurements are not corrected for carbonate content, which could be the reason behind the carbonate rich nature of the OMEX 2K sediments in this interpretation. All other magnetic data has been corrected for carbonate content (see Section 4.4.1), and therefore the characteristics discussed in previous sections should not be due to carbonate variations, as suggested by the volume measurements.

Fig. 5.20a shows the biplot of κ v. κ_{arm} for the temporal groups for OMEX 2K. As expected, all the sections fall into the carbonate rich area, however the distributions of the samples within the groups vary quite significantly. The Holocene, H1 and H2 appear to have quite widely distributed samples, while the others (YD, Pre H1, Post H2, the Precursor and Pre H2) have quite tightly grouped

samples. On comparison with the whole-core plot, it is evident that the long “tail” of samples to the left hand side is composed almost entirely of Holocene samples. This suggests that the flux of material to OMEX 2K varied significantly throughout the Holocene, and was also at its lowest. Looking back at the original magnetic data, these lowest points fall towards the top of the core, implying that the flux of sediment has got weaker as the Holocene has progressed. As mentioned previously, H1 and H2 also have relatively widely distributed samples, suggesting that the flux of sediment during these times was also interrupted.

Fig 5.19b shows the plot of κ_{arm}/κ v. $S_{(Bloemendal)}$ for OMEX 2K. A variety of sources and transport pathways is expected for OMEX 2K, due to the known variations in climate during its time-span, and this is evident from the broadly distributed samples shown on Fig 5.19b. The results actually appear to form three clusters with varying κ_{arm}/κ values, which would imply three possible source areas or transport mechanisms. To examine the sources and pathways within these results, and on smaller time-scales, Fig. 5.19b has been re-drawn showing the data for the different temporal groups (Fig. 5.20b). Using the interpretation of the graphs provided by Bloemendal *et al.*, (1992), and comparing with the graphs from that paper (Figs. 5.18a & b), it is apparent that the distribution of samples varies within some of the temporal groups as well as between them. The YD and the Precursor appear to have very tightly clustered samples, suggesting one source, whereas the Holocene, H1 and H2 have relatively broadly distributed results, suggesting two or more. The ambient glacial sediments (Pre H1, Post H2 and Pre H2) are not as tightly clustered as the YD but also do not appear to have distinctly separate groups as does the Holocene. The ambient sediments cover a larger time span than either the YD or the Precursor, which could account for these differences. One source for the material however is still implied for the ambient sediments. When looking back at the whole-core plot (Fig 5.19b), the three separate clusters appear related to different temporal groups. The largest group with the highest κ_{arm}/κ values is made up of Holocene samples, a second group, with the lowest κ_{arm}/κ values is caused by five H2 samples and one H1 sample, while a third, and largest group, contains samples from all of the temporal

groups, including the Holocene, H1 and H2. From these patterns it is suggested that a single source could account for the ambient glacial sediment, which also contributes to part of the HEs and the Holocene; a second source involved in other parts of the HEs; with a third source, which becoming available during the Holocene. Bearing in mind that the Bloemendal *et al.*, (1992) interpretation of these plots argues that they are also influenced by transport mechanisms, the sources referred to here could in fact be methods of sediment delivery rather than actual source areas, or a combination of both.

Overview of Magnetic Results

The magnetic results discussed above reveal relatively detailed information regarding the minerals present in OMEX 2K and how their signature changes over time. Overall, there seems to be a dominant low coercivity signal, specifically magnetite, throughout the core, with no influential presence of magnetotactic bacteria or greigite.

Starting at the base of the core, the Pre H2 section (see Table 5.4) shows a slight increase in magnetic concentration, grain size and both types of magnetic minerals (high and low coercivity). It is dominated by a relatively consistent input of carbonate rich material from one source or transport mechanism. The precursor event has a similar signature to the Pre H2 samples in terms of its sediment type and provenance. Its magnetic characteristics show a lower overall concentration of minerals than Pre H2, but an increase in coarse-grained ferrimagnets. The Heinrich Events display a dramatic increase in multi-domain low coercivity magnetic minerals. Three samples from each HE contain significantly coarser magnetic minerals and are higher in magnetic concentration than the rest of the HE material. This is apparent on the Bloemendal Plots as an intermittent flux of carbonate rich sediments from more than one source area/delivery method. Some of the other HL samples appear to have a signal more closely related to the precursor, this is particularly evident from the biplots in Fig. 5.17.

The ambient glacial sediments (Pre H1 and Post H2) are comprised of low magnetic mineral concentration and fine grains, with the exception of sample 139

(higher concentration of coarse-grained ferrimagnetic minerals and an obvious decline in haematite). Following Bloemendal *et al.*, (1992), it is inferred that they have a carbonate rich sediment type which appears to have an intermittent flux of material, i.e. the transport of these carbonate rich sediments was not constant, though not as disrupted as during the HEs. They also appear to have the same provenance signature as the Pre H2 and precursor samples.

The Younger Dryas shows a drop in magnetic concentration, accompanying an increase in the relative abundance of magnetite, and a decrease in mineral size. These sediments display a tightly grouped distribution of carbonate rich material, with a similar provenance to the ambient, pre H2 and precursor sediments.

Finally, the Holocene possess a different signal altogether. There is a steady magnetic concentration decrease and a reduction in grain size to the lowest seen in the whole core. The sediment type is an intermittent carbonate rich material, with a different provenance to any of the other groups. It is suggested that, due to the changing climate over the Holocene, this alteration in magnetic signature is a reflection in transport mechanism, rather than sediment source. For example, the effect could be modelled as a shift from ice rafting and wind transport to increased distribution by turbidities and bottom currents. Sediment source is likely to be similar to the ambient sediments, and European in origin. The different provenance signature seen within the HEs, however, is probably more to do with source area than delivery method, as the sediment was deposited over a short time period, with both signals showing simultaneously.

5.3 Environmental Interpretation of OMEX 2K

The main aims behind this study (Section 1.3) are to assess the ability of environmental magnetic methods to identify the North Atlantic Heinrich Events, characterise them, and, ultimately, determine the sources of the IRD contained within them. The discussion in Section 5.2 reveals unique magnetic properties occurring within the HLs of OMEX 2K, effectively answering the first two issues

above. The final question, namely whether environmental magnetism can determine HE IRD provenance will be addressed here. Firstly, the non-magnetic data available for HEs in OMEX 2K, described during previous chapters (Section 3.2, 4.1, & 5.2) is summarised, followed by a comparison with the magnetic data from Section 5.2.1. This section concludes with an evaluation of the technique along with its ability to meet the aims set out in Section 1.3.

5.3.1 The Heinrich Events

Non-magnetic data

The bulk of the non-magnetic data consists of the extensive petrological and mineralogical analysis undertaken at the University of Wales, Bangor reported by Scourse *et al.*, (2000) and Furze (unpublished)(Figs. 5.4 & 5.5). These data create a very detailed picture of the types of material brought to the Celtic Margin throughout the last 30 kyr and are described fully in Section 5.2.

Throughout the Heinrich Events represented in this core, sequencing of both provenance signals (LIS and EIS) can be seen, for example, during the onset to H2 (25.16 – 25.00 kyr BP) when there was an increase in IRD input, the signal was dominated by European material. At 24.92 kyr BP, this signal became obscured by an abundance of Laurentide sediment (primarily Dolomite), however, this only lasted for ~240 years, at which point (24.68 kyr BP) European material reappears and dominates until the IRD concentration decreases and the HE ends (c. 24.37 kyr BP). A similar pattern is seen for H1, with European material being prevalent during the onset of the HE (16.61 – 16.25 kyr BP), and replaced or diluted by Laurentide material at 16.13 kyr BP before returning for the final stage of the HE at 15.75 kyr BP. The Laurentide input during H1 lasted approximately 380 years. It must be acknowledged here that a constant sedimentation rate has been assumed to exist throughout the HEs in order to give specific ages to the various events. In reality, this is unlikely to be the case, and errors will be present within the stated ages.

Fig. 5.21 shows the varying concentrations of the main minerals within the 18

samples selected for XRD analysis on a percentage abundance scale. They are not absolute values. During the Holocene, there is a dominance of calcite, with under 20% of the material consisting of other minerals. At 54 cm depth, the position of the Vedde Ash (Scourse *et al.*, 2000), there is an increase in both the total clay content and quartz. At the peaks of both HEs, there is a drop in clay content and an increase in plagioclase and dolomite. H1 also shows an increase in calcite in the lower sample (82 cm), which is replaced by K-feldspar in the second (83 cm) sample. H2, however, displays a massive increase in quartz in the peak (181 cm) sample with all other minerals remaining low. The second H2 sample (180 cm) shows quartz returning to ambient levels and plagioclase and dolomite peaking. The quartz and sodium chloride content stays approximately constant throughout the core. The minerals of the ambient glacial samples (92 cm – 168 cm), are dominated by clay. The remaining minerals are approximately the same as at the end of H2. Pre H2, the XRD data suggests that the mineral concentration was returning to ambient glacial levels, with high clay content.

OMEX 2K has an average sedimentation rate of 0.18mka^{-1} . There appears to be a lower sedimentation rate during the Holocene than during the Pleistocene, however problems arise at around 21 ka where there is a negative calculated sedimentation rate (Fig. 5.3). This can be explained by problems with the dating of OMEX 2K, as there is an apparent age reversal at 24 ka (Fig. 5.2). The age model itself is not affected by this issue as it utilises the error ranges of the dates, which in the case of the two dates involved in the reversal, overlap. The variations in sedimentation rate represent changes in the transport of material reaching the core site and generally, there appears to be greater sediment supply during colder climates. When there is a higher rate, transport mechanisms such as ice rafting and cross shelf currents are represented as they are able to move larger quantities of material out beyond the continental shelf. Lower rates suggest mechanisms such as ocean bottom currents, which are less efficient at delivering sediment to the core site, or which may act to prevent the deposition of fine grained material (Hall & McCave, 2000). Overall, this is supported by the sedimentation rates within OMEX 2K.

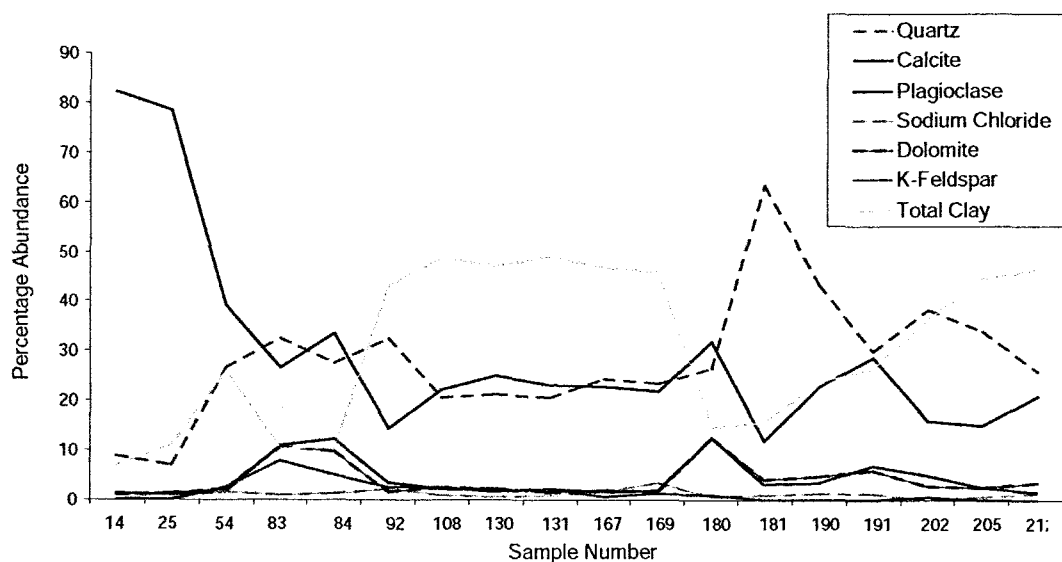


Fig 5.21: XRD mineral abundances for the 18 selected samples from OMEX 2K.

Table 5.5: The magnetic and non-magnetic characteristics of the HEs, and their potential source areas.

HL Sample (by depth)	Age (kyr BP)	Magnetic Characteristics	Non -magnetic Characteristics	Potential Provenance
H1 - 77 cm	15.10	Low concentration (χ_{lf}), low grain size (χ_{arm} , ARM/ χ), harder magnetic mineralogy (IRM ₁₀₀ /SIRM).	Low point in IRD presence, end of H1 dolomite peak	European
- 78 cm	15.23	Low concentration (χ_{lf}), low grain size (χ_{arm} , ARM/ χ , SIRM χ), harder magnetic mineralogy (IRM ₁₀₀ /SIRM) with increase in softer minerals (Soft IRM).	As above	European
- 79 cm	15.36	Low concentration (χ_{lf}), increasing grain size (χ_{arm} , ARM/ χ), harder magnetic mineralogy (IRM ₁₀₀ /SIRM).	As above	European
- 80 cm	15.49	Low concentration (χ_{lf}), increasing grain size (all parameters) increasingly softer mineralogy (Hard IRM, IRM ₁₀₀ /SIRM).	High dolomite content	European
- 81cm	15.62	Increasing concentration (χ_{lf}), higher grain size (all parameters), increasingly softer mineralogy (all parameters).	High dolomite content	European
- 82 cm	15.75	Almost identical to sample 81 in all parameters	Peak in dolomite content	European
- 83 cm	15.88	High concentration (χ_{lf}), large grain size (all parameters), soft magnetic mineralogy (all parameters).	Peak in dolomite content. Decrease in calcite and clay content, increase in dolomite, K-feldspars and plagioclase	Laurentide
- 84 cm	16.00	Very high concentration (χ_{lf}), very large grain size (all parameters), soft magnetic mineralogy (all parameters).	Onset of dolomite peak, slight increase in mica (biotite) and quartz (biotite) concentraion. Drop in clay content, increase in dolomite and plagioclase	Laurentide
- 85 cm	16.13	High concentration (χ_{lf}), very large grain size (all parameters), soft magnetic mineralogy (all parameters).	Low in all mineralogies	Laurentide
- 86 cm	16.25	Decreasing concentration (χ_{lf}), lower grain size (all parameters), harder magnetic mineralogy (Hard IRM, IRM ₁₀₀ /SIRM).	Low in all mineralogies	European

Table 5.5 (cont)

HL (by depth)	Sample (depth)	Age (kyr BP)	Magnetic Characteristics	Non -magnetic Characteristics	Potential Provenance
	- 87 cm	16.37	Low concentration (χ_{lf}), falling grain size (all parameters), harder magnetic mineralogy (all parameters).	Increasing quartz content	European
	- 88 cm	16.49	Low concentration (χ_{lf}), low grain size (χ_{arm} , ARM/ χ), harder magnetic mineralogy (IRM ₁₀₀ / SIRM).	Increasing quartz content	European
	- 89 cm	16.61	Low concentration (χ_{lf}), low grain size (all parameters), harder magnetic mineralogy (all parameters).	Abundance in quartz lithologies	European
H2	- 175 cm	24.37	Low concentration (χ_{lf}), low grain size (SIRM/ χ , SIRM/ARM, SIRM/ χ_{arm}), hard magnetic mineralogy (Hard IRM).	End of large dolomite peak	European
	- 176 cm	24.45	Low concentration (χ_{lf}), low grain size (SIRM/ χ , SIRM/ARM, SIRM/ χ_{arm}), hard magnetic mineralogy (all parameters).	End of dolomite peak, onset of quartz dominated material	European
	- 177 cm	24.53	Low concentration (χ_{lf}), increasing grain size (SIRM/ARM, SIRM/ χ_{arm} parameters), harder magnetic mineralogy (Hard IRM).	Slight second peak in dolomite	European
	- 178 cm	24.60	Low concentration (χ_{lf}), increasing grain size (SIRM/ARM, SIRM/ χ_{arm}), increasingly softer magnetic mineralogy (all parameters).	Dolomite abundance	European
	- 179 cm	24.68	Low concentration (χ_{lf}), relatively large grain size (ARM/ SIRM), softer magnetic mineralogy (IRM ₁₀₀ /SIRM).	High dolomite presence	European
	- 180 cm	24.76	Very high concentration (χ_{lf}), large grain size (ARM/ SIRM), SIRM/ARM), soft magnetic mineralogy (all parameters).	Main dolomite peak, slight peak in chalk too. Slight increase in calcite, drop in clay content, increase in plagioclase and dolomite	Laurentide
	- 181 cm	24.84	Very high concentration (χ_{lf}), large grain size (ARM/ SIRM), SIRM/ARM), soft magnetic mineralogy (all parameters).	High dolomite concentration. Drop in dolomite, plagioclase and clay content, increase in quartz.	Laurentide
	- 182 cm	24.92	High concentration (χ_{lf}), large grain size (ARM/ χ , SIRM/ χ , SIRM/ARM), soft magnetic mineralogy (all parameters).	Onset of dolomite peak, end of mice (biotite), quartz and tephra peaks	Laurentide
	- 183 cm	25.00	Low concentration (χ_{lf}), low grain size (SIRM/ χ , SIRM/ARM, SIRM/ χ_{arm}), hard magnetic mineralogy (all parameters).	Onset of dolomite peak, end of mice (biotite), quartz and tephra peaks	European
	- 184 cm	25.08	Low concentration (χ_{lf}), low grain size (SIRM/ χ , SIRM/ARM, SIRM/ χ_{arm}), hard magnetic mineralogy (all parameters).	Large quantities of quartz and tephra, peaks in mice (biotite) and phylitic grains	European

Comparison of magnetic and non-magnetic data

This section compares the various compositional datasets from OMEX 2K, mainly concentrating on the sections containing the two HEs, but also referring to the other temporal groups of the core. As noted in section 5.2, there are distinctive magnetic properties found in the peak HE samples, which are a very high concentration of coarse-grained ferrimagnets, though there also appears to be a definite structure to the whole HE, from onset to finale. During the onset and end phase of the HEs, the magnetic characteristics build up to, and diminish from, these peak properties. During the first stage of the HEs, higher than ambient concentration of magnetic minerals, which appear slightly higher in coercivity than the peak samples, coincide with inputs of tephra, quartz, mica (biotite) and phylitic grains for H2, and a dominant quartz lithology for H1. The main HE peaks (81-84 cm and 180-181 cm), with very high concentrations of MD ferrimagnetic grains, correspond to large dolomite peaks in the IRD. H2 does see a slight increase in chalk at this point too, but all other signals are absent, or diluted by the abundance of dolomite. XRD data for the HE peaks indicate large increases in the percentage abundance of both dolomite and plagioclase minerals. They are exceeded by the amount of calcite and quartz in these samples, although the calcite record does fall at these points. H1 shows an increase in the relative abundance of K-feldspars, whilst H2 has an increase in quartz at the onset of the main peak (181 cm). Both HEs, however, display a drop in the total clay percentage of the sediments. As the magnetic characteristics of the HEs decline to ambient levels, so does the input of dolomite, which is replaced by a low IRD content dominated by various quartz lithologies. These data are summarised in Fig. 5.22.

Table 5.5 contains descriptions of the magnetic characteristics and non-magnetic properties for all of the Heinrich Layer samples, along with a proposal of their provenance based on the descriptions. Samples labelled as Laurentide are not likely to be “pure” Laurentide material. Mixing with other material (European, Icelandic, Greenland etc) is typical, but these samples will contain significantly more Laurentide material than those samples labelled as European, and are therefore

more representative of that ice sheet.

In order to ascertain the appropriateness of assigning different provenances to the two sets of samples, Mann Whitney U tests were performed on the magnetic data for the HL subsets identified in Table 5.5. The Mann Whitney U tests for all the parameters except χ_{arm} , SIRM and Soft IRM returned a P-value of < 0.05 , therefore the null hypothesis of no difference between the HL subsets can be rejected, confirming that they are statistically different populations. For χ_{arm} , SIRM and Soft IRM, however, this null hypothesis cannot be rejected, and it must be said that there is no statistical difference between the two subsets for these particular parameters. The Mann Whitney U tests can be found in Appendix 2biv (Pg 343).

Based on the information in Section 5.3.1, and Table 5.5 basic environmental magnetic methods do not distinguish between specific lithological or mineral types, although they do differentiate between materials from different provenance areas with confidence. Environmental magnetism has several advantages over the more traditional techniques currently employed to analyse IRD provenance, being highly sensitive, quick, cheap and non-destructive. Additionally, they characterise differences in the composition of IRD within the HLs. Also, magnetic measurements are performed on the bulk sediments, they are perhaps reflect all the components of the IRD, as fine grained sediments are transported by ice rafting along with the coarse grains. As mentioned above, however, environmental magnetic techniques do not identify specific mineralogies, or necessarily quantify the contributions of each mineral to a mixture. Environmental magnetic analysis is useful at the beginning of a project to help select areas of interest where more time consuming, traditional methods can be concentrated.

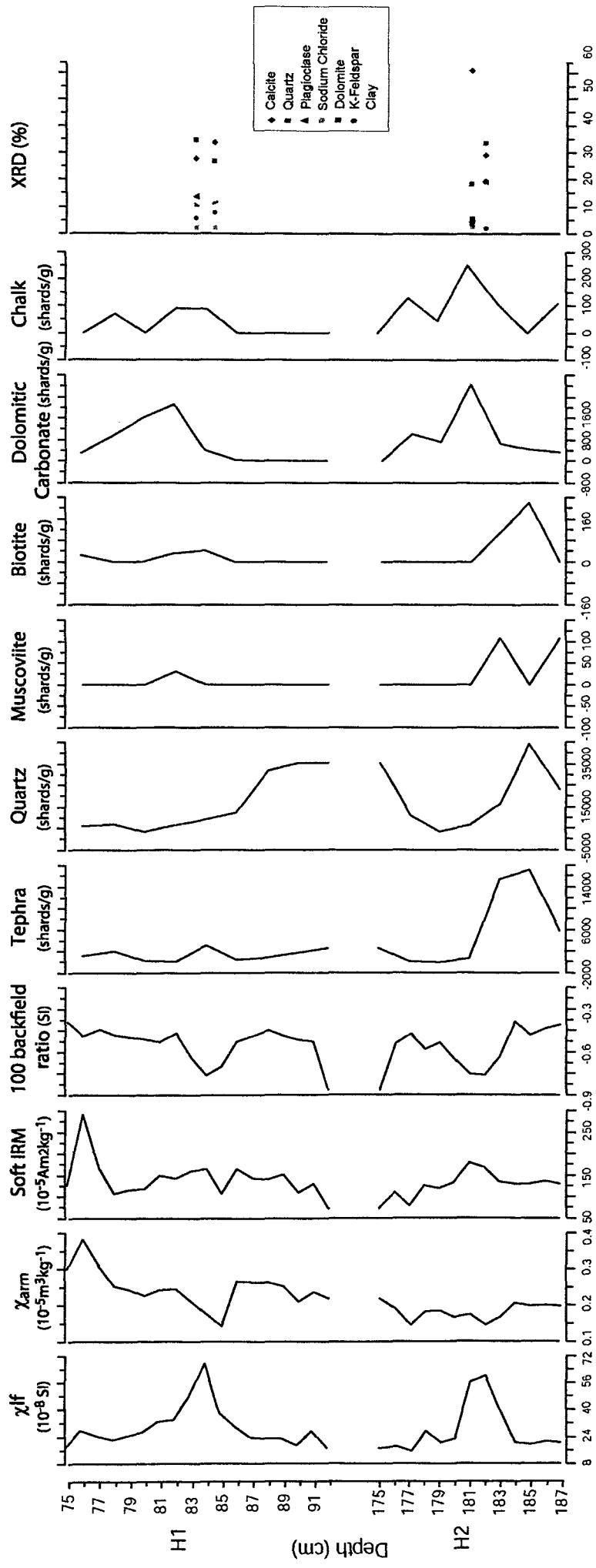


Fig. 5.22: Synthesis of data for the Heinrich Event sections of OMEX 2K.

5.3.2 Other aspects of OMEX 2K

In addition to the information provided by the magnetic analysis on the provenance of Heinrich Event IRD, several other points of interest have been recognised in the data obtained for OMEX 2K.

The tephra identified during the lithological analysis performed at the University of Wales, Bangor, displays distinct magnetic signatures. This is part of the reason that the Pre H2 group in the biplots (Fig. 5.17) has a different, less clustered, signal to the other ambient sediments. There is a slight increase in magnetic concentration in comparison to the ambient sediments when tephra are present, along with a very fine magnetic grain size and an increase in both mineral types. This could be due to the specific magnetic characteristics of the tephra, or a response to the origin of the material, which is likely to be Icelandic, a source that has not yet been discussed in this thesis.

The Younger Dryas also has a distinctive signature, which appears to be somewhere between the HL characteristics and those of the Holocene. The magnetic concentration appears to increase slightly, corresponding to an input of tephra. It is known that the BIS during the Younger Dryas did not terminate in a marine environment, and that no rafting of ice into the North Atlantic occurred from the BIS (Lambeck, 1995). Whether this increase in magnetic concentration is a result of the tephra, or a representation of a return to glacial conditions is, as yet, unconstrained. The magnetic grain size decreases dramatically throughout the YD and into the Holocene, with the magnetic mineralogy appearing to exhibit lower coercivity behaviour. The biplots show clustering of the YD samples, usually falling between the ambient glacial sediments and the Holocene samples.

The Holocene has a very low magnetic concentration; a very fine magnetic grain size; and a slightly higher coercivity magnetic mineralogy than is seen in the HLs, which is comparable to the ambient sediments. All this is indicative of delivery mechanisms that are unable to transport material of large grain sizes, such as

ocean currents. Austin & Kroon, (2001) have also suggested that bottom currents are stronger during the Holocene than the YD and glacial stadials, and therefore are able to transport significant amounts of material without deposition. This would account for the low sedimentation rate and the low concentration of magnetic minerals throughout the Holocene.

Factor Analysis

As described in Section 4.5.4, factor analysis is a statistical tool which determines underlying factors within a data set and identify any pattern to their influences. Factor analysis techniques (both R and Q mode) were applied to the OMEX 2K dataset to assess statistically the interpretations presented above (Section 5.3).

Factor analysis was preformed on OMEX 2K using Minitab version 14. The plot (Fig. 5.23) uses the same key as used in previous graphs. Six HE samples plot to the far top right corner of the graph, (along the χ_{lf} and χ/χ_{arm} axes), showing a strong relationship with the concentration dependent parameters, but a weak relationship with χ_{arm} . The mineralogical parameters have little influence on the factor analysis, and this is probably due to the very small changes in magnetite mineralogy that are evident in the routine magnetic data but are disguised by concentration differences.

The other temporal groups plot together in distinct clusters, though some overlapping does occur, possibly due to the relatively low sedimentation rate in OMEX 2K. The Holocene plots at the bottom left corner with very low loadings on factor 1, with a low χ_{lf} and a high χ_{arm} relationship; the ambient sediments plot towards the centre of the graph with low loadings on both factor 1 and 2 and no apparent connection to the Holocene, HEs or Pre H2 samples; Pre H2, some H1 and H2 samples, and the Precursor appear to have both quite high loadings on factor 1 but low loadings on factor 2, they display a hard and soft IRM influence, and again cluster in a separate portion of the graph.

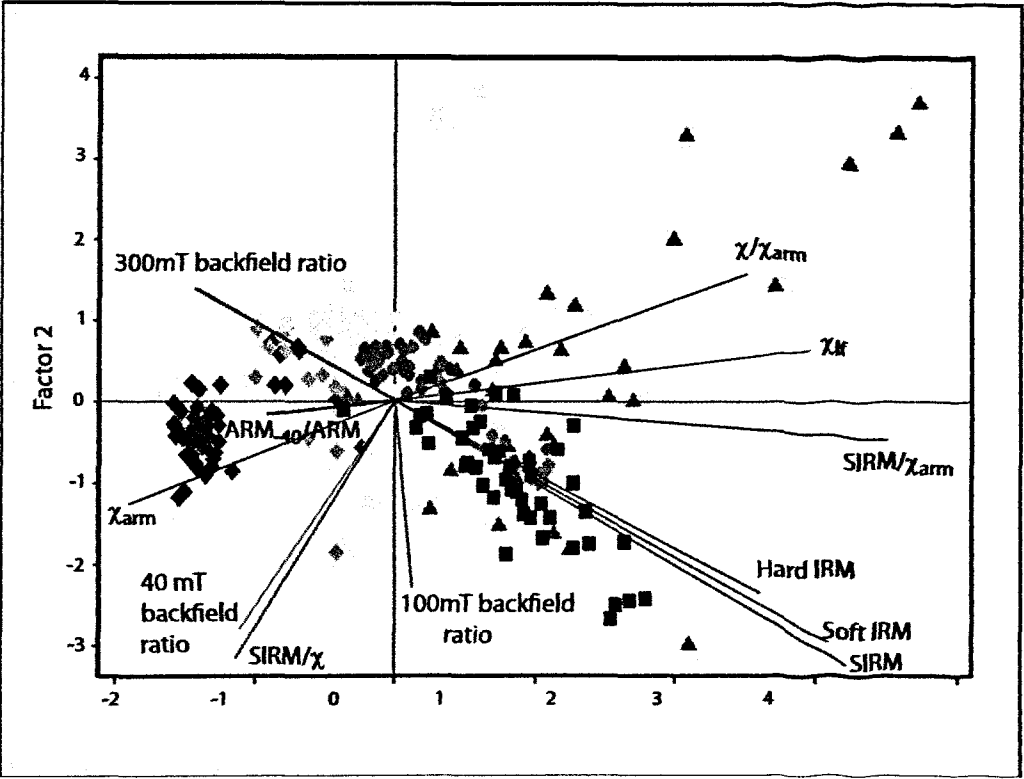


Fig 5.23: Factor analysis results for OMEK 2K.

As the HL IRD that is not attributed to the LIS in Table 5.5 plots with the other glacial material (Precursor, Pre H2 etc), it is therefore presumed to be composed of material from the same source. The slight differences observed between some of the temporal groups could be dependent on climatic conditions and transport mechanisms, as discussed in the Bloemendal plots in Section 5.2.1, though the larger differences are likely to be due to differences in provenance.

Overall, the factor analysis for OMEX 2K appears to support the initial interpretation of the data set using the graphical methods.

5.4 MD01-2461

The success of the analysis on OMEX 2K led to the opportunity to perform further analysis on a longer core. MD01-2461 is a 25.3m long core retrieved in 2001 on which little work has been done to date. The top 15 m were made available for magnetic analysis using the methods discussed in Section 4.3.

5.4.1 Chronology

As MD01-2461 is a relatively new core, no radiocarbon age model exists as yet, and so, an alternative method was used to establish a basic chronology for MD01-2461 to enable the same graphs as in Section 5.2.1 to be drawn. Initially a combination of the IRD counts and magnetic susceptibility data was used to constrain the location of the HEs, which was successful in determining depths for each HE peak, with the exception of H1. North Atlantic Ash Zone II was also located during IRD analysis by Vicky Peck (V. Peck, Pers. Comm. 2003).

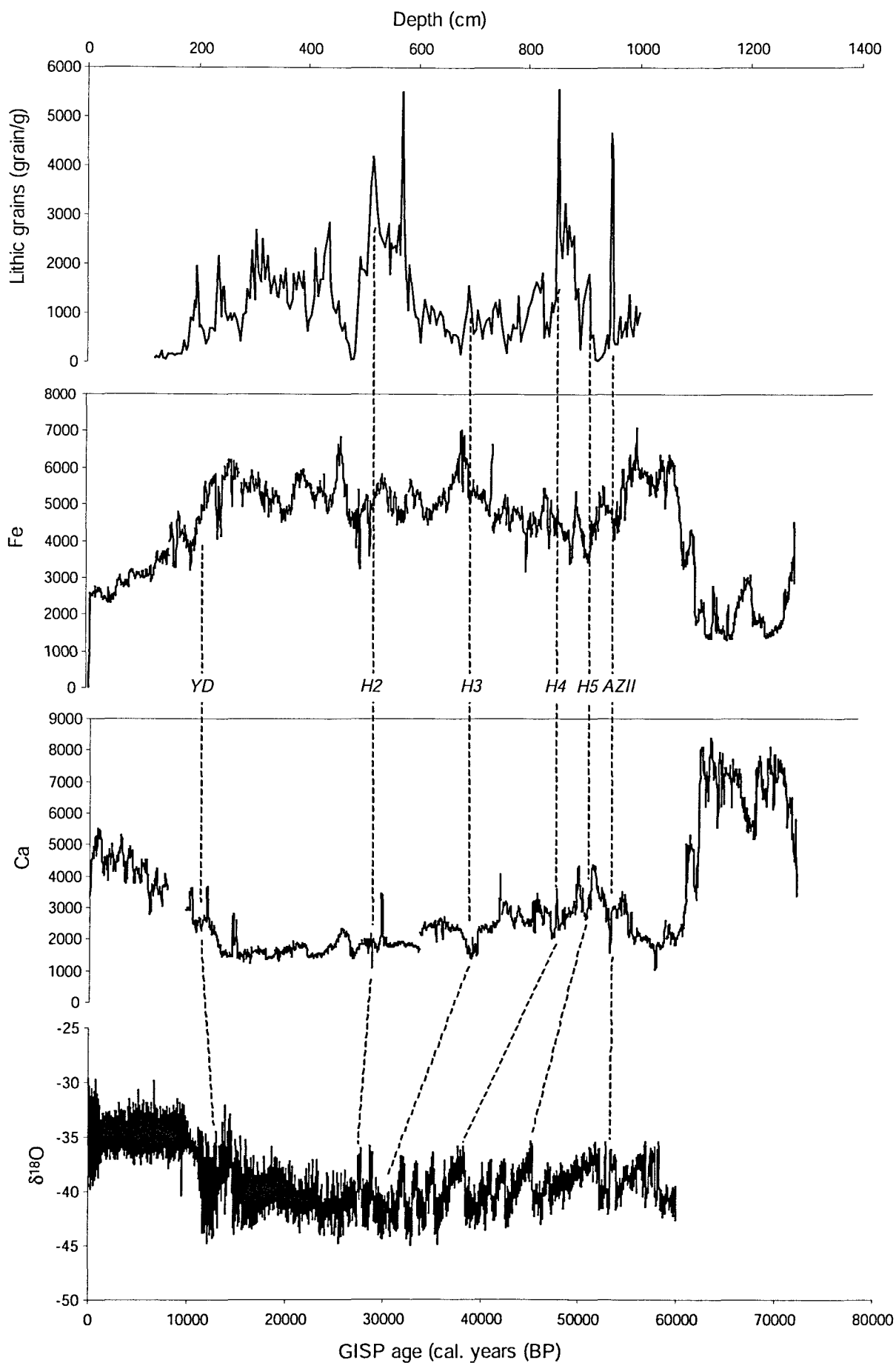


Fig. 5.24: IRD count and Fe:Ca data for MD01-2461 showing the tie-points to the GISP2 oxygen isotope record used to develop a crude chronology for the core.

Calcium/Iron XRF line intensity scans were provided by Dr B. Austin and Dr N. Norgaard-Pedersen (St Andrews) for the top 1300 cm of the core. The Ca/Fe content of marine sediments is taken to show the stadial-interstadial cycles seen in the $\delta^{18}\text{O}$ GRIP and GISP2 ice core records, as they represent the dilution of CaCO_3 by inorganic material (Stoner & Andrews, 1999; Evans & Heller, 2003). Hence, during cold stadials, dips in the Ca record correlate with peaks in Fe, as the amount of biological productivity decreases, and *vice versa* in the interstadials. Therefore, by determining “markers” of known ages in the core (e.g. tephra layers, HEs etc), the interstadials in the GISP2 records before and after these markers may be identified. Once depths for each of the interstadials in the core have been selected, these depths can be assigned an age from the ice core $\delta^{18}\text{O}$ chronology, by looking up the age for the corresponding interstadial (Fig. 5.24).

In a similar way to the age-model construction in Section 5.1, once the interstadial depths were assigned ages, they were plotted onto an age-depth graph and an equation provides an age (kyr BP) for any depth (cm) along the core, using a 5th order trendline (Fig. 5.25). The 5th order polynomial was selected for this model as it matched all the “known” ages with more consistency than any others, which were wrong by up to 5000 years at the older and younger parts of the core. The equation provided by the 5th order trendline is still very approximate, and still presents some problems around H2. The age suggested by the model is c. 2000 years older than the GISP2 age given for H2, however, after comparison with the IRD trace, and confirmation that the IRD peak at 517 cm depth was dolomite in composition (V. Peck, Pers. Comm. 2003), it was decided to assign H2 the age suggested by the model, despite the disparity from GISP2.

Other problems with this method arise during the selection of the tie points (i.e. in this case, the depths of the interstadials in the core and the corresponding ages in GISP2). It is possible that not all the interstadials are represented in the core, or that stretching during core retrieval (Section 3.3) has distorted the age-depth relationship. Additionally, as each interstadial spans millennial timescales, there is room for error when selecting the ages from the GISP2 record.

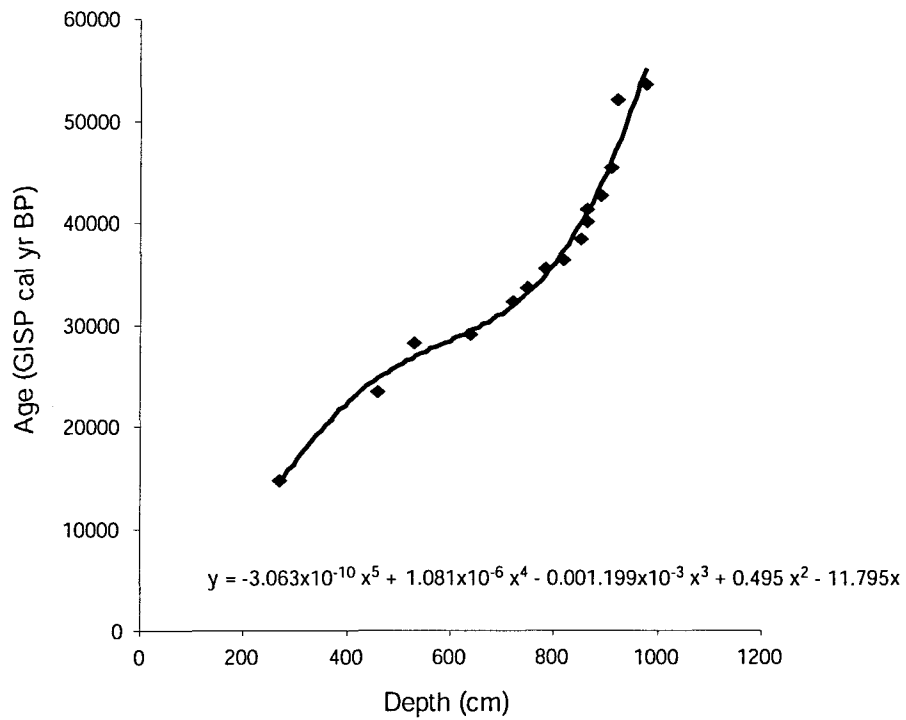


Fig. 5.25: Age model for MD01-2461. The equation of the fifth order polynomial trendline will give an age for any depth along the core.

Depths and corresponding ages were selected from the onset of each interstadial, however there is still likely to be some discrepancy between the two.

In addition to this issue, there is also concern about the precision of the GISP2 record, particularly at depth (Shackleton *et al.*, 2004). Up to 40 ka BP, GISP2 is thought to have errors of $\pm 2\%$, beyond which the error increases to $\pm 5-10\%$ (Meese *et al.*, 1997). Shackleton *et al.*, (2004) have also estimated that below 31 ka BP, the GISP2 record is around 1000 years too young, even with these errors taken into account.

Despite these areas of concern the above method was deemed suitable for the needs of this project, namely to devise a way to split MD01-2461 into temporal groups, until a more detailed radiocarbon chronology becomes available. This approach is thought adequate within the context of this work as most of the errors occur below 40 ka BP, and MD01-2461 has the added constraint of Ash Zone II (55 ka) to improve the precision at depth.

5.4.2 Magnetic Analysis

The routine magnetic analysis for MD01-2461 differed slightly from that for OMEX 2K. The measurement of volume susceptibility was unavailable due to the problems mentioned in Section 4.3, therefore, mass susceptibility (χ) at high and low frequencies were the first measurements to be made, including the calculation of frequency dependence of susceptibility ($\chi_{fd\%}$). The low frequency susceptibility (χ_{lf}) is shown in Fig. 5.26, along with the susceptibility taken onboard ship shortly after the retrieval of the core, the initial IRD counts undertaken by Vicky Peck at Cardiff University (Peck, unpublished data), and the CaCO_3 record modelled from the measurements by Dr Ian Hall (Cardiff University)(See Section 4.4.1).

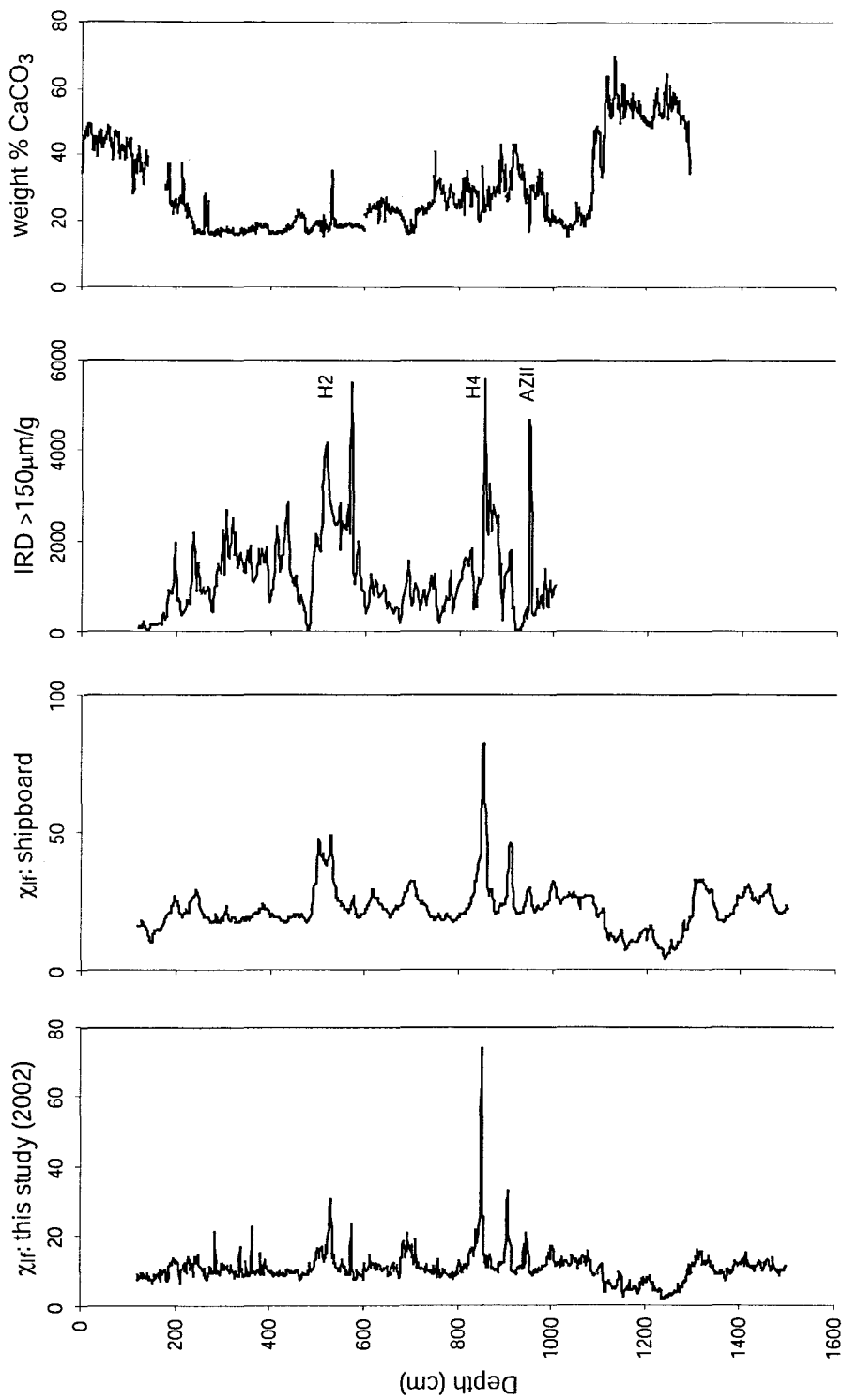


Fig. 5.26: Magnetic susceptibility measured in this study in comparison to that taken onboard ship; the IRD counts of grains >150µm per gram of sediment (Peck, unpublished data); and carbonate content modelled from measurements by Dr I. Hall.

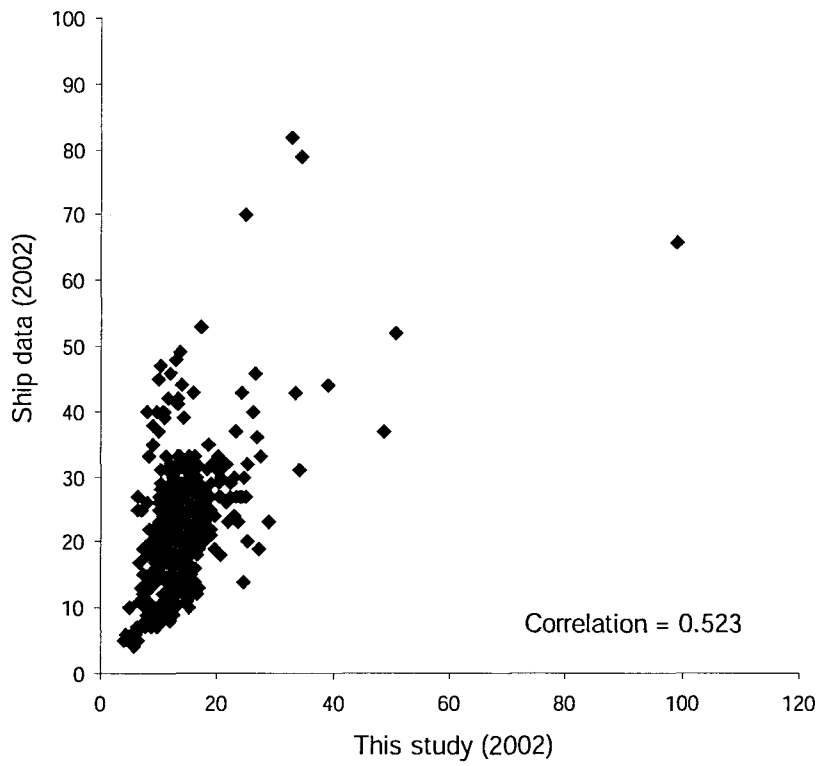


Fig. 5.27: Correlation between the susceptibility measured during this study (2002) and that taken onboard ship. The result of 0.523 suggests an adequate correlation.

The general trends within the two susceptibility records follow the same patterns. However, there are some specific differences, for example, the 2002 record (measured during this study) seems to be more sensitive to small variations in susceptibility. Most of these differences can be attributed to the differences in measurement type, equipment and the environment of measurement. Some, however, such as the lack of a double susceptibility peak at 505 - 530 cm (H2) in the 2002 data, cannot be explained by this. The two main IRD peaks at 500-550 cm and 850-900 cm, and their corresponding susceptibility peaks have been labelled as Heinrich 2 and Heinrich 4 respectively (Peck, unpublished). The smaller susceptibility peak below H4 has been called H5, due to the proximity of Ash Zone II (950 cm depth) found by Vicky Peck during the separation of the IRD (Peck, Pers. Comm. 2003). In general the IRD trace appears to match the susceptibility records well, with the exception of the missing H2 peak in the 2002 record. The Pearsons product moment coefficient correlation between the two records is 0.52 (Fig. 5.27), which is statistically significant.

The other measurements made were ARM, ARM₄₀, followed by SIRM (IRM₃₀₀₀) and the backfields of 40, 100, 300 and 1000 mT (See Section 4.3). The magnetic ratios found in Table 4.9 were calculated in a broadly similar way as for OMEX 2K. Fig. 5.28 shows the down-core profiles for each of the magnetic parameters against depth. These parameters have been defined previously (Section 5.2), so discussion here focuses on their interpretation.

The magnetic data obtained during analysis of MD01-2461 show remarkable similarity to the trends and patterns seen in OMEX 2K. However, the absolute values of the data are different, with MD01-2461 yielding higher results. This is thought to be due to the distance between the two cores; close enough to be influenced by the same factors delivering the magnetic material, but far enough apart to be affected by different levels of biologic productivity and sediment focussing.

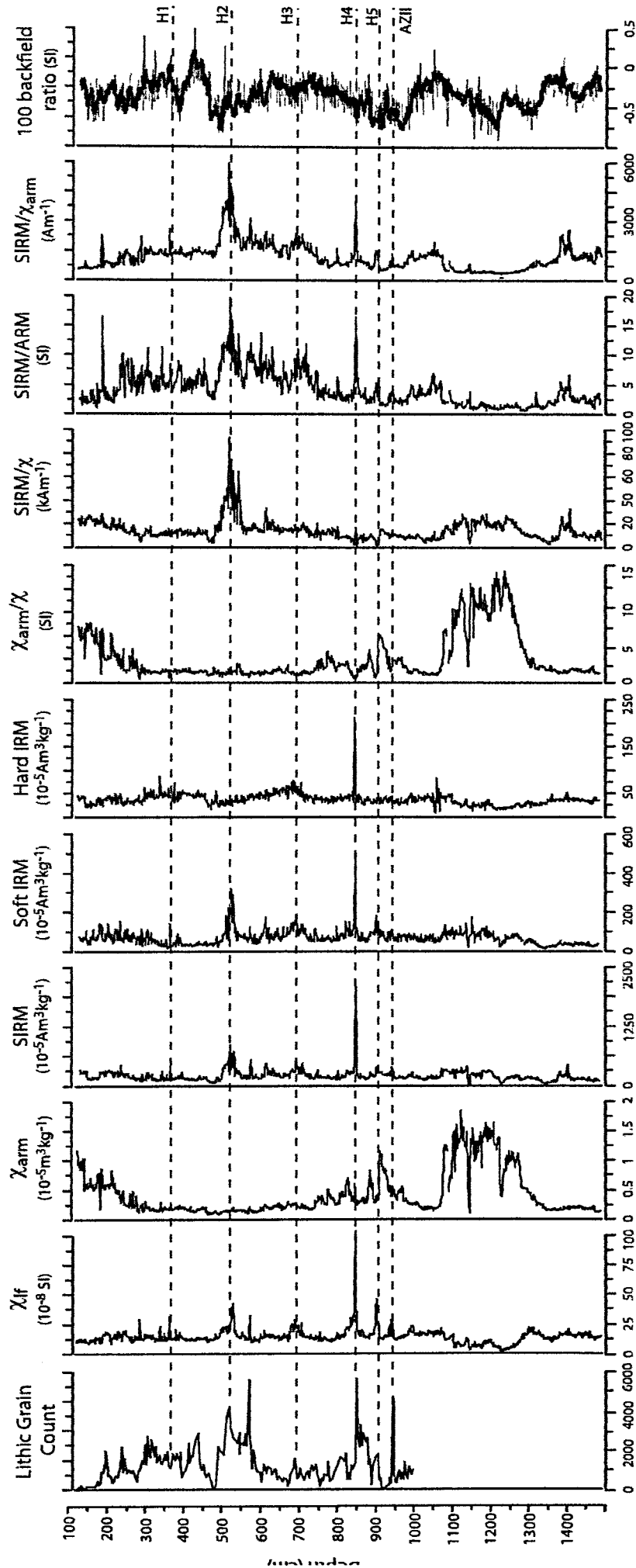


Fig. 5.28: Down-core plots of the magnetic parameters and ratios measured and calculated for MD01-2461. The dashed lines are the positions of the Heinrich Events. On the 100 backfield ratio plot, the thick black line represents the running mean and helps to smooth the alternating signal. See text for a full discussion.

χ_{arm} is very large below c. 1059 cm depth, indicating the presence of fine grained ferrimagnetic minerals, this is supported by the massive increase in χ_{arm}/χ below 1100 cm. χ_{arm}/χ itself displays several peaks between 1000 and 750 cm depth, but remains fairly constant between 750 and 300 cm depth, suggesting that the size of the ferrimagnetic minerals varied significantly during the early part of the glacial cycles, but then became relatively constant. This pattern is also in agreement with the χ_{arm} record. A large increase in both variables begins at 300 cm and continues through to the top of the core, similar to the signal seen by these records in OMEX 2K.

The Soft IRM record displays slightly lower values between 1100 and 1300 cm depth, implying a decrease in the concentration of ferrimagnetic minerals. As this also occurs in the Hard IRM record, which suggests a decrease in the concentration of harder magnetic minerals. An overall decrease in the presence of magnetic minerals as a whole is indicated, in agreement with χ_{lf} . Peaks in ferrimagnetic minerals are found at 843-879 cm (H4) and 489-587 cm (H2), with smaller rises at 920 cm, 670-740 cm and from 400 cm upwards. The Hard IRM trace also shows a sharp increase in higher coercivity minerals at 857-875 cm (H4). The general rise in magnetic concentration (seen by χ_{lr}) is responsible for this rise in both Soft and Hard IRM. Hard IRM then rises to around 670-700 cm and slowly declines before rising again at 350-400 cm and tailing off towards the top of the core.

The third mineralogical parameter used, IRM₋₁₀₀/SIRM (100 backfield ratio) seems to alternate between high values of near zero and low values of around -0.6. There is a large decrease in the ratio between 1350 and ~1050 cm and then again between 1050 and 750cm, 750 and 450 cm and finally from 450 cm to the top of the core. This suggests the alternation between a higher coercivity signal (the highest points, ~1350, ~1050, ~750 and ~450) and a lower coercivity signal (the lowest points, ~1200, ~900, ~500 and ~150). However, values never rise above 0, and a more magnetite-like signal is implied throughout.

The parameter of SIRM/ χ suggests there is a dominant magnetite signature with grain size variations at 1059 – 1331 cm (smaller), 815-929 cm (larger) and 617cm (smaller). The large peak in SIRM/ χ at 490-590 cm does potentially creep into the range for haematite. The grain size parameters of SIRM/ARM and SIRM/ χ_{arm} show a large decrease over 1339 – 1059 cm indicating finer magnetic grains and peaks at 900-933 cm, 841-877 cm, 670-747 cm and 493-580 cm demonstrating coarser grains. Three peaks of larger grains are also found above 400 cm depth, at 363 cm, 285 cm, and 183 cm.

Summary

The base of the core shows some very interesting magnetic characteristics, which are only matched by a few results occurring at the top of the core. Between 1321 – 1059 cm there are significant declines in both grain size and concentration, which are similar characteristics to those found during the Holocene in OMEX 2K. This, therefore, is proposed to represent the last interglacial, Marine Isotope Stage 5e. There appears to be larger drops in magnetic concentration and grain size below 1321 cm depth than above 280 cm (the Holocene in MD01-2461). Kandiano *et al.*, (2004) state that during MIS 5e, sea surface temperatures were up to 2°C warmer than during the Holocene, and had a significant impact on the oceanography of the North Atlantic by influencing the THC. It is suggested that this temperature difference is the cause of the differing interglacial magnetic signals between the Holocene and MIS 5e.

At ~950 cm there are increases in concentration, grain size and the presence of high coercivity minerals (such as haematite). IRD analysis by V. Peck shows this to be Ash Zone II (Peck, unpublished).

Between 900-940 cm depth, there is a small increase in magnetic concentration, along with rises in grain size and the concentration of low coercivity minerals. These characteristics are consistent with those of Heinrich Events (see discussion for OMEX 2K), and using the placing of AZII and H4, it is possible to label this feature as Heinrich Layer 5. H4 (840-880 cm) has a peak in magnetic

concentration and grain size, and there are increases in both hard and soft magnetic minerals due to the sharp overall increase of minerals, although the low coercivity mineral increase is prolonged relative to the high coercivity increase, spanning a further 18 cm.

At 670-740 cm there are smaller increases in all the same characteristics, namely concentration, grain size, soft and hard minerals. These are not of the same magnitude as those seen in H2 or H4, but are clearly present. This is potentially Heinrich Layer 3. H3 is documented as displaying a number of different characteristics relative to the other HLs (Grousset *et al.*, 1993).

H2 spans the depths 490-580 cm. It has a small χ_{if} peak at 575 cm, but two in SIRM at 575 cm and 499-533 cm suggesting an overall double peak in concentration, similar to that found in the onboard susceptibility measurements. There are also two significant increases in grain size at corresponding depths and two peaks in ferrimagnetic mineral concentration. There is also a decrease in high coercivity magnetic minerals, which rise slowly towards the end of the HL and peak at 475 cm. In contrast to this, the SIRM/ χ record has values over 50 at H2, possibly suggesting the presence of haematite.

Above 400cm, there is quite a detailed record, involving a general decrease in magnetic grain size, with peaks occurring at 363 cm, 285 cm, and 183 cm and a decline at 339cm. Overall, there is a constant background concentration of magnetic minerals, with peaks again occurring at 363 cm, 339 cm, and 285 cm. There are increases in ferrimagnetic minerals at 363 cm, 285 cm, and 229 cm with peaks of canted antiferromagnetic minerals at 377 cm and 339 cm. It is suggested that 363 cm corresponds to H1, and 285cm as the YD, with sediments above this representing the Holocene.

At the base of the core the magnetic data begin during glacial conditions prior to the onset of MIS 5e. It is therefore suggested that the analysed section of MD01-2461 dates back to MIS 6, a glacial stadial. The chronology discussed in Section

5.4.1 does not maintain its precision at this depth, so this conclusion is speculative.

IRM Acquisition Curves

IRM acquisition curves for the backfield measurements were drawn and compared to the “standard” curves from Walden, 1999 (Fig. 5.28), as well as the acquisition curves for OMEX 2K. It appears that MD01-2461 is dominated by low coercivity mineral behaviour. As with the OMEX 2K curves, the sample that saturates the earliest is a peak HE sample, in this case H4.

Magnetotactic Bacteria

As discussed earlier (Section 5.2), it is essential to eliminate, or account for the presence of magnetotactic bacteria within a sediment. Again, the most appropriate parameters for MD01-2461 are ARM/SIRM, χ_{arm}/χ and $\chi_{\text{arm}}/\chi_{\text{fd}}$, as they are measured during routine magnetic analysis. Oldfield, (1994) suggests that values of $\chi_{\text{arm}}/\chi > 40$ and $\chi_{\text{arm}}/\chi_{\text{fd}} > 1$ are representative of bacterial magnetite. ARM/SIRM values of between 0.15 - 0.25 kAm⁻¹ are indicative of MTB (Moskowitz *et al.*, 1993).

Figs. 5.30a & b show the graphs of χ_{arm}/χ versus $\chi_{\text{arm}}/\chi_{\text{fd}}$ and ARM/SIRM against depth, respectively. Both graphs clearly show the MD01-2461 material falling below the area attributed to MTB, with the exception of a few interglacial samples on the ARM/SIRM plot. On the basis of Fig. 5.30, it can be inferred that organic magnetic minerals contribute minimally to the sediments on the Celtic Margin, particularly during the glacial cycles.

Greigite

As discussed in the Section 4.5, for this study, the parameters appropriate to assessing the contribution of greigite to the sediments in MD01-2461 are the magnetic ratios of SIRM/ χ , ARM₄₀/ARM and IRM₁₀₀/SIRM, all of which were measured during the routine magnetic analysis of the samples. For MD01-2461, the analysis of the loss of susceptibility is not likely to be diagnostic, as only 1

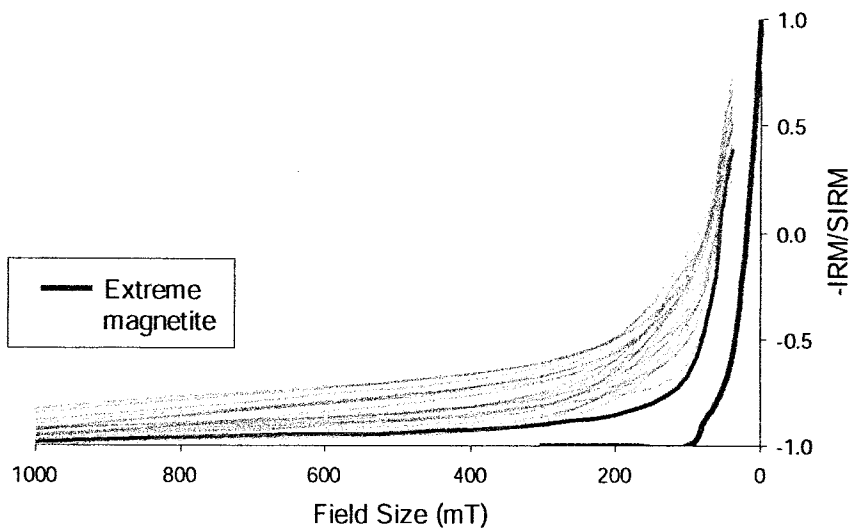


Fig. 5.29: Acquisition curve for MD01-2461. Only backfields were used during this analysis, and so only the one "standard" example can be used. However, it still suggests that MD01-2461 is dominated by ferrimagnetic material. The purple line is an H4 sample.

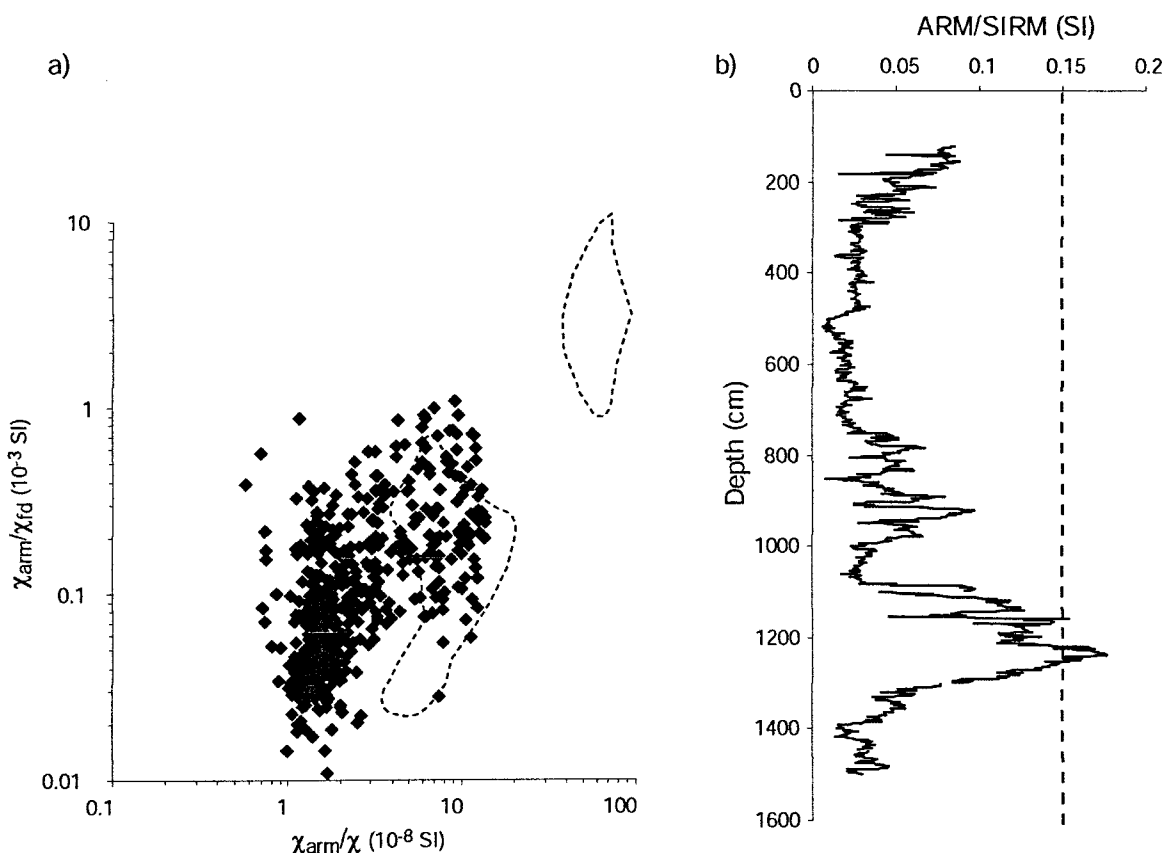


Fig. 5.30: a) graph of χ_{arm}/χ versus χ_{arm}/χ_{fd} used for the identification of magnetotactic bacteria. Oldfield (1992) states that any bacterial magnetic material should plot with χ_{arm}/χ values of >40 and χ_{arm}/χ_{fd} values of >1 (dashed lines). This is not the case for the MD01-2461 sediments. b) graph of ARM/SIRM for MD01-2461, used as an indication for the presence of magnetotactic bacteria. Values for MD01-2461 only appear to reach the levels for magnetotactic bacteria during the last interglacial, MIS 5e.

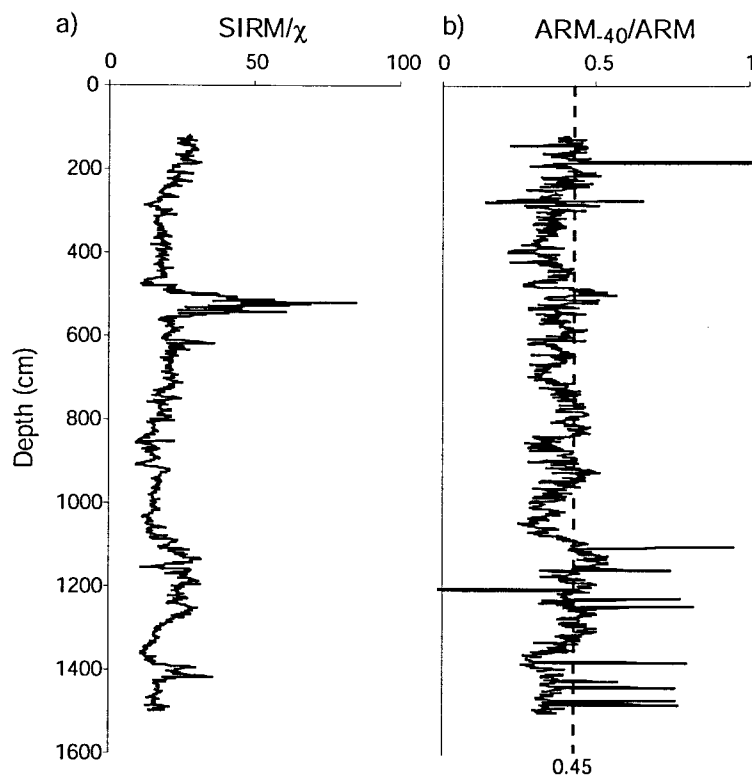


Fig. 5.31: a) Down-core plot of $SIRM/\chi$ for MD01-2461 used for the assessment for the presence of greigite. Values should fall >70 kAm^2 . b) Down-core plot of ARM_{40}/ARM . Values of greigite fall within the range 0.45-0.85.

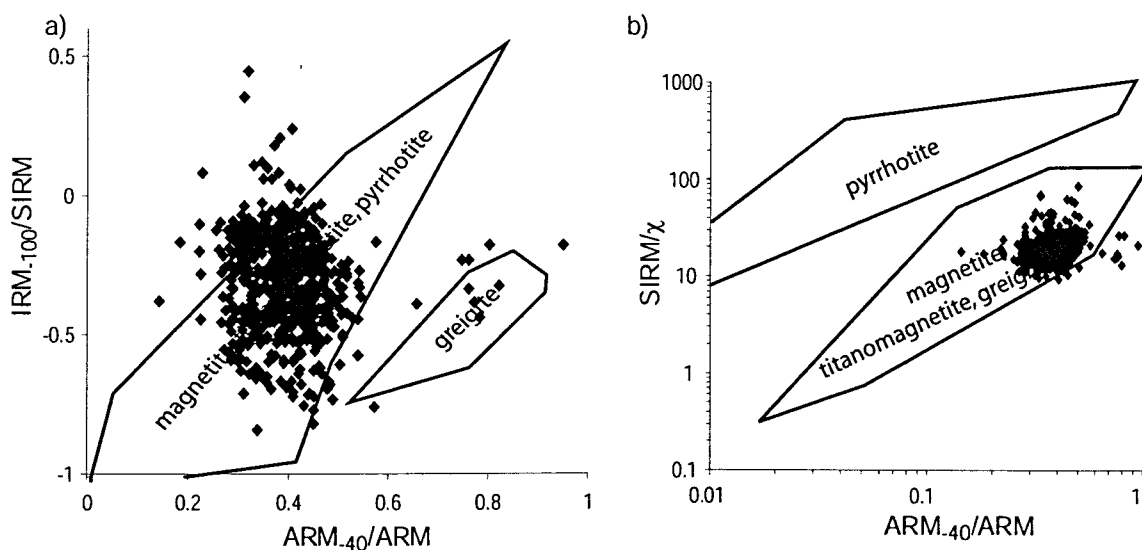


Fig. 5.32: a) Plot of ARM_{40}/ARM versus IRM_{100}/IRM_{1000} , used by Peters & Thompson, 1998) for the differentiation of magnetic minerals. b) Plot of ARM_{40}/ARM versus IRM_{1000}/χ also used by Peters & Thompson (1998) for the identification of greigite.

year had elapsed between the separate susceptibility measurements. This makes the likelihood of any obvious changes very low. In addition, the saturation properties are unavailable for analysis, as only backfield measurements were made with MD01-2461.

SIRM/ χ ratios above 70 kAm⁻¹ coupled with ARM₄₀/ARM values between 0.45-0.85 are indicative of the presence of greigite. Fig. 5.31a & b shows down-core plots of these two ratios. The ratio of SIRM/ χ suggests only a limited presence of greigite, as the only samples to fall within the appropriate values are at the H2 area. As discussed earlier, H2 has significantly lower χ_{lf} values than expected when compared to the onboard trace, which will disproportionally increase SIRM/ χ ratios. As the ratios in this section of the core are so much larger than elsewhere, it is suggested that χ_{lf} measurements are the cause, rather than presence of greigite. The plot of ARM₄₀/ARM, however, shows several areas within appropriate ranges for greigite, such as the Holocene, the last interglacial (MIS 5e) and occasional samples within MIS 6. Although, as these are not coupled with SIRM/ χ ratios of >70 kAm⁻¹ a minimal presence of greigite within MD01-2451 is implied. Additionally, as these samples are outwith the main areas of interest to this study, which are the HLs and the last glacial stage, they will not be included in further analysis and discussion.

Biplots used by Peters & Thompson, (1998) to provide a single method with which to distinguish between various magnetic minerals were also generated for MD01-2461 (Fig. 5.32a & b). The plot of ARM₄₀/ARM versus SIRM/ χ shows the MD01-2461 material falling within the magnetite, titanomagnetite and greigite region, as expected. The plot of ARM₄₀/ARM versus IRM₁₀₀/SIRM, however, does show a few samples that fall within the envelope of likely greigite behaviour. These samples are from below 1100 cm depth, and therefore fall into the last interglacial cycle (MIS 5e). Based on this analysis greigite has little influence in MD01-2461 sediments. Any greigite that may be present is found below 1100 cm, (MIS 5e), and therefore not of any great concern in this study.

Biplots

Fig. 5.33 and Appendix 1b shows the biplots for MD01-2461. The same graphs proved helpful in diagnosing potential LIS samples within OMEX 2K. In the case of MD01-2461, some of the finer details are not as obvious as in OMEX 2K, due to the larger quantity of samples used, and the slightly lower resolution analysis (every 2 cm as opposed to every 1 cm). However, similar patterns are found. The temporal units selected for MD01-2461 are presented in Table 5.6, and are based on the chronology discussed in Section 5.4.1.

Kruskal-Wallis tests were also performed on each of the temporal groups in Table 5.6 for each of the magnetic parameters, to test if there is any statistically significant difference between the magnetic characteristics of the separate groups. For each of the parameters discussed in Section 5.2.1, the Kruskal-Wallis tests returned a P-value of 0.000, which means that the null hypothesis of no significant difference must be rejected. Therefore, statistically speaking, there are differences in the magnetic characteristics between all the temporal groups shown in Table 5.6. The Kruskal-Wallis tests can be found in Appendix 2ciii (Pg-348-349).

Several samples, mainly from H4 and H5, display particularly large concentrations of magnetic minerals and larger grains sizes (Fig. 5.33). They also have higher magnetite contents, compared with other samples within H4 and H5. These are similar to the potential LIS samples found in OMEX 2K (Table 5.5), and therefore these samples are probably also LIS in origin. Samples from the H2 section of the core also display some distinctive characteristics, especially in the grain size ratios of SIRM/χ and $\text{SIRM}/\chi_{\text{arm}}$ and very low $\text{IRM}_{-100}/\text{SIRM}$ values. As discussed earlier in this section, the low χ_{if} values measured in this study have an impact on ratios involving the H2 samples and result in some of these characteristics. The causes of these features, are as yet not understood, however, more detailed analysis of the H2 section of MD01-2461 discussed later in the chapter may resolve some of the issues.

Table 5.6: The Division of MD01-2461 into temporal units.

Group	Depth (cm)	Age (kyr BP)
Holocene	121 - 185	3.9 – 8.4
Younger Dryas	186 - 227	8.45 – 11.5
H1	243 - 271	12.7 – 14.7
H2	487 - 555	
H2 (PE)	565 - 597	27.7 – 28.4
H3	673 - 739	30.3 – 32.7
H4	837 - 871	38.6 – 41.7
H4 (PE)	873 - 899	41.9 – 44.6
H5	901 - 919	44.8 – 47.0
Ash Zone II	945 - 955	50.4 – 51.8
MIS 5e	1097 -	

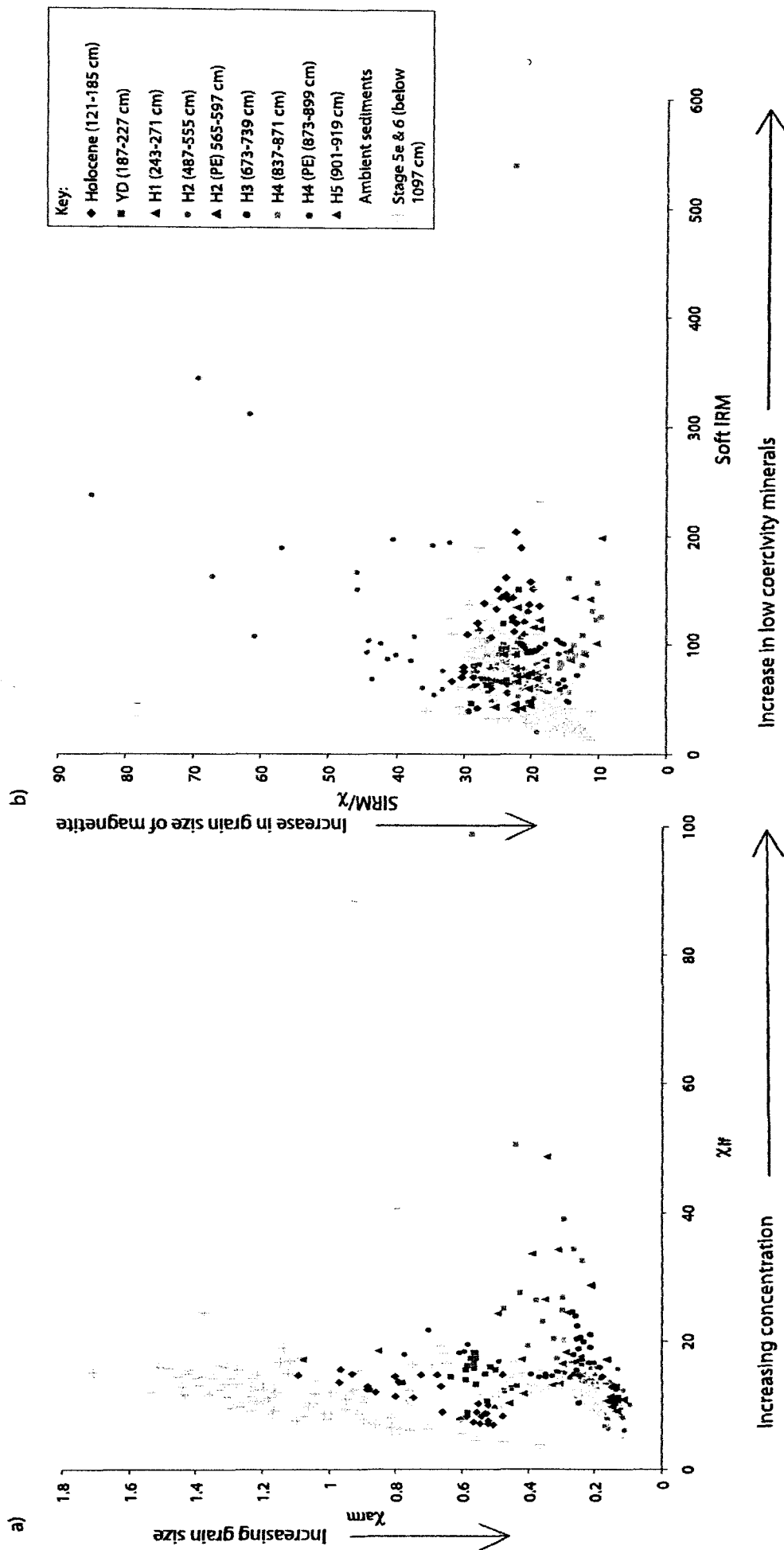


Fig. 5.32: Biplots for some of the magnetic parameters measured on MD01-2461. a) χ_{H} versus χ_{arm}
b) Soft IRM versus $\text{SIRM}/\chi_{\text{H}}$

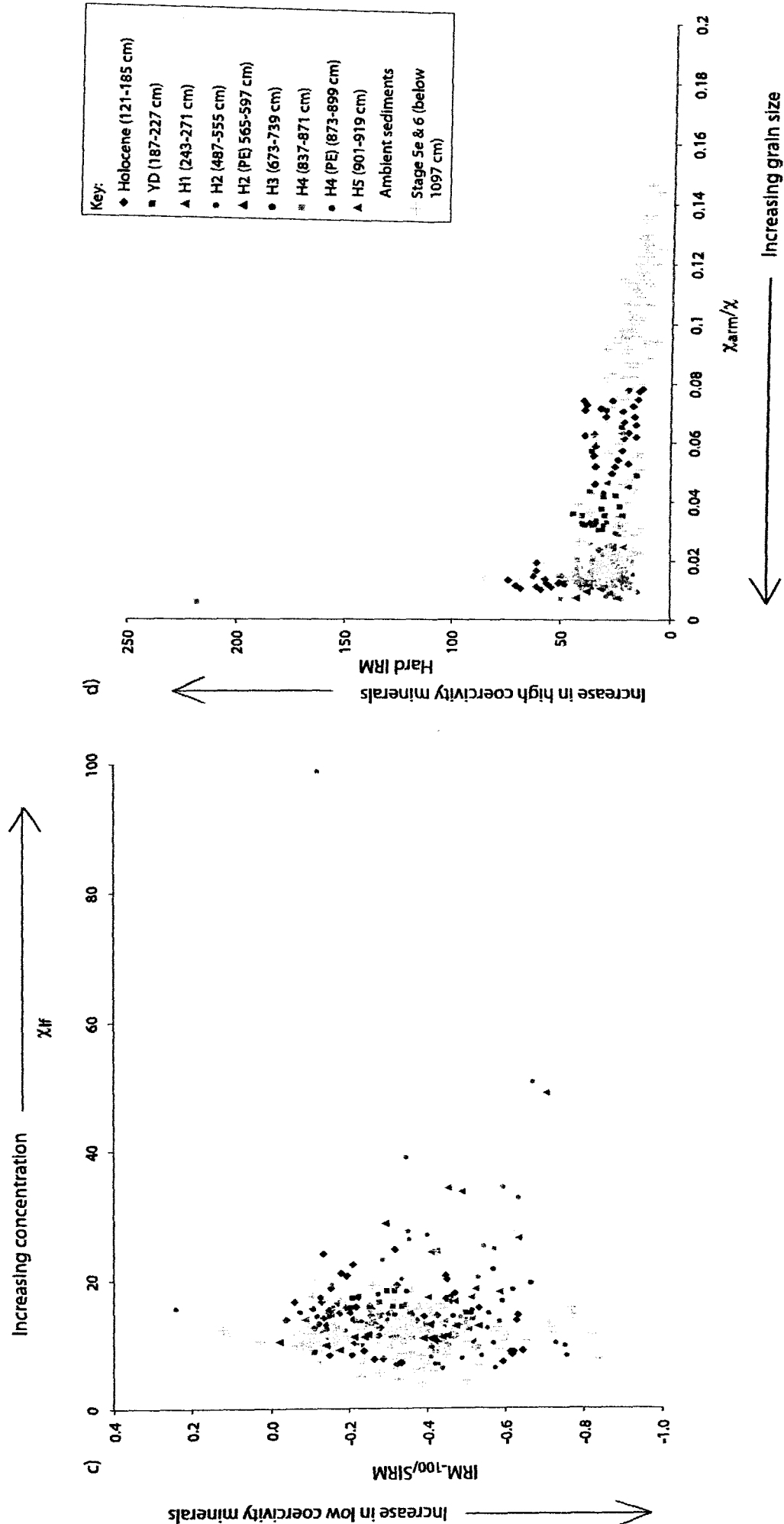


Fig. 5.32: Biplots for some of the magnetic parameters measured on MD01-2461. c) χ_{lf} versus IRM₋₁₀₀/SIRM, d) χ_{arm}/χ versus Hard IRM.

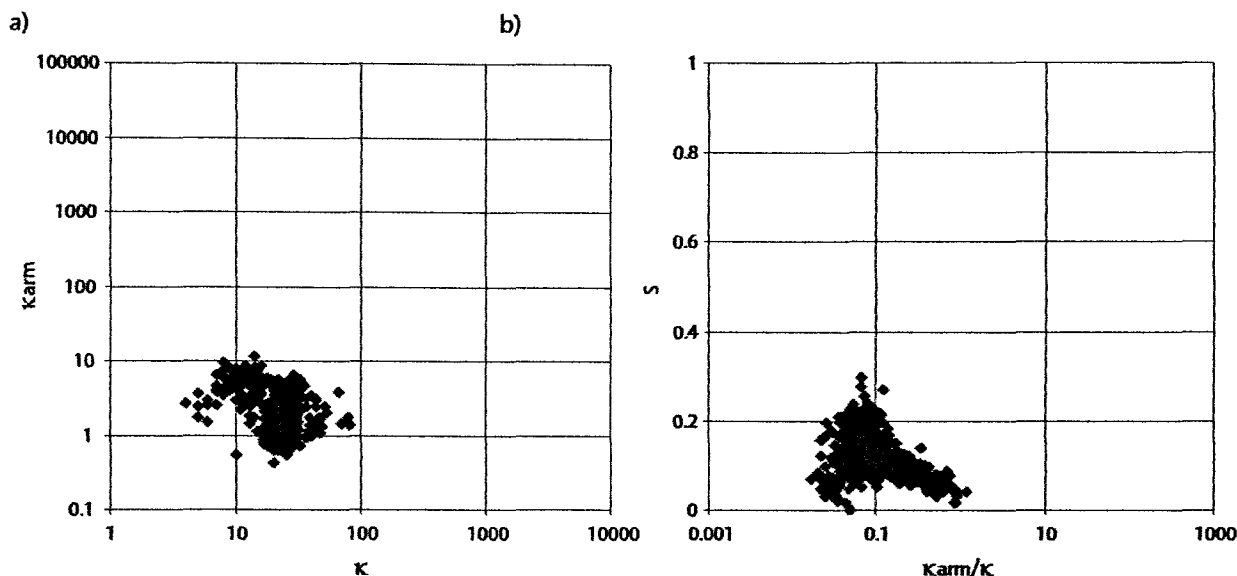


Fig. 5.34: Whole-core plots of: a) κ versus κ_{arm} and b) κ_{arm}/κ versus $S_{(Bloemendal)}$ for MD01-2461. In comparison to the discussion in Bloemendal *et al.*, 1992 and the diagrams taken from that paper (Fig. 5.18), these data suggests a relatively intermittent flux of carbonate-rich sediments from more than one source, or by more than one transport mechanism.

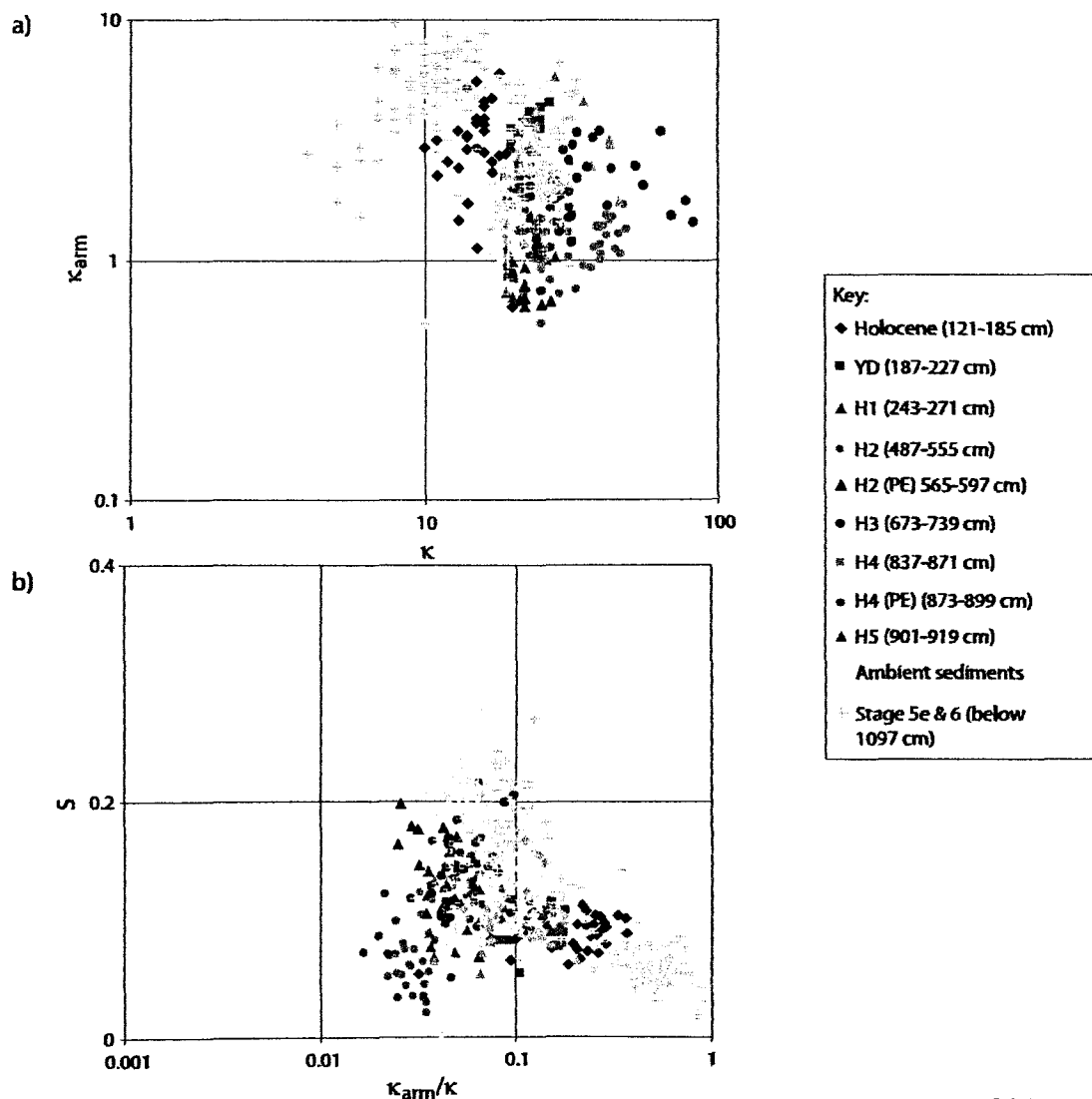


Fig. 5.35: Plots of: a) κ versus κ_{arm} and b) κ_{arm}/κ versus $S_{(Bloemendal)}$ for the temporal groups within MD01-2461. These plots show that there is variation in the sources and transport pathways both between and within the different groups.

As with the OMEX 2K data, graphs of κ versus κ_{arm} and κ_{arm}/κ versus $S_{(Bloemendal)}$ were used to assess the material type within MD01-2461 and to attempt to determine variation in provenance mechanisms (Figs. 5.34a & b and 5.35a & b). Fig. 5.34a shows the plot of κ versus κ_{arm} for the whole core, and indicates that the sediments in MD01-2461 are comprised of carbonate rich material. This is expected given its proximity to OMEX 2K.

Using the temporal units identified for MD01-2461 (Table 5.6), similar patterns are found to those for OMEX 2K (Fig. 5.35a). The Holocene and MIS 5e have widely distributed groups with the lowest κ values, suggesting that carbonate flux to the Celtic margin was sporadic during interglacial periods, when using the interpretation from Bloemendal *et al.*, (1992; Section 5.2.1). All the other core sections appear to be tightly grouped not only within the sections, but also with each other. The exceptions are H4 and H5. The samples with the highest κ values, plotting away from the main cluster, are from H4.

Fig. 5.34b and Fig. 5.35b show the graphs of κ_{arm}/κ versus $S_{(Bloemendal)}$ for the whole-core MD01-2461, and the temporal groups. As with OMEX 2K, there is a broad distribution of samples, though the $S_{(Bloemendal)}$ values are significantly lower for MD01-2461 (see discussion at the beginning of Section 5.4.2). The Holocene and MIS 5e form one end of the distribution, with H2 and H4 samples making up the other end. The rest of the material is grouped in the centre, with higher $S_{(Bloemendal)}$ values. Despite very different $S_{(Bloemendal)}$ values, based upon the ideas of Bloemendal *et al.*, (1992), the interpretation of the graphs is the same as in Section 5.2, i.e. the interglacial material has one transport mechanism, whereas the ambient sediments, along with some of the HE material, have another. The remaining HE samples belonging to a third provenance area or transport pathway.

5.4.3 Environmental Interpretation of MD01-2461

As with the pilot study on OMEX 2K, the main purpose of the research described above is to assess the ability of environmental magnetic measurements to identify and characterise the sediment contained within Heinrich Layers, to build on the information revealed by OMEX 2K, and to extend it into HEs not found in OMEX 2K. The interpretation of MD01-2461 will follow the same format as that for OMEX 2K, discussing any non-magnetic data available and comparing it to the magnetic data, before proposing provenance for the material, and sequencing of the events.

The Heinrich Events

The only non-magnetic data currently available are the IRD counts of grains $>150\ \mu\text{m}$ per gram of sediment calculated by Vicky Peck (see Section 4.1 & Fig. 4.4). Whilst this does not provide the detailed information on specific grain types as available in Section 5.2 and 5.3 it does provide a detailed picture of periods of increased ice-rafting.

As yet, the IRD counts have only been performed down to 10 m depth (Fig. 4.4 & 5.28), however, as this depth encompasses all the HEs known to be present in MD01-2461 it is sufficient for the present analysis. Large pulses of IRD can be seen at 946-954 cm, 852 cm, 570 cm, and 517 cm. Smaller, but still prominent peaks are found at 908 cm, 864-880 cm, 690 cm, 436 cm, 304 cm, 236 cm and 196 cm. The chronology for MD01-2461 indicates the large peaks at 946-954 cm and 852 cm to be Ash Zone 2 (AZII) and H4 respectively, with a possible H4 precursor event at 864-880 cm. The smaller peaks in IRD at 908 cm and 690 cm are likely to be H5 and H3, with the larger peaks at 570 cm and 517 cm being H2 and its possible precursor. The intermediate peaks at 436 cm, 604 cm, 236 cm and 196 cm are un-identified as yet although it is probable that one of them is H1, and another, the YD.

Comparison of magnetic and non-magnetic data

During the onset to H4, there is an increase in IRD at c. 880cm depth, though no rise is seen in χ_{lf} until 859 cm, which is accompanied by a further rise in IRD concentration. This applies to all the magnetic properties, suggesting that the initial input of IRD is somewhat different in composition to the material deposited from 859 cm upwards. The HE magnetic characteristics tail off after the peak at 853 cm, however the IRD concentration appears to drop much more rapidly. A summary diagram for this, plus the data for H2, H3 and H5 can be found on Fig. 5.36.

The IRD and magnetic parameters seem to operate in tandem during H5, with the build up to, and reduction from peak HE characteristics and IRD concentration occurring simultaneously. This is also the case during H3, however the magnetic characteristics and actual IRD concentration during this HE is different from the others. The IRD concentration is approximately one third of that during H4, though spread over a similar interval (the chronology suggests a larger timespan for H3), the susceptibility is also much lower, but still above ambient levels. Increases in both low and high coercivity minerals are seen on comparable levels, suggesting that the IRD is not dominated by a single mineral type. A slight coarsening of the magnetic grain size is also present.

In contrast, H2 follows that same pattern as H4, with a build up of IRD prior to the magnetic parameters that characterise HEs, recording peak conditions at 517 cm depth and then tailing off of ambient levels. The major difference with H2, however, is the lack of any χ peak coinciding with the IRD maxima and other HE magnetic characteristics, although the increase in other concentration dependent parameters (e.g. SIRM) does indicate a rise in magnetic concentration. This low in χ could be due to sampling or measurement errors, and will be examined further later during more detailed analysis of H2.

This, along with the slightly lower resolution of the data for MD01-2461 compared with OMEX 2K and the coarse chronology, makes it difficult to discuss

the exact phasing of events within the MD01-2461 HEs. However, it does appear possible to that during H2, H4 and H5 a similar sequence of events to those in OMEX 2K occurs, and that a dominant EIS IRD signal is obscured or diluted by an input of LIS material during peak HE conditions, and then a reduction of LIS input and renewed dominance of to EIS material. H3, however, does not appear to contain LIS material, and there is not an obvious peak event. It is, therefore, suggested that H3 is characteristic of a prolonged input of EIS IRD. Table 5.7 attempts to separate the HEs within MD01-2461 into LIS and EIS dominated samples, analogous to Table 5.5 for OMEX 2K.

As with OMEX 2K, Mann Whitney U tests were also performed on the separate LIS and EIS samples in Table 5.7, to test for any statistical difference between the two populations. For the H2 subsets, the Mann Whitney U tests for all the parameters except SIRM, $SIRM/\chi$, Soft IRM, $SIRM/ARM$ and $SIRM/\chi_{arm}$ returned a P-value of > 0.05 , therefore the null hypothesis of no difference between the HL subsets cannot be rejected, and there is no statistical difference between the two subsets for these particular parameters. For SIRM, $SIRM/\chi$, $SIRM/ARM$ and $SIRM/\chi_{arm}$, however, this null hypothesis can be rejected, confirming that they are statistically different populations. The Mann Whitney U tests can be found in Appendix 2civ (Pg 350). It is suggested that the acknowledged issues surrounding H2 discussed in the sections above, along with the indecision of provenance in Table 5.7, will have contributed something to these results.

For H4, the tests for all the parameters except χ_{arm} , Hard IRM, $SIRM/\chi$ and $IRM_{100}/SIRM$ returned a P-value of <0.05 , therefore the null hypothesis of no difference between the HL subsets can be rejected, confirming that they are statistically different populations. For χ_{arm} , Hard IRM, $SIRM/\chi$ and $IRM_{100}/SIRM$, however, this null hypothesis cannot be rejected, and it must be said that there is no statistical difference between the two subsets for these particular parameters. The tests can be found in Appendix 2civ (Pg 351).

Mann Whitney U tests have not been performed for H5, as there should be at

least 4 observations in each population. Two samples have a possible LIS provenance (Table 5.7).

Factor Analysis

Fig. 5.37 shows the results of the factor analysis for MD01-2461, the key is the same as the previous MD01-2461 plots to make sample identification easier. Two H4 samples plot on their own on the bottom of the graph, with four more lying between them and the remaining samples, which are identified as the potential LIS samples discussed in Section 5.4.3 and Table 5.7. The rest of the core also shows some interesting clustering within the large group towards the top left of the plot. The ambient glacial sediments and Stage 6, with higher loadings on factor 2 lie towards the top, whereas the Holocene and Stage 5e plot towards the right, with higher factor 1 loadings. H1 and H3 cluster tightly near the ambient sediments, with high factor loadings of almost 0. H1 and H3, as noted in previous discussions, do not appear to show any extreme LIS-type characteristics which possibly results in this tight clustering. The remaining HE samples from H2, H5 and some H2 and H4 precursor samples plot on the left with low loadings on factor 1, and are more widely distributed than either H1 or H3. The LIS samples are the only samples to show any significant change with the two factors, and as with OMEX 2K, are positioned close to the concentration-dependent parameters such as χ_{lf} but away from χ_{arm} , confirming their high concentrations of magnetic minerals but suggesting they are dominated by coarser magnetic grain sizes.

The factor analysis for MD01-2461 appears to support the earlier interpretation of a separate LIS input during the peak HE events which contributes to the very high magnetic concentrations and large magnetic grain size.

Table 5.7: The magnetic characteristics of the MD01-2461 HEs and their probable source areas.

HL sample (by depth)	Magnetic Characteristics	Potential Provenance
H2 – 487 to 499	Low concentration (SIRM), high coercivity mineralogy (Hard IRM, Soft IRM)	European
501 to 513	Increasing concentration (SIRM), increasing in low coercivity minerals (Soft IRM, Hard IRM)	European
513 to 517	Higher concentration (SIRM), softer mineralogy (Soft IRM)	Laurentide
517 to 519	Peak HE conditions; high concentration (SIRM), coarser grain size (χ_{arm}/χ , SIRM/ARM) and lower coercivity mineralogy (Soft IRM)	Laurentide
521 & 523	Slight decrease in concentration (SIRM) and softer minerals (Soft IRM)	
525 to 529	Return to peak conditions; high concentration (SIRM), finer grain size (SIRM/ARM, χ_{arm}/χ) and lower coercivity mineralogy (Soft IRM)	Laurentide
531 to 547	Decreasing concentraion (SIRM) and lower coercivity minerals (Soft IRM)	European
549 to 555	Low concentration (SIRM), higher coercivity mineralogy (Soft IRM, Hard IRM)	European
H4 – 837 to 845	Low concentration (χ , SIRM), finer grain size (χ_{arm}/χ , SIRM/ χ_{arm}), hard mineralogy (100 backfield ratio)	European
847 to 851	Higher concentration (χ , SIRM), coarsening grain size (χ_{arm}/χ , SIRM/ARM, SIRM/ χ_{arm}), softer mineralogy (100 backfield ratio)	Laurentide
853	Peak conditions; very high concentration (χ , SIRM), coarse grain size (χ_{arm}/χ , SIRM/ARM, SIRM/ χ_{arm})	Laurentide
855 to 857	Higher concentration (χ , SIRM), coarsening grain size (χ_{arm}/χ , SIRM/ARM, SIRM/ χ_{arm}), lower coercivity mineralogy (Hard IRM, Soft IRM)	Laurentide
859 to 871	Low concentration (χ , SIRM), finer grain size (χ_{arm}/χ , SIRM/ χ_{arm} , SIRM/ARM), harder mineralogy (100 backfield ratio)	European
H5 – 901 & 903	Low concentration (χ , SIRM), slightly finer grain size (χ_{arm}/χ , SIRM/ χ_{arm} , SIRM/ARM)	European
905 to 907	Increasing concentration (χ , SIRM), coarsening grain size (χ_{arm}/χ , SIRM/ARM, SIRM/ χ_{arm}), rise in low coercivity minerals (Soft IRM)	European
909 & 911	Peak conditions; high concentration (χ , SIRM), coarse grain size (χ_{arm}/χ , SIRM/ARM, SIRM/ χ_{arm}), soft mineralogy (Soft IRM)	Laurentide
913 to 915	Decreasing c oncentration (χ , SIRM), decreasing grain size (χ_{arm}/χ , SIRM/ARM, SIRM/ χ_{arm}), higher coercivity mineralogy (Soft IRM)	European
917 to 919	Low concentration (χ , SIRM), finer grain size (χ_{arm}/χ , SIRM/ARM, SIRM/ χ_{arm})	European

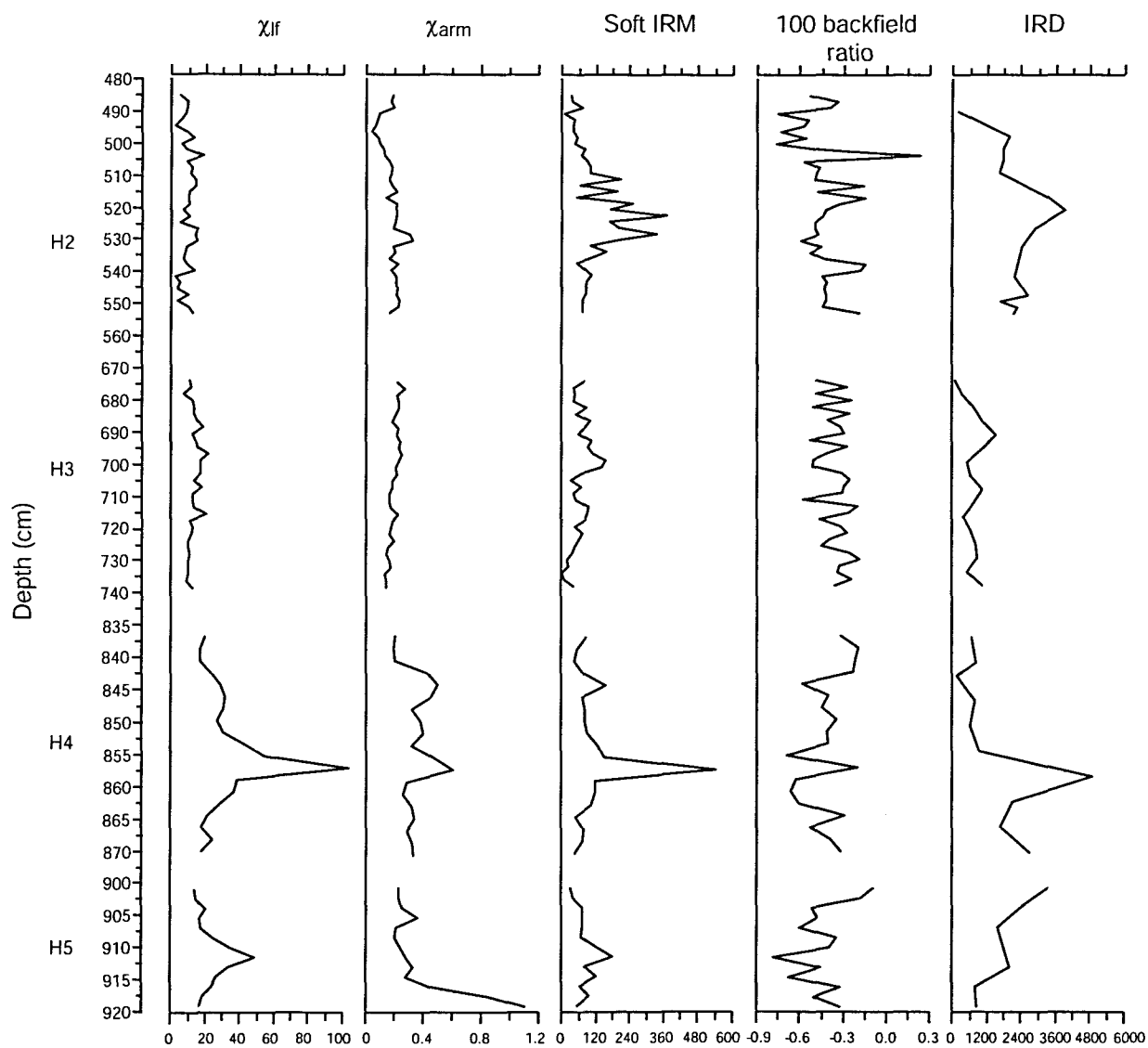


Fig. 5.36: Synopsis of data from H2, H3, H4 and H5 from MD01-2461.

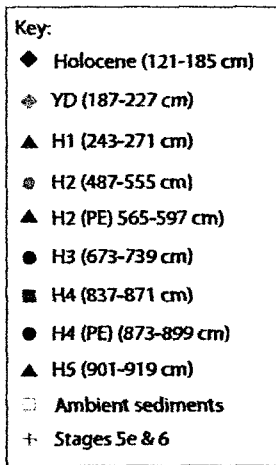
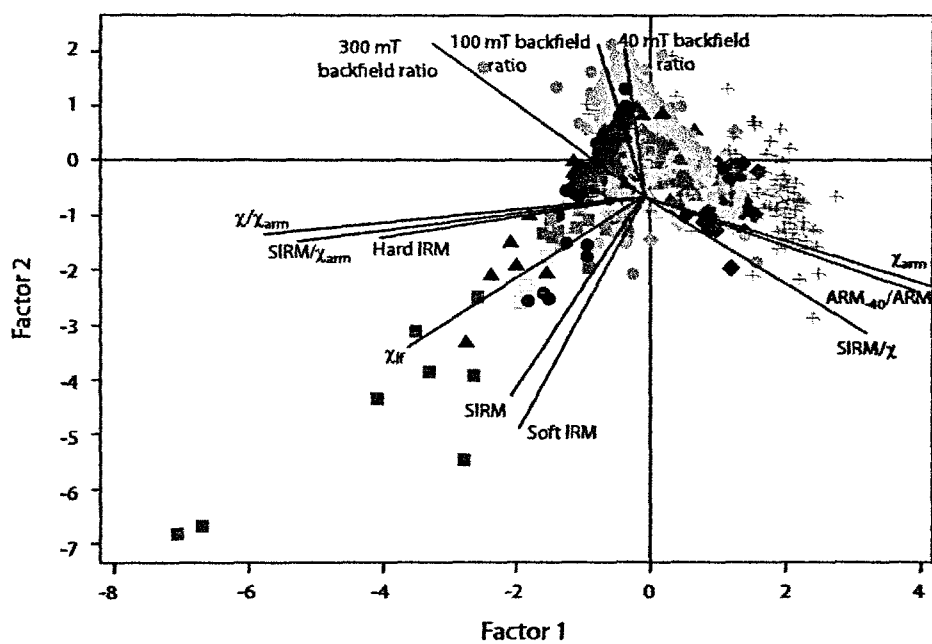


Fig. 5.37: Factor analysis results for MD01-2461.

Other aspects of MD01-2461

Ash Zone II was identified by V. Peck during the initial IRD analysis at 950 cm depth and is represented in the lithic grain count by a large peak comparable in size to H4. The magnetic characteristics at this point of the core display a slight increase in magnetic concentration of both high and low coercivity minerals and an increase in magnetic grain size. This signal is different to the tephra signature noted in OMEX 2K, which has a very low magnetic grain size. There could be several reasons for this, including different concentrations and types of tephra, and a different background matrix of sediment.

The Younger Dryas within MD01-2461 (285 cm depth) demonstrates a slight increase in magnetic concentration and grain size. The dominant minerals present appear to be of higher coercivity mineralogy. The biplots place the YD signature between the interglacial sediments and the Heinrich Event material, and are supported by the graphs taken from Bloemendal *et al.*, (1992)(Figs. 5.34 & 5.35).

The Holocene is characterised by an overall decrease in magnetic concentration, though the minerals present seem to be dominated by ferrimagnets. Magnetic grain size also decreases through the Holocene, though there are two abrupt and rapid pulses of coarser-grained material at 141 cm and 183 cm depth. The biplots show the Holocene to have a totally different signature to the glacial component of MD01-2461, and appears to operate a much less efficient transport system to those during the glacial stadial. The section of the core thought to span MIS 5e shows similar characteristic to the Holocene, though the increases and decreases are much bigger. Kandiano *et al.*, (2004) have established that temperatures in MIS 5e were up to 2°C warmer than during the Holocene. These differences would have had an effect on ocean circulation and the THC, which could be a cause for the enhanced Holocene-like magnetic signal. While this is interesting in its own right, the cause for these differences are not central to the aims of this thesis and will, therefore, not be considered further.

5.4.4 Comparison to OMEX 2K

Comparisons between the magnetic results and environmental interpretation of OMEX 2K and MD01-2461 can be made to help assess how successful the method has been in addressing the aims set out in Section 1.3. The provenance of the various sections of the cores are compared, as are the sequencing of the different inputs of material.

The Heinrich Events

OMEX 2K detailed a magnetic signature of a high concentration, large magnetic grain size and dominant ferrimagnetic minerals for the Heinrich Events. This is supported by the magnetic results from MD01-2461, though there is some disparity surrounding H2 when using χ . Statistically different groupings were also found within the HE sediments of both OMEX 2K and MD01-2461, suggesting more than one sediment source has contributed to the HL material. When examined with petrological data, these groupings were found to represent different pulses of sediment to those from the Celtic margin, creating a three-stepped structure to the HLs. An increase in European-sourced material was found at the onset of the HEs, which was either diluted, or completely replaced by Laurentide sediments before a second European input of material was discussed towards the end of the events. These patterns were also found during H2, H4, H5, and to some extent in H3 in MD01-2461, however because of the lack of detailed mineralogical data for MD01-2461, there is no non-magnetic confirmation that the steps are due to different lithologies, as was demonstrated for OMEX 2K. Acknowledging that fact, it does seem possible to identify sediments of different provenance within the HLs using magnetic methods alone.

Non-Heinrich Event ambient marine glacial sediments also appear to have a diagnostic signature. Both OMEX 2K and MD01-2461 display parameters of similar magnitudes, showing constantly low magnetic concentrations, a higher coercivity mineralogy and a grain size that is neither particularly fine nor coarse. It must be noted, following the discussion on the differing absolute values between OMEX 2K

and MD01-2461 (Section 5.4.2), that the similarity mentioned here is only seen within the ambient glacial sediments themselves and does not apply to the HEs or the interglacial/Holocene samples. The ambient glacial signal is not only shown between the two cores, but also within a core; the lowest section of MD01-2461 shows a return to the kinds of values discussed above suggesting that the record spans back to MIS 6.

The Younger Dryas and the Holocene can also be compared between the cores. The YD appears less consistent in magnitude between the cores in some parameters (IRM₁₀₀/SIRM, Soft IRM, for example), however the values still fall between the HE and Holocene sediments. The Holocene itself displays a contrast to the sediments previously discussed, as there is a significant decrease in the size of magnetic minerals along with an overall decrease in concentration and the reemergence of dominant low coercivity minerals. This pattern is also seen during what is thought to be MIS 5e in MD01-2461. The changes are greater (i.e. there is an even smaller concentration and a finer grain-size) than in the Holocene, which could be a reflection of a slightly warmer climate.

5.5 Zooming in on the Heinrich Events: H2 and H4

In order to provide a more detailed examination of possible IRD provenance variation, it was decided to focus on H2 and H4 (as 'typical' HEs) from MD01-2461 and study them at 1 cm resolution. These HLs were selected as they were easily identifiable in the core, and because detailed work had been done on H2 and H4 in other cores by various workers (e.g. Gwiazda *et al.*, 1996a; Cortijo *et al.*, 1997; Vidal *et al.*, 1997; Hemming *et al.*, 1998; Benson *et al.*, 2003). Also, due to the discrepancy in χ_{lf} at H2 between the onboard data and the measured data from this study, it was thought that a closer examination of H2 was required. The previously employed methods were performed (Section 5.4.2), though much of the data analysis was refined to reproduce, using the same approach as successfully applied in studying OMEX 2K and MD01-2461 (Sections 5.2 & 5.4.2).

5.5.1 H2 Magnetic Analysis

Down-core profiles

The close-up magnetic picture of H2 is more complex than the original whole-core analysis would suggest (Fig. 5.38). The susceptibility trace shows a larger peak at 520 – 530 cm depth than the one at 576 cm, whereas in the whole MD01-2461 record, no peak is present at 520-530 cm. The $>150\ \mu\text{m}$ IRD plot (Fig. 4.4 & 5.38; picked at a 2 cm resolution) has peaks corresponding to both the 520-530 cm and 570 cm susceptibility maxima. SIRM is also indicative of concentration, and demonstrates peaks at 522 cm, 528 cm, 530 cm, 576-577 cm and 588 cm.

The rest of the magnetic data also show some interesting results. χ_{arm} displays several peaks, demonstrating an increase in smaller ferrimagnetic grain sizes. These are found at 522 cm, 528 cm, 530 cm and 576-577 cm. Minima in χ_{arm} are found at 506 cm and 541 cm, possibly indicating the presence of larger ferrimagnetic grains. The χ_{arm} minima previously discussed in the chapter, have been associated with susceptibility peaks. In H2 however, this does not seem to be the case. Soft IRM also increases dramatically at 522 cm, 528-530 cm and 576-577 cm, as well as at 588 cm; there are smaller rises at 508 cm, 542 cm and 557 cm.

Hard IRM decreases at several of the points at which Soft IRM increases: notably at 508 cm, 527-532 cm and 541 cm. However, it also increases at 540 cm and 576-577 cm, suggesting an overall increase in magnetic grains, not just of a single mineral. This is supported by the overall increase found in the χ_{ir} record. The IRM₁₀₀/SIRM ratio is sensitive to the changes in relative concentrations in haematite and magnetite. There are significant declines in the ratio at 513 cm, 522 cm, 526-533 cm and 588 cm, along with smaller ones at 558 cm and 277 cm. This is indicative of decreasing haematite presence and increasing magnetite.

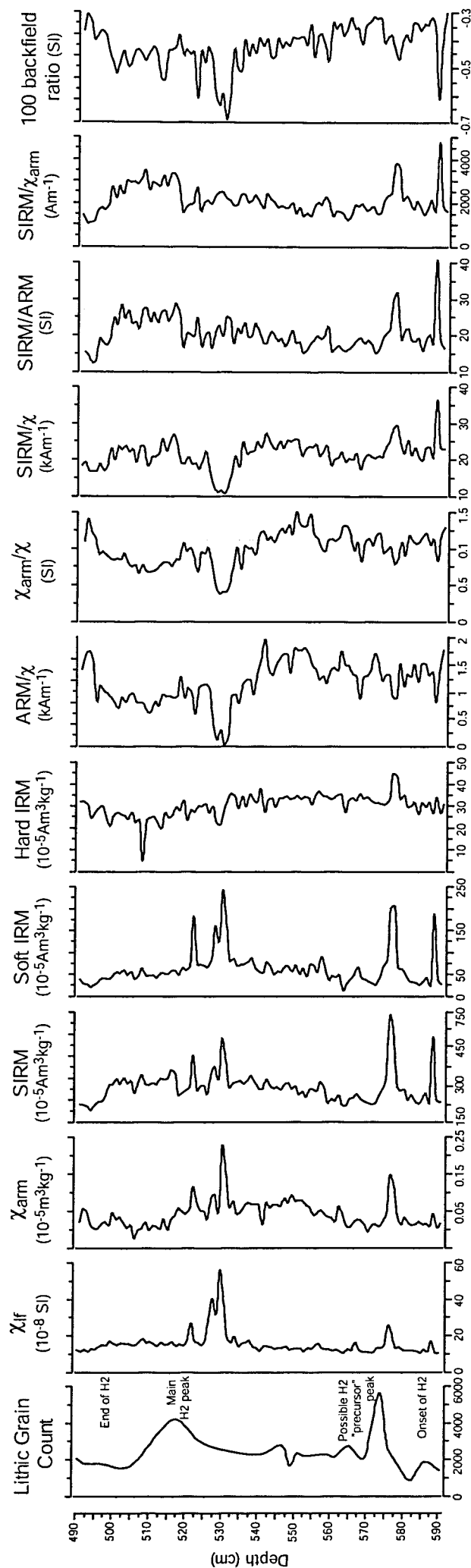


Fig. 5.38: Down-core magnetic results for the H2 section of MD01-2461. Annotations for the lithic grain count were provided by V. Peck (Pers Comm).

The grain size parameters of SIRM/χ , χ_{arm}/χ and $\text{SIRM}/\chi_{\text{arm}}$ however, are not in such agreement. SIRM/χ displays generally low values (i.e. <40), suggesting the dominance of softer magnetic minerals, however there is a substantial drop at 526-533 cm, a small one at 522 cm (increases in grain size) and two peaks at 577 cm and 588 cm (decreases in grain size). $\text{SIRM}/\chi_{\text{arm}}$ shows very little variation except for three peaks at 577 cm, 588 cm and 522 cm. These ratios suggest an increase in grain size at these depths. χ_{arm}/χ displays two peaks at 493 cm and 549-553 cm, with a series of somewhat higher values at 518 cm, 525 cm, 540 cm, 563 cm, 571 cm and 585 cm, which are representative of fine ferrimagnetic grains. There are also decreases in χ_{arm}/χ at 522 cm, 526-533 cm, 567 cm, and 576 cm, which are indicative of coarser ferrimagnetic grains, and in agreement with the SIRM/χ record. All three of the above ratios show a coarsening of magnetic grain size around the main H2 peak, as with OMEX 2K, even if χ_{arm} does not.

Summary

There are three major increases in magnetic concentration, at 576-577 cm, 526-533 cm and 522 cm and smaller rises at 588 cm, 567 cm and 557 cm. Mineralogically, these appear to be consistent with an increase in lower coercivity, softer magnetic minerals like magnetite, and a decrease in harder minerals such as haematite. The sole exception to this is at 576-577 cm depths, where an increase in both mineralogy types is seen. In terms of magnetic grain size, the pattern is a little more complicated. The parameters SIRM/χ and χ_{arm}/χ agree that 522 cm and 526-533 cm have an increased grain size, whilst χ_{arm} suggests a higher concentration of SD grains, therefore a smaller overall size. χ_{arm}/χ also indicates that the high concentration peaks at 588 cm, 576-577 cm, and 567 cm have larger grain sizes, which is supported at 588 cm, 576-577 cm and 522 cm by $\text{SIRM}/\chi_{\text{arm}}$. Again, χ_{arm} is not consistent. Overall, the grain size parameters suggest a coarse grain size at 522 cm, 526-533 cm, and 588 cm.

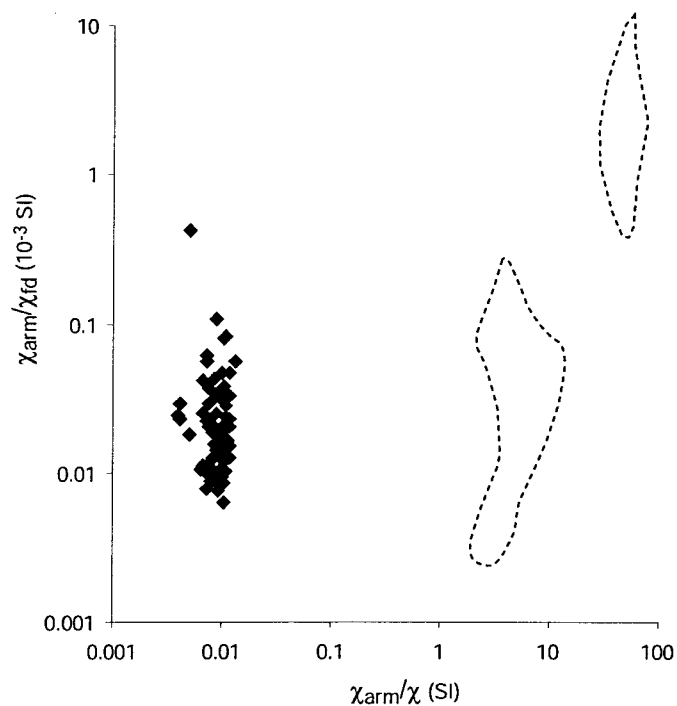


Fig. 5.39: Graph of χ_{arm}/χ versus χ_{arm}/χ_{fd} for the identification of magnetotactic bacteria within the H2 section of MD01-2461. χ_{arm}/χ values of >40 and χ_{arm}/χ_{fd} values of >1 are indicative of organic magnetite.

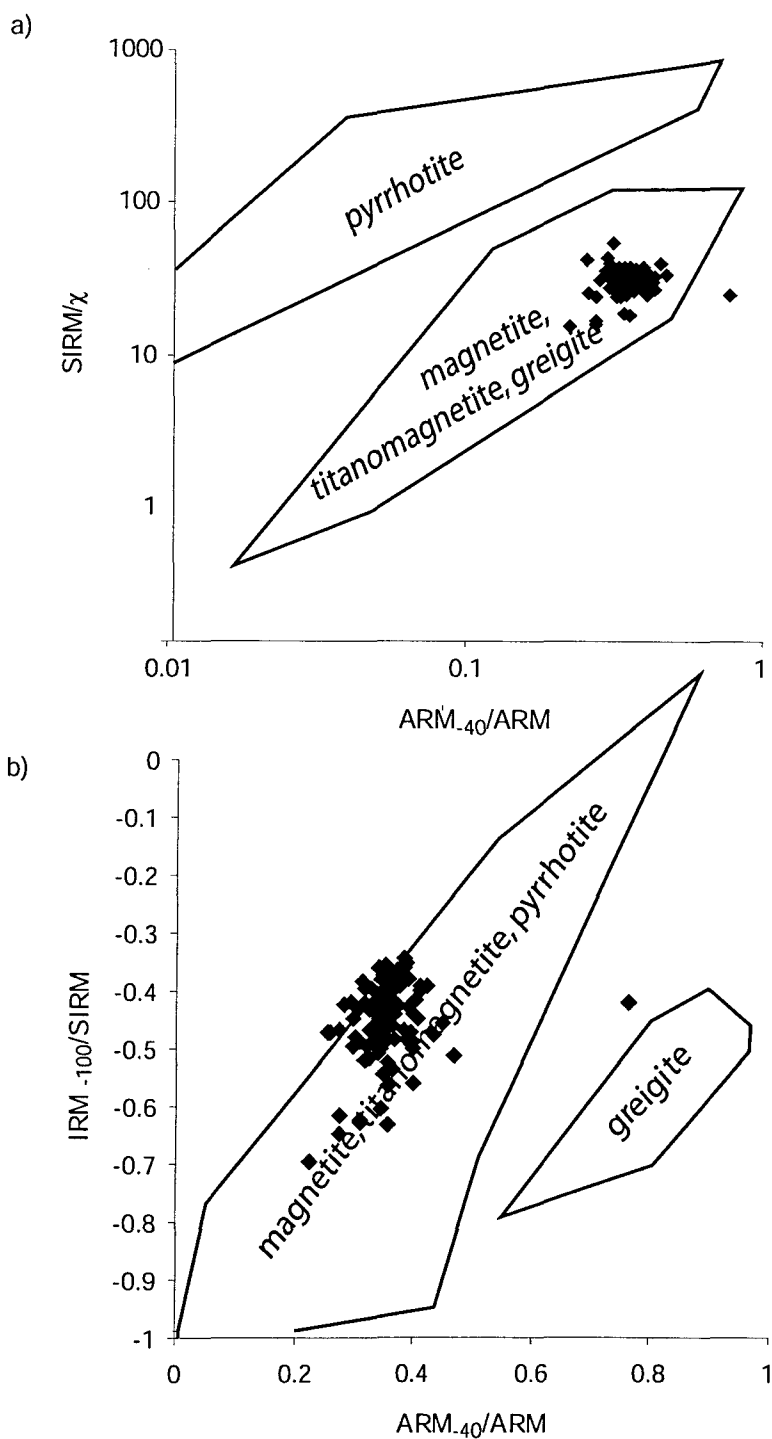


Fig. 5.40: a) Graph of ARM_{.40}/ARM versus SIRM/ χ and b) ARM_{.40}/ARM versus IRM₋₁₀₀/SIRM for the identification of the mineral greigite in the H2 subsection of MD01-2461.

Magnetotactic Bacteria and Greigite

The plots in Figs. 5.30, 5.31 & 5.32 for the analysis of magnetotactic bacteria and diagenetic greigite in core MD01-2461 have shown that there is little influential presence of either. Therefore, it was decided unnecessary to repeat the procedures for H2 and H4. However, given the very different χ_{lf} measurements obtained on the discrete H2 samples compared with the whole-core data, the most diagnostic graphs were re-drawn for H2 to check the robustness of the previous interpretations. The graphs were χ_{arm}/χ versus χ_{arm}/χ_{fd} from Oldfield, (1992) for the detection of MTB, and the two graphs from Peters & Thompson, (1998) (ARM_{-40}/ARM versus $SIRM/\chi$ and ARM_{-40}/ARM versus $IRM_{-100}/SIRM$), for the detection of greigite (Figs. 5.39 & 5.40). No differences were seen in the new greigite plots, but as they are not affected by susceptibility, this was to be expected. The MTB graph, however, plots at significantly lower values than the whole-core data, but as this does not put the sediment into the range of MTB, any effect can safely be discounted.

Therefore, based on the information above, and that discussed in Section 5.4.2, it can be assumed that MTB and digenetic greigite do not influence the magnetic characteristics of the H2 and H4 material from MD01-2461.

Biplots

Fig. 5.41 shows the biplots drawn for the H2 section of MD01-2461. They replicate the plots in Fig. 5.17 for OMEX 2K and Fig. 5.33 for MD01-2461, as these have proven to be most diagnostic of provenance in this study.

The plots display significant variations in sediment characteristics within H2. Five specific samples (527-530 cm) show a much higher concentration than the rest, along with a large grain size and dominant low coercivity mineralogy. Other samples also show distinctive behaviour: 508 cm displays a significantly low coercivity mineralogy but no increase in general concentration, 522 cm has a high concentration of magnetite-type material without the increased grain size seen at 527-530 cm, 588 cm displays coarse grains of low coercivity mineralogy but no

overall increase in concentration, and 576-577 cm shows an increase in concentration with no other obvious magnetic traits. Using the interpretation discussed in Sections 5.2 and 5.4.2, it is suggested that the material at 527-530 cm originates from North America, whilst the rest of H2 is European-sourced sediment. Within this European material however, further variations are seen in the magnetic data, such as the high concentration at 576-577 cm and 522 cm. Without access to petrological data or an accurate age chronology, as yet, it is difficult to assess whether these differences are due to sediment type, or simply inputs from varying sections of the European Ice Sheets or ice streams. However, following suggestions by Scourse *et al.*, (2000), and the extent of the BIS during the LGM described by Hall & McCave, (1998b), it is speculated that the first pulse of material (576-577 cm) is what has been called the H2 “precursor” in OMEX 2K, whilst the second input (522 cm) corresponds to the post H2 chalk deposition noted during the OMEX 2K detailed mineralogical analysis (Furze. Pers. Comm. 2003)(Fig. 5.5). The differences are possibly due to deposition by different ice streams or outwash channels flowing from the BIS as depicted by Hall & McCave, (1998b) and Scourse *et al.*, (2000). It is reiterated that, without further petrological data these are tentative speculations.

5.5.2 Environmental Interpretation

The higher resolution magnetic analysis of the H2 subset from MD01-2461 appears to resolve some of the issues raised during the whole-core work. Firstly, a susceptibility trace more comparable to the onboard data is seen with a double peak at c. 530 cm depth. This means that some of the inter-parametric ratios, such as χ_{arm}/χ and SIRM/ χ , are also brought into line with values seen in the other HEs and OMEX 2K. In addition, this more detailed analysis has enabled a more confident identification of the possible provenance of selected samples through H2 and, in particular, the identification of samples displaying magnetic properties characteristic of an LIS source.

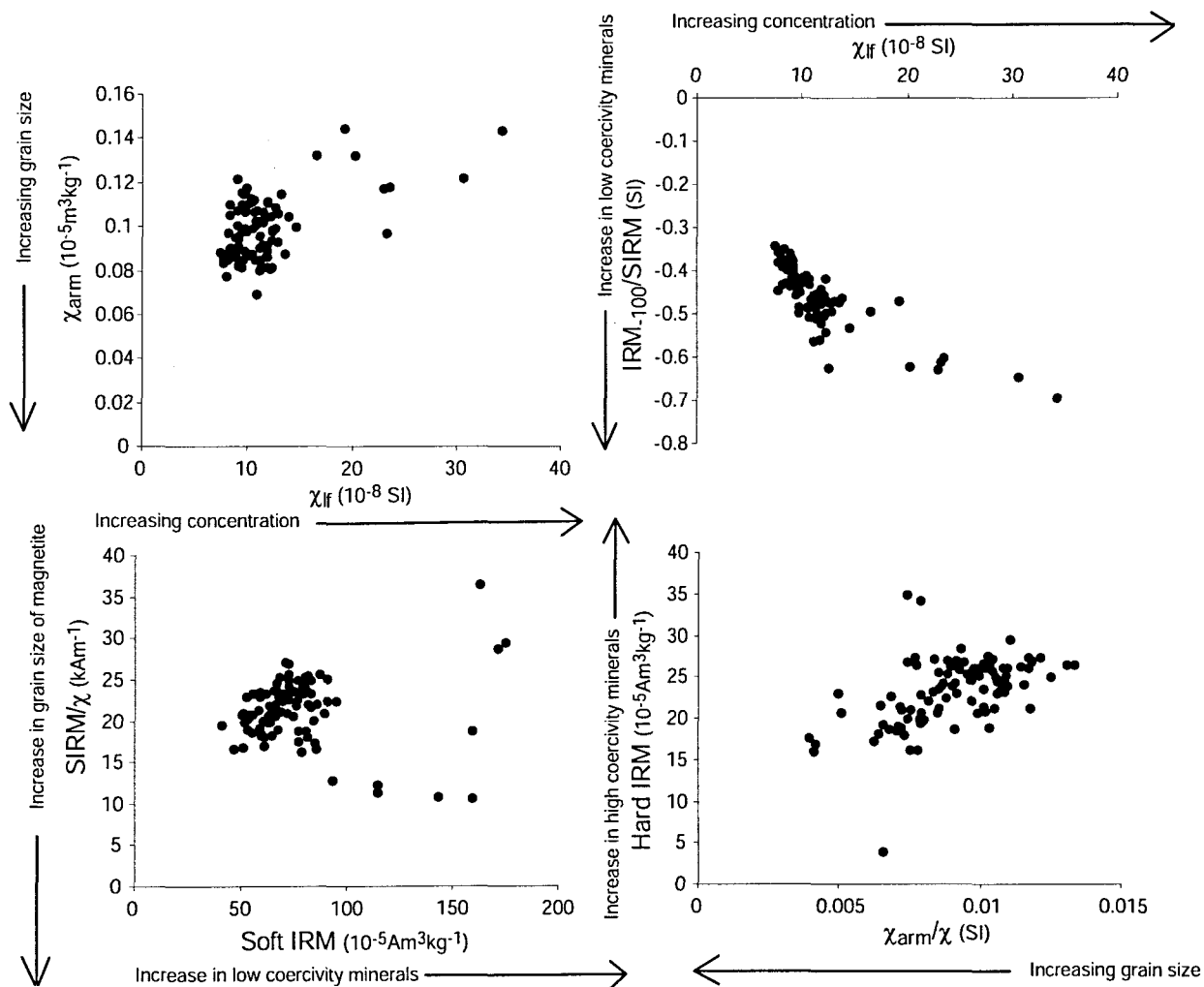


Fig. 5.41: Biplots for the H2 section of MD01-2461

Table 5.8: The magnetic characteristics of the H2 section of core MD01-2461 and its probable source areas.

HL sample (by depth)	Magnetic Characteristics	Potential Provenance
490 to 521	Low concentration (χ , SIRM), varying grain size, however remains relatively fine in comparison to peak HE grain size (χ_{arm}/χ , SIRM/ χ), higher coercivity mineralogy (Hard IRM, Soft IRM)	European
522	Relatively high concentration (χ , SIRM), slight coarsening of grain size (χ_{arm}/χ), low coercivity mineralogy (Soft IRM, 100 backfield ratio)	Other source?
523 to 526	Low concentration (χ , SIRM), fine grain size (SIRM/ χ , χ_{arm}/χ), relatively hard mineralogy (Hard IRM, Soft IRM, 100 backfield ratio)	European
527	Higher concentration (χ , SIRM), coarser grain size (SIRM/ χ , χ_{arm}/χ), softer mineralogy (Soft IRM, Hard IRM, 100 backfield ratio)	Laurentide
528 to 530	Peak HE conditions; high concentration (χ , SIRM), coarser grain size (χ_{arm}/χ , SIRM/ χ) and lower coercivity mineralogy (Hard IRM, Soft IRM, 100 backfield ratio)	Laurentide
531	Higher concentration (χ , SIRM), coarser grain size (SIRM/ χ , χ_{arm}/χ), softer mineralogy (Soft IRM, Hard IRM, 100 backfield ratio)	Laurentide
532 to 575	Low concentration (χ , SIRM), varying grain size, however remains relatively fine in comparison to peak HE grain size (χ_{arm}/χ , SIRM/ χ), higher coercivity mineralogy (Hard IRM, Soft IRM)	European
576 & 577	Relatively high concentration (χ , SIRM), coarsening of grain size (all parameters), increase in high and low coercivity minerals (Soft IRM, Hard IRM)	Other source?
579 to 587	Low concentration (χ , SIRM), finer grain size (χ_{arm}/χ , SIRM/ χ), high coercivity mineralogy (all parameters)	European

Table 5.9: The magnetic characteristics of the H4 section of core MD01-2461 and its probable source areas.

HL sample (by depth)	Magnetic Characteristics	Potential Provenance
837 to 845	Low concentration (χ , SIRM), finer grain size (χ_{arm}/χ , SIRM/ χ_{arm}), hard mineralogy (100 backfield ratio)	European
846 to 848	Slightly higher concentration (χ), fine grain size (χ_{arm} , SIRM/ARM), relatively hard mineralogy (100 backfield ratio, Hard IRM)	European with the introduction of Laurentide material
849 to 851	Higher concentration (χ , SIRM), coarsening grain size (χ_{arm}/χ , SIRM/ARM, SIRM/ χ_{arm}), softer mineralogy (100 backfield ratio)	Laurentide
852 & 853	Peak conditions; very high concentration (χ , SIRM), coarse grain size (χ_{arm}/χ , SIRM/ARM, SIRM/ χ_{arm})	Laurentide
854 & 855	Higher concentration (χ , SIRM), coarsening grain size (χ_{arm}/χ , SIRM/ARM, SIRM/ χ_{arm}), lower coercivity mineralogy (Hard IRM, Soft IRM)	Laurentide
856 to 858	Lower concentration (χ , SIRM), still a relatively coarse grain size (χ_{arm} , χ_{arm}/χ), relatively soft mineralogy (Soft IRM, Hard IRM, 100 backfield ratio)	Laurentide with a re-emergence of European material
859 to 871	Low concentration (χ , SIRM), finer grain size (χ_{arm}/χ , SIRM/ χ_{arm} , SIRM/ARM), harder mineralogy (100 backfield ratio)	European

Table 5.8 contains a revised list of potential LIS and EIS samples from H2. Table 5.8 has helped to constrain the sequence of events during H2 within MD01-2461, though some of the samples still have a question mark over their provenance. This can be resolved with further petrological and detailed geochemical analysis. Table 5.8 reveals a similar three-step structure to H2 in MD01-2461 as the HEs in OMEX 2K, with an initial input of European material, followed by the main Laurentide HE peak, and then a re-emergence of European material towards the end of the HE. Timescales can not be discussed for this sequencing due to the lack of a detailed age model (see Section 5.4.1).

Mann Whitney U tests were performed on the subset of H2, using the sample identified in Table 5.8 to try to constrain the earlier data (Section 5.4.3) further. The tests can be found in Appendix 2diii (Pg 356) and return P-values of <0.05 for all parameters except Hard IRM, SIRM/ARM and SIRM/ χ_{arm} (the latter two parameters are essentially the same, see Section 5.2.1 and Table 4.9). Therefore, there is a significant difference between the LIS and EIS fractions of the H2 subset for all parameters except Hard IRM, SIRM/ARM and SIRM/ χ_{arm} .

5.5.3 Comparison with H2 from other cores

MD95-2006 is a 30 m long giant piston core (see Section 3.3) originating from the Barra Fan (North West Scotland, 57°01.82N, 10°03.48W). Extensive work has been carried out on this core (e.g. Kroon *et al.*, 2000; Knutz *et al.*, 2001), with H2 and H4 being well constrained and subjected to much analysis. Access to samples from H2 and H4 was provided by Dr B. Austin and Miss S. Leigh (St Andrews), and the same magnetic analysis was performed as for MD01-2461, enabling a comparison between the same HEs in cores from different areas around the BIS.

H2 spans 70 cm between the depths 1600 – 1670cm, with material available at a 1 cm resolution. The sediment was collected and prepared following the methods described in Section 4.3. Carbonate content had been measured

previously and the data made available to this study. The MD95-2006 samples were corrected using the methods outlined in Section 4.4.1 for OMEX 2K. Fig. 5.42 shows the down-core magnetic results and IRD concentration for MD95-2006 H2.

The susceptibility trace shows two large, and two smaller peaks at 1617 cm, 1645 cm, 1651 cm and 1661 cm respectively, all of which also display peaks in IRD. The first, and largest peak coincides with maxima in χ_{arm} , SIRM, Soft IRM, SIRM/ARM and SIRM/ χ_{arm} and minima in Hard IRM, χ_{arm}/χ , SIRM/ χ and IRM-100/SIRM. This indicates an abundance of coarse-grained ferrimagnetic minerals. The second χ increase (1645 cm depth), has been confirmed as a dolomitic carbonate peak (S. Leigh, Pers. Comm. 2004), and corresponds to a decrease in χ_{arm} , a slight increase in SIRM and Soft IRM, a larger declines in Hard IRM, χ_{arm}/χ and IRM-100/SIRM than the first χ peak, and larger increases in SIRM/ARM and SIRM/ χ_{arm} . This, too, is indicative of coarse-grained ferrimagnets, however the larger increases in SIRM/ARM and SIRM/ χ_{arm} , along with the decline in χ_{arm} and the bigger drops in Hard IRM and IRM-100/SIRM, suggest coarser grains of much lower coercivity. The two smaller χ peak samples show increases in SIRM, Soft IRM, SIRM/ARM and SIRM/ χ_{arm} and slight drops in χ_{arm}/χ and IRM-100/SIRM.

Figs. 5.43, 5.44 and 5.45 show the graphs that are thought to be diagnostic of magnetotactic bacteria and greigite, in order to assess the sediments of MD95-2006 for the presence of either of these minerals. None of the plots identify MTB or greigite within the H2 section of MD95-2006.

The biplots seen in Figs. 5.17, 5.33 and 5.41 are proven to differentiate between potential LIS and EIS samples, therefore they are re-drawn here (Fig. 5.44). Four very distinct samples are identifiable on all four biplots; 1617 cm, 1644 cm, 1645 cm and 1661 cm, with the obvious LIS-type signal described in Table 5.5 and 5.8.

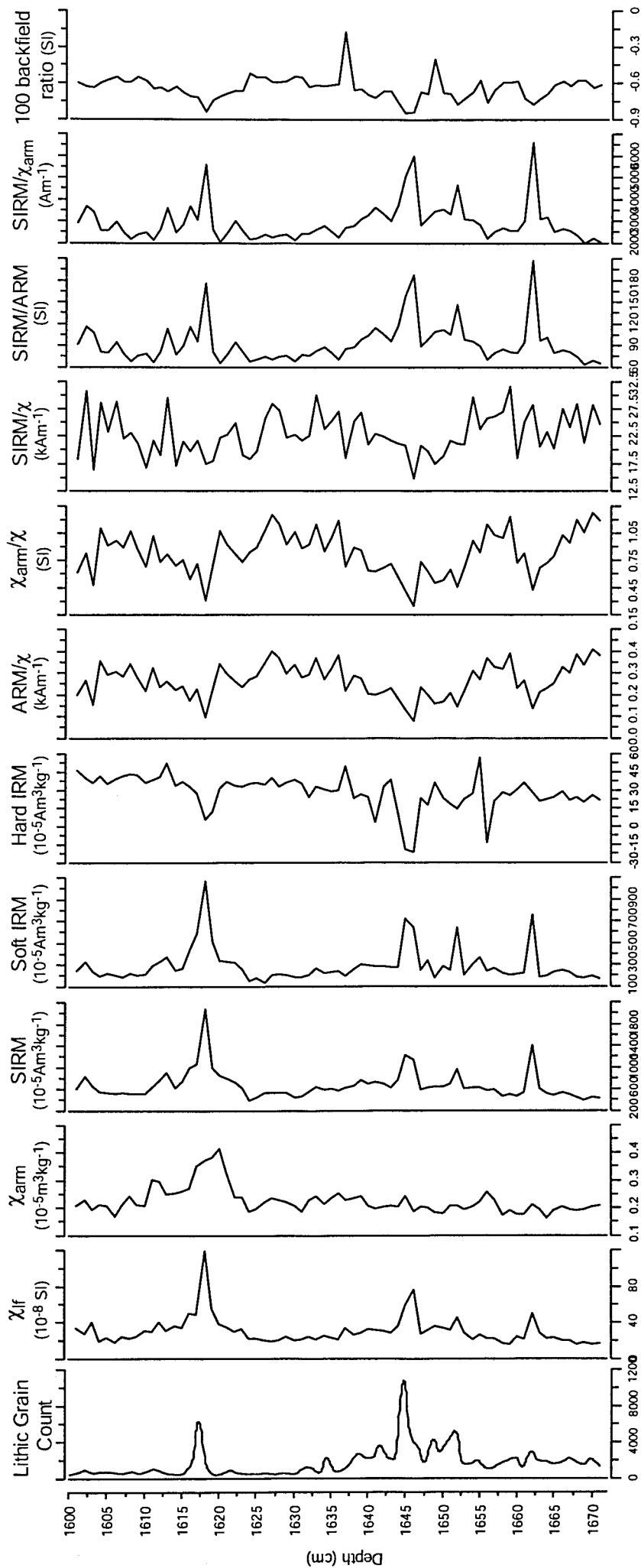


Fig. 5.42: Down-core magnetic results for the H2 section of MD95-2006. IRD data courtesy of Miss S. Leigh.

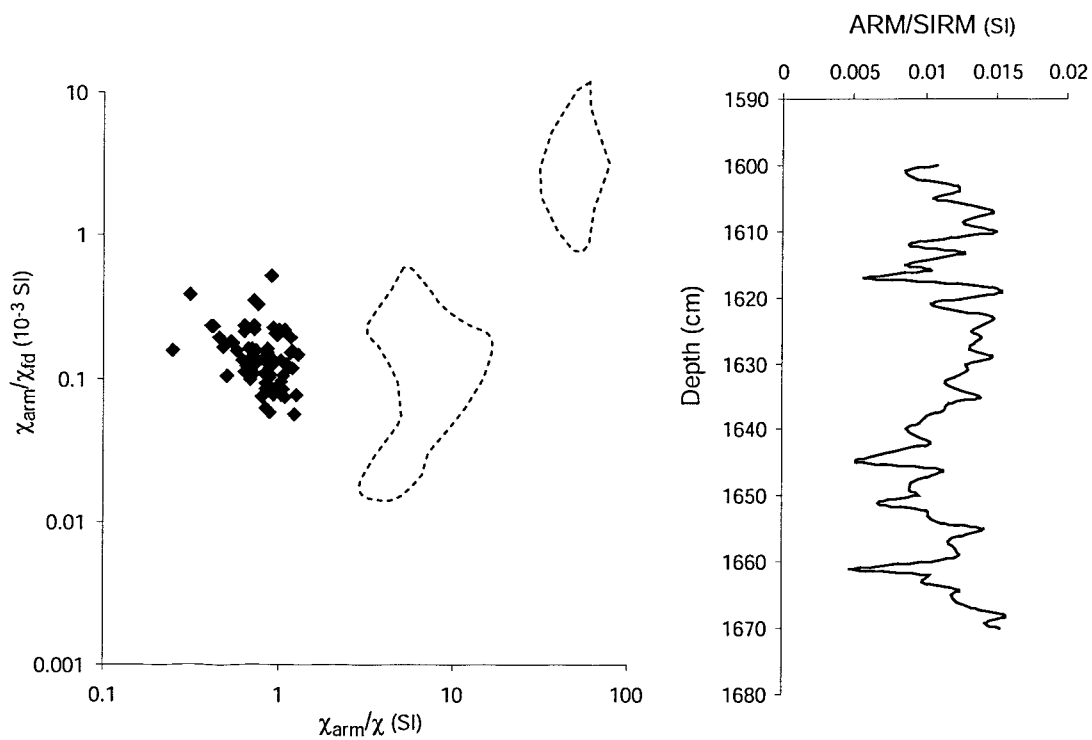


Fig. 5.43: Plots used for the identification of magnetotactic bacteria in the H2 section of MD95-2006.

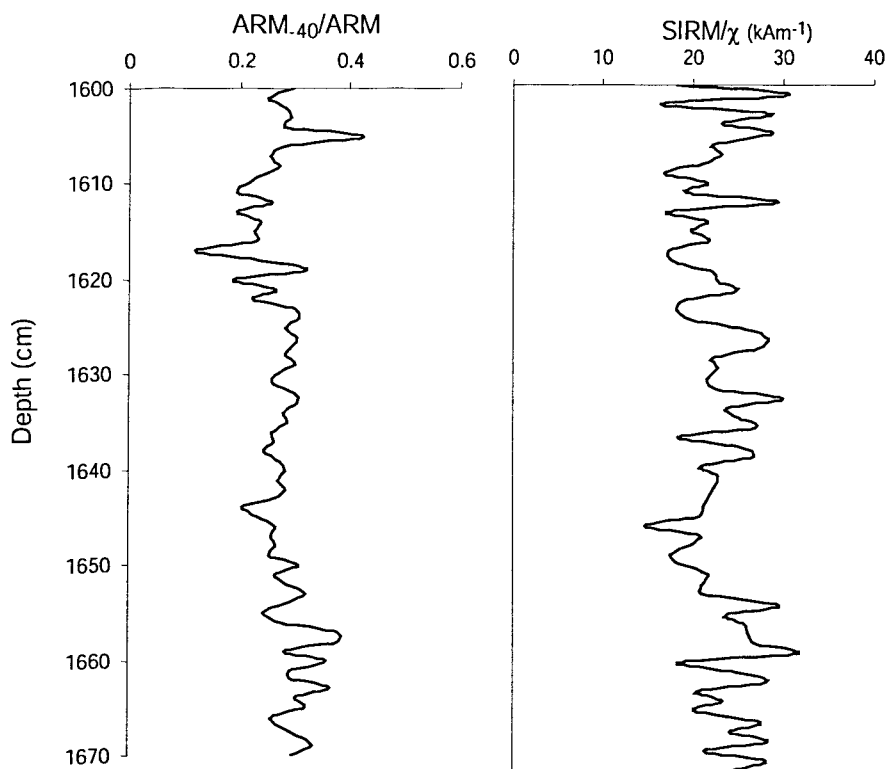


Fig. 5.44: Plots used for the identification of the minerals greigite in the H2 section of MD95-2006.

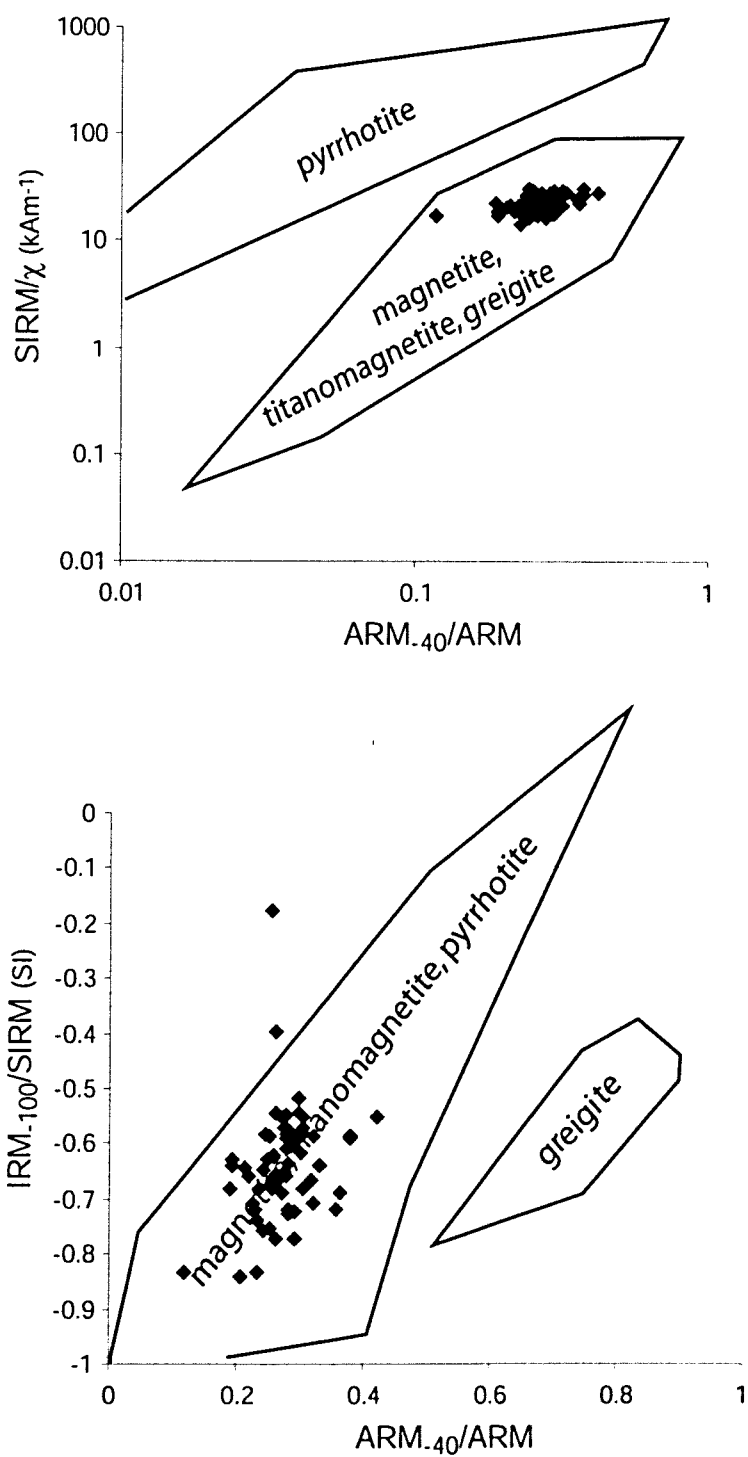


Fig. 5.45: Biplots for the analysis for the presence of greigite in the H2 section of MD95-2006.

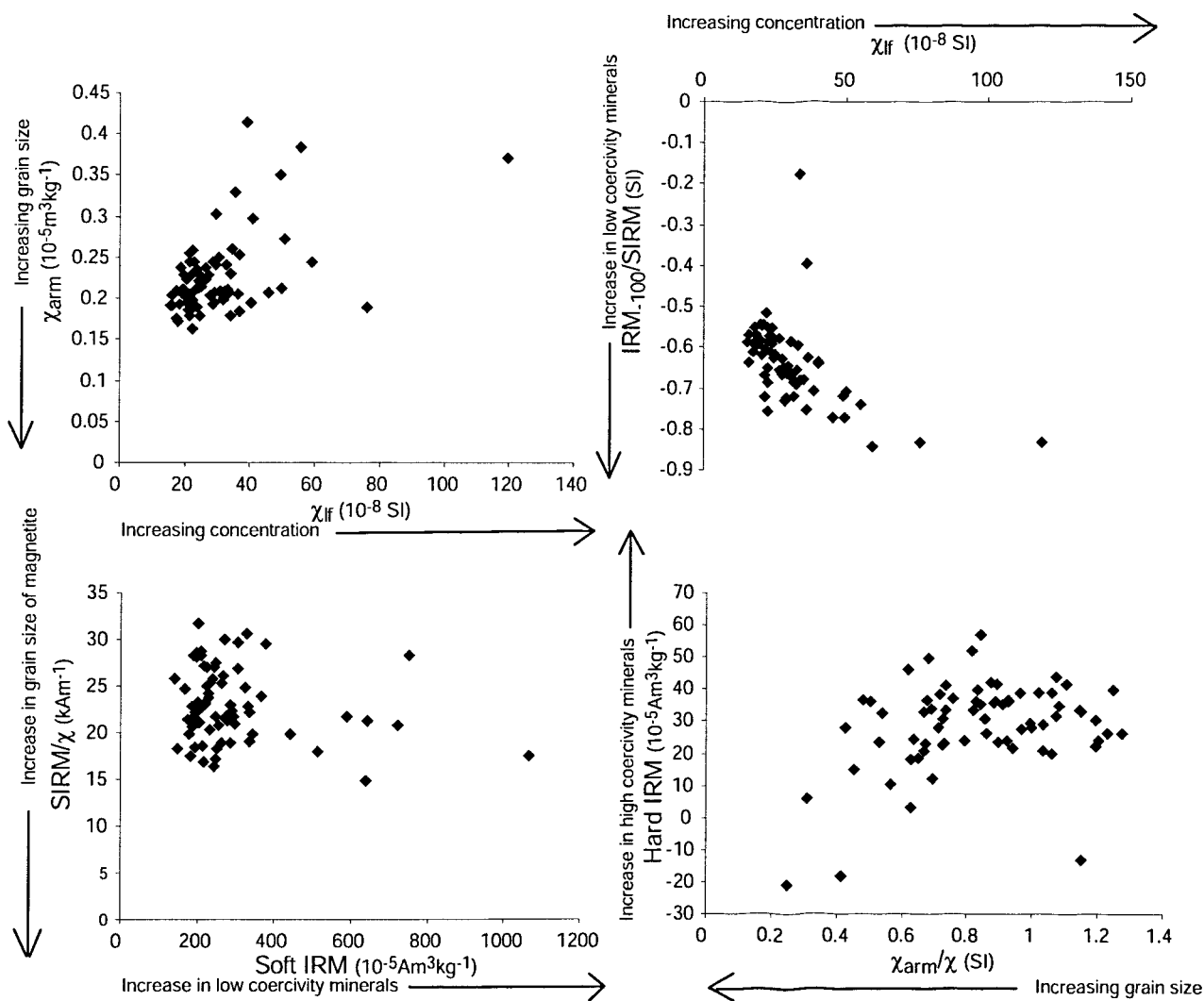


Fig. 5.46: Biplots for the H2 section of MD95-2006.

Comparison of H2 between MD01-2461, OMEX 2K and MD95-2006

In MD01-2461 and OMEX 2K, H2 displays a three-stepped structure, which has been identified using petrological analysis on OMEX 2K as an input of European material, followed by Laurentide sediment and then European material again. However, this pattern is less clear in MD95-2006. In MD95-2006, there appear to be four pulses of material over the H2 interval here, in addition to the background sediments; the third of which has been confirmed as dolomitic carbonate by mineralogy (S. Leigh Pers. Comm. 2004). Two pulses occur prior to this LIS input, one of which is represented by a much smaller χ increase suggesting a European origin, and one with a χ peak of similar magnitude as the LIS sample. The mineralogy of the peaks suggests low coercivity. After the main LIS peak, there is another high χ peak which is larger than the LIS peak and displays similar characteristics to the lower peak, with the exception of the parameter χ_{arm} .

In Section 5.5.1 the possibility of different ice streams causing slight differences in European magnetic characteristics was introduced, following a suggestion by Scourse *et al.*, (2000). It is known that during H2 the location of the BIS was very close to the site of MD95-2006, and that large quantities of material were being released into the area (Wilson *et al.*, 2002). Therefore, it is suggested that the peak found at 1645 cm is the main LIS HE peak and the others are various inputs of European material. This discussion has revealed, however, that the structure of H2 in MD95-2006 is actually similar to that found in both MD01-2461 and OMEX 2K even if the quantities of material are different. There appear to be several different inputs of European material during the first section of H2, followed by a pulse of Laurentide material, which in turn is replaced by European material. Hence, the European-Laurentide-European sequence is still observed.

5.5.4 H4 Magnetic Analysis

Down-core profiles

The H4 data is slightly more straight-forward to interpret than the H2 results (Fig. 5.47). The IRD plot is much clearer, with a significant peak at 849-857 cm and smaller ones at 863 cm, 871 cm and 879 cm. There is also a rise below 900 cm, which could be attributed to H5. The susceptibility record displays a very large peak, similar to the ones seen in OMEX 2K at 857-849 cm. There are also smaller peaks at 842 cm, 872 cm and 913-906 cm (H5). The rises in concentration are supported by SIRM data at 842 cm, 850-856 cm and 906-913 cm.

χ_{arm} decreases in size (increases in value) at 830-833 cm and 888-897 cm, and increases in size (decreases in value) at 811 cm, 858 cm, 886 cm and 906 cm. Soft IRM demonstrates significant increases in ferrimagnetic minerals at 842cm, 850-856 cm and 906-913 cm and a less significant rise at 859 cm. There is a slight drop in Soft IRM for one sample, 811 cm, which consists of a large clast (2.5 cm diameter) with little surrounding sediment. This sample displays a very large peak in Hard IRM, suggesting that the pebble contains haematite, and is supported by another very large peak seen in the IRM-100/SIRM ratio record. There are also maxima in the Hard IRM record at 842 cm, and 852-856 cm and a slight rise at 830-839 cm. The IRM-100/SIRM backfield ratio falls significantly at 795 cm and 840 cm and smaller dips at 850-855 cm, 865 cm and 897-922 cm.

SIRM/ χ shows one sample with a very high value, sample 811 cm, suggesting that it has a higher coercivity signal than the rest of H4. The individuality of the clast found at 811 cm depth can account for the distinct magnetic properties displayed at this depth, but without further investigation using more advanced techniques cannot be described in more detail. The other samples in H4 have a softer signature, with increases in grain size at 848-855 cm, 872 cm and 906-913 cm, and decreases in size at 842 cm and 855 cm. SIRM/ χ_{arm} has large peaks at 811 cm, 841-843 cm, 850-856 cm, 905-911 cm, with a smaller peak at 864

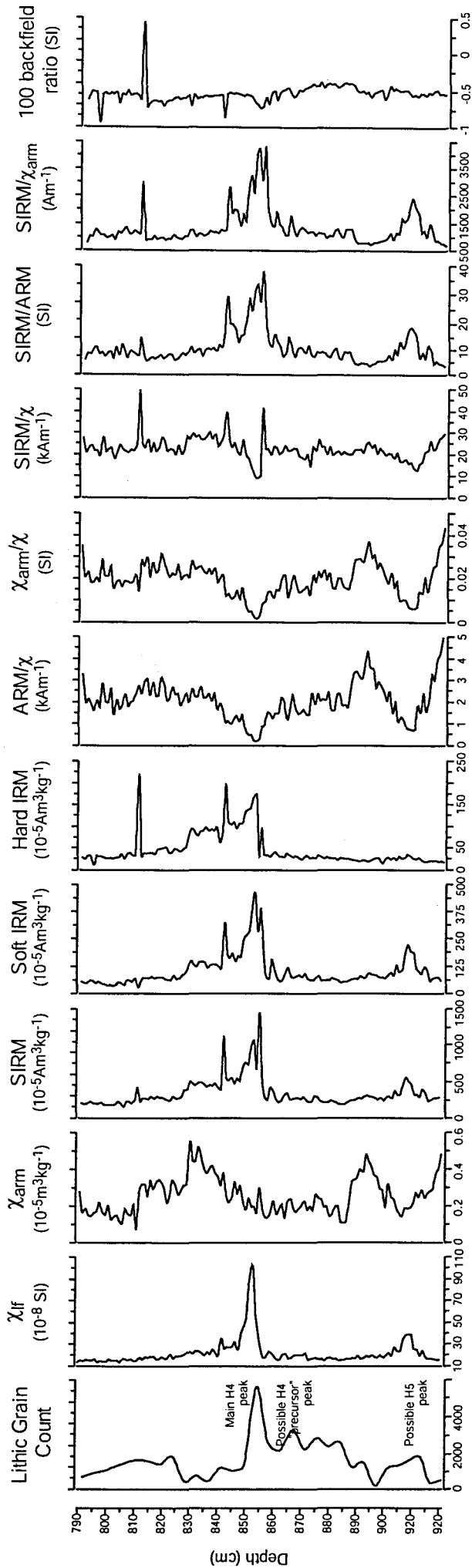


Fig. 5.47: Down-core magnetic results for the H4 section of MD01-2461. Annotations for the lithic grain counts provided by V. Peck (Pers Comm)

cm, all suggesting grain size rises. Finally, χ_{arm}/χ displays the presence of fine grained ferrimagnetic minerals with maxima at 790-830 cm and 887-898 cm. Minima occur at 840-858 cm and 903-912 cm, representing coarser grained ferrimagnetic minerals.

Summary

Significant increases in magnetic concentration occur at 849-857 cm depth, with smaller rises at 842 cm and 906-913 cm. The area between 906 cm and 915 cm probably corresponds to H5 on the basis of both the provisional chronology and magnetic data. Rises in both hard and soft minerals also occur at 850-856 cm and 842 cm. Soft minerals appear to increase at H5, whereas hard minerals do not. There is also a slight rise in hard minerals between 830-839 cm. At 811 cm, soft minerals decrease slightly while hard minerals show a very significant peak. Sample 811 cm consists of one large pebble, with very little surrounding sediment, which seems to be composed of largely high coercivity material. The size parameters dependent on ferrimagnetic minerals (χ_{arm} and χ_{arm}/χ) show sample 811 as a decrease in size. As sample 811 cm is high coercivity in type, other grain size parameters not so dependent on ferrimagnetic minerals must be examined (e.g. SIRM/ χ and SIRM/ARM). These display an increase in size. Increases in magnetic grain size are also shown by all parameters at 903-913 cm and 840-858 cm. Decreases in size are found at 887-900 cm and 830-833 cm.

Biplots

Again, biplots were drawn for the H4 subsection of MD01-2461, and differences in magnetic characteristics were observed (Fig. 5.48). As with OMEX 2K, and the whole-core measurements of MD01-2461, including H2, some samples have a high concentration of large-grained ferrimagnetic minerals, most notably between 850-854 cm. Samples 907-910 cm also display most of these characteristics, but to a lesser degree, χ_{arm}/χ seeming most able to discriminate this behaviour. These are potentially H5 samples, as it is possible that H5 was sub-sampled along with H4 (see Section 4.3). Other samples from H4 also have distinctive magnetic signals, such as sample 811 cm, which demonstrated a marked rise in Hard IRM

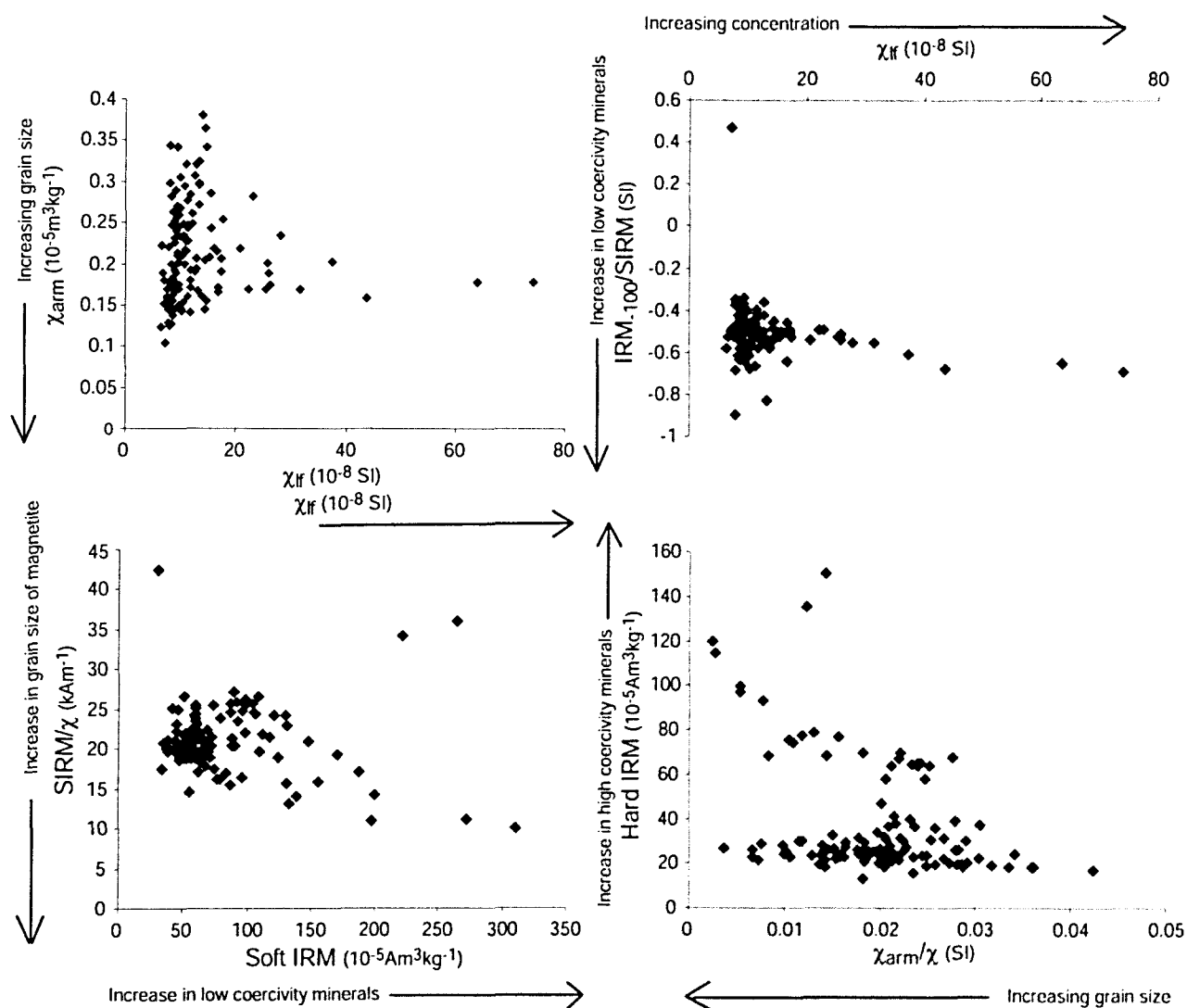


Fig. 5.48: Biplots for the H4 section of MD01-2461

picked up in the down-core profiles. Here, it shows a massive IRM₁₀₀/SIRM value of +0.5, one of the smallest Soft IRM values and a large SIRM/ χ value, all of which suggest a dominant high coercivity mineralogy, for example, haematite. Sample 842 cm also demonstrates an intriguing magnetic signature, with either a fine-grained ferrimagnetic content, as suggested by the Soft IRM v. SIRM/ χ plot, or a coarse-grained high coercivity mineral content (χ_{arm}/χ v. Hard IRM). SIRM/ χ is, however, dependent on mineralogy, with higher values indicative of haematite, supporting the latter proposal of a coarse-grained antiferromagnetic input.

Again, the results of Sections 5.2 and 5.4.2, indicate the material in samples 850-854 cm should be attributed to the LIS, with the remaining sediment being predominantly European. The magnetic characteristics at 811 cm depth are associated with the large pebble sampled, the mineralogy of which is as yet, unknown. Sample 842 cm also displays some interesting magnetic data, but as with H2 and sample 811 cm, without any petrological data, interpretation of these variations in terms of lithology and provenance is hampered.

2.5.5 Environmental Interpretation

The analysis of the H4 subsection of MD01-2461 serves to reinforce the interpretation of the whole-core analysis, with large increases in concentration, grain size and both low and high coercivity minerals. The higher resolution analysis performed over the H4 interval has also allowed some additional information to be gleaned regarding the depositional sequence of H4. The main H4 peak appears to be positioned at 850-854 cm depth, with some sort of magnetic “post-cursor” at 842 cm that is not particularly prominent in the IRD data. There is also a higher concentration of IRD input between the depths of 863-885 cm, however, very little else is noted throughout the other magnetic records at this depth.

The biplots from the H4 subsection of MD01-2461 highlights the same “peak HE” samples as the whole-core analysis, including the extra samples created by the 1 cm resolution. Table 5.9 expands the list of potential sources for the samples

found in Table 5.7 for the H4 subsection.

Mann Whitney U tests for the samples in Table 5.9 (Appendix 5eiii, Pg 361) return P-values of <0.05 for all parameters except χ_{arm} . Therefore, there is a significant difference between the potential LIS and EIS fractions of H4 for all parameters, with the exception of χ_{arm} .

2.5.6 Comparison to H4 in other cores (MD95-2006)

Fig. 5.49 shows the down-core magnetic results and IRD concentrations for H4 from MD95-2006. H4 in this core, spanned a total of 60 cm, however, it has been extensively sampled during previous analysis and therefore material was only available from every second centimeter for magnetic measurements.

The susceptibility trace for H4 shows a large peak at 2481 cm depth, which coincides with the largest IRD peak and declines in χ_{arm} , Hard IRM, ARM/ χ , SIRM/ χ , χ_{arm}/χ , and IRM-100/SIRM with increases in Soft IRM, SIRM/ χ_{arm} and SIRM/ARM. These results suggest an increase in concentration and grain size of magnetic minerals of a lower coercivity signature. Further up the H4 section there are three more susceptibility peaks in close succession to each other, all much smaller than the first peak. The IRD trace here shows several inputs of lithic material. The first of these three χ peaks is found at 2461 cm depth and is associated with a large peak in χ_{arm} , and increases in Soft IRM and Hard IRM (a greater increase in Hard IRM than Soft IRM is seen). The grain size parameters are very varied over this period, however, there does appear to be a slight increase in SIRM/ARM and a small decrease in χ_{arm}/χ . This is indicative of a slight increase in coarser minerals of both high and low coercivity, though the IRM-100/SIRM ratio (and larger increase in Hard IRM) suggests an overall, higher coercivity mineralogy. The second susceptibility peak (2457 cm) also displays a slight increase in both Hard and Soft IRM, as well as in SIRM/ARM and SIRM/ χ_{arm} and decreases in χ_{arm}/χ and SIRM/ χ , which are all suggestive of coarser grained minerals. A slight dip in the IRM-100/SIRM ratio suggests a softer than ambient mineralogy, however there is still an increase in

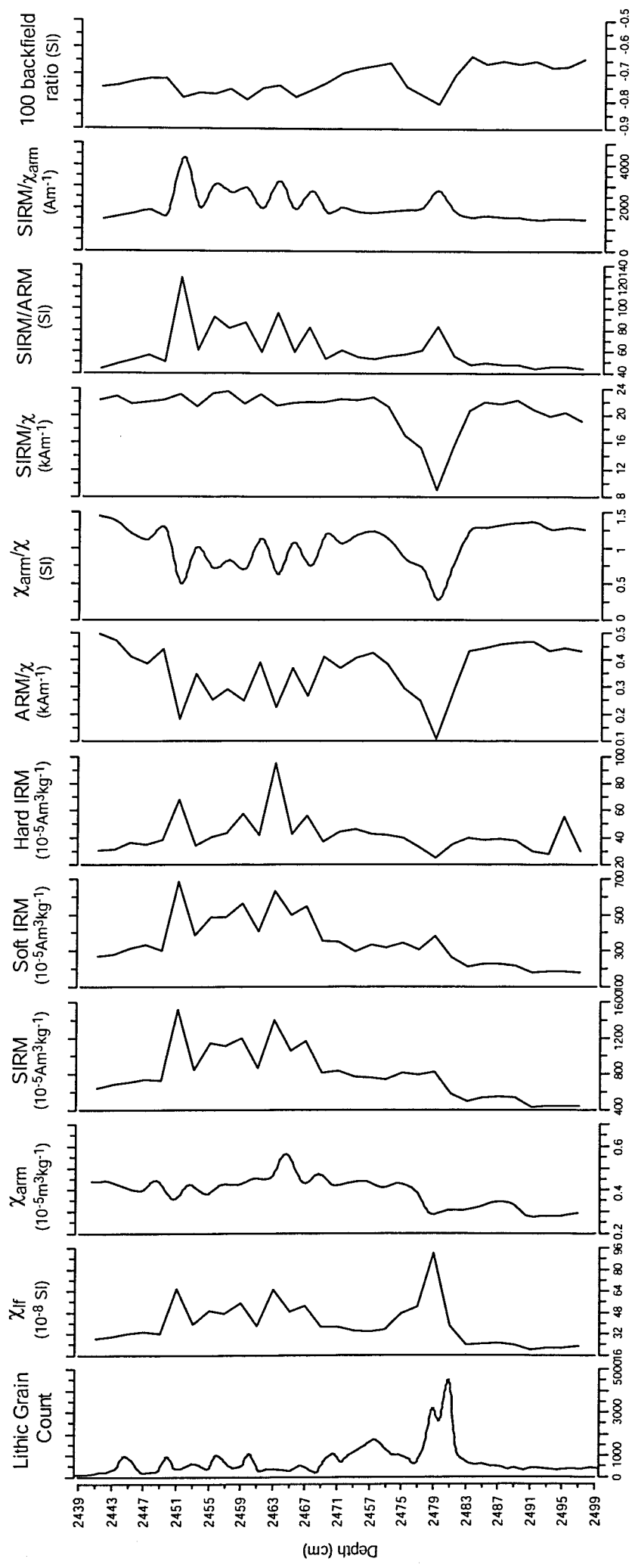


Fig. 5.49: Down-core magnetic results for the H4 section of MD95-2006. IRD data courtesy of Miss S. Leigh.

both mineral types. The third, and final, susceptibility peak (2449 cm) also shows increases in Hard and Soft IRM (a larger increase in Soft IRM than Hard IRM) and a slightly lower coercivity signal in the IRM-100/SIRM, as well as rises in SIRM/ARM and SIRM/ χ_{arm} and drops in χ_{arm}/χ and χ_{arm} . This signature is also characteristic of coarser grained minerals, and again, despite an increase in low and high coercivity minerals, the dominant signal is a low coercivity one.

Figs. 5.50, 5.51 and 5.52 show the plots used previously for the identification of magnetotactic bacteria and the mineral greigite, re-drawn for the H4 section of MD95-2006. No samples plot in the necessary regions on any of the graphs, therefore it is concluded that diagenetic and authigenic processes contribute minimally to the magnetic characteristics of MD95-2006 H4.

The biplots also drawn previously to help identify different signatures within the HEs have also been re-drawn here (Fig. 5.53). One sample is picked out by all of the plots in Fig. 5.53 as having LIS-style characteristics; sample 2481 cm. Other samples are also picked out, but for different reasons. The samples mentioned above as having susceptibility peaks are noted in Fig. 5.53a and c. Sample 2499 cm is noted in 5.53a and d, for its very large χ_{arm} value, Samples immediately above and below 2481 cm (2477 cm, 2479 cm and 2483 cm) are also evident in 5.53b.

Comparison between MD01-2461 and MD95-2006.

As with H2, MD01-2461 displays a three-stepped structure to H4 indicative of European-Laurentide-European inputs. However, as with H2, MD95-2006 is slightly different. The first χ peak in MD95-2006 (2481 cm) also shows the other LIS characteristics identified previously, and has been confirmed as dolomitic carbonate in mineralogy (S. Leigh, Pers. Comm. 2004). This would suggest that the first pulse of HE material comes from the LIS, contrary to all other findings for MD01-2461, MD95-2006, and OMEX 2K. The following peaks in χ show values that correspond to the EIS in other HEs and cores, however, only one (2461 cm) has the dominant high coercivity mineralogy also associated with EIS material. The

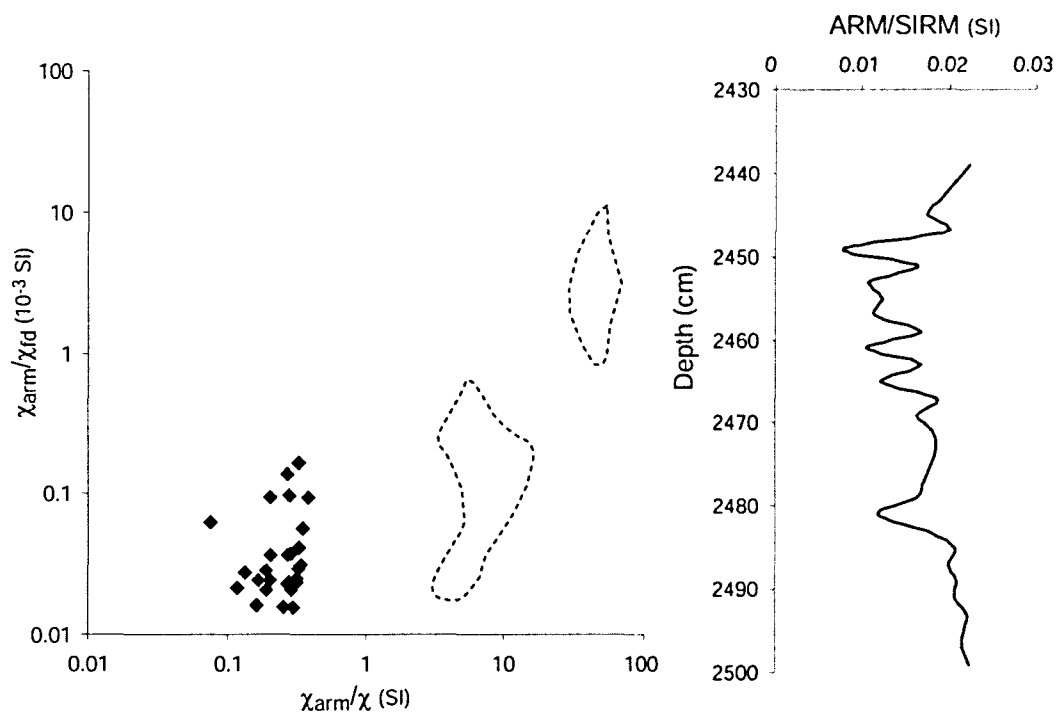


Fig. 5.50: Plots used for the identification of magnetotactic bacteria in the H4 section of MD95-2006

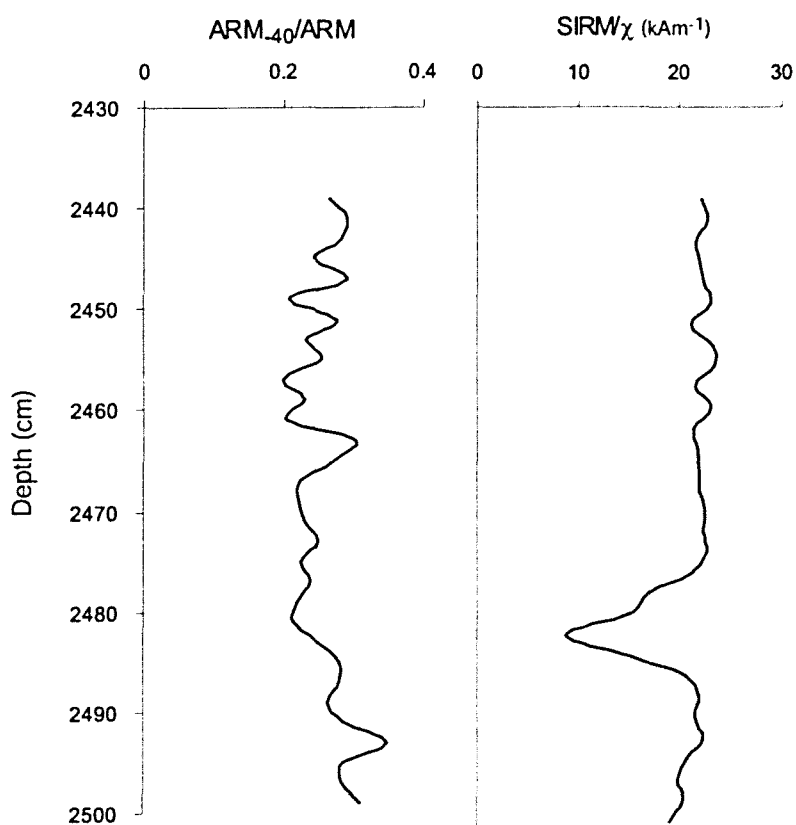


Fig. 5.5 1: Plots used for the identification of greigite in the H4 section of MD95-2006

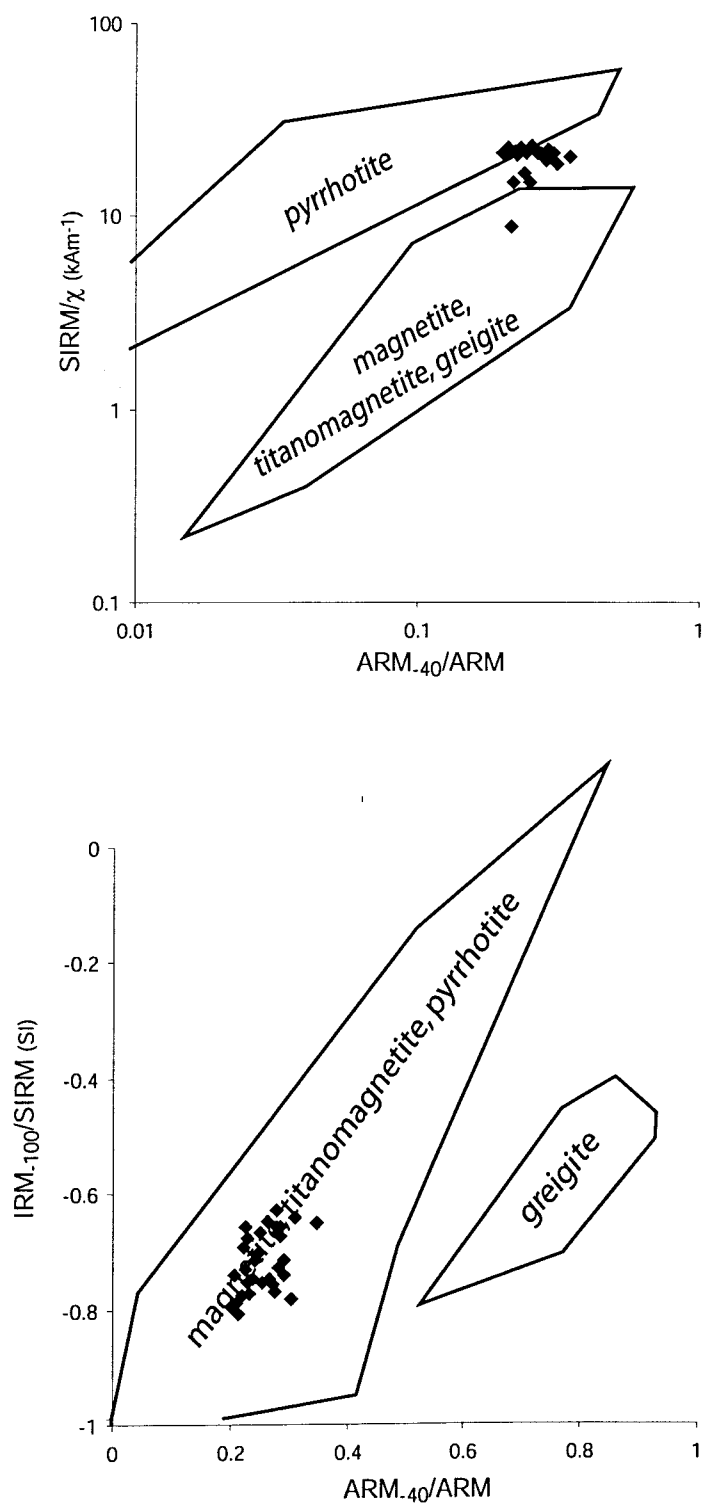


Fig. 5.52: Biplots used for the identification of greigite in the H4 section of MD95-2006

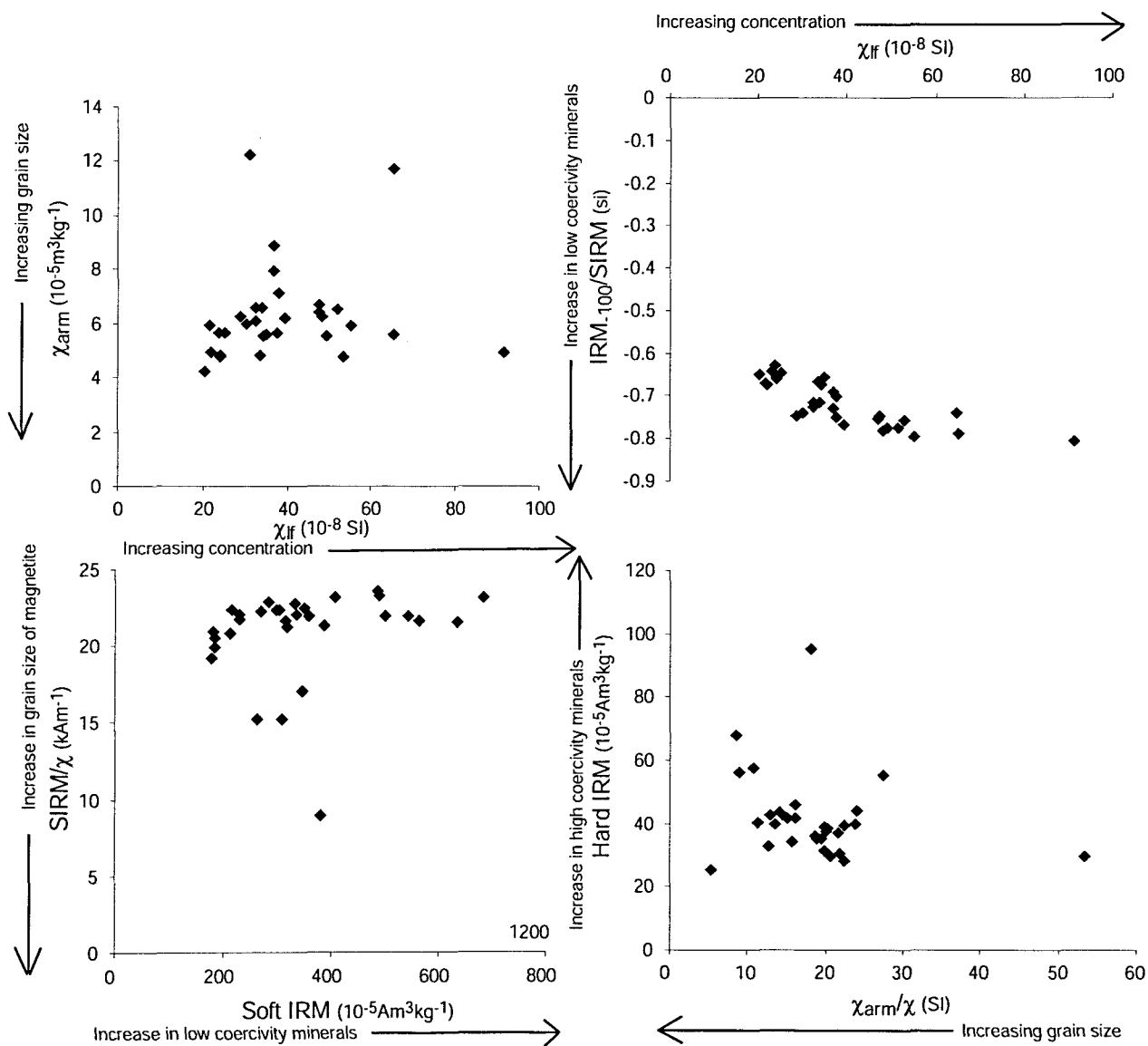


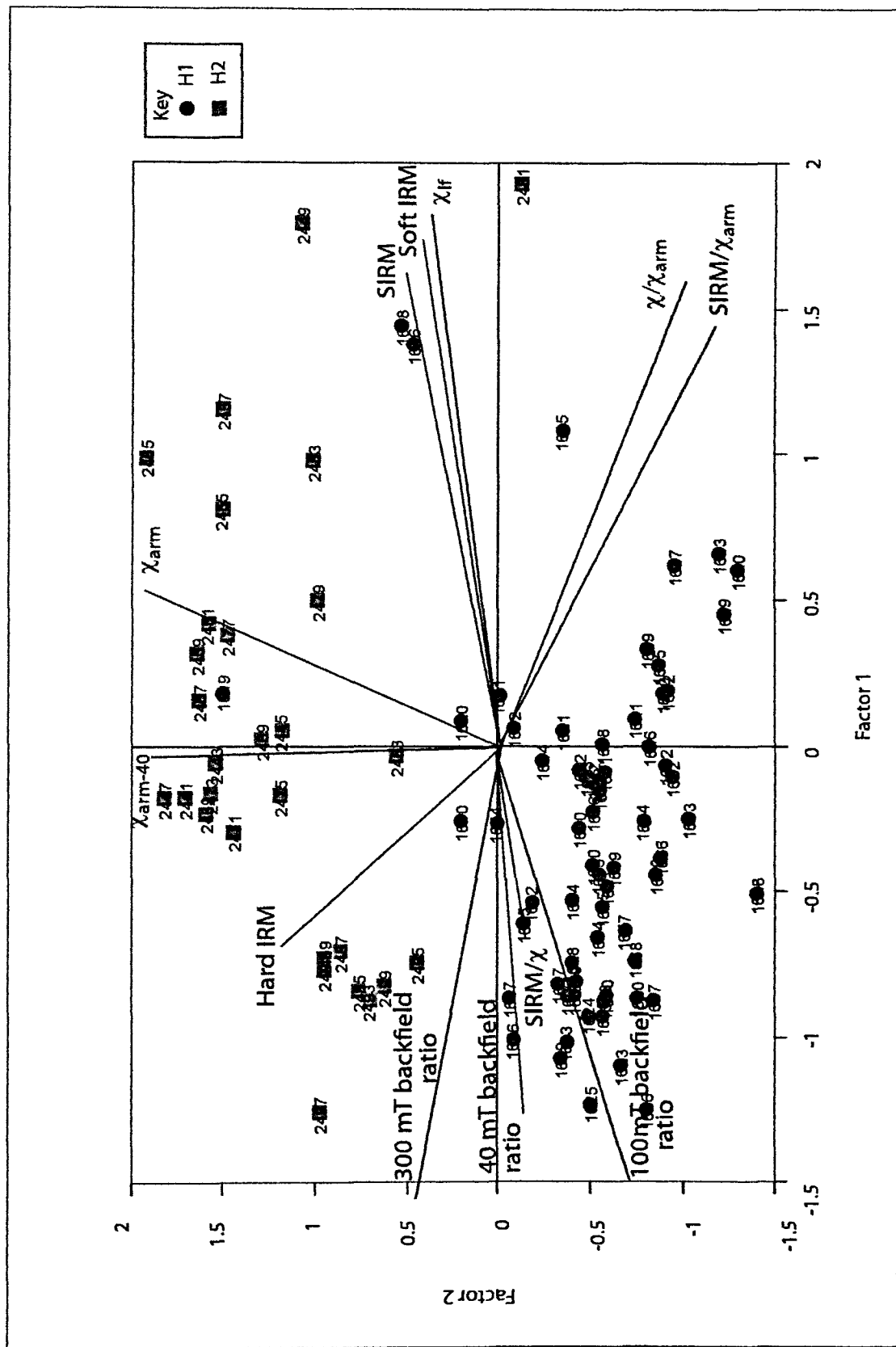
Fig. 5.53: Biplots for the H4 section of MD95-2006

top two have a ferrimagnetic-type signal. The location of the BIS during H4 is not very well documented, however it is thought to have been much smaller than during H2 (which falls near the LGM), and therefore ice rafting from the BIS may have been a relatively insignificant process compared to during H2. Sediments of slightly different composition from various ice streams could have been transported to the site of MD95-2006 during H4 by alternative methods, such as glacial outwash streams and surface run off from the continental shelf which could contribute to the variation in magnetic signature.

The sequence of events during H4 in MD95-2006 suggests an initial input of Laurentide material before the arrival of any European sediment. There are then three pulses of European material probably from at least two different ice streams before a return to ambient glacial conditions. This is a very different sequence to anything depicted in the other HEs examined in any of the cores. This could be due to the exceptionally high resolution of MD95-2006 compared to the other cores, or the location of the core relative to the BIS, or the data here could be picking out a D-O cycle signal predating H4 which due to the lower temporal resolution in MD01-2461 is difficult to make out in that core.

Factor Analysis

Fig 5.54 shows the factor analysis for the H2 and H4 subsections of MD95-2006. Each HE appears to sit in its own area of multivariate space, though looking closely at the individual HEs in isolation also produces some interesting clusters which appear to be grouped by depth, suggesting distinct inputs over time. The main χ_{f} peak within H4 is found on its own on the far right of the graph. The peak H2 samples also plot in the right hand side, but at the bottom. This indicates that, whilst HEs show generally the same characteristics, there are differences between them, even in the same core. Again these samples are found around the concentration axes and at opposite ends to the χ_{arm} axis, indicating a dominance of coarser magnetic grain sizes. This supports the previous interpretation that LIS samples are distinct from the rest of the core, but the HEs in MD95-2006 are more diverse than in OMEX 2K or MD01-2461, possibly due to the location



of the core and the influence of the BIS.

5.6 Overall Summary

The magnetic results discussed in the above sections have revealed some important insights into the North Atlantic Heinrich Events, in terms of their provenance and structure. In all HEs examined, the contribution of Laurentide material displays a very distinct set of magnetic characteristics, which can be identified from a series of biplots and multivariate statistical analysis. Within cores OMEX 2K and MD01-2461, these characteristics can be given specific values that are representative of LIS material. These specific values include χ_{lf} of >35 (10^{-8} SI); χ_{arm} of $0.12-0.25 \times 10^{-5} \text{m}^3 \text{kg}^{-1}$; IRM₁₀₀/SIRM of -0.6 ; Soft IRM of $>100 \times 10^{-5} \text{Am}^2 \text{kg}^{-1}$; Hard IRM of $<25 \times 10^{-5} \text{Am}^2 \text{kg}^{-1}$; SIRM/ χ ratios of $<15 \text{ kAm}^{-1}$; and χ_{arm}/χ ratios of <1 . Within MD95-2006, however, whilst the general descriptive characteristics can identify the HEs, the specific values do not. The similarity of the values between OMEX 2K and MD01-2461 is probably due to the proximity of the core locations, and a similar history of IRD delivery from the Celtic Sea ice-stream draining the southern margin of the BIS. This also explains the difference between both OMEX 2K and MD01-2461, and MD95-2006 – with the latter being fed from a northern ice-stream of the BIS. These results confirm the usefulness of environmental magnetic techniques in the identification and characterisation of IRD sediments, and indicate that the Heinrich Events within North Atlantic sediments are identifiable by magnetic methods alone. This highlights the potential for environmental magnetic techniques to be used as a screening tool, possibly immediately after core capture onboard ship, to identify areas of interest that more time consuming, palaeoceanographic techniques such as isotope analysis, foraminiferal analysis and mineralogical analysis, should concentrate on initially.

Additionally, with the exception of H4 in MD95-2006, each HE examined has demonstrated the same three-stepped structure of IRD provenance consisting of initial European material, followed by probable dilution by Laurentide sediments

and than a return to European dominated material (Fig. 5.55). In H4 from MD95-2006, there appears to be an initial input of Laurentide material before three separate pulses of European sediments. The location and size of the BIS at this time may play a significant part in the lack of initial delivery of European material. The identification of this kind of structure, which has been suggested by authors using other techniques (e.g. Snoeckx *et al.*, 1999; Grousset *et al.*, 2000; Grousset *et al.*, 2001), lends credibility to the use of environmental magnetic methods for the determination of sediment provenance and the sequencing of IRD events throughout the Heinrich Events.

In terms of provenance, all the core sections appear to show groupings that can be interpreted in terms of sediment source through the dependence of transport mechanisms on climate. The Holocene shows a low sedimentation rate, with a reduction in magnetic minerals, suggesting a warmer climate bringing material from proximal sources via bottom current and turbidities, and an increase in biogenic dilution due to a rise in ocean productivity. Suggested parameter ranges for Holocene sediments are χ_{ir} of ~ 10 (10^{-8} SI); χ_{arm} values of $> 0.6 \cdot 10^{-5} \text{ m}^3 \text{ kg}^{-1}$; χ_{arm}/χ values of > 5 ; and SIRM/χ_{arm} values of $< 500 \text{ kAm}^{-1}$. It must be acknowledged, however, that due to the preliminary nature of the MD01-2461 chronology (Section 5.4.1) and definition of the Holocene interval, these specific values are only speculative.

The Younger Dryas has characteristics that fall between the full HE and Holocene signals, with a slight increase in the concentration of higher coercivity minerals, alluding to a shift towards glacial conditions, halting the EIS retreat and re-introducing ice rafting. Conditions, however, were not cold enough to bring icebergs from North America to the Celtic margin. The Younger Dryas shows χ_{ir} values of $\sim 20-25$ (10^{-8} SI); Soft IRM values of $> 125 \cdot 10^{-5} \text{ Am}^2 \text{ kg}^{-1}$; and χ_{arm}/χ values of 2-3.5. Again, the MD01-2461 chronology must be acknowledged as a possible problem when attributing these characteristics. Additionally the presence of tephra in OMEX 2K around this depth could confuse the signal slightly (see Section 5.3.2).

The ambient glacial sediments display similar patterns to the Holocene, however their actual values are higher. This is indicative of a relatively stable cold climatic state delivering material of a European origin to the area. χ_{if} values for the ambient sediments are around 12–15 (10^{-8} SI), with Soft IRM values $\sim 50 \cdot 10^{-5} \text{Am}^2 \text{kg}^{-1}$; Hard IRM values of 30–36 $10^{-5} \text{Am}^2 \text{kg}^{-1}$; and SIRM/ χ values of 22 kAm^{-1} . As with the YD, the presence of tephra within the ambient sediments, particularly below H2 in OMEX 2K, could have an influence on the overall magnetic signal seen.

The interpretations discussed above have wider reaching implications for the use of environmental magnetism in the study of Heinrich Events than just the provision of a useful early diagnostic tool. The identification of parameter ranges associated with different time periods throughout the cores suggests that environmental magnetic signatures vary, quite specifically, with climate, and it may be possible, after further analysis to make assumptions on past climatic conditions based on the magnetic information provided by routine measurements.

The interpretation of the magnetic data contained in this thesis has been constrained by the limits of the traditional techniques currently employed by the majority of HE researchers. As these provide the only universally accepted data on Heinrich Events, they are therefore the only scientifically robust methods to compare with any new data. However, the results of this study suggests that environmental magnetic methods could have a significant impact on the source apportionment of the HE sediments, especially if work on samples from the potential source areas is carried out. This is important to the study of Heinrich Events, as more information regarding ice sheet dynamics and their response to climate forcing and internal variations is vital to the identification of an ultimate causal mechanism for HEs.

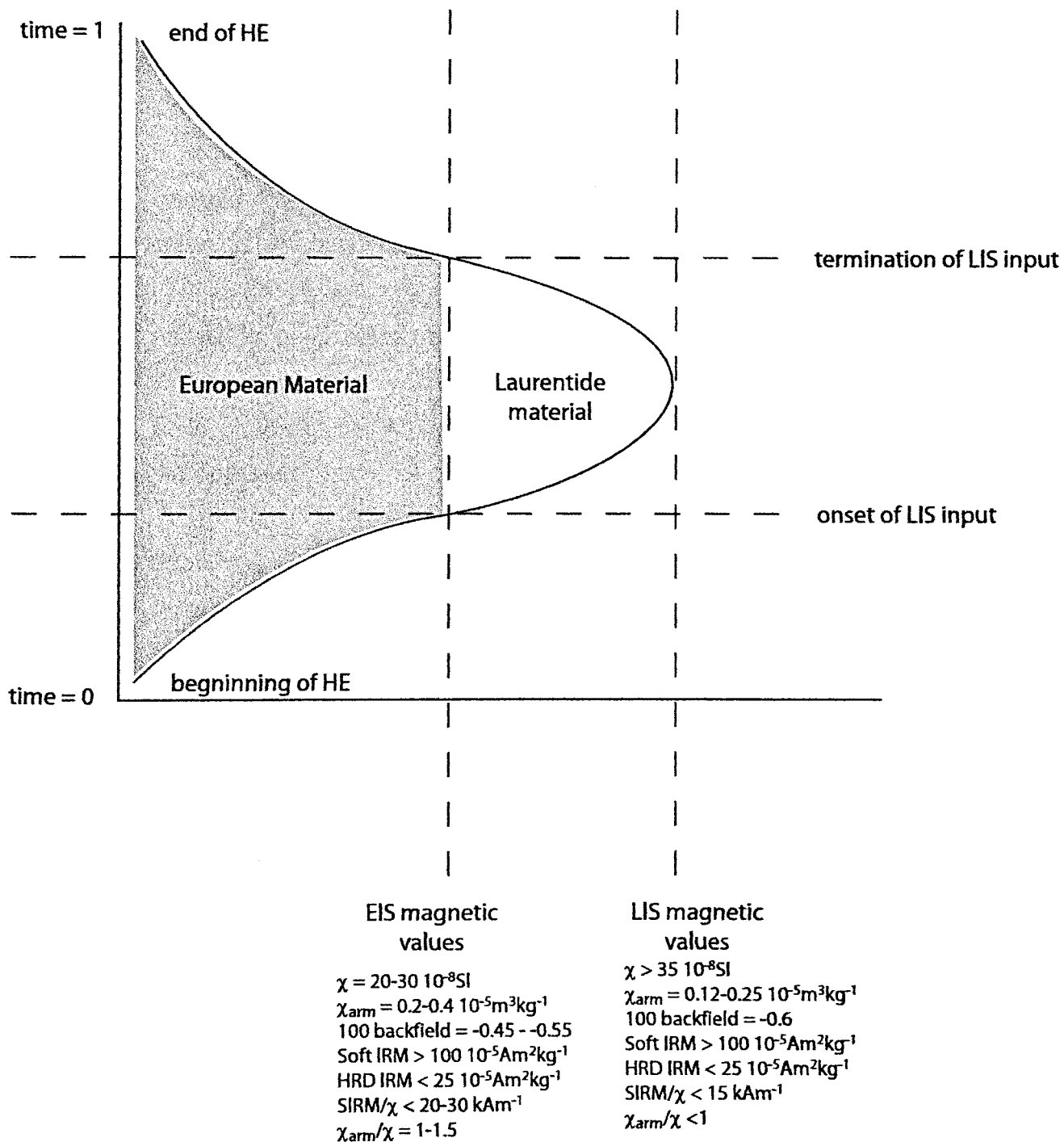


Fig. 5.55: Schematic showing the sequence IRD input through a Heinrich Event as suggested by the magnetic measurements within this study.

6.0 Conclusions and Further Work

When addressing the original aims of the project, set out in Section 1.3, it would appear that environmental magnetic techniques have considerable potential in studying marine sediments. The following specific conclusions can be drawn.

- Environmental magnetic analyses can successfully identify down-core changes in magnetic properties that may represent a response to changing climate and sediment transport mechanisms.
- As well as other areas of interest within a core, environmental magnetic analyses are able to identify and characterise the Heinrich Events and could prove a valuable tool for initial analysis to select areas for more detailed examination.
- Environmental magnetic analyses are able to distinguish between possible provenances of IRD within HEs, with the LIS component of the HEs having a particularly distinct magnetic character.

Several other conclusions can be drawn from the work involved in this thesis:

- Heinrich Events on the Celtic margin seem to have a three-stepped structure to them, starting with an input of European material, followed by the appearance of the Laurentide sediment, and ending with a disappearance of the Laurentide material, leaving the European signal. This suggests, for this area, at least, the European icebergs were the first to arrive. This is most likely to be a result of the proximal location of the cores to the BIS, reducing the lag time, but may also indicate a more rapid response time of the European ice sheets to an external climatic control.

- Changes within the magnetic signatures of the sediments on the Celtic margin are a response to climatic shifts and the accompanying changes transport mechanism and provenance.

The conclusions above, however, have been drawn from relatively basic measurements on two cores, with some comparison work done on sections of a third. Therefore, further work can be done to test and analyse the ideas begun in this thesis. Suggestions for further work are:

- More detailed magnetic measurements on OMEX 2K, MD01-2461 and MD95-2006, such as temperature dependent magnetic analysis and hysteresis loops, particularly to try to identify further differences between the various inputs of European material in MD95-2006.
- The measurement of the same parameters used here on cores from a more central location in the North Atlantic. This could help determine a sequence of events unaffected by individual ice streams and the varying location of the European Ice Sheets.
- Examination of a core with a large sedimentation rate at a higher resolution to look for any influence of the D-O cycles. This could reinforce the idea that magnetic measurements can identify climatic variations.

References

- Ahnert F., (1996). *Introduction to Geomorphology*. London, Arnold.
- Allen J.R.M. Brandt U. Brauer A. Hubbertens H-W. Huntley B. Keller J. & Kraml M., (1999). Rapid Environmental Changes in Southern Europe during the Last Glacial Period. *Nature*: 400: 740-743.
- Alley R.B., (1998). Icing the North Atlantic. *Nature*: 392: 335-337.
- Alley R.B. & MacAyeal D.R., (1994). Ice-Rafted Debris Associated with Binge/Purge Oscillations of the Laurentide Ice Sheet. *Paleoceanography*: 9(4): 503-511.
- Andrews J.T., (1998). Abrupt changes (Heinrich Events) in Late Quaternary North Atlantic Marine Environments: A History and Review of data and concepts. *Journal of Quaternary Science*: 13(1): 3-16.
- Andrews J.T., (2000). Icebergs and Ice-Rafted Detritus (IRD) in the North Atlantic: Facts and Assumptions. *Oceanography*: 13(3): 100-108.
- Andrews J.T. & Barber D.C., (2002). Dansgaard-Oeschger Events: Is There a Signal off the Hudson Strait Ice Stream? *Quaternary Science Reviews*: 21: 443-454.
- Andrews J.T. Tedesco K. & Jennings A.E., (1993). Heinrich Events: Chronology and Processes, East-central LIS and NW Labrador Sea. *Ice in the Climate System*. Peltier W.P. (ed). NATO AASI Series: 12: 167-186.
- Andrews J.T. Jennings A.E. Kerwin M. Kirby M. Manley W. Miller G.H. Bond G. & MacClean B., (1995). A Heinrich-like Event, H-0 (DC-0): Source(s) for Detrital

Carbonate in the North Atlantic During the Younger Dryas Chronozone.
Paleoceanography: 10(5): 943-952.

Anon (2003). Radiocarbon Dating [online]. Available from:
www1.phys.uu.nl/AMS/Radiocarbon (18/11/2003).

Anon (2004). The Magneto-Lab Research [online]. Bremen. Available from:
www.mpi-bremen.de/magneto/research (16/10/2004).

Anon (2004). CALYPSO: Giant Sediments Cores and Support [online]. Available
from: <http://www.ifremer.fr/ifrtp/> (21/1/2004).

Anon (unknown). What is Radiocarbon dating [online]. Belfast, Queens University
Belfast. Available from: www.qub.ac.uk/c14/whatis14 (7/8/2004).

ANSTO (2003). Radiocarbon Dating [online]. Australia. Available from:
[http://www.ansto.gov.au/ansto/environment1/ams/ams_Radiocarbon-](http://www.ansto.gov.au/ansto/environment1/ams/ams_Radiocarbon-dating.htm)
[dating.htm](http://www.ansto.gov.au/ansto/environment1/ams/ams_Radiocarbon-dating.htm) (14/11/2003).

Auffret G.A. Boelaert A. Vergnaud-Grazzini C. Muller C. & Kerbrat R., (1996).
Identification of Heinrich Layers in Core KS 01 North Eastern Atlantic (46°N,
17°W), Implications for their Origin. *Marine Geology*: 131: 5-20.

Auffret G.A. Zaragosi S. Dennielou B. Cortijo E. Rooij D. Grousset F. Pujol C.
Eynaud F. & Siebert M., (2002). Terrigenous Flux at the Celtic Margin during
the past Glacial Cycle. *Marine Geology*: 188: 79-108.

Augustin L. Barbante C. Barnes P.R.F. Marc Barnola J. Bigler M. Castellano E.
Cattani O. Chappellaz J. Dahl-Jensen D. Delmonte B. Dreyfus G. Durand G.
Falourd S. Fischer H. Fluckiger J. Hansson M.E. Huybrechts P. Jugie G. Johnsen
S.J. Jouzel J. Kaufmann P. Kipfstuhl J. Lambert F. Lipenkov V.Y. Littot G.C.
Longinelli A. Lorrain R. Maggi V. Masson-Delmotte V. Miller H. Mulvaney R.

- Oerlemans J. Oerter H. Orombelli G. Parrenin F. Peel D.A. Petit J-R. Raynaud D. Ritz C. Ruth U. Chwander J. Siegenthaler U. Souchez R. Stauffer B. Peder Steffensen J. Stenni B. Stocker T.F. Tabacco I.E. Udisti R. van de Wal R.S.W. van den Broeke M. Weiss J. Wilhelms F. Winther J-G. Wolff E.W. & Zucchelli M., (2004). Eight Glacial Cycles from an Antarctic Ice Core. *Nature*: 429(6992): 623-628.
- Austin W. E. N. and Kroon D., (2001). Deep sea ventilation of the Northeastern Atlantic during the last 15,000 years. *Global and Planetary Change*: 30(1-2): 13-31.
- Austin W.E.N. Bard E. Hunt J.B. Kroon D. & Peacock J.D., (1995). The ^{14}C Age of the Icelandic Vedde Ash: Implications for Younger Dryas Marine Reservoir Age Corrections. *Radiocarbon*: 37(1): 53-62.
- Backman J., (1984). Cenozoic Calcareous Nannofossil Biostratigraphy from the Northeastern Atlantic Ocean Deep-Sea Drilling Project, Leg 81. *Initial Reports of the DSDP*. Roberts S.D. & Schnokter D.G., *et al.*, (eds). Washington, US Govt Printing Office, 81: 403-428.
- Bader R.G. & Paquette R.G., (1956). Piston Coring Device (Instrumental Note). *Deep Sea Research*: 3(4): 289.
- Balsam W. Ji J. & Chen J., (2004). Climatic interpretation of the Luochuan and Lingtai loess sections, China, based on changing iron oxide mineralogy and magnetic susceptibility. *Earth and Planetary Science Letters*: 223(3-4): 335-348.
- Banerjee S.K. Hunt C.P. & Lui X-M., (1993). Separation of Local Signals from the Regional Palaeomonsoon Record of the Chinese Loess Plateau: A Rock Magnetic Approach. *Geophysical Research Letters*: 20: 843-846.

- Bard E. Arnold M. Duprat J. Moyes J. & Duplessy J-C., (1987). Reconstruction of the Last Deglaciation: Deconvolved Records of $\delta^{18}\text{O}$ profiles, Micropalaeontological Variations and AMS ^{14}C dating. *Paleoceanography*: 1: 101-112.
- Bard E. Hamelin B. Fairbanks R G. & Zindler A., (1990). Calibration of the ^{14}C Timescale over the Past 30000 years using Mass Spectrometric U-Th ages from Barbados Corals. *Nature*: 245: 405-410.
- Bard E. Arnold M. Mangerud J. Paterne M. Labeyrie L Duprat J. Melieres M-A. Sonstegaard E. & Duplessy J-C., (1994). The North Atlantic atmosphere-sea surface ^{14}C gradient during the Younger Dryas climate event. *Earth and Planetary Science Letters*: 126: 275-287.
- Bard E. Arnold M. Hamelin B. Tisnerat-Laborde N. & Cabioch G., (1998). Radiocarbon Calibration by means of Mass Spectrometric $^{230}\text{Th}/^{234}\text{U}$ and ^{14}C ages of corals: An updated database including samples from Barbados, Mururoa and Tahiti. *Radiocarbon*: 40(1): 1085-1092.
- Bartlein P. J. Edwards M. E. Shafer S. L. & Barker Jr E. D., (1995). Calibration of Radiocarbon Ages and the Interpretation of Paleoenviromental Records. *Quaternary Research*: 44(3): 417-424.
- Batt C.M., (1999). Preliminary Investigations into the Acquisition of Remanence in Archaeological Sediments. *Palaeomagnetism and Diagenesis in Sediments*. Tarling D.H. & Turner P. (eds). London, The Geological Society. Special Publication 151: 9-20.
- Bauch D. Darling K. Simstich J. Bauch H.A. Erienkeusser H. & Kroon D., (2003). Palaeoceanographic Implications of Genetic Variation in living North Atlantic *Neogloboquadrina pachyderma*. *Nature*: 424: 299-302.

- Beaufort L. *et al.*, (2002). Mona cruise leg 1 and 2 [online]. Available from: www.images.pclab.ifg.uni-kiel.de/mona (29/1/2004).
- Behl R.J. & Kennett J.P., (1996). Brief Interstadial Events in the Santa Barbara Basin, NE Pacific During the Past 60kyr. *Nature*: **379**: 243-246.
- Behling H. Arz H.W. Patzold J. & Wefer G., (2000). Late Quaternary Vegetational and Climate Dynamics in Northeast Brazil, Inferences from Marine Core GeoB 3104-1. *Quaternary Science Reviews*: **19**: 981-994.
- Begét J.E. & Hawkins D.B., (1989). Influence of Orbital Parameters on Pleistocene Loess Deposition in Central Alaska. *Nature*: **337**: 151-153.
- Begét J.E. Stone D.B. & Hawkins D.B., (1990). Palaeoclimate Forcing of Magnetic Susceptibility Variations in Alaskan Loess during the Late Quaternary. *Geology*: **18**: 40-43.
- Bell F.G. & Walker D.J.H., (2000). A further examination of the nature of dispersive soils in Natal, South Africa. *Quarterly Journal of Engineering, Geology and Hydrogeology*: **33**: 187-199.
- Benn D.I. & Evans D.J.A., (1998). *Glaciers and Glaciation*. London, Arnold.
- Benson L.V. Lund S.P. Burdett J.W. Kashgari M. Rose T.P. Smoot J.P. & Schwartz M., (1998). Correlation of Late Pleistocene Lake-Level Oscillations in Mono Lake, California, with North Atlantic Climate Events. *Quaternary Research*: **49**: 1-10.

- Benson L.V. Barber D. Andrews J.T. Taylor H. & Lamothe P., (2003). Rare Earth Elements and Nd and Pb Isotopes as source indicators for Labrador Sea clay-sized sediments during Heinrich Event 2. *Quaternary Science Reviews*: 22: 881-889.
- Berger A. Loutre M.F. & Dehant V., (1989). Pre-Quaternary Milankovitch Frequencies. *Nature*: 342: 133.
- Bianchi G.C. & McCave I.N., (1999). Holocene Periodicity in North Atlantic Climate and Deep Ocean Flow South of Iceland. *Nature*: 397: 515-517.
- Bindler R. Brannvall M-L. Renberg I. Emteryd O. & Grip H., (1999). Natural Lead Concentrations in Pristine Boreal Forest Soils and Past Pollution Trends: A Reference for Critical Load Models. *Environmental Science and Technology*: 33(19): 3362-3367.
- Birkeland A. Nordgulen O. Cumming G.L. & Bjorlykke A., (1993a). Pb-Nd-Sr Isotopic Constraints on the Origin of the Caledonian Bindal Batholith, central Norway. *Lithos*: 29: 257-271.
- Birkeland A. Ihlen P.M. & Bjorlykke A., (1993b). The Sources of Metals in Sulphide Deposits in the Helgeland Nappe Complex, North-Central Norway: Pb Isotopic Evidence. *Economic Geology*: 88: 1810-1829.
- Bjorlykke A. Vokes F.M. Birkeland A. & Thorpe R.I., (1993). Lead Isotope Systematics of Strata-Bound Sulphide Deposits in the Caledonides of Norway. *Economic Geology*: 88: 397-417.
- Blakemore R., (1975). Magnetotactic Bacteria. *Science*: 190: 377-379.

- Blakemore R., (1982). Magnetotactic Bacteria. *Annual Reviews of Microbiology*: 36: 217-238.
- Bloemendal J., (1983). Palaeoenvironmental Implications of the Magnetic Characteristics of Sediments from Deep Sea Drilling Project Site 541, South East Argentine Basin. *Initial Reports of the Deep Sea Drilling Project*: 71(2): 1097-1108.
- Bloemendal J. & de Menocal P., (1989). Evidence for a Change in the Periodicity of Tropical Climate Cycles at 2.4 Myr from Whole-core Magnetic Susceptibility Measurements. *Nature*: 342: 897-899.
- Bloemendal J. Lamb B. & King J., (1988). Palaeoenvironmental Implications of Rock-Magnetic Properties of Late Quaternary Cores from the Eastern Equatorial Atlantic. *Paleoceanography*: 3(1): 61-87.
- Bloemendal J. King J.W. Hall F.R. & Doh S-J., (1992). Rock Magnetism of Late Neogene and Pleistocene Deep-Sea Sediments: Relationship to Sediment Source, Diagenetic Processes and Sediment Lithology. *Journal of Geophysical Research*: 97(B4): 4361-4375.
- Bloemendal J. King J.W. Hunt A. de Menocal P. & Hayashida A., (1993). Origin of the Sediment Magnetic Record at Ocean Drilling Program Sites on the Owen Ridge, Western Arabian Sea. *Journal of Geophysical Research*: 98(B3): 4199-4219.
- Blomquist S., (1985). Reliability of Core Sampling of Soft Bottom Sediment: an *in situ* study. *Sedimentology*: 32(4): 605-612.
- Bond G. & Lotti R., (1995). Iceberg Discharges into the North Atlantic on Millennial Time-Scales During the Last Glaciation. *Science*: 267: 1005-1010.

- Bond G. Heinrich H. Broecker W. Labeyrie L. McManus J. Andrews J. Huon S. Jantschik R. Clasen S. Simet C. Tedesco K. Klas M. Bonani G. & Ivy S., (1992). Evidence for Massive Discharges of Icebergs into the North Atlantic Ocean during the Last Glacial Period. *Nature*: 360: 245-249.
- Bond G. Broecker W. Johnsen S. McManus J. Labeyrie L. Jouzel J. & Bonani G., (1993). Correlations between Climate Records from North Atlantic Sediments and Greenland Ice. *Nature*: 365: 143-147.
- Bond G. Showers W. Cheeseby M. Lotti R. Almasi P. de Menocal P. Priore P. Cullen H. Hajdas I. & Bonani G., (1997). A Pervasive Millennial-Scale Cycle in North Atlantic Holocene and Glacial Climates. *Science*: 278: 1257-1266.
- Bond G.C. Showers W. Elliot M. Evans M. Lotti R. Hajdas I. Bonani G. & Johnson S., (1999). The North Atlantic 1-2 kyr Climate Rhythm: Relation to Heinrich Events, Dansgaard-Oeschger Cycles and the Little Ice Age. *Mechanisms of Global Climate Change at Millennial Timescales*. Clark P.U (ed). AGU. Geophysical Monograph 112: 35-58.
- Bouma A.H. & Boerma J.A.K., (1968). Vertical Distributions in Piston Cores. *Marine Geology*: 6: 231-241.
- Bowen D.Q. Rose J. McCabe A.M. & Sutherland D. G., (1986). Correlation of Quaternary Glaciations in England, Ireland, Scotland and Wales. *Quaternary Science Reviews*: 299-340.
- Bowman S., (1990). *Interpreting the Past: Radiocarbon Dating*. London, British Museums Publications Ltd.
- Brannvall M-L. Bindler R. Renberg I. Emteryd O. Bartnicki J. & Billström K., (1999). The Medieval Metal Industry was the Cradle of Modern Large-scale

- Atmospheric Lead Pollution in Northern Europe. *Environmental Science and Technology*: 33(24): 4391-4395.
- Brannvall M-L. Bindler R. Emteryd O. & Renberg I., (2001). Four Thousand Years of Atmospheric Lead Pollution in Northern Europe: a summary from Swedish Lake Sediments. *Journal of Palaeolimnology*: 25: 451-435.
- Bramlette M.N. & Bradley W.H., (1941). Lithology and Geological Interpretations: Geology and Biology of North Atlantic Deep-Sea Cores. *US Geological Survey Prof Paper*: 196: 1-34.
- Brasier M.D., (1980). *Microfossils*. Herts, UK, Allen & Unwin.
- Briggs D. Smithson P. Addison K. & Atkinson K., (1997). *Fundamentals of the Physical Environment*. London, Routledge.
- Broecker W.S., (1994). Massive Iceberg Discharges as Triggers for Global Climate Change. *Nature*: 421-424.
- Broecker W.S., (1995). *The Glacial World According to Wally*. USA, Columbia University.
- Broecker W.S., (2000). Abrupt Climate Change: Causal Constraints Provided by the Palaeoclimate Record. *Earth-Science Reviews*: 51: 137-154.
- Broecker W.S., (2003). Does the Trigger for Abrupt Climate Change Reside in the Ocean or in the Atmosphere? *Science*: 300: 1519-1522.
- Broecker W. Mix A. Andree M. & Oeschger H., (1984). Radiocarbon measurements on coexisting benthic and planktic foraminifera shells: potential for reconstructing ocean ventilation times over the past 20 000 years. *Nuclear*

Instruments and Methods in Physics Research Section B: Beam Interactions with Materials and Atoms: 5(2): 331-339.

Broecker W. Andree M. Bonani G. Wolfli W. Klas M. Mix A. & Oeschger H., (1988). Comparison Between Radiocarbon Ages Obtained on Co-existing Planktonic Foraminifera. *Paleoceanography*: 3(6): 647-657.

Broecker W. Bond G. Klas M. Clark E. & McManus J., (1992). Origin of the North Atlantic Heinrich Events. *Climate Dynamics*: 6: 265-273.

Broecker W. Bond G. & McManus J. (1993). Heinrich Events: Triggers of Ocean Circulation Change. *Ice In the Climate System*. Peltier W.P. (ed). NATO ASI Series: 12: 161-166.

Bronk Ramsey C., (1995). Radiocarbon Calibration and Analysis of Stratigraphy: The OxCal Program. *Radiocarbon*: 37(2): 425-430.

Buckley D.E. MacKinnon W.G. Cranston R.E. & Christian H.A., (1994). Problems with Piston Core Sampling: Mechanical and Geochemical Diagnosis. *Marine Geology*: 117: 95-106.

Calais E. Deverchère J. Peypouquet J.P., (2003). The Marion Dufresne Research Vessel [online]. Available from: http://www.univ-brest.fr/IUEM/Universite_flottante/md.html (29/1/2004).

Calanchi N. Cattaneo A. Dinelli E. Gasparotto G. & Lucchini F., (1998). Tephra layers in Late Quaternary sediments of the central Adriatic Sea. *Marine Geology*: 149(1-4): 191-209.

Capo R.C. Stewart B.W. & Chadwick O.A., (1998). Strontium Isotopes as Tracers of Ecosystem Processes: Theory and Methods. *Geoderma*: 82: 197-225.

- Chang S-B R. & Kirschvink J.L. (1989). Magnetofossils, the Magnetisation of Sediments and the Evolution of Magnetite Biomineralisation. *Annual Reviews of Earth and Planetary Science*: 17: 169-195.
- Channell J.E.T. & Hawthorne T., (1990). Progressive Dissolution of Titanomagnetite at ODP site 653 (Tyrrhenian Sea). *Earth and Planetary Science Letters*: 96: 469-480.
- Chappell J., (2002). Sea Level Changes Forced Ice Breakouts in the Last Glacial Cycles: New Results from Coral Terraces. *Quaternary Science Reviews*: 21: 1229-1240.
- Chernicoff S.E., (1983). Glacial Characteristics of a Pleistocene Ice Lobe in East-Central Minnesota. *Geological Society of America Bulletin*: 94: 1401-1414.
- Chillrud S. N. Hemming S. Shuster E.L. Simpson H.J. Bopp R.F. Ross J.M. Pederson D.C. Chaky D.A. Tolley L-R. & Estabrooks F., (2003). Stable lead isotopes, contaminant metals and radionuclides in upper Hudson River sediment cores: implications for improved time stratigraphy and transport processes. *Chemical Geology*: 199(1-2): 53-70.
- Clark P.U., (1994). Unstable Behaviour of the Laurentide Ice Sheet Over Deforming Sediment and its Implications for Climate Change. *Quaternary Research*: 41: 19-25.
- Colmenero E. Flores J.A. Lowemark L. Schonfeld J. & Sierro F.J., (2000). Palaeoceanographic Reconstruction of the Gulf of Cadiz During the Last Glacial Cycle as Revealed by Cocco-lithophore Assemblages. *Journal of Nannofossil Research*: 2: 22.

- Conolly J.R. & Ewing M., (1965). Pleistocene Glacial-Marine Zones in North Atlantic Deep-Sea Sediments. *Nature*: **208**: 135-138.
- Coope G.R., (1997). Fossil Coleopteran Assemblages as Sensitive Indicators of Climatic Changes during the Devensian (Last) Cold Stage. *Philosophical Transactions of the Royal Society of London Series B*: **280**: 313-340.
- Cortijo E. Yiou P. Laybrie L. & Cremer M., (1995). Sedimentary Records of Rapid Climate Variability in the North Atlantic Ocean during the Last Glacial Cycle. *Paleoceanography*: **10**(2): 911-926.
- Cortijo E. Labeyrie L. Vidal L. Vautravers M. Chapman M. Duplessy J-C. Elliot M. Arnold M. Turon J-L. & Auffret G., (1997). Changes in Sea Surface Hydrology Associated with Heinrich Event 4 in the North Atlantic Ocean between 40° and 60° N. *Earth and Planetary Science Letters*: **146**: 29-45.
- Cranfield D.E. & Berner R.A., (1987). Dissolution and Pyritisation of Magnetite in Anoxic marine sediments. *Geochimica et Cosmochimica Acta*: **51**: 645-659.
- Dansgaard W. & Oeschger H., (1989). Past Environmental Long-term Records from the Arctic. *The Environmental Record in Glaciers and Ice Sheets*. Oeschger H. & Langway Jr C.C. (eds) Wiley: 287-318.
- Dansgaard W. Johnsen S.J. Clausen H.B. Dahl-Jensen D. Gundstrup N.S. Hammer C.U. Hvidberg C.S. Steffensen J.P. Sveinbjorndottir A.E.J., (1993). Evidence for General Instability of Past Climate from a 250 kyr Ice-Core Record. *Nature*: **364**: 218-220.
- Davis J.C., (2002). *Statistics and Data Analysis in Geology*. New York, Wiley.
- Dawson A.G., (1992). *Ice Age Earth: Late Quaternary Geology and Climate*. London, Routledge.

- Dearing J., (1999). Magnetic Susceptibility. Chapter 4: *Environmental Magnetism: A Practical Guide*. Walden J. Oldfield F. & Smith J. (eds). London, Quaternary Research Association. Technical Guide No 6: 35-62.
- Dearing J. & Flower R., (1982). The Magnetic Susceptibility of Sedimentary Material Trapped in Lough Neagh, Northern Ireland and its Erosional Significance. *Limnology & Oceanography*: 17(5): 969-975.
- de Graciansky P.C. Poag C.W. & Foss G., (1981). Drilling on the Goban Spur: Objectives, Regional Geological Setting and Operational Summary. *Initial Reports of the Deep Sea Drilling Project*: 80 (1): 5-13.
- De Dekker P., (1997). The Significance of the Oceans in the Australasian Region with respect to Global Palaeoclimates: Future Directions. *Palaeogeography, Palaeoclimatology, Palaeoecology*: 131: 511-515.
- Dekkers M.J., (1997). Environmental Magnetism: An Introduction. *Geologie en Mijnbouw*: 76: 163-182.
- Dixon P.R. LeHuray A.P. & Rye D.M., (1990). Basement Geology and Tectonic Evolution of Ireland as Deduced from PB Isotopes. *Journal of the Geological Society, London*: 147: 121-132.
- Dokken T.M. & Hald H., (1996). Rapid Climate Shifts during Isotope Stages 2 - 4 in the Polar North Atlantic. *Geology*: 24(7): 599-602.
- Donally D.M., (1989). Calcareous Nannofossils of the Norwegian-Greenland Sea: ODP Leg 104. *Proceeding of the Ocean Drilling Project, Scientific Results*: 104: 459-478.

- Dowdeswell J.A. Maslin M.A. Andrews J.T. & McCave I.N., (1995). Iceberg Production, Debris Rafting, and the Extent and Thickness of Heinrich Layers (H1, H2) in North Atlantic Sediments. *Geology*: 23(4): 301-304.
- Doyle P. Bennett M.R. & Baxter A.N., (1994). *The Key to Earth History: An Introduction to Stratigraphy*. Chichester, Wiley.
- Dreger D., (1999). Decadal-to-Millennial Scale Sediment Records of Ice Advance on the Barents Shelf and Meltwater Discharge in to the North-East Norwegian Sea over the Past 40kyr. *Berichte-Repots Institut fur Geowissenschaften 3*: 80: Christian-Albrechts Universitat Kiel, Germany.
- Dunlop D.J. & Özdemir O., (1997). *Rock Magnetism: Fundamentals and Frontiers*. Cambridge, Cambridge University Press.
- Elderfield H., (1986). Strontium Isotope Stratigraphy. *Palaeogeography, Palaeoclimatology, Palaeoecology*: 57: 71-90.
- Elliot M. Labeyrie L. Bond G. Cortijo E. Turon J-L. Tisnerat N. & Duplessy J-C., (1998). Millennial-Scale Iceberg Discharges in the Irminger Basin during the Last Glacial Period: Relationship with the HEs and Environmental Settings. *Paleoceanography*: 13(5): 433-446.
- Elliot M. Labeyrie L. & Duplessy J-C., (2002). Changes in North Atlantic Deep-Water Formation Associated with the Dansgaard-Oeschger Temperature Oscillations (10-60 ka). *Quaternary Science Reviews*: 21: 1153-1165.
- Emery K.O. & Hulsemann J., (1964). Shortening of Sediment cores collected in Open Barrel Gravity Corers. *Sedimentology*: 3: 144-154.

- Eriksson M.G. & Sandgren P., (1999). Mineral Magnetic Analysis of Sediment Cores Recording Recent Soil Erosion History in Central Tunisia. *Palaeogeography, Palaeoclimatology, Palaeoecology*: 152: 365-383.
- Evans T.E. & Heller F., (1994). Magnetic Enhancement and Palaeoclimate: Study of Loess/Palaeosol Couplet Across the Loess Plateau of China. *Geophysical Journal Interim*: 117: 257-264.
- Evans M.E. & Heller F., (2001). Magnetism in Loess/Palaeosol Sequences: Recent Developments. *Earth-Science Reviews*: 54: 129-144.
- Evans M.E. & Heller F., (2003). *Environmental Magnetism: Principles and Applications of Environmagnetics*. USA, Elsevier.
- Ewen T.L. Weaver A.J. & Schmitter A., (2004). Modeling Carbon Cycle Feedbacks during Abrupt Climate Change. *Quaternary Science Reviews*: 23: 531-448.
- Fairchild I. Hendry G. Quest M. & Tucker M., (1988). Chemical Analysis of Sedimentary Rocks, Chapter 9: *Techniques in Sedimentology*. Tucker M. (ed). Oxford, Blackwell Scientific Publications: 274-354.
- Farmer G.L. Barber D. & Andrews J.T., (2003). Provenance of Late Quaternary Ice-Proximal sediments in the North Atlantic: Nd, Sr and Pb Isotopic Events. *Earth and Planetary Science Letters*: 209: 227-243.
- Faure G., (1986). *Principles of Isotope Geology*. New York, Wiley & Sons.
- Findlay C.S. & Giraudeau J., (2000). Extant Calcareous Nannoplankton in the Australian Sector of the Southern Ocean (austral summers of 1994 and 1995). *Marine Micropaleontology*: 40: 417-439.

- Fillon R.H. & Duplessy J.C., (1980). Labrador sea bio-, tephro-, oxygen isotopic stratigraphy and Late Quaternary Palaeoceanographic trends. *Canadian Journal of Earth Sciences*: 17: 831-854.
- Forster T.H. & Heller F., (1997). Magnetic Enhancement Paths in Loess Sediments from Tajikistan, China and Hungary. *Geophysical Research Letters*: 24: 17-20.
- Fowler J. Cohen L. & Jarvis P., (1998). *Practical Statistics for Field Biology*. Chichester, Wiley.
- Frankel R.B. Blakemore R.P. & Wolfe R.S., (1979). Magnetite in Freshwater Magnetotactic Bacteria. *Science*: 203: 1355-1356.
- Frankel R.B. Blakemore R.P. Torres de Araujo F.F. Esquivel D.M.S. & Danon J., (1981). Magnetotactic Bacteria at the Geomagnetic Equator. *Science*: 212: 1269-1270.
- Frederichs T. Bleil U. Daumler K. von Dobeneck T. & Schmidt A.M., (1999). The Magnetic View on the Marine Palaeoenvironment: Parameters, Techniques and Potentials of Rock Magnetic Studies as a Key to Palaeoclimatic and Palaeoceanographic Changes. *Use of Proxies in Palaeoceanography: Examples from the South Atlantic*. Fischer G. & Wefer G. (eds). Berlin, Springer-Verlag: 575-599.
- Geyh M.A. & Schluchter C., (1998). Calibration of the ^{14}C Timescale beyond 22000 BP. *Radiocarbon*: 40(1): 475-482.
- Gibbons J. D., (1993). *Non-Parametric Statistics: An Introduction*. Newbury Park, Sage University Publications.
- Gillespie R. Hedges R.E.M. & Humm M.J., (1986). Routine AMS Dating of Bone and Shell fragments. *Radiocarbon*: 28: 451-456.

- Goodhew P.J., (1975). *Electron Microscopy and Analysis*. London, Wykeham Publications Ltd.
- Goslar T. Arnold M. Bard E. Kuc T. Pazdur M.F. Raiska-Jasiewiczowa M. Rozanski K. Tisnerat N. Walanus A. Wicik B & Wieckowski K., (1995). High Concentration of atmospheric ^{14}C during the Younger Dryas Cold Episode. *Nature*: **377**: 414-417.
- Gravenor C.P. & Stipavsky M., (1974). Magnetic Susceptibility of the Surface Tills of Southern Ontario. *Canadian Journal of Earth Sciences*: **11**: 658-663.
- Grimm E.C. Jacobson G.L. Watts W.A. Hansen B.C.S. & Maasch K.A., (1993). A 50000 year Record of Climate Oscillations from Florida and its Temporal Correlation with the Heinrich Events. *Science*: **261**: 198-200.
- GRIP Members (1993). Climate Instability During the Last Interglacial Period Recorded in the GRIP Ice Core. *Nature*: **364**: 203-207.
- Gröger M. Heinrich R. & Bicket T., (2003). Glacial-Interglacial Variability in Lower North Atlantic Deep Water: Inference from Silt grain-sized Analysis and Carbonate Preservation in the Western Equatorial Atlantic. *Marine Geology*: **201**: 321-332.
- Grousset F.E. Labeyrie L. Sinko J.A. Cremer M. Bond G. Duprat J. Cortijo E. & Huon S., (1993). Patterns of Ice-rafted Detritus in the Glacial North Atlantic (40° - 55°). *Paleoceanography*: **8**(2): 175-192.
- Grousset F.E. Pujol C. Labeyrie L. Auffret G. & Boelaert A., (2000). Were the North Atlantic Heinrich Events Triggered by the Behaviour of the European Ice Sheets? *Geology*: **28**(2): 123-126.
- Grousset F.E. Cortijo E. Houn S. Herve L. Richter T. Burdloff D. Duprat J. & Weber O., (2001). Zooming in on Heinrich Layers. *Paleoceanography*: **16**(3): 240-259.

- Gwiazda R.H. Hemming S.R. & Broecker W.S., (1996a). Tracking the Sources of Icebergs with Lead Isotopes: The Provenance of Ice-Rafted Debris in Heinrich Layer 2. *Paleoceanography*: 11(1): 77-93.
- Gwiazda R.H. Hemming S.R. & Broecker W.S., (1996b). Provenance of Icebergs during Heinrich Event 3 and the Contrast to their Sources during Other Heinrich Episodes. *Paleoceanography*: 11(4): 371-378.
- Hall I.R., (2002). Personal Communication: E. Wadsworth.
- Hall I.R. & McCave I.N., (1998a). Late Glacial to Recent Accumulation Fluxes of Sediments at the Shelf Edge and Slope of NW Europe 48-50°N. In Stoker M.S. Evans D. & Cramp A. (eds). *Geological Processes on Continental Margins: Sedimentation, Mass Wasting and Stability*. Geological Society London Special Publication: 129: 339-350.
- Hall I.R. & McCave I.N., (1998b). Glacial-Interglacial Variation in Organic Carbon Burial on the Slope of the NW European Continental Margin (48-50°N). *Progress in Oceanography*: 42: 37-60.
- Hall I.R. & McCave I.N., (2000). Palaeocurrent Reconstruction, Sediment and Thorium Focusing on the Iberian Margin over the Last 140 kyr. *Earth and Planetary Science Letters*: 178: 151-164.
- Hall I.R. McCave I.N. Chapman M.R. & Shackleton N.J., (1998). Coherent Deep Flow Variations in the Iceland and American Basins during the Last Interglacial. *Earth and Planetary Science Letters*: 134: 15-21.
- Hallam D.F. & Maher B.A., (1994). A Record of Reversed Polarity carried by the Iron Sulphide Greigite in British Early Pleistocene Sediments. *Earth and Planetary Science Letters*: 121: 71-80.

- Hardy R. & Tucker M., (1988). X-ray Powder Diffraction of Sediments, Chapter 7: *Techniques in Sedimentology*. Tucker M. (ed). Oxford, Blackwell Scientific Publications: 191-228.
- Hearle J.W.S., (1972). Introduction to Scanning Electron Microscopy. *The Use of the Scanning Electron Microscope*. Hearle J.W.S. Sparrow J.T. & Cross P.M. (eds). Oxford, Pergamon Press Ltd.
- Heezen & Laughton (1960). Chapter 14. *The Sea*: 3: 312-364.
- Heier-Nielsen S. Heinemeier J. Nielsen H.L. & Rid N., (1995). Recent Reservoir Ages of Danish Fjords and Marine Waters. *Radiocarbon*: 37(3): 875-882.
- Heinrich H., (1988). Origin and Consequences of Cyclic Ice-rafting in the North Atlantic Ocean during the past 130 000yrs. *Quaternary Research*: 29: 142-152.
- Heller F. & Liu T., (1984). Magnetism of Chinese Loess Deposits. *Geophysical Journal of the Royal Astronomical Society*: 77: 125-141.
- Helmke J.P. Schulz M. & Bauch H.A., (2002). Sediment Color Record from the Northeast Atlantic Reveals Patterns of Millennial-Scale Climate Variability during the Past 500 000 Years. *Quaternary Research*: 57: 49-57.
- Hemming S. R., (2004). Heinrich Events: Massive Late Pleistocene Detritus Layers of the North Atlantic and their Global Climate Imprint. *Reviews of Geophysics*: 42(1): 1-43.
- Hemming S.R. Broecker W.S. Sharp W.D. Bond G.C. Gwiazda R.H. McManus J.K. Klas M. & Hajdas I., (1998). Provenance of Heinrich Layers in Core V28-82, NE Atlantic: $^{40}\text{Ar}/^{39}\text{Ar}$ Ages of Ice-Rafted Hornblende, Pb isotopes in Feldspar and

- Nd-Sr-Pb isotopes in the fine sediment fraction. *Earth and Planetary Science Letters*: 164: 317-333.
- Hemming S.R. Vorren T.O. & Kleman J., (2002). Provinciality of Ice Rafting in the North Atlantic: Application of $^{40}\text{Ar}/^{39}\text{Ar}$ Dating of Individual Hornblende Grains. *Quaternary International*: 95-96: 75-85.
- Heslop D. Dekkers M.J. & Langereis C.G., (2002). Timing and Structure of the mid-Pleistocene transition: records from the loess deposits of northern China. *Palaeogeography, Palaeoclimatology, Palaeoecology*: 185: 133-143.
- Heywood V.H., (1971). The Characteristics of the Scanning Electron Microscope and their Importance in Biological Studies. *Scanning Electron Microscopy*. Heywood V.H. (ed). London, Academic Press Inc. 4: 1-16.
- Higham T., (2003). Corrections to Radiocarbon Dates [online]. Oxford University, Available from: www.c14dating.com (14/11/2003).
- Hilton. J., (1986). Normalised Magnetic Parameters and Their Applicability to Palaeomagnetism and Environmental Magnetism. *Geology*: 14: 887-889.
- Hilton J., (1990). Greigite and the Magnetic Properties of Sediments. *Limnology and Oceanography*: 35(2): 509-520.
- Hilton J. & Lishman J.P., (1985). The Effect of the Redox Change on the Magnetic Susceptibility of Sediments from a Seasonally Anoxic Lake. *Limnology & Oceanography*: 30: 907-909.
- Hollister C.D. Silva A.J. & Driscoll A., (1973). A Giant Piston Corer. *Ocean Engineering*: 2: 159-168.

- Hong C-S. Torii M. Shea K-S. & Kao S-J., (1998). Inconsistent Magnetic Polarities between Greigite and Pyrrhotite bearing Marine Sediments from the Tsailiao-chi section, Southwestern Taiwan. *Earth and Planetary Science Letters*: 164: 467-481.
- Hughen K.A. Overpeck J.T. Peterson L.C. & Trumbore S., (1996). Rapid Climate Changes in the Tropical Atlantic Region during the Last Deglaciation. *Nature*: 380: 51-54.
- Hughen K.A. Overpeck J.T. Lehman S.J. Kashgarians M. Southons J. Peterson L.C. Alley R. & Sigman D.M., (1998). Deglacial Changes in Ocean Circulation from and Extended Radiocarbon Calibration. *Nature*: 391: 65-68.
- Hughen K.A. Southon J.R. Lehman S.J. & Overpeck J.T., (2000). Synchronous Radiocarbon and Climate Shifts During the Last Deglaciation. *Science*: 290: 1951-1954.
- Hughen K.A. Lehman S.J. Overpeck J.T. Southons J. Marchal O. Herring C. & Turnbull J., (2004). ^{14}C Activity and Global Carbon Cycle Changes over the Past 50 000 years. *Science*: 303: 202-207.
- Hull S., (1998). Crash Course in Statistics for Scientists. *Personal Communication*. E. Wadsworth.
- Hunt A., (1986). The Application of Mineral Magnetic Methods to Atmospheric Aerosol Discrimination. *Physics of the Earth and Planetary Interiors*: 42: 10-21.
- Hunt A.G. & Malin P.E., (1998). Possible Triggering of Heinrich Events by Ice-Land induced earthquakes. *Nature*: 393: 155-158.
- Jansen E. & Veum T., (1990). Evidence for Two-Step Deglaciation and it's impact on North Atlantic Deep-Water Circulation. *Nature*: 343: 612-612.

- Jansen J. H. F. Van der Gaast S. J. Koster B. & Vaars A. J., (1998). CORTEX, a shipboard XRF-scanner for element analyses in split sediment cores. *Marine Geology*: 151(1-4): 143-153.
- Johnsen S.J. Clausen H.B. Dansgaard W. Fuhrer K. Gundestrup N. Hammer C.U. Iversen P. Jouzel J. Stauffer B. & Steffensen J.P., (1992). Irregular Glacial Interstadials Recorded in a New Greenland Ice Core. *Nature*: 359: 311-313.
- Kandiano E. S. Bauch H.A. & Muller A., (2004). Sea Surface Temperature Variability in the North Atlantic during the Last Two Glacial-Interglacial cycles: Comparison of Faunal, Oxygen Isotopic, and Mg/Ca-derived Records. *Palaeogeography, Palaeoclimatology, Palaeoecology*: 204(1-2): 145-164.
- Kanfoush S.L. Hodell D.A. Charles C.D. Guilderson T.P. Mortyn G. & Ninnemann U.S., (2000). Millennial-Scale Instability of the Antarctic Ice Sheet during the Last Glaciation. *Science*: 288: 1815-1818.
- Karega A., (1995). Cretaceous foraminifers from the Mandawa Basin, southern Tanzania: Preliminary Results. *Marine Micropaleontology*: 26(1-4): 419-423.
- Karlin R. Lyle. M. Heath. G.R., (1987). Authigenic Magnetite Formation in Suboxic Marine Sediments. *Nature*: 326: 490-492.
- Karlin R., (1990a). Magnetic Mineral Diagenesis in Suboxic Sediments at Bettis Site W-N, NE Pacific Ocean. *Journal of Geophysical Research*: 95(B4): 4421-4436.
- Karlin R., (1990b). Magnetite Diagenesis in Marine Sediments from the Oregon Continental Margin. *Journal of Geophysical Research*: 95(B4): 4405-4419.
- Kellogg T.B., (1976). Late Quaternary Climate Changes: Evidence from Deep-Sea Cores of Norwegian and Greenland Seas. *Investigations of Late Quaternary*

- Palaeoceanography and Palaeoclimates*. Cline R.M. & Hays J.D. (eds). Geological Society of America Memoir 145: 77-110.
- Kent. D.V., (1982). Apparent Correlation of Palaeomagnetic Intensity and Climate Records in Deep-Sea Sediments. *Nature*: 299: 538-539.
- Kidd R.B. & Hailwood E.A., (1993). High Resolution Stratigraphy in Modern and Ancient Marine Sequences: Ocean Sediment Core to Palaeozoic Outcrop. *High Resolution Stratigraphy*. Hailwood E.A. & Kidd R.B. (eds). London, Geological Society Special Publication. 70: 1-8.
- King C.A.M., (1974). *Introduction to Marine Geology*. London, Arnold.
- King C.A.M. & Buckley J.T., (1968). The Analysis of Stone Size and Shape in Arctic Environments. *Journal of Sedimentary Petrology*: 38(1): 200-214.
- King J.W. & Channell J.E.T., (1991). Sedimentary Magnetism, Environmental Magnetism and Magnetostratigraphy. *Reviews of Geophysics: Supplement*: 358-370.
- Kirby M.E. & Andrews J.T., (1999). Mid-Wisconsin Laurentide Ice Sheet Growth and Decay: Implications for Heinrich Events 3 & 4. *Paleoceanography*: 14(2): 211-223.
- Kirschvink J.L. & Lowenstam H.A., (1979). Mineralisation and Magnetisation of Chiton Teeth: Palaeomagnetic, Sedimentologic and Biological Implications of Organic Magnetite. *Earth and Planetary Science Letters*: 44: 193-204.
- Kirschvink J.L. & Chang S-B.R., (1984). Ultra-Fine-Grained Magnetite in Deep-Sea Sediments: Possible Bacterial Magnetofossils. *Geology*: 12: 559-562.

- Kirtay V. J. Kellum J. H. & Apitz S. E., (1998). Field-portable X-ray fluorescence spectrometry for metals in marine sediments: results from multiple sites. *Water Science and Technology*: 37(6-7): 141-148.
- Kissel C. Laj C. Lehman B. Labeyrie L. & Bout-Raumazeilles V., (1997). Changes in the Strength of Iceland-Scotland Overflow Water in the last 200,000 years: Evidence from Magnetic Anisotropy Analysis of core SU90-33. *Earth and Planetary Science Letters*: 152: 25-36.
- Kissel C. Laj C. Labeyrie L. Dokken T. Voelker A. & Blamart D., (1999). Rapid Climatic Variations During Marine Isotopic Stage 3: Magnetic Analysis of Sediments from Nordic Seas and North Atlantic. *Earth and Planetary Science Letters*: 171: 489-502.
- Kitagawa H. & van der Plicht J., (1998). A 40 000yr Varve Chronology from Lake Suigetsu, Japan: Extension of the ^{14}C Calibration curve. *Radiocarbon*: 40(1): 505-515.
- Kitagawa H. & van der Plicht J., (2000). Atmospheric Radiocarbon Calibration beyond 11900 Cal BP from Lake Suigetsu Laminated Sediments. *Radiocarbon*: 42(3): 369-380.
- Knutz P.C. Austin W.E.N. & Jones E.J.W., (2001). Millennial-Scale Depositional Cycles Related to British Ice Sheet Variability and North Atlantic Palaeocirculation Since 45 kyr BP, Barra Fan, UK Margin. *Paleoceanography*: 16(1): 53-64.
- Knutz P.C. Hall I.R. Zahn R. Rasmussen T.L. Kuijpers A. Moros M. Shackleton N.J., (2002). Multidecadal Ocean Variability and NW European Ice Sheet Surges during the last Deglaciation. *Geochemistry Geophysics Geosystems*: 3(12).

- Kris M. Krsova M. Pruner P. Zeman A. Novak F. & Jansa J., (1990). A Petromagnetic Study of Miocene Rocks Bearing Micro-Organic Material and the Magnetic Mineral Greigite. *Physics of the Earth and Planetary Interiors*: 63: 98-112.
- Kroon D. Austin W.E.N. Chapman M.R. & Ganssen G.M., (1997). Deglacial Surface Circulation Changes in the Northeastern Atlantic: Temperature and Salinity Records off NW Scotland on a Century Scale. *Paleoceanography*: 12(6): 755-763.
- Kuehl S.A. Nittrouer C.A. DeMaster D.J. & Curtin T.B., (1985). A Long Square-Barrel Gravity Corer for Sediment and Geochemical Investigation of Fine-Grained Sediments. *Marine Geology*: 62: 365-370.
- Lagerklint I.M. & Wright J.D., (1999). Late Glacial Warming Prior to Heinrich Event 1: The Influence of Ice-Rafting and Large Ice Sheets on the Timing of Initial Warming. *Geology*: 27(12): 1099-1102.
- Lagroix F. & Banerjee S.K., (2002). Paleowind Directions from the Magnetic Fabric of Loess Profiles in Central Alaska. *Earth and Planetary Science Letters*: 195: 99-112.
- Laj C. Mazaud A. & Duplessy C., (1996). Geomagnetic Intensity and ^{14}C Abundance in the Atmosphere and Ocean during the past 50 kyr. *Geophysical Research Letters*: 23(16): 2045-2048.
- Lal D., (2004). Assessing Past Climate Changes from Proxy Records: An Iterative Process between Discovery and Observations. *Quaternary International*: 117: 5-16.

- Lambeck K., (1995). Late Devensian and Holocene Shorelines of the British Isles and North Sea from Models of Glacio-hydro-isostatic Rebound. *Journal of the Geological Society, London*: 152: 437-448.
- Lean C. M. B. & McCave I.N., (1998). Glacial to Interglacial Mineral Magnetic and Palaeoceanographic Changes at Chatham Rise, SW Pacific Ocean. *Earth and Planetary Science Letters*: 163(1-4): 247-260.
- Lee C.H. & Jin J-H., (1995). Authigenic Greigite in Mud from the Continental Shelf off the Yellow Sea, off the Southwestern Korean Peninsula. *Marine Geology*: 128: 11-15.
- Lees J. & Dearing J., (1999). Additional Measurements Using a Vibrating Sample Magnetometer. Chapter 10: *Environmental Magnetism: A Practical Guide*. Walden J. Oldfield F. & Smith J., (eds). London, Quaternary Research Association. Technical Guide No 6: 185-196.
- Leuschner D.C. & Sirocko F., (2000). The Low-Latitude Monsoon Climate During Dansgaard-Oeschger cycles and Heinrich Events. *Quaternary Science Reviews*: 19: 245-254.
- Leigh S., (2004). Personal Communication. E. Wadsworth.
- Lindsley D.H. *et al.*, (1966). Magnetic Properties of Rocks and Minerals. *Handbook of Physical Constants*. S.P. Clark (ed). New York, Geological Society of America. Memoir 97: 544-551.
- Liu X.M. Rolph T.C. Bloemendal J. Shaw J. & Liu T.S., (1995). Quantitative Estimates of Palaeoprecipitation in the Loess Plateau of China. *Palaeogeography, Palaeoclimatology, Palaeoecology*: 113: 243-248.

- Liu Q. Banerjee S. & Jackson M., (2002). A New Method in Mineral Magnetism for the Separation of Weak Antiferromagnetic Signal from a Strong Ferrimagnetic Background. *Geophysical Research Letters*: **29**(12): 6-1 – 6-4.
- Liu X.M. Rolph T. An Z. & Hesse P., (2003a). Palaeoclimatic Significance of Magnetic Properties on the Red Clay underlying the Loess and Palaeosols in China. *Palaeogeography, Palaeoclimatology, Palaeoecology*: **199**: 153-166.
- Liu J. Zhu R. & Li G., (2003b). Rock magnetic properties of the fine-grained sediment on the outer shelf of the East China Sea: implications for provenance. *Marine Geology*: **193**: 195-206.
- Lowe J.J. & Walker M.J.C., (1997). *Reconstructing Quaternary Environments*. Essex, Longman.
- Lowell T.V. Heusser C.J. Anderson B.G. Moreno P.I. Hauser A. Heusser L.E. Schichter C. Marchant D.R. & Denton G.H., (1995). Interhemispheric Correlation of Late Pleistocene Glacial Events. *Science*: **269**: 1541-1549.
- Lowrie W. & Fuller M., (1971). On the Alternating Field Demagnetisation Characteristics of Multidomain Thermoremanent Magnetisation in Magnetite. *Journal of Geophysical Research*: **76**: 6339-6349.
- Lowry R.K. Downer R.M. & Loncar Z., (1997). Ocean Margin EXchange: OMEX 1 Data Set CD ROM. Birkenhead, British Oceanographic Data Centre.
- MacAyeal D.R., (1993). Binge/Purge Oscillations of the Laurentide Ice Sheet as a Cause of the North Atlantic Heinrich Events. *Paleoceanography*: **8**(6): 775-784.
- MacKenzie A. B. Logan E.M. Cook G.T. & Pulford I.D., (1998). Distributions, Inventories and Isotopic Composition of Lead in ^{210}Pb -dated Peat Cores from

Contrasting Biogeochemical Environments: Implications for Lead Mobility. *The Science of The Total Environment*: 223(1): 25-35.

Mackereth F.J.H., (1965). Chemical Investigation of Lake Sediments and their Interpretation. *Proceedings of the Royal Society of London Series B*(161): 295-309.

Mackereth F.J.H., (1966). Some Chemical Observations on Post-glacial Lake Sediments. *Transitions of the Royal Society of London, Series B*: 250: 165-213.

Mackereth F.J.H., (1971). On the Variation in Direction of the Horizontal Component of Remanent Magnetism in Lake Sediments. *Earth and Planetary Science Letters*: 12: 332-338.

Maher B A., (1988). Magnetic Properties of Some Synthetic Sub-Micron Magnetites. *Geophysical Journal*: 94: 83-96.

Maher B A., (1998). Magnetic Properties of Modern Soils and Quaternary Loessic Palaeosols: Palaeoclimatic Implications. *Palaeogeography, Palaeoclimatology, Palaeoecology*: 137: 25-54.

Maher B. & Taylor R.M., (1988). Formation of Ultrafine Grained Magnetite in Soils. *Nature*: 336: 368-370.

Maher B. & Thompson R., (1992). Palaeoclimatic Significance of the Mineral Magnetic Record of the Chinese Loess and Palaeosols. *Quaternary Research*: 37: 155-170.

Maher B.A. & Thompson R., (1999). Palaeomonsoons I: The Magnetic Record of Palaeoclimate in the Terrestrial Loess and Palaeosol Sequences. Chapter 3:

- Quaternary Climates, Environments and Magnetism*. Maher B.A. & Thompson R. (eds). Cambridge, Cambridge University Press: 81-125.
- Maher B A. Thompson R. & Zhou L.P., (1994). Spatial and Temporal Reconstructions of Changes in the Asian Palaeomonsoon: A New Mineral Magnetic Approach. *Earth and Planetary Science Letters*: 125: 461-471.
- Maher B A. Thompson R. & Hounslow M.W., (1999). Introduction. Chapter 1: *Quaternary Climates, Environments and Magnetism*. Maher B.A. & Thompson R. (eds). Cambridge, Cambridge University Press: 1-48.
- Manabe & Stouffer R.J., (1995). Simulation of Abrupt Climate Change Induced by Freshwater Input to the North Atlantic Ocean. *Nature*: 378: 165-167.
- Manighetti B. & McCave I.N., (1995). Late Glacial and Holocene Palaeocurrents around Rockall Bank, N.E. Atlantic. *Paleoceanography*: 10: 512-525.
- Maslin M. Shackleton N. J. & Pflaumann U., (1995). Surface Water Temperature, Salinity and Density Changes in the Northeast Atlantic During the Last 45 000 years: Heinrich Events, Deep-water Formation and Climate Rebounds. *Paleoceanography*: 10(3): 527-244.
- McCave I.N. Hall I.R. Antia A.N. Chou L. Dehairs F. Lampitt R.S. Thomsen L. van Weering T.C.E. & Wollast R., (2001). Distribution, Composition and Flux of Particulate Material over the European Margin at 47-50°N. *Deep-Sea Research II*: 48: 3107-3139.
- McCave I.N., (2004). Personal Communication. E. Wadsworth.
- McCabe A.M. & Clark P.U., (1998). Ice Sheet Variability Around the North Atlantic Ocean During the last Deglaciation. *Nature*: 392: 373-377.

- McClellan R.G. & Kean W.F., (1993). Contributions of Wood Ash Magnetism to Archaeomagnetic Properties of Fire Pits and Hearths. *Earth and Planetary Science Letters*: 119: 387-394.
- McCoy F. W., (1985). Mid-core Flow-in; Implications for Stretched Stratigraphic Sections in Piston Cores. *Journal of Sedimentary Petrology*: 55(4): 608-610.
- McManus J.F. Oppo D.W. & Cullen J.L., (1999). A 0.5 Million Year Record of Millennial Scale Climate Variability in the North Atlantic. *Science*: 283: 971-975.
- Meese D.A. Gow A.J. Alley R.B. Zielinski G.A. Grootes P.M. Ram M. Taylor K.C. Mayewski P.A. & Bolzan J.F., (1997). The Greenland Ice Sheet Project 2 Depth-Age Scale: Methods and Results. *Journal of Geophysical Research*: 102: 26411-26423.
- Molspin (unknown). Molspin products [online]. Newcastle. Available from: www.molspin.com (6/7/2004).
- Monna F. Dominik J. Loizeau J-L. Pardos M. & Arpagaus P., (1999). Origin and evolution of Pb in sediments of Lake Geneva (Switzerland- France). Establishing a stable Pb record. *Environmental Science and Technology*: 33(17): 2850-2857.
- Moreno E. Thouveny N. Delanghe D. McCave I.N. & Shackleton N.J., (2002). Climate and Oceanographic Changes in the NE Atlantic Reflected by Magnetic Properties of Sediments deposited on the Portuguese Margin during the past 340 kyr. *Earth and Planetary Science Letters*: 6316: 1-16.
- Moros M. McManus J.F. Rasmussen T. Kuijpers A. Dokken T. Snowball I. Nielsen T. & Jansen E., (2004). Quartz Content and the Quartz to Plagioclase Ratio Determined by X-Ray Diffraction: A Proxy for Ice Rafting in the Northern North Atlantic. *Earth and Planetary Science Letters*: 218: 389-401.

- Moskowitz B.M. Frankel R.B. Flanders P.J. Blakemore R.P. & Schwartz B.B., (1988). Magnetic Properties of Magnetotactic Bacteria. *Journal of Magnetism and Magnetic Materials*: 73: 273-288.
- Moskowitz B.M. Frankel R.B. & Bazylinski D A., (1993). Rock Magnetic Criteria for the Detection of Biogenic Magnetite. *Earth and Planetary Science Letters*: 120: 283-300.
- Muhs D.R. Ager T.A. Bettis E.A. McGeechin J. Been J.M. Begét J.E. Pavich M.J. Stafford T.W. & Stevens S.P., (2003). Stratigraphy and Palaeoclimate significance of Late Quaternary Loess-Palaeosol Sequences of the Last Interglacial-Glacial cycles in Central Alaska. *Quaternary Science Reviews*: 22: 1947-1986.
- Mulitza S. Arz H. Kemle-von Mucke S. Moos C. Niebler H-S. Patzold J. & Segl M., (1999). The South Atlantic Carbon Isotope Record of Planktic Foraminifera. *Use of Proxies in Palaeoceanography: Examples from the South Atlantic*. Fischer. G. & Wefer G. (eds). Berlin, Springer-Verlag: 427-445.
- Mullins C.E., (1977). Magnetic Susceptibility of the Soil and its Significance in Soil Science - A Review, *Journal of Soil Science*: 28: 223-246.
- Norrish K. & Chappell B., (1967). X-Ray Fluorescence Spectrography. Chapter 4: *Physical Methods in Determinative Mineralogy*. Zussman Z. (ed). London, Academic Press Inc.
- Oerlemans J., (1993). Evaluating the Role of Climate Cooling in Iceberg Production and the Heinrich Events. *Nature*: 364: 783-785.
- Oldfield F., (1991). Environmental Magnetism - A Personal Perspective. *Quaternary Science Reviews*: 10: 73-85.

- Oldfield F., (1992). The Source of Fine-grained Magnetite in Sediments. *The Holocene*: 2(2): 180-182.
- Oldfield F., (1994). Towards the Discrimination of Fine-grained Ferrimagnets by Magnetic Measurements in Lake and near shore Marine Sediments. *Journal of Geophysical Research*: 95(B5): 9045-9050.
- Oldfield F., (1999). Environmental Magnetism: The Range of Applications. Chapter 12: *Environmental Magnetism: A Practical Guide*. Walden J. Oldfield F. & Smith J. (eds), London, Quaternary Research Association. Technical Guide No 6: 98-112.
- Oldfield F. Hunt A. Jones M.D.H. Chester R. Dearing J.A. Olsson L. & Prospero J.M., (1985). Magnetic Differentiation of Atmospheric Dusts. *Nature*: 317: 516-518.
- Oppo D.W. & Lehman S.J., (1995). Suborbital Timescale Variability of North Atlantic Deep Water during the Past 200 kyr. *Paleoceanography*: 10(5): 901-910.
- Oppo D.W. McManus J.F. & Cullen J.L., (1998). Abrupt Climate Events 500 000 to 340 000 years age: Evidence from Subpolar North Atlantic Sediments. *Science*: 279: 1335-1338.
- Paasche O. Lovlie R. Dahl S.O. Bakke J. & Nesje A., (2004). Bacterial magnetite in lake sediments: late glacial to Holocene climate and sedimentary changes in northern Norway. *Earth and Planetary Science Letters*: 223(3-4): 319-333.
- Palliard D. & Labeyrie L., (1994). Role of the Thermohaline Circulation in the Abrupt Warming after Heinrich Events. *Nature*: 372: 162-164.
- Parkin D.W., (1974). Trade-Winds During the Glacial Cycles. *Proceedings of the Royal Society Series A*: 377: 73-100.

- Peck J.A. King J.W. Colman S.M. & Kravchinsky V.A., (1994). A Rock Magnetic Record from Lake Baikal, Siberia: Evidence for Late Quaternary Climate Change. *Earth and Planetary Science Letters*: 122: 221-238.
- Peck V., (2003). Personal Communication. E. Wadsworth.
- Pennington *et al.*, (1972). Lake Sediments in Northern Scotland. *Transitions of the Royal Society of London, Series B*: 264: 191-294.
- Peters C. & Thompson R., (1998). Magnetic Identification of Selected Natural Oxides and Sulphides. *Journal of Magnetism and Magnetic Materials*: 183: 365-374.
- Peters C. & Turner G., (1999). Lake Paringa: a Catchment Study Using Magnetic Techniques. *Physics and Chemistry of the Earth A*: 24(9): 753-757.
- Peters C. & Dekkers M.J., (2003). Selected Room Temperature Magnetic Parameters as a Function of Mineralogy, Concentration and Grain Size. *Physics and Chemistry of the Earth*: 28: 659-667.
- Petersen N. von Dobeneck T. & Vali H., (1986). Fossil Bacterial Magnetite in Deep-Sea Sediments from the South Atlantic Ocean. *Nature*: 320: 611-615.
- Petit J.R. Jouzel J. Raynaud N.I. Barnola J-M. Basile I. Benders M. Chappellaz J. Davis M. Delaygue G. Delmotte M. Kotlyakov V.M. Legrand Lipenkov V.Y. Lorius C. Pepin L. Ritz C. Saltzman E. & Stievenard M., (1999). Climate and the Atmospheric History of the Past 420 000yrs from the Vostok Ice Core, Antarctica. *Nature*: 399: 429-436.
- Piepgas D.P. & Wasserburg G.J., (1980). Neodymium Isotopic Variations in Seawater. *Earth and Planetary Science Letters*: 50: 128-138.

- Pilcher J., (1991). Radiocarbon Dating for the Quaternary Scientist. *Radiocarbon Dating: Recent Applications and Future Potential*. Lowe J.J.(ed), Cambridge, QRA. Quaternary Proceedings 1: 27-33.
- Piotrowski A.M. Goldstein S.L. Hemming S.R. & Fairbanks R.G., (2004). Intensification and Variability of Ocean Thermohaline Circulation through the Last Deglaciation, *Earth and Planetary Science Letters*: 225(1-2): 205-220.
- Porter S.C. & Zhisheng A., (1995). Correlation between Climate Events in the North Atlantic and China during the Last Glaciation. *Nature*: 375: 305-308.
- Prange M. Lohmann G. Romanova V. & Butzin M., (2004). Modelling Temp-Spatial Signatures of Heinrich Events: Influence of the Climatic Background State. *Quaternary Science Reviews*: 23: 521-527.
- Prohaska T. Watkins M. Latkoczy C. Wenzel W.W. & Stingeder G. (2000). Lead Isotope Ratio Analysis by Inductively Coupled Plasma Sector Field Mass Spectrometry (ICP-SMS) in soil digests of a depth profile. *Journal of Analytical Atomic Spectrometry*: 15(4): 365-369.
- Rahman A., (1995). Reworked Nannofossils in the North Atlantic Ocean and Subpolar Basins: Implications for Heinrich Events and Ocean Circulation. *Geology*: 23(6): 487-490.
- Rashid H. Hesse R. & Piper D.J.W., (2003). Distribution, Thickness and Origin of Heinrich Layer 3 in the Labrador Sea. *Earth and Planetary Science Letters*: 205: 281-293.
- Rasmussen T.L. van Weering T.C.E. & Labeyrie L., (1997). Climatic Instability, Ice Sheets and Ocean Dynamics during the Last Glacial Period (58-10 kyr BP). *Quaternary Science*: 16: 71-80.

- Raymo M.E. Ruddiman W.F. Shackleton N.J. & Oppo D.W., (1990). Evolution of Atlantic-Pacific ^{13}C gradients over the last 2.5 my. *Earth and Planetary Science Letters*: 97: 353-368.
- Renberg, I. Brannvall M-L. Bindler R. Emteryd O., (2002). Stable Lead Isotopes and Lake Sediments--a Useful Combination for the Study of Atmospheric Lead Pollution History. *The Science of The Total Environment*: 292(1-2): 45-54.
- Rendle R. H. & Reijmer J. J. G., (2002). Quaternary Slope Development of the Western, Leeward Margin of the Great Bahama Bank. *Marine Geology*: 185(1-2): 143-164.
- Revel M. Sinko J.A. Grousset F.E. & Biscaye P.E., (1996). Sr and Nd Isotopes as Tracers of North Atlantic Lithic Particles: Palaeoclimatic Implications. *Paleoceanography*: 11(1): 95-113.
- Richards A.F., (1966). Principles of Piston Coring Fine-Grained Sediments with Minimum Deformation. *Geological Society of America: Abstracts for 1965*(87): 136.
- Richter T.O. Lassen S. van Weering T.C.E. & de Haas H., (2001). Magnetic Susceptibility Patterns and Provenance of Ice-Rafted Material at Feni Drift, Rockall Trough: Implications for the History of the British-Irish Ice Sheet. *Marine Geology*: 173: 37-54.
- Roberts D.G. & Montadert L., (1979). Objectives of Passive Margin Drilling. *Initial Reports of the Deep Sea Drilling Project*: 48: 5-8.
- Roberts A.P. & Turner G.M., (1993). Diagenetic Formation of Ferrimagnetic Iron Sulphide Minerals in Rapidly deposited Marine Sediments, South Island, New Zealand. *Earth and Planetary Science Letters*: 115: 257-273.

- Roberts A.P., (1995). Magnetic properties of Sedimentary Greigite (Fe₃S₄). *Earth and Planetary Science Letters*: **134**: 227-236.
- Robinson S.G., (1986). The Late Pleistocene Palaeoclimate Record of North Atlantic Deep-Sea Sediments revealed by Mineral Magnetic Measurements. *Physics of the Earth and Planetary Interiors*: **42**: 22-47.
- Robinson S.G., (1990). Applications of Whole-core Magnetic Susceptibility Measurements of Deep-Sea Sediments: ODP Leg 115, Results. *Proceedings of the Ocean Drilling Project*: **115**: 737-771.
- Robinson S.G. Maslin M.A. & McCave N., (1995). Magnetic Susceptibility Variations in Upper Pleistocene Deep Sea Sediments of the North East Atlantic: Implications for Ice-Rafting and Palaeocirculation at the Last Glacial Maximum. *Paleoceanography*: **10**(2): 221-250.
- Rochette P. Fillion G. Mattei J-L. & Dekkers M.J. (1990). Magnetic Transition at 30-34 Kelvin in Pyrrhotite: Insight into a Widespread Occurrence of the Mineral in Rocks. *Earth and Planetary Science Letters*: **98**: 319-328.
- Röhl U. Bralower T.J. Norris R.D. & Wefer G., (2000). New Chronology for the Late Pleistocene Thermal Maximum and its Environmental Implications. *Geology*: **28**(10): 927-930.
- Rosenbaum J.G. Reynolds R.L. Adam D.P. Drexler J. Sarna-Wojcicki A.M. & Whitney G.C., (1996). A Middle Pleistocene Climate Record from Buck Lake, Cascade Range, Southern Oregon: Evidence from Sedimentary Magnetism, Trace Element Geochemistry, and Pollen. *Geological Society of America Bulletin*: **108**: 1328-1341.

- Rosman K. J. R. Chisholm W. *et al.*, (1997). Lead from Carthaginian and Roman Spanish Mines Isotopically Identified in Greenland Ice Dated from 600 B.C. to 300 A.D. *Environmental Science and Technology*: **31**(12): 3413-3416.
- Ruddiman W.F., (1977). Late Quaternary Deposition of Ice-rafted Sand in the Subpolar North Atlantic (40° - 60°). *Geological Society of America: Bulletin* **88**: 1813-1827.
- Ruddiman W.F., (2003). Orbital Insolation, Ice Volume and Greenhouse Gases. *Quaternary Science Reviews*: **22**: 1597-1629.
- Ruddiman W.F. & McIntyre A., (1976). Northeast Atlantic Palaeoclimate Changes over the last 600 kyr. *Geological Society of America: Memoir* **145**: 111-146.
- Sagnotti L. & Winkler A., (1999). Rock magnetism and Palaeomagnetism of Greigite-bearing mudstones in the Italian Peninsula. *Earth and Planetary Science Letters*: **165**: 67-80.
- Sagnotti L. Macri P. Camerlenghi A. & Rebesco M., (2001). Environmental Magnetism of Antarctic Late Pleistocene Sediments and Interhemispheric Correlation of Climatic Events. *Earth and Planetary Science Letters*: **192**: 65-80.
- Sartori M. Heller F. Forster T. Borkovec M. Hammann J. & Vincent E. (1999). Magnetic Properties of Loess Grain Size Fractions from the Section at Paks (Hungary). *Physics of the Earth and Planetary Interiors*: **116**: 53-64.
- Schilling J. van Weering T.C.E. & Eisma D., (1988). Advantages of Light-weight Kevlar Rope for Ocean Bottom Sampling with the Piston Corer and Box Corer. *Marine Geology*: **79**: 149-152.

- Schmelzer I., (1998). *High-Frequency Event Stratigraphy and Palaeoceanography of the Red Sea*, D.Sc Thesis, Eberhard-Karis-Universitat, Tübingen, Germany, 124pp.
- Schüler D., (1999). Formation of Magnetosomes in Magnetotactic Bacteria. *Journal of Molecular Microbiology and Biotechnology*: 1(1): 79-86.
- Schulz H. von Rad U. & Erlenkeuser H., (1998). Correlation Between Arabian Sea and Greenland Climate Oscillations of the Past 110 000 years. *Nature*: 393: 54-57.
- Scourse J.D. Hall I.R. McCave I.N. Young J.R. & Sugdon C., (2000). The Origin of Heinrich Events: Evidence from H₂ for European Precursor Events. *Earth and Planetary Science Letters*: 182: 187-195.
- Seibold E. & Berger W.H., (1982). *The Sea Floor*.
- Seidov D. & Maslin M., (1999). North Atlantic Deep Water Circulation Collapse During Heinrich Events. *Geology*: 27(1): 23-26.
- Shackleton N., (1963). Oxygen Isotope Analysis and Pleistocene Temperatures Re-Assessed. *Nature*: 215: 15-17.
- Shackleton N.J., (1987). Oxygen Isotopes, Ice Volume and Sea Level. *Quaternary Science Reviews*: 6: 183-190.
- Shackleton N.J. Hall M.A. & Vincent E., (2000). Phase Relationships Between Millennial Scale Events, 64000 - 24000 ka. *Paleoceanography*: 15(6): 565-569.

- Shu J. Dearing J.A. Morse A.P. Yu L. & Yuan N., (2001). Determining the Sources of Atmospheric Particles in Shanghai, China, from Magnetic and Geochemical Properties. *Atmospheric Environment*: 35: 2615-2625.
- Shaw J., (unknown). Magnetic Measurements [online]. Lancashire. Available from: www.magnetic-measurements.com 2004.
- Sinclair J.M., (consultant)(2001). *Collins Concise Dictionary*. Aylesbury, England, HarperCollins.
- Simonetti A. Gariépy C. & Carignan J., (2000). Pb and Sr Isotopic Evidence for Sources of Atmospheric Heavy Metals and their Deposition Budgets in Northeastern North America. *Geochimica et Cosmochimica Acta*: 64(20): 3439-3452.
- Skinner B.J. Erd R.C. & Grimaldi F.S., (1964). Greigite, the thio-spinel of Iron; A new Mineral. *American Mineralogist*: 49(5-6): 543-555.
- Skinner L.C. & McCave I.N., (2003). Analysis and Modelling of Gravity and Piston Coring Based on Soil Mechanics. *Marine Geology*: 199: 181-204.
- Smith J., (1999). An Introduction to the Magnetic Properties of Natural Minerals. Chapter 2: *Environmental Magnetism: A Practical Guide*. Walden J. Oldfield F. & Smith J. (eds), London, Quaternary Research Association. Technical Guide No 6: 5-25
- Snoeckx H. Grousset F. Revel M. & Boelaert A., (1999). European Contribution of Ice-Rafted Sand to Heinrich Layers H3 & H4, *Marine Geology*: 158: 197-208.
- Snowball I., (1991). Magnetic Hysteresis Properties of Greigite (Fe₃S₄) and a New Occurrence in Holocene Sediments from Sweddish Lapland. *Physics of the Earth and Planetary Interiors*: 68: 32-40.

- Snowball I., (1994). Bacterial Magnetite and the Magnetic Properties of Sediments in a Swedish Lake. *Earth and Planetary Science Letters*: 126: 129-142.
- Snowball I. & Thompson R., (1988). The Occurrence of Greigite in Sediments from Loch Lomond. *Journal of Quaternary Science*: 3(2): 121-125.
- Snowball I. & Torii M., (1999). Incidence and Significance of Magnetic Iron Sulphides in Quaternary Sediments and Soils. Chapter 7: *Quaternary Climates, Environments and Magnetism*. Maher B A. & Thompson R. (eds). Cambridge, Cambridge University Press: 199-230.
- Stallard M. O. Apitz S. E. & Dooley C. A., (1995). X-ray Fluorescence Spectrometry for Field Analysis of Metals in Marine Sediments. *Marine Pollution Bulletin*: 31(4-12): 297-305.
- Stauffer B., (1999). Cornucopia of Ice Core Results. *Nature*: 399: 412-413.
- Sternberg R.S., (1987). Archaeomagnetism and Magnetic Anomalies in the American Southwest. *Geophysics*: 52: 368-371.
- Stocker T.F., (1998). The Role of the Deep Ocean Circulation for Past and Future Climate Change. *Nature*:
- Stockhausen H. & Zolitschka B., (1999). Environmental Changes Since 13,000 cal. BP Reflected in Magnetic and Sedimentological Properties of Sediments from Lake Holzmaar (Germany). *Quaternary Science Reviews*: 18(7): 913-925.
- Stolz J.F. Chang S-B. R. & Kirschvink J.L., (1986). Magnetotactic Bacteria And Single Domain Magnetite in Hemipelagic Sediments. *Nature*: 321: 849-851.

- Stoner J.S. & Andrews J.T., (1999). The North Atlantic as a Quaternary Magnetic Archive. Chapter 2: *Quaternary Climates, Environments and Magnetism*. (eds) Maher B.A. & Thompson R. Cambridge, Cambridge University Press: 49-80.
- Stoner J.S. Channell J.E.T. & Hillaire-Marcel C., (1996). The Magnetic Signature of Rapidly Deposited Layers from the Deep Labrador Sea: Relationship to North Atlantic Heinrich Layers. *Paleoceanography*: 11(3): 309-325.
- Stordal M.C. & Wasserburg G.J., (1986). Neodymium Isotopic Study of Baffin Bay Water: Sources of REE from Very Old Terrains. *Earth and Planetary Science Letters*: 77: 259-272.
- Stow D.A.V. & Aksu A.E., (1978). Disturbances in Soft Sediments due to Piston Coring. *Marine Geology*: 28: 135-144.
- Stuiver M. & Reimer P.J., (1993). Extended ^{14}C Data Base and Revised Calib 3.0 ^{14}C Age Calibration Program. *Radiocarbon*: 40(1): 215-230.
- Stuiver M. Reimer P.J. Bard E. Beck J.W. Burr G.S. Hughen K.A. Kromer B. McCormac G. van der Plicht J. & Spurk M., (1998). Intcal98 Radiocarbon Age Calibration, 24000-0 cal BP. *Radiocarbon*: 40(1): 1041-1083.
- Tang Y. Jia J. & Xie X., (2003). Records of magnetic properties in Quaternary Loess and its Palaeoclimate Significance: A Brief Review. *Quaternary International*: 108: 33-50.
- Tarling D.H. & Turner P. (eds). (1999). *Palaeomagnetism and Diagenesis in Sediments*. London, Geological Society Special Publications. 151: 205-208.
- Telford R.J. Heegaard E. & Birks H.J.B., (2004a). The Intercept is a Poor Estimate of a Calibrated Radiocarbon Age. *The Holocene*: 12(2): 296-298.

- Telford R.J. Heegaard E. & Birks H.J.B., (2004b). All Age-Depth Models are Wrong: But How Badly? *Quaternary Science Reviews*: **23**: 1-5.
- Texasoft (2004). Kruskal-Wallis Test [online]. Available from: www.texasoft.com/winkkrus (8/7/2004).
- Thierstein H. R., (1976). Mesozoic Calcareous Nannoplankton Biostratigraphy of Marine Sediments. *Marine Micropaleontology*: **1**: 325-362.
- Thompson R., (1973). Palaeolimnology and Palaeomagnetism. *Nature*: **242**: 182-184.
- Thompson R. & Morton D.J., (1979). Magnetic Susceptibility and Particle-Size Distribution in Recent Sediments of the Loch Lomond Drainage Basin, Scotland, *Journal of Sedimentary Petrology*: **49**(3): 801-812.
- Thompson R. & Oldfield F., (1986). *Environmental Magnetism*. London, Allen & Unwin.
- Thompson R. Batterbee R.W. O'Sullivan P. E. Oldfield F., (1975). Magnetic Susceptibility of Lake Sediments. *Limnology and Oceanography*: **20**(5): 687-398.
- Thompson R. Bloemendal J. Dearing J.A. Oldfield F. Rummary T.A. Stober J.C. Turner G.M., (1980). Environmental Applications of Magnetic Measurements, *Science*: **207**(4430): 481-486.
- Thouveny N. Beaulieu J-L. Bonifay E. Creer K.M. Guiot J. Icole M. Johnson S. Jouzel J. Reille M. Williams T. & Williamson D., (1994). Climate Variations in Europe over the past 140 kyr Deduced from Rock Magnetism. *Nature*: **371**: 503-506.

- Thouveny N. Moreno E. Delanghe D. Candon L. Lancelot Y. & Shackleton N.J., (2000). Rock Magnetic Detection of Distal Ice-Rafted Debris: Clue for the Identification of Heinrich Layers on the Portuguese Margin. *Earth and Planetary Science Letters*: 180: 61-75.
- Times Books (1999). *Times Concise Atlas of the World*. Wembing, Aprinta GmbH & Co.
- Towe K.M. & Moench T.T., (1981). Electron-Optical Characterisation of Bacterial Magnetite. *Earth and Planetary Science Letters*: 52: 213-220.
- Tucker L.R. & MacCallum R.C., (1997). Exploratory Factor Analysis [online]. Available from: (07/2002).
- Union of Concerned Scientists (2004). Global Environment: Abrupt Climate Change [online]. USA. Available from: <http://www.ucsusa.org> (21/09/2004).
- Valkovic O. & Bogdanovic I., (1996). PIXE and XRF analysis of marine sediments. *Nuclear Instruments and Methods in Physics Research Section B: Beam Interactions with Materials and Atoms*: 109-110: 488-492.
- Vali H. Forster O. Amarantidis G. & Petersen N., (1987). Magnetotactic Bacteria and the Magnetofossils in Sediments. *Earth and Planetary Science Letters*: 86: 389-400.
- van der Biest O. & Thomas G., (1976). Fundamentals of Electron Microscopy. *Electron Microscopy in Mineralogy*. Wenk H.R. (ed). Berlin, Springer-Verlag.
- van Krevelde S.A. Knappertsbusch M. Ottens J. Ganssen G.M. & van Hinte J.E., (1996). Biogenic Carbonate and Ice Rafted Debris (Heinrich Layer) Accumulation in Deep Sea Sediments from a North Eastern Atlantic Piston Core. *Marine Geology*: 131: 21-46.

- van Kreveld S. Sarnthein M. Erlenkeuser H. Grootes P. Jung S. Nadeau M.J. Pflaumman U. & Voelker A., (2000). Potential Links Between Surging Ice Sheets, Circulation Changes, and the Dansgaard-Oeschger Cycles in the Irminger Sea, 60-18 kyr. *Paleoceanography*: 15(4): 425-442.
- van Weering T.C.E. McCave I.N. & Hall I.R., (1998a). Ocean Margin Exchange (OMEX I) Benthic Processes Study. *Progress in Oceanography* 42: 1-4.
- van Weering T.C.E. Hall I.R. de Stiger H.C. McCave I.N. & Thimsen L., (1998b). Recent Sediments, Sediment Accumulation and Carbon Burial at Goban Spur, NW European Continental Margin (47-50°N). *Progress in Oceanography*: 42: 2-35.
- van Weering T.C.E. Stigter H.C. Balzer W. Epping E.H.G. Graf G. Hall R. Helder W. Khripounoff A. Lohse L. McCave I.N. Thomsen L. & Vangriesheim A., (2001). Benthic Dynamics and Carbon Fluxes on the NW European Continental Margin. *Deep-Sea Research II*: 48: 3191-3221.
- Vance D. & Burton K., (1999). Nd Isotopes in Planktonic Foraminifera: A Record of the Response of Continental Weathering and Oceanic Circulation Rates to Climate Change. *Earth and Planetary Science Letters*: 173: 365-379.
- Vaniman D. T. Chipera S. J. Bish D. L. Duff M. C. & Hunter D. B., (2002). Crystal Chemistry of Clay-Mn Oxide Associations in Soils, Fractures, and Matrix of the Bandelier Tuff, Pajarito Mesa, New Mexico. *Geochimica et Cosmochimica Acta*: 66(8): 1349-1374.
- Verosub K.L. & Roberts A.P., (1995). Environmental Magnetism: Past, Present and Future, *Journal of Geophysical Research*: 100(B2): 2175-2192.
- Vidal L. Layebrie L. Cortijo E. Duplessy J.C. Michel E. Becque S. & van Weering T.C.E., (1997). Evidence for Changes in the North Atlantic Deep Water linked

- to Meltwater Surges during the Heinrich Events. *Earth and Planetary Science Letters*: 146: 13-27.
- Vitrac A.M. Albarende F. & Allegre C.J., (1981). Lead Isotope Composition of Hercynian Granitic K-Feldspars Constrains Continental Genesis. *Nature*: 291: 461-464.
- Vlag P. Rochette P. Thouveny N. & van Velzen A.J., (1996). A Rock Magnetic Study of the Soils and Basalts in the Catchment Area of Lac St. Front, Chapter 5. *PhD Thesis, P. Vlag Cerege University Aix Marseille III*: 65-96.
- Voelker A.H.L., (2002). Global Distribution of Centennial-scale Records for Marine Isotope Stage (MIS) 3: A Database. *Quaternary Science Reviews*: 21: 1185-1212.
- Vonder Haar S.P. & Johnson W.H., (1973). Mean Magnetic Susceptibility: A Useful Parameter for Stratigraphic Studies of Glacial Till. *Journal of Sedimentary Petrology*: 43(4): 1148-1151.
- Waelbroeck C. Duplessy J-C. Michel E. Labeyrie L. Palliard D. & Duprat J., (2001). The Timing of the Last Deglaciation in North Atlantic Climate Records. *Nature*: 412: 724-727.
- Walden J., (1999a). Sample Collection and Preparation. Chapter 3: *Environmental Magnetism: A Practical Guide*. Walden J. Oldfield F. & Smith J. (eds), London, Quaternary Research Association. Technical Guide No 6: 25-34
- Walden J., (1999b). Remanence Measurements. Chapter 5: *Environmental Magnetism: A Practical Guide*. Walden J. Oldfield F. & Smith J. (eds), London, Quaternary Research Association. Technical Guide No 6: 63-88

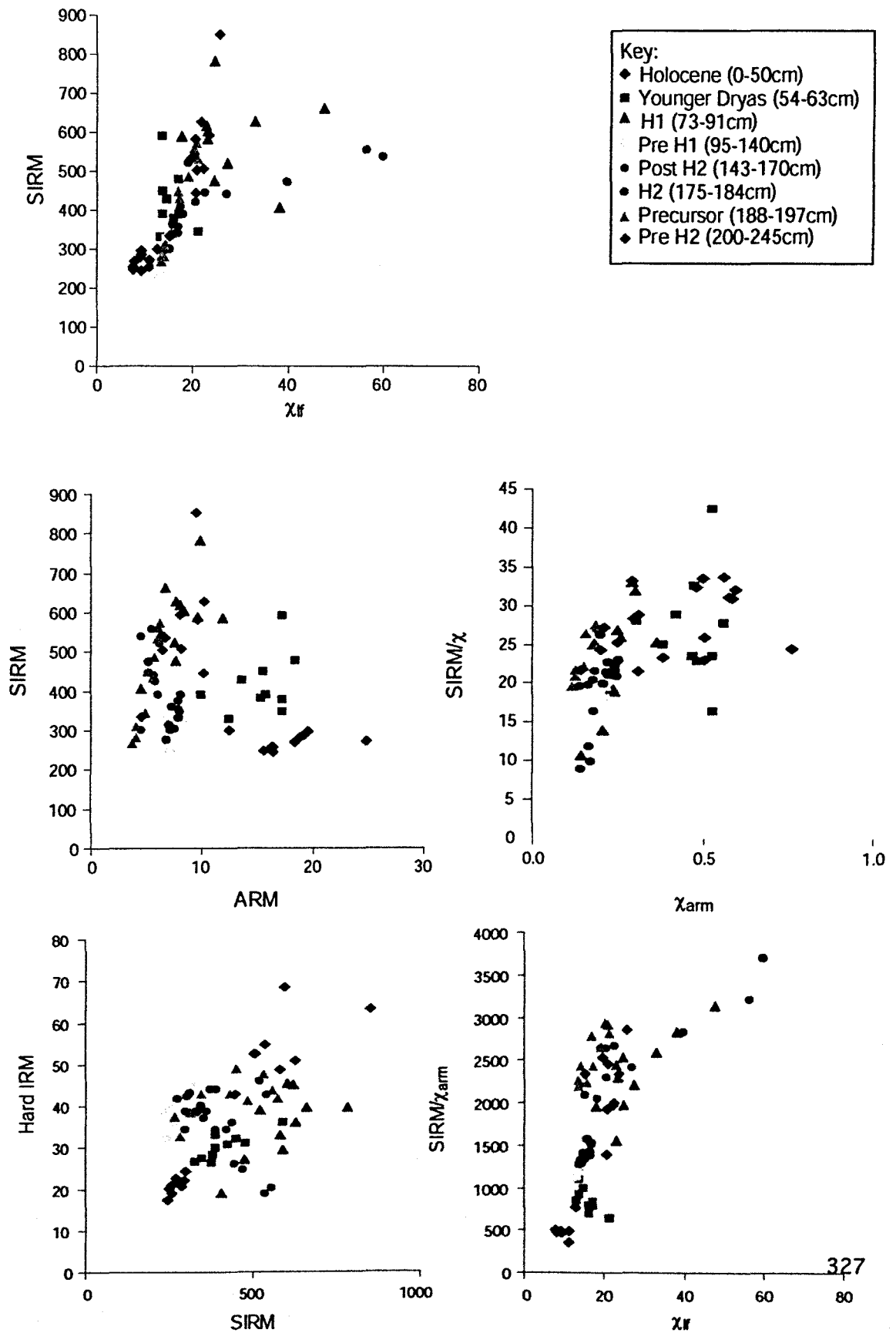
- Walden J. & Slattery M.C., (1993). Verification of a Simple Gravity Technique for Separation of Particle Size Fractions Suitable for Mineral Magnetic Analysis. *Earth Surface Processes and Landforms*: 18: 829-833.
- Walden J. & Addison K., (1995). Mineral Magnetic Analysis of a "Weathering" Surface within Glaciogenic Sediments at Glanllynau, North Wales. *Journal of Quaternary Science*: 10: 367-378.
- Walden J. & Smith J.P., (1995). Factor Analysis: A Practical Application. *Statistical Modeling of Quaternary Science Data*. Maddy D. & Brew J.S. (eds). Cambridge, Quaternary Research Association. Technical Guide No 5: 39-64.
- Walden J. & Ballantyne C.F., (2002). Use of Environmental Magnetic Measurements to Validate the Vertical Extent of Ice Masses at the Last Glacial Maximum. *Journal of Quaternary Science*: 17(3): 193-200.
- Walden. J. Smith. J.P. Dackombe R.V., (1987). The Use of Mineral Magnetic Analysis in the Study of Glacial Diamicts: A Pilot Study. *Journal of Quaternary Science*: 2: 73-80.
- Walden J. Smith J.P. & Dackombe R.V., (1991). The Use of Simultaneous R- and Q- mode Factor Analysis as a Tool for Assisting Interpretation of Minerals Magnetic Data. *Mathematical Geology*: 24(3): 227-247.
- Walden J. Smith J.P. & Dackombe R.V., (1992). Mineral Magnetic Analyses as a Means of Lithostratigraphic Correlation and Provenance Indication of Glacial Diamicts: Intra- and Inter- Unit Variation. *Journal of Quaternary Science*: 7(3): 257-270.
- Walden J. Smith J.P. & Dackombe R.V., (1996). A Comparison of Mineral Magnetic, Geochemical and Mineralogical Techniques for Compositional Studies of Glacial Diamictons. *Boreas*: 25: 115-130.

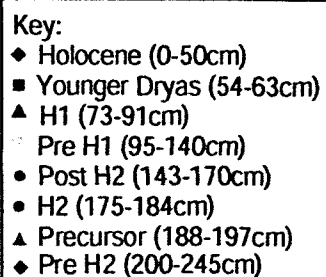
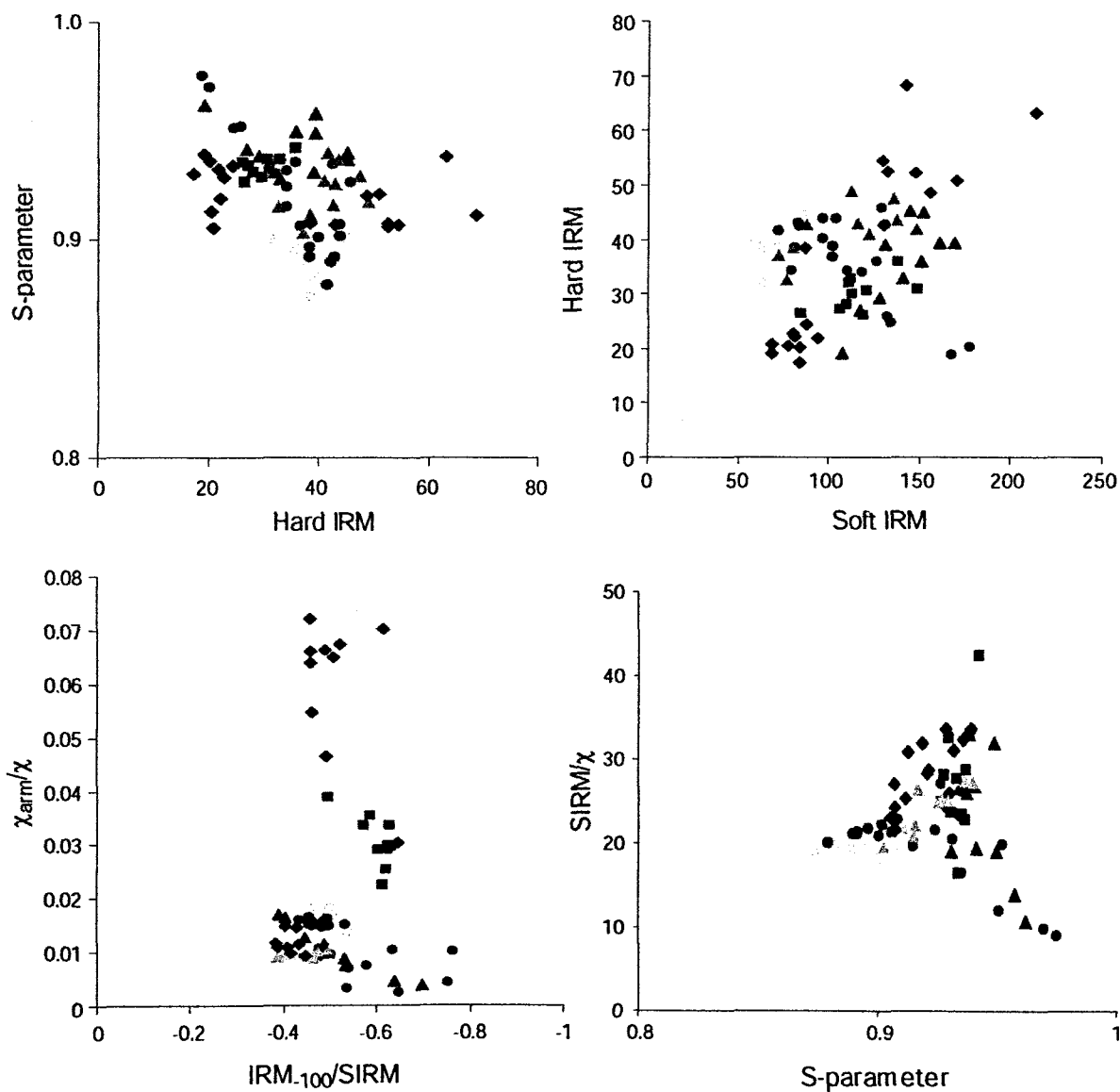
- Walker M.J.C., (2001). Rapid Climate Change during the Last Glacial-Interglacial Transition: Implications for Stratigraphic Subdivision, Correlation and Dating. *Global and Planetary Change*: **30**: 59-72.
- Wand J.O. Gillespie R. & Hedges R.E.M., (1984). Sample Preparation for Accelerator-based Radiocarbon Dating. *Journal of Archaeological Science*: **10**: 159-163.
- Wang L. Sarnthein M. Erlenkeuser H. Grimalt J. Grootes P. Heilig S. Ivanova E. Kienast M. Pelejero C. & Pflaumann U., (1999). East Asian Monsoon Climate During the Late Pleistocene: High Resolution Sediment Records from the South China Sea. *Marine Geology*: **156**: 245-284.
- Watkins S.J. & Maher B.A. (2003). Magnetic Characterisation of Present-day Deep-sea Sediments and Sources in the North Atlantic. *Earth and Planetary Science Letters*: **214**: 379-394.
- Weaver P.P.E. & Schulthesis P.J., (1983). Detection of Re-penetration and Sediment Disturbance in Open-barrel Gravity Cores. *Journal of Sedimentary Petrology*: **53**(2): 649-678.
- Weaver P.P.E. & Schulthesis P.J., (1990). Current Methods for Obtaining, Logging and Splitting Marine Cores. *Marine Geophysical Researches*: **12**: 85-100.
- Wefer G. Berger W.H. Bijma J. & Fischer G., (1999). Clues to Ocean History: A Brief Overview of Proxies. *Use of Proxies in Palaeoceanography: Examples from the South Atlantic*. Fischer G. & Wefer G. (eds). Berlin, Springer-Verlag: 1-68.
- Weiss, D. Shotyk W. Kramers J.D. & Gloor M., (1999). Sphagnum Mosses as Archives of Recent and Past Atmospheric Lead Deposition in Switzerland. *Atmospheric Environment*: **33**(23): 3751-3763.

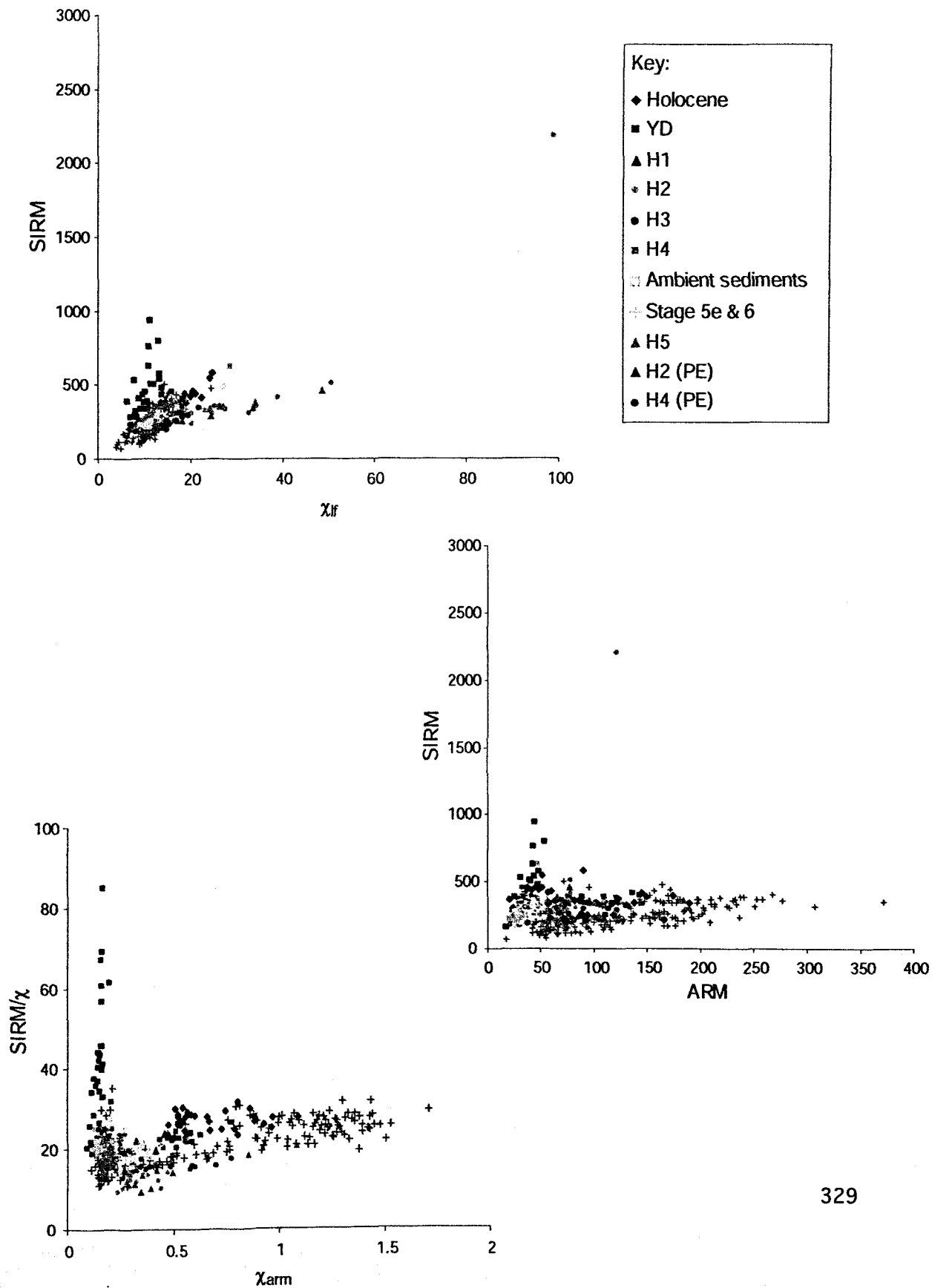
- Whitlock C. & Bartlein P.J., (1997). Vegetation and Climate Change in Northwest America during the Past 125 kyr. *Nature*: **388**: 57-61.
- Whittow J., (1984). *Dictionary of Physical Geography*. London, Penguin.
- Williams K.L., (1987). *An Introduction to X-Ray Spectrometry*. London, Allen & Unwin.
- Williams M. Dunkerly D. De Dekker P. Kershaw P. & Chappell J., (1998). *Quaternary Environments*. London, Arnold.
- Willman H.B. Glass H.D. & Frye J.D., (1963). Mineralogy of Glacial Tills and their Weathering Profiles in Illinois; Part 1, Glacial tills. *Circular - Illinois State Geological Survey*.
- Willman H.B. Glass H.D. & Frye J.D., (1966). Mineralogy of Glacial Tills and their Weathering Profiles in Illinois; Part 2, Weathering profiles. *Circular - Illinois State Geological Survey*.
- Wilson L.J. & Austin W.E.N., (2001). Millennial and Sub-Millennial Variability in Sediment Colour from the Barra Fan, NW Scotland: Implications for British Ice Sheet Dynamics. In *Glacier-influenced Sedimentation on High Latitude Continental Margins*. Dowdeswell J.A. & O'Cofaigh C. (eds). Geological Society London Special Publication: **203**: 349-365.
- Wilson L.J. Austin W.E.N. & Jansen E., (2002). The Last British Ice Sheet: Growth, Maximum Extent and Deglaciation. *Polar Research*: **21**: 243-230.
- Winterhalter B., (1970). An Automatic-release Piston for use in Piston coring. *Marine Geology*: **8**: 371-375.

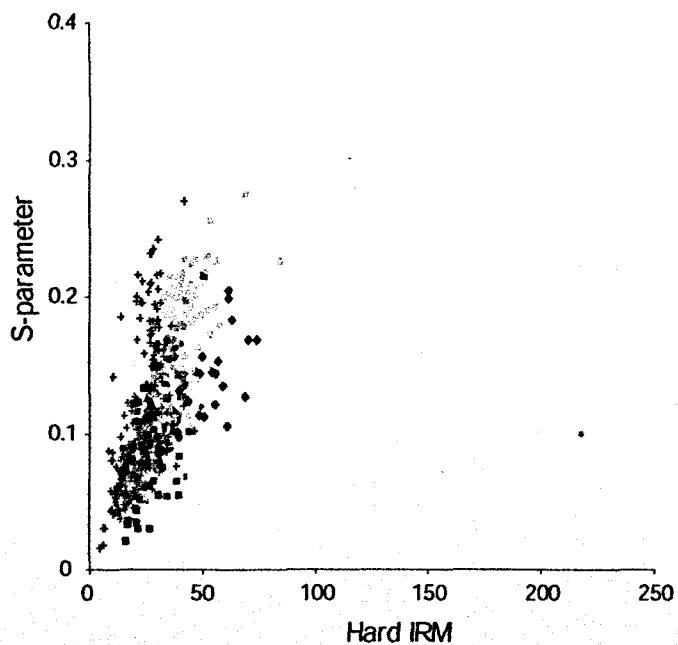
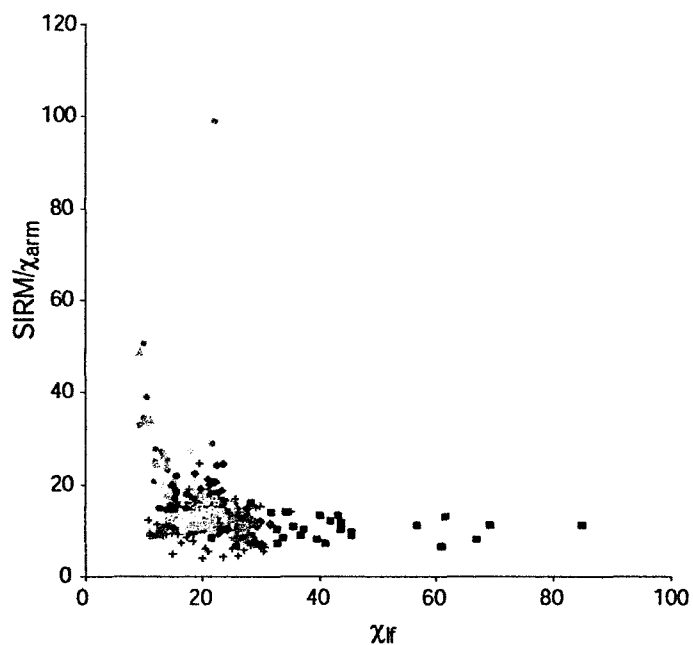
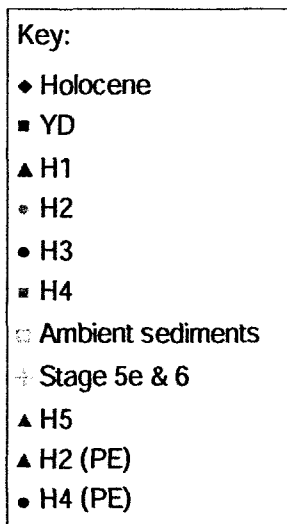
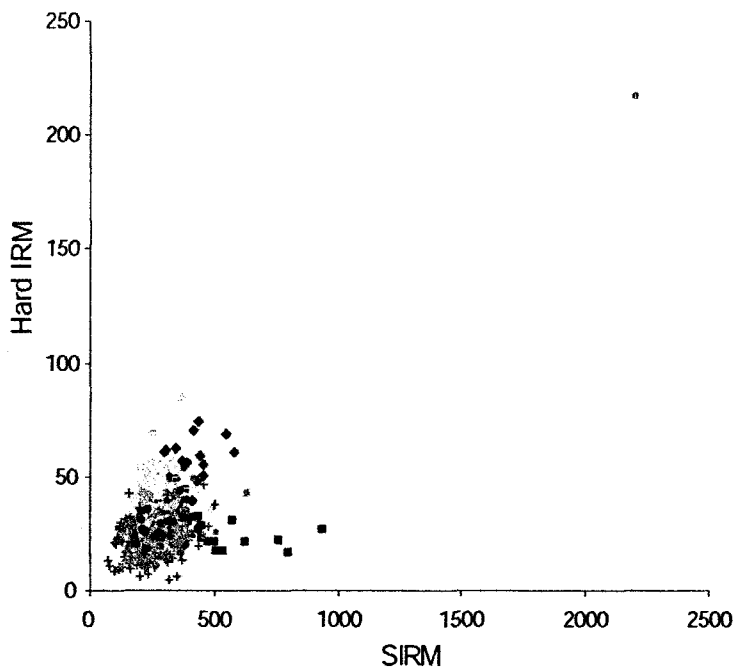
- Wolin G. Ryan W.B.F. & Ericson D.B., (1978). Climate Changes, Magnetic Intensity Variations and Fluctuations of the Eccentricity of the Earth's Orbit during the Past 2000 kyr and a Mechanism which may be Responsible for the Relationship. *Earth and Planetary Science Letters*: 41: 395-397.
- Yu L. & Oldfield F., (1989). A Multivariate Mixing Model for Identifying Sediment Source from Magnetic Measurements. *Quaternary Research*: 32: 168-181.
- Yu L. & Oldfield F., (1993). Quantitative Sediment Source Ascription Using Magnetic Measurements in a Reservoir Catchment System near Nijar, Spain. *Earth Surface Processes and Landforms*: 18: 441-454.
- Zablotskii V. Yurchenko V. Kamysa Y. & Chelombetskaya M., (2001). Calculations of Magnetic Susceptibility of Magnetotactic Bacteria Culture. *Journal of Magnetism and Magnetic Materials*: 234: 575-583.
- Zahn R. Schonfeld J. Kudrass H-R. Park M-O. Erlenkeuser H. & Grootes P., (1997). Thermohaline Instability in the North Atlantic During Meltwater Events: Stable Isotope and Ice-Rafted Detritus Records from core S075-26KL, Portuguese Margin. *Paleoceanography*: 12(5): 696-710.
- Zangger E. & McCave I.N., (1990). A Re-designed Kasten Core Barrel and Sampling Techniques. *Marine Geology*: 94: 165-171.
- Zhu R. Liu Q. & Jackson M., (2004). Paleoenvironmental Significance of the Magnetic Fabrics in Chinese Loess-Paleosols since the Last Interglacial (<130 ka). *Earth and Planetary Science Letters*: 221(1-4): 55-69.

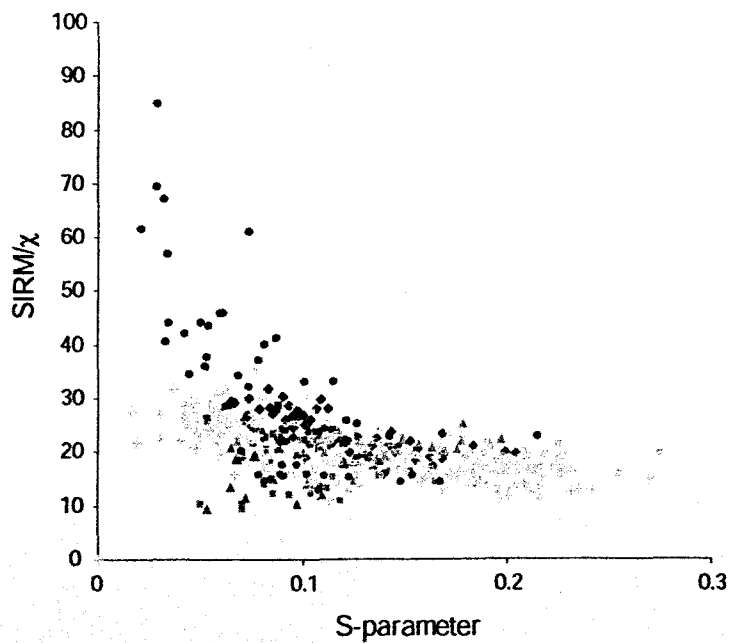
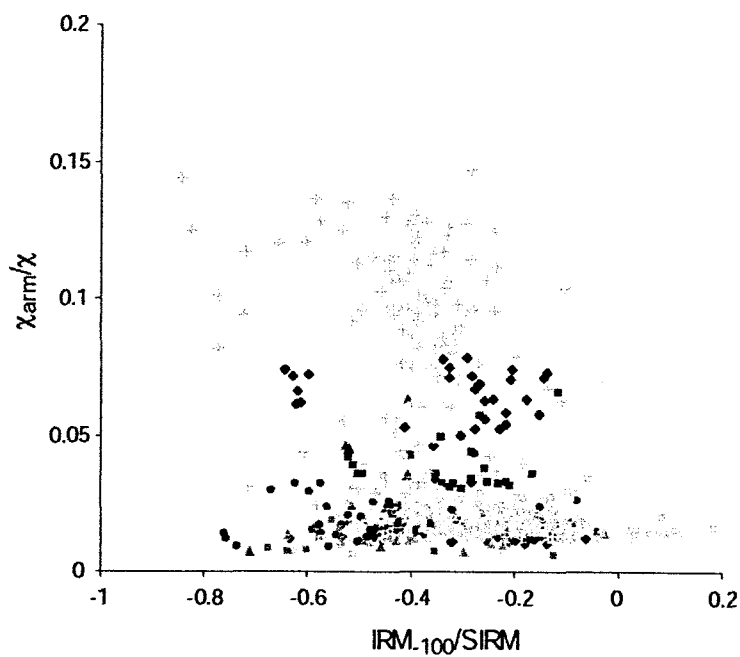
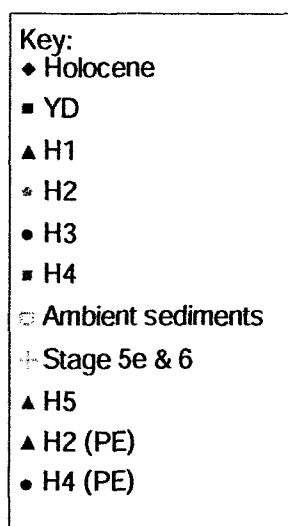
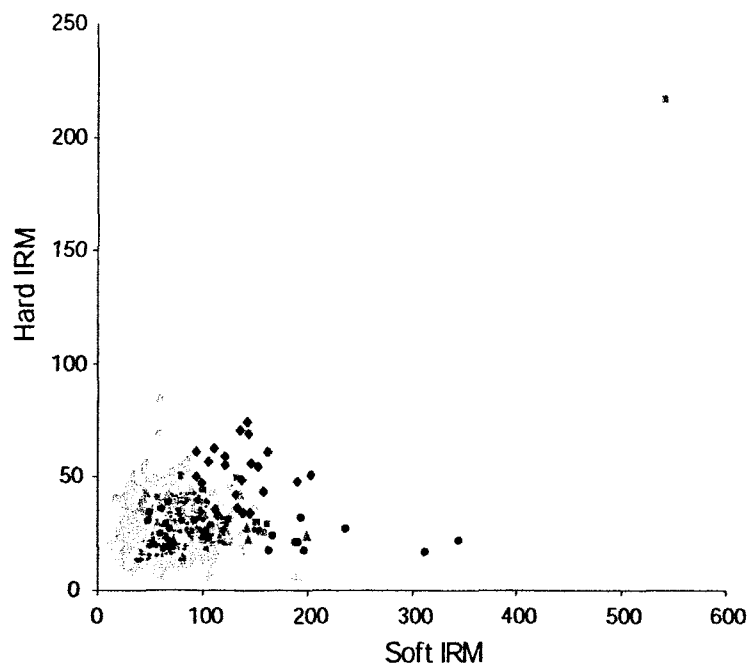
Appendix 1a) Biplots for OMEX 2K











Appendix 2: Statistics

Appendix 2a) General methods and procedure tables.

Kruskal Wallis test formula and procedure

$$H = \frac{12 \sum [n_i(R_i - R)^2]}{N(N+1)} \quad (\text{Gibbons, 1993})$$

Where: n_i = number of observations in group i .

N = total sample size.

R_i = average rank of group i .

R = average of all the ranks, which is also equal to $(N+1)/2$

Step	Procedure (based on Fowler <i>et al.</i> , 1998 and Minitab help.)
1	Assemble all n_i measurements in all k samples into a single set, N .
2	Organise all measurements into rank order from the lowest to the highest
3	Return the resulting ranks to the original samples, substituting them for the raw values.
4	Calculate the average rank for each of the k samples (R_i), and the average rank for the set N (R).
5	Subtract each R_i value from R , and square each separate result. Multiply each separate result by the corresponding n_i value to give $(n_i(R_i - R))^2$.
6	Add together and multiply by 12. Divide by $N(N+1)$.
7	The resultant value is the test statistic H . Using a χ^2 table, look up the value for the appropriate degrees of freedom ($k - 1$) and significance level (P -value). If the H value is above the χ^2 value, then there is a significant difference between the medians of the groups.

χ^2 distribution table, to be used with the Kruskal Wallis tests (from Gibbons, 1993).

df	0.99	0.98	0.95	0.9	0.8	0.7	0.5	0.3	0.2	0.1	0.05	0.02	0.01	0.001
1	0.00016	0.00063	0.00390	0.01600	0.06400	0.15	0.46	1.07	1.64	2.71	3.84	5.41	6.64	10.83
2	0.02	0.04	0.10	0.21	0.45	0.71	1.39	2.41	3.22	4.60	5.99	7.82	9.21	13.82
3	0.12	0.18	0.35	0.58	1.00	1.42	2.37	3.66	4.64	6.25	7.82	9.84	11.34	16.27
4	0.30	0.43	0.71	1.06	1.65	2.20	3.36	4.88	5.99	7.78	9.49	11.67	13.28	18.46
5	0.55	0.75	1.14	1.61	2.34	3.00	4.35	6.06	7.29	9.24	11.07	13.39	15.09	20.52
6	0.87	1.13	1.64	2.20	3.07	3.83	5.35	7.23	8.56	10.64	12.59	15.03	16.81	22.46
7	1.24	1.56	2.17	2.83	3.82	4.67	6.35	8.38	9.80	12.02	14.07	16.62	18.48	24.32
8	1.65	2.03	2.73	3.49	4.59	5.53	7.34	9.52	11.03	13.36	15.51	18.17	20.09	26.12
9	2.09	2.53	3.32	4.17	5.38	6.39	8.34	10.66	12.24	14.68	16.92	19.68	21.67	27.88
10	2.56	3.06	3.94	4.86	6.18	7.27	9.34	11.78	13.44	15.99	18.31	21.16	23.21	29.59
11	3.05	3.61	4.58	5.58	6.99	8.15	10.34	12.90	14.63	17.28	19.68	22.62	24.72	31.26
12	3.57	4.18	5.23	6.30	7.81	9.03	11.34	14.01	15.81	18.55	21.03	24.05	26.22	32.91
13	4.11	4.76	5.89	7.04	8.63	9.93	12.34	15.12	16.98	19.81	22.36	25.47	27.69	34.53
14	4.66	5.37	6.57	7.79	9.47	10.82	13.34	16.22	18.15	21.06	23.68	26.87	29.14	36.12
15	5.23	5.98	7.36	8.55	10.31	11.72	14.34	17.32	19.31	22.31	25.00	28.26	30.58	37.70
16	5.81	6.61	7.96	9.31	11.15	12.62	15.34	18.42	20.46	23.54	26.30	29.63	32.00	39.29
17	6.41	7.26	8.67	10.08	12.00	13.53	16.34	19.51	21.62	24.77	27.59	31.00	33.41	40.75
18	7.02	7.91	9.39	10.86	12.86	14.44	17.34	20.60	22.76	25.99	28.87	32.35	34.80	42.31
19	7.63	8.57	10.12	11.65	13.72	15.35	18.34	21.69	23.90	27.20	30.14	33.69	36.19	43.82
20	8.26	9.24	10.85	12.44	14.58	16.27	19.34	22.78	25.04	28.41	31.41	35.02	37.57	45.32
21	8.90	9.92	11.59	13.24	15.44	17.18	20.34	23.86	26.17	29.62	32.67	36.34	38.93	46.80
22	9.54	10.60	12.34	14.04	16.31	18.10	21.34	24.94	27.30	30.81	33.92	37.66	40.29	48.27
23	10.20	11.29	13.09	14.85	17.19	19.02	22.34	26.02	28.43	32.01	35.17	38.97	41.64	49.73
24	10.86	11.99	13.85	15.66	18.06	19.94	23.34	27.10	29.55	33.20	36.42	40.27	42.98	51.15
25	11.52	12.70	14.61	16.47	18.94	20.87	24.34	28.17	30.68	34.38	37.65	41.57	44.31	52.62
26	12.20	13.41	15.38	17.29	19.82	21.79	25.34	29.25	31.80	35.56	38.88	42.86	45.64	54.25
27	12.88	14.12	16.15	18.11	20.70	22.72	26.34	30.32	32.91	36.74	40.11	44.14	46.96	55.48
28	13.56	14.85	16.93	18.94	21.59	23.65	27.34	31.39	34.03	37.92	41.34	45.42	48.28	56.89
29	14.26	15.57	17.71	19.77	22.48	24.58	28.34	32.46	35.14	39.09	42.56	46.69	49.59	58.30
30	14.95	16.31	18.49	20.60	23.36	25.51	29.34	33.53	36.25	40.26	43.77	47.96	50.89	59.70

Mann Whitney U test procedure

Step	Procedure (based on Fowler <i>et al.</i> , 1998; Davis 2002).
1	Combine the two populations (n^1 and n^2)
2	Organise all measurements into rank order from the lowest to the highest
3	Return the resulting ranks to the original samples, substituting them for the raw values.
4	Sum the ranks of the two populations (R^1 and R^2).
5	Calculate the test statistic U^1 and U^2 . $U^1 = n^1 n^2 + \frac{n^2(n^2+1)}{2} - R^2$ $U^2 = n^1 n^2 + \frac{n^1(n^1+1)}{2} - R^1$
6	Select the smaller of the two U values. This is the test statistic and should be compared with Mann Whitney table using appropriate n^1 and n^2 values. If U is smaller than the critical value provided by the table, the null hypothesis is rejected and there is a significant difference between the populations.

Factor Analysis procedure

Step	Procedure (from Walden & Smith, 1995).
1	Compile a raw data matrix of n samples (rows) by m variables (columns) denoted by $[X]$, as in conventional matrix algebra.
2	Standardise $[X]$ to give $[W]$. Each element of $[X]$ has its column (variable) mean subtracted from it. It is then divided by the product of the column (variable) standard deviation, and the square root of n .
3	$[W]$ is then transposed to give $[W]'$. This involves turning the rows of $[W]$ into the columns of $[W]'$ and the columns into rows.
4	$[R]$ is created by matrix multiplication of $[W]' \cdot [W]$. The matrix $[R]$ represents a correlation matrix between the variables.
5	Eigenvectors and eigenvalues are extracted from $[R]$. The eigenvectors are used to form a matrix $[U]$. The eigenvalues can be used to compute the percentage of the total variation in the original data set explained by the new "underlying" factors.
6	The square roots of the eigenvalues are placed in the top left to bottom right diagonal elements of matrix $[\Lambda]$. All other elements are set to zero.
7	$[A^R]$ is computed by matrix multiplication of $[U] \cdot [\Lambda]$. The matrix $[A^R]$ contains the R- mode (variable) factor loadings. Each column represents the loadings of the original variables on an individual factor (column 1 on factor 1, etc). These are the values used when plotting the variables in "factor space" in the form of scatter diagrams.
8	$[A^Q]$ is computed by matrix multiplication of $[W] \cdot [U]$. The matrix $[A^Q]$ contains the Q- mode (sample) factor loadings. Each column represents the loadings of the original variables on an individual factor (column 1 on factor 1, etc). These are the values used when plotting the variables in "factor space" in the form of scatter diagrams.

The hypothetical data set below consists of 16 samples, upon which 6 variables were measured. The samples fall into 2 clear groups, and factor analysis is used to see if the groups can be differentiated by these variables alone. The measurements, along with the sample numbers and group numbers form the original matrix [X] that is fed into Minitab. [X] must firstly be standardised, to eliminate any influence of measurement scale differences between the variables ([X] becomes [W]). This done using a short macro:

```
let ck2=(ck1-mean(ck1))
let k3= sqrt(ssq(ck2)/n(ck2))
let ck2=ck2/(k3*(sqrt(n(ck2))))
let k1=k1+1
let k2=k2+1
```

This macro should be created before the factor analysis commences and saved as a text file with a .MTB extension (e.g. stand.mtb). Now the factor analysis can start:

```
MTB > print c1-c7
```

ROW	sample	varA	varB	varC	varD	varE	varF
1	P1	3.4	122	0.76	25.3	46.9	3.63986
2	P2	3.7	143	0.72	39.6	61.2	4.15790
3	P3	3.2	165	0.75	22.4	41.9	3.44037
4	P4	3.4	129	0.78	55.9	77.5	4.67896
5	P5	4.0	150	0.79	43.9	65.5	4.30149
6	P6	3.8	137	0.75	22.8	44.4	3.54152
7	P7	3.6	143	0.71	37.1	58.7	4.07209
8	Q1	3.9	130	0.69	39.0	60.6	4.13747
9	Q2	3.8	143	0.69	25.6	47.2	3.65148
10	Q3	3.8	132	0.70	29.8	43.9	3.52152
11	Q4	3.7	154	0.71	43.0	64.6	4.27184
12	Q5	3.8	163	0.69	47.3	68.9	4.41172
13	Q6	3.9	132	0.72	37.3	58.9	4.07902
14	Q7	4.0	147	0.73	50.3	68.3	4.39247
15	Q8	4.1	142	0.72	22.6	44.2	3.53354
16	Q9	3.9	143	0.70	22.9	44.5	3.54551

This is the measured data that form [X]. This must be standardised into [W]:

```
MTB> let k1=2
MTB> let k2=21

MTB> execute 'stand' 6

MTB> copy c21-c26 m1
```

Here, the first column of raw data is specified, along with the empty column in which the standardised data can be placed. 'stand' is the name of the file containing the macro for standardization, it has been executed six times, once for each variable. The final command places the standardised data into matrix format.

```
MTB > print m1

MATRIX M1

-0.368932 -0.435939 0.278875 -0.233885 -0.209418 -0.206982
-0.052705 0.017546 -0.045634 0.100571 0.116977 0.126858
... ..
0.158114 0.017546 -0.207889 -0.290017 -0.264197 -0.267786
```

Next, [W] must be transposed to give [W]':

```
MTB > transpose m1 m2
MTB > print m2
```

MATRIX M2

```
-0.368932 -0.052705 ..... 0.158114
-0.435939 0.017546 ..... 0.017546
0.278875 -0.045634 ..... -0.207889
-0.233885 0.100571 ..... -0.290017
-0.209418 0.116977 ..... -0.264197
-0.206982 0.126858 ..... -0.267786
```

[W] and [W]' are then multiplied to give [R]:

```
MTB > multiply m2 m1 m3
MTB > print m3
```

MATRIX M3

```
1.00000 -0.03301 -0.33779 0.05375 0.04956 0.06436
.....
0.06436 0.08306 0.17526 0.98119 0.99927 1.00000
```

Eigenvectors and eigenvalues are extracted from [R]. The eigenvectors are stored in [U]. The eigenvalues are stored in an empty column in the MINITAB worksheet:

```
MTB > eigen m3 c30 m4
MTB > print m4
```

MATRIX M4

```
-0.022119 -0.686603 0.364600 0.628536 0.007152 0.006703
.....
-0.570807 -0.048584 0.024104 -0.074759 -0.451345 -0.679659
```

```
MTB > print c30
```

```
ROW    C30
1    3.03245
2    1.34041
3    1.01803
4    0.58545
5    0.02321
6    0.00046
```

The square roots of these eigenvalues are then placed in the top left to bottom right diagonal elements of a new matrix [Λ], with the remaining elements set to 0:

```
MTB > sqrt c30 c31
MTB > diagonal c31 m5
MTB > print m5
```

MATRIX M5

```
1.7413932 0.0000000 0.0000000 0.0000000 0.0000000 0.0000000
0.0000000 1.1577595 0.0000000 0.0000000 0.0000000 0.0000000
.....
0.0000000 0.0000000 0.0000000 0.0000000 0.0000000 0.0213351
```


[U] and [Λ] are multiplied to create [A^R], the R-mode (i.e. variable) factor loadings:

```
MTB > multiply m4 m5 m6
MTB > print m6

MATRIX M6

-0.038518 -0.794921 0.367872 0.480923 0.001090 0.000143
-0.105970 -0.245420 -0.935130 0.232533 0.000551 -0.000052
.....
-0.993999 -0.056249 0.024320 -0.057201 -0.068765 -0.014501
```

[W] and [U] are multiplied to create [A^Q], the Q-mode (i.e. sample) factor loadings:

```
MTB > multiply m1 m4 m7
MTB > print m7

MATRIX M7

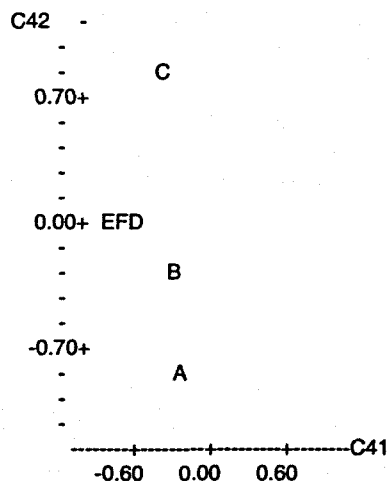
0.365215 0.565793 0.278449 -0.117268 -0.022620 -0.004835
-0.189730 -0.013519 -0.031824 -0.086567 -0.018426 -0.005710
0.502200 0.470582 -0.672335 -0.000897 0.022392 -0.000337
.....
0.493928 -0.221619 0.006793 0.023075 -0.021020 0.006683
```

The contents of [A^R] and [A^Q] are then copied into empty column in the worksheet, so they may be plotted. Each matrix should have a column of "labels" before it (the original variables and samples), so that they can be distinguished in the plots:

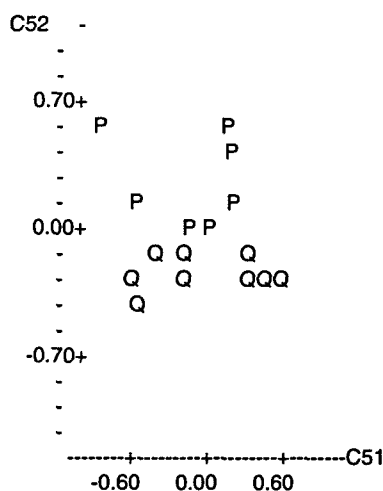
```
MTB > copy m6 c41-c46
MTB > copy m7 c51-c56
MTB > set c40
DATA> 1 2 3 4 5 6
DATA> end
MTB > set c50
DATA> 1 1 1 1 1 1 1 2 2 2 2 2 2 2 2
DATA> end
```

The MINITAB Lplot command is used to produce scatter plots with labels of both the variables and the samples on factor 1 versus factor 2. The last of the three columns specified in the Lplot command contains numerical values, which are transferred into their equivalent letters of the alphabet within the plot itself. The same axis is used in both plots to allow the relationship between the samples and the variables in factor space to be judged more clearly.

```
MTB > lplot c42 c41 c40;
SUBC> ystart -1 1;
SUBC> xstart -1 1.
```



```
MTB > lplot c52 c51 c50;
SUBC> ystart -1 1;
SUBC> xstart -1 1.
```



The final stage of the analysis involves the production of scatter graphs showing the positions of both the original variables and the samples in the new 'factor space'. This is achieved by plotting the factor loadings for either the variables or samples for any two of the factors. Two such plots are shown at the end of Appendix 1 for factors 1 and 2. It can be seen, that with respect to the origin of the graph (0,0), the two sample sets (P and Q) both show a spread of values on factor 1 but have distinctly different factor loadings on factor 2. It would appear then, that factor 2 provides a useful way of distinguishing between the two sample sets, suggesting that the sample sets can be distinguished on the basis of some or all of the 6 original variables.

It is also possible to distinguish a small group of 4 samples from set Q, with relatively high loadings on factor 1. This sort of separation on the factor diagram can be used in an exploratory way, encouraging the original data and context of the samples to be re-examined to seek a possible explanation for such patterns.

Variables A and C appear to be most strongly related to factor 2. It could therefore be suggested that it is these variables that are providing the distinction between the two sample sets. Variables D, E and F appear closely related to factor 1. They also plot in close proximity to one another, suggesting the samples are responding to these variables in a similar manner (i.e. these variables are strongly positively correlated). Variable C plots almost directly opposite variable A with respect to the origin. This suggests that variable C is negatively correlated with variable A.

Variable B does not appear to be strongly related to either factor 1 or factor 2. It may be related to other factors, or it may simply be a redundant measurement, offering no explanation of pattern, either between or within sample sets.

The insights gained from such factor plots, may help direct future work. For example, if all that is required is to separate unknown samples into either groups P or Q, then analysis could concentrate on variables A and B. Detection of variables that appear to offer duplicate information (such as D, E and F) or seem redundant altogether, can also help reduce the number of variables assessed in future analyses, especially if this offers important savings in time or cost.

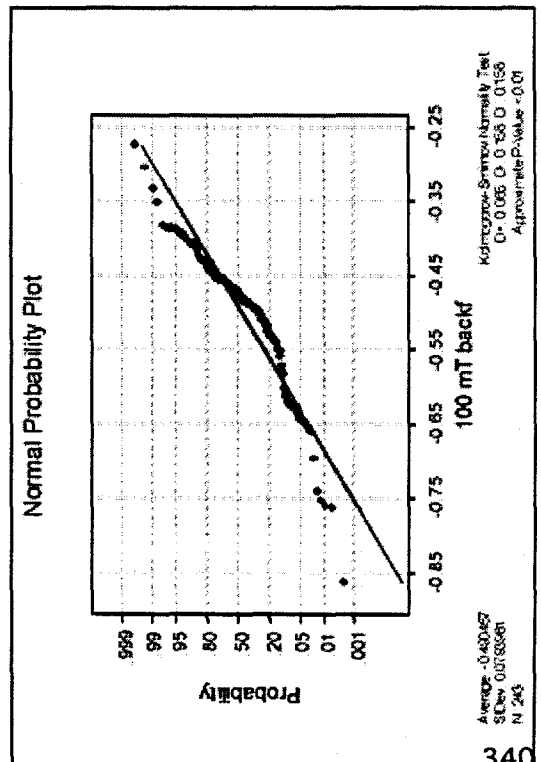
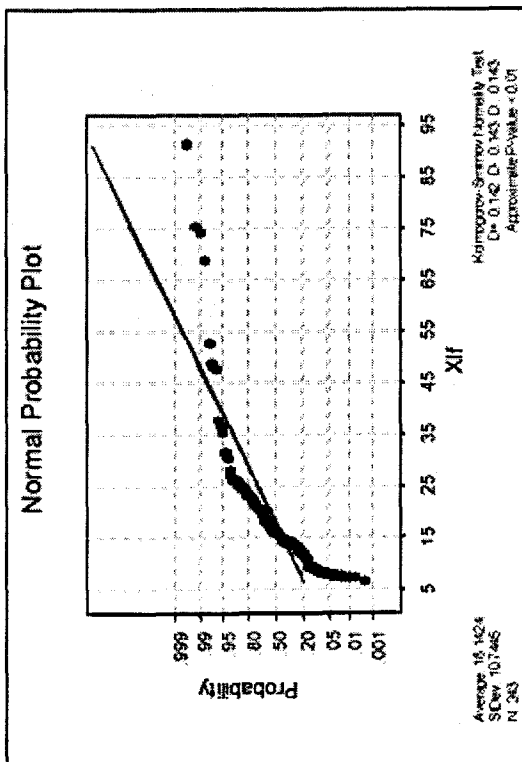
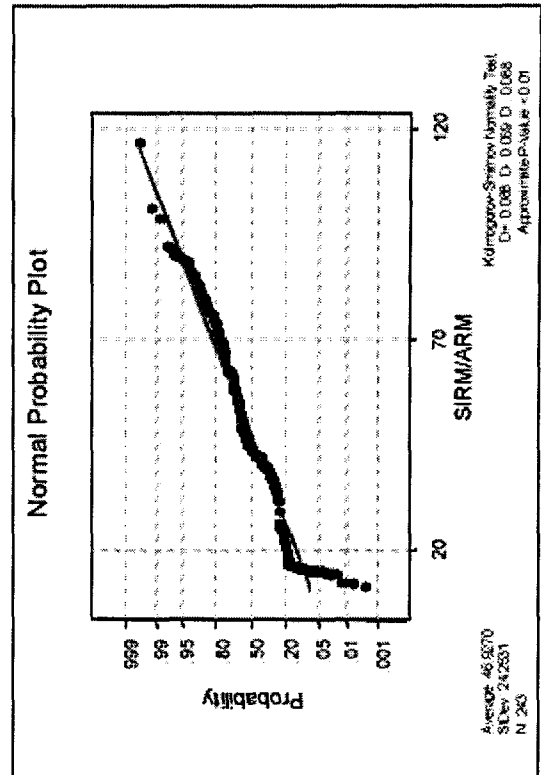
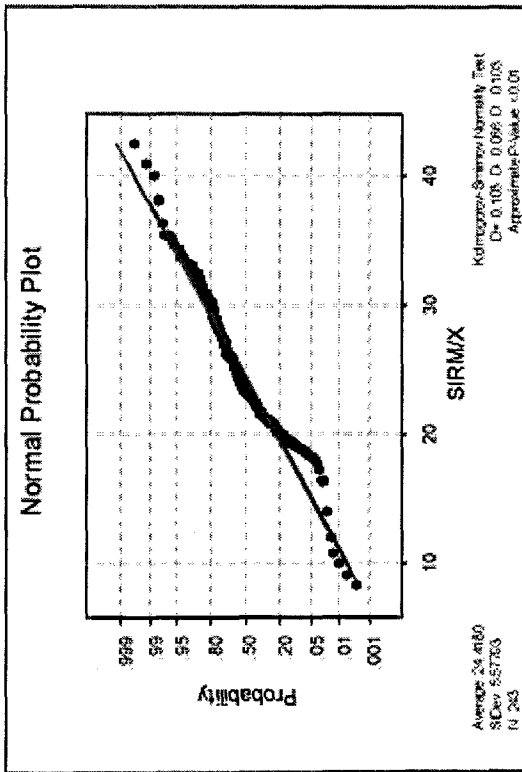
Appendix 2: Statistics

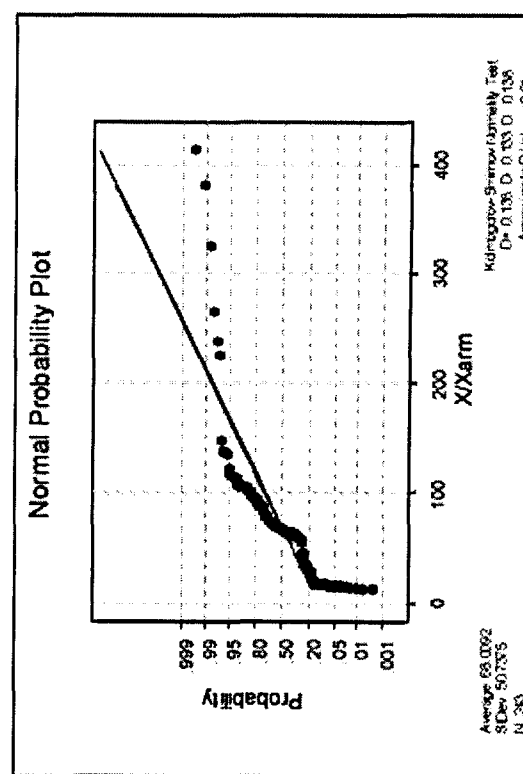
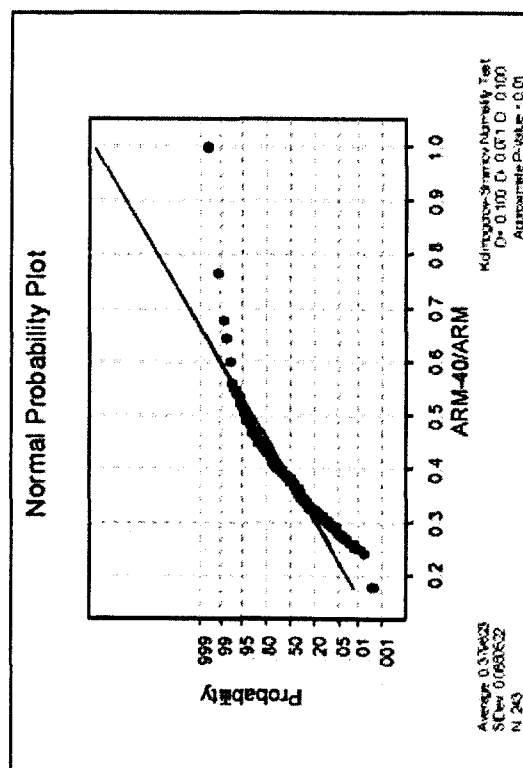
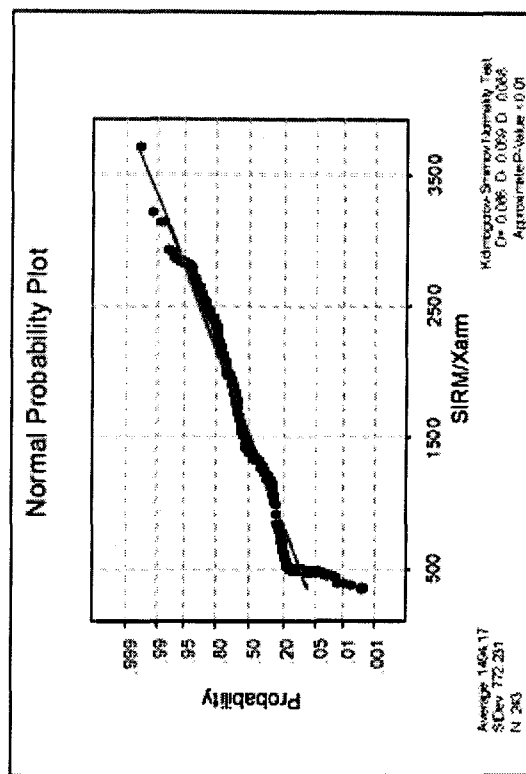
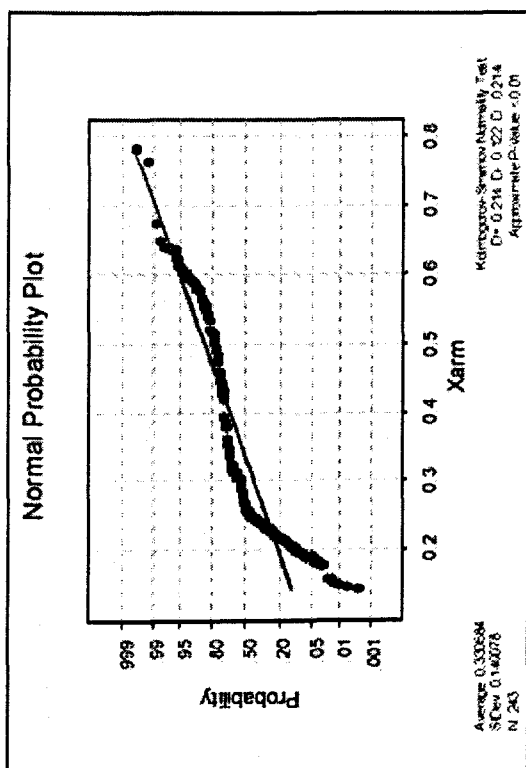
Appendix 2b) OMEX 2K.

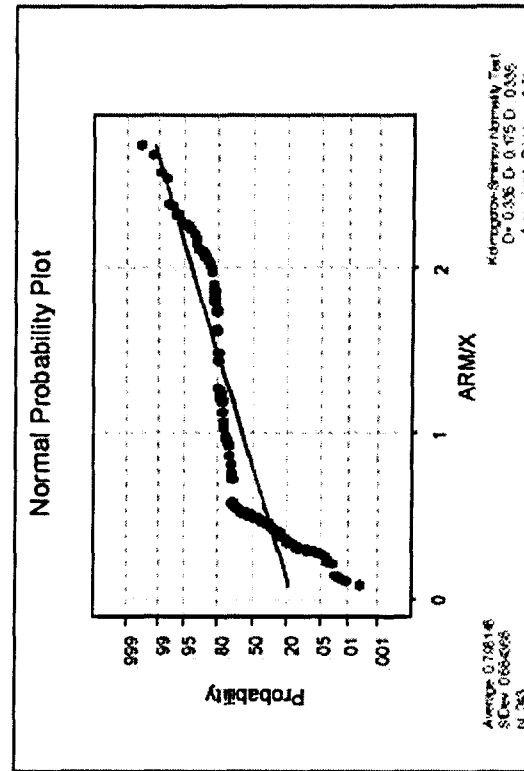
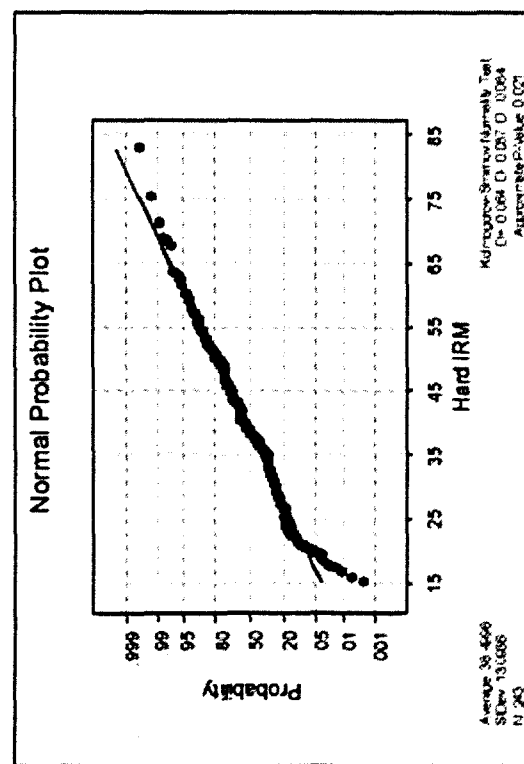
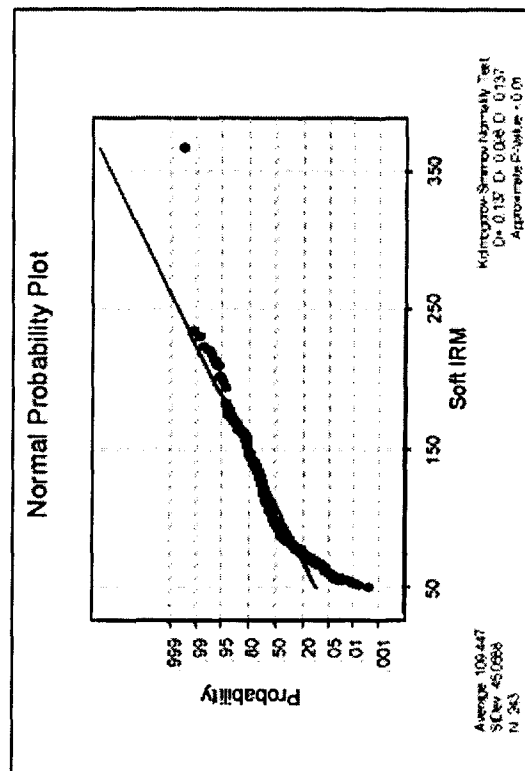
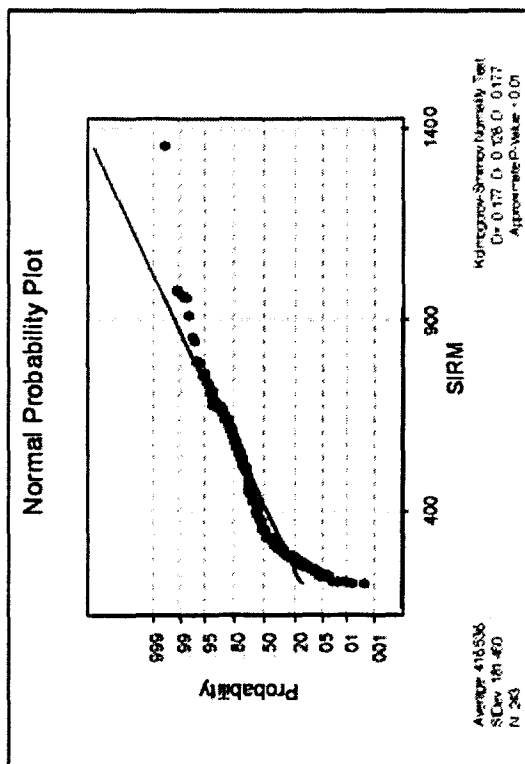
2bi) Descriptive Statistics

Variable	N	Mean	Median	Truncated Mean	Standard Deviation	Standard Error of the Mean	Minimum	Maximum	Lower Quartile	Upper Quartile
χ_H	243	18.14	15.76	16.76	10.74	0.69	6.41	91.18	12.72	21.27
χ_{arm}	243	0.33	0.25	0.32	0.15	0.01	0.14	0.78	0.22	0.44
SIRM	243	109.45	94.30	105.93	45.06	2.89	49.40	366.20	76.40	138.20
Soft IRM	243	0.80	0.49	0.74	0.68	0.04	0.08	2.74	0.37	0.96
Hard IRM	243	24.42	23.16	24.32	5.58	0.36	8.25	42.42	20.63	27.99
χ_{arm}/χ	243	0.02507	0.01541	0.02335	0.0215	0.00138	0.00242	0.08619	0.01159	0.03022
ARM/ χ	243	68.01	64.88	62.64	50.74	3.25	11.60	413.10	33.09	86.25
SIRM/ χ	243	0.46	0.46	0.46	0.01	0.00	0.43	0.48	0.45	0.46
SIRM/ARM	243	3.13	3.36	3.17	0.73	0.05	1.19	4.64	3.04	3.58
SIRM/ χ_{arm}	243	1494.20	1378.10	1469.60	772.20	49.50	348.40	3705.10	795.20	2081.2
IRM ₁₀₀ /SIRM	243	-0.49046	-0.47600	-0.48552	0.07940	0.00509	-0.86400	-0.27400	-0.51300	-0.44800

2bii) Normality tests







2biii) Kruskal Wallis tests

Kruskal Wallis test on χ_{lf}

Group Code	N	Median	Ave Rank	Z
1 - Holocene	50	8.54	29.6	-10.18
2 - YD	10	15.47	109.2	0.06
3 - H1	17	26.9	193.1	5.87
4 - Pre H1	45	13.65	77.9	-3.66
5 - Post H2	28	15.75	115.3	0.67
6 - H2	10	21.65	175.8	3.53
7 - Precursor	10	17.15	127	0.99
8 - Pre H2	45	21.01	169.1	7.41
Overall	215		108	

H = 178.42 DF = 7 P = 0.000

H = 178.42 DF = 7 P = 0.000 (adjusted for ties)

Kruskal Wallis test on χ_{arm}

Group Code	N	Median	Ave Rank	Z
1	50	0.565	188.3	10.42
2	10	0.4935	170.4	3.25
3	17	0.245	96.1	-0.82
4	45	0.212	59.7	-5.86
5	28	0.24	93.2	-1.35
6	10	0.1775	19.9	-4.59
7	10	0.1695	14.9	-4.85
8	45	0.281	107.2	-0.1
Overall	215		108	

H = 165.26 DF = 7 P = 0.000

H = 165.27 DF = 7 P = 0.000 (adjusted for ties)

Kruskal Wallis test on ARM₄₀/ARM

Group Code	N	Median	Ave Rank	Z
1	50	0.381	126	2.34
2	10	0.4925	181.1	3.8
3	17	0.319	74.5	-2.31
4	45	0.35	89.9	-2.19
5	28	0.3675	98.9	-0.83
6	10	0.407	136.2	1.47
7	10	0.462	187.1	4.12
8	45	0.327	84.3	-2.87
Overall	215		108	

H = 52.06 DF = 7 P = 0.000

H = 52.07 DF = 7 P = 0.000 (adjusted for ties)

Kruskal Wallis test on SIRM

Group Code	N	Median	Ave Rank	Z
1	50	275.8	50.1	-7.51
2	10	388.9	139.3	1.63
3	17	602.6	184.4	5.27
4	45	270.5	58.8	-5.96
5	28	324.3	102	-0.55
6	10	459.3	152.1	2.3
7	10	440.8	132.3	1.27
8	45	535.2	174.2	8.03
Overall	215		108	

H = 157.33 DF = 7 P = 0.000

H = 157.33 DF = 7 P = 0.000 (adjusted for ties)

Kruskal Wallis test on Soft IRM

Group Code	N	Median	Ave Rank	Z
1	50	79.5	69.1	-5.04
2	10	111.9	145.6	1.95
3	17	142.4	174.9	4.62
4	45	68	41.9	-8.02
5	28	91.25	99.6	-0.77
6	10	129.8	160	2.7
7	10	113.5	124.9	0.88
8	45	139.9	173.6	7.96
Overall	215		108	

H = 151.99 DF = 7 P = 0.000

H = 151.99 DF = 7 P = 0.000 (adjusted for ties)

Kruskal Wallis test on Hard IRM

Group Code	N	Median	Ave Rank	Z
1	50	20.6	28.8	-10.27
2	10	30.3	68	-2.08
3	17	38.9	112.8	0.33
4	45	37.3	108	0
5	28	40.85	1345	2.42
6	10	34.15	79.8	-1.47
7	10	42.15	139.5	1.64
8	45	52.3	185.8	9.44
Overall	215		108	

H = 165.39 DF = 7 P = 0.000

H = 165.40 DF = 7 P = 0.000 (adjusted for ties)

Kruskal Wallis test on ARM/ χ

Group Code	N	Median	Ave Rank	Z
1	50	2.095	190.3	10.68
2	10	0.95	161.4	2.78
3	17	0.31	36.4	-4.94
4	45	0.51	116.9	1.08
5	28	0.48	101.5	-0.59
6	10	0.255	17.5	-4.71
7	10	0.3	23.1	-4.42
8	45	0.39	65.9	-5.11
Overall	215		108	

H = 179.09 DF = 7 P = 0.000

H = 179.21 DF = 7 P = 0.000 (adjusted for ties)

Kruskal Wallis test on SIRM/ARM

Group Code	N	Median	Ave Rank	Z
1	50	15.07	25.6	-10.69
2	10	26.14	57.4	-2.63
3	17	77.24	182	5.11
4	45	39.61	93.3	-1.78
5	28	42.68	107.4	-0.06
6	10	82.84	190.3	4.28
7	10	79.9	190	4.27
8	45	62.76	161.4	6.48
Overall	215		108	343

H = 188.97 DF = 7 P = 0.000

H = 188.98 DF = 7 P = 0.000 (adjusted for ties)

Kruskal Wallis test on SIRM/ χ

Group Code	N	Median	Ave Rank	Z
1	50	31.29	172.7	8.39
2	10	26.32	135.2	1.42
3	17	20.44	83.5	-1.69
4	45	19.96	56.1	-6.29
5	28	20.94	63.9	-4.03
6	10	19.69	52.4	-2.89
7	10	25.04	111.8	0.2
8	45	24.32	130.2	2.69
Overall	215		108	

H = 117.72 DF = 7 P = 0.000

H = 117.72 DF = 7 P = 0.000 (adjusted for ties)

Kruskal Wallis test on IRM₁₀₀/SIRM

Group Code	N	Median	Ave Rank	Z
1	50	146.5	143.58	-4.07
2	10	219.5	213.4	-0.062
3	17	159	153.88	-1.997
4	45	134	124.56	-4.875
5	28	132	125.46	-3.781
6	10	207.5	182.2	-0.815
7	10	77	75.3	-3.393
8	45	37	43.93	-9.174
Overall	215		108	

H = 162.482 DF = 7 P = 0.000

H = 162.482 DF = 7 P = 0.000 (adjusted for ties)

2biv) Mann Whitney U tests on the separate fractions of H1 and H2

χ_{lf} N = 6 Median = 43.65

$\chi_{lf} b$ N = 13 Median = 22.60

Point estimate for ETA1-ETA2 is 21.85

95.2 Percent CI for ETA1-ETA2 is (11.10,33.81)

W = 95.5

Test of ETA1

The test is significant at 0.0021 (adjusted for ties)

SIRM N = 6 Median = 506.7

SIRM b N = 13 Median = 521.2

Point estimate for ETA1-ETA2 is 5.6

95.2 Percent CI for ETA1-ETA2 is (-120.6,114.9)

W = 60.0

Test of ETA1 = ETA2 vs ETA1 not = ETA2

is significant at 1.0000

Cannot reject at alpha = 0.05

Hard IRM N = 6 Median = 22.35

Hard IRM b N = 13 Median = 36.00

Point estimate for ETA1-ETA2 is -14.50

95.2 Percent CI for ETA1-ETA2 is (-20.10,-5.80)

W = 31.0

Test of ETA1 = ETA2 vs ETA1 not = ETA2

is significant at 0.0124

SIRM/ χ N = 6 Median = 11.265

SIRM/ χ b N = 13 Median = 21.590

Point estimate for ETA1-ETA2 is -10.280

95.2 Percent CI for ETA1-ETA2 is (-16.400,-6.467)

W = 24.0

Test of ETA1 = ETA2 vs ETA1 not = ETA2

is significant at 0.0018

The test is significant at 0.0018 (adjusted for ties)

χ_{arm} N = 6 Median = 0.17000

$\chi_{arm} b$ N = 13 Median = 0.20500

Point estimate for ETA1-ETA2 is -0.03850

95.2 Percent CI for ETA1-ETA2 is (-0.09303,0.00601)

W = 40.5

Test of ETA1 = ETA2 vs ETA1 not = ETA2 is significant at 0.0956

The test is significant at 0.0955 (adjusted for ties)

Cannot reject at alpha = 0.05

Soft IRM N = 6 Median = 146.80

Soft IRM b N = 13 Median = 130.40

Point estimate for ETA1-ETA2 is 12.75

95.2 Percent CI for ETA1-ETA2 is (-16.19,41.81)

W = 70.0

Test of ETA1 = ETA2 vs ETA1 not = ETA2 is significant at 0.4047

Cannot reject at alpha = 0.05

ARM/ χ N = 6 Median = 0.1250

ARM/ χ b N = 13 Median = 0.3200

Point estimate for ETA1-ETA2 is -0.1850

95.2 Percent CI for ETA1-ETA2 is (-0.2400,-0.0900)

W = 27.0

Test of ETA1 = ETA2 vs ETA1 not = ETA2 is significant at 0.0044

The test is significant at 0.0043 (adjusted for ties)

SIRM/ARM N = 6 Median = 93.85

SIRM/ARM b N = 13 Median = 75.90

Point estimate for ETA1-ETA2 is 19.29

95.2 Percent CI for ETA1-ETA2 is (6.09,33.38)

W = 87.0

Test of ETA1 = ETA2 vs ETA1 not = ETA2 is significant at 0.0201

100 mT N = 6 Median = -0.6950

100 mT b N = 13 Median = -0.5050

Point estimate for ETA1-ETA2 is -0.1535

95.2 Percent CI for ETA1-ETA2 is (-0.2640,-0.0540)

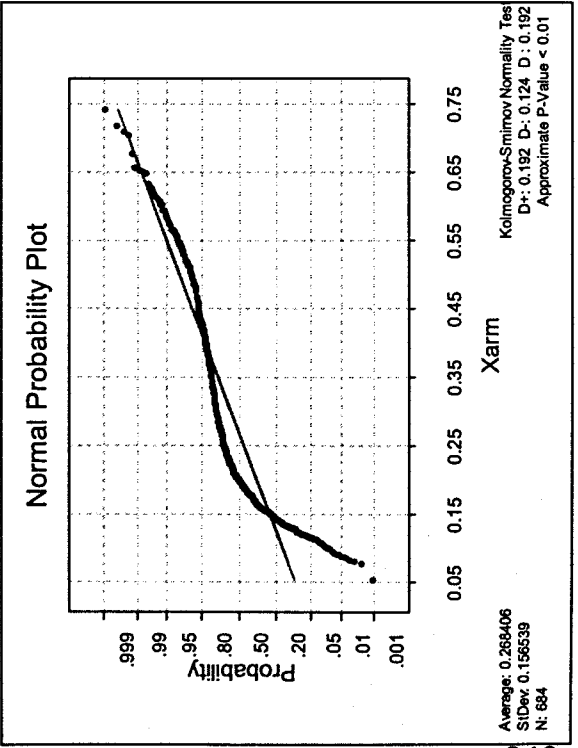
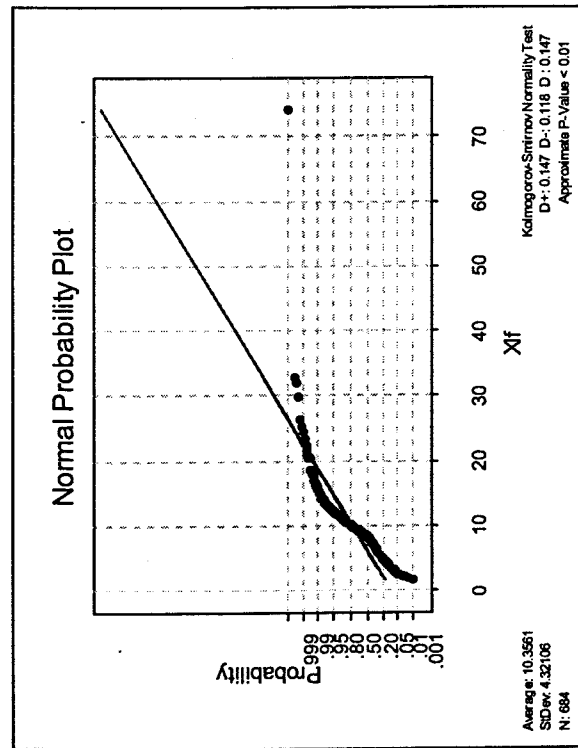
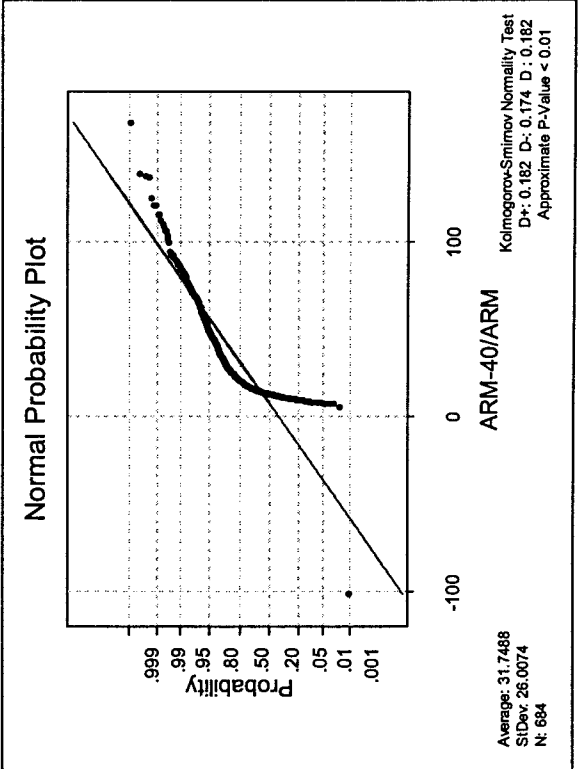
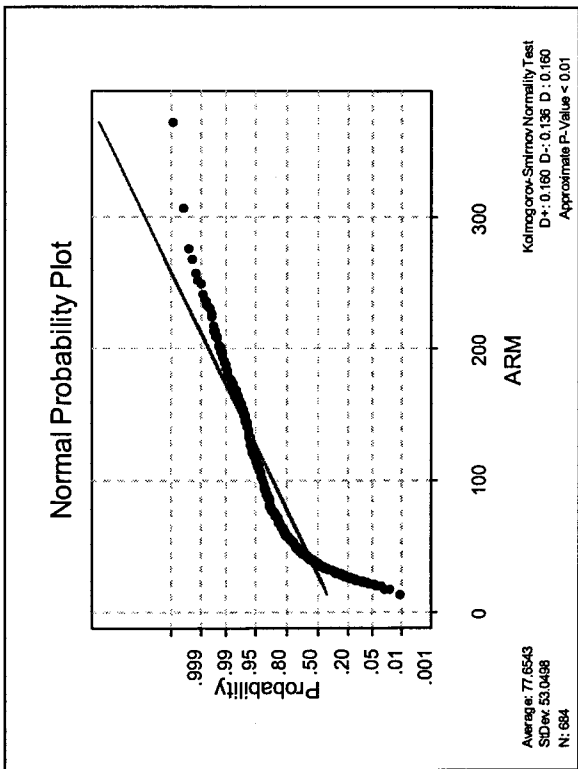
W = 36.0

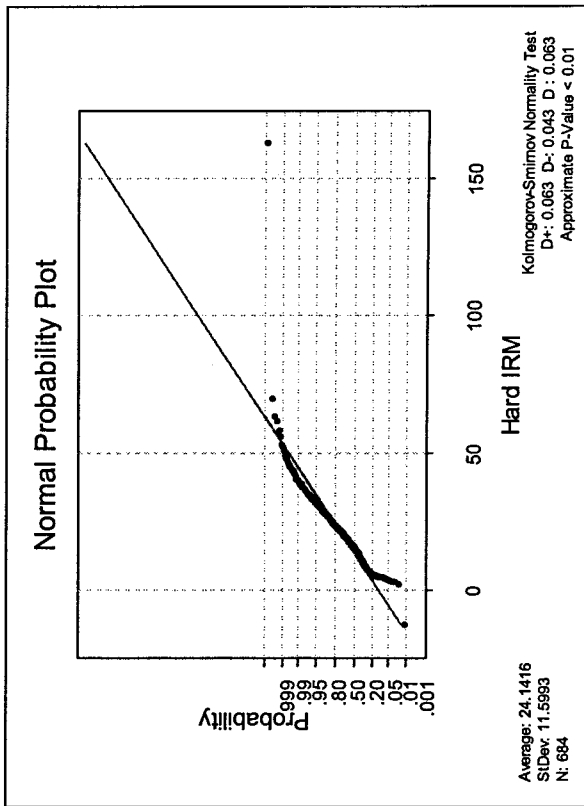
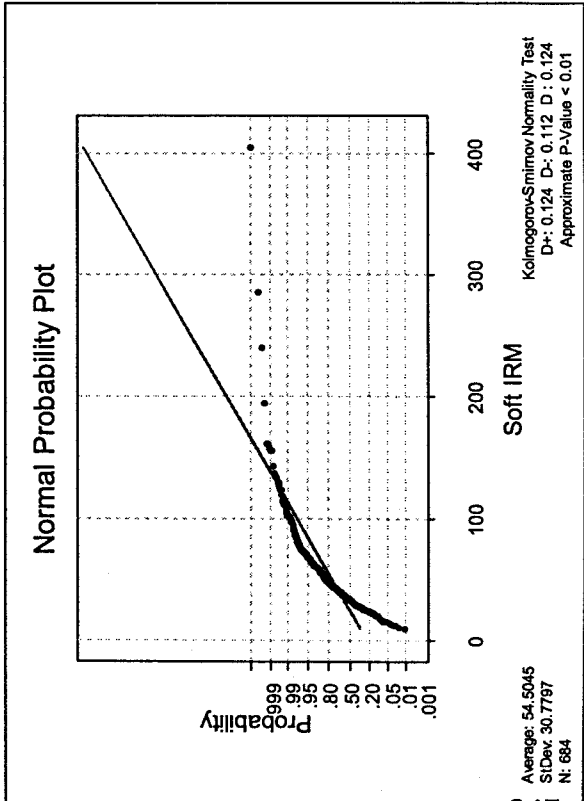
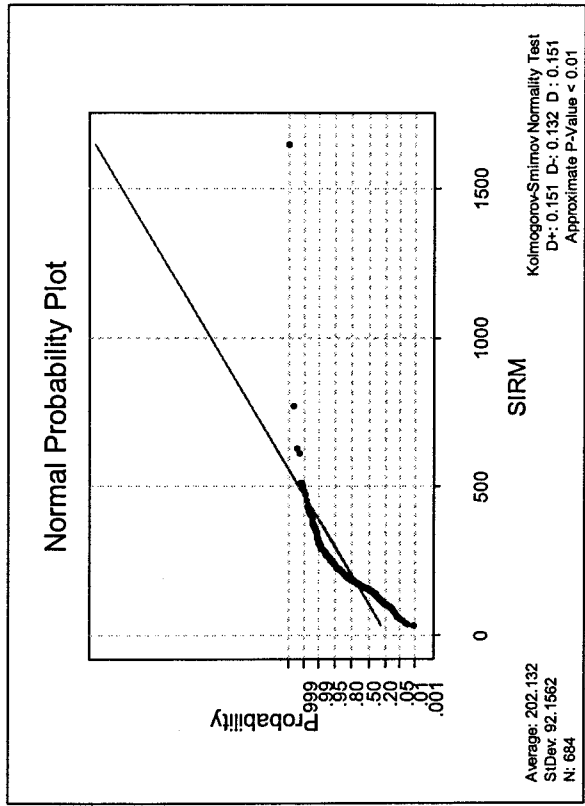
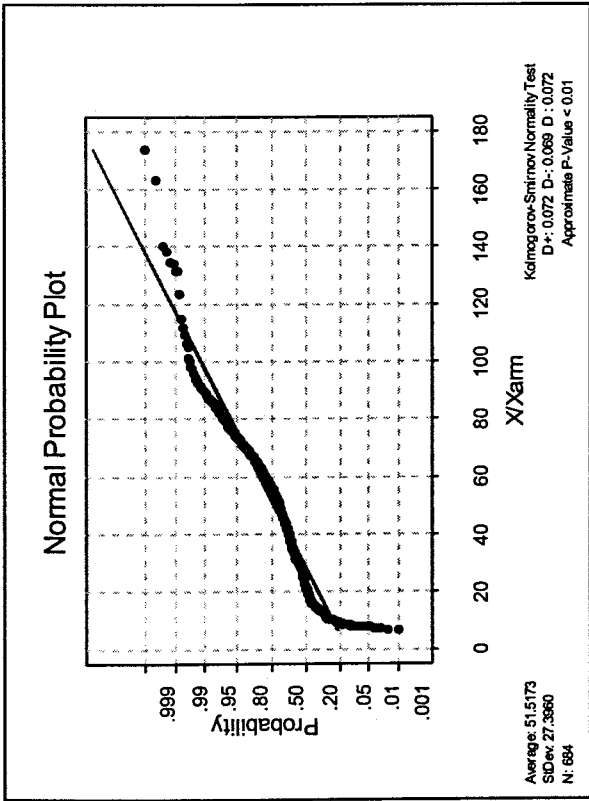
Test of ETA1 = ETA2 vs ETA1 not = ETA2 is significant at 0.0393

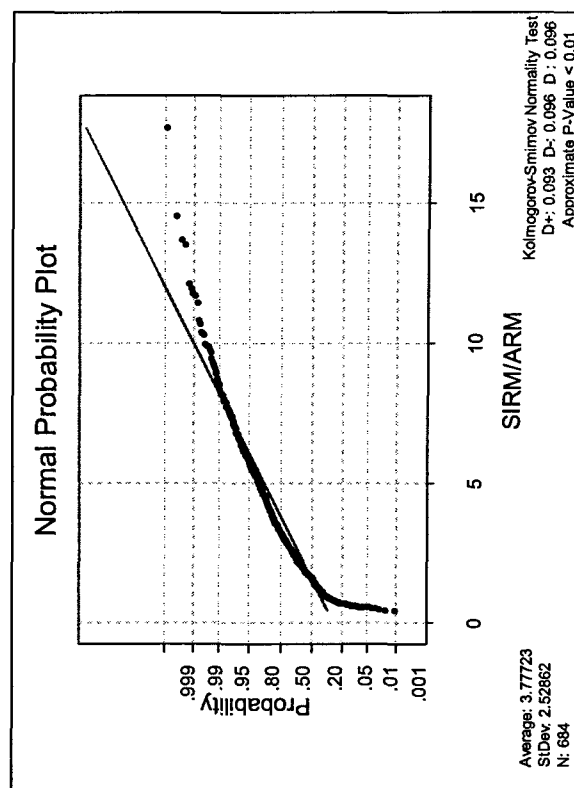
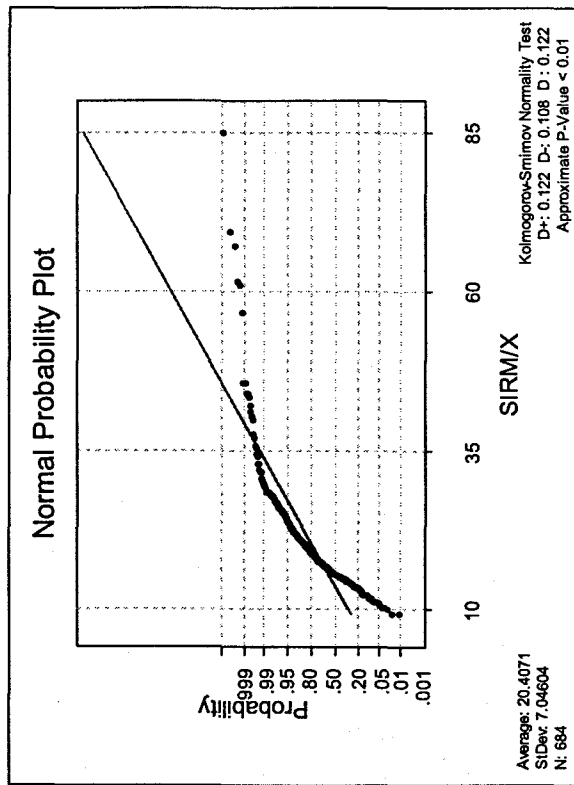
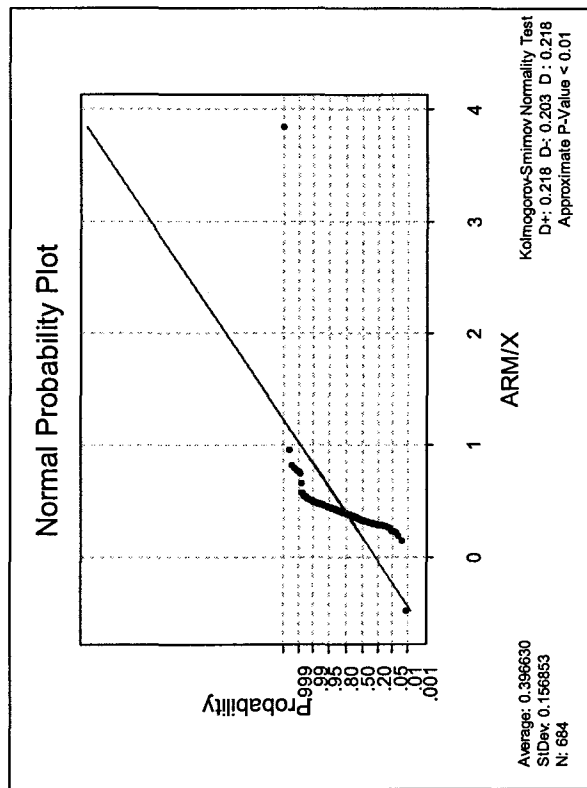
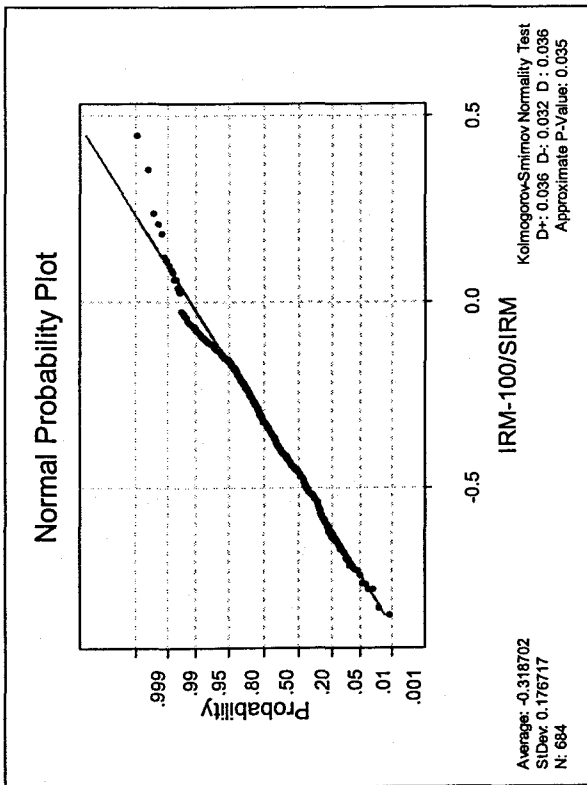
2ci) Descriptive Statistics

Variable	N	Mean	Median	Truncated Mean	Standard Deviation	Standard Error of the mean	Minimum	Maximum	Lower Quartile	Upper Quartile
χ_{if}	660	13.719	12.89	13.214	5.64	0.22	3.836	98.968	10.996	15.399
χ_{arm}	660	0.4109	0.2474	0.3741	0.3449	0.0134	0.0958	1.7082	0.1838	0.5132
SIRM	660	270.37	246.3	261.67	120.52	4.69	74.71	2199.85	207.33	322.48
Soft IRM	660	74	68.93	70.48	41.7	1.62	12.45	540.25	45.59	91.6
Hard IRM	660	31.047	30.379	30.374	13.659	0.532	0.313	217.553	22.684	37.499
χ_{arm}/χ	660	0.03297	0.0178	0.02924	0.03118	0.00121	0.0058	0.1465	0.0142	0.0349
ARM/ χ	660	6.228	4.545	5.755	4.604	0.179	1.232	26.019	3.019	7.573
SIRM/ χ	660	20.371	18.926	19.661	7.136	0.278	9.365	84.959	16.048	22.705
SIRM/ARM	660	4.739	3.943	4.462	3.074	0.12	0.949	21.515	2.391	6.393
SIRM/ χ_{arm}	660	998.9	929.1	933.6	667.8	26	181.2	5733.9	521.8	1282.6
IRM-100/SIRM	660	-0.31668	-0.31725	-0.31517	0.17785	0.00692	-0.8419	0.4469	-0.43353	-0.17892

2cii) Normality test







2ciii) Kruskal-Wallis tests

Kruskal-Wallis test of χ_{lf}

Group Code	N	Median	Ave Rank	Z
1 = Holocene	33	11.16	210.2	-3.72
2 = YD	21	15.53	439	2.65
3 = H1	14	13.18	349.7	0.38
4 = H2	32	10.3	164.2	-5.06
5 = H2 PE	17	10.98	230.3	-2.19
6 = H3	33	15.67	497	5.15
7 = H4	18	24.97	606.6	6.23
8 = H4 PE	14	15.13	519.1	3.74
9 = H5	10	24.27	625.6	4.93
10 = MIS 5e/6	197	11.45	228.6	-8.95
11 = Ambient	271	13.66	376.5	5.17
Overall	660		330.5	

H = 221.68 DF = 10 P = 0

H = 221.68 DF = 10 P = 0 (adjusted for ties)

Kruskal-Wallis test on χ_{arm}

Group Code	N	Median	Ave Rank	Z
1	33	0.6029	524	5.98
2	21	0.5577	510	4.39
3	14	0.2497	349.5	0.38
4	32	0.1514	69.3	-7.95
5	17	0.1426	56.8	-6
6	33	0.2135	262.8	-2.09
7	18	0.3046	406.5	1.71
8	14	0.3768	456.9	2.51
9	10	0.3683	452.9	2.05
10	197	0.4713	403.7	6.43
11	271	0.2147	279	-5.79
Overall	660		330.5	

H = 213.91 DF = 10 P = 0

Kruskal-Wallis test on SIRM

Group Code	N	Median	Ave Rank	Z
1	33	327.7	406	2.33
2	21	340	521.2	4.66
3	14	253.7	340.3	0.19
4	32	385.4	504.2	5.28
5	17	231.2	322.9	-0.17
6	33	335.5	498	5.18
7	18	318.4	473.3	3.22
8	14	246.1	321.1	-0.19
9	10	341.4	510.3	3
10	197	224.5	270.8	-5.25
11	271	232.2	293.4	-4.17
Overall	660		330.5	

H = 126.91 DF = 10 P = 0

Kruskal-Wallis test on Soft IRM

Group Code	N	Median	Ave Rank	Z
1	33	75.6	388.5	1.79
2	21	76.65	426.1	2.34
3	14	78.64	419.2	1.76
4	32	92.24	464.1	4.06
5	17	68.89	309.1	-0.47
6	33	105.03	527.2	6.08
7	18	92.02	489.8	3.59
8	14	71.04	379.3	0.97
9	10	98.75	541.9	3.53
10	197	53.43	260.8	-6.13
11	271	63.55	302.9	-3.11
Overall	660		330.5	

H = 120.24 DF = 10 P = 0

Kruskal-Wallis test on Hard IRM

Group Code	N	Median	Ave Rank	Z
1	33	25.13	253.9	-2.37
2	21	32.33	356.4	0.63
3	14	25.52	236.3	-1.87
4	32	24.5	216.3	-3.47
5	17	36.73	458.4	2.8
6	33	47.63	558.6	7.05
7	18	35.28	410.7	1.81
8	14	25.84	258.4	-1.43
9	10	26.98	267.9	-1.05
10	197	22.09	188.8	-12.45
11	271	35.21	424.1	10.52
Overall	660		330.5	

H = 255.71 DF = 10 P = 0

Kruskal-Wallis test on SIRM/ χ

Group Code	N	Median	Ave Rank	Z
1	33	26.88	582	7.77
2	21	22.61	496	4.04
3	14	19.06	342.4	0.24
4	32	37.34	600.8	8.22
5	17	21.83	439.6	2.39
6	33	20.99	409.5	2.44
7	18	13.77	84.8	-5.54
8	14	15.48	129.6	-3.99
9	10	13.73	98	-3.89
10	197	20.38	362.1	2.77
11	271	17.39	250.4	-9.01
Overall	660		330.5	

H = 262.37 DF = 10 P = 0

Kruskal-Wallis test on SIRM/ARM

Group Code	N	Median	Ave Rank	Z
1	33	2.843	252.3	-2.42
2	21	3.468	301.5	-0.71
3	14	7.696	531.4	3.98
4	32	11.317	610.9	8.53
5	17	9.708	602.3	5.95
6	33	7.367	541.6	6.53
7	18	4.011	376.9	1.05
8	14	3.071	246.7	-1.66
9	10	3.791	318.4	-0.2
10	197	1.952	140.7	-16.68
11	271	4.862	395.7	7.33
Overall	660		330.5	

H = 396.52 DF = 10 P = 0

Kruskal-Wallis test on ARM/ χ

Group Code	N	Median	Ave Rank	Z
1	33	9.881	503.7	5.35
2	21	6.52	443	2.75
3	14	2.676	124	-4.1
4	32	3.485	223.2	-3.26
5	17	2.258	60.6	-5.91
6	33	2.632	127.7	-6.27
7	18	3.526	184.7	-3.29
8	14	4.979	361.8	0.62
9	10	3.225	233.1	-1.63
10	197	9.651	518.6	16.53
11	271	3.392	240.6	-10.13
Overall	660		330.5	

H = 398.09 DF = 10 P = 0

Kruskal-Wallis test on SIRM/ χ_{arm}

Group Code	N	Median	Ave Rank	Z
1	33	412.8	145.8	-5.71
2	21	633	211.2	-2.91
3	14	1015.5	353.8	0.46
4	32	2491.2	630.3	9.12
5	17	1734.8	593.7	5.77
6	33	1609.3	555.9	6.97
7	18	935.1	379.8	1.11
8	14	596.1	202.1	-2.55
9	10	884.9	299.8	-0.51
10	197	484.4	200.7	-11.41
11	271	1108.2	380.6	5.63
Overall	660		330.5	

H = 314.8 DF = 10 P = 0

Kruskal-Wallis test on χ_{arm}/χ

Group Code	N	Median	Ave Rank	Z
1	33	0.0658	540.4	6.49
2	21	0.0356	499	4.12
3	14	0.0183	351.6	0.42
4	32	0.0147	179.7	-4.59
5	17	0.0123	88.3	-5.31
6	33	0.0131	131	-6.17
7	18	0.0149	187.1	-3.24
8	14	0.02565	433	2.03
9	10	0.01455	235.6	-1.59
10	197	0.0363	453.1	10.77
11	271	0.0159	266.7	-7.17
Overall	660		330.5	

H = 268.56 DF = 10 P = 0

H = 268.56 DF = 10 P = 0 (adjusted for ties)

Kruskal-Wallis on IRM₋₁₀₀/SIRM

Group Code	N	Median	Ave Rank	Z
1	33	-0.2803	321.3	-0.28
2	21	-0.301	327.3	-0.08
3	14	-0.4234	238	-1.83
4	32	-0.4634	185.6	-4.41
5	17	-0.3912	309.8	-0.45
6	33	-0.1973	422.4	2.84
7	18	-0.355	242.1	-1.99
8	14	-0.4921	232.2	-1.95
9	10	-0.5028	107.6	-3.73
10	197	-0.3355	312.2	-1.61
11	271	-0.2432	376.4	5.16
Overall	660		330.5	

H = 68.49 DF = 10 P = 0

H = 68.49 DF = 10 P = 0 (adjusted for ties)

2cvi) Mann Whitney U tests for H2. a is the material suggested to be European, b is the Laurentide material.

χ_{lf} a N = 32 Median = 10.299
 χ_{lf} b N = 9 Median = 11.027
 Point estimate for ETA1-ETA2 is -0.707
 95.1 Percent CI for ETA1-ETA2 is (-2.609,1.034)
 W = 640.5
 Test of ETA1 = ETA2 vs ETA1 not = ETA2 is significant at 0.3289
 The test is significant at 0.3287 (adjusted for ties)
 Cannot reject at alpha = 0.05

SIRM a N = 32 Median = 385.4
 SIRM b N = 9 Median = 571.7
 Point estimate for ETA1-ETA2 is -195.5
 95.1 Percent CI for ETA1-ETA2 is (-347.5,-64.7)
 W = 587.5
 Test of ETA1 = ETA2 vs ETA1 not = ETA2 is significant at 0.0082
 The test is significant at 0.0081 (adjusted for ties)

Hard IRM a N = 32 Median = 24.499
 Hard IRM b N = 9 Median = 21.326
 Point estimate for ETA1-ETA2 is 1.822
 95.1 Percent CI for ETA1-ETA2 is (-2.198,6.049)
 W = 705.5
 Test of ETA1 = ETA2 vs ETA1 not = ETA2 is significant at 0.2986
 The test is significant at 0.2984 (adjusted for ties)
 Cannot reject at alpha = 0.05

SIRM/ARM a N = 32 Median = 11.317
 SIRM/ARM b N = 9 Median = 14.575
 Point estimate for ETA1-ETA2 is -3.178
 95.1 Percent CI for ETA1-ETA2 is (-5.651,-0.002)
 W = 606.5
 Test of ETA1 = ETA2 vs ETA1 not = ETA2 is significant at 0.0406
 The test is significant at 0.0405 (adjusted for ties)

SIRM/ χ_{arm} a N = 32 Median = 2491.2
 SIRM/ χ_{arm} b N = 9 Median = 3786.7
 Point estimate for ETA1-ETA2 is -996.9
 95.1 Percent CI for ETA1-ETA2 is (-1752.8,-274.4)
 W = 590.5
 Test of ETA1 = ETA2 vs ETA1 not = ETA2 is significant at 0.0107
 The test is significant at 0.0107 (adjusted for ties)

χ_{arm}/χ a N = 32 Median = 0.01470
 χ_{arm}/χ b N = 9 Median = 0.01470
 Point estimate for ETA1-ETA2 is 0.00000
 95.1 Percent CI for ETA1-ETA2 is (-0.00290,0.00210)
 W = 669.5
 Test of ETA1 = ETA2 vs ETA1 not = ETA2 is significant at 0.9498
 The test is significant at 0.9497 (adjusted for ties)
 Cannot reject at alpha = 0.05

χ_{arm} a N = 32 Median = 0.15142
 χ_{arm} b N = 9 Median = 0.16079
 Point estimate for ETA1-ETA2 is -0.00838
 95.1 Percent CI for ETA1-ETA2 is (-0.03079,0.00144)
 W = 623.5
 Test of ETA1 = ETA2 vs ETA1 not = ETA2 is significant at 0.1306
 The test is significant at 0.1304 (adjusted for ties)
 Cannot reject at alpha = 0.05

Soft IRM a N = 32 Median = 92.2
 Soft IRM b N = 9 Median = 189.3
 Point estimate for ETA1-ETA2 is -83.8
 95.1 Percent CI for ETA1-ETA2 is (-136.0,-0.0)
 W = 608.5
 Test of ETA1 = ETA2 vs ETA1 not = ETA2 is significant at 0.0472
 The test is significant at 0.0471 (adjusted for ties)

SIRM/ χ a N = 32 Median = 37.34
 SIRM/ χ b N = 9 Median = 56.75
 Point estimate for ETA1-ETA2 is -16.57
 95.1 Percent CI for ETA1-ETA2 is (-28.87,-2.22)
 W = 594.5
 Test of ETA1 = ETA2 vs ETA1 not = ETA2 is significant at 0.0153
 The test is significant at 0.0153 (adjusted for ties)

ARM/ χ a N = 32 Median = 3.4852
 ARM/ χ b N = 9 Median = 3.9488
 Point estimate for ETA1-ETA2 is -0.2785
 95.1 Percent CI for ETA1-ETA2 is (-0.6771,0.0138)
 W = 618.5
 Test of ETA1 = ETA2 vs ETA1 not = ETA2 is significant at 0.0950
 The test is significant at 0.0949 (adjusted for ties)
 Cannot reject at alpha = 0.05

100 bacfield a N = 32 Median = -0.4634
 100 bacfield b N = 9 Median = -0.4415
 Point estimate for ETA1-ETA2 is -0.0387
 95.1 Percent CI for ETA1-ETA2 is (-0.1691,0.0306)
 W = 640.5
 Test of ETA1 = ETA2 vs ETA1 not = ETA2 is significant at 0.3289
 The test is significant at 0.3287 (adjusted for ties)
 Cannot reject at alpha = 0.05

2cvi) Mann Whitney U tests for H4. a is the material suggested to be European, b is the Laurentide material.

χ_{lf}^2 b N = 6 Median = 36.65
 Point estimate for ETA1-ETA2 is -18.08
 95.6 Percent CI for ETA1-ETA2 is (-35.58,-8.97)
 W = 80.0
 Test of ETA1 = ETA2 vs ETA1 not = ETA2 is
 significant at 0.0017

SIRM a N = 12 Median = 302.9
 SIRM b N = 6 Median = 384.7
 Point estimate for ETA1-ETA2 is -110.3
 95.6 Percent CI for ETA1-ETA2 is (-268.7,-25.3)
 W = 87.0
 Test of ETA1 = ETA2 vs ETA1 not = ETA2 is
 significant at 0.0131

Hard IRM a N = 12 Median = 35.3
 Hard IRM b N = 6 Median = 32.0
 95.6 Percent CI for ETA1-ETA2 is (-23.2,14.4)
 Point estimate for ETA1-ETA2 is 0.6
 W = 116.0
 Test of ETA1 = ETA2 vs ETA1 not = ETA2 is
 significant at 0.8883
 Cannot reject at alpha = 0.05

SIRM/ARM a N = 12 Median = 3.815
 SIRM/ARM b N = 6 Median = 6.367
 95.6 Percent CI for ETA1-ETA2 is (-3.791,-0.256)
 Point estimate for ETA1-ETA2 is -2.544
 W = 92.0
 Test of ETA1 = ETA2 vs ETA1 not = ETA2 is
 significant at 0.0440

SIRM/ χ_{arm} a N = 12 Median = 809.9
 SIRM/ χ_{arm} b N = 6 Median = 1323.2
 95.6 Percent CI for ETA1-ETA2 is (-682.2,-185.9)
 Point estimate for ETA1-ETA2 is -476.8
 W = 82.0
 Test of ETA1 = ETA2 vs ETA1 not = ETA2 is
 significant at 0.0032

χ_{arm}/χ a N = 12 Median = 0.01680
 χ_{arm}/χ b N = 6 Median = 0.00750
 Point estimate for ETA1-ETA2 is 0.00830
 95.6 Percent CI for ETA1-ETA2 is (0.00440,0.01240)
 W = 148.0
 Test of ETA1 = ETA2 vs ETA1 not = ETA2 is significant at 0.0017

χ_{arm} N = 12 Median = 0.3046
 χ_{arm} N = 6 Median = 0.3327
 Point estimate for ETA1-ETA2 is 0.0058
 95.6 Percent CI for ETA1-ETA2 is (-0.1429,0.0655)
 W = 117.0
 Test of ETA1 = ETA2 vs ETA1 not = ETA2 is
 significant at 0.8149
 Cannot reject at alpha = 0.05

Soft IRM a N = 12 Median = 83.9
 Soft IRM b N = 6 Median = 129.4
 Point estimate for ETA1-ETA2 is -47.5
 95.6 Percent CI for ETA1-ETA2 is (-95.5,-21.0)
 W = 84.0
 Test of ETA1 = ETA2 vs ETA1 not = ETA2 is
 significant at 0.0057

SIRM/ χ a N = 12 Median = 14.248
 SIRM/ χ b N = 6 Median = 10.453
 95.6 Percent CI for ETA1-ETA2 is (-1.131,5.199)
 Point estimate for ETA1-ETA2 is 2.923
 W = 134.0
 Test of ETA1 = ETA2 vs ETA1 not = ETA2 is
 significant at 0.0678
 Cannot reject at alpha = 0.05

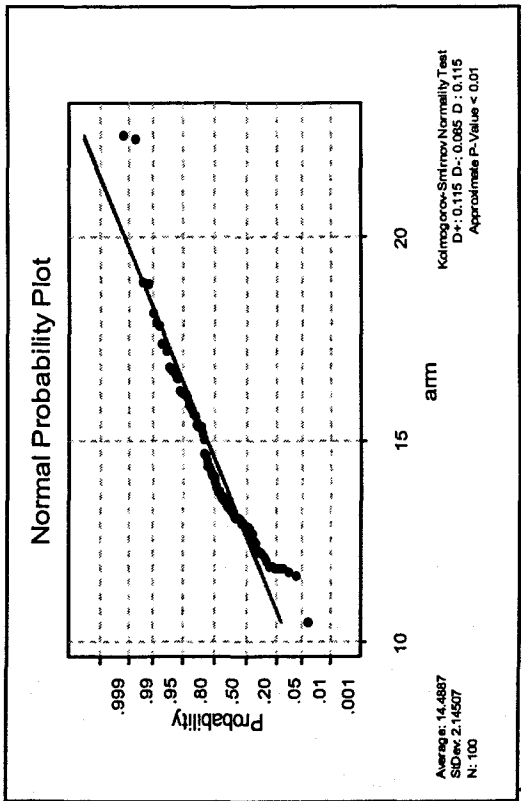
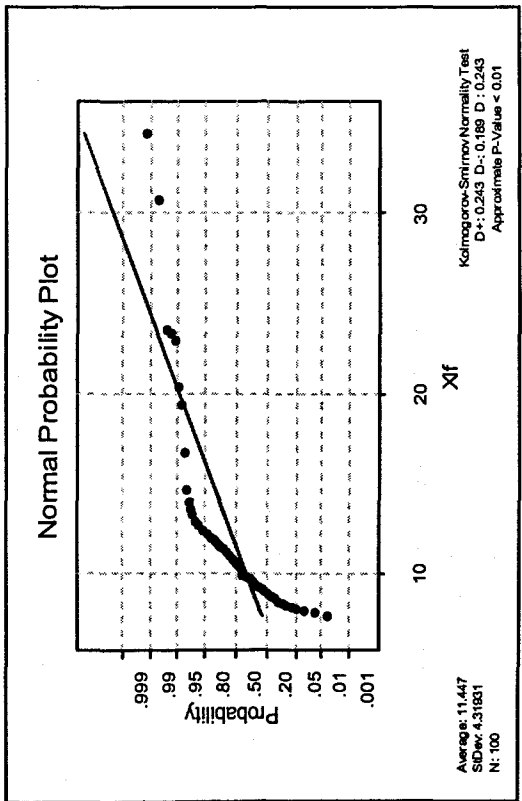
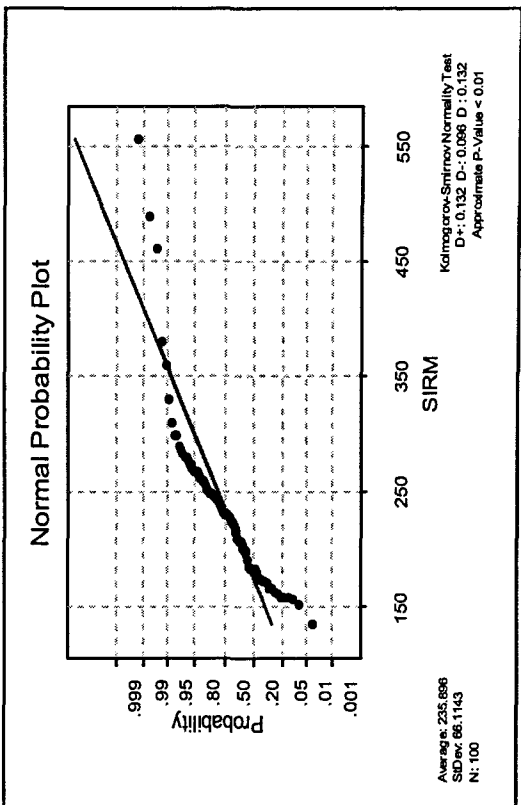
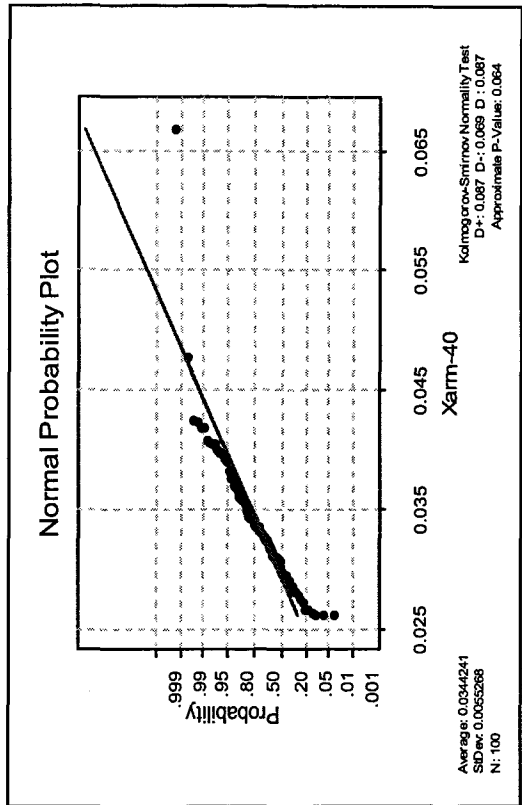
ARM/ χ a N = 12 Median = 3.847
 ARM/ χ b N = 6 Median = 1.596
 95.6 Percent CI for ETA1-ETA2 is (0.484,2.946)
 Point estimate for ETA1-ETA2 is 2.134
 W = 142.0
 Test of ETA1 = ETA2 vs ETA1 not = ETA2 is
 significant at 0.0100

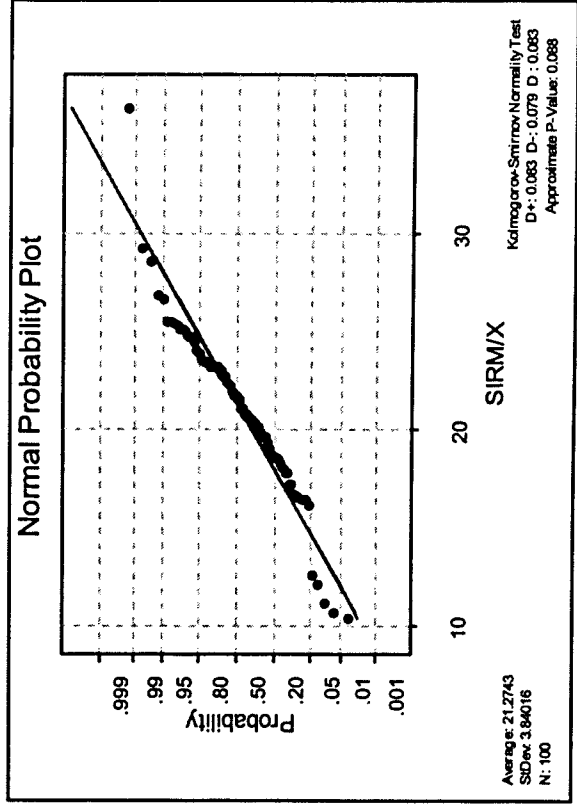
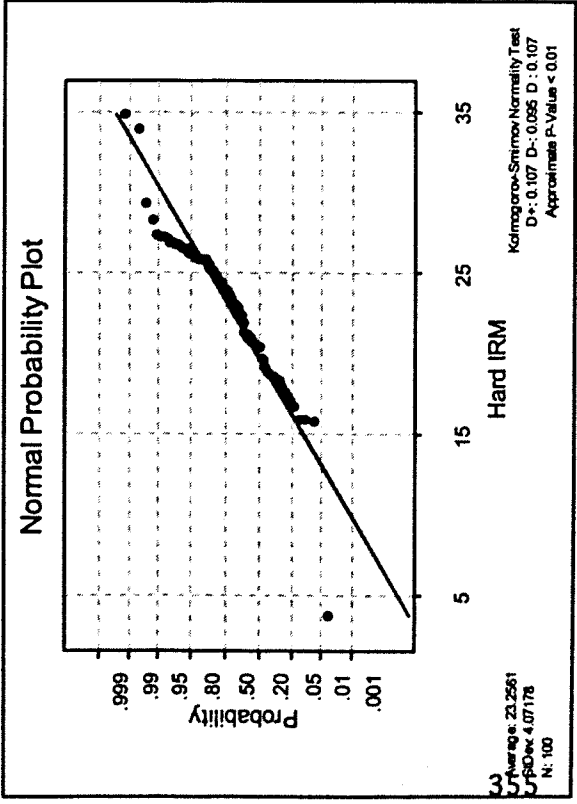
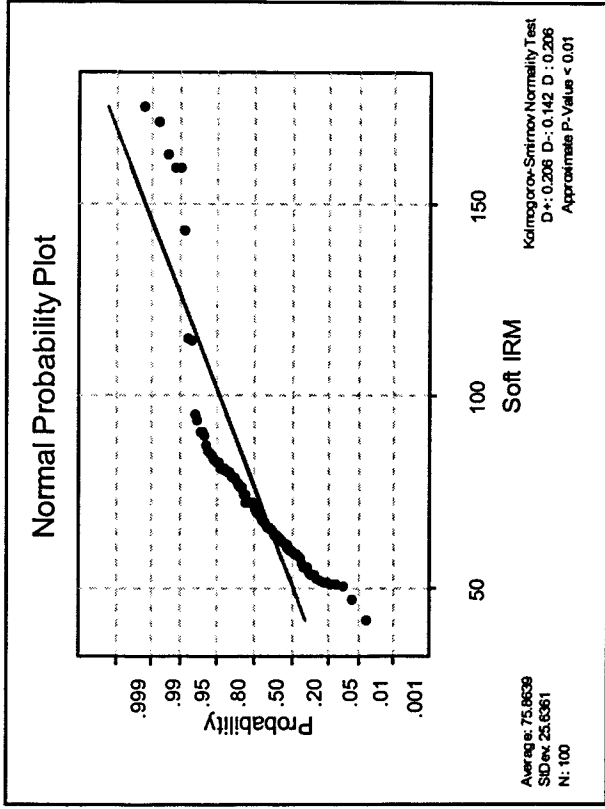
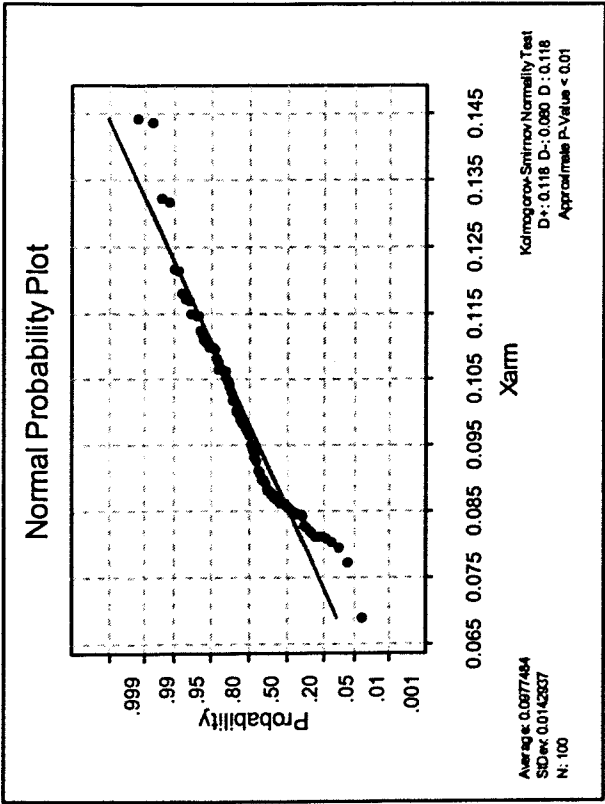
100 backfield a N = 12 Median = -0.3451
 100 backfield b N = 6 Median = -0.4785
 95.6 Percent CI for ETA1-ETA2 is (-0.1619,0.3211)
 Point estimate for ETA1-ETA2 is 0.0951
 W = 127.0
 Test of ETA1 = ETA2 vs ETA1 not = ETA2 is
 significant at 0.2417
 Cannot reject at alpha = 0.05

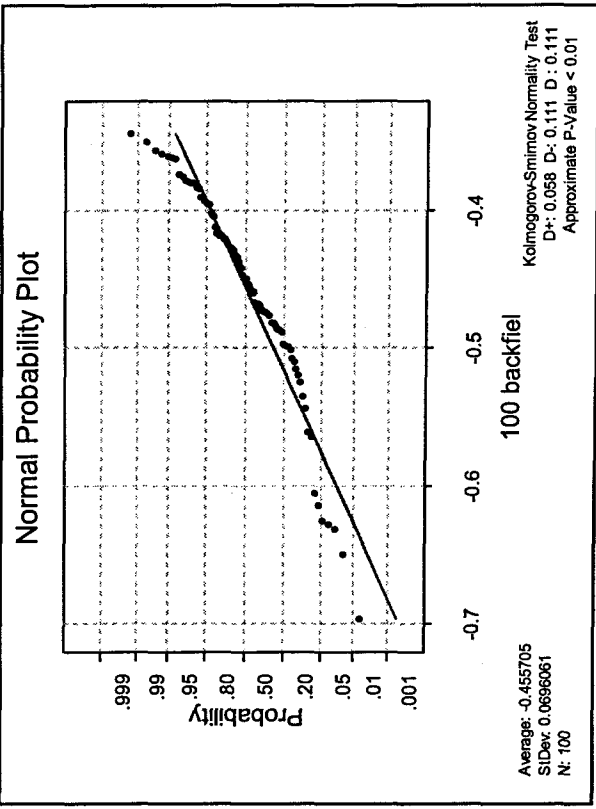
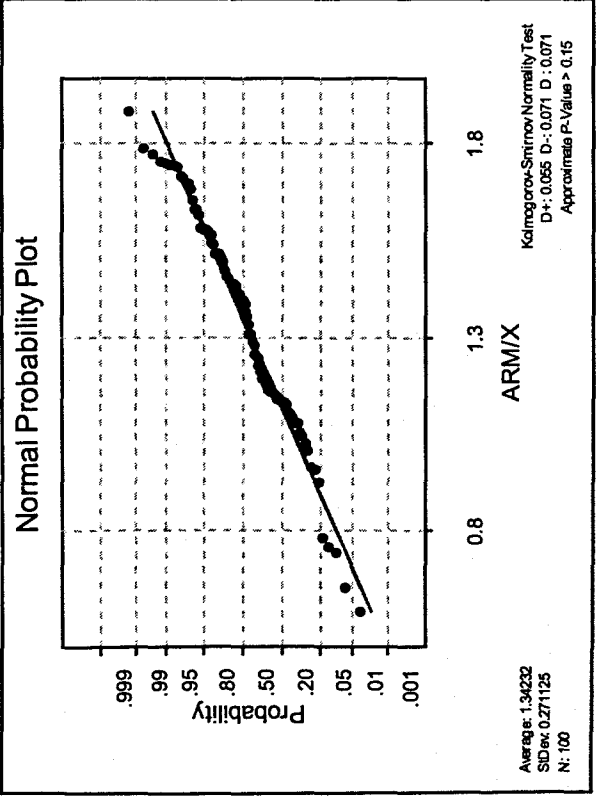
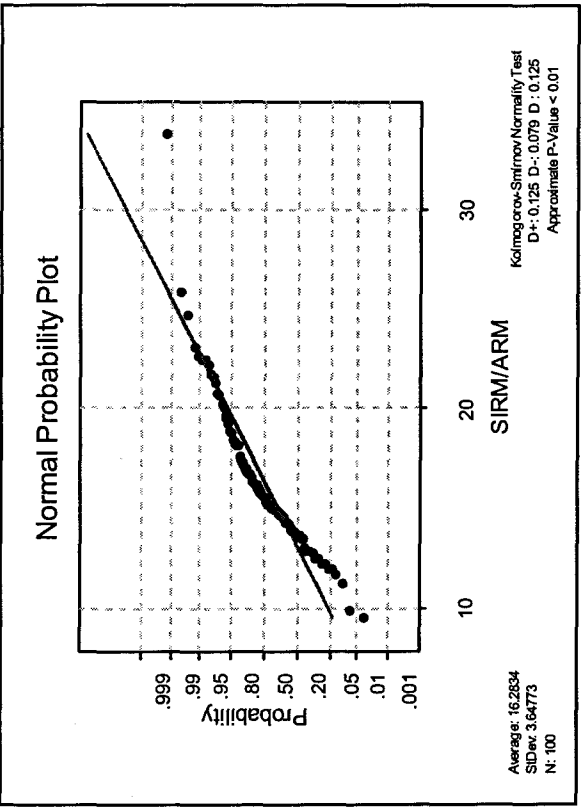
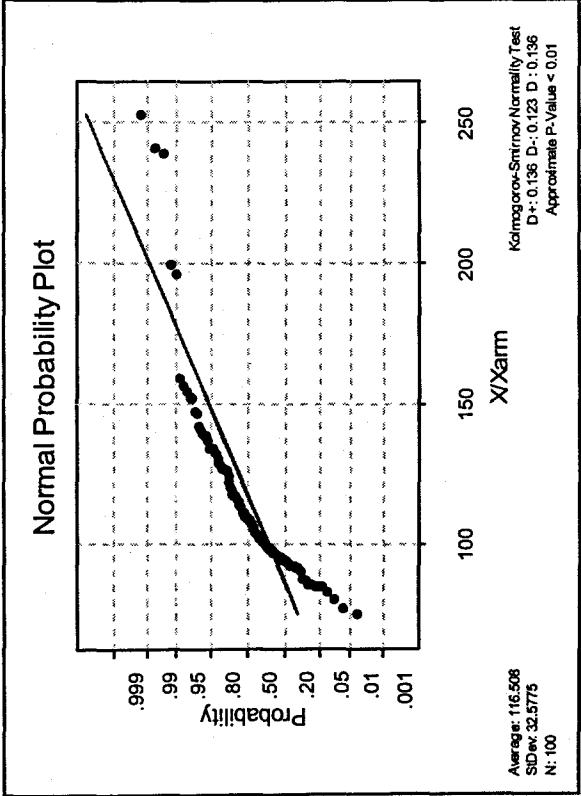
2di) Descriptive Statistics

Variable	N	Mean	Median	Truncated Mean	Standard Deviation	Standard Error of the Mean	Minimum	Maximum	Lower Quartile	Upper Quartile
χ_I	100	11.447	10.55	10.781	4.319	0.432	7.6	34.4	9.1	12
χ_{arm}	100	0.09775	0.09593	0.09683	0.01429	0.00143	0.06891	0.14418	0.08627	0.10661
SIRM	100	235.9	230.8	228.69	66.11	6.61	135	555.61	185.94	261.12
Soft	100	75.86	71.21	72.38	25.64	2.56	41.84	175.47	61.49	81.04
Hard	100	23.256	23.978	23.37	4.072	0.407	3.779	34.844	20.783	25.956
χ_{arm}/χ	100	0.00908	0.0092	0.00915	0.00193	0.00019	0.00395	0.01335	0.00776	0.01049
ARM/ χ	100	1.3423	1.3848	1.3528	0.2711	0.0271	0.5891	1.884	1.1461	1.5444
SIRM/ χ	100	21.274	21.595	21.359	3.84	0.384	10.453	36.358	19.128	23.442
SIRM/ARM	100	16.283	15.543	16.043	3.648	0.365	9.575	33.724	13.87	18.024
SIRM/ χ_{arm}	100	2414.8	2309.3	2379.6	542.3	54.2	1512.9	4692.3	2055.3	2665.5
IRM-100/SIRM	100	-0.4557	-0.44923	-0.45078	0.06961	0.00696	-0.69593	-0.34471	-0.48529	-0.40605

2dii) Normality tests







2diii) Mann Whitney U tests - sample set a) are the European samples, b) are the Laurentide samples

χ_{lf} a N = 92 Median = 12.80
 χ_{lf} b N = 5 Median = 35.39
 Point estimate for ETA1-ETA2 is -21.99
 95.1 Percent CI for ETA1-ETA2 is (-26.92,-17.43)
 W = 4278.0
 Test of ETA1 = ETA2 vs ETA1 not = ETA2 is significant at 0.0002

SIRM a N = 92 Median = 282.8
 SIRM b N = 5 Median = 405.4
 Point estimate for ETA1-ETA2 is -126.8
 95.1 Percent CI for ETA1-ETA2 is (-206.6,-72.0)
 W = 4299.0
 Test of ETA1 = ETA2 vs ETA1 not = ETA2 is significant at 0.0007

Hard IRM a N = 92 Median = 29.770
 Hard IRM b N = 5 Median = 25.962
 Point estimate for ETA1-ETA2 is 3.554
 95.1 Percent CI for ETA1-ETA2 is (-0.679,7.978)
 W = 4612.0
 Test of ETA1 = ETA2 vs ETA1 not = ETA2 is significant at 0.0913
 Cannot reject at alpha = 0.05

SIRM/ARM a N = 92 Median = 18.848
 SIRM/ARM b N = 5 Median = 22.342
 Point estimate for ETA1-ETA2 is -2.907
 95.1 Percent CI for ETA1-ETA2 is (-5.764,0.511)
 W = 4398.0
 Test of ETA1 = ETA2 vs ETA1 not = ETA2 is significant at 0.0740
 Cannot reject at alpha = 0.05

ARM/ χ a N = 92 Median = 1.1288
 ARM/ χ b N = 5 Median = 0.5064
 Point estimate for ETA1-ETA2 is 0.5922
 95.1 Percent CI for ETA1-ETA2 is (0.4372,0.7555)
 W = 4738.0
 Test of ETA1 = ETA2 vs ETA1 not = ETA2 is significant at 0.0002

IRM₁₀₀/SIRM a N = 92 Median = -0.44395
 IRM₁₀₀/SIRM b N = 5 Median = -0.63118
 Point estimate for ETA1-ETA2 is 0.19438
 95.1 Percent CI for ETA1-ETA2 is (0.14784,0.23714)
 W = 4736.0
 Test of ETA1 = ETA2 vs ETA1 not = ETA2 is significant at 0.0002
 The test is significant at 0.0002 (adjusted for ties)

χ_{arm} a N = 92 Median = 0.09479
 χ_{arm} b N = 5 Median = 0.11809
 Point estimate for ETA1-ETA2 is -0.02374
 95.1 Percent CI for ETA1-ETA2 is (-0.03576,-0.00930)
 W = 4334.0
 Test of ETA1 = ETA2 vs ETA1 not = ETA2 is significant at 0.0046

Soft IRM a N = 92 Median = 85.61
 Soft IRM b N = 5 Median = 176.18
 Point estimate for ETA1-ETA2 is -80.56
 95.1 Percent CI for ETA1-ETA2 is (-109.96,-50.11)
 W = 4291.0
 Test of ETA1 = ETA2 vs ETA1 not = ETA2 is significant at 0.0004

SIRM/ χ a N = 92 Median = 21.680
 SIRM/ χ b N = 5 Median = 11.203
 Point estimate for ETA1-ETA2 is 10.156
 95.1 Percent CI for ETA1-ETA2 is (7.941,12.386)
 W = 4738.0
 Test of ETA1 = ETA2 vs ETA1 not = ETA2 is significant at 0.0002

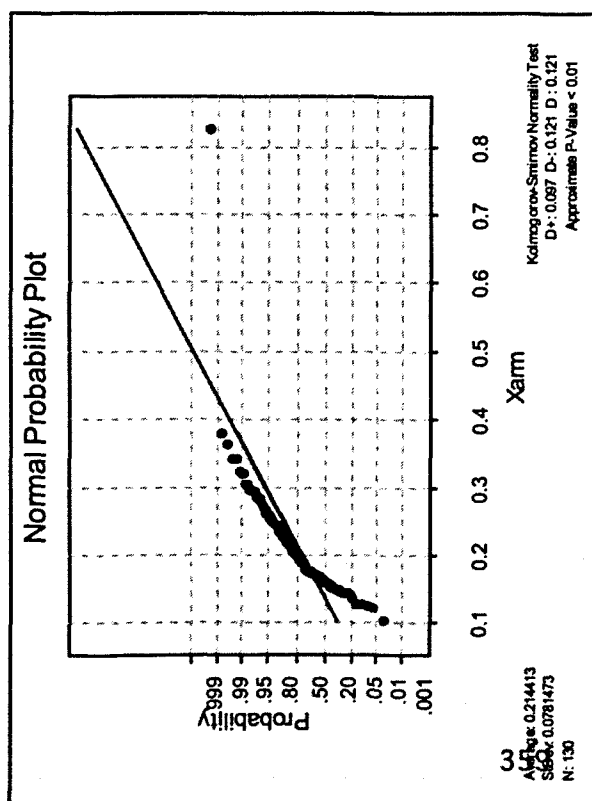
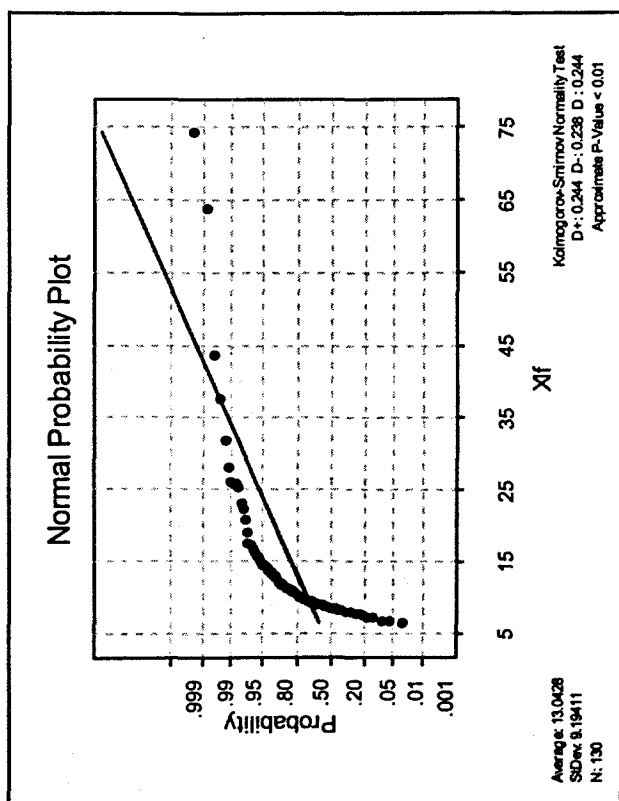
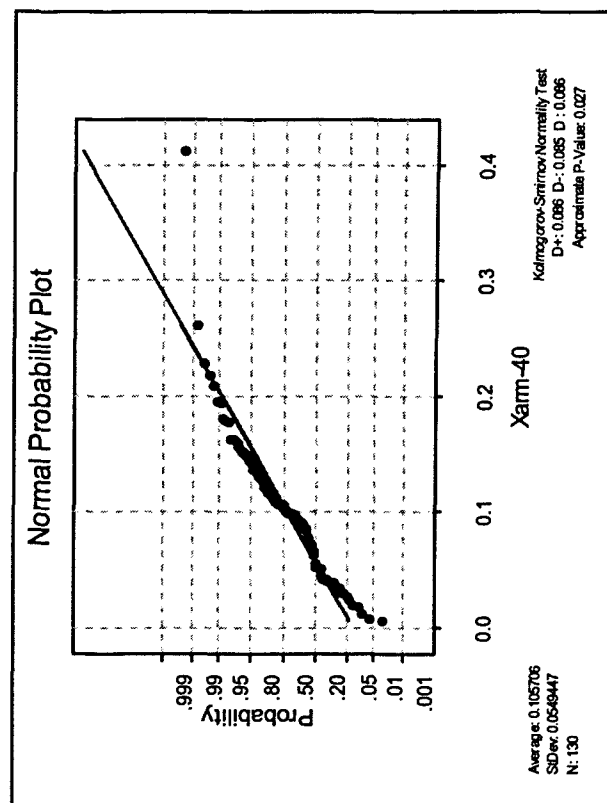
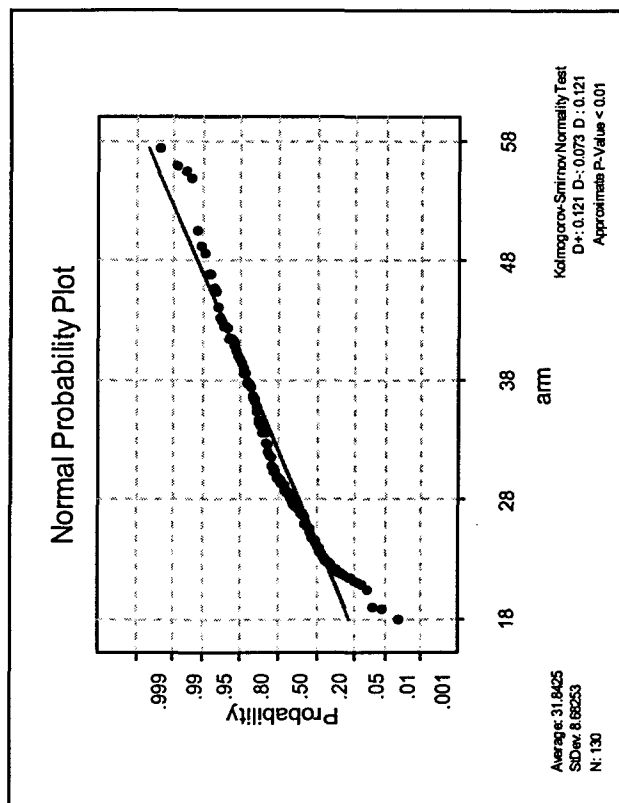
SIRM/ χ_{arm} a N = 92 Median = 2270.4
 SIRM/ χ_{arm} b N = 5 Median = 2524.7
 Point estimate for ETA1-ETA2 is -292.7
 95.1 Percent CI for ETA1-ETA2 is (-568.2,150.0)
 W = 4409.0
 Test of ETA1 = ETA2 vs ETA1 not = ETA2 is significant at 0.1080
 Cannot reject at alpha = 0.05

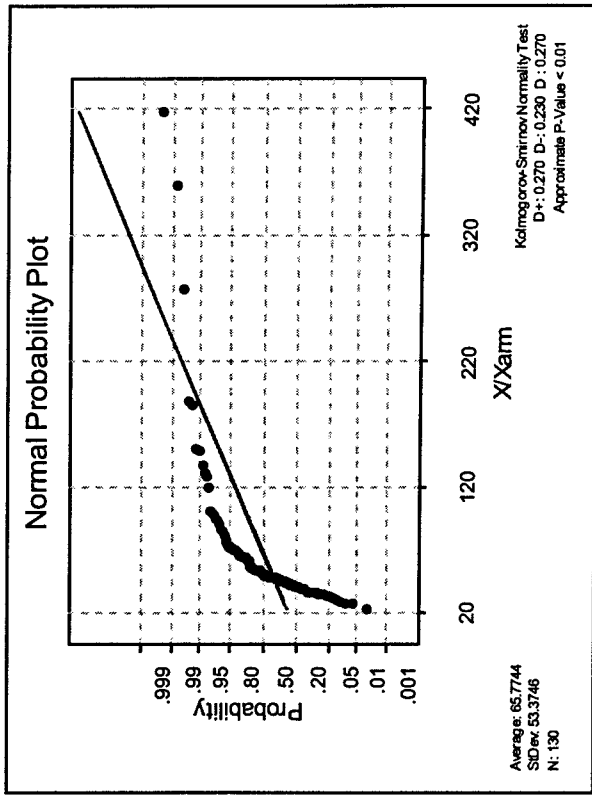
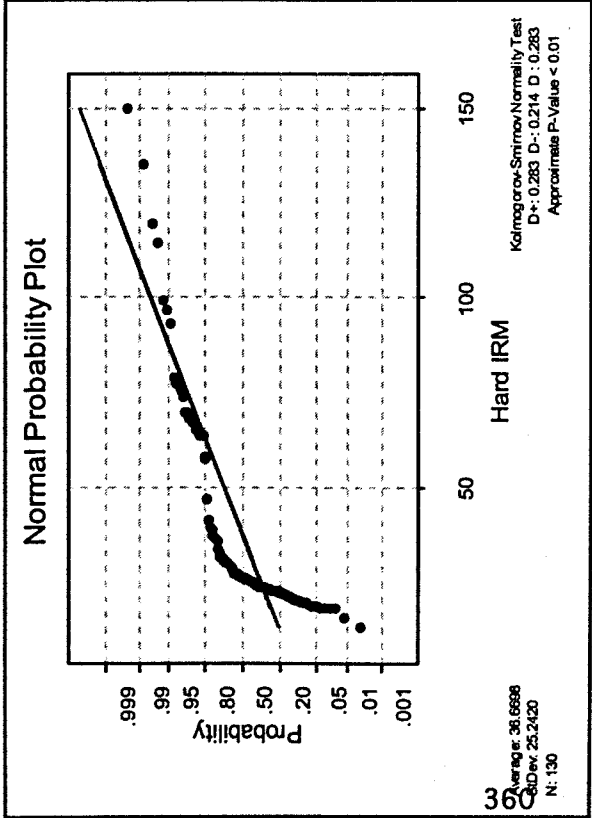
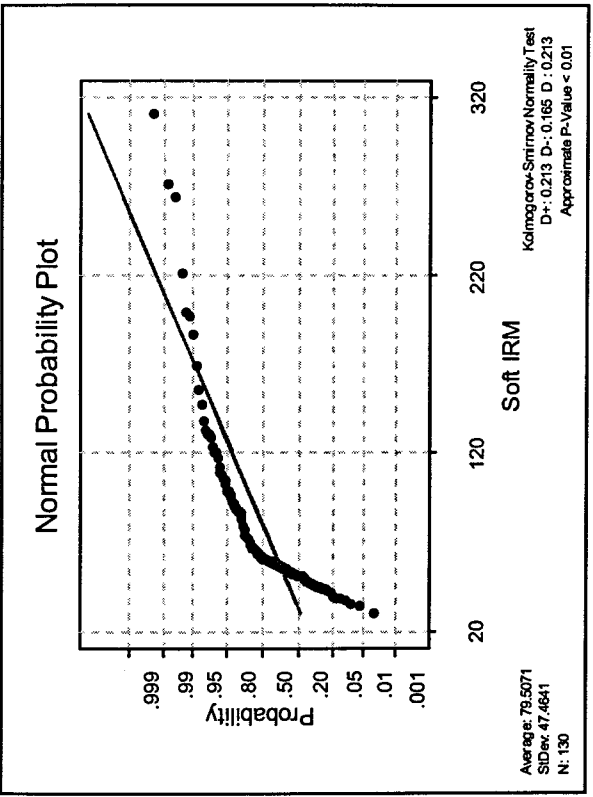
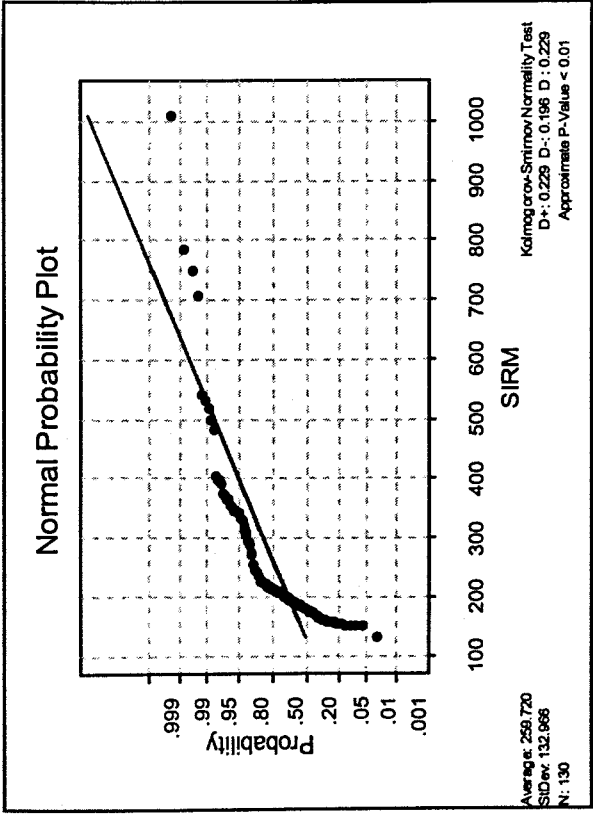
χ_{arm}/χ a N = 92 Median = 0.00931
 χ_{arm}/χ b N = 5 Median = 0.00418
 Point estimate for ETA1-ETA2 is 0.00488
 95.1 Percent CI for ETA1-ETA2 is (0.00344,0.00610)
 W = 4738.0
 Test of ETA1 = ETA2 vs ETA1 not = ETA2 is significant at 0.0002

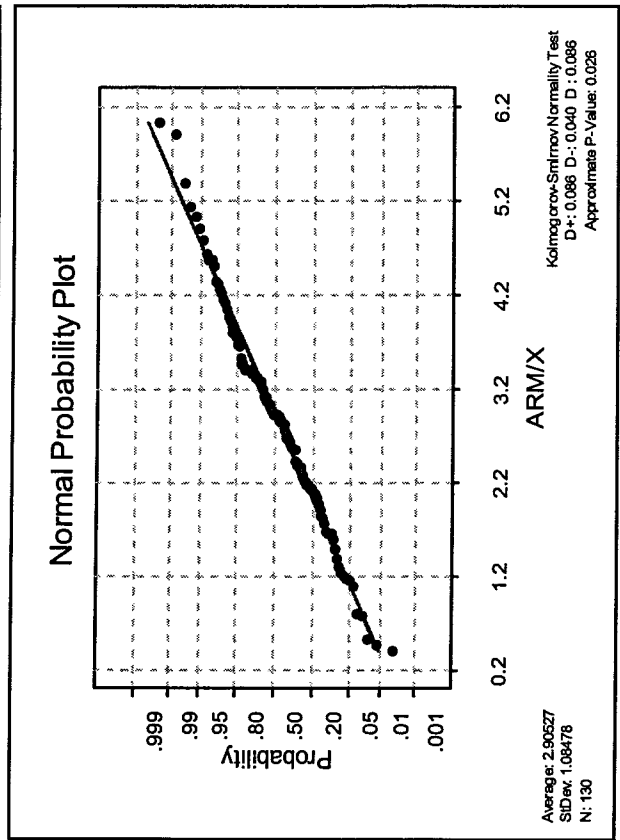
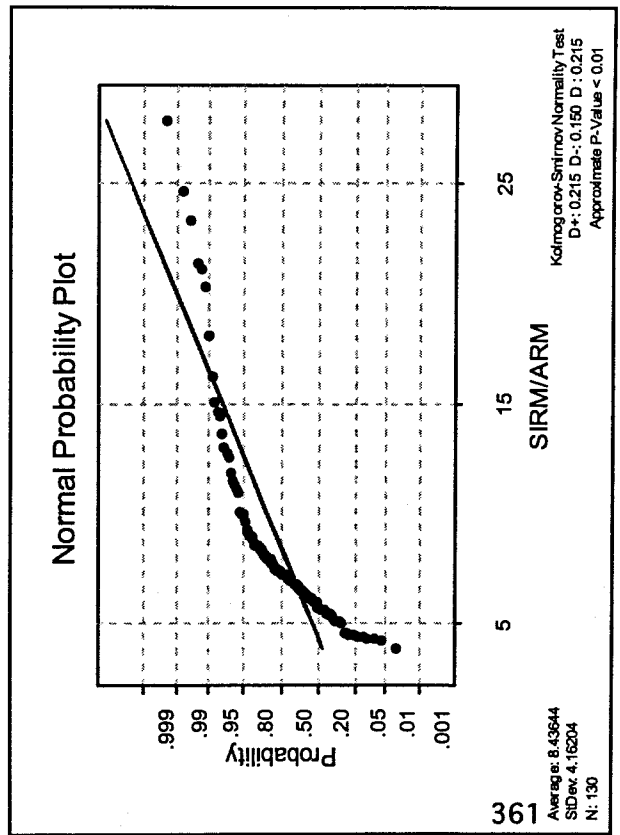
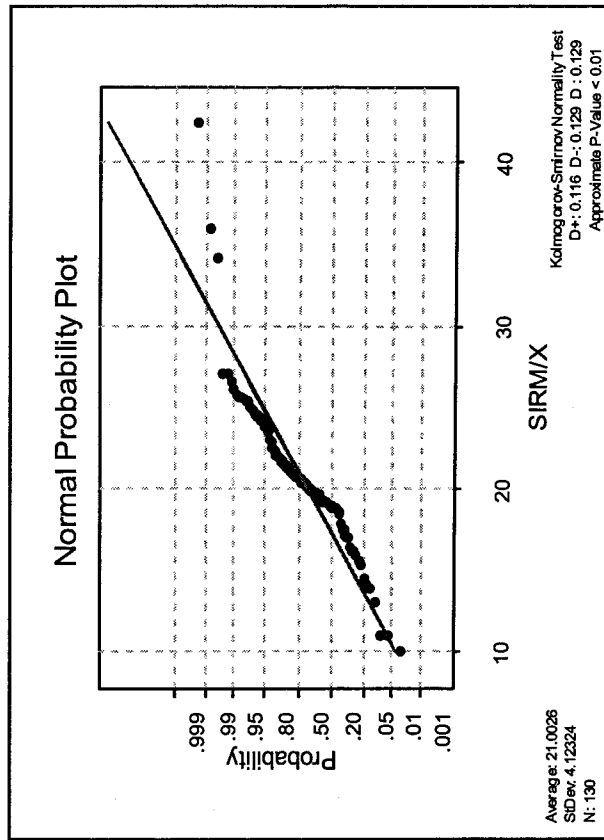
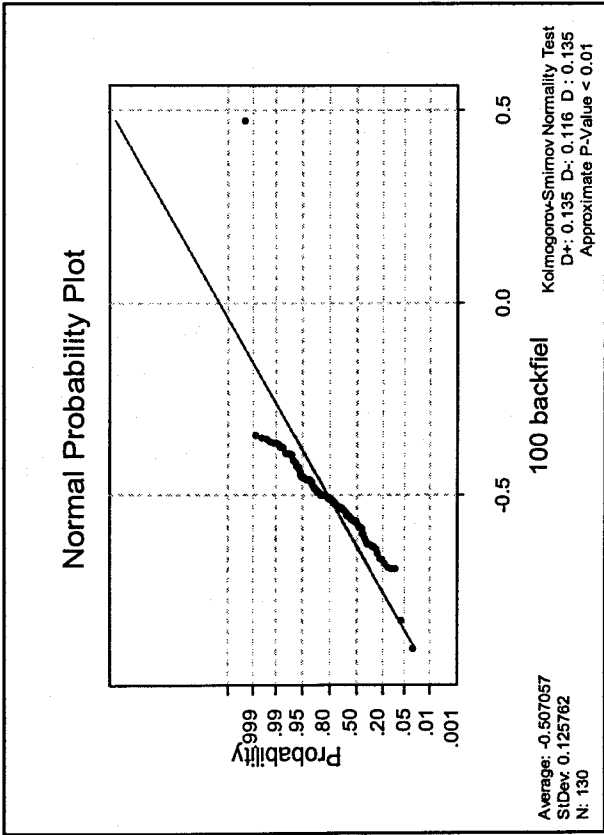
2e) Descriptive Statistics

Variable	N	Mean	Median	Truncated Mean	Standard Deviation	Standard error of the mean	Minimum	Maximum	Lower Quartile	Upper Quartile
χ_{if}	130	13.043	10.25	11.561	9.194	0.806	6.5	74.3	8.7	13.5
χ_{arm}	130	0.21441	0.20074	0.20775	0.07815	0.00685	0.10476	0.82572	0.16751	0.24746
SIRM	130	259.7	212.4	240.3	133	11.7	132.2	1009.1	184.3	304.7
Soft IRM	130	79.51	60.61	72.66	47.46	4.16	30.44	310.47	51.88	90.51
Hard IRM	130	36.67	25.93	33.09	25.24	2.21	12.98	149.99	22.7	37.15
SIRM/ χ	130	21.003	20.653	20.886	4.123	0.362	10.087	42.433	19.162	22.692
SIRM/ARM	130	8.436	7.284	7.843	4.162	0.365	3.887	27.838	6.062	8.973
SIRM/ χ_{arm}	130	1273	1070.2	1173.3	665.6	58.4	626.7	4298.9	916	1286.8
ARM/ χ	130	2.9053	2.9334	2.8889	1.0848	0.0951	0.4085	6.0412	2.1922	3.4189
χ_{arm}/χ	130	0.1938	0.02005	0.01933	0.0072	0.00063	0.00239	0.04233	0.01452	0.02356
SIRM ₁₀₀ /SIRM	130	-0.5071	-0.5088	-0.5094	0.1258	0.011	-0.9017	0.4732	-0.5606	-0.4575

2eii) Normality tests







2eiii) Mann Whitney U tests - a is the sample set using the European material, b is the sample set using Lauretide material.

χ_{lf} a N = 28 Median = 17.21
 χ_{lf} b N = 7 Median = 51.36
 Point estimate for ETA1-ETA2 is -33.47
 95.5 Percent CI for ETA1-ETA2 is (-64.87,-22.12)
 W = 406.0
 Test of ETA1 = ETA2 vs ETA1 not = ETA2 is significant at 0.0001
 The test is significant at 0.0001 (adjusted for ties)

SIRM a N = 28 Median = 388.3
 SIRM b N = 7 Median = 741.0
 Point estimate for ETA1-ETA2 is -437.1
 95.5 Percent CI for ETA1-ETA2 is (-671.0,-278.5)
 W = 412.0
 Test of ETA1 = ETA2 vs ETA1 not = ETA2 is significant at 0.0002

Hard IRM a N = 28 Median = 40.80
 Hard IRM b N = 7 Median = 132.27
 Point estimate for ETA1-ETA2 is -60.03
 95.5 Percent CI for ETA1-ETA2 is (-98.31,-26.12)
 W = 438.0
 Test of ETA1 = ETA2 vs ETA1 not = ETA2 is significant at 0.0069

SIRM/ARM a N = 28 Median = 12.371
 SIRM/ARM b N = 7 Median = 28.836
 Point estimate for ETA1-ETA2 is -15.979
 95.5 Percent CI for ETA1-ETA2 is (-20.148,-11.509)
 W = 410.0
 Test of ETA1 = ETA2 vs ETA1 not = ETA2 is significant at 0.0001

ARM/ χ a N = 28 Median = 1.5850
 ARM/ χ b N = 7 Median = 0.5721
 Point estimate for ETA1-ETA2 is 1.0330
 95.5 Percent CI for ETA1-ETA2 is (0.7321,1.3334)
 W = 602.0
 Test of ETA1 = ETA2 vs ETA1 not = ETA2 is significant at 0.0001

IRM₁₀₀/SIRM a N = 28 Median = -0.5059
 IRM₁₀₀/SIRM b N = 7 Median = -0.6114
 Point estimate for ETA1-ETA2 is 0.1114
 95.5 Percent CI for ETA1-ETA2 is (0.0419,0.1709)
 W = 583.0
 Test of ETA1 = ETA2 vs ETA1 not = ETA2 is significant at 0.0012

χ_{arm} a N = 28 Median = 0.26215
 χ_{arm} b N = 7 Median = 0.24286
 Point estimate for ETA1-ETA2 is 0.01274
 95.5 Percent CI for ETA1-ETA2 is (-0.03182,0.06729)
 W = 518.0
 Test of ETA1 = ETA2 vs ETA1 not = ETA2 is significant at 0.5777
 Cannot reject at alpha = 0.05

Soft IRM a N = 28 Median = 120.3
 Soft IRM b N = 7 Median = 273.2
 Point estimate for ETA1-ETA2 is -180.3
 95.5 Percent CI for ETA1-ETA2 is (-251.4,-130.4)
 W = 410.0
 Test of ETA1 = ETA2 vs ETA1 not = ETA2 is significant at 0.0001

SIRM/ χ a N = 28 Median = 21.06
 SIRM/ χ b N = 7 Median = 14.13
 Point estimate for ETA1-ETA2 is 7.13
 95.5 Percent CI for ETA1-ETA2 is (1.94,10.29)
 W = 567.0
 Test of ETA1 = ETA2 vs ETA1 not = ETA2 is significant at 0.0100

SIRM/ χ_{arm} a N = 28 Median = 1323.5
 SIRM/ χ_{arm} b N = 7 Median = 3220.0
 Point estimate for ETA1-ETA2 is -1919.7
 95.5 Percent CI for ETA1-ETA2 is (-2746.6,-1336.6)
 W = 408.0
 Test of ETA1 = ETA2 vs ETA1 not = ETA2 is significant at 0.0001

χ_{arm}/χ a N = 28 Median = 0.01480
 χ_{arm}/χ b N = 7 Median = 0.00530
 Point estimate for ETA1-ETA2 is 0.01024
 95.5 Percent CI for ETA1-ETA2 is (0.00731,0.01339)
 W = 602.0
 Test of ETA1 = ETA2 vs ETA1 not = ETA2 is significant at 0.0001